The 10th International Seminar on Climate System and Climate Change

第十届气候系统与气候变化国际讲习班（ISCS）

References of the Lectures

by Jonathon Wright, Albertus Dolman, Martin Todd, Yokeling Chee

参考文献 （下）

2013 年 7 月 15-21 日，北京

15-26 July 2013, Beijing, China

Contents

Dr. Jonathon S. Wright — Curriculum Vitae

Tsinghua University Center for Earth System Science
Yifu Keji Building Room S917
100084 Beijing, PRC

+86 13581950705
jswright@tsinghua.edu.cn
http://www.damtp.cam.ac.uk/user/jw660

Education

Ph. D., Georgia Institute of Technology
Earth and Atmospheric Sciences, 2006

B. S., Gettysburg College
Summa Cum Laude, Mathematics, 2001

Research interests

Diagnosis of mechanisms controlling atmospheric water vapor using observations and global models; Transport of water vapor and pollutants in the troposphere and lower stratosphere; Stable water isotopes, particularly their utility in diagnosing transport pathways and constraining cloud parameterizations; Cloud formation, evolution, and environmental interactions.

Research Experience

Associate Professor January 2012 to present
Tsinghua University, Center for Earth System Science. I study the atmospheric water cycle, atmospheric transport, and atmospheric composition. I have been awarded research fellowships through the Young Thousand Talents Plan and the National Natural Science Foundation of China Research Fund for Young International Scientists.

Research Scientist V August 2011 to December 2011
University of Texas at Austin, Jackson School of Geosciences. I conducted research on atmospheric transport and composition, particularly in the tropical upper troposphere and lower stratosphere.

Postdoctoral Research Associate November 2009 to May 2011
University of Cambridge, Department of Applied Mathematics and Theoretical Physics. I worked within the Atmospheric Dynamics Group to characterize influences of clouds on the transport of water vapor and other constituents into the stratosphere.

Postdoctoral Research Scientist October 2006 to September 2009
Columbia University, Department of Applied Physics and Applied Mathematics. I worked within the research group of Prof. Adam Sobel developing and employing techniques to diagnose water vapor transport in global climate model simulations.

Graduate Research Assistant August 2001 to August 2006
Georgia Institute of Technology, School of Earth and Atmospheric Sciences. I worked within Prof. Rong Fu's research group, using a combination of satellite data and Lagrangian models to study the influences of tropical deep convection and Rossby wave breaking on upper tropospheric and lower stratospheric humidity and carbon monoxide.

Graduate Research Assistant June 2004 to August 2004
Goddard Earth Science and Technology Center, Graduate Student Summer Program in Earth Systems Science. I worked with Dr. Andrew Dessler at the Goddard Space Flight Center, where I investigated relationships between tropical deep convection and upper tropospheric water vapor using data from the TRMM and Aqua satellites.

Teaching and Supervisory Experience

Associate Professor January 2012 to present
Tsinghua University, Center for Earth System Science. I have taught the graduate level course "Atmosphere–Ocean Interactions" and contributed lectures to the graduate level courses "Stable Isotope Ecology" and "Earth System Science Seminar Series". I currently supervise two Masters students. I also co-supervise one Ph.D. student at the China Meteorological Administration and have advised the undergraduate dissertation of one student at Sun Yat-Sen University.

Research Scientist V August 2011 to December 2011
University of Texas at Austin, Jackson School of Geosciences. I worked directly with graduate students and assisted with organizing group meetings and activities.

Graduate Teaching Assistant August 2005 to December 2005
Georgia Institute of Technology, School of Earth and Atmospheric Sciences. I directed and graded two weekly labs for EAS 1601: How to Build a Habitable Planet.

Graduate Teaching Assistant January 2003 to May 2003
Georgia Institute of Technology, School of Earth and Atmospheric Sciences. I was selected by faculty to assist in the teaching of EAS 4610/6130: Earth Systems Modeling. I assisted students during open office hours and graded assignments.

Student Associate August to December 1999 & 2000
Gettysburg College, Department of Mathematics. I was selected by faculty to assist in the teaching of Abstract Mathematics I. I graded assignments, ran help sessions, and assisted in class.

Student Associate January 1999 to May 1999
Gettysburg College, Department of Mathematics. I was selected by faculty to assist in the teaching of Calculus II. I graded assignments and led external help sessions.

Student Associate August 1998 to December 1998
Gettysburg College, Department of Mathematics. I helped to lead external help sessions for the introductory course Quantitative Methods.

Service and Editorial Experience

Invited Editor April 2012 to present
Acta Meteorologica Sinica. I edit manuscripts for the English-language edition of the journal.

Freelance Editor June 2011 to February 2012
Stallard Scientific Editing. I provided professional editing services for manuscripts in the areas of meteorology, climatology, and numerical modeling.

Publications

[8] **Wright, J. S.** and S. Fueglistaler (2013): Large differences in the diabatic heat budget of the tropical UTLS in reanalyses, *Atmos. Chem. Phys. Disc.*, **13**, 8805–8830.

[7] Huang, L., R. Fu, J. H. Jiang, **J. S. Wright**, and M. Luo (2012): Geographic and seasonal distributions of CO transport pathways and their roles in determining CO centers in the upper troposphere, *Atmos. Chem. Phys.*, **12**, 4683–4698.

[6] Noone, D., J. Galewsky, Z. Sharp, J. Worden, J. Barnes, D. Baer, A. Bailey, D. Brown, L. Christensen, E. Crosson, F. Dong, J. Hurley, L. Johnson, M. Strong, D. Toohey, A. Van Pelt, and **J. S. Wright** (2011), Properties of air mass mixing and humidity in the subtropics from measurements of the D/H isotope ratio of water vapor at the Mauna Loa Observatory, *J. Geophys. Res.*, **116**, D22113, doi:10.1029/2011JD015773.

[5] **Wright, J. S.**, R. Fu, S. Fueglistaler, Y. Liu, and Y. Zhang (2011), The influence of summertime convection over South–East Asia on water vapor in the tropical stratosphere, *J. Geophys. Res.*, **116**, D12302, doi:10.1029/2010JD015416.

[4] **Wright, J. S.**, A. H. Sobel, and J. Galewsky (2010), Diagnosis of zonal mean relative humidity changes in a warmer climate using tracers of last saturation, *J. Clim.*, **23**, 4556–4570.

[3] **Wright, J. S.**, A. H. Sobel, and G. Schmidt (2009), The influence of condensate evaporation on water vapor and its stable isotopes in a GCM, *Geophys. Res. Lett.*, 36, L12804, doi:10.1029/2009GL039091

[2] **Wright, J. S.**, R. Fu, and A. J. Heymsfield (2009), A statistical analysis of the influence of deep convection on water vapor variability in the tropical upper troposphere, *Atm. Chem. Phys.*, **9**, 5847–5865.

[1] Fu, R., Y. Hu, **J. S. Wright**, J. H. Jiang, R. E. Dickinson, M. Chen, M. Filipiak, W. G. Read, J. W. Waters, and D. L. Wu (2006), Convective transport over the Tibetan Plateau - A short-circuit of water vapor and polluted air to the global stratosphere, *Proc. Natl. Acad. Sci.* USA, **103**, 5664–5669.

Recent Presentations

Wright, J. S. and S. Fueglistaler (2013), Effects of differences in reanalysis diabatic heating on transport and composition in the Asian monsoon anticyclone, *Workshop on Atmospheric Composition and the Asian Summer Monsoon*, Kathmandu, poster presentation.

Wright, J. S. and S. Fueglistaler (2013), Reanalysis estimates of the diabatic heat budget in the tropical UTLS, *SPARC Reanalysis Intercomparison Project Planning Workshop*, Exeter, UK, poster presentation.

Wright, J. S. and S. Fueglistaler (2012), Reanalysis estimates of the diabatic heat budget in the tropical UTLS, *AOGS-AGU (WPGM) Joint Assembly*, Singapore, oral presentation.

Wright, J. S. (2012), Estimating the influence of summertime deep convection over the Tibetan Plateau on water transport into the tropical lower stratosphere, *Sixth Workshop on Surface-Troposphere-Stratosphere Interaction Over the Tibetan Plateau*, Austin, TX, oral presentation.

Wright, J. S. (2011), Exploring influences of deep convection and cloud processes on tropical stratospheric water vapor, *Atmospheric Sciences Seminar*, Texas A&M University, College Station, TX, oral presentation.

Wright, J. S. (2011), Influences of microphysical processes on atmospheric humidity: Observations and model results, *Centre for Atmospheric Science Seminar Series*, Cambridge, UK, oral presentation.

Wright, J. S. (2011), Diagnosis of relative humidity changes in a warmer climate using tracers of last saturation, *Vortex Dynamics Group Seminar*, University of St. Andrews, St. Andrews, UK, oral presentation.

Honors and Fellowships

Research Fund for Young International Scientists (2013)
National Natural Science Foundation of China

Young Thousand Talents Plan (2012)

Most Outstanding Oral Presentation (Fall 2004)
2^{nd} annual School of Earth and Atmospheric Sciences Graduate Student Symposium

Graduate Student Summer Program in Earth Systems Science (Summer 2004)
Goddard Earth Sciences and Technology Center

National Defense Science and Engineering Graduate Fellowship (2001–2004)

President's Fellowship, Georgia Institute of Technology (2001–2006)

Phi Beta Kappa (Gettysburg College, 2001)

Budapest Semester in Mathematics (Spring 2000)

Memberships

American Geophysical Union (AGU), 2002–present

American Meteorological Society (AMS), 2006–present

European Geophysical Union (EGU), 2010–present

Royal Meteorological Society, 2010–present

Asia–Oceania Geosciences Society, 2012–present

Surv Geophys (2012) 33:585–608
DOI 10.1007/s10712-011-9159-6

Energetic Constraints on Precipitation Under Climate Change

Paul A. O'Gorman · Richard P. Allan · Michael P. Byrne · Michael Previdi

Received: 17 August 2011 / Accepted: 2 November 2011 / Published online: 23 November 2011
© Springer Science+Business Media B.V. 2011

Abstract Energetic constraints on precipitation are useful for understanding the response of the hydrological cycle to ongoing climate change, its response to possible geoengineering schemes, and the limits on precipitation in very warm climates of the past. Much recent progress has been made in quantifying the different forcings and feedbacks on precipitation and in understanding how the transient responses of precipitation and temperature might differ qualitatively. Here, we introduce the basic ideas and review recent progress. We also examine the extent to which energetic constraints on precipitation may be viewed as radiative constraints and the extent to which they are confirmed by available observations. Challenges remain, including the need to better demonstrate the link between energetics and precipitation in observations and to better understand energetic constraints on precipitation at sub-global length scales.

Keywords Precipitation · Global change · Energetics

1 Introduction

It is not surprising that energetics play an important role in determining global-mean precipitation given that surface evaporation is ultimately driven by solar radiation.[1]

[1] See Peixoto and Oort (1992), Trenberth et al. (2009), and Stevens and Schwartz (2011) for reviews of the energy budget of the Earth.

P. A. O'Gorman (✉) · M. P. Byrne
Department of Earth, Atmospheric, and Planetary Sciences, Massachusetts Institute of Technology, 77 Massachusetts Avenue, Cambridge, MA 02139, USA
e-mail: pog@mit.edu

R. P. Allan
Department of Meteorology, National Centre for Atmospheric Science, University of Reading, Reading, UK

M. Previdi
Lamont-Doherty Earth Observatory, Columbia University, 61 Route 9W, Palisades, NY 10964, USA

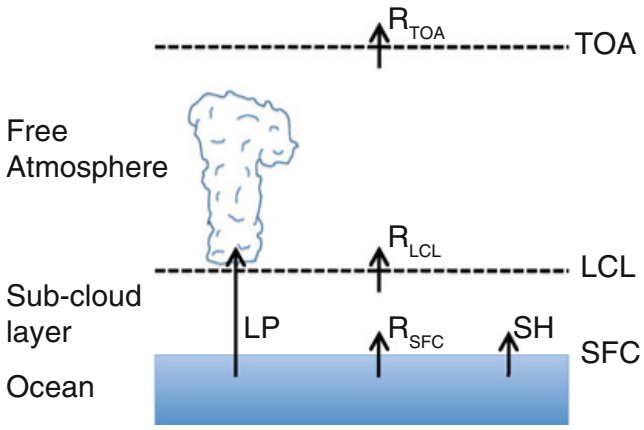

Fig. 1 Schematic of the energy budgets of the atmosphere and of the atmosphere above cloud base, as described in the text; LCL is the lifted condensation level. [Following Fig. 1 of Takahashi (2009a)]

In the context of climate change, we speak of energetics placing a constraint on precipitation in the sense that precipitation must change in such a way that the energy budget of the atmosphere (or the surface) continues to balance. We will work primarily with the energy budget of the atmosphere because its relatively small heat capacity facilitates analysis of transient changes in precipitation; the surface energy budget may also be usefully analyzed in a climate change context (Boer 1993; Richter and Xie 2008; Andrews et al. 2009; Lorenz et al. 2010). A schematic view of the global atmospheric energy budget is shown in Fig. 1. We begin by considering the energy budget of the entire atmosphere from the surface to the top of the atmosphere. The perturbation budget between two climates may be written as

$$L\delta P = \delta R_{\mathrm{TOA}} - \delta R_{\mathrm{SFC}} - \delta SH \tag{1}$$

where L is the latent heat of condensation (assumed constant for simplicity), P is the precipitation rate, R_{TOA} and R_{SFC} are the net radiation fluxes at the top of the atmosphere (TOA) and at the surface (SFC), respectively, SH is the surface sensible heat flux, and δ denotes the difference between the two climates.[2] Thus, changes in precipitation are directly related to changes in the radiative cooling of the atmosphere and the surface sensible heat flux. For a change in surface temperature, the resulting change in radiative cooling may be calculated to first order by assuming invariant relative humidity and a moist adiabatic lapse rate in the free troposphere. More generally, the changes in all radiative forcing agents, surface air temperature difference, and surface sensible heat flux must also be taken into account. This energetic approach is often more straightforward than understanding the precipitation response in terms of changes in large-scale circulations or convective mass fluxes that are themselves mediated by relatively subtle changes in atmospheric stability.

The energetic constraint described above was already discussed in some detail in the early work of Mitchell et al. (1987). Allen and Ingram (2002) showed how it could be used to understand the response of precipitation to climate change in different climate model simulations, and Pierrehumbert (2002) showed how the surface energy budget constrained precipitation in very warm climates. More recently, there has been considerable progress in using the energetic perspective to better quantify and understand several aspects of the response of precipitation to climate change: the feedbacks influencing the rate of change of precipitation under warming (e.g., Stephens and Ellis 2008; Previdi 2010), how the

[2] Positive fluxes of energy are upwards and all fluxes are averaged globally and over sufficiently long times that we may neglect changes in energy and water storage in the energy budget of a given climate state.

response of precipitation varies depending on the climate forcing agent (e.g., Andrews et al. 2010), and how precipitation responds on "fast" and "slow" timescales (e.g., Lambert and Faull 2007; Bala et al. 2010). In all of these cases, it is useful and natural to think of precipitation and evaporation as energy fluxes. Even for regional changes in precipitation, it is possible to usefully adopt an energetic approach (Muller and O'Gorman 2011).

The energetic constraint does not suggest that global-mean precipitation scales with the amount of water vapor in the atmosphere, although water vapor does play an important radiative role and can, therefore, be related to changes in precipitation through energetic arguments (Stephens and Ellis 2008; Allan 2009; Stephens and Hu 2010). Precipitation intensity or precipitation extremes, on the other hand, could be expected to be more directly affected by changes in water vapor concentrations and increase with warming at a faster rate than global-mean precipitation (Allen and Ingram 2002; Trenberth et al. 2003; Pall et al. 2007); recent results suggest that vertical gradients of specific humidity or surface specific humidities are relevant for precipitation extremes (O'Gorman and Schneider 2009a, b; Schneider et al. 2010; Muller et al. 2011; Romps 2011). Several authors have argued that this implies a reduction in the overall frequency of precipitation (e.g., Trenberth 1999, 2011; Allen and Ingram 2002; Trenberth et al. 2003; Stephens and Hu 2010). Decreases in precipitation frequency are seen in the subtropics in model simulations of warmed climates (e.g., Sun et al. 2007), and there is observational evidence for decreases in mean precipitation in tropical regions with mean descent (e.g., Allan et al. 2010), but it is important to note that the precipitation distribution could adjust in ways other than a simple decrease in frequency (Muller et al. 2011). Similar arguments have been made for a decrease in the strength of the circulation (e.g., Held and Soden 2006), although, again, the required magnitude of the circulation change is difficult to estimate from first principles (Schneider et al. 2010). We do not pursue the implications for precipitation frequency or circulation changes further, but rather focus on the radiative or energetic constraints themselves.

The purpose of this paper is to provide an overview of the modern understanding of energetic constraints on precipitation under climate change, to describe some of the major recent developments, and to examine in detail some of the key open questions. We begin by discussing the extent to which the atmospheric energetic constraint on global-mean precipitation may be viewed as a radiative constraint (Sect. 2) and to what extent energetics place an upper bound on global-mean precipitation (Sect. 3). We discuss the factors contributing to the rate of change of precipitation under climate change (Sect. 4), how these combine to determine the transient precipitation response (Sect. 5), and how the energetic perspective on precipitation changes may be extended to regional precipitation (Sect. 6). We then address the important issue of the extent to which observed changes in precipitation may be related to observed changes in net radiative cooling (Sect. 7). We conclude with a summary and a discussion of remaining challenges (Sect. 8).

2 Radiative or Energetic Constraint?

The energetic constraint on global-mean precipitation is often thought of as a radiative constraint in which latent heat release balances radiative cooling, but it clearly also involves the surface sensible heat flux (Eq. 1). Changes in surface sensible heat flux under climate change are not negligible; the upward sensible heat flux decreases in climate model simulations of greenhouse-gas driven warming (O'Gorman and Schneider 2008; Stephens

and Ellis 2008; Liepert and Previdi 2009; Bala et al. 2010) and in response to increases in insolation (Bala et al. 2010), but may increase with warming in response to aerosol forcing (Liepert and Previdi 2009). One might, therefore, question if the radiative cooling of the atmosphere is really a constraint on precipitation, since the sensible heat flux could in principle adjust to accommodate a given radiative cooling (e.g., by changes in the air-sea temperature difference), so that a minimal model of the atmospheric or surface energy balance must take into account boundary layer transfer in order to constrain precipitation (Pierrehumbert 2002; Le Hir et al. 2009). Takahashi (2009a) proposed a simple model that avoids some of these difficulties by working with the atmospheric energy balance above cloud base (Fig. 1). Assuming that condensation only occurs above the lifted condensation level (LCL), it may be argued that the primary relevant balance is between latent heating and the radiative cooling above the LCL

$$L\delta P \simeq \delta R_{\mathrm{TOA}} - \delta R_{\mathrm{LCL}}. \tag{2}$$

This approximate balance relies on the lower level used (nominally the LCL) being below the level of substantial latent heating and above the level of substantial boundary layer dry sensible heat fluxes. It also neglects vertical dry static energy fluxes across the LCL associated with the large-scale circulation. We will refer to it as the free-atmospheric radiative constraint on precipitation (even though the LCL and the top of the boundary layer need not coincide).

Here, we test the accuracy of the free-atmospheric radiative constraint on precipitation in statistical-equilibrium simulations with an idealized general circulation model (GCM) over a wide range of climates (Fig. 2). The GCM is based on a version of the Geophysical Fluid Dynamics Laboratory (GFDL) dynamical core, but with simplified moist parameterizations,

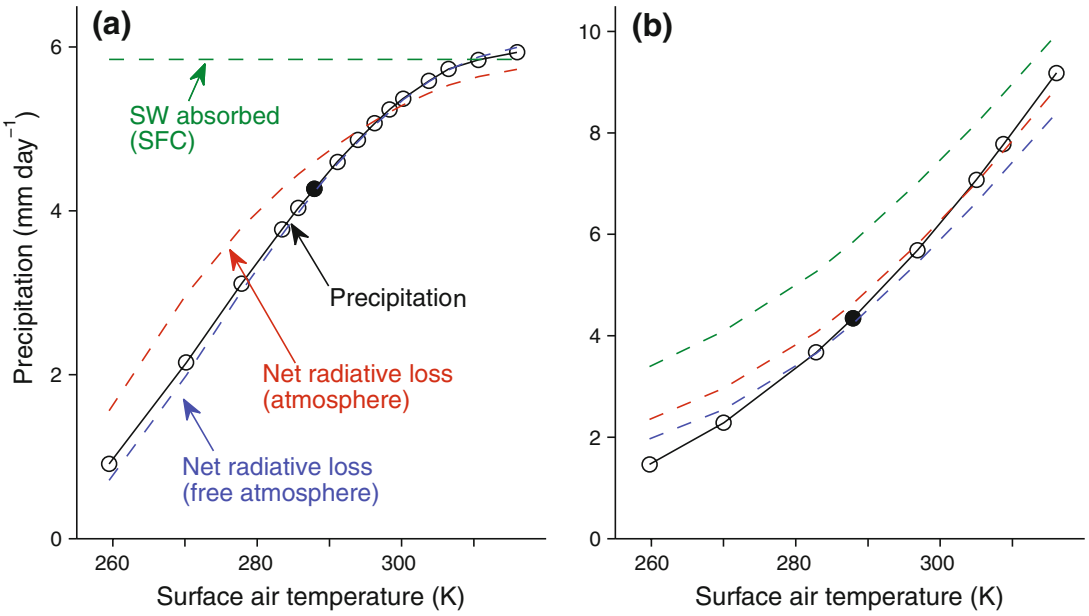

Fig. 2 Global-mean precipitation (*solid line with circles*) versus global-mean surface air temperature in two series of statistical-equilibrium simulations with an idealized GCM in which **a** the optical depth of the longwave absorber is varied and **b** the solar constant is varied. The *filled circles* indicate the reference simulation (common to both series) which has the climate most similar to present-day Earth's. The *red dashed lines* show the net radiative loss of the atmosphere, the *blue dashed lines* show the net radiative loss of the free atmosphere (above $\sigma = 0.86$), and the *green dashed lines* show the net absorbed solar radiation at the surface (all in equivalent precipitation units of mm day^{-1})

a two-stream semi-gray radiation scheme without cloud radiative effects, and a slab-ocean lower boundary condition (Frierson et al. 2006; Frierson 2007; O'Gorman and Schneider 2008). The climate is varied in one set of simulations by changing the longwave optical depth to mimic changes in greenhouse-gas concentrations with shortwave (SW) radiative heating held constant (Fig. 2a), as described in O'Gorman and Schneider (2008). We also present a new set of simulations in which the climate is varied by changing the solar constant over a range from 0.58 to 1.70 of the reference value (Fig. 2b). Although the radiation scheme is highly simplified, these simulations serve to illustrate the basic role of energetic constraints on precipitation over a wide range of climates—more realistic radiative transfer will be discussed in later sections. In addition, the GCM includes processes (boundary-layer turbulence and large-scale circulations) that could cause the free-atmospheric radiative constraint on global-mean precipitation (Eq. 2) to be inaccurate, and as such the idealized simulations provide a test of this constraint.

Global-mean precipitation increases with warming for both sets of simulations (Fig. 2a, b). The behavior in the limits of very low and high temperatures is broadly consistent with what might be expected from a simple analysis of the surface energy balance using bulk transfer formulae (Pierrehumbert 2002): precipitation tends to zero for sufficiently low temperatures because of low-specific humidities, and precipitation is limited at high temperatures by the availability of solar radiation at the surface (as discussed in the next section). In the "greenhouse-gas" simulations, the approximation of global-mean precipitation by the net radiative loss of the atmosphere (the dashed red line in Fig. 2a) is not accurate because of substantial changes in the surface sensible heat flux over the range of climates. The net radiative loss of the free atmosphere gives much better agreement (the dashed blue line in Fig. 2a). The free atmosphere is defined here as the atmosphere above the level $\sigma = 0.86$, where σ is pressure normalized by surface pressure. This level is chosen to give the best overall fit of radiative loss to precipitation and is taken to be representative of the nominal LCL in the approximate radiative constraint given by Eq. 2. But, the global-mean LCL is actually lower in the atmosphere ($\sigma \simeq 0.93$), a discrepancy which likely relates to the occurrence of substantial boundary layer fluxes at levels somewhat higher than the LCL. The rate of change of global-mean precipitation is 2.5% K^{-1} near the reference climate (the climate most similar to present-day Earth), compared to 1.5% K^{-1} for the net radiative loss of the atmosphere and 2.6% K^{-1} for the net radiative loss of the free atmosphere. The improvement gained from considering the free atmosphere is not as great in the solar series of simulations, but the overall accuracy of the free-atmospheric radiative constraint is not much worse; the rates of change at the reference climate are 3.2% K^{-1} for precipitation, 2.6% K^{-1} for the net radiative loss of the atmosphere, and 2.9% K^{-1} for the net radiative loss of the free atmosphere.

Our results provide some support for the approximation of global-mean precipitation under climate change using the net radiative loss of the free atmosphere. We will also find this to be a useful approximation in Sect. 4.2 when considering the effect on precipitation of black carbon aerosols at different levels in the atmosphere.

3 Upper Bound on Precipitation

Figure 2a shows that the rate of growth of global-mean precipitation with temperature declines sharply in the very warm climates of the "greenhouse-gas" series of simulations, despite the quasi-exponential increase with temperature of atmospheric water vapor content (O'Gorman and Schneider 2008), and suggesting the possibility of an upper bound on

precipitation for a given solar constant (Pierrehumbert 1999, 2002; O'Gorman and Schneider 2008). In very warm climates, the atmosphere is optically thick in the longwave and the net longwave radiative flux at the surface becomes small. As discussed by Pierrehumbert (2002), the boundary layer becomes stable (with the near-surface air temperature greater than the surface temperature), and boundary layer turbulence is suppressed. To the extent that the surface sensible heat flux is small, the surface energy budget implies that the surface latent heat flux should then be equal to the absorbed shortwave radiation at the surface, corresponding to the horizontal line in Fig. 2a (the shortwave fluxes are held constant in this idealized set of simulations). The absorbed shortwave radiation is not exactly an upper bound because the surface sensible heat flux becomes directed downward providing additional energy for the evaporation of water (Pierrehumbert 2002). Similarly, in the simulations in which the solar constant is increased, precipitation approaches (but does not reach) the limit given by the absorbed shortwave radiation at the surface (Fig. 2b).

Thus, the energetic constraint on precipitation becomes relatively simple in the limit of very warm climates, although the exact amount of precipitation achievable may depend on poorly understood details of boundary-layer turbulence and radiative transfer. It is useful to remember the limiting case of very warm climates when considering the differences in scaling of water vapor concentrations and precipitation and, as discussed in the next section, the different responses of precipitation to solar and CO_2 forcings. The upper bound on global-mean precipitation given by the absorbed surface shortwave radiation is also relevant to very warm climates of the past, in which continental runoff plays an important role in the weathering thermostat (Pierrehumbert 2002; Le Hir et al. 2009). Le Hir et al. (2009) found that global-mean precipitation and continental runoff behaved similarly in the global mean as the climate changed, but it is not clear that this is a general result, and a better understanding of the constraints on precipitation over land is desirable.

4 Contributions to Changes in Precipitation

We next discuss the different contributions to changes in precipitation and how they lead to different responses of precipitation compared with temperature depending on the forcing agent. The response of global-mean precipitation to temperature change is clearly quite different for greenhouse-gas versus solar forcing, as evidenced by the leveling-off of precipitation at high temperatures in Fig. 2a compared with the continuous growth in Fig. 2b. Figure 3 [reproduced from Andrews et al. (2009)] shows a similar difference in behavior, but now for subsequent years following an instantaneous doubling of CO_2 or an instantaneous increase in solar irradiance in an atmospheric GCM coupled to a slab ocean. The response to CO_2 forcing is characterized by an initial decrease in precipitation, followed by a quasi-linear increase with temperature (e.g., Yang et al. 2003; Andrews et al. 2009). The response to solar forcing has a similar form but with a smaller initial decrease (extrapolating the precipitation curve to zero temperature change). As a result, the hydrological sensitivity, defined as the ratio of precipitation change to temperature change, is quite different at equilibrium for the CO_2 and solar forcings (compare the dotted lines in Fig. 3).[3] But, note that the slopes of the precipitation curves are similar for both forcings

[3] Interestingly, if the hydrological sensitivity is instead defined in terms of TOA radiative forcing rather than temperature change, it is not very different between solar and CO_2 forcing (Lambert and Faull 2007).

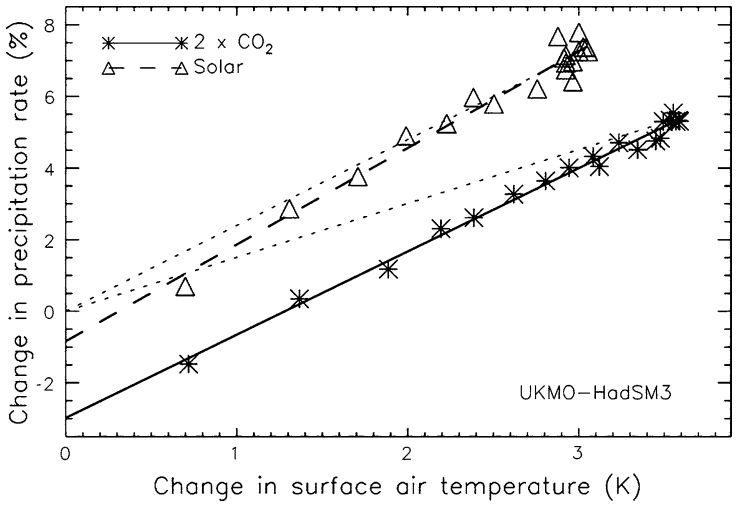

Fig. 3 Change in global-mean precipitation versus change in global-mean surface air temperature averaged over individual years subsequent to an instantaneous increase in CO_2 (*asterisks*) or solar irradiance (*triangles*) in simulations with the Hadley Centre Slab-Ocean Model version 3. There is a large initial decrease in precipitation in response to CO_2 forcing, but the slopes of the subsequent linear responses are similar for the solar and CO_2 simulations. *Dotted lines* show the slopes corresponding to the hydrological sensitivities calculated from the initial and final states [Fig. 7 from Andrews et al. (2009). © American Meteorological Society. Reprinted with permission]

(the solid and dashed lines in Fig. 3), so that the differential dependence of precipitation on temperature is similar.

The linear dependence of precipitation on temperature shown in Fig. 3 suggests that it may be useful to rewrite the atmospheric energy budget (Eq. 1), decomposing the right hand side (and the precipitation change) into a temperature-dependent part ($k\delta T$) and a temperature-independent part G,

$$L\delta P = k\delta T + G, \tag{3}$$

where k is a constant, and δT is the change in global-mean surface temperature (e.g., Allen and Ingram 2002). There are several ways to make this decomposition in practice. Previdi (2010) considers G to include the direct radiative forcing, while $k\delta T$ represents all feedbacks, including the change in surface sensible heat flux. Alternatively, one may decompose the response based on timescale into a "fast" component that occurs before sea surface temperatures (SSTs) respond substantially, and a "slow" component that increases in magnitude as the SSTs change on a multiyear timescale (Yang et al. 2003; Lambert and Faull 2007; Lambert and Webb 2008; Lambert and Allen 2009; Andrews et al. 2009, 2010; Takahashi 2009b; Bala et al. 2010; Andrews and Forster 2010; Frieler et al. 2011). The "slow" and "fast" responses may be calculated using fixed SST simulations or by regressing transient changes in precipitation and temperature (e.g., by calculating the slope and offset of the solid and dashed lines in Fig. 3).

4.1 Feedbacks

We first focus on the temperature-dependent part of the precipitation response and ask what physical processes contribute to its magnitude and the range of roughly 1.4–3.4% K^{-1} found in modern climate model simulations (Lambert and Webb 2008).

We make use of the radiative kernel technique (Soden et al. 2008) as applied to feedbacks on global-mean precipitation within the framework of the atmospheric energy budget by Previdi (2010). The simulations used are drawn from the World Climate Research Programme's (WCRP's) Coupled Model Intercomparison Project phase 3 (CMIP3) archive. We present results based on the climate change from 2001–2010 to 2101–2110 under an emissions scenario for greenhouse gases and aerosols (SRES A1B). The feedback analysis quantifies the contributions to $k\delta T$ in Eq. 3 from radiative feedbacks due to changes in tropospheric temperature, water vapor, clouds, and albedo, and from changes in surface sensible heat flux. We further decompose the temperature feedback into a Planck feedback (associated with vertically uniform warming) and a lapse rate feedback (associated with vertically nonuniform warming). We adopt the convention of Previdi (2010) that a positive feedback corresponds to a gain of energy for the atmospheric column and a negative feedback on precipitation. The feedbacks are shown in Fig. 4 for the nine climate models for which the necessary data were available [see Previdi (2010) for details]. This figure may be compared with Fig. 1 of Bony et al. (2006), which shows TOA radiative feedbacks rather than the atmospheric energy budget feedbacks shown here.

The water vapor feedback tends to suppress precipitation as a result of both increased shortwave heating and reduced longwave cooling [Previdi (2010); although Mitchell et al. (1987) and Hall and Manabe (2000) conclude that longwave radiative feedback enhances precipitation under warming based on different simulations and analysis]. The reduced longwave cooling is a residual of opposing effects of increases in specific humidity in the lower troposphere which tend to cool the atmospheric column and increases in specific humidity in the upper troposphere which tend to warm the atmospheric column (Previdi 2010). The effect of changes in water vapor concentrations is, therefore, strongly altitude dependent. Takahashi (2009b) argued that inter-model scatter in the change in clear-sky absorption of shortwave radiation by water vapor is important for inter-model scatter in the precipitation response and that the source of the inter-model scatter was not from different radiative transfer schemes or different changes in the amount of column water vapor. The

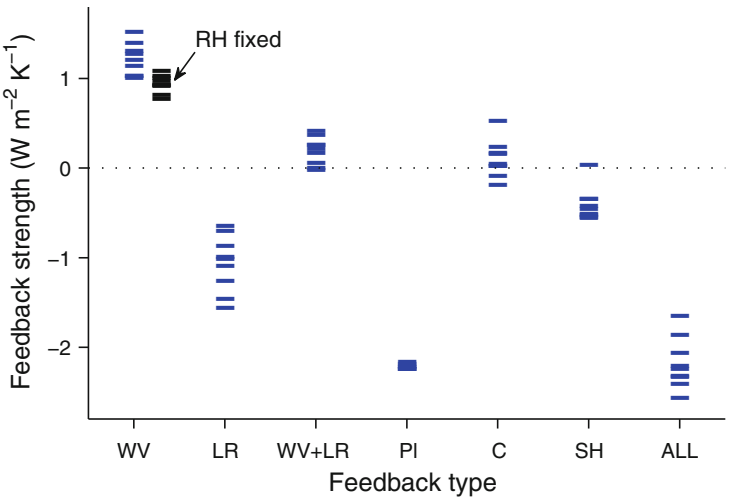

Fig. 4 Feedbacks (*blue dashes*) on the atmospheric energy budget in coupled simulations with nine climate models. *Positive values* indicate a gain in energy for the atmospheric column and a negative feedback on precipitation. Feedbacks shown are water vapor (WV), lapse rate (LR), the sum of water vapor and lapse rate (WV + LR), Planck (Pl), cloud (C), surface sensible heat flux (SH), and the sum ALL = WV + LR + Pl + C + SH. Albedo feedback is negligible and is not shown. *Black dashes* show the water vapor feedback for invariant relative humidity (RH)

water vapor feedback is slightly stronger and has greater inter-model scatter than the feedback that would result from an invariant relative humidity distribution (black dashes in Fig. 4). A consistent pattern of relative humidity changes is found in response to warming in climate model simulations (e.g., Mitchell et al. 1987; Sherwood et al. 2010), and although the fractional changes in relative humidity are not as large as the fractional changes in saturation vapor pressure, they may still be expected to affect radiative fluxes.

The lapse rate feedback is of similar strength to the water vapor feedback, but it tends to enhance precipitation. The magnitudes of the lapse rate and water vapor feedbacks are correlated between models, but they have opposite sign, so that the sum of the two feedbacks (WV + LR) has less inter-model scatter than might otherwise be expected. A similar relationship between lapse rate and water vapor feedbacks has been found for TOA radiative feedbacks (e.g., Bony et al. 2006; Soden et al. 2008).

The cloud feedback is calculated by adjusting the change in cloud radiative forcing to account for cloud-masking effects (Soden et al. 2008; Previdi 2010). It can be positive or negative depending on the model, but tends to suppress precipitation in the multi-model mean. Stephens and Ellis (2008) also found that cloud effects tended to mute the increase in precipitation in the multi-model mean. Although shortwave cloud radiative feedbacks contribute strongly to inter-model scatter in climate sensitivity, they might be expected to have less impact on the atmospheric cooling that controls changes in precipitation (Lambert and Webb 2008). Nonetheless, cloud radiative feedback is the single biggest contributor to inter-model scatter if the water vapor and lapse rate feedbacks are considered as one contribution.

With the exception of one model, the surface sensible heat flux feedback tends to increase precipitation and has relatively little inter-model scatter. The Planck feedback is large in magnitude and has almost the same value in all models considered (-2.1 to -2.2 W m^{-2} K^{-1}). The albedo feedback is very small in magnitude and is not shown. The sum of the feedbacks has a value of ~ -2W m^{-2} K^{-1} and must be combined with the forcing to give the change in precipitation found in these simulations. Compared with previous analyses of TOA radiative feedbacks (e.g., Bony et al. 2006), some of the primary differences are the negligible albedo feedback, the addition of the surface sensible heat flux, a possibly smaller contribution to scatter from the cloud feedback, and a possibly greater contribution from changes in relative humidity.

4.2 Dependence on Forcing Agent

We next consider the dependence of the precipitation response on the nature of the forcing agent. The direct radiative effect of increased concentrations of CO_2 is to decrease the net upwelling longwave radiation at the top of the atmosphere (TOA) and increase the net downwelling longwave radiation at the surface, with a net decrease in the radiative loss of the atmosphere [contributing to $G < 0$ in Eq. 3] (Ramanathan 1981; Mitchell et al. 1987). Consequently, if surface temperature is held fixed and CO_2 concentrations are increased, then global-mean precipitation decreases (e.g., Yang et al. 2003), consistent with Fig. 3. The direct radiative effect of increased insolation is much smaller in the atmospheric energy budget than in the TOA budget since much of the increased shortwave radiation passes through the atmosphere or is scattered back to space. Nonetheless, an increase in insolation does lead to increased shortwave absorption in the atmosphere, which tends to decrease precipitation. Because of the difference in the fast response of precipitation to solar and CO_2 forcing (Fig. 3), we expect global-mean precipitation to decrease in an idealized geoengineering experiment in which the effect on global-mean surface

temperature of higher concentrations of greenhouse gases is offset by the effect of a decrease in solar constant. Bala et al. (2008) find that global-mean precipitation is reduced by $\sim 2\%$ for a doubling of CO_2 in such a geoengineering experiment, which is roughly consistent with what might be inferred from Fig. 3.

Figure 5a [based on Table 2 of Andrews et al. (2010)] shows that the slow temperature-dependent part of the response is quite similar for solar, CO_2, and aerosol, forcing, so that the different responses to different forcing agents arises primarily because of the fast component of the response.[4] Aerosols affect precipitation in a number of different ways (e.g., Ramanathan et al. 2001), but here we will discuss their effect on precipitation through their radiative role in the energetic constraint on precipitation. Figure 5a shows that sulfate aerosols yield a similar precipitation response to solar forcing, as might be expected given that they scatter shortwave radiation. However, increases in the burden of black carbon aerosols may decrease global-mean precipitation even as they increase global-mean surface temperature because of a strongly negative fast response (Fig. 5a).

The negative fast response of precipitation to black carbon aerosols results from absorption of shortwave radiation in the troposphere (induced changes in cloud radiative effects may also play a role). Whether or not the total precipitation response is negative depends on the level in the atmosphere at which the black carbon aerosols occur (Ming et al. 2010; Ban-Weiss et al. 2011). This was demonstrated by Ming et al. (2010) in a set of simulations in which the burden of black carbon aerosols was increased at different levels in the troposphere [Fig. 5b, which is based on Table 1 of Ming et al. (2010)]. Roughly speaking, precipitation decreases when black carbon aerosols are added in the free troposphere, but it increases when they are added near the surface. In all cases shown in Fig. 5b, the surface temperature increases, changes in shortwave absorption provide a negative contribution to the precipitation change, and changes in surface sensible heat flux and temperature provide a positive contribution.[5] If black carbon aerosols are added near the surface, the increased shortwave absorption is partially canceled by a decrease in the upward sensible heat flux, and precipitation increases because of the increase in radiative cooling related to the increase in temperature. The sensible heat flux response is considerably smaller if the aerosol is added in the free troposphere, and the increase in shortwave heating is then partially balanced by a decrease in latent heating (and precipitation).

The precipitation response to black carbon aerosols is more easily understood using the approximate balance of precipitation and free-atmospheric radiative cooling (Eq. 2) in which radiative heating near the surface and surface sensible heat fluxes do not enter. In the case of the addition of black carbon aerosols near the surface, the only effect on free atmosphere radiative cooling is through the temperature increase, and precipitation increases accordingly. When black carbon aerosols are added higher up in the atmosphere, they directly affect the free-atmospheric radiative heating and precipitation decreases.

[4] Andrews et al. (2010) show that the temperature dependence of the slow precipitation response is similar for nine different forcing scenarios. The precipitation sensitivities are normalized by a temperature change that is different for the slow and total responses because the fast response includes a change in land surface temperature and the slow response is calculated as the difference between total and fast responses.

[5] Ming et al. (2010) consider the change in surface sensible heat flux to be part of the fast or temperature-independent response.

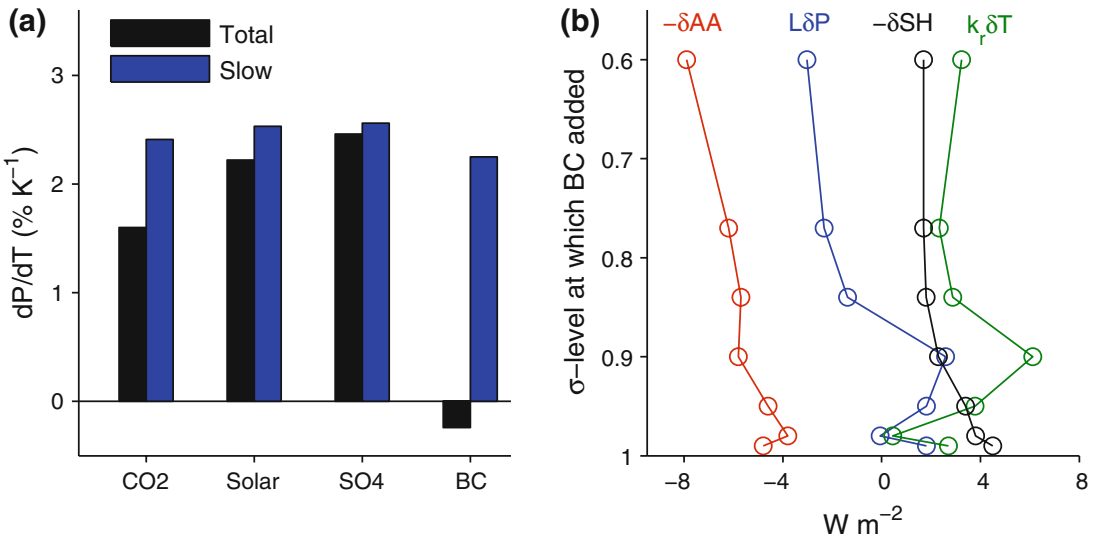

Fig. 5 **a** Sensitivities of the total and slow precipitation responses for different forcings (CO_2, solar, sulfate aerosols, and black carbon aerosols) in simulations with an atmospheric model coupled to a mixed-layer ocean. The total response is the sum of the slow and fast responses [based on Table 2 of Andrews et al. (2010)]. **b** Terms in the perturbation atmospheric energy budget in response to additional black carbon aerosols at different σ-levels in simulations with an atmospheric GCM coupled to a mixed-layer ocean. The terms shown are the changes in atmospheric absorption induced directly by the absorbing aerosols (δAA), radiative feedbacks ($k_r \delta T$) with surface temperature T and $k_r = 1.8$ W m^{-2} K^{-1}, the change in latent heating associated with precipitation $L\delta P$, and the change in upward sensible heat flux (δSH). We show $-\delta AA$ and $-\delta SH$ so that all terms are positive when contributing to a positive change in precipitation [based on Table 1 of Ming et al. (2010)]

5 Transient Changes in Precipitation

The discussion of the preceding section makes clear that changes in surface temperature are not sufficient to determine the equilibrium response of precipitation, but rather that changes in atmospheric radiative forcing must also be specified. Temperature changes may occur on an entirely different timescale to the radiative forcing, and the transient evolution of precipitation depends on the evolution of both radiative forcing and temperature. For example, we expect a slower rate of increase in precipitation with respect to temperature in a period in which both greenhouse-gas concentrations and temperature are increasing than in a period in which greenhouse-gas concentrations have stabilized but temperature continues to increase (Andrews and Forster 2010).

Some further nonintuitive properties of the transient precipitation response have recently been illustrated in coupled climate model simulations (Wu et al. 2010; Cao et al. 2011). Wu et al. (2010) showed that, in response to a change in the trend of atmospheric CO_2 concentrations from upward to downward, temperature begins to fall almost immediately, but the rate of increase in precipitation actually accelerates, before eventually decreasing after several decades. Cao et al. (2011) found a similar behavior in response to a rampdown of CO_2 concentrations [Fig. 6c; reproduced from Cao et al. (2011)] and also demonstrated an extreme limit of the same behavior in which CO_2 concentrations are changed in a step-like manner, first upward and then downward, resulting in downward and then upward spikes in precipitation (red lines in Fig. 6a, b; see also Fig. 3). As discussed by Wu et al. (2010) and Cao et al. (2011), these transient responses may be understood using the energetic constraint on precipitation. For example, a sudden decrease in CO_2 concentrations leads to an increase in radiative cooling and an increase in precipitation. Only on the slow timescale of the

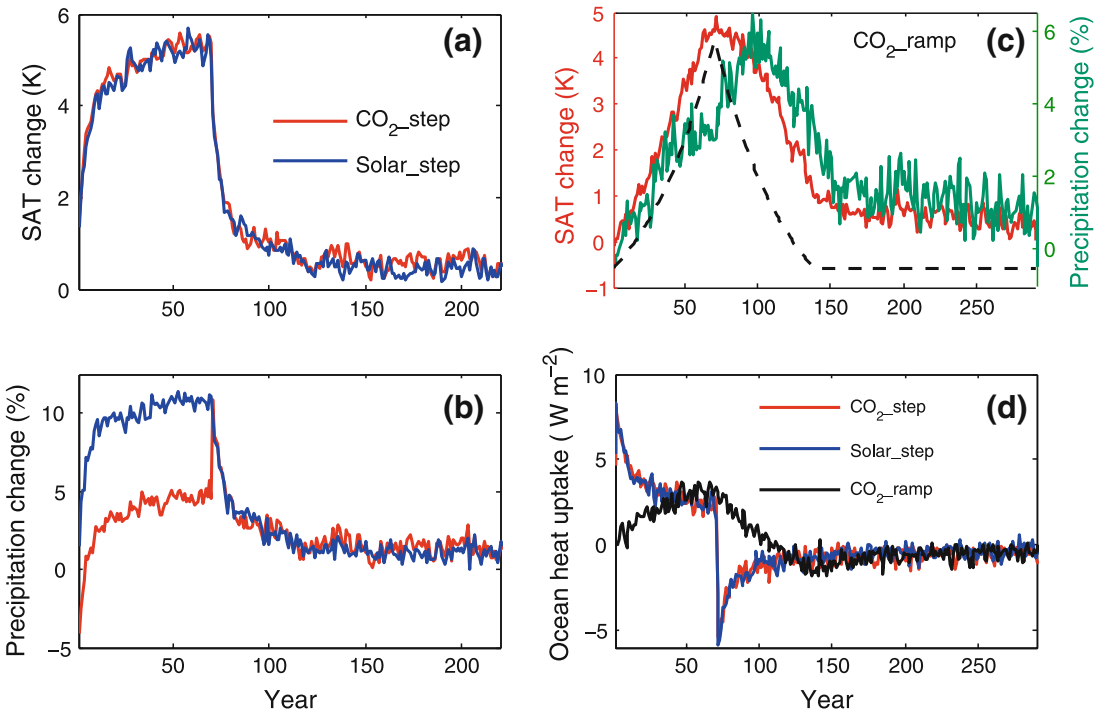

Fig. 6 Temporal variations in **a**, **c** surface air temperature, **b**, **c** precipitation, and **d** ocean heat uptake in three simulations with a coupled climate model (HadCM3L). In the "step" simulations (**a**, **b**, **d**), atmospheric CO_2 or the solar constant are instantaneously increased and then instantaneously returned to their initial value after 70 years (CO_2 is quadrupled or the solar constant is increased by 4.54%). In the CO_2 ramp simulation (**c**, **d**), atmospheric CO_2 is increased by 2% per year until quadrupling after 70 years, and then decreased by 2% per year until the original value is reached [*dashed black line* in (**c**)]. Note the downward and upward spikes in precipitation in the CO_2 step simulation at years 0 and 70, respectively [reproduction of Fig. 1 of Cao et al. (2011)]

ensuing temperature decrease does the radiative cooling and precipitation decrease. The precipitation and temperature responses are more qualitatively similar to one another in a simulation in which the step-like changes are in the solar constant (blue lines in Fig. 6a, b), consistent with the much smaller fast response of precipitation for solar forcing. (The magnitude of the changes in solar constant are chosen to give similar surface temperature variations as for the CO_2 simulation). From the surface energy budget perspective, the rate of ocean heat uptake should be expected to influence the transient response of evaporation and precipitation. However, the time history of ocean heat uptake is almost identical in the simulations with solar and CO_2 step-like changes (Fig. 6d), which shows that the sudden reduction in ocean heat uptake at year 70 is not necessarily sufficient to give a temporary increase in precipitation, depending on the nature of the radiative forcing.

The energetic perspective also makes clear that radiative feedbacks will be important for low-frequency variability of precipitation. For example, Hall and Manabe (2000) found a reduction in the interannual variability of global-mean precipitation in a climate model simulation in which the longwave radiative feedback of water vapor was suppressed.

6 Regional Changes in Precipitation

We have focused on the energetic constraint on global-mean precipitation, but regional changes in precipitation are of greater importance for impacts of climate change. Regional

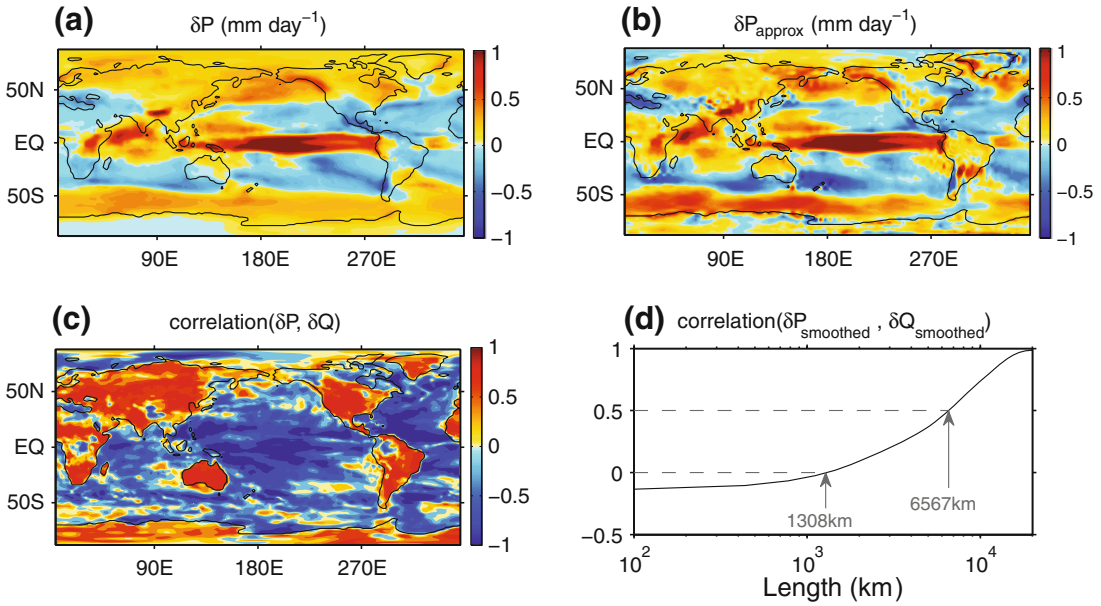

Fig. 7 Energetic perspective on local precipitation changes in the multi-model mean of CMIP3 simulations: **a** change in precipitation (mm day^{-1}), **b** an approximation $\delta P_{\text{approx}} = \delta\langle P\rangle + \delta H_m/L$ that neglects changes in eddy dry static energy (DSE) fluxes and spatial variations in the change in diabatic cooling, **c** the inter-model correlation coefficient of the change in precipitation and diabatic cooling, and **d** the global-mean of this correlation coefficient as a function of the length scale of a spatial filter that is first applied to the changes in precipitation and diabatic cooling [see Muller and O'Gorman (2011) for details]

precipitation changes have been conventionally analyzed in terms of column water vapor balance, relating the difference between precipitation and evaporation to the water vapor flux convergence (e.g., Held and Soden 2006; Seager et al. 2010). The energy budget has sometimes been used as an additional constraint to account for changes in the circulation which are an important regional contributor to the changes in precipitation (Chou and Neelin 2004; Chou et al. 2009; Levermann et al. 2009; Chou and Chen 2010). Alternatively, the energetic approach to global-mean precipitation changes may be extended to local precipitation changes by including changes in horizontal transports of dry static energy (DSE),

$$L\delta P = \delta Q + \delta H, \tag{4}$$

where δH is the change in the vertical integral of the DSE flux divergence, and we will refer to $Q = R_{\text{TOA}} - R_{\text{SFC}} - SH$ as the diabatic cooling (excluding latent heating).[6] The vertical integral in δH is taken over the atmospheric column, although it could be approximated by a vertical integral over the troposphere. Increases in DSE flux divergence cool the atmospheric column and tend to increase precipitation for fixed diabatic cooling. Muller and O'Gorman (2011) used this local energy budget to analyze changes in precipitation in simulations drawn from the CMIP3 archive under the A1B emissions scenario (Fig. 7a). They showed that a simple approximation δP_{approx} for the change in local

[6] In the case of tropical precipitation extremes, the primary balance is between latent heating and DSE flux divergence (Muller et al. 2011).

precipitation δP is given in terms of the change in the vertical integral of the DSE flux divergence by the mean circulation (δH_m) and the change in global-mean precipitation ($\delta\langle P\rangle$), such that $L\delta P_{\text{approx}} = L\delta\langle P\rangle + \delta H_m$ (Fig. 7b). Further simple approximations may then be made to relate components of δH_m to changes in temperature and mid-tropospheric vertical velocity (Muller and O'Gorman 2011), resulting in approximate relations comparable to those used in the water vapor budget approach (e.g., Held and Soden 2006).

Locally, changes in diabatic cooling may be balanced by changes in precipitation or changes in DSE flux divergence. A fundamental question then arises as to what extent local changes in diabatic cooling δQ are in fact reflected in local changes in precipitation δP. For example, one might ask to what extent localized radiative forcing from aerosols will be related to a corresponding local change in precipitation. Muller and O'Gorman (2011) addressed this question by examining the inter-model correlation coefficient between changes in precipitation δP and changes in diabatic cooling δQ and found that, while δP and δQ were positively correlated over land, they were negatively correlated over ocean because of cloud and water vapor feedbacks (Fig. 7c). The scale dependency of the relationship between δP and δQ was addressed by smoothing over a range of length scales prior to calculation of the correlation coefficient. The global-mean correlation coefficient reaches a value of 0.5 for a smoothing length scale of $\sim$7,000 km (Fig. 7d), implying that only on relatively large scales or over land are δP and δQ strongly positively correlated. Further work is needed to understand the physical processes that contribute to the correlation between changes in precipitation and diabatic cooling at different length scales and to better understand the contrast between their relationship over land and ocean (cf. Trenberth and Shea 2005; Lambert and Allen 2009).

7 Observations of the Atmospheric Energetic Constraint on Precipitation

The energetic constraint on global precipitation is difficult to confirm observationally. Long-term (50 or more years) observations of precipitation (surface rain gauges) are primarily confined to northern hemisphere land regions (e.g., Min et al. 2011), while spatially complete ocean estimates are only available through satellite retrievals of infrared radiances since 1979 and microwave radiances since 1987 (Huffman et al. 2009) and contain substantial uncertainties relating to sampling and calibration (Adler et al. 2001). Reconstructions of past precipitation may be made using reanalyses or surface pressure and temperature measurements (e.g., Arkin et al. 2010), but they are limited by the homogeneity of input data and the physical relationships employed.

Estimates of Earth's radiative energy balance are limited to an even greater extent: satellite data have provided near-global estimates of variability for much of the period since 1985 (Wielicki et al. 2002; Loeb et al. 2009) but with substantial calibration and sampling issues (Trenberth 2002; Wong et al. 2006). Surface measurements are limited to solar radiometers available for a handful of locations over land since the 1950s (Wild 1999), increasing to around 50 well-calibrated longwave and shortwave radiation measurements for the recent decade (Ohmura et al. 1998). Therefore, estimating recent changes in the surface and atmospheric radiative balance is currently possible only through the additional use of reanalyses data sets combined with additional modeling (Zhang et al. 2004).

Current global variability in P and its driving variables are compared in Fig. 8. During this period, global-mean surface air temperature (T) varied by almost 1 K, primarily

relating to El Niño Southern Oscillation (ENSO), but also a cooling in 1992 following the eruption of Mt. Pinatubo in June 1991 and a warming trend during the 1990s.

7.1 Observed Changes in Surface Temperature and Water Vapor

Atmospheric moisture is tightly coupled to global temperatures (Fig. 8a, b) as evidenced by column integrated water vapor (W) from the Special Sensor Microwave Imager [SSM/I; Wentz and Schabel (2000)] and the European Centre for Medium-range Weather Forecasts (ECMWF) Interim ReAnalysis [ERA Interim; Dee et al. (2011)] and also by surface-specific humidity (q) from HadCRUH observations (Willett et al. 2008). Global SSM/I estimates are constructed using ocean-only SSM/I data between 50°S–50°N and applying ERA Interim values elsewhere. ERA Interim W reduces with time compared with the SSM/I estimates, attributable to differences over the tropical oceans (John et al. 2009), and

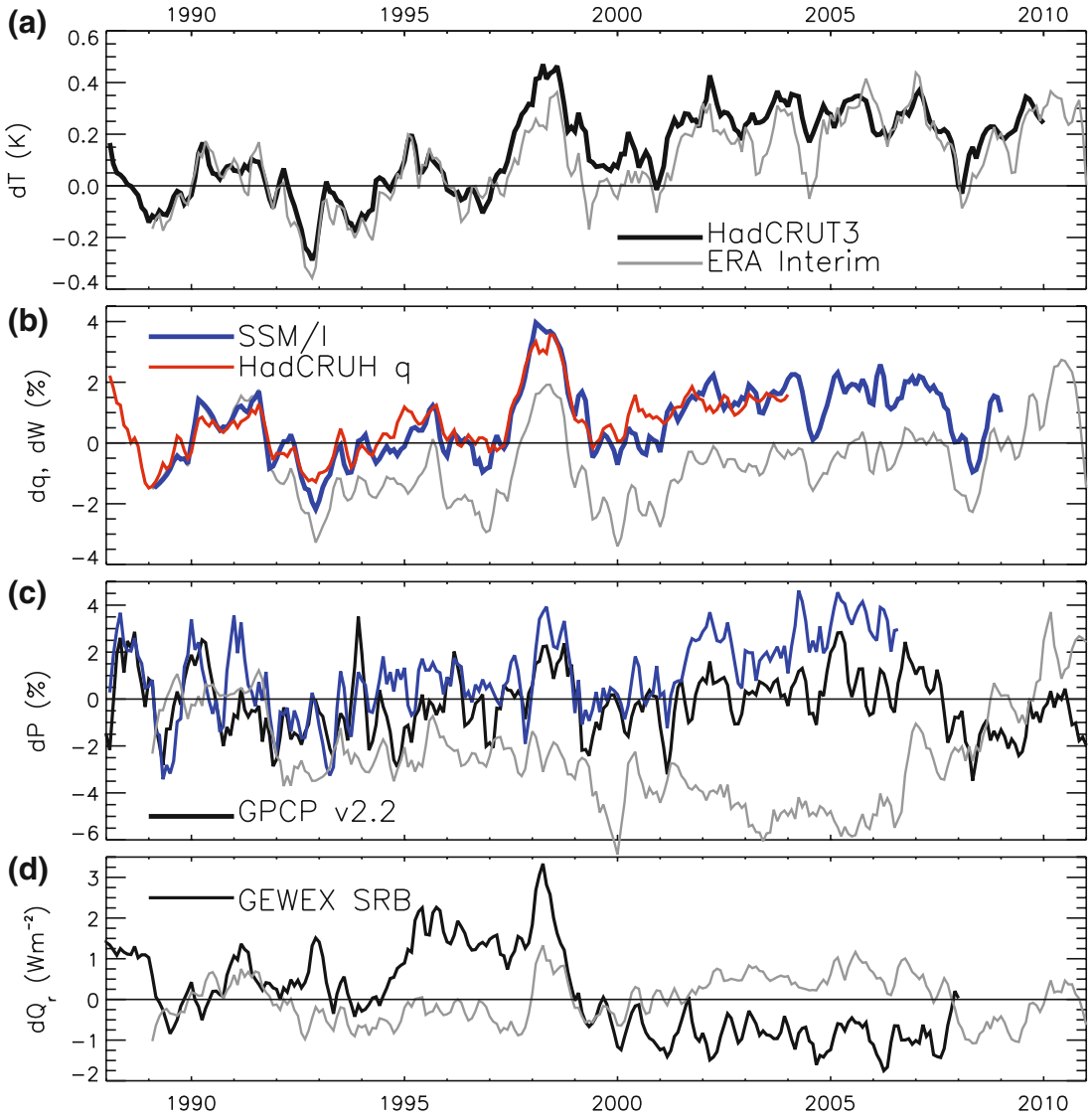

Fig. 8 Global-mean de-seasonalized monthly anomalies in **a** surface air temperature, **b** column integrated water vapor and surface-specific humidity, **c** precipitation and **d** total net radiative cooling of the atmosphere. A 3-month smoothing is applied for clarity. The mean anomaly for January 1989 to December 1990 is subtracted from each time series

Table 1 Linear least squares fits for selected deseasonalized global-mean monthly variables and data sets over the period 1989–2008

Variables (dy/dx)	Data set (y)	Data set (x)	dy/dx ± SE	r
dW/dT	SSM/I, ERA Interim	HadCRUT	6.6 ± 0.4% K^{-1}	0.87
dP/dT	GPCP	HadCRUT	3.4 ± 0.9% K^{-1}	0.40
dQ_r/dT	ERA Interim	ERA Interim	2.5 ± 0.3 W $m^{-2}K^{-1}$	0.71
LdP/dQ_r	GPCP	ERA Interim	1.0 ± 0.2	0.54

may be an artifact of the observing system as documented previously (Trenberth et al. 2001; Allan et al. 2002; Bengtsson et al. 2004).

Similarity between HadCRUH and SSM/I-ERA interim estimates of global moisture variability ($r = 0.86$) is striking, both demonstrating the robust relationship between low-level moisture and temperature (dW/d$T \sim 7\%$ K^{-1}; Table 1), close to that expected from the Clausius–Clapeyron equation (O'Gorman and Muller 2010). This has been documented previously using surface observations (Willett et al. 2008), satellite data (Wentz and Schabel 2000; Santer et al. 2007; Allan 2009), and radiosonde soundings (Durre et al. 2009). The dependence of atmospheric water vapor amounts on temperature is important in accounting for observed contrasting regional precipitation responses (Zhang et al. 2007), in particular for the ascending and descending portions of the tropical circulation (Allan et al. 2010) and enhanced tropical seasonality (Chou et al. 2007), and for the observed increase in the intensity of precipitation (Rajeevan et al. 2008; O'Gorman and Schneider 2009a; Zolina et al. 2010; Allan et al. 2010; Min et al. 2011). Importantly for the energetic constraint on precipitation, increases in atmospheric water vapor content are also physically consistent with enhanced longwave radiative cooling of the atmosphere to the surface (Allan 2006; Stephens and Ellis 2008; Philipona et al. 2009) and enhanced shortwave radiative heating of the atmosphere (Allan 2009; Takahashi 2009b).

7.2 Observed Changes in Precipitation

Observed global precipitation changes (Fig. 8c) are from the Global Precipitation Climatology Project [GPCP v2.2; Huffman et al. (2009)], which combines infrared and SSM/I microwave radiances over ice-free oceans since 1988 and rain gauges over land, and an estimate from Wentz et al. (2007), who combined SSM/I data over ice-free oceans with GPCP data over remaining regions. Simulated precipitation from ERA Interim is also shown and displays a negative trend up until 2005, as noted by John et al. (2009), and a rapid increase over the period 2006–2010, variations which are known to be erroneous (Dee et al. 2011). Since the hydrological cycle in reanalyses is not well-constrained globally, their representation of decadal changes in water vapor and precipitation is unlikely to be realistic.

Global precipitation from GPCP shows a weak positive relationship with surface temperature from HadCRUT (dP/d$T = 3.4\%$ K^{-1}) over the period 1989–2008 (Table 1), similar to values estimated by Adler et al. (2008) for the period 1979–2006. Allowing for autocorrelation using the method of Yang and Tung (1998), which estimates 36 degrees of freedom in the time series, this is only just significant at the 95% confidence level. The autocorrelation timescale for precipitation (6 months) is notably shorter than for water vapor and net radiation (both around 20 months); the timescale dependence of the

controlling processes may provide further insight into the role of forcing, feedback, and response (Harries and Futyan 2006).

There is considerable sensitivity of precipitation response to the data set and time period chosen (Quartly et al. 2007; Wang et al. 2008; John et al. 2009). The relationship with temperature changes found above ($dP/dT = 3.4\%\ K^{-1}$) is weaker than calculated by Wentz et al. (2007), who estimated a $7\%\ K^{-1}$ response for a shorter time period (Adler et al. 2008), and is also weaker than estimated changes in ocean evaporation (Yu 2007; Li et al. 2011). These estimates were based upon linear trends in precipitation and temperature which introduce substantial uncertainty given the short length of the climate record and the influence of ENSO and volcanic eruptions (Gu et al. 2007; Lambert et al. 2008); the estimated observed responses are, therefore, not inconsistent with the large spread in responses calculated from climate models using similar methods (Previdi and Liepert 2008; Liepert and Previdi 2009; Allan 2009). The larger response over the period 1987–2006 (Wentz et al. 2007) may be consistent with an apparent intensification of the Walker and Hadley circulation since 1979 (Sohn and Park 2010; Zahn and Allan 2011; Li et al. 2011) although declines in circulation have also been identified by other authors (Vecchi et al. 2006; Power and Smith 2007; Gastineau and Soden 2011), based upon reanalyses and satellite wind data. A blended reconstruction of twentieth century precipitation by Arkin et al. (2010), based upon gauge observations over land and surface temperature and pressure patterns over ocean, suggests a smaller hydrological sensitivity of $2.5\%\ K^{-1}$.

7.3 Estimating Net Radiative Cooling

The energetic constraint on precipitation discussed in previous sections implies that changes in global-mean precipitation depend both on changes in the radiative cooling of the atmosphere and changes in surface sensible heat flux. As discussed in Sect. 2, the net atmospheric radiative cooling above the sub-cloud layer may provide a more direct link to global-mean precipitation (Takahashi 2009a), but given the difficulties of generating such a data set, we instead use the approach of Allan (2006) and show estimates of the net radiative cooling of the atmosphere (Q_r, longwave radiative cooling minus shortwave radiative heating) in Fig. 8d.

There is poor agreement between estimates of Q_r from the NASA Global Energy and Water Cycle Experiment (GEWEX) Surface Radiation Budget (SRB) project, which uses cloud and radiation information retrieved from satellite and atmospheric profiles from reanalyses as input to radiative transfer models (Stackhouse et al. 2011) and the ERA Interim reanalysis project. Variability from the International Satellite Cloud Climatology Project (ISCCP) D2 radiative flux products (Zhang et al. 2004) is substantially larger (not shown), showing poor agreement with SRB and ERA Interim. John et al. (2009) also found larger differences in atmospheric longwave and shortwave radiative divergence between data sets for the tropical ocean. One of the problems with the approach adopted by SRB and ISCCP is that surface radiative fluxes are not well constrained by the satellite measurements, in particular for the longwave fluxes, and homogeneity of the ISCCP data set is questionable (Evan et al. 2007).

Although ERA Interim clouds are generated by model parameterizations, the simulation of changes in net radiation at the top of the atmosphere is reasonable based upon comparison with satellite data (Allan 2011) and, notwithstanding issues with drifts in W shown in Fig. 8b and the lack of account for changes in aerosol optical depth, appear physically reasonable based upon the relationship with surface temperature ($dQ_r/dT = 2.5\ W\ m^{-2}\ K^{-1}$, Table 1) and previous analysis (Allan 2009; John et al. 2009). Although

clouds contribute to heating of the moist tropical troposphere and cooling of the atmospheric column for stratocumulus regions and higher latitudes (Sohn 1999), their impact upon decadal changes in the atmospheric radiative budget may be weak, as discussed by John et al. (2009). (For climate models, Fig. 4 shows that the cloud radiative feedback on precipitation is not different from zero to within the inter-model scatter.)

7.4 Observed Link Between Precipitation and Atmospheric Net Radiative Cooling

The relationship between GPCP P (converted into units of W m^{-2} by multiplying by the latent heat of condensation L) and ERA Interim Q_r, $L\mathrm{d}P/\mathrm{d}Q_r = 1.0 \pm 0.2$, is weak (Table 1) although statistically significant at the 95% confidence level allowing for autocorrelation and it is also physically reasonable. Accounting more carefully for changes in aerosol, cloud and water vapor may improve the observational constraint on precipitation changes. For example, decadal trends in aerosol optical depth associated with global "dimming" and "brightening" (Wild et al. 2005; Mishchenko et al. 2007) are thought to explain increases in rainfall over land during the 1990s (Wild et al. 2008; Wild and Liepert 2010).

Within the framework of the atmospheric energy budget constraint on precipitation, scattering aerosols influence atmospheric radiative cooling and precipitation through the surface temperature response, but absorbing aerosols also directly lead to radiative heating of the atmosphere and thus may affect precipitation independent of surface temperature changes (Lambert et al. 2008; Andrews et al. 2009; Ming et al. 2010; Ban-Weiss et al. 2011), as discussed in Sect. 4.2. A further influence on hydrological sensitivity relates to greenhouse gases. Decadal trends in P are influenced by the secular rises in CO_2 concentrations which act in a similar way to absorbing aerosols by radiatively heating the atmosphere. Based upon these arguments, rising CO_2 concentrations in the 2000s, combined with stable decadal temperature, should result in a negative precipitation trend; this is not immediately obvious from Fig. 8c.

8 Conclusions

We have given a review of many of the insights to be gained from the energetic perspective on the response of precipitation to climate change. A number of open questions remain, several of which we now discuss briefly.

While it is clear that the atmospheric energy budget constrains the possible changes in global-mean precipitation, especially in warm climates, there is still some uncertainty as to the nature of the constraint. For example, we have discussed whether it may be approximated as a purely radiative constraint by balancing latent heating with the radiative cooling of the free atmosphere. Results presented here based on simulations with an idealized GCM over a wide range of climates provide some support for this free-atmospheric radiative constraint. Further work is needed to evaluate its accuracy, although the necessary radiative fluxes near the top of the boundary layer are not readily available in global observational or climate model data sets. It would be straightforward to further test the accuracy of the free-atmospheric radiative constraint using simulations with a comprehensive climate model in which the necessary radiative fluxes were stored. Even if the free-atmospheric radiative constraint is not very accurate, it may still be useful conceptually. For example, we have shown that it gives a particularly simple explanation for the simulated response of precipitation to radiative forcing from black carbon aerosols (Sect. 4.2).

Considerable progress has been made in quantifying the different feedbacks that contribute to changes in global-mean precipitation. The results presented here [extending the analysis of Previdi (2010)] suggest that cloud radiative feedbacks are a primary contributor to the inter-model scatter in the response of precipitation. Further characterization of the sources of uncertainty in the response of precipitation is desirable, with the aim of clarifying the extent to which these are similar to the sources of uncertainty for climate sensitivity and of identifying the processes whose parameterization is most problematic in this context. The need to include the changes in surface sensible heat fluxes (unless the free-atmospheric radiative constraint is proven adequate) distinguishes the problem from that of TOA radiative feedbacks, and it is important to develop a better understanding of the response of surface sensible heat fluxes on different timescales and for different forcings (cf., Liepert and Previdi 2009).

The different responses to different forcing agents have also been described, including recent progress in quantifying the fast response of precipitation to different types of aerosol forcing. The vertical structure of changes in water vapor, black carbon aerosols, and clouds is expected to be important in determining the magnitude and even the sign of the precipitation response. The combination of slow and fast responses means that it is not necessarily straightforward to relate observed or simulated transient changes in precipitation to changes in temperature. An intriguing possibility is that it is more appropriate to relate changes in precipitation to changes in radiative forcing rather than changes in temperature; in addition to the closer agreement then found between hydrological sensitivities for different forcing agents (Lambert and Faull 2007), it may be more appropriate to relate changes in energy fluxes to one another than to changes in temperature.

We have discussed how the energetic perspective on global-mean precipitation changes may be extended to regional precipitation changes by including horizontal energy fluxes (DSE fluxes) in the analysis. One important question that could be addressed in such a framework is the extent to which energetics can be used to give a simple constraint on changes in precipitation over land (for example, in terms of radiative forcings and changes in surface temperature). Such a constraint would be particularly useful because many of the available historical observations of precipitation are over land rather than ocean. Lambert and Allen (2009) found that a simple regression model for precipitation changes that was adequate in the global-mean was not adequate over land alone, even when land-ocean energy transports were accounted for. Nonetheless, starting from the full local energy budget, it should be possible to systematically make approximations to derive the minimal energetic model needed to account for changes in precipitation over land.

Currently available observations do not allow us to definitively link changes in global-mean precipitation with changes in the radiative energy budget of the atmosphere. Uncertainties arise for both the observed changes in radiative fluxes and precipitation, and more extensive and longer-term observations are clearly desirable. The observations we do have raise a number of important questions. For example, what sets the different autocorrelation timescales of global-mean precipitation, column water vapor, and net radiative cooling? And what are the contributions of different forcing agents to the observed hydrological sensitivity over different time periods? These basic questions are important for understanding observations of ongoing changes in the global hydrological cycle.

Progress could be made on several of the open questions identified here using simulations which have recently become available from the Coupled Model Intercomparison Project phase 5. In particular, the experiments designed to probe fast and slow responses and the impacts of changes in clouds and aerosols could be used to better understand precipitation responses in different models and emissions scenarios.

Acknowledgments M. Byrne is supported through the MIT Joint Program on the Science and Policy of Global Change. R. Allan is funded through the National Environment Research Council PREPARE project (NE/G015708/1) and National Centre for Atmospheric Sciences. We thank the American Meteorological Society (AMS) and T. Andrews for reproduction of Fig. 3, the American Geophysical Union (AGU) and L. Cao for reproduction of Fig. 6, and C. J. Muller for Fig. 7. The SSM/I data were extracted from Remote Sensing Systems, the GPCP data from the NASA Goddard Space Flight Center, the HadCRUH and HadCRUT data from http://www.metoffice.gov.uk/hadobs/ and ERA Interim data from http://www.ecmwf.int. We acknowledge the modeling groups, the Program for Climate Model Diagnosis and Intercomparison (PCMDI) and the WCRP's Working Group on Coupled Modelling (WGCM) for their roles in making available the WCRP CMIP3 multi-model data set. Support of this data set is provided by the Office of Science, US Department of Energy.

References

Adler RF, Kidd C, Petty G, Morissey M, Goodman HM (2001) Intercomparison of global precipitation products: the third precipitation intercomparison project (PIP-3). Bull Am Meteorol Soc 82:1377–1396

Adler RF, Gu G, Wang JJ, Huffman GJ, Curtis S, Bolvin D (2008) Relationships between global precipitation and surface temperature on interannual and longer timescales (1979–2006). J Geophys Res 113:D22,104

Allan RP (2006) Variability in clear-sky longwave radiative cooling of the atmosphere. J Geophys Res 111:D22, 105

Allan RP (2009) Examination of relationships between clear-sky longwave radiation and aspects of the atmospheric hydrological cycle in climate models, reanalyses, and observations. J Clim 22:3127–3145

Allan RP (2011) Combining satellite data and models to estimate cloud radiative effect at the surface and in the atmosphere. Meteorol Appl 18:324–333

Allan RP, Slingo A, Ramaswamy V (2002) Analysis of moisture variability in the European Centre for medium-range weather forecasts 15-year reanalysis over the tropical oceans. J Geophys Res 107:4230

Allan RP, Soden BJ, John VO, Ingram WI, Good P (2010) Current changes in tropical precipitation. Environ Res Lett 5:025205

Allen MR, Ingram WJ (2002) Constraints on future changes in climate and the hydrologic cycle. Nature 419:224–232

Andrews T, Forster PM (2010) The transient response of global-mean precipitation to increasing carbon dioxide levels. Environ Res Lett 5:025212

Andrews T, Forster PM, Gregory JM (2009) A surface energy perspective on climate change. J Clim 22:2557–2570

Andrews T, Forster PM, Boucher O, Bellouin N, Jones A (2010) Precipitation, radiative forcing and global temperature change. Geophys Res Lett 37:L14701

Arkin PA, Smith TM, Sapiano MRP, Janowiak J (2010) The observed sensitivity of the global hydrological cycle to changes in surface temperature. Environ Res Lett 5:035201

Bala G, Duffy PB, Taylor KE (2008) Impact of geoengineering schemes on the global hydrological cycle. Proc Nat Acad Sci 105:7664–7669

Bala G, Caldeira K, Nemani R (2010) Fast versus slow response in climate change: implications for the global hydrological cycle. Clim Dyn 35:423–434

Ban-Weiss GA, Cao L, Bala G, Caldeira K (2011) Dependence of climate forcing and response on the altitude of black carbon aerosols. Clim Dyn doi:10.1007/s00382-011-1052-y

Bengtsson L, Hagemann S, Hodges KI (2004) Can climate trends be calculated from reanalysis data?. J Geophys Res 109:D11111

Boer GJ (1993) Climate change and the regulation of the surface moisture and energy budgets. Clim Dyn 8:225–239

Bony S, Colman R, Kattsov VM, Allan RP, Bretherton CS, Dufresne JL, Hall A, Hallegatte S, Holland MM, Ingram W, Randall DA, Soden BJ, Tselioudis G, Webb MJ (2006) How well do we understand and evaluate climate change feedback processes?. J Clim 19:3445–3482

Cao L, Bala G, Caldeira K (2011) Why is there a short-term increase in global precipitation in response to diminished CO_2 forcing?. Geophys Res Lett 38:L06703

Chou C, Chen CA (2010) Depth of convection and the weakening of tropical circulation in global warming. J Clim 23:3019–3030

Chou C, Neelin JD (2004) Mechanisms of global warming impacts on regional tropical precipitation. J Clim 17:2688–2701

Chou C, Tu JY, Tan PH (2007) Asymmetry of tropical precipitation change under global warming. Geophys Res Lett 34:L17708
Chou C, Neelin JD, Chen CA, Tu JY (2009) Evaluating the "Rich-Get-Richer" mechanism in tropical precipitation change under global warming. J Clim 22:1982–2005
Dee DP, Uppala SM, Simmons AJ, Berrisford P, Poli P, Kobayashi S, Andrae U, Balmaseda MA, Balsamo G, Bauer P, Bechtold P, Beljaars ACM, van de Berg L, Bidlot J, Bormann N, Delsol C, Dragani R, Fuentes M, Geer AJ, Haimberger L, Healy SB, Hersbach H, Hólm EV, Isaksen L, Kållberg P, Köhler M, Matricardi M, McNally AP, Monge-Sanz BM, Morcrette JJ, Park BK, Peubey C, de Rosnay P, Tavolato C, Thépaut JN, Vitart F (2011) The ERA-Interim reanalysis: configuration and performance of the data assimilation system. Q J R Meteorol Soc 137:553–597
Durre I, Williams CN Jr, Yin X, Vose RS (2009) Radiosonde-based trends in precipitable water over the Northern Hemisphere: an update. J Geophys Res 114:D05112
Evan AT, Heidinger AK, Vimont DJ (2007) Arguments against a physical long-term trend in global ISCCP cloud amounts. Geophys Res Lett 34:L04701
Frieler K, Meinshausen M, von Deimling TS, Andrews T, Forster P (2011) Changes in global-mean precipitation in response to warming, greenhouse gas forcing and black carbon. Geophys Res Lett 38:L04702
Frierson DMW (2007) The dynamics of idealized convection schemes and their effect on the zonally averaged tropical circulation. J Atmos Sci 64:1959–1976
Frierson DMW, Held IM, Zurita-Gotor P (2006) A gray-radiation aquaplanet moist GCM. Part I: static stability and eddy scale. J Atmos Sci 63:2548–2566
Gastineau G, Soden BJ (2011) Evidence for a weakening of tropical surface wind extremes in response to atmospheric warming. Geophys Res Lett 38:L09706
Gu G, Adler RF, Huffman GJ, Curtis S (2007) Tropical rainfall variability on interannual-to-interdecadal and longer time scales derived from the GPCP monthly product. J Clim 20:4033–4046
Hall A, Manabe S (2000) Effect of water vapor feedback on internal and anthropogenic variations of the global hydrologic cycle. J Geophys Res 105:6935–6944
Harries JE, Futyan JM (2006) On the stability of the Earth's radiative energy balance: response to the Mt. Pinatubo eruption. Geophys Res Lett 33:L23814
Held IM, Soden BJ (2006) Robust responses of the hydrological cycle to global warming. J Clim 19:5686–5699
Huffman GJ, Adler RF, Bolvin DT, Gu G (2009) Improving the global precipitation record: GPCP version 2.1. Geophys Res Lett 36:L17808
John VO, Allan RP, Soden BJ (2009) How robust are observed and simulated precipitation responses to tropical ocean warming. Geophys Res Lett 36:L14702
Lambert FH, Allen MR (2009) Are changes in global precipitation constrained by the tropospheric energy budget?. J Clim 22:499–517
Lambert FH, Faull NE (2007) Tropospheric adjustment: the response of two general circulation models to a change in insolation. Geophys Res Lett 34:L03701
Lambert FH, Webb MJ (2008) Dependency of global mean precipitation on surface temperature. Geophys Res Lett 35:L16706
Lambert FH, Stine AR, Krakauer NY, Chiang JCH (2008) How much will precipitation increase with global warming?. Eos Trans AGU 89:193–194
Le Hir G, Donnadieu Y, Goddéris Y, Pierrehumbert RT, Halverson GP, Macouin M, Nédélec A, Ramstein G (2009) The snowball Earth aftermath: exploring the limits of continental weathering processes. Earth Planet Sci Lett 277:453–463
Levermann A, Schewe J, Petoukhov V, Held H (2009) Basic mechanism for abrupt monsoon transitions. Proc Nat Acad Sci 106:20,572–20,577
Li G, Ren B, Yang C, Zheng J (2011) Revisiting the trend of the tropical and subtropical Pacific surface latent heat flux during 1977–2006. J Geophys Res 116:D10115
Liepert BG, Previdi M (2009) Do models and observations disagree on the rainfall response to global warming?. J Clim 22:3156–3166
Loeb NG, Wielicki BA, Doelling DR, Smith GL, Keyes DF, Kato S, Manalo-Smith N, Wong T (2009) Toward optimal closure of the Earth's top-of-atmosphere radiation budget. J Clim 22:748–766
Lorenz DJ, DeWeaver ET, Vimont DJ (2010) Evaporation change and global warming: the role of net radiation and relative humidity. J Geophys Res 115:D20118
Min SK, Zhang X, Zwiers FW, Hegerl GC (2011) Human contribution to more-intense precipitation extremes. Nature 470:378–381
Ming Y, Ramaswamy V, Persad G (2010) Two opposing effects of absorbing aerosols on global-mean precipitation. Geophys Res Lett 37:L13701

Mishchenko MI, Geogdzhayev IV, Rossow WB, Cairns B, Carlson BE, Lacis AA, Liu L, Travis LD (2007) Long-term satellite record reveals likely recent aerosol trend. Science 315:1543

Mitchell JFB, Wilson CA, Cunnington WM (1987) On CO_2 climate sensitivity and model dependence of results. Q J R Meteorol Soc 113:293–322

Muller CJ, O'Gorman PA (2011) An energetic perspective on the regional response of precipitation to climate change. Nat Clim Change 1:266–271

Muller CJ, O'Gorman PA, Back LE (2011) Intensification of precipitation extremes with warming in a cloud resolving model. J Clim 24:2784–2800

O'Gorman PA, Muller CJ (2010) How closely do changes in surface and column water vapor follow Clausius–Clapeyron scaling in climate-change simulations?. Environ Res Lett 5:025207

O'Gorman PA, Schneider T (2008) The hydrological cycle over a wide range of climates simulated with an idealized GCM. J Clim 21:3815–3832

O'Gorman PA, Schneider T (2009a) The physical basis for increases in precipitation extremes in simulations of 21st-century climate change. Proc Natl Acad Sci 106:14,773–14,777

O'Gorman PA, Schneider T (2009b) Scaling of precipitation extremes over a wide range of climates simulated with an idealized GCM. J Clim 22:5676–5685

Ohmura A, Dutton EG, Forgan B, Fröhlich C, Gilgen H, Hegner H, Heimo A, König-Langlo G, McArthur B, Müller G, Philipona R, Pinker R, Whitlock CH, Dehne K, Wild M (1998) Baseline surface radiation network (BSRN/WCRP): new precision radiometry for climate research. Bull Am Meteorol Soc 79:2115–2136

Pall P, Allen MR, Stone DA (2007) Testing the Clausius–Clapeyron constraint on changes in extreme precipitation under CO_2 warming. Clim Dyn 28:351–363

Peixoto JP, Oort AH (1992) Physics of climate. American Institute of Physics, New York

Philipona R, Behrens K, Ruckstuhl C (2009) How declining aerosols and rising greenhouse gases forced rapid warming in Europe since the 1980s. Geophys Res Lett 36:L02806

Pierrehumbert RT (1999) Subtropical water vapor as a mediator of rapid global climate change. In: Clarks PU, Webb RS, Keigwin LD (eds) Mechanisms of global climate change at millennial time scales. Geophys. Monogr. Ser., vol 112, American Geophysical Union, Washington, p 339

Pierrehumbert RT (2002) The hydrologic cycle in deep-time climate problems. Nature 419:191–198

Power SB, Smith IN (2007) Weakening of the Walker circulation and apparent dominance of El Niño both reach record levels, but has ENSO really changed?. Geophys Res Lett 34:L18702

Previdi M (2010) Radiative feedbacks on global precipitation. Environ Res Lett 5:025211

Previdi M, Liepert BG (2008) Interdecadal variability of rainfall on a warming planet. Eos Trans AGU 89:193–195

Quartly GD, Kyte EA, Srokosz MA, Tsimplis MN (2007) An intercomparison of global oceanic precipitation climatologies. J Geophys Res 112:D10121

Rajeevan M, Bhate J, Jaswal AK (2008) Analysis of variability and trends of extreme rainfall events over India using 104 years of gridded daily rainfall data. Geophys Res Lett 35:L18707

Ramanathan V (1981) The role of ocean-atmosphere interactions in the CO_2 climate problem. J Atmos Sci 38:918–930

Ramanathan V, Crutzen PJ, Kiehl JT, Rosenfeld D (2001) Aerosols, climate, and the hydrological cycle. Science 294:2119–2124

Richter I, Xie SP (2008) Muted precipitation increase in global warming simulations: A surface evaporation perspective. J Geophys Res 113:D24118

Romps DM (2011) Response of tropical precipitation to global warming. J Atmos Sci 68:123–138

Santer BD, Mears C, Wentz FJ, Taylor KE, Gleckler PJ, Wigley TML, Barnett TP, Boyle JS, Brüggemann W, Gillett NP, Klein SA, Meehl GA, Nozawa T, Pierce DW, Stott PA, Washington WM, Wehner MF (2007) Identification of human-induced changes in atmospheric moisture content. Proc Natl Acad Sci 104:15,248–15,253

Schneider T, O'Gorman PA, Levine XJ (2010) Water vapor and the dynamics of climate changes. Rev Geophys 48:RG3001

Seager R, Naik N, Vecchi GA (2010) Thermodynamic and dynamic mechanisms for large-scale changes in the hydrological cycle in response to global warming. J Clim 23:4651–4668

Sherwood SC, Ingram W, Tsushima Y, Satoh M, Roberts M, Vidale PL, O'Gorman PA (2010) Relative humidity changes in a warmer climate. J Geophys Res 115:D09104

Soden BJ, Held IM, Colman R, Shell KM, Kiehl JT, Shields CA (2008) Quantifying climate feedbacks using radiative kernels. J Clim 21:3504–3520

Sohn BJ (1999) Cloud-induced infrared radiative heating and its implications for large-scale tropical circulations. J Atmos Sci 56:2657–2672

Sohn BJ, Park SC (2010) Strengthened tropical circulations in past three decades inferred from water vapor transport. J Geophys Res 115:D15112
Stackhouse PW Jr, Gupta SK, Cox SJ, Zhang T, Mikovitz JC, Hinkelman LM (2011) 24.5-year SRB data set released. GEWEX News 21:10–12
Stephens GL, Ellis TD (2008) Controls of global-mean precipitation increases in global warming GCM experiments. J Clim 21:6141–6155
Stephens GL, Hu Y (2010) Are climate-related changes to the character of global-mean precipitation predictable?. Environ Res Lett 5:025209
Stevens B, Schwartz SE (2011) Observing and modeling Earth's energy flows. Surv Geophys (submitted)
Sun Y, Solomon S, Dai A, Portmann RW (2007) How often will it rain?. J Clim 20:4801–4818
Takahashi K (2009a) Radiative constraints on the hydrological cycle in an idealized radiative-convective equilibrium model. J Atmos Sci 66:77–91
Takahashi K (2009b) The global hydrological cycle and atmospheric shortwave absorption in climate models under CO_2 forcing. J Clim 22:5667–5675
Trenberth KE (1999) Conceptual framework for changes of extremes of the hydrological cycle with climate change. Clim Change 42:327–339
Trenberth KE (2002) Changes in tropical clouds and radiation. Science 296:2095a
Trenberth KE (2011) Changes in precipitation with climate change. Clim Res 47:123–138
Trenberth KE, Shea DJ (2005) Relationships between precipitation and surface temperature. Geophys Res Lett 32:L14703
Trenberth KE, Stepaniak DP, Hurrell JW, Fiorino M (2001) Quality of reanalyses in the tropics. J Clim 14:1499–1510
Trenberth KE, Dai A, Rasmussen RM, Parsons DB (2003) The changing character of precipitation. Bull Am Meteorol Soc 84:1205–1217
Trenberth KE, Fasullo JT, Kiehl J (2009) Earth's global energy budget. Bull Am Meteorol Soc 90:311–323
Vecchi GA, Soden BJ, Wittenberg AT, Held IM, Leetmaa A, Harrison MJ (2006) Weakening of tropical Pacific atmospheric circulation due to anthropogenic forcing. Nature 441:73–76
Wang JJ, Adler RF, Gu G (2008) Tropical rainfall-surface temperature relations using Tropical Rainfall Measuring Mission precipitation data. J Geophys Res 113:D18115
Wentz FJ, Schabel M (2000) Precise climate monitoring using complementary satellite data sets. Nature 403:414–416
Wentz FJ, Ricciardulli L, Hilburn K, Mears C (2007) How much more rain will global warming bring?. Science 317:233–235
Wielicki BA, Wong T, Allan RP, Slingo A, Kiehl JT, Soden BJ, Gordon CT, Miller AJ, Yang S, Randall DA, Robertson F, Susskind J, Jacobowitz H (2002) Evidence for large decadal variability in the tropical mean radiative energy budget. Science 295:841–844
Wild M (1999) Discrepancies between model-calculated and observed shortwave atmospheric absorption in areas with high aerosol loadings. J Geophys Res 104:27,361–27,371
Wild M, Liepert B (2010) The Earth radiation balance as driver of the global hydrological cycle. Environ Res Lett 5:025003
Wild M, Gilgen H, Roesch A, Ohmura A, Long CN, Dutton EG, Forgan B, Kallis A, Russak V, Tsvetkov A (2005) From dimming to brightening: decadal changes in solar radiation at Earth's surface. Science 308:847–850
Wild M, Grieser J, Schär C (2008) Combined surface solar brightening and increasing greenhouse effect support recent intensification of the global land-based hydrological cycle. Geophys Res Lett 35:L17706
Willett KM, Jones PD, Gillett NP, Thorne PW (2008) Recent changes in surface humidity: development of the HadCRUH dataset. J Clim 21:5364–5383
Wong T, Wielicki BA, Lee RB, Smith GL, Bush KA, Willis JK (2006) Reexamination of the observed decadal variability of the Earth radiation budget using altitude-corrected ERBE/ERBS nonscanner WFOV data. J Clim 19:4028–4040
Wu P, Wood R, Ridley J, Lowe J (2010) Temporary acceleration of the hydrological cycle in response to a CO_2 rampdown. Geophys Res Lett 37:L12705
Yang F, Kumar A, Schlesinger ME, Wang W (2003) Intensity of hydrological cycles in warmer climates. J Clim 16:2419–2423
Yang H, Tung KK (1998) Water vapor, surface temperature, and the greenhouse effect—a statistical analysis of tropical-mean data. J Clim 11:2686–2697
Yu L (2007) Global variations in oceanic evaporation (1958–2005): the role of the changing wind speed. J Clim 20:5376–5390
Zahn M, Allan RP (2011) Changes in water vapor transports of the ascending branch of the tropical circulation. J Geophys Res 116:D18111

Zhang X, Zwiers FW, Hegerl GC, Lambert FH, Gillett NP, Solomon S, Stott PA, Nozawa T (2007) Detection of human influence on twentieth-century precipitation trends. Nature 448:461–465

Zhang Y, Rossow WB, Lacis AA, Oinas V, Mishchenko MI (2004) Calculation of radiative fluxes from the surface to top of atmosphere based on ISCCP and other global data sets: refinements of the radiative transfer model and the input data. J Geophys Res 109:D19105

Zolina O, Simmer C, Gulev SK, Kollet S (2010) Changing structure of European precipitation: longer wet periods leading to more abundant rainfalls. Geophys Res Lett 37:L06704

Diagnosis of Zonal Mean Relative Humidity Changes in a Warmer Climate

JONATHON S. WRIGHT* AND ADAM SOBEL

Department of Applied Physics and Applied Mathematics, Columbia University, New York, New York

JOSEPH GALEWSKY

Department of Earth and Planetary Sciences, University of New Mexico, Albuquerque, New Mexico

(Manuscript received 23 October 2009, in final form 24 March 2010)

ABSTRACT

The zonal mean relative humidity response to a doubling of CO_2 in a climate model is examined using a global climate model and an offline tracer transport model. Offline tracer transport model simulations are driven by the output from two configurations of the climate model, one with 1979 concentrations of atmospheric greenhouse gases and one with doubled CO_2. A set of last saturation tracers is applied within the tracer transport model to diagnose the dynamics responsible for features in the water vapor field. Two different methods are used to differentiate the effects of circulation and transport shifts from spatially inhomogeneous temperature changes. The first of these uses the tracer transport model and is achieved by decoupling the input temperature and circulation fields; the second uses the reconstruction of humidity from the last saturation tracers and is achieved by decoupling the tracer concentrations from their saturation specific humidities. The responses of the tropical and subtropical relative humidities are found to be largely dependent on circulation and transport changes, particularly a poleward expansion of the Hadley cell, a deepening of the height of convective detrainment, a poleward shift of the extratropical jets, and an increase in the height of the tropopause. The last saturation tracers are used to illustrate the influence of changes in transport pathways within the GCM on the zonal mean relative humidity, particularly in the tropical upper troposphere and subtropical dry zones. Relative humidity changes near the extratropical tropopause and in the lower troposphere are largely dependent on changes in the distribution and gradients of temperature. Increases in relative humidity near the extratropical tropopause in both hemispheres are coincident with increases in the occurrence of local saturation and high cloud cover.

1. Introduction

Climate models indicate that the water vapor feedback is roughly equivalent to that expected from constant global mean relative humidity (RH; Soden and Held 2006; Randall et al. 2007). Analyses of observed climate variations in the recent historical record are consistent with this view (Soden et al. 2002; Dessler et al. 2008). A constant global mean RH does not necessarily correspond to a static distribution of RH, however, and even small changes can be consequential for other aspects of the climate (e.g., Sherwood et al. 2010).

Relative humidity is an important factor in determining the distribution and occurrence of clouds (Sundqvist 1978; Price and Wood 2002). An increase in the fraction of optically thin high clouds with warming would represent a positive feedback, as such clouds are relatively transmissive to sunlight, largely opaque to outgoing longwave radiation, and have a substantially different emission temperature than the surface. The converse is true for low clouds, as the increase in solar albedo that they provide outweighs their effect as longwave absorbers (Manabe and Strickler 1964; Hartmann et al. 1992; Chen et al. 2000). A greater understanding of the underlying causes of simulated RH changes and their plausibility may therefore be helpful in constraining cloud feedbacks, which currently represent the largest source of intermodel spread in

* Current affiliation: Department of Applied Mathematics and Theoretical Physics, University of Cambridge, Cambridge, United Kingdom.

Corresponding author address: Jonathon Wright, Dept. of Applied Mathematics and Theoretical Physics, University of Cambridge, Wilberforce Road, Cambridge CB3 0WA, United Kingdom.
E-mail: j.wright@damtp.cam.ac.uk

DOI: 10.1175/2010JCLI3488.1

© 2010 American Meteorological Society

climate sensitivity (Randall et al. 2007). Inhomogeneity in RH changes also impacts the distribution of both latent and radiative heating, which may then project onto the atmospheric circulation (Schneider et al. 2010), large-scale convective organization (Gray and Jacobson 1977), and the level at which deep convection detrains (Hartmann and Larson 2002). Regional shifts of the climatological distribution of RH thus have the potential to influence climate on a wide range of scales.

Several studies have noted that the simulated RH response to warming exhibits a distinctive zonal mean pattern (Mitchell and Ingram 1992; Lorenz and DeWeaver 2007a; Sherwood et al. 2010). This pattern is characterized by a horseshoe-shaped decrease of relative humidity throughout the tropical upper troposphere, subtropics, and extratropical free troposphere, with a slightly more pronounced decrease in the Southern Hemisphere. This horseshoe is bracketed by an increase in relative humidity in the tropical midtroposphere and extratropical tropopause layer, as shown in Fig. 1. The RH difference shown in Fig. 1 is averaged over 10 models in the World Climate Research Program's (WCRP's) Coupled Model Intercomparison Project phase 3 (CMIP3) multimodel dataset, and is calculated using time mean zonal mean relative humidities from the final 5 yr of the slab-ocean control (SlabCNTL) and doubled carbon dioxide (2xCO2) experiments. Although the details of the signal vary among constituent models, the qualitative pattern is largely robust. The relative humidities used to derive Fig. 1 are those reported by the individual models and may, thus, be calculated by using different formulations or transitions from saturation with respect to liquid to saturation with respect to ice.

Relative humidity is defined in this analysis as the ratio of specific humidity to saturation specific humidity. Saturation specific humidity is a function of local temperature as expressed by the Clausius–Clapeyron equation. Free tropospheric specific humidity is in turn determined to leading order by the temperature and circulation fields, where the latter includes the distribution of convective transport, with condensate evaporation playing a minor role (Sherwood 1996; Pierrehumbert and Roca 1998; Galewsky et al. 2005; Sherwood and Meyer 2006; Wright et al. 2009).

Unsaturated air parcels conserve specific humidity. To the extent that condensate evaporation is unimportant, the specific humidity in unsaturated air equals the saturation specific humidity at the point at which it was last saturated. Galewsky et al. (2005, hereafter GSH) used "tracers of last saturation" to trace the pathways taken by air parcels since their points of last saturation. This technique provides insight into the ways in which the circulation and temperature fields together determine

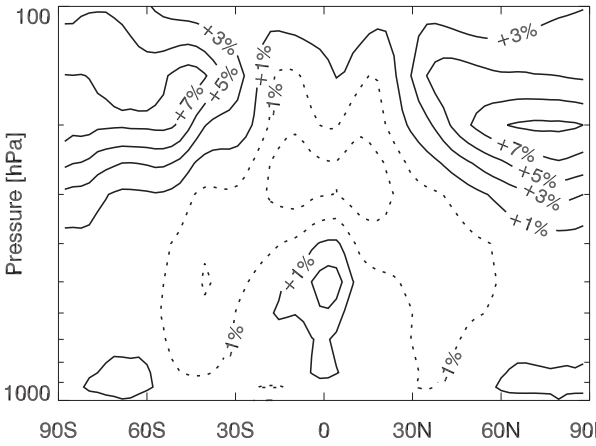

FIG. 1. Zonal mean changes in RH averaged over 10 different slab-ocean GCMs. Dotted contours represent decreases in the $2 \times CO_2$ runs as compared to the control runs. Contour intervals are 2% RH; the first dashed contour represents a 1% absolute decrease in RH and the first solid contour represents a 1% absolute increase in RH.

the distributions of atmospheric specific and relative humidities. Here, we apply an updated formulation of this tracer technique to the output of two integrations of a GCM, one of which simulates the modern climate and one of which simulates a climate with doubled CO_2. The results help to establish the relative influences of shifts in atmospheric circulation and convective transport as compared to inhomogeneous changes in temperature on the characteristic RH response shown in Fig. 1.

2. Model configuration

This study employs a two-level global modeling procedure to investigate the mechanisms behind relative humidity change in a warmer climate. First, a GCM is run to provide 6-hourly circulation and temperature fields that are representative of both a modern (CTL) and doubled CO_2 (WRM) climate. These meteorology fields are then used as inputs to a global tracer transport model, which includes an independent hydrologic cycle and is outfitted with a last saturation tracer scheme (GSH; Hurley and Galewsky 2010a,b).

a. General circulation model

The base meteorology for this study is generated by two integrations of the Goddard Institute for Space Studies (GISS) ModelE (Schmidt et al. 2006). The first of these, designated CTL, uses atmosphere and ocean conditions that are consistent with the year 1979, including greenhouse gas concentrations and sea surface temperatures. The second simulation is designated WRM, and is performed using a slab-ocean version of the model with the atmospheric CO_2 doubled from the

1979 value at the outset. The concentration of atmospheric CO_2 is held constant at 337.1 ppmv for the CTL simulation and 674.2 ppmv for the WRM simulation.

Both model simulations are run at 2° × 2.5° latitude–longitude resolution with 20 vertical levels. Advection of temperature and water vapor conserves the potential enthalpy and mass, and is computed using a quadratic upstream scheme with nine higher-order moments (Prather 1986). This yields an effective tracer resolution of approximately 0.7° × 0.8°. The model physics and radiation are described in detail by Schmidt et al. (2006).

The sea surface temperatures and sea ice extent for the CTL simulation follow a fixed annual cycle averaged over 1975–84, with all other boundary conditions set to 1979 values, as discussed by Schmidt et al. (2006). This simulation is run for 10 yr; output from the last 5 yr is used for this analysis.

The WRM simulation is similar to the CTL simulation, with the addition of a mixed layer heat flux model (q-flux). The initial mixed layer heat transport is prescribed using implied values from a 5-yr climatology generated during the CTL simulation. The net global heating at the surface during the CTL run is 0.09 W m^{-2}, well within the ±0.5 W m^{-2} threshold recommended for a q-flux setup run (Schmidt et al. 2006). The mixed layer depth varies according to a fixed seasonal cycle and is assumed to be isothermal with depth. Energy is conserved by incorporating fluxes between the mixed layer and a deeper layer between the base of the current mixed layer and the base of the mixed layer at its annual maximum depth. The sea surface temperatures and sea ice extent are determined dynamically during the model integration.

Instantaneous meteorological variables are saved every 6 h during each model run. Saved surface variables include orography, surface geopotential, surface temperature, surface pressure, latent heat flux, sensible heat flux, and the zonal and meridional components of the surface stress. Atmospheric variables are saved at all 20 vertical levels and include the temperature, specific humidity, and zonal and meridional winds. For compatibility with the tracer transport model, these data are interpolated from the ModelE's 2° × 2.5° latitude–longitude grid onto a T42 Gaussian grid using bilinear interpolation. The vertical coordinate is unchanged.

Relative humidity is calculated from the ModelE results using the modified formulas for saturation vapor pressure provided by the World Meteorological Organization (WMO 1988), with a linear transition from liquid to ice between $T = 273.16$ and 253.16 K. Note that this differs from the ModelE diagnostic contributed to the CMIP3 archive, for which RH is calculated with respect to liquid water everywhere. We have chosen this formulation for consistency with the other models used in this study.

b. Tracer transport model

Tracer transport is accomplished using the offline Model for Atmospheric Transport and Chemistry (MATCH) developed at the National Center for Atmospheric Research (NCAR) (Rasch et al. 1997). The MATCH model uses a semi-Lagrangian advection scheme, and includes an independent hydrologic cycle with parameterizations for cloud physics and convection.

The MATCH integrations presented here are performed using a 30-min time step, with linear interpolation between the 6-hourly meteorological fields. The model is run on a T42 Gaussian horizontal grid with 20 hybrid sigma vertical levels, matching the input meteorological data. Tracer advection is calculated using a semi-Lagrangian transport scheme with enforced mass conservation (Rasch and Williamson 1990; Rasch et al. 1995). Subgrid-scale turbulent mixing is represented by a vertical eddy diffusion parameterization.

The parameterizations for clouds and convection are based on those developed for version 3 of the NCAR Community Climate Model (CCM3). In particular, MATCH uses the prognostic cloud parameterization presented by Rasch and Kristjansson (1998) and the convection scheme described by Hack et al. (1998). The convective parameterization partitions the convective transport into deep convection (Zhang and McFarlane 1995) and shallow convection (Hack 1994). Tracers are advected both within the convective parameterization and by the large-scale circulation.

The relative humidity in MATCH is also calculated using the formulation given by the WMO (1988), although the transition from saturation with respect to liquid to saturation with respect to ice differs from that used for the ModelE results. In MATCH, this transition is accomplished by using an empirical fifth-order polynomial fit between $T = 273.16$ and 253.16 K.

c. Tracer formulation

The base formulation of the tracers of last saturation follows that of GSH. Specifically, a set of N zonally symmetric tracer domains is chosen to cover the global troposphere. The overall distribution of tracer domains is shown as dashed gray lines in Fig. 2. Note that each tracer covers a limited range in latitude and a limited range in pressure, but is global in longitude. Each grid point between the surface and 110 hPa in the model is contained by a domain. For any given grid point, we will call the tracer associated with its containing domain the local tracer ($\mathcal{L}$) and all other tracers will be nonlocal tracers ($\mathcal{T}_i$; $i = 1, \ldots, N - 1$).

All tracers are initially set to zero. During model integration, whenever the free-tropospheric RH exceeds

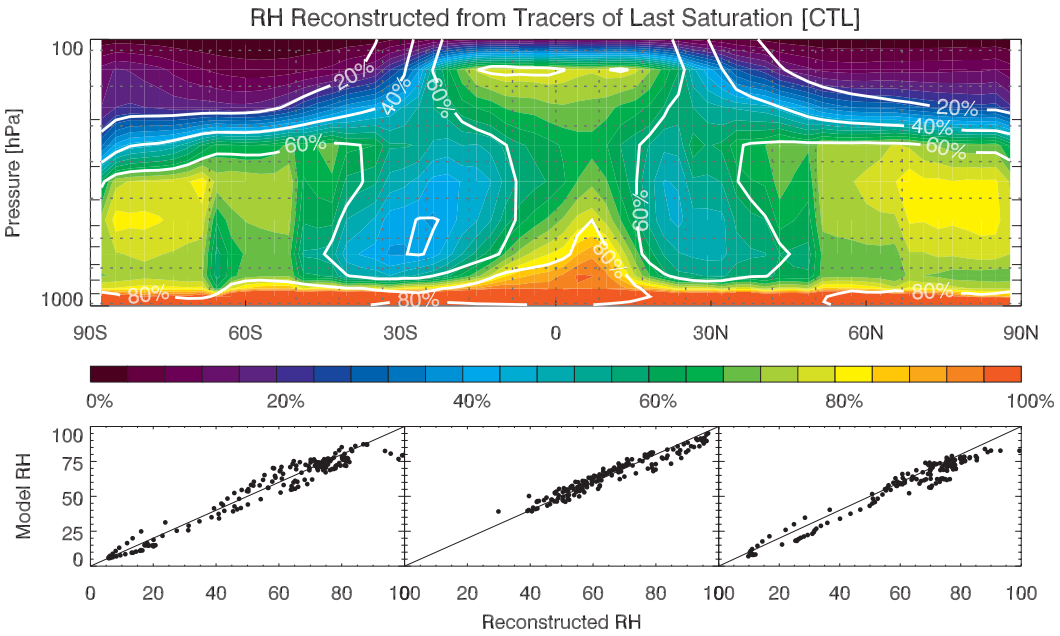

FIG. 2. Zonal mean relative humidity reconstructed from the last saturation tracers for the CTL run (filled contours), overplotted with RH as calculated by the MATCH internal hydrologic cycle (white contours; contour interval is 20% RH). Dashed gray lines show the distribution of the tracer domains. (bottom) A point-by-point comparison between the two modeled and reconstructed RHs for the latitude bands matching the abscissa above. Left to right, these regions correspond to 90°–30°S, 30°S–30°N, and 30°–90°N. Black solid lines represent a 1:1 correspondence and are not fits to the data.

a saturation threshold of 90%, the local tracer is set to one and all nonlocal tracers are set to zero at that point:

$$\mathcal{L}(\lambda, \phi, p, t) = 1$$
$$\mathcal{T}_i(\lambda, \phi, p, t) = 0|_{i=1,\ldots,N-1}$$
$$\mathcal{S}(\lambda, \phi, p, t) = 0$$
$$\mathcal{S}_{\text{amt}}(\lambda, \phi, p, t) = 0,$$

where λ and ϕ represent the longitude and latitude of the saturated grid cell, respectively; p represents the vertical coordinate; and t denotes the model time step. As defined below, $\mathcal{S}$ and $\mathcal{S}_{\text{amt}}$ are the surface source tracers. Whenever the local RH is below the threshold value, the tracers of last saturation are permitted to advect and mix unchanged. An RH threshold of 90% is chosen to reflect the fact that saturation operates at spatial scales well below the grid scale; that is, some air parcels in the grid volume may be at saturation even though the mean RH for the entire volume is below 100%. The results of the tracer calculations presented in this paper are qualitatively insensitive within reasonable perturbations to this threshold (±10% RH). This insensitivity to reasonable perturbations was also noted by GSH, and results from the sharp gradients between locations with high and low RH. That is, the locations that experience 80% RH are very similar to the locations that experience 90% RH, which are in turn quite similar to the locations that experience 100% RH. Shifting the humidity threshold down (up) leads to a slightly more dilute (concentrated) tracer distribution, but does not change the qualitative nature of the results (i.e., the large-scale distribution of where air is last saturated). We chose 90% because it gives the best reconstruction. Using a saturation threshold of 80% results in a slight dry bias in the reconstruction (~−3% RH), while using a threshold of 100% results in a slight moist bias (~+7% RH). Saturation for the tracer scheme is determined according to MATCH's internal hydrologic cycle, rather than the GCM output.

The evaporative source at the surface is incorporated by treating the lowest model layer separately: all last saturation tracers in this layer are set to zero and a source tracer ($\mathcal{S}$) is defined with a value equal to the current specific humidity (q) in the grid cell:

$$\mathcal{T}_i(\lambda, \phi, p_b, t) = 0|_{i=1,\ldots,N}$$
$$\mathcal{S}(\lambda, \phi, p_b, t) = q(\lambda, \phi, p_b, t)$$
$$\mathcal{S}_{\text{amt}}(\lambda, \phi, p_b, t) = 1,$$

where p_b denotes the lowest model layer. For bookkeeping purposes we also define a source amount tracer

$\mathcal{S}_{\text{amt}}$ that follows the definitions of $\mathcal{L}$ and $\mathcal{T}$. Note that $\mathcal{S}_{\text{amt}}$ is by definition the local tracer $\mathcal{L}$ in the lowest model layer, so that there are N nonlocal tracers rather than $N - 1$. The source tracer is permitted to mix, so that the value of $\mathcal{S}$ at any location may reflect several excursions to the surface.

The local specific humidity $q(\lambda, \phi, p, t)$ can then be reconstructed via the linear combination

$$q(\lambda, \phi, p, t) = \mathcal{L}(\lambda, \phi, p, t)q^*(\lambda, \phi, p, t) + \sum_{i}^{N-1} \mathcal{T}_i(\lambda, \phi, p, t)\langle q_i^* \rangle + \mathcal{S}(\lambda, \phi, p, t), \quad (1)$$

where $q^*(\lambda, \phi, p, t)$ is the local saturation mixing ratio and $\langle q_i^* \rangle$ represents the density-weighted mean saturation specific humidity for tracer domain i. As with the ModelE results, the saturation specific humidity in the tracer scheme is calculated using the formulas provided by the WMO (1988), with a linear transition from saturation over liquid to saturation over ice as described in section 2a.

The tracers generally obey the constraint

$$\mathcal{L}(\lambda, \phi, p, t) + \sum_{i}^{N-1} \mathcal{T}_i(\lambda, \phi, p, t) + \mathcal{S}_{\text{amt}}(\lambda, \phi, p, t) = 1 \quad (2)$$

in our simulations; after a brief initial spinup period, significant deviations from this constraint occur only above the uppermost tracer boundary at 110 hPa. RH is then reconstructed as

$$\text{RH}(\lambda, \phi, p, t) = \frac{q(\lambda, \phi, p, t)}{q^*(\lambda, \phi, p, t)}, \quad (3)$$

with $q(\lambda, \phi, p, t)$ determined by Eq. (1). GSH discuss technical issues involved in this reconstruction and quantify several sources of error. Note that although the tracers are used to reconstruct the water vapor field, they do not directly represent the water vapor itself; the concentration of tracer $\mathcal{T}_i$ in a grid cell is the fraction of air in that grid cell that was last saturated in domain i.

Figure 2 shows a direct comparison between the modeled and reconstructed zonal mean RH fields for the MATCH integration using CTL meteorological fields as input. The qualitative patterns match up remarkably well, and the point-to-point comparison also indicates excellent agreement in both the tropics and extratropics. Excluding the model layers below 900 hPa and above 110 hPa, where boundary layer or stratospheric influences render the reconstruction less effective, the Pearson correlation coefficients between modeled and reconstructed RHs are greater than 0.95. The reconstruction breaks down somewhat near the poles, as the tracer domains get larger. This pixilation effect is discussed in GSH.

Figure 2 includes two adjustments to the tracer scheme presented by GSH. First, we have altered the distribution of the tracer domains (defined by dotted black lines). Although the chosen domains remain zonally axisymmetric, they now provide global coverage (as opposed to 50°S–50°N in GSH). The horizontal resolution of the tracer domains is approximately 5° latitude equatorward of 50°, with a ~15° domain out to 65° and a 25° domain extending to the pole in both hemispheres. We also increase the tracer domain resolution with altitude, so that the vertical domain sizes are roughly equivalent in $\log(p)$ space. This allows us to better diagnose the mechanisms influencing the upper-tropospheric humidity, particularly in the tropics. Second, we have adjusted the online tracer calculation to correct for extremely high upper-tropospheric humidities (in some locations supersaturation with respect to liquid water) in the reconstructions obtained using the GSH formulation. This bias resulted from the transport of trace amounts of source and lower-tropospheric tracers into the upper troposphere. Although these tracer concentrations were quite small, they were associated with values of $\langle q^* \rangle$ that were comparatively quite high and, thus, exerted a disproportionately large influence on the reconstructed humidity. We have addressed this issue by including an online calculation of the density-weighted mean temperature $\langle T_i(t) \rangle$ for each tracer domain, which is dependent only on time. Thus, $\langle T_i(t) \rangle$ is an estimate of the remote temperature at which an air parcel containing only $\mathcal{T}_i$ was saturated. At each time step, we loop through the grid cells and assess whether the local temperature $T(\lambda, \phi, p, t)$ is less than the tracer domain temperature $\langle T_i(t) \rangle$ for any tracer $\mathcal{T}_i$ with nonzero concentration in that grid cell. If so, then the entirety of tracer $\mathcal{T}_i$ is converted to local tracer $\mathcal{L}$:

$$\mathcal{L}(\lambda, \phi, p, t) = \mathcal{L}(\lambda, \phi, p, t) + \mathcal{T}_i(\lambda, \phi, p, t)|_{\langle T_i(t) \rangle > T(\lambda, \phi, p, t)}$$

$$\mathcal{T}_i(\lambda, \phi, p, t) = 0|_{\langle T_i(t) \rangle > T(\lambda, \phi, p, t)}.$$

This adjustment to the tracer calculation compensates for any spurious vertical tracer transport that could lead to supersaturation in the reconstruction, and is physically equivalent to assuming that condensate is immediately removed at the subgrid scale in both parameterized convective updrafts and vertical advection.

3. Simulated climate changes

Investigation of the mechanisms underlying the characteristic pattern shown in the multimodel mean RH

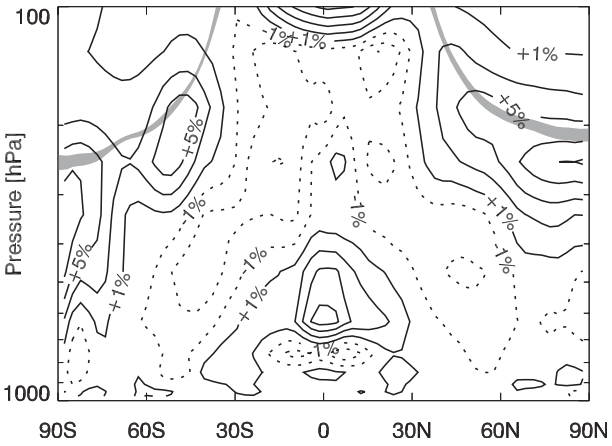

FIG. 3. Changes in zonal mean RH between the WRM and CTL runs of the GISS ModelE. Contour intervals are 2% RH as in Fig. 1. The gray shading represents the range of pressures between the 5-yr mean CTL tropopause pressure and the 5-yr mean WRM tropopause pressure, calculated according to the WMO definition of tropopause (WMO 1957).

changes (Fig. 1) requires meteorological output from a GCM that exhibits this pattern of change as climate warms. Figure 3 shows the RH difference between the WRM and CTL runs of the GISS ModelE. The changes between these two simulations agree quite well with the multimodel mean change qualitatively, and are of similar magnitude. This indicates that the ModelE is a reasonable choice for examining the root causes behind the pattern of RH changes.

A number of studies have examined the distribution of circulation and temperature changes in the model simulations submitted to the CMIP3 intercomparison project (e.g., Randall et al. 2007; Lorenz and DeWeaver 2007b; Vecchi and Soden 2007; Lu et al. 2008; Gastineau et al. 2008). In general, these studies find that the tropopause height increases; the tropical overturning circulation expands poleward, deepens, and weakens; the extratropical jets shift poleward; the lapse rate of temperature with altitude is reduced; and the equator-to-pole temperature gradient in the upper troposphere is increased. These findings are consistent with observational studies that focus on recent historical trends in atmospheric temperature and circulation (e.g., Santer et al. 2003; Seidel and Randel 2006; Hu and Fu 2007; Allen and Sherwood 2008; Santer et al. 2008), although there is some disagreement with observed trends in the strength and rate of the poleward expansion of the Hadley cell (Mitas and Clement 2006; Johanson and Fu 2009).

Figure 4 shows simulated circulation and temperature changes between the CTL and WRM runs of the ModelE GCM. The troposphere warms nearly everywhere (Fig. 4a, shading), with the strongest warming in

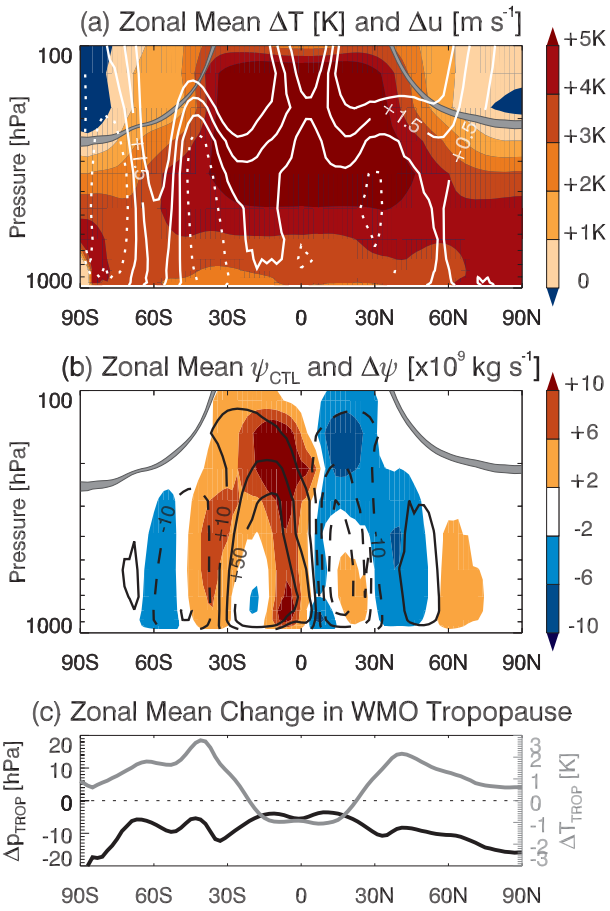

FIG. 4. (a) Annual mean zonal mean changes in simulated temperature and zonal wind in the GISS ModelE. Shading shows temperature with a contour interval of 1 K; white contours show zonal wind with a contour interval of 1 m s^{-1}, with dotted contours representing decreases. (b) Zonal mean streamfunction from the CTL simulation (black contours) and changes in the zonal mean streamfunction between the CTL and WRM simulations (shading). The zonal mean streamfunction is shown with a contour interval of 20×10^9 kg s^{-1}. Dashed contours (blue shading) represent (more) clockwise circulation and solid contours (red shading) represent (more) counterclockwise circulation. (c) Annual mean zonal mean changes in the pressure and temperature of the model-simulated tropopause, according to the WMO definition. The range of zonal mean tropopause pressures (as in Fig. 3) for both simulations is shaded in gray in (a) and (b) for reference.

the tropical upper troposphere. This reduces the tropospheric lapse rate in the tropics and subtropics. The equator-to-pole temperature gradient is reduced in the lower troposphere and increased in the upper troposphere. Changes in zonal mean streamfunction (Fig. 4b, shading) indicate that the Hadley cell expands poleward and deepens, and that tropical deep convection detrains at a higher level. Taken together with the warming in the tropical upper troposphere, the latter is at least qualitatively consistent with the fixed anvil temperature

hypothesis, which postulates that tropical convective detrainment is constrained to occur at roughly the same temperature as climate changes (Hartmann and Larson 2002). The strength of the Hadley circulation is very similar between the CTL and WRM slab-ocean simulations of the ModelE, with a slight strengthening or weakening depending on the metric used. Vecchi and Soden (2007) and others report that the tropical overturning circulation weakens in the CMIP3 models; however, this decrease is primarily manifested in the Walker circulation rather than the Hadley cell. The strength of the longitudinal Walker circulation in the ModelE decreases in our WRM simulation (not shown), consistent with this consensus. Gastineau et al. (2008) show that changes in the strength of the Hadley cell are much more variable in CMIP3 models. Within the context of current scientific understanding, the representation of changes in the strength of the tropical overturning circulation is reasonable and consistent with these expectations.

Shifts in the zonal mean zonal wind (Fig. 4a, white contours) indicate that the extratropical jets intensify and shift poleward in the ModelE, consistent with the CMIP3 multimodel mean (Lorenz and DeWeaver 2007b). Figure 4c shows the zonal mean tropopause height and temperature changes for the WMO (1957) tropopause. Tropopause pressure (height) decreases (increases) globally with a minimum shift in the tropics, while tropopause temperature increases everywhere but in the deep tropics, which exhibit a slight cooling trend. Both of these are consistent with the CMIP3 multimodel means (Lorenz and DeWeaver 2007b) and with observations of recent historical trends (Santer et al. 2003).

If multimodel mean trends (which in some cases are consistent with recent historical trends in the observations) are considered as a baseline consensus, the circulation and temperature changes simulated by the GISS ModelE are generally consistent with this consensus. One important caveat is that the ozone levels in the simulations presented here are fixed at 1979 values, so the impacts of stratospheric ozone recovery on circulation and temperature changes (Son et al. 2008, 2009) are not included in this analysis.

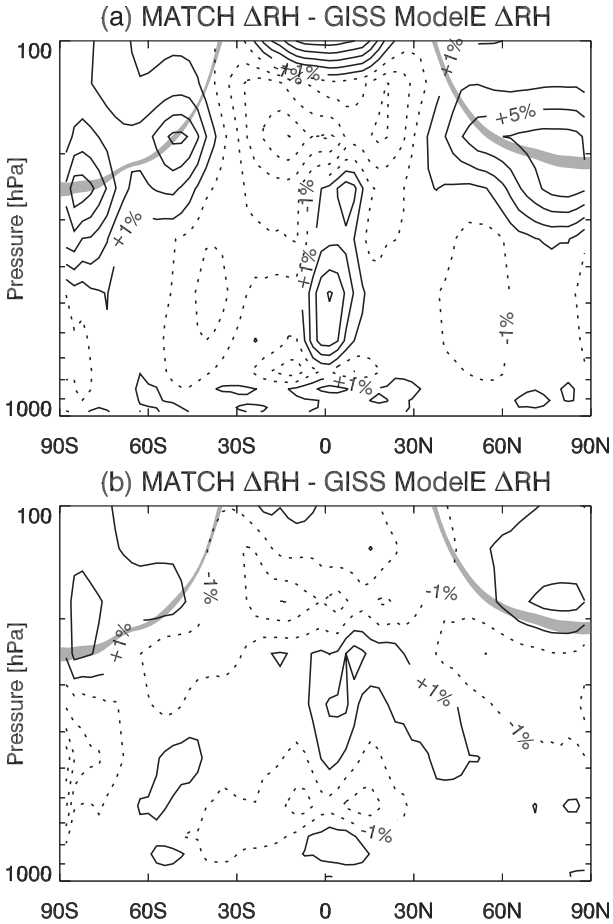

FIG. 5. (a) Zonal mean changes in RH between the CTL and WRM runs determined by the MATCH internal hydrologic cycle using the prescribed temperatures and circulation from the GCM simulations. Contour intervals are 2% RH as in Fig. 1. (b) Differences between the changes in RH simulated by the ModelE and the RH simulated by MATCH. Contour intervals are 2%; negative values mean that MATCH predicts a stronger decrease or weaker increase. The range of zonal mean tropopause pressures (as in Fig. 3) is shaded in gray in both panels for reference.

4. Tracer model experiments

The GCM simulations provide a means by which to describe the control and doubled CO_2 climates. The MATCH tracer transport model is employed at the second level because it affords greater flexibility. By separating calculations of the tracer distribution from the circulation and temperature fields that determine them, the mechanisms that control the distribution of RH changes can be better identified and isolated. It is therefore important that the results of the MATCH runs using GISS output are similarly able to reproduce the expected pattern of RH change. Figure 5a shows the zonal mean difference of RH between the WRM and CTL runs for the MATCH model hydrologic cycle. The contents of this figure follow the same general pattern and are of similar magnitude to those of Fig. 3. Relative errors between the two sets of simulations are on the order of 20%–25% of the simulated changes in RH (Fig. 5b).

The MATCH runs are forced using ModelE output. This leaves two significant differences between the simulations used to prepare Fig. 3 and those used to prepare Fig. 5: the advection scheme and the hydrologic cycle parameterizations. The close correspondence between

the pattern of RH change in MATCH and that in the GCM suggests that the distribution of RH changes is not strongly sensitive to the details of these two parameterizations. This conclusion is supported by the robust nature of the pattern among the CMIP3 model simulations, which also contain a variety of advection and microphysical parameterizations. We note, however, that the MATCH model (Fig. 5b) and most of the individual CMIP3 models (not shown) indicate larger changes in RH than in the ModelE, particularly in the deep tropics, in the tropical upper troposphere, and along the extratropical tropopause.

In the absence of condensate evaporation, the relative humidity at any given point will remain constant under climate change so long as the saturation mixing ratio changes by the same fraction at the point in question and at the relevant point(s) of last saturation. Loosely speaking (in particular, neglecting the nonlinearity of the Clausius–Clapeyron relation), this would occur over the entire atmosphere if the transport pathways remain relatively constant and the temperature changes are spatially uniform. As discussed above, however, climate model simulations of warming predict shifts in the large-scale circulation and distribution of convective transport, and indicate that temperature changes will have spatial structure (e.g., Randall et al. 2007; Lorenz and DeWeaver 2007b; Lu et al. 2008). We wish to attribute the changes in RH shown in Fig. 1 to these two factors. To what extent are these changes driven by circulation shifts, and to what extent are they driven by spatially inhomogeneous temperature changes?

As a brute force method of separating the roles of circulation and temperature, we run the MATCH model with temperature and circulation fields chosen from different GCM simulations. MATCH is run with WRM temperatures and CTL circulation and vice versa. This is dynamically inconsistent, since the temperature and winds are related through the equations of motion. On the other hand, it is kinematically acceptable for the purpose of diagnosing the mechanisms controlling water vapor; the water vapor simply evolves in space and time according to a given set of temperature and wind fields. This approach leverages the offline tracer transport to separate the temperature and circulation in a way that could not be done in a dynamically consistent calculation.

Figure 6a shows RH changes between the CTL MATCH simulation and a simulation in which the WRM atmospheric temperatures are combined with the CTL circulation. This difference does not show the characteristic horseshoe-shaped pattern of RH decrease throughout the troposphere, particularly in the tropical and subtropical upper troposphere. It does capture the RH increases near the extratropical tropopause and in the

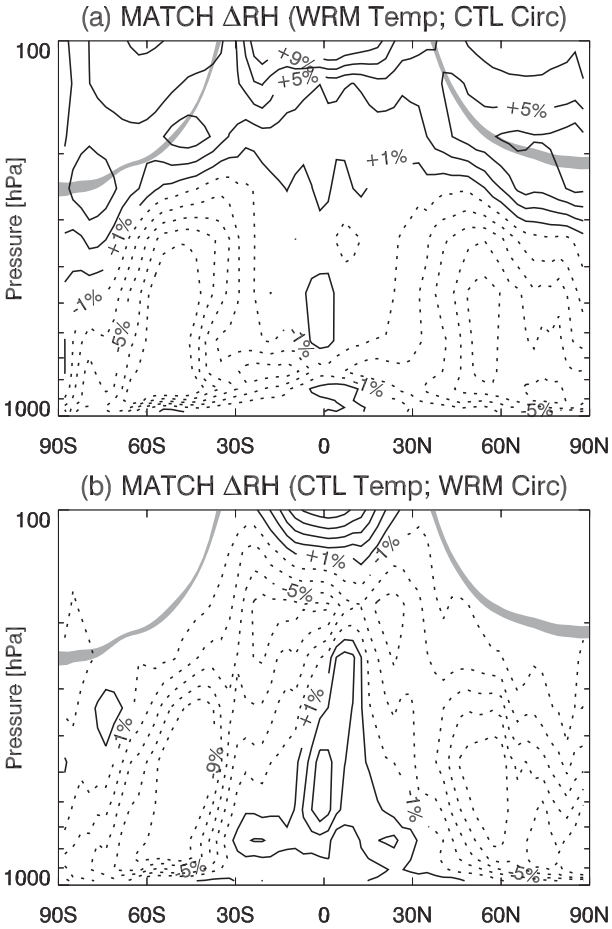

FIG. 6. Zonal mean relative humidity changes in the MATCH hydrologic cycle for (a) a run in which the input files contain WRM temperatures and CTL dynamics and (b) a run in which the input files contain WRM dynamics and CTL temperatures. Contour intervals are 2% RH, as in Fig. 1. The range of zonal mean tropopause pressures (as in Fig. 3) is shaded in gray in both panels for reference.

tropical tropopause layer, however, as well as many aspects of the lower-tropospheric response. Figure 6b shows the same quantity for a MATCH simulation in which the WRM circulation is combined with CTL atmospheric temperatures. In this case, the tropical and subtropical free-tropospheric response is captured quite well, although the RH increase near the extratropical tropopause does not appear. Figure 6 thus suggests that RH changes in the tropical and subtropical troposphere are controlled primarily by circulation changes, whereas the increase near the extratropical tropopause and changes in near-surface RH are controlled primarily by temperature changes.

The high-latitude tropospheric response is far too strong in both perturbation simulations; in fact, Figs. 3 and 5 indicate that changes in these regions should be

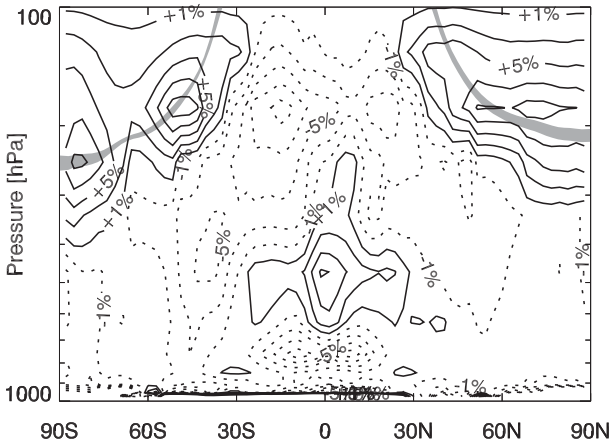

FIG. 7. Annual mean zonal mean changes in RH reconstructed from the last saturation tracers. Contour intervals are 2% RH as in Fig. 1. The range of zonal mean tropopause pressures (as in Fig. 3) is shaded in gray for reference.

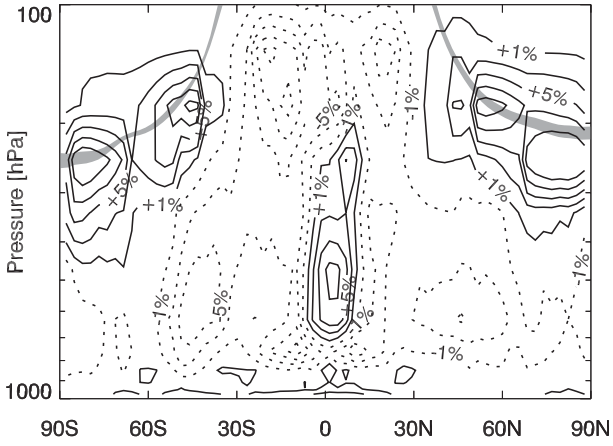

FIG. 8. Annual mean zonal mean changes in local tracer concentration. Contour intervals are 2%; the first dashed contour represents a 1% absolute decrease and the first solid contour represents a 1% absolute increase. The range of zonal mean tropopause pressures (as in Fig. 3) is shaded in gray for reference.

small and of variable sign, rather than the strongly negative response shown in both panels of Fig. 6. This mismatch may be a consequence of removing the strong covariability between the circulation and temperature in the midlatitudes. It could also simply be a result of nonlinearities: tracer transport is linear, while saturation is nonlinear. In the tropics above 200 hPa, the RH response is again too strong, such that both simulations predict RH increases that are similar in sign and magnitude to those in the WRM simulation. In the simulation with WRM temperature and CTL circulation, this increase is spatially quite uniform, and likely due to sharpened temperature gradients near the tropopause (Fig. 4). In the simulation with CTL temperature and WRM circulation, the RH increases are confined primarily to convective regions, such as over the ITCZ and ascending branches of the Walker circulation, and are likely related to changes in the overturning circulation. While these simulations predict an increase in the zonal mean RH in both cases, they do so for different reasons. Thus, the results in Figs. 6a and 6b need not add up to those in Fig. 5 in general, although they do so (approximately) in the tropical and subtropical troposphere, and at the extratropical tropopause.

5. Last saturation tracers

Figure 2 indicates that the tracer reconstruction of RH agrees both qualitatively and quantitatively with the RH simulated by MATCH using the CTL meteorology. This agreement translates to RH changes between the CTL and WRM runs, as shown in Fig. 7. The reconstruction captures much of the structure observed in both the GISS model (Fig. 3) and the online MATCH hydrologic cycle (Fig. 5), in particular the horseshoe-shaped RH decrease and the increases in the tropical middle troposphere and the extratropical tropopause layer. The tracer reconstruction of RH does not capture the increase of RH in the tropical tropopause layer. This is because the reconstructed RH is approximately 100% in both simulations. Because the tracer domains are global in longitude, the convective and nonconvective regions cannot be effectively distinguished, so that the convective regions set the local tracer $\mathcal{L}$ to be approximately 1 throughout the domain. Since the nonconvective regions were typically last saturated in the convective regions within the domain, they appear saturated in the reconstruction as well, leaving no potential for an increase in the zonal mean RH as seen in Figs. 1, 3, and 5.

The broad agreement between the changes in the simulated and reconstructed RH provides a check on the consistency of the tracer formulation. Since the RH reconstruction successfully captures the pattern of RH changes in the warmer climate, the tracers can be applied to diagnose some of the relevant mechanisms.

A simple diagnostic that can be constructed from the last saturation tracers involves separating the contribution of the changes in the local tracer $\mathcal{L}(\lambda, \phi, p)$, which represents the fraction of air in a grid cell (λ, ϕ, p) that was last saturated with the tracer domain containing that cell, from that of all the nonlocal tracers $\sum_i^{N-1} T_i(\lambda, \phi, p)$. Although it only makes use of a small fraction of the information carried by the tracers, this diagnostic appears to explain much of the spatial structure and sign of the RH change. Figure 8 shows the zonal and time mean changes in the concentration of $\mathcal{L}$. The pattern of changes in $\mathcal{L}$ agrees remarkably well with the

pattern of changes in the simulated RH. In particular, if the proportion of air that is last saturated locally decreases, then the RH tends to decrease, and vice versa. This correspondence is expected, as air that was last saturated nearby is likely to be closer to saturation now.

The close correspondence between the pattern of changes in RH and the pattern of changes in $\mathcal{L}$ is particularly relevant near the extratropical tropopause in both hemispheres. These regions experience an increase in the concentration of local tracer $\mathcal{L}$, which acts to increase the RH by increasing the contribution of $q^*(\phi, p)$ to $q(\phi, p)$ [Eq. (1)]. This is driven in large part by the gradient of temperature changes in the upper troposphere. In the CTL simulation, humidity near the extratropical tropopause is determined to a significant extent by equatorward zones of last saturation. The greatest warming occurs in the tropical upper troposphere, with gradually diminished warming toward the poles (Fig. 4). This pattern of warming results in an increase in the equator-to-pole temperature gradient in the upper troposphere and along the extratropical tropopause. Local temperatures in the extratropical tropopause layer have thus cooled relative to any equatorward zones of last saturation. This leads to an increase in the occurrence of local saturation, which drives an increase in the RH. Figure 9a shows the mean concentration of individual tracers in the CTL simulation for an example point along the extratropical tropopause. Figure 9b shows how these concentrations change in the WRM simulation, and illustrates the shift from equatorward last saturation to local saturation that occurs in this region. This increase of local saturation may in turn lead to an increase in the occurrence of high thin clouds near the extratropical tropopause, with implications for cloud radiative forcing. Examination of the ModelE output indicates that the zonal mean ice cloud cover in these regions increases by between 1% and 5% (not shown), a result that is consistent with the CMIP3 multimodel mean changes in Arctic high cloud cover presented by Vavrus et al. (2009).

As with the MATCH perturbation simulations presented in section 4, the tracer reconstruction of RH [Eqs. (1) and (3)] can be broken down into two components: one representing the circulation (the tracers) and one representing temperatures (q^*) (cf. Hurley and Galewsky 2010a). This attribution is not clean, because the temperature field influences the tracers as well; if the circulation were held fixed, changes in temperature would change the locations at which saturation occurs, thus changing the tracer fields. Nonetheless, the correspondence of many aspects of the results below with those in the previous section—in which an entirely different method with different limitations was used to separate

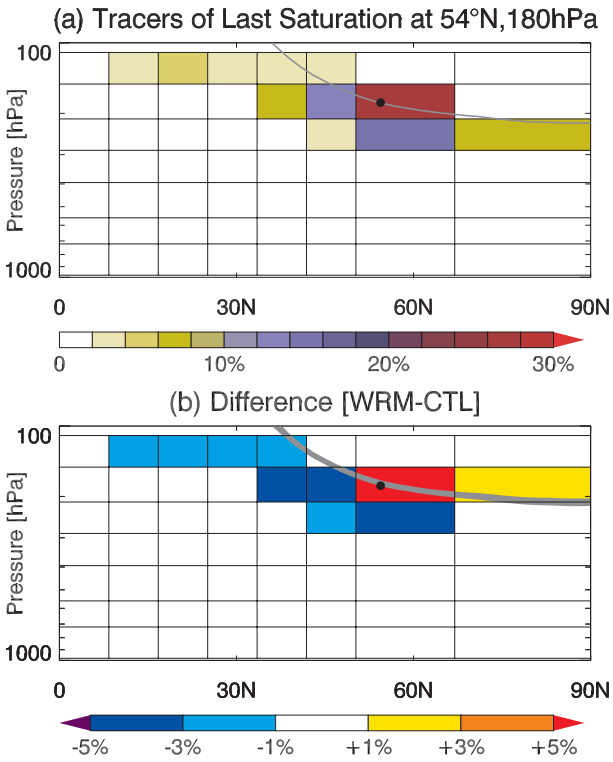

FIG. 9. (a) Zonal mean concentration of tracers at 54.42°N and 180 hPa according to the CTL simulation. Black outlines show the boundaries of individual tracer domains; shading shows the concentration of tracer. The gray line represents the zonal mean tropopause from the CTL simulation according to the WMO definition (WMO 1957). (b) The change in zonal mean tracer concentrations at 54.42°N and 180 hPa between the CTL and WRM simulations. Gray shading represents the range of zonal mean tropopause pressures, as in Fig. 3.

the roles of temperature and circulation—suggests that there is some validity to the conclusions.

Figure 10 shows zonal mean changes in reconstructed RH using WRM calculations of q^* with CTL tracers (Fig. 10a), and WRM tracers with CTL q^* (Fig. 10b).

These results support the conclusions drawn from Fig. 6. In particular, circulation changes appear to play a dominant role in the RH changes in the tropical and subtropical troposphere, while inhomogeneous changes in temperature appear to control the RH increase near the extratropical tropopause. These responses can be illustrated in further detail using the last saturation tracer distributions.

Figure 11 shows changes in the concentration of two sets of tracers in the tropical upper troposphere. The first set (Fig. 11, left panels) indicates air that was last saturated in the layer between 288 and 212 hPa, while the second set (Fig. 11, right panels) indicates air that was last saturated in the layer immediately above (212–150 hPa). There is a dramatic transfer of influence from the lower level to the upper one in the WRM simulation; the

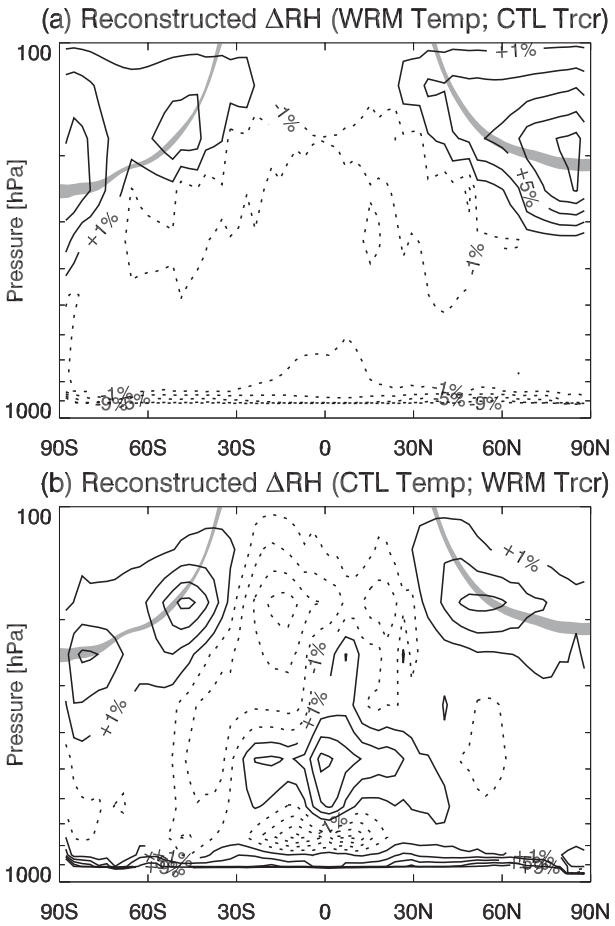

FIG. 10. Zonal mean changes in RH reconstructed from the last saturation tracers using (a) WRM temperatures and CTL tracers and (b) WRM tracers and CTL temperatures. Contour intervals are 2%, as in Fig. 1. The range of zonal mean tropopause pressures (as in Fig. 3) is shaded in gray in both panels for reference.

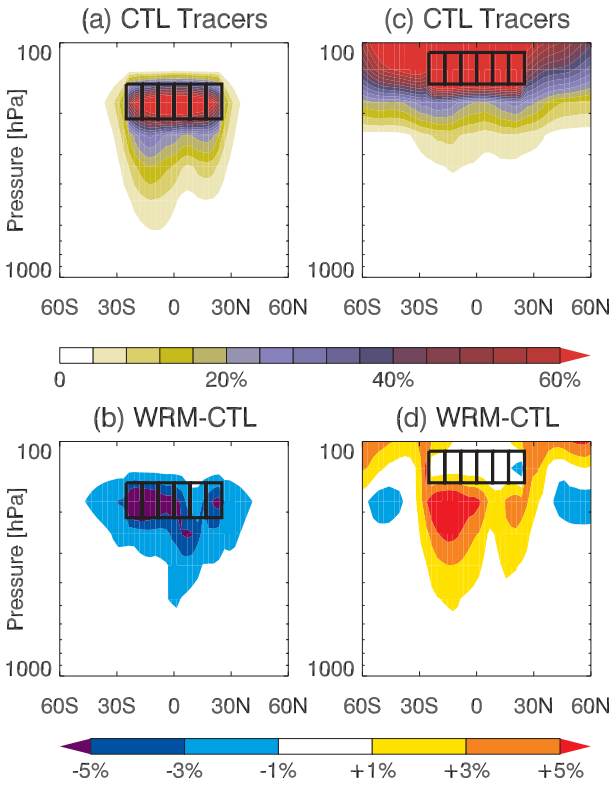

FIG. 11. (a),(c) The percentage of air parcels that reached last saturation within the outlined tracer domains, and (b),(d) the absolute differences in this percentage between the WRM and CTL MATCH simulations. The left panels show tracers indicating last saturation in the 288–212-hPa layer between approximately 25°S and 25°N; the right panels show tracers indicating last saturation with the same latitude range but for the 212–150-hPa pressure layer.

concentration of the lower set of tracers decreases throughout the tropical troposphere and appears to be largely replaced by tracer from the upper set. This transfer represents an upward shift in the zones of last saturation throughout the tropics, consistent with an upward shift in the tropopause as shown in Fig. 4b, and as expected from the fixed anvil temperature hypothesis (Hartmann and Larson 2002). The minimum in tracer concentration change within the layer of interest in Fig. 11d occurs because the tracers in this region are composed of nearly 100% local tracer ($\mathcal{L}$) in both the CTL and WRM simulations, so that there is no potential for increase.

Figure 12 shows changes in the tracer concentrations associated with humidity in the subtropical free troposphere. Figure 12 also shows that the extratropical zones of last saturation for the subtropical dry zones shift upward and poleward in the warmer climate (see also Hurley and Galewsky 2010b). These changes are consistent with an expansion of the tropical Hadley cell and a poleward shift in the extratropical jets, as shown in Fig. 4. In particular, both circulation and tracer shifts are more pronounced in the Southern Hemisphere. The decrease of RH in the Southern Hemisphere is also stronger in the ModelE, MATCH, tracer reconstruction, and CMIP3 multimodel mean. As mentioned above, these model runs do not include stratospheric ozone recovery, so these asymmetries are likely due to differences in the distribution of the continents and orography between the Northern and Southern Hemispheres.

6. Summary

The zonal mean signature of the relative humidity response to a doubling of CO_2 is qualitatively robust across climate models. This signature is characterized by a horseshoe-shaped decrease of relative humidity in the tropical upper troposphere, subtropics, and extratropical

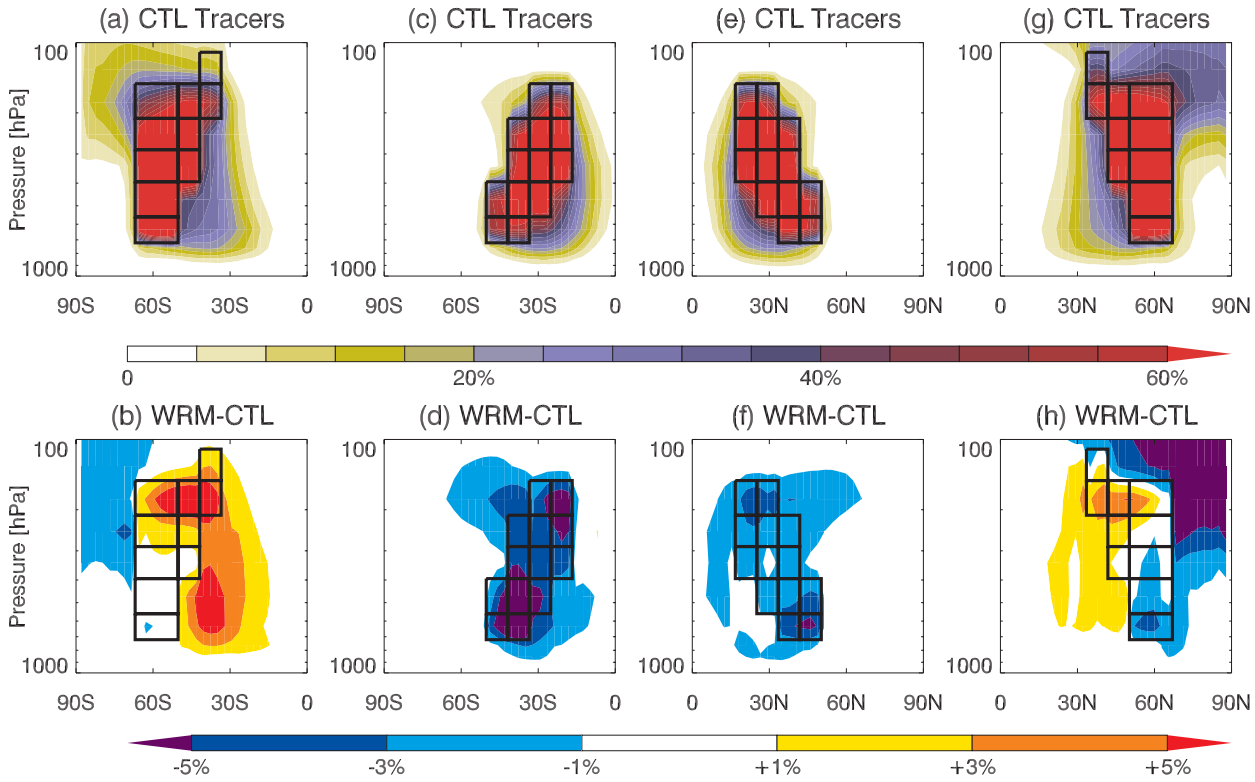

FIG. 12. As in Fig. 11, but for tracers controlling humidity in the (a)–(d) Southern Hemisphere subtropics and (e)–(h) Northern Hemisphere subtropics.

free troposphere, with a stronger decrease in the Southern Hemisphere, and an increase in RH in the tropical midtroposphere and extratropical tropopause layer.

Two climate model simulations are performed: one of modern climate and one with doubled CO_2. The humidity and circulation changes between these simulations are generally representative of the model simulations submitted to the CMIP3 model intercomparison project. Six-hourly meteorological output from the GCM simulations is used to drive a three-dimensional offline tracer transport model that contains both an independent hydrologic cycle and a zonally axisymmetric last saturation tracer scheme. The tracers are capable of quantitatively and qualitatively capturing both the modeled RH field and the pattern of the RH response to warming. Two different methods are then used to separate the role of circulation and transport from that of temperature.

Two perturbation simulations are performed using the tracer transport model that pairs the modern circulation with the doubled CO_2 temperatures and vice versa. The results of these simulations indicate that the horseshoe-shaped pattern of the RH decrease is driven primarily by circulation shifts, particularly in the tropical and subtropical upper troposphere, while the RH increases near the extratropical tropopause and changes near the surface appear to be controlled by inhomogeneities in the temperature response to a doubling of CO_2. Similar conclusions are reached by manipulating the tracer reconstruction of RH to better differentiate between the contributions of circulation, local temperature, and nonlocal temperatures.

Much of the zonal mean RH response is captured by the binary distinction between local and nonlocal last saturation tracers; that is, if the amount of air in a grid cell that was last saturated nearby increases, the RH generally increases as well, and vice versa. This correspondence is particularly relevant near the extratropical tropopause, which exhibits an increase in RH that is associated primarily with an increase in local last saturation. Both of these are driven in large part by the gradient of temperature changes in the upper troposphere and at the tropopause, and lead to an increase in high clouds with substantial implications for cloud radiative forcing in the extratropics and Polar regions.

The last saturation tracers are used to illustrate the influence of simulated circulation shifts on the zonal mean RH. In particular, last saturation zones for the tropical upper troposphere shift upward in the doubled CO_2 climate, resulting in a RH decrease. This shift is consistent with the upward shift of the tropopause and the

deepening of tropical convection associated with the Hadley cell observed in the simulation. Similarly, the tracers of last saturation that control RH in the subtropical dry zones shift upward and poleward in the warmer climate, consistent with a poleward expansion of the tropical circulation and a poleward shift of the extratropical jets.

The response of relative humidity to a doubling of atmospheric CO_2 is robust among current climate models, as are the changes in circulation and temperature that this study identifies as key drivers of that response (e.g., Randall et al. 2007; Lorenz and DeWeaver 2007b; Vecchi and Soden 2007; Lu et al. 2008; Gastineau et al. 2008). Moreover, independent studies of global and regional simulations of RH changes in a warmer climate have reached similar conclusions regarding the mechanisms that underlie these changes (Sherwood et al. 2010; Hurley and Galewsky 2010b). We are thus confident that the results of this study are broadly representative of the RH response and its fundamental causes in current climate model projections of warming. Observational studies of recent historical trends in temperature and circulation are generally consistent with model-simulated trends (e.g., Santer et al. 2003; Seidel and Randel 2006; Hu and Fu 2007; Allen and Sherwood 2008; Santer et al. 2008), although significant uncertainties remain regarding the ability of climate models to accurately reproduce the full character and amplitude of these changes (e.g., Mitas and Clement 2006; Johanson and Fu 2009). These uncertainties must necessarily be considered when assessing the applicability of these results to the natural world. In practice, however, it is not possible to independently prove whether individual simulations of future climate are correct or not. Robust model predictions, such as those regarding the zonal mean response of RH humidity to increases in well-mixed greenhouse gases and the changes in circulation and temperature that drive it, represent our best guess as to how the physical climate system will respond to external forcings.

Acknowledgments. We thank Gavin Schmidt and Tony Del Genio for assistance with the ModelE. We also acknowledge the modeling groups for making their model output available for analysis, the Program for Climate Model Diagnosis and Intercomparison (PCMDI) for collecting and archiving this data, and the WCRP's Working Group on Coupled Modelling (WGCM) for organizing the model data analysis activity. The WCRP CMIP3 multimodel dataset is supported by the Office of Science, U.S. Department of Energy. This work was supported by NASA Grant NNX06AB01G and NSF Grant ATM-0542736.

REFERENCES

Allen, R. J., and S. C. Sherwood, 2008: Warming maximum in the tropical upper troposphere deduced from thermal winds. *Nat. Geosci.,* **1,** 399–403.

Chen, T., W. B. Rossow, and Y. Zhang, 2000: Radiative effects of cloud-type variations. *J. Climate,* **13,** 264–286.

Dessler, A. E., Z. Zhang, and P. Yang, 2008: Water-vapor climate feedback inferred from climate fluctuations, 2003–2008. *Geophys. Res. Lett.,* **35,** L20704, doi:10.1029/2008GL035333.

Galewsky, J., A. Sobel, and I. Held, 2005: Diagnosis of subtropical humidity dynamics using tracers of last simulation. *J. Atmos. Sci.,* **62,** 3353–3367.

Gastineau, G., H. Le Treut, and L. Li, 2008: Hadley circulation changes under global warming conditions indicated by coupled climate models. *Tellus,* **60A,** 863–884.

Gray, W. M., and R. W. Jacobson, 1977: Diurnal variation of deep cumulus convection. *Mon. Wea. Rev.,* **105,** 1171–1188.

Hack, J., 1994: Parameterization of moist convection in the NCAR Community Climate Model, CCM2. *J. Geophys. Res.,* **99,** 5551–5568.

——, J. Kiehl, and J. Hurrell, 1998: The hydrologic and thermodynamic characteristics of the NCAR CCM3. *J. Climate,* **11,** 1179–1206.

Hartmann, D. L., and K. Larson, 2002: An important constraint on tropical cloud–climate feedbacks. *Geophys. Res. Lett.,* **29,** doi:10.1029/2002GL015835.

——, M. E. Ockert-Bell, and M. L. Michelsen, 1992: The effect of cloud type on Earth's energy balance: Global analysis. *J. Climate,* **5,** 1281–1304.

Hu, Y., and Q. Fu, 2007: Observed poleward expansion of the Hadley circulation since 1979. *Atmos. Chem. Phys.,* **7,** 5229–5236.

Hurley, J. V., and J. Galewsky, 2010a: A last-saturation analysis of ENSO humidity variability in the subtropical Pacific. *J. Climate,* **23,** 918–931.

——, and ——, 2010b: A last-saturation diagnosis of subtropical water vapor response to global warming. *Geophys. Res. Lett.,* **37,** L06702, doi:10.1029/2009GL042316.

Johanson, C., and Q. Fu, 2009: Hadley cell widening: Model simulations versus observations. *J. Climate,* **22,** 2713–2725.

Lorenz, D. J., and E. T. DeWeaver, 2007a: The response of the extratropical hydrological cycle to global warming. *J. Climate,* **20,** 3470–3484.

——, and ——, 2007b: Tropopause height and zonal wind response to global warming in the IPCC scenario integrations. *J. Geophys. Res.,* **112,** D10119, doi:10.1029/2006JD008087.

Lu, J., G. Chen, and D. W. Frierson, 2008: Response of the zonal mean atmospheric circulation to El Niño versus global warming. *J. Climate,* **21,** 5835–5851.

Manabe, S., and R. F. Strickler, 1964: Thermal equilibrium of the atmosphere with a convective adjustment. *J. Atmos. Sci.,* **21,** 361–385.

Mitas, C. M., and A. Clement, 2006: Recent behavior of the Hadley cell and tropical thermodynamics in climate models and reanalyses. *Geophys. Res. Lett.,* **33,** L01810, doi:10.1029/2005GL024406.

Mitchell, J. F. B., and W. J. Ingram, 1992: Carbon dioxide and climate: Mechanisms of changes in cloud. *J. Climate,* **5,** 5–21.

Pierrehumbert, R. T., and R. Roca, 1998: Evidence for control of Atlantic subtropical humidity by large scale advection. *Geophys. Res. Lett.,* **25,** 4537–4540.

Prather, M. J., 1986: Numerical advection by conservation of second-order moments. *J. Geophys. Res.,* **91,** 6671–6680.

Price, J., and R. Wood, 2002: Comparison of probability density functions for total specific humidity and saturation deficit humidity, and consequences for cloud parametrization. *Quart. J. Roy. Meteor. Soc.,* **128,** 2059–2072.

Randall, D. A., and Coauthors, 2007: Climate models and their evaluation. *Climate Change 2007: The Physical Science Basis,* S. Solomon et al., Eds., Cambridge University Press, 589–662.

Rasch, P. J., and D. Williamson, 1990: Computational aspects of moisture transport in global models of the atmosphere. *Quart. J. Roy. Meteor. Soc.,* **116,** 1071–1090.

——, and J. Kristjansson, 1998: A comparison of the CCM3 model climate using diagnosed and predicted condensate parameterizations. *J. Climate,* **11,** 1587–1614.

——, B. Boville, and G. Brasseur, 1995: A three-dimensional general circulation model with coupled chemistry for the middle atmosphere. *J. Geophys. Res.,* **100,** 9041–9072.

——, N. M. Mahowald, and B. Eaton, 1997: Representations of transport, convection, and the hydrologic cycle in chemical transport models: Implications for the modeling of short-lived and soluble species. *J. Geophys. Res.,* **102** (D23), 28 127–28 138.

Santer, B. J., and Coauthors, 2003: Contributions of anthropogenic and natural forcing to recent tropopause height changes. *Science,* **301,** 479–483.

——, and Coauthors, 2008: Consistency of modelled and observed temperature trends in the tropical troposphere. *Int. J. Climatol.,* **28,** 1703–1722, doi:10.1002/joc.1756.

Schmidt, G. A., and Coauthors, 2006: Present-day atmospheric simulations using GISS ModelE: Comparison to in situ, satellite, and reanalysis data. *J. Climate,* **19,** 153–192.

Schneider, T., P. A. O'Gorman, and X. Levine, 2010: Water vapor and the dynamics of climate changes. *Rev. Geophys.,* **48,** RG3001, doi:10.1029/2009RG000302.

Seidel, D. J., and W. J. Randel, 2006: Variability and trends in the global tropopause estimated from radiosonde data. *J. Geophys. Res.,* **111,** D21101, doi:10.1029/2006JD007363.

Sherwood, S. C., 1996: Maintenance of the free-tropospheric tropical water vapor distribution. Part II: Simulation by large-scale advection. *J. Climate,* **9,** 2919–2934.

——, and C. L. Meyer, 2006: The general circulation and robust relative humidity. *J. Climate,* **19,** 6278–6290.

——, W. Ingram, Y. Tsushima, M. Satoh, M. Roberts, P. L. Vidale, and P. A. O'Gorman, 2010: Relative humidity changes in a warmer climate. *J. Geophys. Res.,* **115,** D09104, doi:10.1029/2009JD012585.

Soden, B. J., and I. M. Held, 2006: An assessment of climate feedbacks in coupled ocean–atmosphere models. *J. Climate,* **19,** 3354–3360.

——, R. T. Wetherald, G. L. Stenchikov, and A. Robock, 2002: Global cooling after the eruption of Mount Pinatubo: A test of climate feedback by water vapor. *Science,* **296,** 727–730.

Son, S.-W., and Coauthors, 2008: Impact of stratospheric ozone recovery on the Southern Hemisphere westerly jet. *Science,* **320,** 1486–1489.

——, and Coauthors, 2009: The impact of stratospheric ozone recovery on tropopause height trends. *J. Climate,* **22,** 429–445.

Sundqvist, H., 1978: A parameterization scheme for nonconvective condensation including prediction of cloud water content. *Quart. J. Roy. Meteor. Soc.,* **104,** 677–690.

Vavrus, S., D. Waliser, A. Schweiger, and J. Francis, 2009: Simulations of 20th and 21st century Arctic cloud amount in the global climate models assessed in the IPCC AR4. *Climate Dyn.,* **33,** 1099–1115, doi:10.1007/s00382-008-0475-6.

Vecchi, G. A., and B. J. Soden, 2007: Global warming and the weakening of the tropical circulation. *J. Climate,* **20,** 4316–4340.

WMO, 1957: Meteorology—A three-dimensional science: Second session of the commission for aerology. *WMO Bull.,* **IV,** 134–138.

——, 1988: General meteorological standards and recommended practices: Appendix A. WMO Tech. Regulation WMO-No. 49, 88 pp.

Wright, J. S., A. H. Sobel, and G. A. Schmidt, 2009: Influence of condensate evaporation on water vapor and its stable isotopes in a GCM. *Geophys. Res. Lett.,* **36,** L12804, doi:10.1029/2009GL038091.

Zhang, G., and N. McFarlane, 1995: Sensitivity of climate simulations to the parameterization of cumulus convection in the Canadian Climate Centre general circulation model. *Atmos.–Ocean,* **33,** 407–446.

Robust Responses of the Hydrological Cycle to Global Warming

ISAAC M. HELD

National Oceanic and Atmospheric Administration/Geophysical Fluid Dynamics Laboratory, Princeton, New Jersey

BRIAN J. SODEN

Rosenstiel School for Marine and Atmospheric Science, University of Miami, Miami, Florida

(Manuscript received 13 September 2005, in final form 17 March 2006)

ABSTRACT

Using the climate change experiments generated for the Fourth Assessment of the Intergovernmental Panel on Climate Change, this study examines some aspects of the changes in the hydrological cycle that are robust across the models. These responses include the decrease in convective mass fluxes, the increase in horizontal moisture transport, the associated enhancement of the pattern of evaporation minus precipitation and its temporal variance, and the decrease in the horizontal sensible heat transport in the extratropics. A surprising finding is that a robust decrease in extratropical sensible heat transport is found only in the equilibrium climate response, as estimated in slab ocean responses to the doubling of CO_2, and not in transient climate change scenarios. All of these robust responses are consequences of the increase in lower-tropospheric water vapor.

1. Introduction

There remains considerable uncertainty concerning the magnitude of the temperature response to a given increase in greenhouse gases. But there are a number of climatic responses that are tightly coupled to the temperature response. Most of these are related, directly or indirectly, to lower-tropospheric water vapor. We are confident that lower-tropospheric water vapor will increase as the climate warms. We can predict, with nearly as much confidence, that certain other changes will occur that are coupled to this increase in water vapor. In this article we describe some of these robust hydrological responses to warming.

We use the archive of coupled climate models results organized by the Program for Climate Model Diagnosis and Intercomparison (PCMDI) for the Fourth Assessment Report (AR4) of the Intergovernmental Panel on Climate Change as our primary tool in assessing robustness. Some aspects of the hydrological responses to warming are consistent among these models and some are not. To study the latter requires one to understand the consequences of different model formulations, often at a detailed level. When studying a consistent part of the response, in contrast, one is not concerned with the specifics of individual models, but with providing simple physical arguments that add additional support for the plausibility of the response. Some of these robust responses to warming are already well appreciated, but we gather several together here, partly for pedagogical reasons, and partly with the hope of motivating new observational studies to determine whether these responses, which the models predict are already occurring, are detectable.

As in many discussions of water vapor and global warming, our starting point is the Clausius–Clapeyron (CC) expression for the saturation vapor pressure:

$$\frac{d \ln e_s}{dT} = \frac{L}{RT^2} \equiv \alpha(T), \tag{1}$$

where L is the latent heat of vaporization and R is the gas constant. At temperatures typical of the lower troposphere, $\alpha \approx 0.07\ \mathrm{K}^{-1}$; the saturation vapor pressure increases by about 7% for each 1-K increase in temperature. If the equilibrium response of lower-tropospheric temperatures to a doubling of CO_2 is close to the canonical mean value of 3 K, this corresponds to

Corresponding author address: Dr. Brian J. Soden, Rosenstiel School for Marine and Atmospheric Science, University of Miami, 4600 Rickenbacker Causeway, Miami, FL 33149.
E-mail: b.soden@miami.edu

© 2006 American Meteorological Society

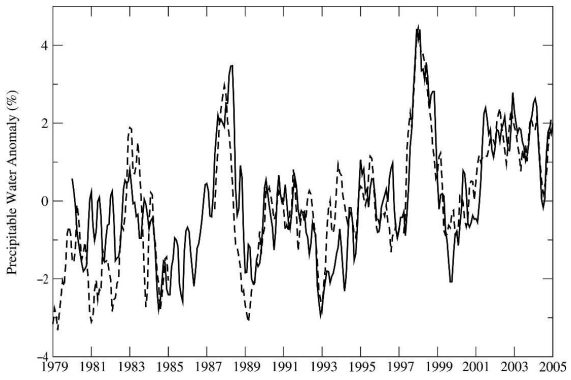

FIG. 1. A time series of the tropical-mean (30°N–30°S), ocean-only column-integrated water vapor from satellite observations (dashed) and GFDL GCM simulations with prescribed SST (solid). The satellite observations for 1979–84 are from the SMMR (Wentz and Francis 1992) and for 1987–2004 are from the SMM/I (Wentz 1997). The mean seasonal cycle is removed from both the observations and model simulations, and the SMMR anomalies are adjusted such that their mean equals that of the model for their overlapping time period (1980–84). All time series are smoothed using a 3-month running mean.

a 20% increase in e_s. Given the size of this increase, it is important to understand which aspects of the climate response are tightly coupled to the increase in e_s and which are not. We discuss the increase in column-integrated water vapor, the decrease in convective mass fluxes, the increase in horizontal moisture transport, the associated enhancement of the pattern of evaporation minus precipitation and its temporal variance, and the decrease in horizontal sensible heat fluxes in the extratropics (in steady state), all of which are robust responses to the increase in temperature and e_s.

2. Column-integrated water vapor

Before turning to the coupled model results, we show in Fig. 1 a time series of the ocean-only tropical-mean column-integrated water vapor based on microwave satellite measurements from the Scanning Multichannel Microwave Radiometer (SMMR; Wentz and Francis 1992) and the Special Sensor Microwave Imager (SSM/I; Wentz 1997). Also shown is the corresponding simulated time series, using a version of the AM2/LM2 developed at the Geophysical Fluid Dynamics Laboratory (GFDL Global Atmospheric Model Development Team 2004). No external parameters or forcing agents are changing in time, except for the lower boundary condition, which is the observed sea surface temperatures (and sea ice). The quality of the agreement is consistent with a very tight relation between sea surface temperatures and integrated water vapor (Wentz and Schabel 2000; Trenberth et al. 2005). Interannual variability, dominated by ENSO events and the longer-term trend, is captured with some fidelity.

It is well known that climate models tend to maintain a fixed tropospheric relative humidity as they warm. The modest changes in relative humidity that the models do generate are worthy of study, but they are too small to substantially modify the increase in column-integrated vapor resulting from the increase in saturation vapor pressure. The data in Fig. 1 do not raise any concerns in this regard, over the tropical oceans at least.

It is perhaps worth emphasizing that column-integrated vapor is dominated by the lower troposphere, whereas infrared water vapor feedback is dominated by the upper tropical troposphere (see Held and Soden 2000). Our focus here is not on water vapor feedback nor on climate sensitivity but on the hydrological response given a lower-tropospheric temperature change.

Using the PCMDI/AR4 archive we examine the change in climate in the A1B scenario between the first 20 yr and the last 20 yr of the twenty-first century. We consider only one realization from each of 20 models (listed in Table 1). Figure 2a shows the globally averaged total column water vapor plotted against the global-mean surface air temperature increase. Not surprisingly, climate models obey CC scaling fairly closely. A linear fit has a slope that is slightly greater than what one would expect from CC scaling with global-mean surface air temperature.

Figure 2c shows the results obtained from the 20C3M simulations of the years 1860–2000, using the difference between the first 20 yr and the last 20 yr of the twentieth century. The result is nearly identical to that obtained from the twenty-first-century projections, with CC scaling fitting the results quite well. The larger spread in the temperature responses in this figure is in part a consequence of a larger contribution from noise as compared to the smaller forced response. The fact that the correlation is nearly as tight as in the twenty-first-century integrations suggests that temperature fluctuations generated internally are also accompanied by CC scaled water vapor fluctuations, consistent with the GFDL AM2/LM2 results in Fig. 1 on shorter time scales.

3. The global-mean hydrological cycle

It is important that the global-mean precipitation or evaporation, commonly referred to as the strength of the hydrological cycle, does *not* scale with Clausius–Clapeyron (see also Betts 1998; Boer 1993; Trenberth

TABLE 1. A list of PCMDI AR4 model simulations used in the analysis of the 20C3M and SRES A1B scenarios. Some models are omitted from figures due to missing variables.

Model	Modeling center
BCCR BCM2	Bjerknes Center for Climate Research
CCCMA CGCM3	Canadian Centre for Climate Modelling and Analysis
CNRM CM3	Center National de Recherches Meteorologiques
CSIRO Mk3	Commonwealth Scientific and Industrial Research Organisation (CSIRO) Atmospheric Research
GFDL CM2.0	Geophysical Fluid Dynamics Laboratory
GFDL CM2.1	Geophysical Fluid Dynamics Laboratory
GISS AOM	Goddard Institute for Space Studies
GISS EH	Goddard Institute for Space Studies
GISS ER	Goddard Institute for Space Studies
IAP FGOALS1	Institute for Atmospheric Physics
INM CM3	Institute for Numerical Mathematics
IPSL CM4	Institut Pierre Simon Laplace
MIROC(hires)	Center for Climate System Research
MIROC(medres)	Center for Climate System Research
MIUB ECHO	Meteorological Institute University of Bonn
MPI ECHAM5	Max Planck Institute for Meteorology
MRI CGCM2	Meteorological Research Institute
NCAR CCSM3	National Center for Atmospheric Research
NCAR PCM1	National Center for Atmospheric Research
UKMO HadCM3	Met Office's Hadley Centre for Climate Prediction

1998; Allen and Ingram 2002). Figures 2b–d show how this strength of the global hydrological cycle responds to warming in the A1B scenario and in the 20C3M simulations in the AR4 archive. While there is an increase in strength that is correlated with increased temperature across the models, there is substantial scatter and, more importantly, the sensitivity is on the order of 2% K^{-1} (with a median value of 1.7% K^{-1}), much weaker than CC scaling. In the twentieth century, precipitation is reduced rather uniformly below the fit for the twenty-first-century projections by about 1%. As a result, it is only the models that warm the most strongly that clearly show an increase in precipitation over the twentieth century. We presume that this ~1% reduction is due to an increase over the century in absorbing aerosols (Ramanathan et al. 2001).

The change in global-mean precipitation, or evaporation, can be decomposed into a part associated with the change in Bowen's ratio and a part due to the net change in radiative flux at the surface. Using an atmospheric model (GFDL Global Atmospheric Model Development Team 2004), we have computed instantaneous radiative flux perturbations created by increasing atmospheric and surface temperatures throughout the troposphere by 1 K, holding relative humidity and clouds fixed. Averaging over a year and the globe, the result is an increase of only 0.7 W m^{-2} in the net downward radiation at the surface. The increase in absorbed solar flux associated with the reduction in surface albedo is ~0.3 W m^{-2} K^{-1} warming averaged over the AR4 models (Soden and Held 2006; Winton 2006). The combination of the radiative effect of uniform warming and the increase in albedo can explain at best 1 W m^{-2}, or about a 1% K^{-1} increase. A doubling of CO_2 holding the atmospheric state fixed increases the net flux by 0.66 W m^{-2}, or roughly 0.7%, but this term should cause a small positive intercept along the precipitation axis in Fig. 2b rather than a change in slope. A decrease in Bowen's ratio plays a significant role in generating the δP versus δT slope generated by the models, but it also cannot compete with CC scaling; the latent heating is already dominant over the sensible, so there is little room for an increase with fixed radiative flux. Cloud feedbacks likely contribute to the scatter among the models. In any case, a sensitivity smaller than that implied by CC scaling is clearly to be expected. [For reasons that are unclear, some one-dimensional radiative–convective models predict sensitivities of the global hydrological cycle as large as 4% K^{-1} (Lindzen et al. 1982; Pierrehumbert 2002).]

4. Mass exchange between the boundary layer and free troposphere

The fact that the strength of the global-mean hydrological cycle increases more slowly than does the mixing ratio near the surface has important consequences for the atmospheric circulation (Betts 1998). We can think of parcels of air leaving the boundary layer for the free

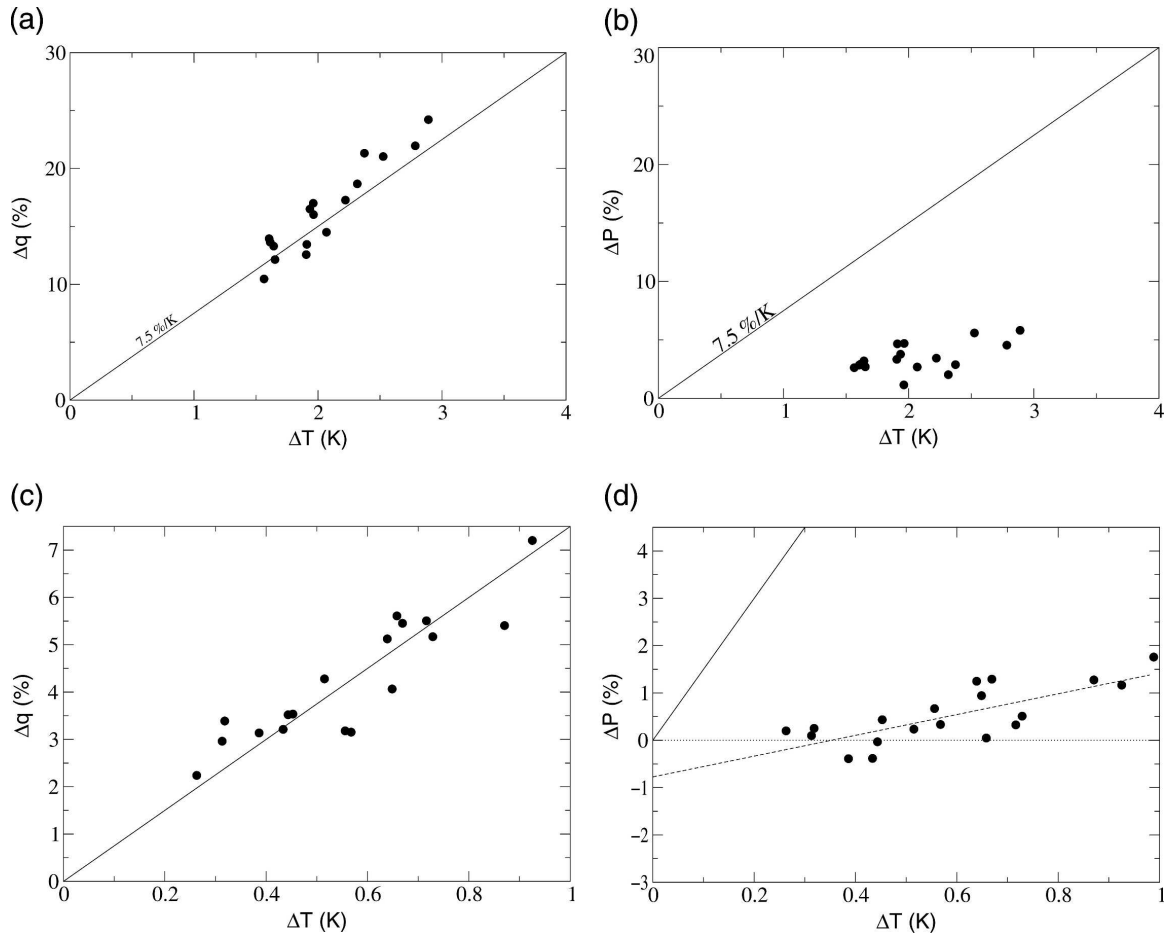

FIG. 2. Scatterplot of the percentage change in global-mean column-integrated (a),(c) water vapor and (b),(d) precipitation vs the global-mean change in surface air temperature for the PCMDI AR4 models under the (a),(b) Special Report on Emissions Scenarios (SRES) A1B forcing scenario and (c),(d) 20C3M forcing scenario. The changes are computed as differences between the first 20 yr and last 20 yr of the twenty-first (SRES A1B) and twentieth (20C3M) centuries. Solid lines depict the rate of increase in column-integrated water vapor (7.5% K^{-1}). The dashed line in (d) depicts the linear fit of ΔP to ΔT, which increases at a rate of 2.2% K^{-1}.

troposphere carrying large boundary layer mixing ratios, condensing and precipitating much of this vapor, and returning with much smaller vapor content. If we ignore this return flow of vapor, we have simply, in the global mean, $P = Mq$, where P is the precipitation, M is the mass exchanged per unit time, and q is a typical boundary layer mixing ratio. (The mass flux in nonprecipitating shallow convection should be excluded from M.) Since q scales with CC but P increases more slowly, M must decrease rapidly, albeit a bit less rapidly than the CC rate. There are a number of ways of measuring the strength of the atmospheric circulation, but by this particular measure, the circulation must weaken as the climate warms. We can, alternatively, speak of the mean residence time of water vapor in the troposphere as increasing with increasing temperature (Roads et al. 1998; Bosilovich et al. 2005).

Since the bulk of the evaporation and precipitation occurs in the Tropics, this argument is relevant for the Tropics in isolation. We therefore expect the mass flux in precipitating convective towers to decrease with increasing temperature. In most comprehensive climate models, this convective mass flux is not explicitly simulated by the resolved motions but is estimated by subgrid-scale closure theories. One might think that little confidence should be placed in the rate of change of convective mass transport with increasing temperature predicted by these models, given the uncertainties in

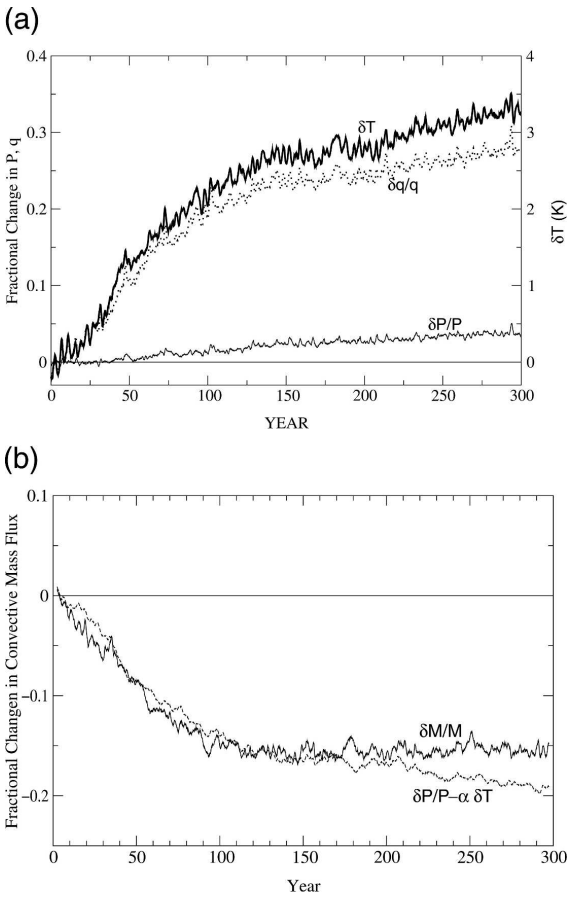

FIG. 3. (a) The change in global-mean surface air temperature, δT (solid), fractional change in precipitation, $\delta P/P$ (dashed), and column-integrated water vapor, $\delta q/q$ (dotted). (b) The fractional change in global-mean convective mass flux $\delta M/M$ (solid) and the corresponding change in $\delta P/P - \alpha\delta T$ (dashed). All results are from the GFDL CM2.1, and the time series are smoothed using a 5-yr running mean.

these closure theories. But the constraints described above operate in the models whether or not the mass flux is resolved by the model or contained in the subgrid-scale closure. Figure 3a is a plot of the time evolution of the fractional changes in global-mean precipitation and column-integrated water vapor. Figure 3b is the corresponding plot of the global-mean subgrid-scale convective mass flux in GFDL's CM2.1 model at 500 mb as a function of time in its A1B scenario, and that predicted from P/q assuming that q follows CC scaling at 7% K^{-1} and taking P from the model: $\delta M/M = \delta P/P - 0.07\delta T$. The temperature change δT and the fractional precipitation change $\delta P/P$ are also shown in the figure.

We do not have access to the convective mass fluxes from most of the models in the PCMDI/AR4 archive to test directly for the robustness of this result, but to the extent that one can simply set $M \propto P/q$, the results in Fig. 2 show that this mass flux decreases in all models.

The reduced upward convective mass flux implies a reduction in the compensating radiatively induced subsidence in the Tropics. An alternative argument for weaker tropical mass exchange is provided by Knutson and Manabe (1995), who focus on the compensating subsidence. Temperatures in the Tropics are dynamically constrained to be very uniform above the planetary boundary layer. In the deep convecting regions, the atmosphere is close to the moist adiabat determined by the moisture content in the boundary layer in those regions. In nonconvecting regions, the free-tropospheric temperatures must be close to the same moist adiabat. [See Santer et al. (2005) for confirmation that the AR4 models behave in this simple way.] In regions with no deep convection, the radiative cooling Q balances the adiabatic warming associated with the subsidence: $Q = \omega\partial\theta/\partial p$, where θ is the potential temperature and ω is the vertical p velocity. On a moist adiabat, $\partial\theta/\partial p$ averaged over the troposphere is proportional to Lq, where q is the boundary layer mixing ratio. The dry stability in the model Tropics increases as the temperature and the low-level moisture increase, following CC scaling. Since $Q \approx P$ the radiative cooling of the troposphere does not increase as rapidly as the increase in stability, and the subsidence weakens, at the rate of $\delta\omega/\omega \approx \delta P/P - \delta q/q$, just as before.

The observed trend over the past two decades in the tropical lapse rate remains a subject of controversy (see Santer et al. 2005). In the context of this paper, we provisionally assume that this controversy will be settled in favor of a tropical atmosphere that stays close to a moist adiabat. Otherwise the models are seriously deficient, and aspects of these arguments will need to be revisited.

A reduction in the mass exchange in the Tropics does not necessarily entail a proportional reduction in the strength of the mean tropical circulation. In the idealized problem of horizontally homogeneous radiative convective equilibrium, there is no mean circulation, yet the argument presented continues to hold and one still expects a reduction in convective mass flux with increasing temperature. One can think of the mean circulation as the superposition of a radiatively driven subsidence and an upward convective mass flux. Redistribution of the latter can change the strength of the circulation independently of the radiatively driven subsidence.

The spatial variance over the Tropics of the convec-

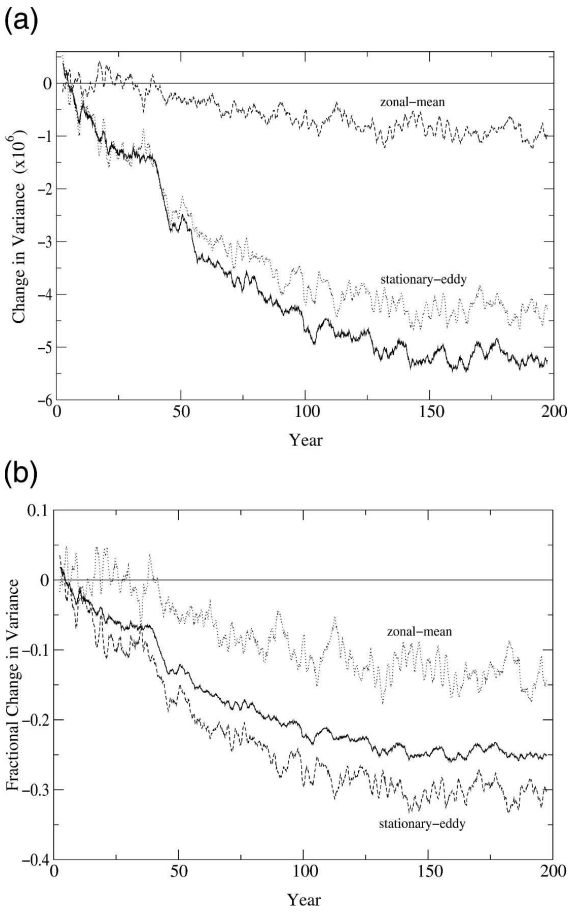

FIG. 4. Time series of the (a) absolute and (b) fractional change in spatial variance of monthly mean convective mass flux at 500 mb over the Tropics. Results are shown separately for the total (solid), zonal-mean (dashed), and eddy (dotted) components of the variance. All results are from the GFDL CM2.1, and the time series are smoothed using a 5-yr running mean.

tive mass flux is a convenient measure of the strength of the circulation driven by convection. If the reduction in the mass flux is everywhere proportional to the preexisting mass flux, then the variance should decrease at twice the rate of the mean mass flux: $2(\delta P/P - \delta q/q) \equiv 10\%\ \mathrm{K}^{-1}$. The rate of reduction in CM2.1 (Fig. 4) is ~25% for a ~3-K warming, somewhat smaller than the expectation based on a proportional reduction, indicating that there is modest redistribution of convection toward less uniformity, causing the circulation to weaken more slowly than one would expect based on the total mass flux scaling itself. (In this calculation, we compute the variance for each monthly mean and then average over time, and define the Tropics to be between 30°N and 30°S). We can divide this variance of the tropical convective mass flux into a part due to the zonal-mean mass flux and a part due to the stationary eddy mass flux (we refer to this eddy contribution as due to "stationary" eddies since we start with monthly mean data). One can then ask if the reduction in variance takes place in the stationary eddy component or in the zonal mean. (In CM2.1, the zonal-mean variance accounts for 40% of the total variance.) As the climate warms, the reduction in total variance is dominated by a reduction of the stationary eddy component (Fig. 4a). The fractional reduction (Fig. 4b) in the stationary eddy component ($10\%\ \mathrm{K}^{-1}$) is consistent with CC scaling, while the fractional reduction in the zonal-mean component ($4\%\ \mathrm{K}^{-1}$) is substantially smaller than that expected from CC scaling.

The implication is that the *redistribution* of convection is such as to increase the variance of the zonal mean, so that the circulation consistent with this component, the zonal-mean Hadley cell, does not decrease in strength as fast as CC scaling of the mass flux would suggest. See Mitas and Clement (2005) for a discussion of the modest weakening of the (wintertime) Hadley cell in most of the AR4 models. We suspect that the zonal-mean Hadley cell is restricted by other factors from decreasing in strength as strongly as implied by the CC scaling of the mass flux

Mitas and Clement (2005) also discuss the trend toward *increasing* strength of the Hadley cell in the National Centers for Environmental Prediction–National Center for Atmospheric Research (NCEP–NCAR) reanalysis and 40-yr European Centre for Medium-Range Weather Forecasts (ECMWF) Re-Analysis (ERA-40) over the past 20 yr. We are aware of no models that simulate such an increase, but it would not necessarily be inconsistent with our line of argument if there were sufficient reorganization of the convection strengthening meridional contrasts at the expense of zonal contrasts. But our tentative working hypothesis is that these trends are artifacts of the reanalysis related to the fact that the tropical lapse rate in the radiosonde data is increasing (Santer et al. 2005) rather than staying close to a moist adiabat. Inappropriately nudging a model toward a more unstable tropical lapse rate in an analysis cycle, by this hypothesis, will result in an artificial increase in convection and artificial intensification of the Hadley cell.

5. Moisture transport

A very important consequence of the increase in lower-tropospheric water is the increase in horizontal

vapor transport within the atmosphere. Consider the time-averaged, vertically integrated, horizontal transport of vapor F. The convergence of this transport balances the difference between evaporation and precipitation. A seemingly simplistic but useful starting point for discussion is the assumption that the response of F is everywhere dominated by the change in lower-tropospheric mixing ratios rather than changes in the flow field, so that the transport also exhibits CC scaling:

$$\frac{\delta F}{F} \approx \frac{\delta e_s}{e_s} \approx \alpha \delta T. \tag{2}$$

The relevant temperature change is the change in the lowest 2 km or so since this is where the bulk of the water vapor resides.

A somewhat different argument can be made based on a simple diffusive picture of midlatitude eddy fluxes. If moisture and temperature are diffused with the same diffusivity, then the ratio of the latent heat transport $F_L = LF$ to the sensible heat transport F_S will be the ratio of the gradient of c_pT to the gradient of $Lq = Lhq_s$, where h is the relative humidity (assumed to be constant once again). Setting $(\partial q_s/\partial y) = (dq_s/dT)(\partial T/\partial y)$ and $\xi \equiv (L/c_p)(dq_s/dT)$, we have $F_L/F_S = h\xi$. As temperatures increase, ξ increases, and the fractional change in the moisture transport is

$$\frac{\delta F_L}{F_L} = \frac{\delta F_s}{F_s} + \frac{\delta \xi}{\xi} \approx \frac{\delta F_s}{F_s} + \frac{1}{\xi}\frac{d\xi}{dT}\delta T = \frac{\delta F_s}{F_s} + \frac{d^2 e_s/dT^2}{de_s/dT}\delta T. \tag{3}$$

Since the temperature dependence of e_s is predominately exponential, the ratio of the second derivative of e_s to its first derivative is essentially α once again:

$$\frac{\delta F_L}{F_L} \approx \frac{\delta F_S}{F_S} + \alpha \delta T. \tag{4}$$

If one assumes that the eddy sensible heat transport does not change, one finds a similar result to that obtained above with the simpler assumption of fixed flow. We return to the relationship between latent and sensible transports below.

We compute δF per unit global warming in each of the AR4 integrations and then average over the model ensemble and plot the result in Fig. 5a. Also shown is the simple prediction, $\alpha \delta T F$, where δT is the zonal- and annual-mean temperature change per unit global warming. (We compute this estimate for each model and then average over all models.) For Fig. 5b, we locate the midlatitude maximum in the annual-mean poleward moisture transport in each model (and each hemisphere) and plot the fractional change in this flux at this latitude in the A1B scenario, as a function of the change in global-mean surface temperature. Despite some scatter, the correlation is clear, with a slope of roughly 5% K^{-1}. If one plots against the temperature change at this latitude, rather than the change in global-mean temperature, the slope in the Northern Hemisphere is reduced (to roughly 4% K^{-1}) while the slope in the Southern Hemisphere is increased. The quantitative departures from precise CC scaling are significant, especially in the Northern Hemisphere when

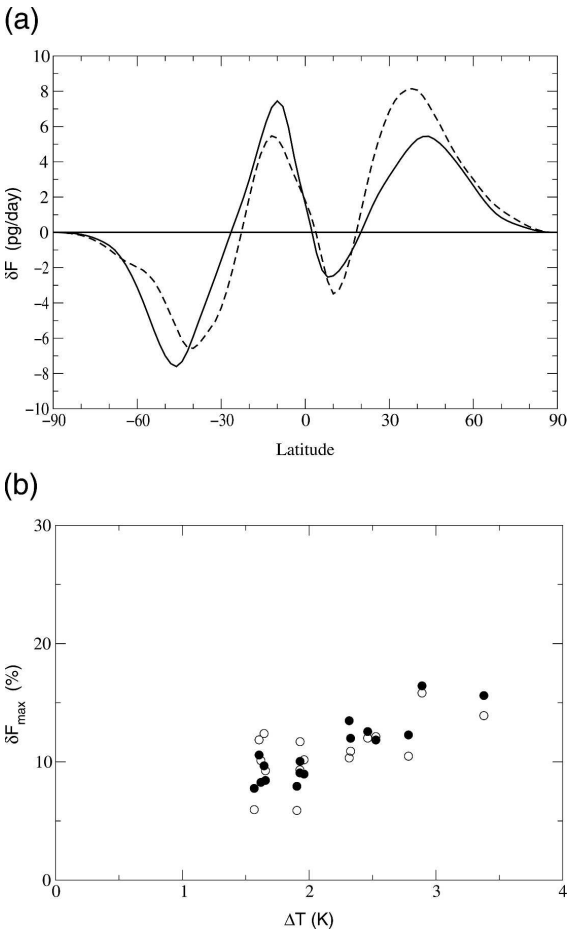

FIG. 5. (a) The change in zonal-mean northward moisture transport, F, from the ensemble mean of PCMDI AR4 models under SRES A1B scenario (solid) and the corresponding thermodynamic contribution (dashed) predicted from (2). (b) Scatterplot of the percentage change in the maximum poleward moisture transport, F_{max}, vs the global-mean δT for individual models. Results are shown separately for the Northern Hemisphere (filled) and Southern Hemisphere (open).

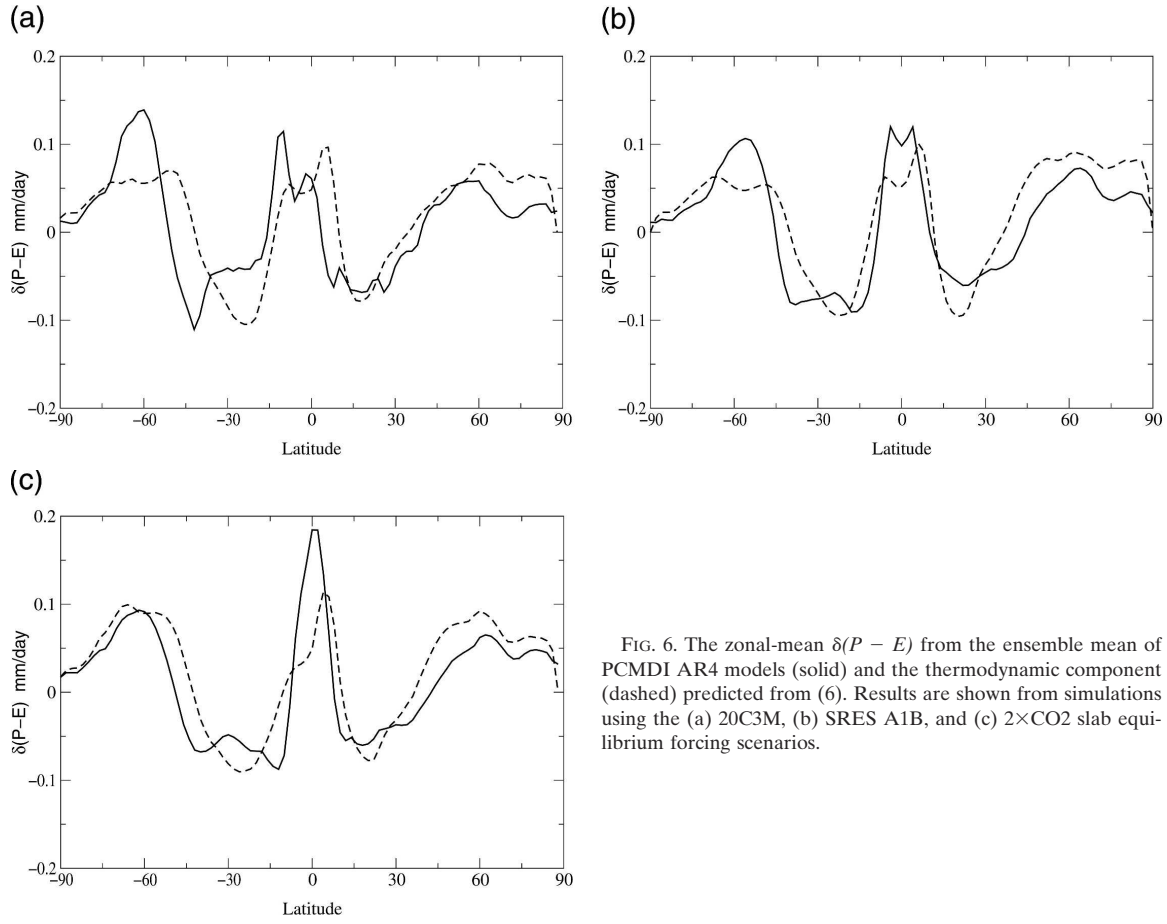

FIG. 6. The zonal-mean $\delta(P - E)$ from the ensemble mean of PCMDI AR4 models (solid) and the thermodynamic component (dashed) predicted from (6). Results are shown from simulations using the (a) 20C3M, (b) SRES A1B, and (c) 2×CO2 slab equilibrium forcing scenarios.

using the local rather than global-mean temperature responses, but it is apparent that the CC increase in vapor determines the basic structure of the response.

An increasing poleward moisture flux with increasing temperature is explicitly assumed or is implicitly generated in most simple energy balance climate models in which one tries to include the poleward moisture flux (e.g., Nakamura et al. 1994) and has been remarked upon in GCM global warming simulations since the inception of this field (Manabe and Wetherald 1975). It is reassuring but not surprising to find this behavior in the comprehensive AR4 models as well.

The result for precipitation minus evaporation is

$$\delta(P - E) = -\nabla \cdot (\alpha \delta T F). \tag{5}$$

If one can remove δT from the derivative, assuming that $P - E$ has more meridional structure than δT, then $P - E$ itself satisfies CC scaling:

$$\delta(P - E) = \alpha \delta T (P - E). \tag{6}$$

The pattern of $P - E$ is simply enhanced, becoming more positive where it is already positive and more negative where it is negative.

One expects this simple balance to be most relevant over the oceans, where low-level relative humidity is strongly constrained, as well as over well-watered land regions. Over arid or semiarid land surfaces, changes in mean low-level relative humidity are not constrained to be small. In these regions, it is, rather, the runoff, $P - E$, and the flux divergence that are constrained to remain small. The approximation in (5) can potentially predict the unphysical result that $P - E < 0$ over land; the modified version (6) has the accidental advantage in this regard that it predicts that $P - E$ will simply remain small where it is already small.

Figure 6 shows the composited change in the zonal- and annual-mean $P - E$ and the change predicted by (6). We use the zonal- and annual-mean change in the surface air temperature, and simply assume that $\alpha = 0.07\ \mathrm{K}^{-1}$ to predict a $\delta(P - E)$ distribution for each

model from its zonal- and annual-mean $P - E$, from (6). We then divide by the global-mean temperature change before averaging over all models to compute both the model and the predicted change in $P - E$ per unit global warming. There are three panels in the figure, corresponding to the change simulated by the AR4 models in the twentieth century (between the periods 1900–20 and 1980–2000; Fig. 6a), the change between the years 2000–20 and 2080–2100 in the A1B scenario (Fig. 6b), and the equilibrium response to a doubling of CO_2 in slab ocean versions of these models (Fig. 6c). The latter equilibrium responses with fixed (implied) oceanic heat fluxes are particularly distinguished from the transient integrations by much larger warming in high southern latitudes.

The fit, which has no free parameters, is rather impressive for these composites; it can be somewhat less accurate for individual models, presumably because the part of the response of $P - E$, related to changes in circulation and, potentially, relative humidity, differs from model to model more than does this simple thermodynamic component.

The fit is somewhat better than one might expect in fact, given the many simplifications made in the derivation, including the neglect of the correlation between F and δT in the seasonal cycle.

The difference between the actual response and this simple fixed flow-fixed relative humidity response clearly shows the effects of the poleward movement of the storm tracks in both hemispheres, which displaces the poleward boundary of the dry subtropical zones with $P - E < 0$ farther poleward. The differences between response and prediction are especially large over the Southern Ocean, where the increase in poleward moisture flux is underestimated, most substantially in the twentieth century. This overestimate in the Southern Hemisphere is reduced in the A1B twenty-first-century simulations, while in the equilibrated slab ocean runs, which allow the Southern Ocean to warm, the prediction is equally good in both hemispheres.

Given the discussion in the preceding section of the reduction in mass exchange between the boundary layer and the interior of the troposphere, especially in the Tropics, one might wonder why this prediction for the change in $P - E$, assuming no change in flow or low-level relative humidity, works as well as it does in the Tropics. If the mass flux in the Hadley cell were reduced in strength following CC scaling, for example, it should cancel the effects of increasing vapor and result in no increase in equatorial rainfall. Clearly this does not occur (although there is a tendency for the simple theory to overestimate the subtropical drying). We have argued that slowdown of the mean meridional circulation need not follow the CC scaling of the reduction in the mass exchange, but we admit to being surprised that this simple expression works as well as it does in the zonal mean. A methodology for a more satisfying analysis of tropical precipitation responses to global warming is outlined by Chou and Neelin (2004). The fixed flow-fixed relative humidity response is but one term in their analysis.

Figure 7 shows the geographical distribution of the annual-mean change in $P - E$ as well as the prediction, $0.07\delta T\,(P - E)$. Here δT is the local annual-mean temperature change. Once again, we composite across the models after normalization by the global-mean temperature response. While it is not accurate enough in isolation to be used as a basis for projections of regional hydrology, this simple thermodynamic constraint is clearly an important component of many regional changes, at least for subtropical to subpolar latitudes. The impression from this figure is that this thermodynamic constraint combined with a simple theory for the poleward expansion of the subtropics might provide a useful first approximation outside of the deep Tropics.

There are other interesting ways of dividing the local hydrologic response into "thermodynamic" and "dynamic" components—see, for example, Emori and Brown (2005), who also find a "dynamical" weakening of precipitation consistent with a reduction in convective mass flux.

To convert this prediction for $\delta(P - E)$ into a theory for δP, we need an expression for δE. A simple choice is to assume that the evaporation increases proportionally to the control evaporation. The global-mean increase in evaporation is 2% K^{-1} so the resulting expression for the precipitation response per unit global warming is

$$\delta P = 0.07\,\delta T\,(P - E) + 0.02E. \qquad (7)$$

Figure 8 shows the result for the zonal means in the A1B runs for both δP and δE.

Because the interesting reduction in evaporation in the Southern Ocean is not captured by this simple fit to δE, the resulting fit for $\delta(P - E)$ substantially overestimates the increase in precipitation in these southern latitudes.

Droughts and floods can be thought of as produced by low-frequency variability in the flow field and therefore in the moisture transport. If we make the conservative assumption once again that the statistics of this variability remain unchanged while the magnitude of F increases, then the intensity of both floods and droughts will increase, as more water is transported by any particular anomalous flow from the region of anomalous vapor convergence to the region of anoma-

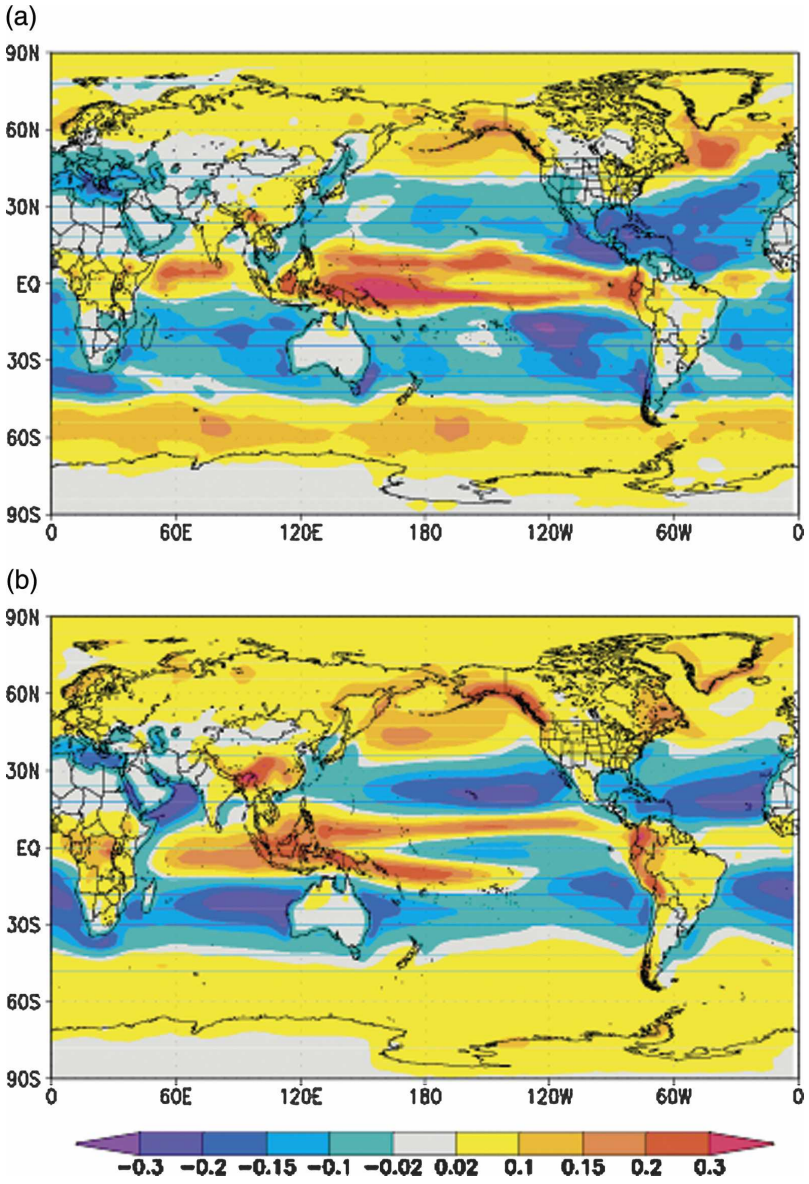

FIG. 7. The annual-mean distribution of $\delta(P - E)$ from the ensemble mean of (a) PCMDI AR4 models and (b) the thermodynamic component predicted from (6) from the SRES A1B scenario.

lous vapor divergence. Dry and marginal land areas, where sensitivity to drought is the greatest, are once again not strongly constrained by his kind of argument. Figure 9 shows the zonal-mean change in variance V of monthly mean anomalies in $P - E$ (local anomalies from the respective climatological seasonal cycles, with the zonal averaging performed after computing the local variance) and the CC scaling prediction: $\delta V/V \approx 2\alpha\delta T$. [See Raisanen (2005) for a related analysis of the CMIP2 models.] The models' increase in variability is uniformly smaller than anticipated from CC scaling of the flux, a result that we are tempted to attribute to the weakening in the mass exchange discussed in section 4.

6. Poleward energy transport

The increased amplitude of the poleward vapor transport implies increased amplitude in the meridional

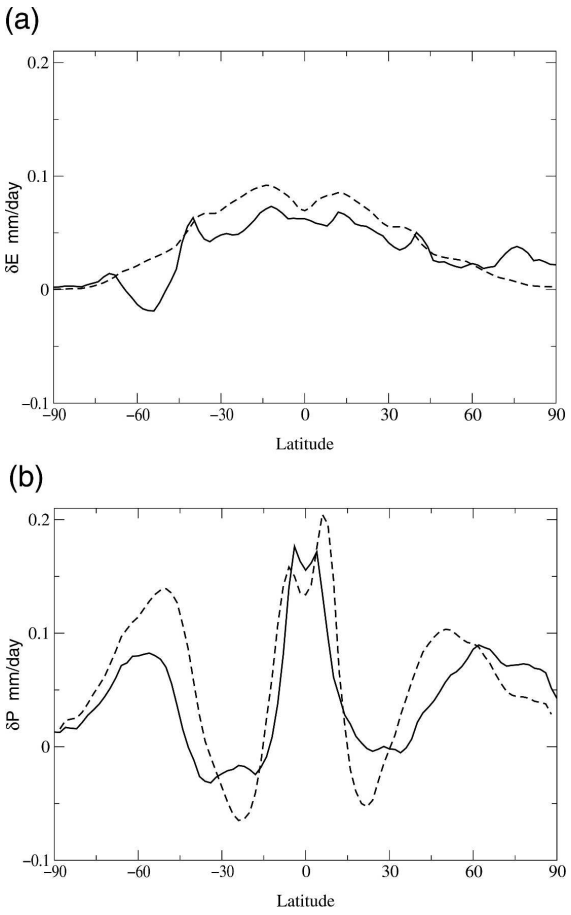

FIG. 8. The zonal-mean (a) δE and (b) δP from the ensemble mean of PCMDI AR4 models (solid) and the thermodynamic component (dashed) predicted from (7) from the SRES A1B scenario.

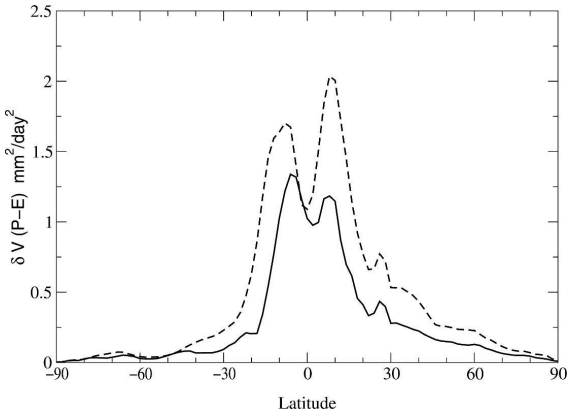

FIG. 9. The zonal-mean change in variance of monthly mean $(P - E)$, δV, from the ensemble mean of PCMDI AR4 models (solid) and the thermodynamic component (dashed) from the SRES A1B scenario.

transport of latent energy. The total poleward energy transport is the sum of this latent energy transport plus the transport of dry static energy. It is of interest to examine the extent to which changes in sensible heat transport compensate for the changes in latent transport. This compensation is clearly seen in a variety of equilibrium responses of GCMs to warming and cooling [see the first such calculation in Manabe and Wetherald (1975)].

We first examine this compensation in the equilibrium responses to doubling CO_2 using the flux-adjusted slab ocean models. This is a simpler case than the transient warming experiments in that there is no change in the flux into the oceans. The composite over all models (Fig. 10a) shows the expected compensation. Since the latent transport is equatorward in the Tropics but poleward in midlatitudes, one sees an increased poleward dry static energy transport in the Tropics but a decreased transport in midlatitudes, a fundamental distinction between the tropical and extratropical responses to warming. The tropical increase is accomplished by an increase in the depth of the Hadley circulation and a reduction in the lapse rate, both of which contribute to the needed increase in the dry static energy difference between poleward and equatorward flows, overcompensating for any reduction in Hadley cell strength. The reduction in the extratropical poleward dry static energy transport is generated by a reduction in the eddy sensible heat transport.

If one inspects the magnitude of the total transport and its moist and dry components, one finds that the decrease in the sensible component compensates for about 70% of the latent transport increase at 45° latitude, near the maximum in the total transport. It would be of interest to try to understand this number, but here we are primarily concerned with the implications of this compensation for the CC scaling of the moisture transport. Returning to (4), rather than assuming that the eddy sensible heat transport is unchanged, we consider the implications of a compensation of given strength μ:

$$\delta F_S / F_S = \mu \delta F_L / F_L, \tag{8}$$

where $\mu \cong 0.7$ for these slab ocean simulations. We also need the ratio of latent to sensible transport in the unperturbed climate $F_L \equiv \xi F_S$. The constant ξ is a strong function of temperature and therefore of latitude. Its value is ≈ 1 at the maximum in the total transport. The resulting modification to CC scaling is

$$\frac{\delta F_L}{F_L} \approx \frac{\alpha \delta T}{1 + \mu \xi}. \tag{9}$$

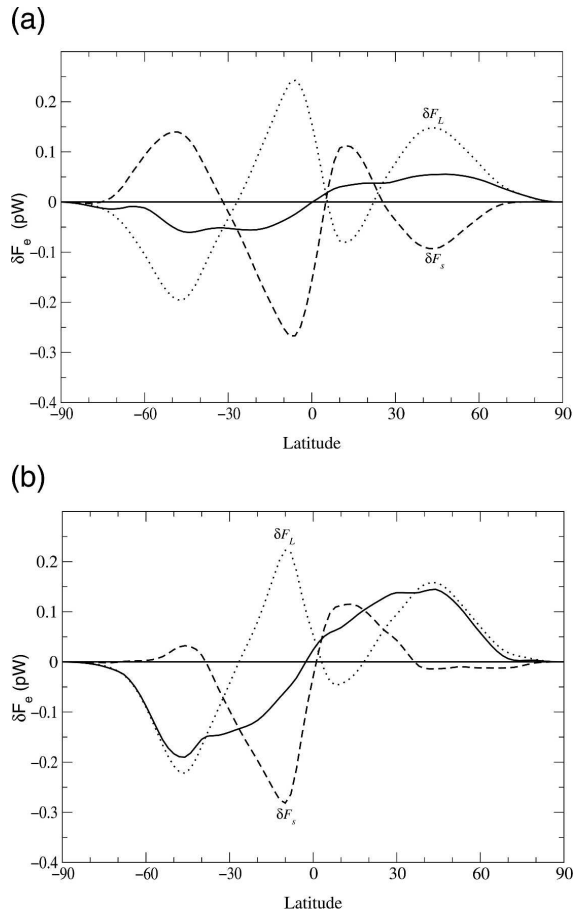

FIG. 10. The change in zonal-mean northward atmospheric energy transports (a) from 2×CO2 slab equilibrium simulations and (b) from SRES A1B transient simulations. Results are shown for the total atmospheric energy transport (solid), the sensible energy transport δF_s (dashed), and the latent energy transport δF_L (dotted).

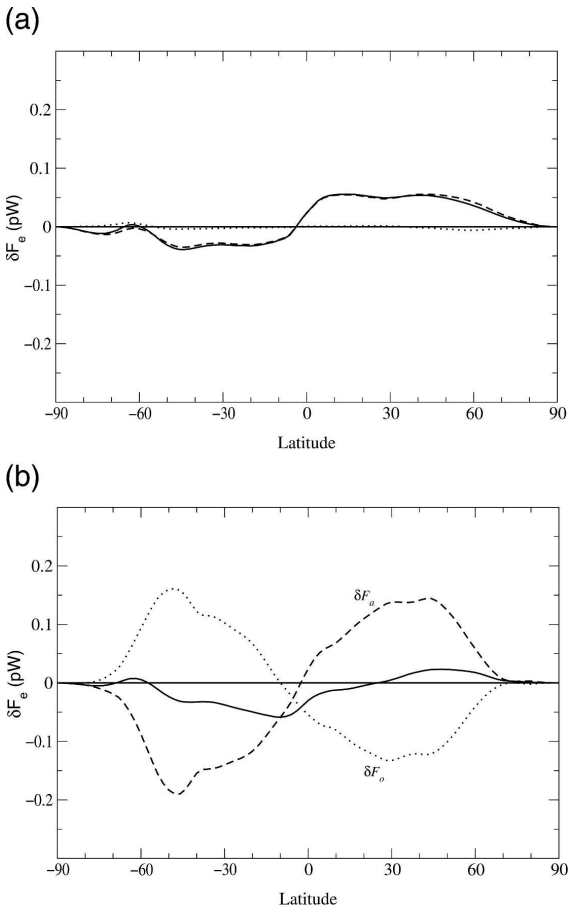

FIG. 11. The change in zonal-mean energy transports for the atmosphere δF_a (dashed), ocean δF_o (dotted), and atmosphere + ocean (solid) from (a) the 2×CO2 slab equilibrium simulations and (b) SRES A1B simulations. The oceanic contribution includes the differential heat storage, as described in the text.

The expression predicts that the increase in the extratropical moisture flux will be about 60% of the CC scaling value at 45° latitude. This estimate is only meant as a rough indication of how much difference we might expect between models in which the increased latent flux is compensated by a decrease in the sensible flux and models in which there is no compensation. As one moves poleward, ξ decreases, and the effects of compensation on the latent flux response should be smaller.

Turning to the integrations for the A1B transient scenario, the results for the heat fluxes are provided in Fig. 10b. A surprising result here is that there is little or no compensation of the increased extratropical latent flux in either hemisphere. The difference between the transient warming scenario and the equilibrated slab ocean models in this respect is striking. Inspection of the fluxes at the top of the atmosphere (Fig. 11) shows that this increased total atmospheric poleward flux in the transient experiments is not radiating out the top of the atmosphere but is passed to the oceans instead. In constructing this figure, we first take the flux into the ocean, remove its global mean, and then integrate from one pole to the other, yielding the sum of ocean transport and differential heat storage. The change in this quantity is the dotted line labeled "ocean" in the figure. The "total" is the sum of this ocean contribution and the change in atmospheric transport and can be computed by integrating the fluxes at the top of the atmosphere, after removing the global mean. One sees that the changes in the top of atmosphere fluxes are not very different than in the slab ocean case. It is the oceanic

contribution that compensates the increased latent transport in the extratropics in the transient warming, rather than a reduction in sensible transport. This oceanic differential storage plus transport should, therefore, obey CC scaling.

One lesson that this result provides is that it is not that the atmosphere prefers to maintain the same total atmospheric flux, but that it prefers not to change the basic gradient in the top-of-the-atmosphere net radiative flux. In the face of the unavoidable increase in the poleward extratropical latent heat transport, in the equilibrated system there is no alternative but a decrease in the sensible transport. In the transient case, one can divide the necessary adjustment between the sensible heat transport and differential oceanic heat storage plus transport. If we assume that the sensible heat transport reacts to changes in meridional temperature gradients, it is plausible that the reduction of the sensible heat transport in the Southern Hemisphere in the transient experiments is retarded, since the Southern Ocean temperatures are very slow to warm and the resulting increased meridional gradient would work against any such reduction. What is unanticipated is that the results look very similar in the Northern and Southern Hemispheres, despite the polar amplification at low levels and the resulting reduction in the meridional gradient in the Northern Hemisphere. One possible interpretation is that the polar amplification over land has little impact on the oceanic storm tracks where much of the heat transport takes place.

On the basis of the diffusive picture leading to (9), one would expect a model with compensation to show a smaller response in the moisture flux, per unit warming, than a model without compensation. This does seem to be the case in the Southern Hemisphere in Fig. 6, since the scaled $P - E$ decreases as one moves from the twentieth century and A1B simulations to the equilibrium slab runs, but the results in the Northern Hemisphere are less clear. These distinctions between equilibrated and transient simulations are deserving of closer examination.

7. Conclusions

A number of important aspects of the hydrological response to warming are a direct consequence of the increase in lower-tropospheric water vapor. Because the increase in strength of the global hydrological cycle is constrained by the relatively small changes in radiative fluxes, it cannot keep up with the rapid increase in lower tropospheric vapor. The implication is that the exchange of mass between boundary layer and the midtroposphere must decrease, and, since much of this exchange occurs in moist convection in the Tropics, the convective mass flux must decrease. In many popular, and in some scientific, discussions of global warming, it is implicitly assumed that the atmosphere will, in some sense, become more energetic as it warms. By the fundamental measure provided by the average vertical exchange of mass between the boundary layer and the free troposphere, the atmospheric circulation must, in fact, slow down. This large-scale constraint has little direct relevance to the question of how tropical storms will be affected by global warming, since the mass exchange in these storms is a small fraction of the total tropical exchange.

In contrast, assuming that the lower-tropospheric relative humidity is unchanged and that the flow is unchanged, the poleward vapor transport and the pattern of evaporation minus precipitation ($E - P$) increases proportionally to the lower-tropospheric vapor, and in this sense wet regions get wetter and dry regions drier. Since the changes in precipitation have considerably more structure than the changes in evaporation, this simple picture helps us understand the zonally averaged pattern of precipitation change. In the extratropics, one can alternatively think of the diffusivity for vapor and for sensible heat as being the same, with similar consequences for the change in the vapor transport. If one assumes that the statistics of the flow are also unchanged, one obtains estimates of the increase in variance of $E - P$ (the increased intensity of "droughts and floods") that are reasonable but overestimate the response of the model variances, perhaps because of the decrease in the strength of the mass exchange.

In the Tropics, one confidently expects compensation between the increase in the equatorward latent heat transport and an increase in poleward dry static energy transport; otherwise the net transport in the Tropics would change sign. One also expects a decrease in the poleward sensible heat flux in the extratropics, as seen in many previous GCM studies. Surprisingly we see this decrease only in the equilibrium climate response as estimated with slab ocean models, and not in the transient climate change experiments. Particularly intriguing is the response in the Northern Hemisphere, where there is no reduction in the sensible heat transport despite the reduction in the zonal-mean temperature gradient at low levels associated with polar amplification of the warming. An implication of this result is that one can estimate the differential oceanic heat storage plus transport (the heat entering the ocean, with the global mean removed) directly from the Clausius–Clapeyron-dominated response of the latent heat transport.

To the extent that we have simple plausible physical

arguments that support the model consensus, we believe that one should have nearly as much confidence in these results as one has in the increase in temperature itself.

Acknowledgments. We are grateful for valuable comments and discussions on this work with G. Vecchi, A. Leetmaa, D. Neelin, and an anonymous reviewer. We also acknowledge the international modeling groups for providing their data for analysis, the Program for Climate Model Diagnosis and Intercomparison (PCMDI) for collecting and archiving the model data, the JSC/CLIVAR Working Group on Coupled Modeling and their Climate Simulation Panel for organizing the model data analysis activity, and the IPCC WG1 TSU for technical support. The IPCC Data Archive at Lawrence Livermore National Laboratory is supported by the Office of Science, U.S. Department of Energy. This work was partially supported by a grant from the NASA Energy and Water Cycle Study.

REFERENCES

Allen, M. R., and W. J. Ingram, 2002: Constraints on future changes in the hydrological cycle. *Nature,* **419,** 224–228.

Betts, A. K., 1998: Climate–convection feedbacks: Some further issues. *Climatic Change,* **39,** 35–38.

Boer, G. J., 1993: Climate change and the regulation of the surface moisture and energy budgets. *Climate Dyn.,* **8,** 225–239.

Bosilovich, M. G., S. D. Schubert, and G. K. Walker, 2005: Global changes in water cycle intensity. *J. Climate,* **18,** 1591–1608.

Chou, C., and J. D. Neelin, 2004: Mechanisms of global warming impacts on regional tropical precipitation. *J. Climate,* **17,** 2688–2701.

Emori, S., and S. J. Brown, 2005: Dynamic and thermodynamic changes in mean and extreme precipitation under changed climate. *Geophys. Res. Lett.,* **32,** L17706, doi:10.1029/2005GL023272.

GFDL Global Atmospheric Model Development Team, 2004: The new GFDL global atmosphere and land model AM2–LM2: Evaluation with prescribed SST simulations. *J. Climate,* **17,** 4641–4673.

Held, I. M., and B. J. Soden, 2000: Water vapor feedback and global warming. *Annu. Rev. Energy Environ.,* **25,** 441–475.

Knutson, T. R., and S. Manabe, 1995: Time-mean response over the tropical Pacific to increase CO_2 in a coupled ocean–atmosphere model. *J. Climate,* **8,** 2181–2199.

Lindzen, R. S., A. Y. Hou, and B. F. Farrell, 1982: The role of convective model choice in calculating the climate impact of doubling CO_2. *J. Atmos. Sci.,* **39,** 1189–1205.

Manabe, S., and R. T. Wetherald, 1975: The effect of doubling CO_2 concentration on the climate of the general circulation model. *J. Atmos. Sci.,* **32,** 3–15.

Mitas, C. M., and A. Clement, 2005: Has the Hadley cell been strengthening in recent decades? *Geophys. Res. Lett.,* **32,** L03809, doi:10.1029/2004GL021765.

Nakamura, M., P. H. Stone, and J. Marotzke, 1994: Destabilization of the thermohaline circulation by atmospheric eddy transports. *J. Climate,* **7,** 1870–1882.

Pierrehumbert, R. T., 2002: The hydrologic cycle in deep time climate problems. *Nature,* **419,** 191–198.

Raisanen, J., 2005: Impact of increasing CO_2 on monthly-to-annual precipitation extremes: Analysis of CMIP2 experiments. *Climate Dyn.,* **24,** 309–323.

Ramanathan, V., P. J. Crutzen, J. T. Kiehl, and D. Rosenfeld, 2001: Aerosols, climate and the hydrological cycle. *Science,* **294,** 2119–2124.

Roads, J. O., S. C. Chen, S. Marshall, and R. Oglesby, 1998: Atmospheric moisture cycling rates. *GEWEX News,* Vol. 8, Internatinal GEWEX Project Office, 7–10.

Santer, B. D., and Coauthors, 2005: Amplification of surface temperature trends and variability in the tropical atmosphere. *Science,* **309,** 1551–1556.

Soden, B. J., and I. M. Held, 2006: An assessment of climate feedbacks in coupled atmosphere–ocean models. *J. Climate,* **19,** 3354–3360.

Trenberth, K. E., 1998: Atmospheric moisture residence times and cycling: Implications for rainfall rates with climate change. *Climatic Change,* **39,** 667–694.

——, J. Fasullo, and L. Smith, 2005: Trends and variability in column integrated atmospheric water vapor. *Climate Dyn.,* **24** (7–8), 741–758.

Wentz, F. J., 1997: A well-calibrated ocean algorithm for SSM/I. *J. Geophys. Res.,* **102,** 8703–8718.

——, and E. A. Francis, 1992: Nimbus-7 SMMR Ocean Products, 1979–1984. Remote Sensing Systems Tech. Rep. 033192, Santa Rosa, CA, 36 pp.

——, and M. Schabel, 2000: Precise climate monitoring using complementary data sets. *Nature,* **403,** 414–416.

Winton, M., 2006: Surface albedo feedback estimates for the AR4 climate models. *J. Climate,* **19,** 359–365.

Biographical Sketch
A.J. (Han) Dolman
June 2013

Director Department of Earth Sciences
VU University Amsterdam,
Boelelaan 1085
1081 HV Amsterdam, the Netherlands
Telephone +31-20-5987358/7303
Email: han.dolman@vu.nl

(i) Profile

Professor of Ecohydrology and current head of the Department of Earth Sciences. My research interests are the interaction of the terrestrial biosphere with the carbon and hydrological cycle and the atmosphere. My work is a combination of modeling and experimental work. I am involved in FLUXNET eddy covariance observations of CO2 and methane in the Netherlands (Horstermeer; http://ecoschermnet.falw.vu.nl:81/) and the Far East Siberia. I am further interested in the application of inverse modeling techniques to regional carbon balances and the application of simple models to study fragility, resilience and feedbacks. I was awarded the Vernadsky medal of the EGU in 2013 (http://www.egu.eu/awards-medals/vladimir-ivanovich-vernadsky/).

(ii) Professional Preparation

University of Groningen, Netherlands	Physical Geography	PhD., 1987
University of Groningen, Netherlands	Theoretical Biology	M.Sc., 1982

(iii) Appointments

Director Department Earth Science	2011 – Present
Member Board of Faculty of Earth and Life Sciences Vice Dean	2008-2011
VU University Amsterdam, Professor Ecohydrology	2003 – Present
Alterra, Wageningen, Senior Scientist	1993-2003
CEH, Wallingford, Senior Research Fellow	1988-1993

(iv) Selected papers (for full list http://www.falw.vu.nl/en/research/earth-sciences/earth-and-climate-cluster/staff/publications/publications-han-dolman.asp)

- Jung M, M Reichstein, P Ciais SI Seneviratne, J Sheffield, G Bonan, A Cescatti, J Chen, RAM De Jeu**, A.J. Dolman,** et al., 2010. A recent decline in the global land evaportranspiration trend due to limited moisture supply, Nature, doi: 10.1038/nature09396
- **Dolman A. J.,** G. R. van der Werf, M. K. van der Molen, G. Ganssen, J.-W. Erisman, B. Strengers , 2010. A Carbon Cycle Science Update Since IPCC AR-4. AMBIO 39:402–412 DOI 10.1007/s13280-010-0083-7
- Canadell, Josep G. Philippe Ciais, Shobhakar Dhakal, **Han Dolman,** Pierre Friedlingstein, Kevin R Gurney, Alex Held, Robert B Jackson, Corinne Le Quere, Elizabeth L Malone, Dennis S Ojima, Anand Patwardhan, Glen P Peters, Michael R Raupach, Interactions of the carbon cycle, human

activity, and the climate system: a research portfolio, Current Opinion in Environmental Sustainability, Volume 2, Issue 4, October 2010, Pages 301-311, ISSN 1877-3435, DOI: 10.1016/j.cosust.2010.08.003.

- **Dolman, A.J.** & Jeu, R.A.M. de (2010). Evaporation in Focus. *Nature Geoscience, 3*, 296.
- Schulze, E.D., Ciais, P., Luysaert, S., Freibauer, A., Janssens, I.A., Sousanna, J.F., Smith, P., Grace, J., Levin, I., Thiruchittampalam, B., Heimann, M., **Dolman, A.J.,** Valentini, R., Bousquet, P., Peylin, P., Peters, W., Roedenbeck, C., Etiope, G., Vuichard, N., Wattenbach, M., Nabuurs, G.J., Poussi, Z., Nieschulze, J. & Gash, J.H.C. (2009). Importance of methane and nitrous oxide for Europe's terrestrial greenhouse-gas balance. *Nature Geoscience*, 842-850.

(v) Synergistic Activities

- 2008 –2013 Chairman of the Terrestrial Observation Panel for Climate of GCOS and GTOC (TOPC)
- 2011-present: Member of the Scientific Advisory Council of the Netherlands Royal Meteorological Institute
- 2009- present: Lead GEO Task CL09-03a, Integrated Carbon Observing System
- 2011 – Present: member of the Mission Assessment Group of CarbonSat, European Space Agency.

(vI) Awards

Vladimir Vernadsky Medal of the Biogeosciences Division of the
European Geophysical Union
Gold honorary medal from the President of the republic of Yakutia , 2010
Shared Nobel Peace Prize as Lead author of the IPCC assessment, 2007

(vii) Projects

I am involved in a number of EU funded projects such as GHG-Europe http://www.ghg-europe.eu/ that aims to determine the full Greenhouse Gas balance of Europe. ICOS http://www.icos-infrastructure.eu/ and ICOS-INWIRE http://www.icos-inwire.lsce.ipsl.fr/ that aim to set up a European Infrastructure for GH G monitoring and GEOCARBON http://www.geocarbon.net/ a global analysis and monitoring system for carbon. I am also involved in AMAZALERT http://www.eu-amazalert.org/home where we try to determin e the resilience and fragility of the Amazon rainforest with humans and climate. I am also involved in PA GE21 http://page21.org/ that studies the effects of changing permafrost.

My current PhD projects deal impact of the South Asian Monsoon on extreme rainfall, Possible effects of soil moisture on source evaporation and extreme events in South Asia, The effect of nitrogen deposition on canopy fluxes of carbon, Moisture effects on mid-latitude vegetation carbon exchange and Stability o f permafrost in Siberia.

I also hold a Science without Frontier Fellowship. This is collaboration with INPE, Cachoeira Paulista to st udy stability of Amazonian Climate and carbon pools.

(viii) Collaborators & Other Affiliations (last 48 months)

Current PhD advisor

C. Berridge. Climate carbon feedbacks at midlatitudes and High latitude permafrost carbon coupling Mar ie Curie) Y. Mi, and High latitude permafrost carbon coupling (Marie Curie)**,** T. Chen. Mid latitude drough ts and carbon cycle. (Chimese Academy of Sciences)**,** K. Fleisher. Nitrogen and the carbon cycle. (NWO), T. T van Leeuwen. Forest fire emissions and carbon losses (SRON/NWO). A. Vermeulen. Observation of tr ace gasses at tall towers in the Netherlands. (ECN) Luiz Vilasa. Land surface feedbacks in the East Asian Monsoon (NWO), Lintao Li. East Asian monsoon moisture characteristics.

Under my supervision 15 PhD thesis were completed over the last 5 years.

Collaborators: Detlef Sculze (MPI-BGC, Jena), Philippe Ciais (LSCE, Paris), Dario Papale (Unitus, Italy), Eddy Moors (Alterra, NL), Timo Vesala (UHel, Finland), Annette Freibauer (vTI, Germany), Martin Heiman (MPI, BGC, Jena), Jean Daniel Paris (LSCE, Paris), Tiong Wang (CMA, China), Guojie Wang (Nuist, China), Shilong Piao (UnBeing, China), Hans Hubberten (AWI, Germany), Christopher Heinze (UnBergen, Norway), Sonia Seniveradne (ETHZ, Switzerland), Riccardo Valentini (Unitus, Italy), Richard Harding (CEH, UK), Dennis Baldocchi (Un Berkely, USA), Alex Vermeulen (ECN, NL).

LETTER

doi:10.1038/nature11390

Observations of increased tropical rainfall preceded by air passage over forests

D. V. Spracklen[1], S. R. Arnold[1] & C. M. Taylor[2]

Vegetation affects precipitation patterns by mediating moisture, energy and trace-gas fluxes between the surface and atmosphere[1]. When forests are replaced by pasture or crops, evapotranspiration of moisture from soil and vegetation is often diminished, leading to reduced atmospheric humidity and potentially suppressing precipitation[2,3]. Climate models predict that large-scale tropical deforestation causes reduced regional precipitation[4–10], although the magnitude of the effect is model[9,11] and resolution[8] dependent. In contrast, observational studies have linked deforestation to increased precipitation locally[12–14] but have been unable to explore the impact of large-scale deforestation. Here we use satellite remote-sensing data of tropical precipitation and vegetation, combined with simulated atmospheric transport patterns, to assess the pan-tropical effect of forests on tropical rainfall. We find that for more than 60 per cent of the tropical land surface (latitudes 30 degrees south to 30 degrees north), air that has passed over extensive vegetation in the preceding few days produces at least twice as much rain as air that has passed over little vegetation. We demonstrate that this empirical correlation is consistent with evapotranspiration maintaining atmospheric moisture in air that passes over extensive vegetation. We combine these empirical relationships with current trends of Amazonian deforestation to estimate reductions of 12 and 21 per cent in wet-season and dry-season precipitation respectively across the Amazon basin by 2050, due to less-efficient moisture recycling. Our observation-based results complement similar estimates from climate models[4–10], in which the physical mechanisms and feedbacks at work could be explored in more detail.

To explore the links between vegetation and rainfall, we analysed combined satellite data on precipitation from the Tropical Rainfall Measuring Mission (TRMM) and other satellites[15] (TRMM3B42) and data on leaf area index (LAI) from the Moderate Resolution Imaging Spectroradiometer[16] (MODIS). In these data positive spatial correlations exist between annual mean precipitation and annual mean LAI (Fig. 1a, d; Pearson correlation coefficient, $r = 0.81$), highlighting the role of precipitation in controlling large-scale vegetation patterns. In this study, our aim was to investigate a causal effect of vegetation on tropical (30° S to 30° N) rainfall in subsequent days on a regional scale (over distances of hundreds to thousands of kilometres). To do this, we calculated the origin and atmospheric transport of air

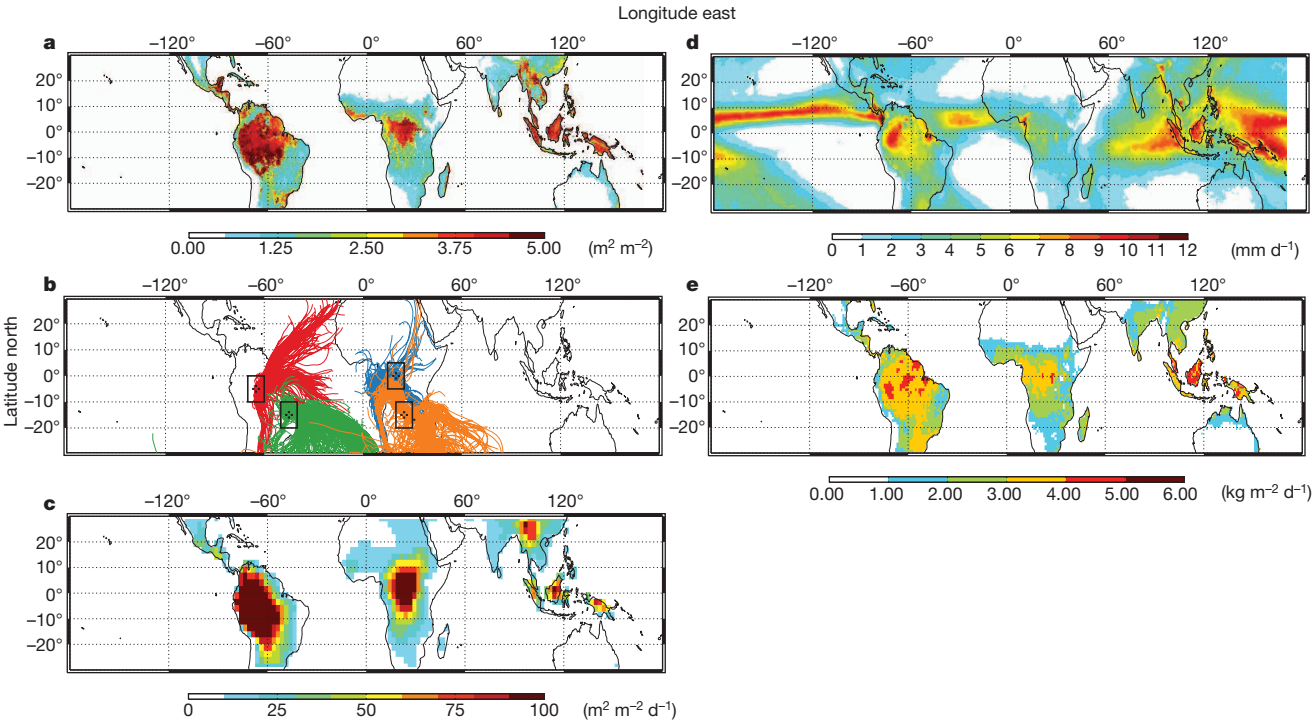

Figure 1 | Annual (2001–2007) mean vegetation, precipitation and evaporation. **a**, Leaf area index (LAI) from MODIS. **b**, Example 10-d back-trajectories arriving daily during 2001. Boxes illustrate the four domains analysed in detail in this study. **c**, Mean cumulative exposure of back-trajectories to LAI over the preceding 10 d. **d**, Precipitation reported by TRMM and other satellites (TRMM3B42). **e**, Evapotranspiration computed as the mean of the four GLDAS models.

[1]School of Earth and Environment, University of Leeds, Leeds LS2 9JT, UK. [2]Centre for Ecology and Hydrology, Wallingford, Oxford OX10 8BB, UK.

©2012 Macmillan Publishers Limited. All rights reserved

masses to determine the prior exposure of air to vegetation. This allowed us to evaluate whether air that had passed over more vegetation produced more rainfall.

To calculate air-mass histories, we used a Lagrangian atmospheric transport model. Such back-trajectory methods have been used previously to identify the transport of atmospheric moisture to continental regions[17,18]. We calculated atmospheric back-trajectories arriving daily at the centre of all continental $1^\circ \times 1^\circ$ grid squares over the tropical domain for 2001–2007. The trajectories were calculated using operational analysis data from the European Centre for Medium-Range Weather Forecasts (ECMWF), and are hence consistent with the large-scale atmospheric flow from the assimilated observations. We tested the sensitivity of our analysis to the length, arrival height and arrival time of the back-trajectories and found consistent results across a broad range of choices (Supplementary Figs 1, 2 and 3). Here we present results for ten-day back-trajectories arriving at the surface at 12:00 UT. Figure 1b shows example back-trajectories arriving at four tropical locations.

For each individual trajectory, we calculated the cumulative LAI (ΣLAI) encountered by the air mass during the last ten days of atmospheric transport. The resulting climatology of ΣLAI (Fig. 1c) is very similar to the *in situ* LAI, although important differences are apparent. For example, there are regions surrounding the Amazon and Congo basins where *in situ* LAI is relatively low but ΣLAI is high owing to exposure of air to large amounts of vegetation as it travels across forested regions upwind.

We analysed relationships between the daily variability in ΣLAI and the daily variability in precipitation. Figure 2a shows these relationships for air masses arriving in a ~1,000 km × 1,000 km region of Minas Gerais, Brazil, near the Amazon basin. To reduce the influence of the initial state of the air mass on our analysis, we stratified the data into that from the wet season and that from the dry season and then further according to the initial specific humidity of the trajectory, on the basis of the ECMWF analyses. We found a strong positive and significant (Student's *t*-test, $P < 0.01$) relationship between the exposure of air masses to vegetation and the precipitation those air masses produce (Fig. 2b). For air masses with low to medium exposure to precedent vegetation (ΣLAI $< 10\ m^2\ m^{-2}\ d$), mean dry- and wet-season rainfall increases by 0.25 mm d^{-1} and, respectively, 0.4 mm d^{-1} for every additional unit of exposure to LAI that is encountered in the preceding 10 d. The impact of vegetation exposure tends to saturate, especially during the wet season, with less sensitivity of rainfall where ΣLAI $> 10\ m^2\ m^{-2}\ d$. Although we find that the initial specific humidity of the air mass does affect precipitation, with moister air masses typically producing more precipitation, the positive trend between precipitation and exposure to LAI is similar for all subsets of the data. Qualitatively similar results are found in a 1,000 km × 1,000 km region south of the tropical forests of the Congo basin (Fig. 2b). Over the moist tropical forests themselves, differences in rainfall between air masses with low and high exposures to LAI are notably smaller (Fig. 2b), although for the Congo basin the differences are significant in the dry season ($P < 0.01$). We note that the positive relationships found between precipitation and ΣLAI are not due to the length of time the trajectories have spent over land, with distance travelled and ΣLAI often poorly correlated (Supplementary Table 1), or to the average topographic height the trajectory has crossed. When we repeated our analysis using the distance travelled by the trajectory over land or the average elevation of the topography crossed by the trajectory (in place of ΣLAI), the relationships were substantially weaker and in some cases negative (Supplementary Figs 4 and 5).

We extended this regional analysis to explore relationships between precipitation and vegetation across the tropics (Fig. 2c). For more than 60% of the tropical land surface, precipitation is a factor of at least two greater in air masses that have been exposed to extensive vegetation in the preceding days (defined as the top decile of ΣLAI), relative to air masses that have been exposed to little (defined as the bottom decile of

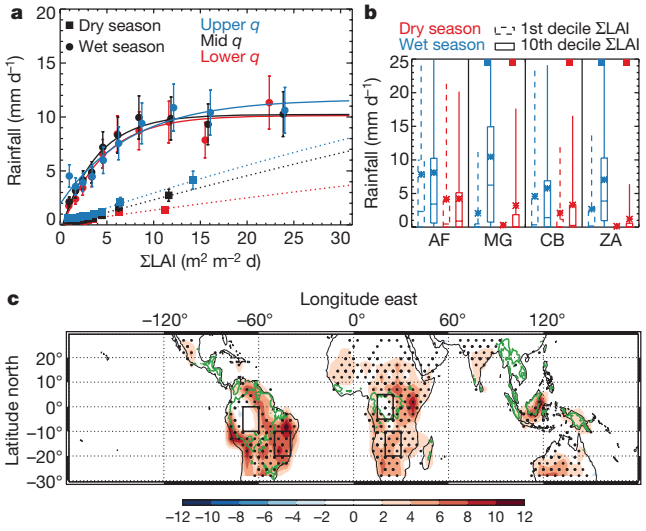

Figure 2 | Relationships between daily precipitation and cumulative exposure of 10-d back-trajectories to vegetation LAI (ΣLAI) for 2001–2007. **a**, Plot for air masses arriving in Minas Gerais, Brazil (10–20° S, 40–50° W). Data binned into deciles of ΣLAI and stratified by initial specific humidity (q). Lines show fit to data (solid, wet season; dotted, dry season) and error bars indicate estimation of error in precipitation (Methods Summary). **b**, Comparison of daily precipitation for air masses that have been exposed to small and large amounts of vegetation (significant ($P < 0.01$) differences indicated by squares at top of panel) during atmospheric transport to the Amazon basin (AB; 10–0° S, 60–70° W), Minas Gerais (MG), the Congo basin (CB; 5° N–5° S, 15–25° E) and south of Congo (ZA; 10–20° S, 20–30° E) (mean, star; median, line; 25th and 75th percentiles, box; 5th and 95th percentiles, whiskers). **c**, Number of calendar months with significant ($P < 0.01$; red, positive; blue, negative) relationships between precipitation and ΣLAI. Stippling denotes regions where precipitation is a factor of at least two greater in air with large exposure to vegetation than in air with small exposure. Green contour delimits areas with $>3\ m^2\ m^{-2}$ annual mean LAI. Black boxes mark the four regions in **b**.

ΣLAI). Significant ($P < 0.01$) positive correlations between precipitation and ΣLAI are common features for much of the year in areas surrounding the Amazon (southern Brazil and Paraguay) and Congo (southern and eastern Africa) forests, matching where previous studies have found large continental precipitation recycling ratios[18]. We find few tropical regions with significant negative correlations, although the relationships between vegetation and precipitation are typically weaker in moist tropical forests. The weaker signal at the centre of extensive forests is probably due to the lack of variability in air-mass exposure to vegetation (Supplementary Fig. 6); however, saturation of the MODIS LAI retrievals for dense tropical forest canopies[19] may have a role.

This analysis demonstrates that there are strong positive relationships between the cumulative exposure of air to vegetation and the amount of precipitation that air will produce, suggestive of a water-cycle feedback. To explore potential mechanisms underlying these relationships, we evaluated the change in atmospheric moisture that occurs along our back-trajectories. To do this we calculated the net change in specific humidity (Δq) that occurred during continental transport in the ECMWF humidity analyses along the 10-d back-trajectories (Fig. 3a). In general, air becomes drier during atmospheric transport over land, owing to lower continental evaporation rates as compared with the oceans. Figure 3a demonstrates that air masses that have been exposed to more vegetation remain significantly moister ($P < 0.01$), and in some cases air can actually moisten when crossing densely vegetated regions. Analysis of the latter cases indicates that typically 70–90% of increases in q occur during the hours of daylight,

©2012 Macmillan Publishers Limited. All rights reserved

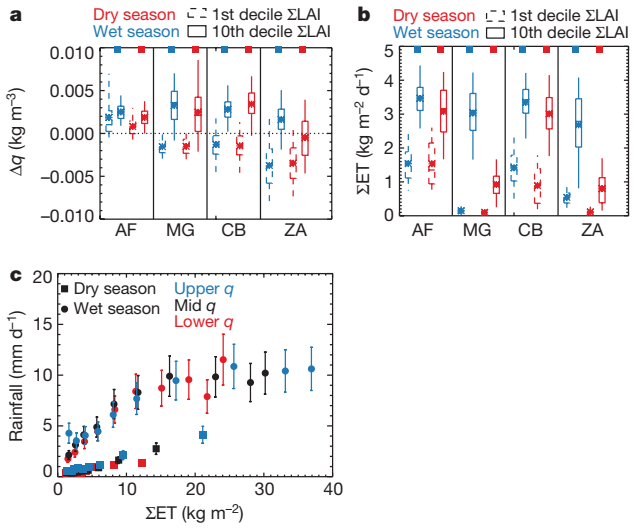

Figure 3 | Atmospheric water-budget components along back-trajectories. **a**, Same as Fig. 2b, but for net change in atmospheric specific humidity (Δq) as a function of ΣLAI. **b**, Same as Fig. 2b, but for cumulative surface evaporation (ΣET) as a function of ΣLAI. **c**, Same as Fig. 2a, but for precipitation as a function of ΣET.

consistent with a dominant forcing from evapotranspiration (Supplementary Fig. 7).

To quantify the contribution of evapotranspiration to the air-mass water budget, we used output from four global land surface models that use the best available estimates of meteorological forcing (those from the Global Land Data Assimilation System[20] (GLDAS)) (Fig. 1e). Figure 3b shows significant ($P < 0.01$) positive relationships between the multi-model mean cumulative surface evaporation (ΣET) and ΣLAI in all four regions examined. Figure 3c shows rainfall as a function of ΣET for the Minas Gerais region, demonstrating that additional moisture from evapotranspiration emitted into air masses with large exposure to vegetation is substantially greater than the additional precipitation observed in these air masses. Indeed, for all four regions the extra ΣET emitted into air masses with large vegetation exposure exceeds the observed additional precipitation by a factor of at least four (Supplementary Table 2).

Our analysis explores the role of regional-scale vegetation patterns on precipitation. Through evapotranspiration, forests maintain atmospheric moisture that can return to land as rainfall downwind. These processes operate on timescales of days over distances of 100–1,000 km (ref. 18) such that large-scale land-use change may alter precipitation hundreds to thousands of kilometres from the region of vegetation change. Land-use patterns and small-scale deforestation may also alter precipitation locally, through changes in the thermodynamic profile and the development of surface-induced mesoscale circulations[21,22]. Natural and pyrogenic emissions from vegetation can also have a role in rainfall initiation over tropical forest regions[23]. The impact of cloud microphysical processes on precipitation is highly uncertain[24], and biogenic emissions could contribute to our observed relationship between rainfall and exposed vegetation. However, our water-balance calculations imply that cumulative increases in evapotranspiration over upstream forested regions more than account for the increase in downstream rainfall.

Rapid land-use change is occurring across large regions of the tropics: 40% of the Amazon is predicted to be deforested by 2050 under a business-as-usual scenario[25]. We used this scenario to explore the potential sensitivity of rainfall to changes in moisture recycling as a result of deforestation. We combined the deforestation scenario with present-day LAI to produce a new spatial distribution of LAI

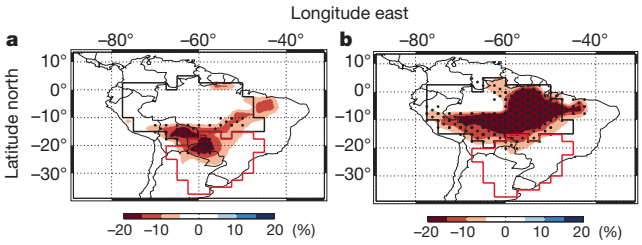

Figure 4 | Simulated percentage change in precipitation due to 2000–2050 business-as-usual deforestation of the Amazon basin. **a**, Wet season; **b**, dry season. Stippling denotes regions where the simulated precipitation anomaly differs from the present-day (1998–2010) rainfall by more than 1 s.d. The Amazon (black) and Rio de la Plata (red) basins are marked.

(Supplementary Fig. 8) and then used our trajectories to calculate ΣLAI under the deforested scenario. We then applied our empirical relationships between ΣLAI and rainfall (Fig. 2b) to estimate the change in rainfall that might occur as a result of this extensive deforestation. In this calculation, we implicitly assumed there to be no change in the large-scale circulation and that the local effects of deforestation on rainfall were negligible downstream. Despite these assumptions, our estimates are broadly consistent with estimates of basin-wide deforestation from climate models[4–10]. Using this method, we estimated a 12% reduction in wet-season precipitation and a 21% reduction in dry-season precipitation across the Amazon basin (Fig. 4). This sensitivity is not restricted to the region of deforestation, and we estimate a 4% decrease in annual total precipitation for the Rio de la Plata basin. Through comparison with TRMM3B42 data, we calculate that the estimated reduction in precipitation is equivalent to the basin-wide drought experienced across the Amazon in 2010. Such a reduction in precipitation may have consequences for the future of remaining Amazonian forests[26,27] and for rainfall-reliant industries both within and outside the Amazon basin, including agriculture and hydroelectric power generation, which contribute substantially to South American economies. The successful efforts to curb Amazon deforestation that have been applied in recent years[28] must be maintained if large-scale clearance of the Amazon and the resulting impacts on regional rainfall are to be avoided.

METHODS SUMMARY

Remote-sensed data. We used precipitation retrievals from the 3B42 3-h 0.25° × 0.25° product of TRMM and other satellites[15] to calculate daily accumulated (24-h) rainfall. We used monthly mean LAI from MODIS[16] using the MOD15_BU_V5 product available at 0.25° × 0.25° resolution. We spatially averaged both products to 1° × 1° resolution. We apply this temporal and spatial averaging to the precipitation data to reduce random error[29]. We estimate the total error to be the random error, estimated according to ref. 28, plus a systematic error estimated as 0.2 times the absolute precipitation[30], combined in quadrature.

Land surface models. We used 1° × 1° monthly mean evaporation from four global land surface models archived on GLDAS[20]. The models are forced by a combination of meteorological data sets including atmospheric analysis, and precipitation from merged gauge–satellite products.

Atmospheric transport. We calculated kinematic atmospheric back-trajectories arriving four times daily (00:00, 06:00, 12:00 and 18:00 UT) on a 1° × 1° grid for the period 2001–2007 using the OFFLINE trajectory model. The position of each trajectory is calculated every 30 min and output every 6 h. We calculated 3-, 5- and 10-d trajectories arriving at the surface and three altitudes above the surface (corresponding to air pressures of 900, 800 and 700 hPa) that are likely to be within the deep tropical boundary layer.

Analysis. For each trajectory, we calculated the total distance travelled over land, the cumulative exposure to LAI (ΣLAI), the average elevation of the topography over which the trajectory travelled and the cumulative evapotranspiration (ΣET; specified by GLDAS). We fitted rainfall data with a function of the form $f(x) = ae^{bx} + c$ (Supplementary Table 2). We calculated ΣLAI regardless of trajectory pressure. Restricting the calculation to when trajectory pressure is greater than 850 hPa gives similar results (Supplementary Fig. 9).

©2012 Macmillan Publishers Limited. All rights reserved

Full Methods and any associated references are available in the online version of the paper.

Received 16 April; accepted 29 June 2012.
Published online 5 September 2012.

1. Bonan, G. B. Forests and climate change: forcings, feedbacks, and the climate benefit of forests. *Science* **320,** 1444–1449 (2008).
2. Shukla, J. & Mintz, Y. Influence of land-surface evapotranspiration on the Earth's climate. *Science* **215,** 1498–1501 (1982).
3. Eltahir, E. A. B. & Bras, R. L. Precipitation recycling in the Amazon basin. *Q. J. R. Meteorol. Soc.* **120,** 861–880 (1994).
4. Henderson-Sellers, A. & Gornitz, V. Possible climatic impacts of land cover transformations, with particular emphasis on tropical deforestation. *Clim. Change* **6,** 231–257 (1984).
5. Lean, J. & Warrilow, D. A. Simulation of the regional climatic impact of Amazon deforestation. *Nature* **342,** 411–413 (1989).
6. Shukla, J., Nobre, C. & Sellers, P. Amazon deforestation and climate change. *Science* **247,** 1322–1325 (1990).
7. Werth, D. & Avissar, R. The local and global effects of Amazon deforestation. *J. Geophys. Res.* **107,** 8087 (2002).
8. Ramos da Silva, R., Werth, D. & Avissar, R. Regional impacts of future land-cover changes on the Amazon basin wet-season climate. *J. Clim.* **21,** 1153–1170 (2008).
9. Hasler, N., Werth, D. & Avissar, R. Effects of tropical deforestation on global hydroclimate: a multimodel ensemble analysis. *J. Clim.* **22,** 1124–1141 (2009).
10. Nobre, P. *et al.* Amazon deforestation and climate change in a coupled model simulation. *J. Clim.* **22,** 5686–5697 (2009).
11. Pitman, A. J. *et al.* Uncertainties in climate responses to past land cover change: first results from the LUCID intercomparison study. *Geophys. Res. Lett.* **36,** L14814 (2009).
12. Butt, N., de Oliveira, P. A. & Costa, M. H. Evidence that deforestation affects the onset of the rainy season in Rondonia, Brazil. *J. Geophys. Res.* **116,** D11120 (2011).
13. Negri, A. J., Adler, R. F., Xu, L. & Surratt, J. The impact of Amazonian deforestation on dry season rainfall. *J. Clim.* **17,** 1306–1319 (2004).
14. Chagnon, F. J. F. & Bras, R. L. Contemporary climate change in the Amazon. *Geophys. Res. Lett.* **32,** L13703 (2005).
15. Huffman, G. *et al.* The TRMM multisatellite precipitation analysis (TMPA): quasi-global, multiyear, combined-sensor precipitation estimates at fine scales. *J. Hydrometeorol.* **8,** 38–55 (2007).
16. Myneni, R. B. *et al.* Global products of vegetation leaf area index and fraction absorbed PAR from year one of MODIS data. *Remote Sens. Environ.* **83,** 214–231 (2002).
17. Gimeno, L., Drumond, A., Nieto, R., Trigo, R. M. & Stohl, A. On the origin of continental precipitation. *Geophys. Res. Lett.* **37,** L13804 (2010).
18. van der Ent, R. J., Savenije, H. H. G., Schaefli, B. & Steele-Dunne, S. C. Origin and fate of atmospheric moisture over continents. *Wat. Resour. Res.* **46,** W09525 (2010).
19. Aragão, L. E. O. C. *et al.* Spatial validation of collection 4 MODIS LAI product in eastern Amazonia. *IEEE Trans. Geosci. Rem. Sens.* **43,** 2526–2534 (2005).
20. Rodell, M. *et al.* The global land data assimilation system. *Bull. Am. Meteorol. Soc.* **85,** 381–394 (2004).
21. Wang, J. F., Bras, R. L. & Eltahir, E. A. B. The impact of observed deforestation on the mesoscale distribution on the mesoscale distribution of rainfall and clouds in Amazonia. *J. Hydrometeorol.* **1,** 267–286 (2000).
22. Garcia-Carreras, L. & Parker, D. J. How does local tropical deforestation affect rainfall? *Geophys. Res. Lett.* **38,** L19802 (2011).
23. Andreae, M. O. *et al.* Smoking rain clouds over the Amazon. *Science* **303,** 1337–1342 (2004).
24. Koren, I. *et al.* Aerosol-induced intensification of rain from the tropics to mid-latitudes. *Nature Geosci.* **5,** 118–122 (2012).
25. Soares-Fihlo, B. S. *et al.* Modelling conservation in the Amazon basin. *Nature* **440,** 520–523 (2006).
26. Phillips, O. L. *et al.* Drought sensitivity of the Amazon rainforest. *Science* **323,** 1344–1347 (2009).
27. Aragão, L. E. O. C. *et al.* Spatial patterns and fire response of recent Amazonian droughts. *Geophys. Res. Lett.* **34,** L07701 (2007).
28. Davidson, E. A. *et al.* The Amazon basin in transition. *Nature* **481,** 321–328 (2012).
29. Huffman, G. J. Estimates of root-mean-square random error for finite samples of estimated precipitation. *J. Appl. Meteorol.* **36,** 1191–1201 (1997).
30. Smith, T. M., Arkin, P. A., Bates, J. J. & Huffman, G. J. Estimating bias of satellite precipitation estimates. *J. Hydrometeorol.* **7,** 841–856 (2006).

Supplementary Information is available in the online version of the paper.

Acknowledgements D.V.S. acknowledges a Natural Environment Research Council grant (NE/G015015/1). The GLDAS data used in this study were acquired as part of the mission of NASA's Earth Science Division and were archived and distributed by the Goddard Earth Sciences Data and Information Services Center.

Author Contributions D.V.S. and S.R.A. initiated the project. All authors participated in discussions, conducted the analysis, assisted with data interpretation and wrote the manuscript.

Author Information Reprints and permissions information is available at www.nature.com/reprints. The authors declare no competing financial interests. Readers are welcome to comment on the online version of the paper. Correspondence and requests for materials should be addressed to D.V.S. (d.v.spracklen@leeds.ac.uk).

©2012 **Macmillan Publishers Limited. All rights reserved**

METHODS

Remote-sensed data. We used precipitation retrievals (from the Tropical Rainfall Measuring Mission (TRMM; http://trmm.gsfc.nasa.gov/) and other satellites) in the 3B42 3-h $0.25^\circ \times 0.25^\circ$ product[15] to calculate daily accumulated (24 h) rainfall. This product reports precipitation from microwave sensors on board polar-orbiting satellites, combined with more frequent cloud-top temperature data, surface rain gauge analysis and the precipitation radar on TRMM. We used the monthly mean leaf area index (LAI) from the Moderate Resolution Imaging Spectroradiometer (MODIS; http://modis.gsfc.nasa.gov/data/dataprod/dataproducts.php?MOD_NUMBER=15)[16] using the MOD15_BU_V5 product available at $0.25^\circ \times 0.25^\circ$ resolution.

The precipitation product includes both systematic and random error[29,30]. Systematic biases of 0.5–1 mm d^{-1}, or 0.2 times the mean precipitation, have been estimated[30]. To reduce the random error we spatially averaged the precipitation product to $1^\circ \times 1^\circ$ resolution and temporally averaged to give daily accumulated (24 h) precipitation. This temporal and spatial averaging applied to TRMM3B42 means that each data point in our analysis (which corresponds to a single trajectory) is the average of 128 TRMM3B42 data points. This substantially reduces the random error that is present in the TRMM3B42 product[29]. We estimate the random error using the method of ref. 29 and assume a systematic error of 0.2 times the mean precipitation[30]. We combine the random and systematic errors in quadrature to give an estimate of the total error, which in any case is substantially smaller than the large effect of vegetation on precipitation. We spatially averaged the LAI data to the same resolution as the precipitation product.

Land surface models. We used $1^\circ \times 1^\circ$ monthly mean evaporation from four global land surface models (Community Land Model (CLM), Variable Infiltration Capacity model (VIC), NOAH and MOSIAC) archived on the Global Land Data Assimilation System (GLDAS; http://disc.sci.gsfc.nasa.gov/services/grads-gds/gldas)[20]. The models are forced by a combination of meteorological data sets including atmospheric analysis, and precipitation from merged gauge–satellite products.

Atmospheric transport. We calculated kinematic atmospheric back-trajectories arriving daily (00:00, 06:00, 12:00 and 18:00 UT) on a $1^\circ \times 1^\circ$ grid for the period 2001–07 using the OFFLINE trajectory model[31]. The position of each trajectory is calculated every 30 min, and output every 6 h. We calculated 3-, 5- and 10-day trajectories arriving at the surface and 3 levels above the surface (900, 800 and 700 hPa) that are likely to be within the deep tropical boundary layer. We demonstrate that our results are robust to the back-trajectory length (Supplementary Fig. 1), arrival pressure (Supplementary Fig. 2) and arrival time (Supplementary Fig. 3) of the trajectory. Throughout the Letter we report analysis of 10-day back-trajectories arriving at the surface at 12:00 UT.

Analysis. For each trajectory we calculated (1) total distance travelled over land (Σdist), (2) cumulative exposure to LAI (ΣLAI), (3) average elevation of the topography (specified by the Climate Research Unit CRU CL 2.0 database, 10′ resolution) over which the air mass travels, and (4) cumulative evapotranspiration (specified by GLDAS; ΣET). We calculate ΣLAI regardless of trajectory pressure but show that restricting the calculation to when trajectory pressure is greater than 850 hPa gives similar results (Supplementary Fig. 9).

We analysed relationships between daily precipitation and the variables calculated from air mass history (Σdist, ΣLAI and ΣET). We stratified trajectories into dry season and wet season and according to the initial specific humidity (q) of the back-trajectory (taken from the ECMWF analyses). The timings of wet and dry season are location dependent. For the purpose of this analysis we defined the dry season at any location as calendar months with below annual average precipitation for that location and the wet season as calendar months with above average precipitation (as observed by TRMM3B42; Supplementary Table 2). We demonstrated that this stratification results in large variability in initial q of the back-trajectory (Supplementary Table 2). We conducted detailed analysis over 4 large ($10^\circ \times 10^\circ$, ~1,000 km × 1,000 km) domains. Our pan-tropical analysis was conducted at a horizontal resolution of $2.5^\circ \times 2.5^\circ$. For our 7-year analysis each $10^\circ \times 10^\circ$ grid box represents 255,000 trajectories whereas each $2.5^\circ \times 2.5^\circ$ grid box represents 15,968 trajectories.

We binned trajectories into deciles of ΣLAI. We then compared back-trajectories with small exposure to vegetation (lowest decile of ΣLAI) to back-trajectories with large exposure to vegetation (largest decile of ΣLAI) and used the Student's t-test to determine the significance of any differences. Accounting for the stratification described above means that each data point (for example, data point in Fig. 2a, box-plot in Fig. 2b) represents 3,650 trajectories. We fitted relationships between precipitation and ΣLAI with functions of the form $y(x) = a\exp(bx) + c$ (see Fig. 2a). Supplementary Table 2 gives the fitted variables for the $10^\circ \times 10^\circ$ domains. Using a linear fit ($y(x) = ax + c$), which does not capture the nonlinear behaviour of the data well, altered our estimated impacts of deforestation on annual mean Amazon basin rainfall from −14% to −10%.

To estimate the impact of Amazonian deforestation on precipitation we combined the functions we fitted above with projected LAI distributions after deforestation. We created an LAI distribution for the year 2050 (see Supplementary Fig. 8) by combining a business-as-usual deforestation scenario[25] with the present-day LAI distribution from MODIS. We assumed that deforested areas are maintained as pasture with a LAI of 1 m^2 m^{-2} (ref. 32). We then ran our present-day trajectories over the projected LAI to calculate the ΣLAI that would occur in the deforestation scenario. We used our empirical relationships (calculated at a resolution of $2.5^\circ \times 2.5^\circ$) along with ΣLAI to estimate the rainfall that would occur after deforestation. We estimated both wet season and dry season rainfall. Our approach only estimates the change in rainfall due to changes in water recycling. It makes the implicit assumption that there is no change in the large-scale circulation, and that the local impacts of deforestation on rainfall are negligible downstream. Calculation of the full impacts of deforestation on rainfall would require a climate model.

We compared the estimated changes in rainfall due to deforestation with present-day (1998–2010) rainfall recorded by TRMM3B42. We make comparisons for both the wet season and the dry season.

31. Methven, J. *Offline Trajectories: Calculation and Accuracy* Technical Report 44, (UK Universities Global Atmospheric Modelling Programme, University of Reading, 1997).
32. Aragão, L. E. O. C., Shimabukuro, Y. E., Santo, F. D. B. E. & Williams, M. Landscape pattern and spatial variability of leaf area index in Eastern Amazonia. *For. Ecol. Mgmt.* **211,** 240–256 (2005).

©2012 **Macmillan Publishers Limited. All rights reserved**

LETTER

doi:10.1038/nature11377

Afternoon rain more likely over drier soils

Christopher M. Taylor[1], Richard A. M. de Jeu[2], Fran□oise Guichard[3], Phil P. Harris[1] & Wouter A. Dorigo[4]

Land surface properties, such as vegetation cover and soil moisture, influence the partitioning of radiative energy between latent and sensible heat fluxes in daytime hours. During dry periods, soil-water deficit can limit evapotranspiration, leading to warmer and drier conditions in the lower atmosphere[1,2]. Soil moisture can influence the development of convective storms through such modifications of low-level atmospheric temperature and humidity[1,3], which in turn feeds back on soil moisture. Yet there is considerable uncertainty in how soil moisture affects convective storms across the world, owing to a lack of observational evidence and uncertainty in large-scale models[4]. Here we present a global-scale observational analysis of the coupling between soil moisture and precipitation. We show that across all six continents studied, afternoon rain falls preferentially over soils that are relatively dry compared to the surrounding area. The signal emerges most clearly in the observations over semi-arid regions, where surface fluxes are sensitive to soil moisture, and convective events are frequent. Mechanistically, our results are consistent with enhanced afternoon moist convection driven by increased sensible heat flux over drier soils, and/or mesoscale variability in soil moisture. We find no evidence in our analysis of a positive feedback—that is, a preference for rain over wetter soils—at the spatial scale (50–100 kilometres) studied. In contrast, we find that a positive feedback of soil moisture on simulated precipitation does dominate in six state-of-the-art global weather and climate models—a difference that may contribute to excessive simulated droughts in large-scale models.

Soil moisture influences precipitation across a range of scales in time and space[5]. In drought-affected continental regions, weak evapotranspiration leads to reduced atmospheric moisture content over a period of days, potentially suppressing subsequent precipitation[6]. When soil moisture anomalies are extensive, surface-induced perturbations to the atmospheric heat budget may modify synoptic-scale circulations[2], in turn affecting moisture advection from the oceans[7]. On smaller scales, the development of convective clouds and precipitation can be influenced by local surface fluxes over the course of the day[1,3]. Theoretical considerations[8,9] suggest that, in an undisturbed atmosphere, the likelihood and sign of a surface feedback will be determined by the atmospheric profiles of temperature and humidity. Thus, one might expect regional variations in the strength and sign of convective sensitivity to soil moisture[10,11]. Mesoscale variability in soil moisture can also influence the feedback through the development of daytime circulations[12], which provide additional convergence to trigger convection[13,14].

Several studies have examined the impact of the land surface on observed rainfall in different regions of the world. Analyses in Illinois[15] and West Africa[16] have indicated positive correlations between antecedent soil moisture and precipitation, consistent with a positive soil moisture feedback. A recent study[17] based on observationally constrained reanalysis data showed an increasing frequency of convective rainfall when evapotranspiration was higher across much of North America. On the other hand, examination of satellite cloud data has indicated locally enhanced afternoon precipitation frequency over surfaces with increased sensible heat fluxes, as a result of mesoscale circulations due either to soil moisture[18] or vegetation cover[19,20].

At the regional scale, climate models tend to agree on where feedbacks occur, these being constrained largely by where soil moisture limits evapotranspiration in the presence of convective activity[4]. But the spread in simulated feedback strength is large, highlighting both the uncertainty in surface flux sensitivity to soil moisture and the response of the planetary boundary layer and convection to surface fluxes[21,22]. Indeed, the feedback sign can change depending on model spatial resolution, with a strong influence of the convective parameterization likely to be responsible[23].

Until recently, there has been a lack of observations with which to evaluate feedbacks in large-scale models. We address that problem here, and focus on the least well understood aspect of the feedback loop between soil moisture and precipitation, namely, the response of daytime moist convection to soil moisture anomalies. In the past decade, global observational data sets of both surface soil moisture[24,25] and precipitation[26] have become available at a resolution of 0.25° × 0.25°, on daily and 3-hourly time steps respectively. We use these to analyse the location of afternoon rain events relative to the underlying antecedent soil moisture. In particular we examine whether rain is more likely over soils that are wetter or drier than the surrounding area.We then apply the same methodology to six global models used in reanalyses or climate projections.

We focus on the development of precipitation events during the afternoon, when the sensitivity of convection to land conditions is expected to be maximized. An event is defined at a 0.25° × 0.25° pixel location (L_{max}) with a maximum in afternoon rainfall, centred in a box measuring 1.25° × 1.25° (see Methods Summary and Supplementary Fig. 3). Each L_{max} is paired with one or more pixels in the box where afternoon rainfall is at a minimum (L_{min}). We compute the difference in pre-rain-event soil moisture, ΔS_e, between L_{max} and L_{min} having first subtracted a climatological mean soil moisture from both locations. We quantify the strength of the soil moisture effect on precipitation using a sample of events, and assess how unexpected the observed sample mean value of ΔS_e is, relative to a control sample, ΔS_c, from the same location pairs on non-event days. More precisely, we examine the difference in ΔS between the event and control samples, $\delta_e = \text{mean}(\Delta S_e) - \text{mean}(\Delta S_c)$, expressed as a percentile of typical δ values (see Methods Summary). Mountainous and coastal areas are excluded because of their effects on mesoscale precipitation, and we are unable to analyse the observations in tropical forest regions, owing to the limitations of soil moisture retrievals beneath dense vegetation.

The map in Fig. 1 shows regions of the world where afternoon precipitation is observed more frequently than expected over wet (blue) or dry (red) soils, based on analysis of δ_e at a scale of 5°. Globally, 28.9% of the grid cells analysed have percentile values, P, less than 10, as compared to an expected frequency (assuming no feedback) of 10%, and just 3.4% with $P > 90$. Clusters of low percentiles are found in semi-arid and arid regions, most notably North Africa, but also in Eastern Australia, Central Asia and Southern Africa. These clusters indicate a clear preference for afternoon rain over drier soils

[1]NERC Centre for Ecology and Hydrology, Maclean Building, Benson Lane, Crowmarsh Gifford, Wallingford OX10 8BB, UK. [2]Vrije Universiteit Amsterdam, Earth and Climate Cluster, Department of Earth Sciences, Faculty of Earth and Life Sciences, De Boelelaan 1085, 1081 HV Amsterdam, The Netherlands. [3]CNRM-GAME (CNRS and Me¨te¨o-France), 42 avenue Coriolis, 31057 Toulouse Cedex, France. [4]Institute of Photogrammetry and Remote Sensing (I.P.F.), Vienna University of Technology, GusshausstraÞe 27-29, 1040 Vienna, Austria.

©2012 Macmillan Publishers Limited. All rights reserved

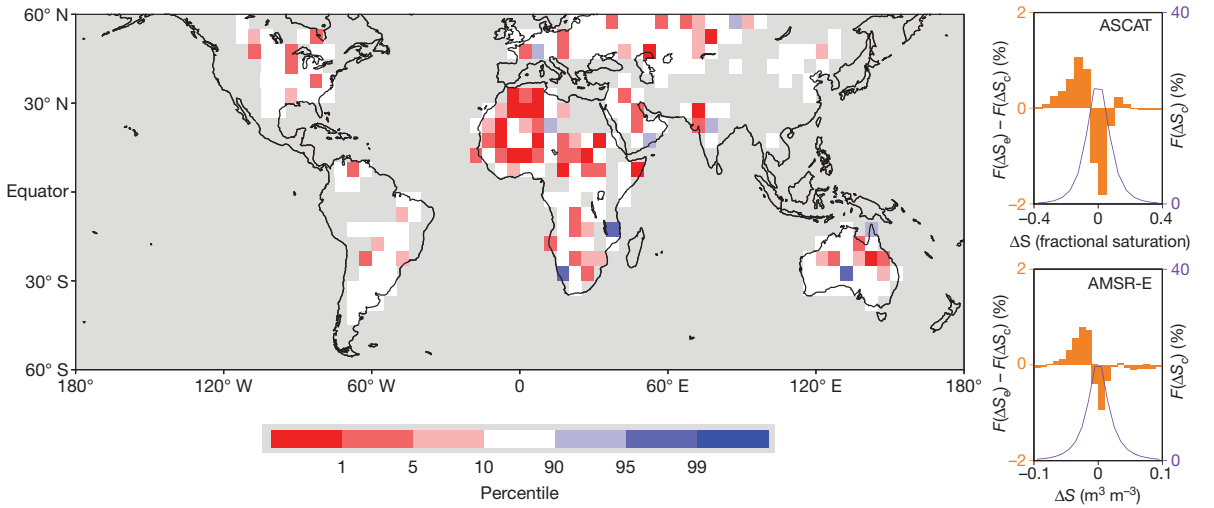

Figure 1 | Preference for afternoon precipitation over soil moisture anomalies. Percentiles of the observed variable $\delta_e = \text{mean}(\Delta S_e) - \text{mean}(\Delta S_c)$ for each $5^\circ \times 5^\circ$ box under a null assumption that no feedback exists. Null sampling distributions of δ values were estimated for each box by re-sampling without replacement from the combined set of event and non-event ΔS values. Low (high) percentiles indicate where rainfall maxima occur over locally dry (wet) soil more frequently than expected. Grey denotes $5^\circ \times 5^\circ$ cells containing fewer than 25 events. The map is based on a merging of two separate analyses using either ASCAT or AMSR-E soil moisture. For each $5^\circ \times 5^\circ$ cell, the relative quality of the two data sets is tested independently to determine which product is used (Supplementary Figs 5, 6). Insets: frequency histograms $F(\Delta S_c)$ of soil moisture difference in the global control sample (purple), and the difference $F(\Delta S_e) - F(\Delta S_c)$ between the histograms of the global event and global control samples (orange shading). The total number of events (n_e) is 29,729 for ASCAT and 73,623 for AMSR-E. Note the different units for ΔS for ASCAT (fractional saturation) and AMSR-E ($m^3\,m^{-3}$).

in those regions, consistent with a previous study over the Western Sahel[18]. This signal is also evident when computing δ_e from all events across the world (Fig. 1 insets). Further analysis (Supplementary Information and Supplementary Tables 3 and 4) demonstrates that this signal is statistically significant at the 99% level over all continents and in all climate zones, with the exception of tropical forests, where accurate soil moisture retrievals are unavailable. We repeated the analysis after degrading the spatial resolution from 0.25° to 1.0° . This produced only about one-tenth of the number of events identified in the 0.25° data, but a statistically robust preference for rain over drier soil was still found across the tropics, and in particular over parts of North Africa and Australia (Supplementary Fig. 10; Supplementary Tables 3, 4).

Using two alternative precipitation data sets, we found the same global preference for rain over drier soil, and similar regions contributing to that signal (Supplementary Fig. 8; Supplementary Tables 3, 4). Although all of the satellite-derived data sets are subject to errors at the event scale, analysing the data over many events should yield more accurate estimates of δ_e. Furthermore, our approach exploits an aspect of rainfall that is relatively well captured by satellite, that is, its spatial structure. Additional analysis (Supplementary Fig. 4) indicates a strong degree of mutual consistency in the spatial variability of soil moisture and rainfall in our independent data sets, providing further evidence to support our methodology.

We now consider whether the observed preference for rain over drier soil is consistent with land surface feedback. For a soil moisture feedback on precipitation, soil water deficit must limit evapotranspiration. This regime is found only in certain seasons and regions of the world[4], where water stress coincides with convective activity. Low percentiles in Fig. 1 occur in areas that are relatively dry, and originate from seasons with convective storms (Supplementary Fig. 9). Using data from across the globe, the sensitivity of δ_e to the areal-mean ($1.25^\circ \times 1.25^\circ$) soil moisture is explored in Fig. 2a. The most negative values (rain over drier soil) are found for the driest mean conditions, and the signal loses significance at the 95% level above 0.20 $m^3\,m^{-3}$. This behaviour is consistent with soil moisture feedback, as the sensitivity of sensible and latent heat fluxes to soil moisture increases as mean soil moisture decreases. Also, the use of surface soil moisture

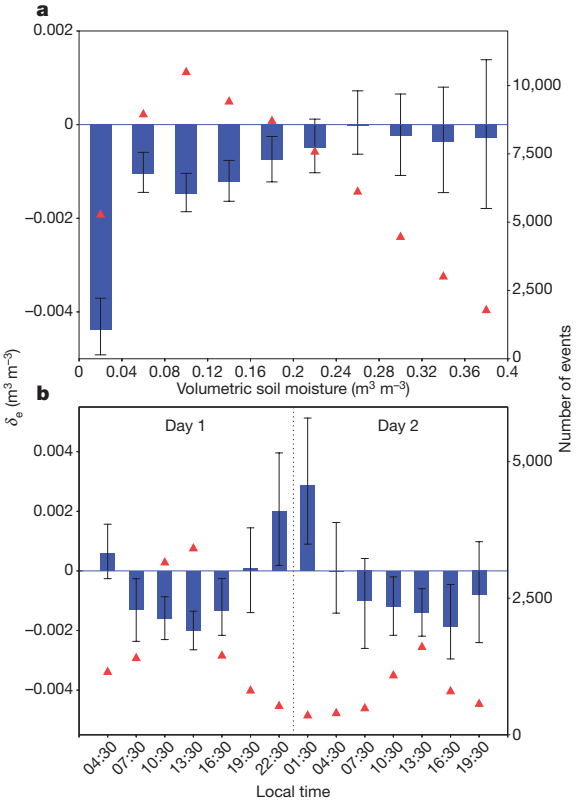

Figure 2 | Sensitivities of pre-rain-event soil moisture to mean soil moisture and time of day. Blue bars denote the anomalous pre-rain-event soil moisture difference, δ_e, averaged over every event globally, as a function of pre-event soil moisture averaged over $1.25^\circ \times 1.25^\circ$ (**a**), and time of first precipitation (at least 1 mm over 3 h), following a soil moisture measurement at 1:30 on day 1 (**b**). Negative values of δ_e indicate a preference for precipitation over drier soil, and error bars show 90% confidence limits. Red triangles denote the number of events used for each δ_e average.

©2012 Macmillan Publishers Limited. All rights reserved

as a proxy for surface flux variability should be most effective for dry and sparsely vegetated surfaces.

A land feedback requires a strong diurnal sensitivity in the observed signal. We repeated our analysis, this time detecting the onset of precipitation at varying lag times after a soil moisture observation at 1:30 (all times are local time). The values of δ_e (Fig. 2b) exhibit a pronounced diurnal cycle, still evident 36 hours after the observation. The most negative values occur during daytime, in particular between 12:00 and 15:00. By contrast, between 21:00 and 3:00 the opposite signal emerges; that is, events are more likely to be found over wetter soils. The early afternoon minimum is consistent with a negative soil moisture feedback on convective initiation, when the effects of surface properties on the planetary boundary layer, convective instability and mesoscale flows are all maximized. Mechanisms to explain the reverse signal in the hours around midnight may be more subtle. The effects of thermals and daytime surface-induced flows are likely to be relatively short-lived after dusk. On the other hand, nocturnal humidity anomalies may persist for longer, depending on the spatial scale of the surface features and wind conditions. From detailed examination of individual events, it appears that, overnight, there is an increasing influence of pre-existing, fast-moving convective systems in our sample, particularly in the Sahel. Distinct mechanisms will be involved in the surface interaction with organized convective systems, which may favour a positive feedback[16].

Finally, we repeat our analysis using 3-hourly diagnostics from six global models, ranging in horizontal resolution from 0.5 to 2.0°. Our results (Fig. 3) indicate a strong preference for rain over wet soils for large parts of the world, in contrast to the observations. Only one model (Fig. 3e) produces more than the expected 10% of grid cells with $P < 10$, largely due to contributions at mid-latitudes. The cross-model signal favouring precipitation over wet soil, particularly across the tropics (Supplementary Table 3), demonstrates a fundamental failing in the ability of convective parameterizations to represent land feedbacks on daytime precipitation. This is likely to be linked to the oft-reported phase lag in the diurnal cycle of precipitation; that is, simulated rainfall tends to start several hours too early[27], and is possibly amplified by a lack of boundary-layer clouds in some models. This weakness has been related to the crude criteria used to trigger deep convection in large-scale models[28]. The onset of convective precipitation is overly sensitive to the daytime increase of moist convective instability, which is typically faster over wetter soils[3], favouring a positive feedback. Early initiation limits the effect of other daytime processes on triggering convection in the models. In contrast, our observational analysis points to the importance of dry boundary-layer dynamics for this phenomenon over land.

The observed preference for afternoon rain over locally drier soil on scales of 50–100 km is consistent with a number of regional studies based on remotely sensed data[18–20]. Our failure to find areas of positive

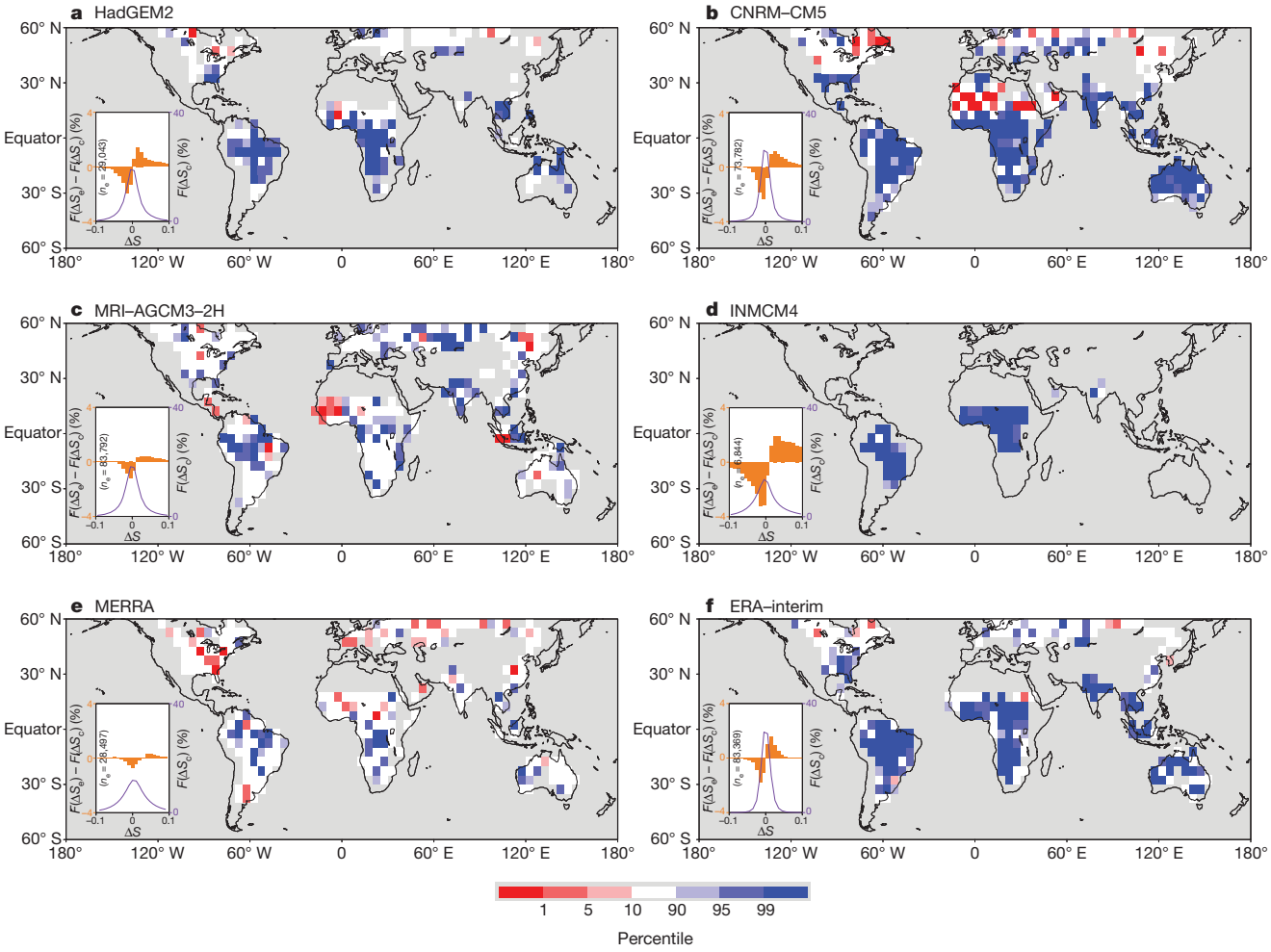

Figure 3 | Simulated preference for afternoon precipitation over soil moisture anomalies. As for Fig. 1 but using diagnostics from integrations by four climate models (**a**–**d**) and two atmospheric reanalysis models (**e**, **f**). Blue (red) shading indicates convective precipitation more likely over wetter (drier) soils. The models used are: **a**, HadGEM2; **b**, CNRM-CM5; **c**, MRI-AGCM3-2H; **d**, INMCM4; **e**, MERRA; and **f**, ERA-Interim. Inset as for Fig. 1, with ΔS in $m^3 m^{-3}$. Further details of the models are in Supplementary Information, with maps of the number of events in each model in Supplementary Fig. 11.

©2012 Macmillan Publishers Limited. All rights reserved

feedback may indicate the importance of surface-induced mesoscale flows in triggering convection[18], although the coarse spatial resolution of our data sets prevents us from drawing firm conclusions on this issue. Equally, mixing processes in the growth stage of convective clouds before precipitation[23,29] may play an important role. Neither of these processes is captured in existing one-dimensional analyses[8]. Furthermore, our results raise questions about the ability of models reliant on convective parameterizations to represent these processes adequately. Although the coarser-resolution models analysed here (HadGEM2, CNRM-CM5 and INMCM4) cannot resolve mesoscale soil moisture structures, nor their potential impacts on convective triggering[18], all the models have a strong tendency towards rain over wetter soils, for which we find no observational support. Our study does not, however, imply that the soil moisture feedback is negative at temporal and spatial scales different from those analysed here. The multi-day accumulation of moisture in the lower atmosphere from a freely transpiring land surface may provide more favourable initial (dawn) conditions for daytime convection than the equivalent accumulation over a drought-affected region. Equally, the large-scale dynamical response to soil moisture may dominate in some regions. However, the erroneous sensitivity of convection schemes demonstrated here is likely to contribute to a tendency for large-scale models to `lock-in' dry conditions, extending droughts unrealistically, and potentially exaggerating the role of soil moisture feedbacks in the climate system[30].

METHODS SUMMARY

Surface soil moisture retrievals are used between 60° S and 60° N from the Advanced Microwave Scanning Radiometer for EOS (AMSR-E; June 2002 to October 2011)[24], and the MetOP Advanced Scatterometer (ASCAT; 2007–11)[25]. They have typically one overpass per pixel per day at either 1:30 or 13:30 (AMSR-E), and 9:30 or 21:30 (ASCAT). Additional soil moisture quality control procedures are described in Supplementary Information. The CMORPH[26] 3-hourly precipitation data set is based on data from a combination of satellites.

Locations of afternoon events, L_{max}, are defined within a box measuring 5×5 pixels by the maximum accumulated precipitation (12:00–21:00) that exceeds 3 mm. We exclude pixels with more than 1 mm rain in the preceding hours, and apply an additional filter to remove cases close to active precipitation when using soil moisture data for 13:30. These steps ensure that the soil moisture measurement precedes the rainfall. Locations where topographic height variability exceeds 300 m are excluded, along with regions containing water bodies or strong climatological soil moisture gradients.

The control sample, ΔS_c, is constructed from daily soil moisture differences between locations L_{max} and L_{min}, using data for the same calendar month but from non-event years. This quantifies typical (non-event) soil moisture differences between the locations. Each value in samples ΔS_e and ΔS_c has an individual climatological mean ΔS subtracted, which is calculated from ΔS values in the same calendar month in non-event years. For the models, soil moisture and rainfall accumulations are available every 3 h (universal time). Because of the models' lower spatial resolution (0.5–2.0°), the event box is reduced to 3×3 pixels and the local time window between 6:00 and 8:59 adopted to calculate ΔS. Convective rain is accumulated in the subsequent 9 h, several hours in the day earlier, to account for diurnal phase bias in model precipitation.

Received 19 March; accepted 29 June 2012.
Published online 12 September 2012.

1. Betts, A. K. & Ball, J. H. FIFE surface climate and site-average dataset 1987–89. *J. Atmos. Sci.* **55,** 1091–1108 (1998).
2. Fischer, E. M. *et al.* Soil moisture-atmosphere interactions during the 2003 European summer heat wave. *J. Clim.* **20,** 5081–5099 (2007).
3. Eltahir, E. A. B. A soil moisture-rainfall feedback mechanism. 1. Theory and observations. *Wat. Resour. Res.* **34,** 765–776 (1998).
4. Koster, R. D. *et al.* Regions of strong coupling between soil moisture and precipitation. *Science* **305,** 1138–1140 (2004).
5. Goessling, H. F. & Reick, C. H. What do moisture recycling estimates tell us? Exploring the extreme case of non-evaporating continents. *Hydrol. Earth Syst. Sci.* **15,** 3217–3235 (2011).
6. van der Ent, R. J., Savenije, H. H. G., Schaefli, B. & Steele-Dunne, S. C. Origin and fate of atmospheric moisture over continents. *Wat. Resour. Res.* **46,** W09525 (2010).
7. Webster, P. J. Mechanisms of monsoon low-frequency variability - surface hydrological effects. *J. Atmos. Sci.* **40,** 2110–2124 (1983).
8. Findell, K. L. & Eltahir, E. A. B. Atmospheric controls on soil moisture-boundary layer interactions. Part I: framework development. *J. Hydrometeorol.* **4,** 552–569 (2003).
9. Ek, M. B. & Holtslag, A. A. M. Influence of soil moisture on boundary layer cloud development. *J. Hydrometeorol.* **5,** 86–99 (2004).
10. Findell, K. L. & Eltahir, E. A. B. Atmospheric controls on soil moisture-boundary layer interactions. Part II: feedbacks within the continental United States. *J. Hydrometeorol.* **4,** 570–583 (2003).
11. Ferguson, C. R. & Wood, E. F. Observed land–atmosphere coupling from satellite remote sensing and reanalysis. *J. Hydrometeorol.* **12,** 1221–1254 (2011).
12. Ookouchi, Y., Segal, M., Kessler, R. C. & Pielke, R. A. Evaluation of soil moisture effects on the generation and modification of mesoscale circulations. *Mon. Weath. Rev.* **112,** 2281–2292 (1984).
13. Cheng, W. Y. Y. & Cotton, W. R. Sensitivity of a cloud-resolving simulation of the genesis of a mesoscale convective system to horizontal heterogeneities in soil moisture initialization. *J. Hydrometeorol.* **5,** 934–958 (2004).
14. Anthes, R. A. Enhancement of convective precipitation by mesoscale variations in vegetative covering in semi-arid regions. *J. Clim. Appl. Meteorol.* **23,** 541–554 (1984).
15. Findell, K. L. & Eltahir, E. A. B. An analysis of the soil moisture-rainfall feedback, based on direct observations from Illinois. *Wat. Resour. Res.* **33,** 725–735 (1997).
16. Taylor, C. M. & Lebel, T. Observational evidence of persistent convective-scale rainfall patterns. *Mon. Weath. Rev.* **126,** 1597–1607 (1998).
17. Findell, K. L., Gentine, P., Lintner, B. R. & Kerr, C. Probability of afternoon precipitation in eastern United States and Mexico enhanced by high evaporation. *Nature Geosci.* **4,** 434–439 (2011).
18. Taylor, C. M. *et al.* Frequency of Sahelian storm initiation enhanced over mesoscale soil-moisture patterns. *Nature Geosci.* **4,** 430–433 (2011).
19. Wang, J. F. *et al.* Impact of deforestation in the Amazon basin on cloud climatology. *Proc. Natl Acad. Sci. USA* **106,** 3670–3674 (2009).
20. Carleton, A. M. *et al.* Synoptic circulation and land surface influences on convection in the Midwest US ``corn belt'' during the summers of 1999 and 2000. Part II: role of vegetation boundaries. *J. Clim.* **21,** 3617–3641 (2008).
21. Santanello, J. A., Peters-Lidard, C. D. & Kumar, S. V. Diagnosing the sensitivity of local land–atmosphere coupling via the soil moisture–boundary layer interaction. *J. Hydrometeorol.* **12,** 766–786 (2011).
22. Guo, Z. C. *et al.* GLACE: The Global Land-Atmosphere Coupling Experiment. Part II: analysis. *J. Hydrometeorol.* **7,** 611–625 (2006).
23. Hohenegger, C., Brockhaus, P., Bretherton, C. S. & Schar, C. The soil moisture-precipitation feedback in simulations with explicit and parameterized convection. *J. Clim.* **22,** 5003–5020 (2009).
24. Owe, M., de Jeu, R. & Holmes, T. Multisensor historical climatology of satellite-derived global land surface moisture. *J. Geophys. Res.* **113,** F01002 (2008).
25. Bartalis, Z. *et al.* Initial soil moisture retrievals from the METOP-A Advanced Scatterometer (ASCAT). *Geophys. Res. Lett.* **34,** L20401 (2007).
26. Joyce, R. J., Janowiak, J. E., Arkin, P. A. & Xie, P. CMORPH: a method that produces global precipitation estimates from passive microwave and infrared data at high spatial and temporal resolution. *J. Hydrometeorol.* **5,** 487–503 (2004).
27. Dai, A. Precipitation characteristics in eighteen coupled climate models. *J. Clim.* **19,** 4605–4630 (2006).
28. Guichard, F. *et al.* Modelling the diurnal cycle of deep precipitating convection over land with cloud-resolving models and single-column models. *Q. J. R. Meteorol. Soc.* **130,** 3139–3172 (2004).
29. Zhang, Y. & Klein, S. A. Mechanisms affecting the transition from shallow to deep convection over land: inferences from observations of the diurnal cycle collected at the ARM southern Great Plains site. *J. Atmos. Sci.* **67,** 2943–2959 (2010).
30. McCrary, R. R. & Randall, D. A. Great Plains drought in simulations of the twentieth century. *J. Clim.* **23,** 2178–2196 (2010).

Supplementary Information is linked to the online version of the paper at www.nature.com/nature.

Acknowledgements This research was partly funded by the European Union (FP6) WATCH Integrated Project (contract 036946), the UK National Centre for Earth Observation and the European Space Agency STSE Water Cycle Multi-mission Observation Strategy (WACMOS) project (ESRIN/contract number 22086/08/I-EC. We thank A. Beljaars, S. Seneviratne and D. Parker for discussions on this topic. We also thank the CMORPH, TRMM, PERSIANN and GPROF teams for the provision of their precipitation data, the World Climate Research Programme's Working Group on Coupled Modelling, and the centres who provided modelling data in Figure 3.

Author Contributions C.M.T. and R.A.M.d.J. conceived the study, C.M.T. performed the analysis and wrote the paper, R.A.M.d.J. and W.A.D. provided expertise on soil moisture data sets, F.G. interpreted the convective responses in models and observations, and P. P.H. devised statistical tests. All authors discussed the results and edited the manuscript.

Author Information Reprints and permissions information is available at www.nature.com/reprints. The authors declare no competing financial interests. Readers are welcome to comment on the online version of this article at www.nature.com/nature. Correspondence and requests for materials should be addressed to C.M.T. (cmt@ceh.ac.uk).

©2012 Macmillan Publishers Limited. All rights reserved

LETTER

doi:10.1038/nature11882

Sensitivity of tropical carbon to climate change constrained by carbon dioxide variability

Peter M. Cox[1], David Pearson[2], Ben B. Booth[2], Pierre Friedlingstein[1], Chris Huntingford[3], Chris D. Jones[2] & Catherine M. Luke[1]

The release of carbon from tropical forests may exacerbate future climate change[1], but the magnitude of the effect in climate models remains uncertain[2]. Coupled climate–carbon-cycle models generally agree that carbon storage on land will increase as a result of the simultaneous enhancement of plant photosynthesis and water use efficiency under higher atmospheric CO_2 concentrations, but will decrease owing to higher soil and plant respiration rates associated with warming temperatures[3]. At present, the balance between these effects varies markedly among coupled climate–carbon-cycle models, leading to a range of 330 gigatonnes in the projected change in the amount of carbon stored on tropical land by 2100. Explanations for this large uncertainty include differences in the predicted change in rainfall in Amazonia[4,5] and variations in the responses of alternative vegetation models to warming[6]. Here we identify an emergent linear relationship, across an ensemble of models[7], between the sensitivity of tropical land carbon storage to warming and the sensitivity of the annual growth rate of atmospheric CO_2 to tropical temperature anomalies[8]. Combined with contemporary observations of atmospheric CO_2 concentration and tropical temperature, this relationship provides a tight constraint on the sensitivity of tropical land carbon to climate change. We estimate that over tropical land from latitude 30° north to 30° south, warming alone will release 53 ± 17 gigatonnes of carbon per kelvin. Compared with the unconstrained ensemble of climate–carbon-cycle projections, this indicates a much lower risk of Amazon forest dieback under CO_2-induced climate change if CO_2 fertilization effects are as large as suggested by current models[9]. Our study, however, also implies greater certainty that carbon will be lost from tropical land if warming arises from reductions in aerosols[10] or increases in other greenhouse gases[11].

We use results from the Coupled Climate Carbon Cycle Model Intercomparison Project[3] (C^4MIP) focusing on changes in tropical land carbon storage in the latitudinal band from 30° N to 30° S. Although C^4MIP included general circulation models (GCMs) and Earth-system models of intermediate complexity, we limit our analysis to the GCMs because our emergent constraint requires models that generate interannual variability. The C^4MIP experimental design[3] forced models using the SRES A2 scenario[12] of anthropogenic CO_2 emissions (including those due to land-use change). For each model, an 'uncoupled' simulation was carried out in which the land and ocean carbon cycles were made insensitive to the climate change caused by the increase in atmospheric CO_2. Comparison between the coupled and uncoupled simulations allows the direct effects of CO_2 on land and ocean carbon sinks to be separated from the effects of climate change[3,13]. We test the emergent constraint derived from the C^4MIP GCMs against results from the recent HadCM3 land carbon-cycle ensemble[14].

Our emergent constraint could also be tested against the recent CMIP5 climate–carbon-cycle models, which will appear in the Fifth Assessment Report of the Intergovernmental Panel on Climate Change. However, models in that report typically use prescribed concentrations of atmospheric CO_2 (ref. 15). This makes direct comparison with the observed interannual variability in the atmospheric CO_2 concentration difficult. Therefore, the emergent constraint we present here is conditional on the relatively simplistic representations of the carbon cycle in the C^4MIP models.

Table 1 summarizes results from six C^4MIP GCMs (A to F) for 1960 to 2099. For all models, the impact of climate change on the carbon cycle results in a larger increase in atmospheric CO_2 in the coupled simulation relative to the uncoupled simulation. This amplification varies by an order of magnitude across the model ensemble (from an extra 18 parts per million by volume (p.p.m.v.) in model D to an extra 212 p.p.m.v. in model A). A large part of this uncertainty arises from differing responses of tropical land carbon to projected climate changes in each model. All models produce a significant increase in tropical land carbon storage in the uncoupled simulations as a result of the direct effects of CO_2 on photosynthesis and water-use efficiency (from +263 gigatonnes of carbon (GtC) in model F to +413 GtC in model C). The neglect of carbon–nitrogen interactions in this first generation of climate–carbon models is arguably a major limitation in the mid and high latitudes[16], but is much less problematic in tropical forests, which are not typically nitrogen-limited[17]. Forest inventories are also consistent with a significant CO_2 fertilization in the tropics[18,19]. Despite the reasonable agreement among models on the effect of CO_2 fertilization, the fully coupled simulations produce very different changes in tropical land carbon storage from 1960 to 2099 (from −11 GtC for model A to +319 GtC for model D).

Figure 1a represents the evolution of tropical land carbon storage in the C^4MIP models, with the upper and lower estimates shown for both the coupled and uncoupled simulations. The lower estimate in the coupled simulation comes from the HadCM3LC model, which projects Amazon forest dieback under CO_2-induced climate change[1,9,10]. In this model, tropical land carbon storage increases owing to direct CO_2 effects until around 2050, but then declines abruptly owing to warming and drying in Amazonia[9]. This projection, along with recent extreme droughts in Amazonia[20–22], suggests that tropical forest dieback is a potential high-impact tipping element that would constitute an abrupt change in Earth's climate system[23].

To separate direct effects of CO_2 from those of climate change, we follow previous analyses[3,13] in writing the change in tropical land carbon storage, ΔC_{LT}, in terms of the change in atmospheric CO_2, ΔC_a, and the change in tropical mean temperature, ΔT_T:

$$\Delta C_{LT} = \beta_{LT}\Delta C_a + \gamma_{LT}\Delta T_T$$

Here β_{LT} (GtC per p.p.m.v.) and γ_{LT} (GtC K^{-1}) are the sensitivities of tropical land carbon storage to direct CO_2 effects and to climate change, respectively. The uncoupled simulations are used to estimate β_{LT} for each model, and then these values are used to isolate γ_{LT} from the coupled simulations[3,13] by subtracting the direct CO_2 effect. Figure 1b is a scatter plot of β_{LT} and γ_{LT} for each C^4MIP model and the three HadCM3 ensemble members. Whereas the β_{LT} values span a factor of two, from about 0.5 to 1 GtC per p.p.m.v., the γ_{LT} values range

[1]College of Engineering, Mathematics and Physical Science, University of Exeter, Exeter EX4 4QF, UK. [2]Hadley Centre, Met Office, Exeter EX1 3PB, UK. [3]Centre for Ecology and Hydrology, Wallingford OX10 8BB, UK.

©2013 Macmillan Publishers Limited. All rights reserved

Table 1 | Summary data for climate-carbon cycle projections

Model		Change in global atmospheric CO_2 (p.p.m.v.)		Change in tropical land carbon (GtC)		Change in tropical temperature (K)
		Coupled	Uncoupled	Coupled	Uncoupled	
A	HadCM3LC	689	477	−11	354	3.93
B	IPSL	453	381	177	365	2.70
C	MPI	524	443	242	413	4.36
D	CCSM1	483	465	319	364	1.53
E	FRCGC	589	465	118	271	3.61
F	LOOP	489	460	185	263	3.30
G	HadCM3C-st	599	331	−148	317	4.41
H	HadCM3C-a	445	333	−6	168	3.76
I	HadCM3C-h	589	246	−165	251	4.08

Changes in atmospheric CO_2, tropical land carbon and tropical near-surface air temperature (30° N–30° S), as simulated by the nine climate–carbon GCMs analysed in this study. Models A to F are from the C^4MIP study[3], which prescribed the SRES A2 CO_2 emissions scenario. For these models, the changes are calculated over the period 1960–2099. Models G to I are from a land carbon-cycle parameter ensemble carried out with the HadCM3 model under the SRES A1B scenario[14], and were run only to 2080, so differences here are for 1960 to 2080. In all cases, model runs were carried out both including and excluding climate effects on the carbon cycle ('coupled' and 'uncoupled', respectively), so that the impacts of climate–carbon-cycle feedbacks could be diagnosed.

over a factor of more than four, from $-29\,\mathrm{GtC\,K^{-1}}$ (model F) to $-133\,\mathrm{GtC\,K^{-1}}$ (model A), with a C^4MIP mean of $-69\,\mathrm{GtC\,K^{-1}}$ and standard deviation of $39\,\mathrm{GtC\,K^{-1}}$. This range is even larger if the HadCM3 ensemble members are included. We therefore focus on reducing the larger uncertainty, namely that in γ_{LT}.

Our inspiration for deriving a multi-model emergent constraint comes from a recent study that showed a strong relationship between the contemporary temperature sensitivity of seasonal snow cover and the magnitude of the snow–albedo feedback, across more than 20 GCMs[7]. Because the seasonal cycle of snow cover can be estimated from observations, this model-derived relationship converts the contemporary observations to a constraint on the size of the snow–albedo feedback in the real climate system, for which there is no direct reliable measurement. Emergent constraints of this type make use of the often bewildering spread among Earth-system model projections to reduce uncertainties in the sensitivities of the real Earth system to anthropogenic forcing. They are distinct and complementary to bottom-up constraints arising from process-based studies.

It made sense a priori to look for an emergent constraint linking the sensitivity of tropical land carbon to interannual variability (IAV) in the growth rate of atmospheric CO_2. Tropical land carbon changes in response to climate through changes in the net land–atmosphere CO_2 flux into and out of this carbon store. Critically, the sensitivity of this net tropical CO_2 flux is revealed by the IAV in the CO_2 growth rate, because this is known to be dominated by the response of the tropical land carbon cycle to climatic anomalies (Supplementary Fig. 1a) such as the El Niño/Southern Oscillation[8,24,25]. Hence, some relationship between the IAV in CO_2 and the longer-term sensitivity of tropical land carbon storage to climate change (γ_{LT}) is to be expected, as long as processes that are not evident in the short-term variation of the CO_2 fluxes (for example forest dynamics or changes in long-lived soil carbon pools) do not dominate the long-term response. This is our working hypothesis to be tested against the C^4MIP models, which include a range of representations of slow vegetation and soil processes[3].

Figure 2a compares the observed IAV in the growth rate of global atmospheric CO_2 (refs 26, 27) with the IAV in the annual mean tropical temperature[28]. In both cases, we have chosen observational variables (global mean atmospheric CO_2 and mean land-plus-ocean temperature between 30° N and 30° S) for consistency with the variables available from the C^4MIP models. Aside from the years immediately after the volcanic eruptions[24] of Mount Agung, El Chichon and Mount Pinatubo, the IAV in the growth rate of atmospheric CO_2 is linearly correlated with the IAV in the tropical temperature ($r = 0.65$ (correlation coefficient), $P < 0.0001$; Fig. 2b), with a best-fit 'IAV sensitivity' of $5.1 \pm 0.9\,\mathrm{GtC\,yr^{-1}\,K^{-1}}$. Excluding these volcano-affected years has an impact on the best-fit sensitivity of less than 5%, but avoids the complication of diffuse-light fertilization of plant growth[29], which is not included in any of the C^4MIP models. We also find a similar sensitivity regardless of which tropical temperature reconstruction we use. There is a greater sensitivity to the choice of the global atmospheric CO_2 data set, but this does not affect our overall conclusions (Supplementary Table 1).

A similar calculation is made for each of the coupled climate–carbon-cycle models, to derive the sensitivity of the CO_2 growth rate to tropical temperature for the period 1960–2010. Compared with the observational data, models tend to overestimate the IAV in the tropical temperature by a factor of up to two, and to overestimate the IAV in the CO_2 growth rate by a factor of up to three. The correlation between these variables is underestimated in some models (F, B and D) and overestimated in others (A, E and C). Hence, IAV sensitivity varies across the C^4MIP model ensemble, from $2.9 \pm 1.4\,\mathrm{GtC\,yr^{-1}\,K^{-1}}$ (model F) to $9.7 \pm 0.7\,\mathrm{GtC\,yr^{-1}\,K^{-1}}$ (model A), with most of this range resulting from differences in the sensitivity of heterotrophic respiration to climate (Supplementary Fig. 1b). The three HadCM3

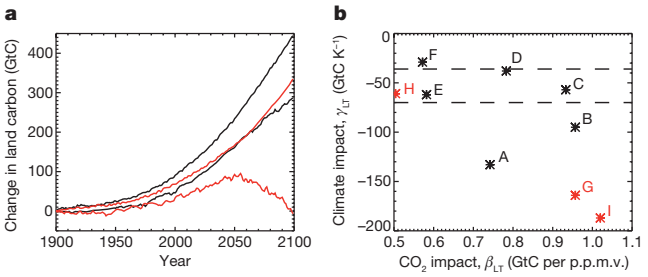

Figure 1 | Projected changes in land carbon storage in the tropics from coupled climate–carbon-cycle models. **a**, Upper and lower estimates from the C^4MIP models[3] (A–F in Table 1) for uncoupled (black lines) and coupled simulations (red lines). **b**, Impact of changes in tropical temperature versus impact of changes in atmospheric CO_2 on tropical land carbon, for the C^4MIP models (black letters) and three variants of the HadCM3C model[14] (red letters). The horizontal lines represent the new constraint presented in this study.

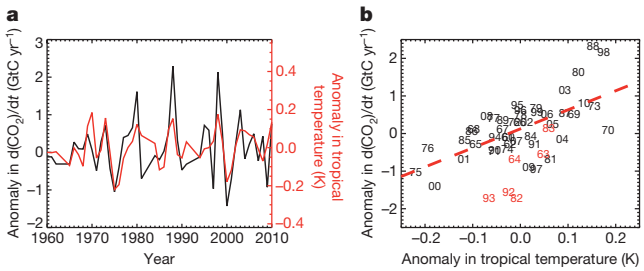

Figure 2 | Observed relationship between variations in the growth rate of atmospheric CO_2 and tropical temperature. **a**, Annual anomalies in CO_2 growth rate (black) and tropical temperature (red) versus year. **b**, Sensitivity of CO_2 growth rate to tropical temperature, with numbers representing the individual years in **a** and the dashed line showing the best-fit straight line, which has a gradient of $5.1 \pm 0.9\,\mathrm{GtC\,yr^{-1}\,K^{-1}}$. The years in red were not included in this fit because they directly followed major volcanic perturbations to the climate.

©2013 Macmillan Publishers Limited. All rights reserved

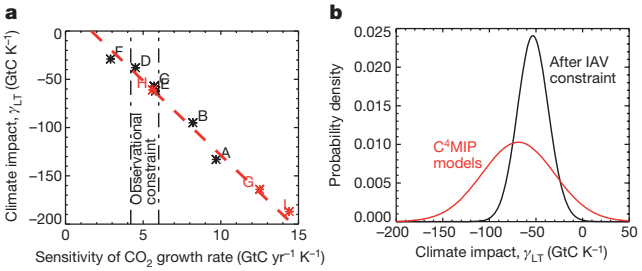

Figure 3 | Emergent constraint on the sensitivity of tropical land carbon to climate change. **a**, Climate sensitivity of tropical land carbon (γ_{LT}) versus the sensitivity of the CO_2 growth rate to tropical temperature, for each of the models shown in Table 1. The dashed line shows the best-fit straight line across the C^4MIP models (black). The red symbols represent a test of this relationship against the three HadCM3C ensemble members. The dot–dash lines indicate the constraint on the observed IAV in the CO_2 growth rate derived from Fig. 2b. **b**, PDF for the climate sensitivity of γ_{LT}. The black line was derived by applying the IAV constraint to the across-model relationship shown in **a**. The red line shows the 'prior' PDF that arises from assuming that all of the C^4MIP models are equally likely to be correct and that they come from a Gaussian distribution.

ensemble members, which were produced by perturbing only parameters in the land carbon-cycle component of the model[13], span an even larger range (5.6–14.4 GtC yr^{-1} K^{-1}), suggesting that uncertainties in the modelling of the tropical land carbon cycle are critical.

Most importantly, these differing IAV sensitivities are strongly correlated ($r = 0.98$, $P = 0.0005$) with variations in γ_{LT} across C^4MIP models (black labels in Fig. 3a). The dashed red line in Fig. 3a shows the best-fit straight line relating these variables for the six C^4MIP GCMs (although in principle a well-defined nonlinear function would also yield an emergent constraint). The red labels in Fig. 3a show how well this relationship would have predicted the variation in γ_{LT} for the three HadCM3 ensemble members given the IAV sensitivity of each. We note that two of the HadCM3 variants have γ_{LT} values beyond the range of the C^4MIP models, but that the extrapolated straight line is nevertheless able to fit these outliers. The dotted vertical black lines in Fig. 3a show the IAV sensitivity (± 1 s.d.), as previously estimated from the contemporary observations, from which we derive tighter bounds on γ_{LT}.

With the model-derived relationship between γ_{LT} and the IAV sensitivity, we can use the observational constraint to estimate a probability density function (PDF) for γ_{LT} (Methods). Figure 3b compares this with the PDF arising from assuming that all C^4MIP models are equally likely to be true and come from an underlying Gaussian distribution (red line). The emergent constraint from the IAV sensitivity of the CO_2 growth rate sharpens the PDF of γ_{LT} and moves its peak to a less negative value (-53 ± 17 as opposed to -69 ± 39 GtC K^{-1}). The application of the IAV constraint reduces the estimated probability of γ_{LT} values more negative than -100 GtC K^{-1}, typically associated with models that project CO_2-induced tropical forest dieback, by almost two orders of magnitude from 21% to 0.24%.

The IAV constraint also gives strong confirmation that tropical land carbon is vulnerable to warming caused by non-CO_2 forcing factors[11]. Remaining uncertainties in tropical land climate–carbon-cycle feedbacks are therefore the magnitude of long-term CO_2 fertilization effects in the tropics, and the extent to which future climate change will be caused by non-CO_2 factors.

METHODS SUMMARY

We used results from six of the eleven models used in C^4MIP[3]. The five excluded models consisted of four Earth-system models of intermediate complexity, which do not typically generate internal variability as required to define the interannual sensitivity of the CO_2 growth rate to tropical temperature anomalies, and one GCM (LLNL), which reported zonal mean land temperatures rather than zonal mean (land and ocean) temperatures. Outputs from the remaining six models were reported as annual means for each 30° latitudinal band (available at https://c4mip.lsce.ipsl.fr/diagnostics_phase2.html). We combined the outputs from the 30° N–0° and 0°–30° S bands to define the projected changes for the 30° N–30° S 'tropical' band.

Models G, H and I in this study, which are used to test the emergent constraint derived from the C^4MIP models, come from a land carbon-cycle ensemble carried out with the HadCM3C model[14]. HadCM3C is similar to C^4MIP model A (HadCM3LC) but includes a higher-resolution ocean model (1.25° × 1.25° rather than 2.5° × 3.75°) and interactive atmospheric sulphur-cycle chemistry. Seventeen HadCM3C ensemble members were defined by perturbations to key land surface parameters including leaf nitrogen concentrations and the temperature sensitivities of photosynthesis and soil respiration[14]. All ensemble members were driven by the SRES A1B emissions scenarios, including changes in non-CO_2 forcing factors (most notably changes in anthropogenic sulphate aerosols[10]). Uncoupled simulations were carried out only for the standard parameter values (HadCM3-st), and the ensemble members leading to the lowest (HadCM3-a) and highest (HadCM3-h) global carbon-cycle feedbacks. We therefore focused on these three variants of HadCM3C in this study.

The analysis of the model outputs and observational data, and the statistical methods employed are outlined in Methods.

Full Methods and any associated references are available in the online version of the paper.

Received 31 May; accepted 28 December 2012.
Published online 6 February 2013.

1. Cox, P. M., Betts, R. A., Jones, C. D., Spall, S. A. & Totterdell, I. J. Acceleration of global warming due to carbon cycle feedbacks in a coupled climate model. *Nature* **408,** 184–187 (2000).
2. Malhi, Y. *et al.* Climate change, deforestation, and the fate of the Amazon. *Science* **319,** 169–172 (2008).
3. Friedlingstein, P. *et al.* Climate-carbon cycle feedback analysis: results from the C^4MIP model intercomparison. *J. Clim.* **19,** 3337–3353 (2006).
4. Jupp, T. E. *et al.* Development of probability density functions for future South American rainfall. *New Phytol.* **187,** 682–693 (2010).
5. Rammig, A. *et al.* Estimating the risk of Amazonian forest dieback. *New Phytol.* **187,** 694–706 (2010).
6. Galbraith, D. *et al.* Multiple mechanisms of Amazonian forest biomass losses in three dynamic global vegetation models under climate change. *New Phytol.* **187,** 647–665 (2010).
7. Hall, A. & Qu, X. Using the current seasonal cycle to constrain snow albedo feedback in future climate change. *Geophys. Res. Lett.* **33,** L03502 (2006).
8. Bacastow, R. Modulation of atmospheric carbon dioxide by the Southern Oscillation. *Nature* **261,** 116–118 (1976).
9. Cox, P. M. *et al.* Amazon dieback under climate-carbon cycle projections for the 21st century. *Theor. Appl. Climatol.* **78,** 137–156 (2004).
10. Cox, P. M. *et al.* Increasing risk of Amazonian drought due to decreasing aerosol pollution. *Nature* **453,** 212–215 (2008).
11. Huntingford, C. *et al.* Highly contrasting effects of different climate forcing agents on ecosystem services. *Phil. Trans. R. Soc. A* **369,** 2026–2037 (2011).
12. Nakicenovic, N. *et al. Emissions Scenarios: Summary for Policymakers*. Spec. Report (Intergovernmental Panel on Climate Change, 2000).
13. Friedlingstein, P., Dufresne, J.-L., Cox, P. M. & Rayner, P. How positive is the feedback between climate change and the carbon cycle? *Tellus* **55B,** 692–700 (2003).
14. Booth, B. B. B. *et al.* High sensitivity of future global warming to land carbon cycle processes. *Environ. Res. Lett.* **7,** 024002 (2012).
15. Moss, R. H. *et al.* The next generation of scenarios for climate change research and assessment. *Nature* **463,** 747–756 (2010).
16. Hungate, B. A. *et al.* Nitrogen and climate change. *Science* **302,** 1512–1513 (2003).
17. Zaehle, S., Friedlingstein, P. & Friend, A. D. Terrestrial nitrogen feedbacks may accelerate future climate change. *Geophys. Res. Lett.* **37,** L01401 (2010).
18. Baker, T. R. *et al.* Increasing biomass in Amazonian forest plots. *Phil. Trans. R. Soc. Lond. B* **359,** 353–365 (2004).
19. Lewis, S. L. *et al.* Increasing carbon storage in intact African tropical forests. *Nature* **457,** 1003–1006 (2009).
20. Marengo, J. A. *et al.* The drought of Amazonia in 2005. *J. Clim.* **21,** 495–516 (2008).
21. Marengo, J. A. *et al.* The drought of 2010 in the context of historical droughts in the Amazon region. *Geophys. Res. Lett.* **38,** L12703 (2011).
22. Phillips, O. *et al.* Drought sensitivity of the Amazon rainforest. *Science* **323,** 1344–1347 (2009).
23. Lenton, T. M. *et al.* Tipping elements in the Earth's climate system. *Proc. Natl Acad. Sci. USA* **105,** 1786–1793 (2008).
24. Jones, C. D. & Cox, P. M. On the significance of atmospheric CO_2 growth rate anomalies in 2002–2003. *Geophys. Res. Lett.* **32,** L14816 (2005).
25. Denman, K. L. *et al.* in *Climate Change 2007: The Physical Science Basis* (eds Solomon, S. *et al.*) 499–587 (Cambridge Univ. Press, 2007).
26. Masarie, K. A. & Tans, P. P. Extension and integration of atmospheric carbon dioxide data into a globally consistent measurement record. *J. Geophys. Res.* **100,** 11593–11610 (1995).
27. Meinshausen, M. *et al.* The RCP greenhouse gas concentrations and their extensions from 1765 to 2500. *Clim. Change* **109,** 213–241 (2011).

©2013 Macmillan Publishers Limited. All rights reserved

28. Smith, T. M. *et al.* Improvements to NOAA's historical merged land-ocean surface temperature analysis (1880–2006). *J. Clim.* **21,** 2283–2296 (2008).
29. Mercado, L. M. *et al.* Impact of changes in diffuse radiation on the global land carbon sink. *Nature* **458,** 1014–1017 (2009).

Supplementary Information is available in the online version of the paper.

Acknowledgements We acknowledge funding from the NERC NCEO programme (P.M.C. and C.M.L.); the EU Greencycles II project (P.M.C. and P.F.); the EU FP7 'CARBONES' project (D.P. and C.D.J.); the Joint DECC/Defra Met Office Hadley Centre Climate Programme (GA01101) (D.P., B.B.B. and C.D.J.); the CEH Science Budget (C.H.) and the Newton Institute programme on 'Mathematical and Statistical Approaches to Climate Modelling and Prediction', during which this research was first formulated (P.M.C., B.B.B. and C.H.). We also acknowledge the modelling groups that provided results to C^4MIP.

Author Contributions P.M.C. led the study and drafted the manuscript. D.P. assisted with the statistical analysis, especially the estimation of the observationally constrained PDF in Fig. 3b. P.F. provided data and guidance on the C^4MIP model ensemble, and B.B.B. did likewise for the HadCM3 carbon-cycle ensemble. C.H. processed observational climate data sets to produce time series of tropical mean temperature anomalies. P.M.C., C.D.J., P.F. and C.H. have had discussions over many years concerning the relationship between the interannual variability and the long-term sensitivity of the land carbon cycle to climate change. C.M.L. provided invaluable insights into the interpretation of the regression line in Fig. 3a. All co-authors commented on and provided edits to the original manuscript.

Author Information Reprints and permissions information is available at www.nature.com/reprints. The authors declare no competing financial interests. Readers are welcome to comment on the online version of the paper. Correspondence and requests for materials should be addressed to P.M.C. (p.m.cox@exeter.ac.uk).

©2013 **Macmillan Publishers Limited. All rights reserved**

METHODS

Choice of models and variables. To make use of the observed interannual variation in atmospheric CO_2 as a constraint, we need climate–carbon-cycle simulations that model CO_2 as a 'free', fully prognostic variable. We therefore make use of the C^{4}MIP simulations[3], which used prescribed SRES A2 CO_2 emissions but calculated the global mean atmospheric CO_2 concentration interactively. We have augmented the C^{4}MIP results with free CO_2 runs from a carbon-cycle parameter ensemble carried out with HadCM3 (ref. 14). These HadCM3 runs allow the emergent constraint derived from the C^{4}MIP models to be tested over a wide range of possible future carbon losses from tropical land.

To derive an emergent constraint, it is of paramount importance that equivalent variables are compared from the models and observations. Therefore, because the C^{4}MIP models reported global mean atmospheric CO_2, and mean land-plus-ocean near-surface temperatures, we compute the same diagnostics from the observational data sets (see below).

Diagnosis of γ_{LT}. The sensitivity of tropical land carbon storage to temperature, γ_{LT}, is calculated as in previous studies[3,13]. First, the sensitivity of tropical land carbon storage to direct CO_2 effects, as given by the parameter β_{LT}, is diagnosed from the uncoupled simulation for each model, $\beta_{LT} = \Delta C^u_{LT}/\Delta C^u_a$, where $\Delta C^u_{LT} = C^u_{LT}(t_1) - C^u_{LT}(t_0)$ is the change in tropical land carbon storage (in GtC) and $\Delta C^u_a = C^u_a(t_1) - C^u_a(t_0)$ is the change in global atmospheric CO_2 concentration (in p.p.m.v.), in both cases between time t_0 and time t_1 for the uncoupled simulation.

This value of β_{LT} is then used to isolate γ_{LT} from the coupled simulation of each model, using the equation

$$\gamma_{LT} = \frac{\Delta C^c_{LT} - \beta_{LT}\Delta C^c_a}{\Delta T^c_T}$$

where $\Delta C^c_{LT} = C^c_{LT}(t_1) - C^c_{LT}(t_0)$ is the change in tropical land carbon storage (in GtC), $\Delta C^c_a = C^c_a(t_1) - C^c_a(t_0)$ is the change in global atmospheric CO_2 concentration (in p.p.m.v.) and $\Delta T^c_T = T^c_T(t_1) - T^c_T(t_0)$ is the change in mean tropical (30° N–30° S) temperature (in K), in all cases between time t_0 and time t_1 for the coupled simulation.

We define the changes relative to 1960 in all cases (that is, $t_0 = 1960$), and use the longest possible common simulation periods over which to diagnose β_{LT} and γ_{LT} for the C^{4}MIP models ($t_1 = 2099$) and the HadCM3C ensemble members ($t_1 = 2080$), respectively.

Sensitivity of CO_2 growth-rate anomaly to tropical temperature anomaly. The sensitivity of the atmospheric CO_2 growth rate to tropical temperature is calculated over the period 1960–2010 inclusive, for the observations and all models. However, for the observational data, and the HadCM3C simulations, which included volcanoes, we exclude the years 1963, 1964, 1982, 1983, 1991 and 1992, which were heavily influenced by the volcanic eruptions[24] of Mount Agung (in 1963), El Chichon (in 1982) and Mount Pinatubo (in 1991). There are two reasons for removing volcanoes. First, not all the models in our ensembles include the climatic effects of volcanic eruptions. Second, volcanoes are believed to affect the land carbon sink through the effects of diffuse radiation fertilization[29], but these effects are not included in the generation of models considered here. We therefore removed 'volcano years' from the observations to maximize consistency between models and observations.

For comparability with the outputs available from the C^{4}MIP models, we also use the global CO_2 concentration and the mean tropical (30° N–30° S) temperature, including both land and ocean points.

As in previous studies[24], the annual CO_2 growth rate for the nth year, $dC_a/dt(t_n)$, is defined as the difference between the annual mean CO_2 concentrations for the nth and $(n-1)$th years: $dC_a/dt(t_n) = C_a(t_n) - C_a(t_{n-1})$. The CO_2 growth rate is therefore centred in time at the beginning of year n. To align the tropical temperature anomalies, we take the associated tropical mean temperature, $\bar{T}_T(t_n)$, to be the mean of the annual mean tropical temperatures for years n and $n-1$:

$$\bar{T}_T(t_n) = \frac{T_T(t_n) + T_T(t_{n-1})}{2}$$

For all model and observational time series, the annual CO_2 growth rate, dC_a/dt, and the associated mean tropical temperature, $\bar{T}_T$, were detrended using an 11-yr running mean, with the residuals defining the annual anomalies (Supplementary Fig. 2). In each case, a least-squares linear regression was found between these anomalies in the CO_2 growth rate and the anomalies in the tropical temperature, with the gradient of the best fit defining the IAV sensitivity (see below).

The IAV sensitivity was calculated for a range of data sets of tropical temperature and atmospheric CO_2 (see below), to explore the uncertainty in the estimate of the IAV sensitivity arising from uncertainties in the observational data. These different estimates are listed in Supplementary Table 1.

To isolate the separate contributions of the tropical net primary productivity and soil respiration, similar regressions against tropical temperature anomalies were carried out separately for each of these fluxes as diagnosed from the C^{4}MIP models (Supplementary Fig. 1). This showed that the IAV sensitivity across the model ensemble is correlated with the response of tropical soil respiration (Supplementary Fig. 1b), rather than net primary productivity (Supplementary Fig. 1c). By contrast, the wide range of longer-term projections of changes in land carbon storage is known to be in part due to the different responses of net primary productivity to climate change[3].

Observational data. Observed annual global CO_2 concentration[26] for 1980 to 2010 was downloaded from the NOAA website (http://www.esrl.noaa.gov/gmd/ccgg/trends/global.html#global_data). Because this data set covers only the period from 1980, global CO_2 concentrations for 1960–1979 were taken from the historical data sets derived for use with the RCP scenarios[27] (http://www.pik-potsdam.de/~mmalte/rcps/index.htm#).

Tropical (30° N–30° S) annual mean temperatures were calculated from NCDC data[28] (http://www.ncdc.noaa.gov/ghcnm/maps.php), from the CRU/Met Office HadCRU3 data set (http://www.metoffice.gov.uk/hadobs/hadcrut3/) and from the GISS data set (http://data.giss.nasa.gov/gistemp/).

Least-squares linear regression. Least-squares linear regressions were calculated using well-established formulae (see, for example, http://mathworld.wolfram.com/LeastSquaresFitting.html). The linear regression, f_n, between a time series given by y_n and a time series given by x_n is defined by a gradient, b, and intercept, a: $f_n = a + bx_n$. Minimizing the least squares error for y_n involves minimizing

$$s^2 = \frac{1}{N-2}\sum_{n=1}^{N}\{y_n - f_n\}^2$$

where N is the number of data points in each time series. In this case, the best-fit gradient is given by $\bar{b} = \sigma^2_{xy}/\sigma^2_x$. Here $\sigma^2_x = \sum_{n=1}^{N}\{x_n - \bar{x}\}^2/N$ is the variance of x_n and $\sigma^2_{xy} = \sum_{n=1}^{N}\{x_n - \bar{x}\}\{y_n - \bar{y}\}/N$ is the covariance of the x_n and y_n time series, which have means of $\bar{x}$ and $\bar{y}$, respectively. The standard error of b is given by $\sigma_b = s/\sigma_x\sqrt{N}$, which defines a Gaussian probability density for b:

$$P(b) = \frac{1}{\sqrt{2\pi\sigma^2_b}}\exp\left\{-\frac{(b-\bar{b})^2}{2\sigma_b}\right\}$$

The 'prediction error' of the regression is the following function of x:

$$\sigma_f(x) = s\sqrt{1 + \frac{1}{N} + \frac{(x-\bar{x})^2}{N\sigma^2_x}}$$

This expression defines contours of equal probability density around the best-fit linear regression, which represent the probability density of y given x:

$$P\{y|x\} = \frac{1}{\sqrt{2\pi\sigma^2_f}}\exp\left\{-\frac{(y-f(x))^2}{2\sigma_f}\right\}$$

where $\sigma_f = \sigma_f(x)$, as above.

Calculation of the PDF for γ_{LT}. The emergent constraint derived in this study is a linear regression across the C^{4}MIP GCMs between the temperature sensitivity of land carbon storage in the tropics, γ_{LT}, and the sensitivity of the annual growth rate in atmospheric CO_2 to the annual tropical temperature anomaly, which we label here as γ_{CO2}. In the context of the least-squares linear regression presented above, γ_{LT} is equivalent to y and γ_{CO2} is equivalent to x.

The linear regression therefore provides an equation for the probability of γ_{LT} given γ_{CO2} (that is, the equation for $P\{y \mid x\}$ above). Supplementary Fig. 3 shows the best-fit straight line (thick dashed red line) and the plus and minus σ_f prediction error contours (as thin dashed red lines) on the same scales as in Fig. 3a.

In addition, the linear regression between the observed annual anomalies in the atmospheric CO_2 growth rate[25,26] and the tropical mean temperature[27] provides an observation-based PDF for γ_{CO2} (via the equation for $P(b)$ above). The best-fit γ_{CO2} from these observations is shown by the thick dashed vertical line in Supplementary Fig. 3, and the uncertainty in this fit is shown by the thin dashed vertical lines representing plus and minus 1 s.e. about the best-fit value.

Given these two PDFs, $P\{\gamma_{LT} \mid \gamma_{CO2}\}$ and $P(\gamma_{CO2})$, the PDF for γ_{LT} is

$$P(\gamma_{LT}) = \int_{-\infty}^{\infty} P\{\gamma_{LT}|\gamma_{CO2}\}P(\gamma_{CO2})\,d\gamma_{CO2}$$

The integrand, $P\{\gamma_{LT}|\gamma_{CO2}\}P(\gamma_{CO2})$, is shown by the continuous black contours in Supplementary Fig. 3, and the integral is the basis for the black PDF for γ_{LT} shown in Fig. 3b.

©2013 Macmillan Publishers Limited. All rights reserved

Earth Syst. Sci. Data Discuss., 5, 1107–1157, 2012
www.earth-syst-sci-data-discuss.net/5/1107/2012/
doi:10.5194/essdd-5-1107-2012
© Author(s) 2012. CC Attribution 3.0 License.

Open Access Earth System Science Data Discussions

This discussion paper is/has been under review for the journal Earth System Science Data (ESSD). Please refer to the corresponding final paper in ESSD if available.

The global carbon budget 1959–2011

C. Le Quéré[1], R. J. Andres[2], T. Boden[2], T. Conway[3], R. A. Houghton[4], J. I. House[5], G. Marland[6], G. P. Peters[7], G. van der Werf[8], A. Ahlström[9], R. M. Andrew[7], L. Bopp[10], J. G. Canadell[11], P. Ciais[10], S. C. Doney[12], C. Enright[1], P. Friedlingstein[13], C. Huntingford[14], A. K. Jain[15], C. Jourdain[1,*], E. Kato[16], R. F. Keeling[17], K. Klein Goldewijk[25], S. Levis[18], P. Levy[14], M. Lomas[19], B. Poulter[10], M. R. Raupach[11], J. Schwinger[20], S. Sitch[21], B. D. Stocker[22], N. Viovy[10], S. Zaehle[23], and N. Zeng[24]

[1]Tyndall Centre for Climate Change Research, University of East Anglia, Norwich Research Park, Norwich, NR4 7TJ, UK
[2]Carbon Dioxide Information Analysis Center (CDIAC), Oak Ridge National Laboratory, Oak Ridge, Tennessee, USA
[3]National Oceanic & Atmosphere Administration, Earth System Research Laboratory (NOAA/ESRL), Boulder, Colorado 80305, USA
[4]Woods Hole Research Centre (WHRC), Falmouth, Massachusetts 02540, USA
[5]Cabot Institute, Dept of Geography, University of Bristol, UK
[6]Research Institute for Environment, Energy, and Economics, Appalachian State University, Boone, North Carolina 28608, USA
[7]Center for International Climate and Environmental Research – Oslo (CICERO), Norway
[8]Faculty of Earth and Life Sciences, VU University Amsterdam, The Netherlands
[9]Department of Physical Geography and Ecosystem Science, Lund University, Sweden

[10]Laboratoire des Sciences du Climat et de l'Environnement, CEA-CNRS-UVSQ, CE Orme des Merisiers, 91191 Gif sur Yvette Cedex, France
[11]Global Carbon Project, CSIRO Marine and Atmospheric Research, Canberra, Australia
[12]Woods Hole Oceanographic Institution (WHOI), Woods Hole, MA 02543, USA
[13]College of Engineering, Mathematics and Physical Sciences, University of Exeter, Exeter, EX4 4QF, UK
[14]Centre for Ecology and Hydrology (CEH), Wallingford, OX10 8BB, UK
[15]Department of Atmospheric Sciences, University of Illinois, USA
[16]Center for Global Environmental Research (CGER), National Institute for Environmental Studies (NIES), Japan
[17]University of California, San Diego, Scripps Institution of Oceanography, La Jolla, California 92093-0244, USA
[18]National Center for Atmospheric Research (NCAR), Boulder, Colorado, USA
[19]Centre for Terrestrial Carbon Dynamics (CTCD), Sheffield University, UK
[20]Geophysical Institute, University of Bergen & Bjerknes Centre for Climate Research, Bergen, Norway
[21]College of Life and Environmental Sciences, University of Exeter, Exeter, EX4 4RJ, UK
[22]Physics Institute, and Oeschger Centre for Climate Change Research, University of Bern, Switzerland
[23]Max-Planck-Institut für Biogeochemie, P.O. Box 600164, Hans-Knöll-Str. 10, 07745 Jena, Germany
[24]Department of Atmospheric and Oceanic Science, University of Maryland, USA
[25]PBL Netherlands Environmental Assessment Agency, The Hague/Bilthoven, The Netherlands
[*]now at: Food and Agriculture Organization of the United Nations (FAO), Rome, Italy

Received: 20 November 2012 – Accepted: 21 November 2012 – Published: 2 December 2012

Correspondence to: C. Le Quéré (c.lequere@uea.ac.uk)

Published by Copernicus Publications.

Abstract

Accurate assessment of anthropogenic carbon dioxide (CO_2) emissions and their redistribution among the atmosphere, ocean, and terrestrial biosphere is important to better understand the global carbon cycle, support the climate policy process, and project future climate change. Present-day analysis requires the combination of a range of data, algorithms, statistics and model estimates and their interpretation by a broad scientific community. Here we describe datasets and a methodology developed by the global carbon cycle science community to quantify all major components of the global carbon budget, including their uncertainties. We discuss changes compared to previous estimates, consistency within and among components, and methodology and data limitations. Based on energy statistics, we estimate that the global emissions of CO_2 from fossil fuel combustion and cement production were 9.5 ± 0.5 PgC yr^{-1} in 2011, 3.0 percent above 2010 levels. We project these emissions will increase by 2.6 % (1.9–3.5 %) in 2012 based on projections of Gross World Product and recent changes in the carbon intensity of the economy. Global net CO_2 emissions from Land-Use Change, including deforestation, are more difficult to update annually because of data availability, but combined evidence from land cover change data, fire activity in regions undergoing deforestation and models suggests those net emissions were 0.9 ± 0.5 PgC yr^{-1} in 2011. The global atmospheric CO_2 concentration is measured directly and reached 391.38 ± 0.13 ppm at the end of year 2011, increasing 1.70 ± 0.09 ppm yr^{-1} or 3.6 ± 0.2 PgC yr^{-1} in 2011. Estimates from four ocean models suggest that the ocean CO_2 sink was 2.6 ± 0.5 PgC yr^{-1} in 2011, implying a global residual terrestrial CO_2 sink of 4.1 ± 0.9 PgC yr^{-1}. All uncertainties are reported as ±1 sigma (68 % confidence assuming Gaussian error distributions that the real value lies within the given interval), reflecting the current capacity to characterise the annual estimates of each component of the global carbon budget. This paper is intended to provide a baseline to keep track of annual carbon budgets in the future.

All carbon data presented here can be downloaded from the Carbon Dioxide Information Analysis Center (doi:10.3334/CDIAC/GCP_V2012).

1 Introduction

The concentration of carbon dioxide (CO_2) in the atmosphere has increased from approximately 278 parts per million (ppm) in 1750, the beginning of the Industrial Era, to 391.4 at the end of 2011 (Conway and Tans, 2012). This increase was caused initially mainly by the anthropogenic release of carbon to the atmosphere from deforestation and other land-use change activities. Emissions from fossil fuel combustion started before the Industrial Revolution and became the dominant source of anthropogenic emissions to the atmosphere from around 1920 until present. Anthropogenic emissions occur on top of an active natural carbon cycle that circulates carbon between the atmosphere, ocean, and terrestrial biosphere reservoirs on time scales from days to many millennia, while geologic reservoirs have even longer timescales (Archer et al., 2009).

The "global carbon budget" presented here refers to the direct and indirect *anthropogenic* perturbation of CO_2 in the atmosphere. It quantifies the input of CO_2 to the atmosphere by emissions from human activities, the growth of CO_2 in the atmosphere, and the resulting changes in land and ocean carbon fluxes directly in response to increasing atmospheric CO_2 levels and indirectly in response to climate and other anthropogenic changes. An understanding of this perturbation budget over time and the underlying variability and trends of the natural carbon cycle are necessary to understand and quantify climate-carbon feedbacks. This also allows potentially earlier detection of any approaching discontinuities or tipping points of the carbon cycle in response to anthropogenic changes (Falkowski et al., 2000).

The components of the CO_2 budget that are reported in this paper include separate estimates for (1) the CO_2 emissions from fossil fuel combustion and cement production (E_{FF}), (2) the CO_2 emissions resulting from deliberate human activities on land,

including land use, land-use change and forestry (shortened to LUC hereafter; E_{LUC}), (3) the growth rate of CO_2 in the atmosphere (G_{ATM}), and (4) the uptake of CO_2 by the "CO_2 sinks" in the ocean (S_{OCEAN}) and on land (S_{LAND}). The CO_2 sinks as defined here include the response of the land and oceans to elevated CO_2 and changes in climate and other environmental conditions. The emissions and their partitioning among the atmosphere, ocean and land are in balance:

$$E_{FF} + E_{LUC} = G_{ATM} + S_{OCEAN} + S_{LAND} \quad (1)$$

Equation (1) subsumes, and partly omits, two kinds of processes. The first is the net input of CO_2 to the atmosphere from the chemical oxidation of reactive carbon-containing gases, primarily methane (CH_4), carbon monoxide (CO), and volatile organic compounds such as terpene and isoprene, which we quantify here for the first time. The second is the anthropogenic perturbations to inland freshwaters, estuaries, and coastal areas carbon cycling, that modify both lateral fluxes transported from land ecosystems to the open ocean, and "vertical" CO_2 fluxes of rivers and estuaries outgassing, and the air-sea CO_2 net exchange of coastal areas (Battin et al., 2008; Aufdenkampe et al., 2011). These flows are omitted in absence of details on the natural versus anthropogenic terms of these loops of the carbon cycle. The inclusion of these fluxes of anthropogenic CO_2 would affect the estimates of S_{LAND} and perhaps S_{OCEAN} in Eq. (1), but not G_{ATM}.

The global carbon budget has been assessed by the Intergovernmental Panel on Climate Change (IPCC) in all Assessment reports (Watson et al., 1990; Schimel et al., 1995; Prentice et al., 2001; Denman et al., 2007), and by others (Conway and Tans, 2012). These included budget estimates for the decades of the 1980s, 1990s and, most recently, the period 2000–2005. The IPCC methodology has been adapted and used by the Global Carbon Project (GCP, www.globalcarbonproject.org), who have coordinated a cooperative community effort for the annual publication of global CO_2 budgets for year 2005 (Raupach et al., 2007; including fossil emissions only), year 2006 (Canadell et al., 2007), year 2007 (published online), year 2008 (Le Quéré et al., 2009), year 2009

(Friedlingstein et al., 2010), and most recently, year 2010 (Peters et al., 2012b). Each of these papers updated previous estimates with the latest available information for the entire time series. From 2008, these publications projected fossil fuel emissions for one additional year using the projected World Gross Domestic Product and estimated improvements in the carbon intensity of the economy.

We adopt a range of ±1 standard deviation (sigma) to report the uncertainties in our annual estimates, representing a likelihood of 68 % that the true value lies within the provided range, assuming that the errors have a Gaussian distribution. This choice reflects the difficulty of characterising the uncertainty in the CO_2 fluxes between the atmosphere and the ocean and land reservoirs individually, as well as the difficulty to update the CO_2 emissions from LUC, particularly on an annual basis. A 68 % likelihood provides an indication of our current capability to quantify each term and its uncertainty given the available information. For comparison, the Fourth Assessment Report of the IPCC (AR4) generally reported 90 % uncertainty for large datasets whose uncertainty is well characterised, or for long time intervals less affected by year-to-year variability. This includes, for instance, attribution statements associated with recorded warming levels since the pre-industrial period. The 90 % number corresponds to the IPCC language of "very likely" or "very high confidence represents at least a 9 out of 10 chance"; our 68 % value is near the 66 % which the IPCC reports as only "likely". The uncertainties reported here combine statistical analysis of the underlying data and expert judgement of the likelihood of results lying outside this range. The limitations of current information are discussed in the paper.

All units are presented in petagrammes of carbon (PgC, 10^{15} gC), which is the same as gigatonnes of carbon (GtC). Units of gigatonnes of CO_2 (or billion tonnes of CO_2) used in policy circles are equal to 3.67 multiplied by the value in units of PgC.

This paper provides a detailed description of the datasets and methodology used to compute the global CO_2 budget and associated uncertainties for the period 1959–2011. It presents the global CO_2 budget estimates by decade since the 1960s, including the last decade (2002–2011), the results for the year 2011, and a projection of

E_{FF} for year 2012. It is intended that this paper will be updated every year using the format of "living reviews", to help keep track of new versions of the budget that result from new data, revision of data, and changes in methodology. Additional materials associated with the release of each new version will be posted at the Global Carbon Project (GCP) website (http://www.globalcarbonproject.org/carbonbudget). With this approach, we aim to provide transparency and traceability in reporting indicators and drivers of climate change.

2 Methods

The original data and measurements to complete the global carbon budget are generated by multiple organizations and research groups around the world. The effort presented here is thus mainly one of synthesis, where results from individual groups are collated, analysed and evaluated for consistency. Descriptions of the measurements, models, and methodologies follow below and in depth descriptions of each component are described elsewhere (e.g. Andres et al., 2012; Houghton et al., 2012).

2.1 CO_2 emissions from fossil fuel combustion and cement production (E_{FF})

2.1.1 Fossil fuel and cement emissions and their uncertainty

The calculation of global and national CO_2 emissions from fossil fuel combustion, including gas flaring and cement production (E_{FF}), relies primarily on energy data, specifically data on hydrocarbon fuels, collated and archived by several organisations (Andres et al., 2012), including the Carbon Dioxide Information Analysis Center (CDIAC), the International Energy Agency (IEA), the United Nations (UN), and the United States Department of Energy (DoE) Energy Information Administration (EIA). We use the emissions estimated by the CDIAC (http://cdiac.ornl.gov) which are based primarily on energy data provided by the UN Statistics Division (UN, 2012a, b) (Table 1), and are typically available 2–3 yr after the close of a given year. CDIAC also provides the

only dataset that extends back in time to 1751 with consistent and well-documented emissions from all fossil fuels, cement production, and gas flaring for all countries (and their uncertainty); this makes the dataset a unique resource for research of the carbon cycle during the fossil fuel era. For this paper, we use CDIAC emissions data up to period 1959–2009, and preliminary estimates based on the BP annual energy review for emissions in 2010 and 2011 (BP, 2012). BP's sources for energy statistics overlap with those of the UN data but are compiled more rapidly, using a smaller group of mostly developed countries and assumptions for missing data. The preliminary estimates are replaced by the more complete CDIAC data when available. Past experience shows that projections based on the BP data provide reliable estimates for the two most recent years when full data are not yet available from the UN (see Sect. 3.2).

Emissions from cement production are based on cement data from the US Geological Survey (Van Oss, 2011) up to year 2009, and from preliminary data for 2010 and 2011 (US Geological Survey, 2012). Emission estimates from gas flaring are calculated in a similar manner as those from solid, liquid, and gaseous fuels, and rely on the UN Energy Statistics to supply the amount of flared fuel. For emission years 2010 and 2011, flaring estimates are assumed constant from the emission year 2009 UN-based data. The basic data on gas flaring have large uncertainty. Fugitive emissions of CH_4 from the so-called upstream sector (coal mining, oil extraction, gas extraction and distribution) are not included in the accounts of CO_2 emissions except to the extent that they get captured in the UN energy data and counted as gas "flared or lost". The UN data are not able to distinguish between gas that is flared or vented.

When necessary, fuel masses/volumes are converted to fuel energy content using coefficients provided by the UN and then to CO_2 emissions using conversion factors that take into account the relationship between carbon content and heat content of the different fuel types (coal, oil, gas, gas flaring) and the combustion efficiency (to account, for example, for soot left in the combustor or fuel otherwise lost or discharged without oxidation). In general, CO_2 emissions for equivalent energy consumptions are about 30 % higher for coal compared to oil, and 70 % higher for coal compared to gas

(Marland et al., 2007). These calculations are based on the mass flows of carbon and assume that the carbon discharged as CO or CH_4 will soon be oxidized to CO_2 in the atmosphere and hence counts the carbon mass with CO_2 emissions.

Emissions are estimated for 1959–2011 for 129 countries and regions. The disaggregation of regions (e.g. the former Soviet Union prior to 1992) is based on the shares of emissions in the first year after the countries are disaggregated.

Estimates of CO_2 emissions show that the global total of emissions is not equal to the sum of emissions from all countries. This is largely attributable to combustion of fuels used in international shipping and aviation, where the emissions are included in the global totals but are not attributed to individual countries. In practice, the emissions from international bunker fuels are calculated based on where the fuels were loaded, but they are not included with national emissions estimates. Smaller differences also occur because globally the sum of imports in all countries is not equivalent to the sum of exports, because of differing treatment of oxidation of non-fuel uses of hydrocarbons (e.g. as solvents, lubricants, feedstocks, etc.).

The uncertainty of the annual fossil fuel and cement emissions for the globe has been estimated at ±5 % (scaled down from the published 10 % at ±2 sigma to the use of ±1 sigma bounds reported here) (Andres et al., 2012). This includes an assessment of the amounts of fuel consumed, the carbon contents of fuels, and the combustion efficiency. While in the budget we consider a fixed uncertainty of 5 % for all years, in reality the uncertainty, as a percentage of the emissions, is growing with time because of the larger share of global emissions from non-Annex B countries with weaker statistical systems (Marland et al., 2009). For example, the uncertainty in Chinese emissions estimates has been estimated at around ±10 % (±1 sigma; Gregg et al., 2008). Generally, emissions from mature economies with good statistical bases have an uncertainty of only a few percent (Marland, 2008).

2.1.2 Emissions embodied in goods and services

National emissions inventories take a territorial (production) perspective by "include[ing] all greenhouse gas emissions and removals taking place within national (including administered) territories and offshore areas over which the country has jurisdiction" (from the Revised 1996 IPCC Guidelines for National Greenhouse Gas Inventories). That is, emissions are allocated to the country where and when the emissions actually occur. The emission inventory of an individual country does not include the emissions from the production of goods and services produced in other countries (e.g. food and clothes) that are used for national consumption. The difference between the standard territorial emission inventories and consumption-based emission inventories is the net transfer (exports minus imports) of emissions from the production of internationally traded goods and services. Complementary emission inventories that allocated emissions to the final consumption of goods and services (e.g. Davies et al., 2011) provide additional information that can be used to understand emission drivers, quantify emission leakages between countries, and potentially design more effective and efficient climate policy.

We estimate consumption-based emissions by enumerating the global supply chain using a global model of the economic relationships between sectors in every country (Peters et al., 2011a). Due to availability of the input data, detailed estimates are made for the years 1997, 2001, 2004, and 2007 (Peters et al., 2011a) using economic and trade data from the Global Trade and Analysis Project (GTAP; Narayanan et al., 2012). The results cover 57 sectors and up to 129 countries and regions. The results are extended into an annual time-series from 1990 to the latest year of the fossil-fuel emissions or GDP data (2010 in this budget), using GDP data by expenditure (from the UN Main Aggregates database, UN, 2012c) and time series of trade data from GTAP (Peters et al., 2012b). We do not provide an uncertainty estimate for these emissions, but based on model comparisons and sensitivity analysis, they are unlikely to be significantly larger than for the territorial emission estimates (Peters et al., 2011b).

Uncertainty is expected to increase for more detailed results (Peters et al., 2011b) (e.g. the results for Annex B will be more accurate than the sector results for an individual country).

It is important to note that the consumption-based emissions defined here consider directly the carbon embodied in traded goods and services, but not the trade in unoxidised fossil fuels (coal, oil, gas). In our consumption-based inventory, emissions from traded fossil fuels accrue to the country where the fuel is burned or consumed, not the exporting country from which it was extracted.

The consumption-based emission inventories in this carbon budget have several improvements over previous years. The detailed estimates for 2004 and 2007 are based on an updated version of the GTAP database (Narayanan et al., 2012). We estimate the sector level CO_2 emissions using our own calculations based on the GTAP data and methodology, but scale the national totals to match the CDIAC estimates from the carbon budget. We do not include international transportation in our estimates. The time-series of trade data provided by GTAP covers the period 1995–2009 and our methodology uses the trade shares of this dataset. For the period 1990–1994 we assume the trade shares of 1995, while in 2010 we assume the trade shares of 2008 since 2009 was heavily affected by the global financial crisis. We identified errors in the trade shares of Taiwan and Netherlands in 2008 and 2009, and for these two countries, the trade shares for 2008–2010 are based on the 2007 trade shares.

This data does not contribute to the global average terms in Eq. (1), but are relevant to the anthropogenic carbon cycle as they reflect the movement of carbon across the Earth's surface in response to human needs (both physical and economic). Furthermore, if national and international climate policies continue to develop in an unharmonised way, then the trends reflected in these data will need to be accommodated by those developing policies.

2.1.3 Emissions projections for the current year

Energy statistics are normally available around June for the previous year. We use the close relationship between the growth in world Gross Domestic Product (GDP) and the growth in global emissions (Raupach et al., 2007) to project emissions for the current year. This is based on the so-called Kaya (also called IPAT) identity, whereby E_{FF} is decomposed by the product of GDP and the fossil fuel carbon intensity of the economy (I_{FF}) as follows:

$$E_{FF} = \mathrm{GDP} \cdot I_{FF} \tag{2}$$

taking a time derivative of this equation gives:

$$\frac{\mathrm{d}E_{FF}}{\mathrm{d}t} = \frac{\mathrm{d}(\mathrm{GDP} \cdot I_{FF})}{\mathrm{d}t} \tag{3}$$

and applying the rules of calculus, assuming that GDP and I_{FF} are independent:

$$\frac{\mathrm{d}E_{FF}}{\mathrm{d}t} = \frac{\mathrm{dGDP}}{\mathrm{d}t} \cdot I_{FF} + \mathrm{GDP} \cdot \frac{\mathrm{d}I_{FF}}{\mathrm{d}t} \tag{4}$$

finally, dividing Eq. (4) by Eq. (2) gives:

$$\frac{1}{E_{FF}} \frac{\mathrm{d}E_{FF}}{\mathrm{d}t} = \frac{1}{\mathrm{GDP}} \frac{\mathrm{dGDP}}{\mathrm{d}t} + \frac{1}{I_{FF}} \frac{\mathrm{d}I_{FFF}}{\mathrm{d}t} \tag{5}$$

where the left hand term is the relative growth rate of E_{FF}, and the right hand terms are the relative growth rates of GDP and I_{FF}, respectively, which can simply be added linearly to give overall growth rate. The growth rates are reported in percent below by multiplying each term by 100. Because preliminary estimates of annual change in GDP are made well before the end of a calendar year, making assumptions on the growth rate of I_{FF} allows us to make projections of the annual change in CO_2 emissions well before the end of a calendar year.

2.1.4 Growth rate in emissions

We report the annual growth rate in emissions for adjacent years in percent by calculating the difference between the two years and then comparing to the emissions in the first year: $[(E_{FF}(t_0+1) - E_{FF}(t_0))/E_{FF}(t_0)] \cdot 100$. This is the simplest method to characterise a one-year growth compared to the previous year. This has strong links with the more general way in which society presents economic change in journalistic circles, most often a comparison of present-day economic activity compared to the previous year.

The growth rate of E_{FF} over time periods of greater than one year can be re-written using its logarithm equivalent as follows:

$$\frac{1}{E_{FF}}\frac{dE_{FF}}{dt} = \frac{d(\ln E_{FF})}{dt} \quad (6)$$

Here we calculate growth rates in emissions for multi-year periods (e.g. a decade) by fitting a linear trend to ln (E_{FF}) in Eq. (6), reported in percent per year. We fit the logarithm of E_{FF} rather than E_{FF} directly because this method ensures that computed growth rates satisfy Eq. (6). This method differs from previous papers (Raupach et al., 2007; Canadell et al., 2007; Le Quéré et al., 2009) who computed the fit to E_{FF} and divided by average E_{FF} directly, but the difference is very small (< 0.05 %) in the case of E_{FF}.

2.2 CO_2 emissions from land-use, land-use change and forestry (E_{LUC})

Net LUC emissions reported in our annual budget (E_{LUC}) include CO_2 fluxes from afforestation, deforestation, logging (forest degradation and harvest activity), shifting cultivation (cycle of cutting forest for agriculture then abandoning), regrowth of forests following wood harvest or abandonment of agriculture, fire-based peatland emissions and other land management practices (Table 2). Our annual estimate combines information from a bookkeeping model (Sect. 2.2.1) primarily based on forest area change and

biomass data from the Forest Resource Assessment (FRA) of the Food and Agriculture Organisation (FAO) (Houghton, 2003) published at intervals of five years, with annual emissions estimated from satellite-based fire activity in deforested areas (Sect. 2.2.2; van der Werf et al., 2010). The bookkeeping model is used mainly to quantify the mean E_{LUC} over the time period of the available data, and the satellite-based method to distribute these emissions annually. The satellite-based emissions are available from year 1997 onwards only. We also use independent estimates from Dynamic Global Vegetation Models (Sect. 2.2.3) to help quantifying the uncertainty in global E_{LUC}.

2.2.1 Bookkeeping method

E_{LUC} calculated using a bookkeeping method (Houghton, 2003) keeps track of the carbon stored in vegetation and soils before deforestation or other land-use change, and the changes in forest age classes, or cohorts, of disturbed lands after land-use change. It tracks the CO_2 emitted to the atmosphere over time due to decay of soil and vegetation carbon in different pools, including wood products pools after logging and deforestation. It also tracks the regrowth of vegetation and build-up of soil carbon pools following land-use change. It considers transitions between forests, pastures and cropland, shifting cultivation, degradation of forests where a fraction of the trees is removed, abandonment of agricultural land, and forest management such as logging and fire management. In addition to tracking logging debris on the forest floor, the bookkeeping model tracks the fate of carbon contained in harvested wood products that is eventually emitted back to the atmosphere as CO_2, although a detailed treatment of the lifetime in each product pool is not performed (Earles et al., 2012). Harvested wood products are partitioned into three pools with different turnover times. All fuel-wood is assumed to be burned in the year of harvest (1.0 yr^{-1}). Pulp and paper products are oxidized at a rate of 0.1 yr^{-1}. Timber is assumed to be oxidized at a rate of 0.01 yr^{-1}, and elemental carbon decays at 0.001 yr^{-1}. The general assumptions about partitioning wood products among these pools are based on national harvest data.

The primary land-cover change and biomass data for the bookkeeping model analysis is the FAO FRA 2010 (FAO, 2010) (Table 1), which is based on countries' self-reporting of statistics on forest cover change and management partially combined with satellite data in more recent assessments. Changes in land cover other than forest are based on annual, national changes in cropland and pasture areas reported by the FAO Statistics Division (FAOSTAT, 2010). The LUC data set is non-spatial and aggregated by regions. The carbon stocks on land (biomass and soils), and their response functions subsequent to LUC, are based on averages per land cover type, per biome and per region. Similar results were obtained using forest biomass carbon density based on satellite data (Baccini et al., 2012). The bookkeeping model does not include land ecosystems' transient response to changes in climate, atmospheric CO_2 and other environmental factors, but the growth/decay curves are based on contemporary data that will implicitly reflect the effects of CO_2 and climate at that time.

2.2.2 Fire-based method

LUC CO_2 emissions calculated from satellite-based fire activity in deforested areas (van der Werf et al., 2010) provide information that is complementary to the bookkeeping approach. Although they do not provide a direct estimate of E_{LUC} as they do not include processes such as respiration, wood harvest, wood products or forest regrowth, they do provide insight on the year-to-year variations in E_{LUC} that result from the interactions between climate and human activity (e.g. there is more burning and clearing of forests in dry years). The "deforestation fire emissions" assumes an important role of fire in removing biomass in the deforestation process, and thus can be used to infer direct CO_2 emissions from deforestation using satellite-derived data on fire activity in regions with active deforestation (legacy emissions such as decomposition from on ground debris or soils are missed by this method). The method requires information on the fraction of total area burned associated with deforestation versus other types of fires, and can be merged with information on biomass stocks and the fraction of the biomass lost in a deforestation fire to estimate CO_2 emissions. The satellite-based fire

emissions are limited to the tropics, where fires result mainly from human activities. Tropical deforestation is the largest and most variable single contributor to E_{LUC}.

Here we used annual estimates from the Global Fire Emissions Database (GFED3), available from http://www.globalfiredata.org. Burned area from Giglio et al. (2010) is merged with active fire retrievals to mimic more sophisticated assessments of deforestation rates in the pan-tropics (van der Werf et al., 2010). This information is used as input data in a modified version of the satellite-driven CASA biogeochemical model to estimate carbon emissions, keeping track of what fraction was due to deforestation (van der Werf et al., 2010). The CASA model uses different assumptions to compute delay functions compared to the bookkeeping model, and does not include historical emissions or regrowth from land use change prior to the availability of satellite data. Comparing coincident CO emissions and their atmospheric fate with satellite-derived CO concentrations allows for some validation of this approach (e.g. van der Werf et al., 2008).

In this paper, we only use emissions based on deforestation fires to quantify the interannual variability in E_{LUC}. We calculate the anomaly in these emissions over the 1997–2011 time period, and add this to average E_{LUC} estimated using the bookkeeping method. We thus assume that all land management activities apart from deforestation do not vary significantly on a year-to-year basis. Other sources of interannual variability (e.g. the impact of climate variability on regrowth) are accounted for in S_{LAND}.

2.2.3 Dynamic Global Vegetation Models (DGVMs) and uncertainty assessment for LUC

Net LUC CO_2 emissions have also been estimated using DGVMs that explicitly represent some processes of vegetation growth, mortality and decomposition associated with natural cycles and also provide a response to prescribed land-cover change and climate and CO_2 drivers (Table 2). The DGVMs calculate the dynamic evolution of biomass and soil carbon pools that are affected by environmental variability and change in addition to LUC transitions each year. They are independent from the other budget

terms except for their use of atmospheric CO_2 concentration to calculate the fertilization effect of CO_2 on primary production. The DGVMs do not provide exactly E_{LUC} as defined in this paper because they represent fewer processes resulting directly from human activities on land, but include the vegetation and soil response to increasing atmospheric CO_2 levels, to climate variability and change (in three models), in addition to atmospheric N deposition in the presence of nitrogen limitation (in one model; Table 2). Nevertheless all methods represent deforestation, afforestation and regrowth, three of the most important components of E_{LUC}, and thus the model spread can help quantify the uncertainty in E_{LUC}.

The DGVMs used here prescribe land-cover change from the HYDE spatially gridded datasets updated to 2009 (Goldewijk et al., 2011; Hurtt et al., 2011), which is based on FAO statistics of change in agricultural area (FAOSTAT, 2010) with assumptions made about change in forest or other land cover as a result of agricultural area change. The changes in agricultural areas are then implemented within each model (for instance, an increased cropland fraction in a grid cell can either use pasture land, or forest, the latter resulting into deforestation). This differs with the data set used in the bookkeeping method (Houghton, 2003 and updates), which is based on forest area change statistics (FAO, 2010). The DGVMs also represent a different methodology of calculating carbon fluxes, and thus provide an independent assessment of LUC emissions to the bookkeeping results (Sect. 2.2.1).

Differences between estimates thus originate from three main sources, firstly the land cover change data set, secondly different approaches in models, and thirdly different process boundaries (Table 2). Four different DGVM estimates are presented here and used to explore the uncertainty in LUC annual emissions (Jain et al., 2012; Kato et al., 2012; Poulter et al., 2010; Stocker et al., 2011b; Table 3). While many published DGVM LUC emissions estimates exist, these model runs were driven by a consistent updated HYDE LUC data set up to year 2009.

We examine the standard deviation of the annual estimates to assess the uncertainty in E_{LUC}. The standard deviation across models in each year ranged from 0.09

to 0.70 PgC yr^{-1}, with an average of 0.42 PgC yr^{-1} from 1960 to 2009. One of the four models (Jain et al., 2012) was used with three different LUC data sets (including HYDE and FAO FRA, 2005) (Jain et al., 2012; Meiyappan and Jain, 2012). The standard deviation for decadal means in these three model runs was ±0.19 PgC yr^{-1} for 1990 to 2005, and ranged from 0.06 to 0.70 PgC yr^{-1} for annual estimates with an average of ±0.27 PgC yr^{-1} from 1960 to 2005. Assuming the two sources of uncertainty are independent, we can combine them using standard error propagation rules. Taking the quadratic sum of the mean annual standard deviation across the four DGVMs (0.42 PgC yr^{-1}) and the standard deviation due to different land cover change data sets (0.27 PgC yr^{-1}) we get a combined standard deviation of 0.5 PgC yr^{-1}.

We use the combined standard deviation ±0.5 PgC yr^{-1} as a quantitative measure of uncertainty for annual emissions, and to reflect our best value judgment that there is at least 68 % chance (±1 sigma) that the true LUC emission lies within the given range, for the range of processes considered here. However, we note that missing processes such as the decomposition of drained tropical peatlands (Ballhorn et al., 2009; Hooijer et al., 2010) could introduce biases which are not quantified here, while the inclusion of the impact of climate variability on land processes by some DGVMs (Table 2) may inflate the standard deviation in annual estimates of LUC emissions compared to our definition of E_{LUC}. The uncertainty of ±0.5 PgC yr^{-1} is slightly lower than that of ±0.7 PgC yr^{-1} estimated in the 2010 CO_2 budget release (Friedlingstein et al., 2010) based on expert assessment of the available estimates. A more recent expert assessment of uncertainty for the decadal mean based on a larger set of published model and uncertainty studies estimated ±0.5 PgC yr^{-1} (Houghton et al., 2012), which partly reflects improvements in data on forest area change using satellite data, and partly more complete understanding and representation of processes in models. We adopt ±0.5 PgC yr^{-1} here for the decadal averages presented Table 4.

2.3 Atmospheric CO_2 growth rate (G_{ATM})

2.3.1 Global atmospheric CO_2 growth rate estimates

The atmospheric CO_2 growth rate is provided by the US National Oceanic and Atmospheric Administration Earth System Research Laboratory (Conway and Tans, 2012), which is updated from Ballantyne et al. (2012). For the 1959–1980 period, the global growth rate is based on measurements of atmospheric CO_2 concentration averaged from the Mauna Loa and South Pole stations, as observed by the CO_2 Program at Scripps Institution of Oceanography (Keeling et al., 1976) and other research groups. For the 1980–2011 time period, the global growth rate is based on the average of multiple stations selected from the marine boundary layer sites (Ballantyne et al., 2012), after fitting each station with a smoothed curve as a function of time, and averaging by latitude band (Masarie and Tans, 1995). The annual growth rate is estimated from atmospheric CO_2 concentration by taking the average of the most recent November–February months (for Mauna Loa) and December–January months (for the globe) corrected for the average seasonal cycle and subtracting this same average one year earlier. The growth rate in units of ppm yr^{-1} is converted to fluxes by multiplying by a factor of 2.123 PgC per ppm (Enting et al., 1994) for comparison with the other components.

The uncertainty around the annual growth rate based on the multiple stations dataset ranges between 0.11 and 0.72 PgC yr^{-1}, with a mean of 0.61 PgC yr^{-1} for 1959–1980 and 0.18 PgC yr^{-1} for 1980–2011, when a larger set of stations were available. It is based on the number of available stations, and thus takes into account both the measurement errors and data gaps at each station. This uncertainty is larger than the uncertainty of ±0.1 PgC yr^{-1} reported for decadal mean growth rate by the IPCC because errors in annual growth rate are strongly anti-correlated in consecutive years leading to smaller errors for longer time scales. The decadal change is computed from the difference in concentration ten years apart based on measurement error of 0.35 ppm (based on offsets between NOAA/ESRL measurements and those of the World Meteorological Organization World Data Center for Greenhouse Gases, NOAA/ESRL, 2012) for the

start and end points (the decadal change uncertainty is the sqrt$(2 \cdot (0.35\,\text{ppm})^2)/10$ yr assuming that each yearly measurement error is independent). This uncertainty is also used in Table 4.

2.3.2 Contribution of anthropogenic CO and CH_4 to the global anthropogenic CO_2 budget

Emissions of CO and CH_4 to the atmosphere are assumed to be mainly balanced by natural land CO_2 sinks for all biogenic carbon compounds, but small imbalances (omitted in Eq. 1) arise through anthropogenic emissions of fugitive fossil fuel CH_4 and CO, and changes in oxidation rates, e.g. in response to climate variability. Emissions of CO from combustion processes are included with E_{FF} and E_{LUC} (for example, CO emissions from fires associated with LUC are included in E_{LUC}). However, fugitive anthropogenic emissions of fossil CH_4 (e.g. gas leaks) from the coal, oil and gas upstream sectors are not counted in E_{FF} because these leaks are not inventoried in the fossil fuel statistics as they are not consumed as fuel.

In the absence of anthropogenic change, natural sources of CO and CH_4 from wildfires and CH_4 wetlands are assumed to be balanced by CO_2 uptake by photosynthesis on continental and long time-scale (e.g. decadal or longer). Anthropogenic land use change (e.g. biomass burning for forest clearing or land management, wetland management) and the indirect anthropogenic effects of climate change on wildfires and wetlands result in an imbalance of sources and sinks of carbon. For the purposes of this study, we assume wildfire and wetland emissions of CO and CH_4 are in balance, and that the non-industrial anthropogenic biogenic sources are captured within estimates of emissions of CO_2 from LUC (included in Sect. 2.2). Peatland draining results in a reduction of CH_4 emissions and an increase in CO_2 (not included in modelled estimates presented here). Thus, none of the CO and CH_4 sources above are included in the (anthropogenic) CO_2 budget of this study.

By contrast to biogenic sources, CO and CH_4 emissions from fossil fuel use are not balanced by any recent CO_2 uptake by photosynthesis, and hence represent a net addition of fossil carbon to the atmosphere. This is implicitly included in this study as estimates of CO_2 emissions are based on the total carbon content of the fuel, and the measured CO_2 growth rate includes CO_2 from CO.

This is not the case for anthropogenic fossil CH_4 emission from fugitive emissions during natural gas extraction and transport, and from the coal and oil industry (gas leaks). This emission of carbon to the atmosphere is not included in the fossil fuel CO_2 emissions described in Sect. 2.1. This CH_4 emission is estimated at 0.09 Pg C yr^{-1} (Kirschke et al., 2012). Fossil CH_4 emissions are assumed to be oxidized with a lifetime of 12.4 yr, the e-folding time of an atmospheric perturbation removal (Prater et al., 2012). After one year, 92 % of these emissions remain in the atmosphere as CH_4 and contribute to the observed CH_4 global growth rate, whereas the rest (8 %) get oxidized into CO_2, and contribute to the CO_2 growth rate. Given that anthropogenic fossil fuel CH_4 emissions represent a fraction of 15 % of the total global CH_4 source (Kirschke et al., 2012), we assumed that a fraction of 0.15 times 0.92 of the observed global growth rate of CH_4 of 6 Tg C-CH_4 yr^{-1} (units of C in CH_4 form) during 2000–2009 is due to fossil CH_4 sources. Therefore, annual fossil fuel CH_4 emissions contribute 0.8 Tg C-CH_4 yr^{-1} to the CH_4 growth rate and 0.8 Tg C-CO_2 yr^{-1} (units of C in CO_2 form) to the CO_2 growth rate. Summing up the effect of fossil fuel CH_4 emissions from each previous year during the past 10 yr, a fraction of which is oxidized into CO_2 in the current year, this defines a contribution of 5 Tg C-CO_2 yr^{-1} to the CO_2 growth rate. Thus the effect of anthropogenic fossil CH_4 fugitive emissions and their oxidation to anthropogenic CO_2 in the atmosphere can be assessed to have a negligible effect on the observed CO_2 growth rate, although they do contribute significantly to the global CH_4 growth rate.

2.4 Ocean CO_2 sink

A mean ocean CO_2 sink of 2.2 ± 0.4 PgC yr^{-1} for the 1990s was estimated by the IPCC (Denman et al., 2007) based on three data-based methods (Mikaloff Fletcher et al., 2006; Manning and Keeling, 2006; McNeil et al., 2003) (Table 1). Here we adopt this mean CO_2 sink, and compute the trends in the ocean CO_2 sink for 1959–2011 using a combination of global ocean biogeochemistry models. The models represent the physical, chemical and biological processes that influence the surface ocean concentration of CO_2 and thus the air-sea CO_2 flux. The models are forced by meteorological reanalysis data and atmospheric CO_2 concentration available for the entire time period. They compute the air-sea flux of CO_2 over grid boxes of 1 to 4 degrees in latitude and longitude.

For 1959–2008, four model estimates were used (Le Quéré et al., 2009). For years 2009 to 2011, we use the interannual variability estimated by the models available to us. These include updates of three of the models used in Le Quéré et al. (2009); Aumont and Bopp (2006); Doney et al. (2009); Buitenhuis et al. (2010) and one further model estimate updated from Assman et al. (2010). We do not recompute the 1959–2008 trend to avoid introducing annual changes in the trend that are associated with the model ensemble rather than with real progress in knowledge or in the number of models available. Instead, we compute the average model anomaly compared to the average of 1999–2008, the ten-year period immediately preceding the end of the trend previously estimated and add this to the estimate presented in Le Quéré et al. (2009). The standard deviation of the ocean model ensemble is generally about 0.1–0.2 PgC yr^{-1}. We estimate that the uncertainty in the annual ocean CO_2 sink is about ±0.5 PgC yr^{-1}, reflecting both the uncertainty in the mean sink and in the interannual variability as assessed by models.

2.5 Terrestrial CO_2 sink

The difference between the fossil fuel (E_{FF}) and LUC net emissions (E_{LUC}), the atmospheric growth rate (G_{ATM}) and the ocean CO_2 sink (S_{OCEAN}) is attributable to the net sink of CO_2 in terrestrial vegetation and soils (S_{LAND}), within the given uncertainties. Thus, this sink can be estimated either as the residual of the other terms in the mass balance budget but also directly calculated using DGVMs. Note the S_{LAND} term does not include gross land sinks directly resulting from LUC (e.g. regrowth of vegetation) as these are estimated as part of the net land use flux (E_{LUC}). The residual land sink (S_{LAND}) is in part due to the fertilising effect of rising atmospheric CO_2 on plant growth, N deposition and climate change effects such as prolonged growing seasons in northern temperate areas. This terrestrial sink was often referred as the "missing sink" prior to the 1990s, before atmospheric CO_2 (Tans et al., 1990), $\delta^{13}C$ (Quay et al., 1992) and O_2 (Keeling et al., 1996) studies independently constrained the ocean and hence the land sinks.

2.5.1 Residual of the budget

For 1959–2011, the terrestrial carbon sink was estimated from the residual of the other budget terms:

$$S_{LAND} = E_{FF} + E_{LUC} - (G_{ATM} + S_{OCEAN}) \quad (7)$$

The uncertainty in S_{LAND} is estimated annually from the quadratic sum of the uncertainty in the right-hand terms assuming the errors are not correlated. The uncertainty averages to $\pm 0.8\,PgC\,yr^{-1}$ over 1959–2011, increasing with time to $\pm 0.93\,PgC\,yr^{-1}$ in 2011. S_{LAND} estimated from the residual of the budget will include, by definition, all the missing processes and potential biases in the other component of Eq. (7).

2.5.2 DGVMs

A comparison of the residual calculation of S_{LAND} in Eq. (7) with outputs from DGVMs similar to those described in Sect. 2.2.3, but designed to quantify S_{LAND} rather than E_{LUC}, provides an independent estimate of the consistency of S_{LAND} with our understanding of the functioning of the terrestrial vegetation in response to CO_2 and climate variability. An ensemble of nine DGVMs are presented here, coordinated by the project "Trends and drivers of the regional-scale sources and sinks of carbon dioxide (Trendy)" (Sitch et al., 2012) (Table 3). These DGVMs were forced with changing climate and atmospheric CO_2 concentration, and a fixed contemporary cropland distribution. These models thus include all climate variability and CO_2 effects over land, but do not include the trend in CO_2 sink capacity associated with human activity directly affecting changes in vegetation cover and management. This effect has been estimated to have lead to a reduction in the terrestrial sink by $0.5\,PgC\,yr^{-1}$ since 1750 (Gitz and Ciais, 2003) but it is neglected here. The models estimate the mean and variability of S_{LAND} based on atmospheric CO_2 and climate, and thus both terms can be compared to the budget residual.

The standard deviation of the annual CO_2 sink across the nine DGVMs ranges from ± 0.8 to $\pm 1.8\,PgC\,yr^{-1}$, with an average of $\pm 1.1\,PgC\,yr^{-1}$ for the period 1960 to 2009. When only the interannual variability is analysed as in Le Quéré et al. (2009) by removing the mean sink of the 1990s from each estimate individually, the standard deviation of the annual CO_2 sink decreases to $0.80\,PgC\,yr^{-1}$, an improvement from the $0.95\,PgC\,yr^{-1}$ presented in Le Quéré et al. (2009) using an ensemble of five models. As this standard deviation across the DGVM models and around the mean trends is of the same magnitude as the combined uncertainty due to the other components (E_{FF}, E_{LUC}, G_{ATM}, S_{OCEAN}), the DGVMs do not provide further constrains on the terrestrial CO_2 sink compared to the residual of the budget (Eq. 7). However (1) they confirm that the sum of our knowledge on annual CO_2 emissions and their partitioning is plausible, (2) they suggest that the uncertainty of $\pm 0.8\,PgC\,yr^{-1}$ for S_{LAND} estimated from Eq. (7)

is an appropriate reflection of current knowledge, and (3) they enable the attribution of the fluxes to the underlying processes and provide a breakdown of the regional contributions (not shown here).

3 Results

3.1 Global CO_2 budget averaged over decades

The global CO_2 budget averaged over the last decade (2002–2011) is shown in Fig. 1. For this time period, 89 % of the total emissions ($E_{FF} + E_{LUC}$) were caused by fossil fuel combustion and cement production, and 11 % by land-use change. The total emissions were partitioned among the atmosphere (46 %), ocean (27 %) and land (28 %). All components except land-use change emissions have grown since 1959 (Figs. 2 and 3), with important interannual variability in the atmospheric growth rate and land CO_2 sink (Fig. 3), and some decadal variability in all terms (Table 4).

Global CO_2 emissions from fossil fuel combustion and cement production have increased every decade from an average of 3.1 ± 0.2 PgC yr^{-1} in the 1960s to 8.3 ± 0.4 PgC yr^{-1} during 2002–2011 (Table 4). The growth rate in these emissions decreased between the 1960s and the 1990s, from 4.5 % yr^{-1} in the 1960s, 2.9 % yr^{-1} in the 1970s, 1.9 % yr^{-1} in the 1980s, 1.0 % yr^{-1} in the 1990s, and increased again since year 2000 at an average of 3.1 % yr^{-1}. In contrast, CO_2 emissions from LUC have remained constant at around 1.5 ± 0.5 PgC yr^{-1} during 1960–1999, and decreased to 1.0 ± 0.5 PgC yr^{-1} since year 2000. The decreased emissions from LUC since 2000 is also reproduced by the DGVMs (Fig. 5).

The growth rate in atmospheric CO_2 increased from 1.7 ± 0.1 PgC yr^{-1} in the 1960s to 4.3 ± 0.1 PgC yr^{-1} during 2002—2011 with important decadal variations (Table 4). The ocean CO_2 sink increased from 1.5 ± 0.5 PgC yr^{-1} in the 1960s to 2.5 ± 0.5 PgC yr^{-1} during 2002–2011, while the land CO_2 sink increased from

1.3 ± 0.8 PgC yr^{-1} in the 1960s to 2.6 ± 0.8 PgC yr^{-1} during 2002–2011, also with important decadal variations.

3.2 Global CO_2 budget for year 2011 and emissions projection for 2012

Global CO_2 emissions from fossil fuel combustion and cement production reached 9.5 ± 0.5 PgC in 2011 (Fig. 4; see also Peters et al., 2012a). The total emissions in 2011 were distributed among coal (43 %), oil (34 %), gas (18 %), cement (4.9 %) and gas flaring (0.7 %). These first four categories increased by 5.4, 0.7, 2.2, and 2.7 % respectively over the previous year, without enough data to calculate the change for gas flaring. Using Eq. (5), we estimate that global CO_2 emissions in 2012 will reach 9.7 ± 0.5 PgC, or 2.6 % above 2011 levels (likely range of 1.9–3.5, Peters et al., 2012a), and that emissions in 2012 will thus be 58 % above emissions in 1990. The expected value is computed using the world GDP projection of 3.3 % made by the IMF (October 2012) and a growth rate for I_{FF} of −0.7 % which is the average from the previous 10 yr. The uncertainty range is based on 0.2 % for GDP growth (the range in IMF estimates published in January, April, July, and October 2012) and the range in I_{FF} due to short term trends of −0.1 % yr^{-1} (2007–2011) and medium term trends of −1.2 % yr^{-1} (1990–2011); the combined uncertainty range is therefore 1.9 % (3.3–1.2–0.2) and 3.5 % (3.3–0.1 + 0.2). Projections made for the 2009, 2010, and 2011 CO_2 budget compared well to the actual CO_2 emissions for that year (Table 5) and were useful to capture the current state of the fossil fuel emissions.

In 2011, global CO_2 emissions were dominated by emissions from China (28 % in 2011), the USA (16 %), the EU (27 member states; 11 %), and India (7 %). The per-capita CO_2 emissions in 2011 were 1.4 tC person^{-1} yr^{-1} for the globe, and 4.7, 2.0, 1.8, and 0.5 tC person^{-1} yr^{-1} for the USA, China, the EU and India, respectively (Fig. 4e).

Territorial-based emissions in Annex B countries have remained stable from 1990–2000, while consumption-based emissions have grown at 0.5 % yr^{-1} (Fig. 4c). In non-Annex B countries territorial-based emissions have grown at 4.4 % yr^{-1}, while

consumption-based emissions have grown at 4.0 % yr^{-1}. In 1990, 65 % of global territorial-based emissions were emitted in Annex B countries, while in 2010 this had reduced to 42 %. In terms of consumption-based emissions this split was 66 % in 1990 and 46 % in 2010. The difference between territorial-based and consumption-based emissions (the net emission transfer via international trade) from non-Annex B to Annex B countries has increased from 0.04 PgC in 1990 to 0.38 PgC in 2010 (Fig. 4), with an average annual growth rate of 9 % yr^{-1}. The increase in net emission transfers of 0.33 PgC from 1990–2008 compares with the emission reduction of 0.2 PgC in Annex B countries. These results clearly show a growing net emission transfer via international trade from non-Annex B to Annex B countries. In 2010, the biggest emitters from a territorial-based perspective were China (26 %), USA (17 %), EU (12 %), and India (7 %), while the biggest emitters from a consumption-based perspective were China (22 %), USA (18 %), EU (15 %), and India (6 %).

Global CO_2 emissions from Land-Use Change activities were 0.9 ± 0.5 PgC in 2011, with the decrease of 0.2 PgC yr^{-1} from the year 2010 estimate based on satellite-detected fire activity.

Atmospheric CO_2 growth rate was 3.6 ± 0.2 PgC in 2011 (1.70 ± 0.09 ppm; Fig. 3). This is slightly below the 2000–2009 average of 4.0 ± 0.1 PgC yr^{-1}, though the interannual variability in atmospheric growth rate is large.

The ocean CO_2 sink was 2.6 ± 0.5 PgC yr^{-1} in 2011, a slight increase compared to the sink of 2.5 ± 0.5 PgC yr^{-1} in 2010 and 2.3 ± 0.5 PgC yr^{-1} in 2000–2009 (Fig. 3). All four models suggest that the ocean CO_2 sink in 2011 was greater than the 2010 sink.

The terrestrial CO_2 sink calculated as the residual from the carbon budget was 4.1 ± 0.9 PgC in 2011, well above the 2.7 ± 0.9 PgC in 2010 and 2.4 ± 0.9 PgC yr^{-1} in 2000–2009 (Fig. 3). This large sink is consistent with enhanced CO_2 sink during the wet and cold conditions associated with the strong La Niña condition that started in the middle of 2010 and ended in March 2012, as discussed for previous events (Peylin et al., 2005; Tian et al., 1998). Results from DGVMs are available to year 2010 only (Fig. 5).

4 Discussion

Each year when the global CO_2 budget is published, each component for all previous years is updated to take into account corrections that are due to further scrutiny and verification of the underlying data in the primary input data sets (Fig. 6). The updates have generally been relatively small and generally focused on the most recent past years, except for LUC between 2008 and 2009 when LUC emissions were revised downwards by 0.56 PgC yr^{-1}, and after 1997 for this budget where we introduced an estimate of interannual variability from management-climate interactions. The 2008/2009 revision was the result of the release of FAO 2010, which contained a major update to forest cover change for the period 2000–2005 and provided the data for the following 5 yr to 2010. Updates were at most 0.24 PgC yr^{-1} for the fossil fuel and cement emissions, 0.19 PgC yr^{-1} for the atmospheric growth rate, 0.20 PgC yr^{-1} for the ocean CO_2 sink. The update for the residual land CO_2 sink was also large, with maximum value of 0.71 PgC yr^{-1}, directly reflecting the revision in other terms of the budget. Likewise, the land sink estimated by DGVMs has also reflected the increasing availability of model output to do these calculations.

Our capacity to separate the CO_2 budget components can be evaluated by comparing the land CO_2 sink estimated with the budget residual (S_{LAND}), which includes errors and biases from all components, with the land CO_2 sink estimates by the DGVM ensemble, which are based on our understanding of processes of how the land responds to increasing CO_2 and climate change and variability. The two estimates are generally close (Fig. 5), both for the mean and for the interannual variability. The DGVMs correlate with the budget residual with $r = 0.34$ to 0.45 (median of $r = 0.43$), and $r = 0.48$ for the model mean (Fig. 5). The DGVMs produce a decadal mean and standard deviation across nine models of 2.6 ± 0.8 PgC yr^{-1}, nearly the same as the estimate produced with the budget residual (Table 4). Analysis of regional CO_2 budgets would provide further information to quantify and improve our estimates, as has been undertaken by the REgional Carbon Cycle Assessment and Processes (RECCAP) exercise (Canadell et al., 2011).

Annual estimations of each component of the global CO_2 budgets have their limitations, some of which could be improved with better data and/or a better understanding of carbon dynamics. The primary limitations involve resolving fluxes on annual time scales and providing updated estimates for recent years for which data-based estimates are not yet available. Of the various terms in the global budget, only the fossil-fuel burning and atmospheric growth rate terms are based primarily on empirical inputs with annual resolution. The data on fossil fuel consumption and cement production are based on survey data in all countries. The other terms can be provided on an annual basis only through the use of models. While these models represent the current state of the art, they provide only estimates of actual changes. For example, the decadal trends in ocean uptake and the interannual variations associated with El Niño/La Niño (ENSO) are not directly constrained by observations, although many of the processes controlling these trends are sufficiently well known that the model-based trends still have value as benchmarks for further validation. Land-use emissions estimates and their variations from year to year have even larger uncertainty, and much of the underlying data are not available as an annual update. Efforts are underway to work with annually available satellite area change data or FAO reported data in combination with fire data and modelling to provide annual updates for future budgets. The best resolved changes are in atmospheric growth (G_{ATM}), fossil-fuel emissions (E_{FF}), and by difference, the change in the sum of the remaining terms ($S_{OCEAN} + S_{LAND} - E_{LUC}$). The variations from year to year in these remaining terms are largely model-based at this time. Further efforts to increase the availability and use of annual data for estimating the remaining terms with annual to decadal resolution are especially needed.

Our approach also depends on the reliability of the energy and land cover change statistics provided at the country level, and are thus potentially subject to biases. Thus it is critical to develop multiple ways to estimate the carbon balance at the global and regional level, including from the inversion of atmospheric CO_2 concentration, the use of other oceanic and atmospheric tracers, and the compilation of emissions using alternative statistics (e.g. sectors). Multiple approaches going from global to regional would

greatly help improve confidence and reduce uncertainty in CO_2 emissions and their fate.

5 Conclusions

The estimation of global CO_2 emissions and sinks is a major effort by the carbon cycle research community that requires a combination of measurements and compilation of statistical estimates and results from models. The delivery of an annual carbon budget serves two purposes. First, there is a large demand for up-to-date information on the state of the anthropogenic perturbation of the climate system and its underpinning causes. A broad stakeholder community relies on the datasets associated with the annual CO_2 budget including scientists, policy makers, businesses, journalists, and the broader civil society increasingly engaged in the climate change debate. Second, over the last decade we have seen rapid changes in the human and biophysical worlds (e.g. acceleration of fossil fuel emissions and the response of land and ocean carbon sinks to global climate phenomena), which require a more frequent assessment of what we can learn regarding future dynamics and the needs for climate change mitigation. In very general terms, both the oceans and the land surface presently mitigate a large fraction of anthropogenic emissions. Any significant change in this situation is of great importance to climate policymaking, as it implies different emissions levels to achieve warming target aspirations such as remaining below the two-degrees of global warming since pre-industrial periods. Better constraints of carbon cycle models against the contemporary datasets raises the hope that they will be more accurate at future projection.

This all requires more frequent, robust, and transparent datasets and methods that can be scrutinized and replicated. After seven annual releases done by the GCP, the effort is growing and the traceability of the methods has become increasingly complex. Here, we have documented in detail the datasets and methods used to compile the annual updates of the global carbon budget, explained the rationale for the choices made,

the limitations of the information, and finally highlighted need for additional information where gaps exist.

This paper via "living reviews" will help to keep track of new budget updates. The evolution over time of the carbon budget is now a key indicator of the anthropogenic perturbation of the climate system and its annual delivery joins a set of climate indicators to monitor the evolution of human-induced climate change, such as the annual updates on the global surface temperature, sea level rise, minimum Arctic sea ice extent and others.

6 Data access

The accompanying database includes one excel file organised in seven spreadsheets:

1. The global carbon budget (1959–2011).
2. Global CO_2 emissions from fossil fuel combustion and cement production by fuel type, and the per-capita emissions (1959–2011).
3. Territorial-based (e.g. as reported to the UN Framework Convention on Climate Change) country CO_2 emissions from fossil fuel combustion and cement production (1959–2011).
4. Consumption-based country CO_2 emissions from fossil fuel combustion and cement production and emissions transfer from the international trade of goods and services (1990–2010).
5. CO_2 emissions from land-use change from the individual methods and models (1959–2011).
6. Ocean CO_2 sink from the individual ocean models (1959–2011).
7. Terrestrial residual CO_2 sink from the DGVMs (1959–2011).

Acknowledgements. We thanks all people and institutions who provided data used in this carbon budget, in particular, G. Hurt, L. Chini, and I. Harris. The observations and modelling analysis were possible thanks to funding from multiple agencies around the world. The UK Natural Environment Research Council provided funding to CLQ and the GCP though their International Opportunities Fund specifically to support this publication (project NE/103002X/1). CLQ, PC, SZ, and JS thank the EU FP7 for funding through projects GEOCarbon (283080), COMBINE (226520) and CARBOCHANGE (264879). GPP acknowledges support from the Norwegian Research Council (221355/E10). SCD acknowledges support from the US National Science Foundation (NSF AGS-1048827). JH was supported by a Leverhulme Research Fellowship and the Cabot Institute, University of Bristol. RJA and TAB were sponsored by US Department of Energy, Office of Science, Biological and Environmental Research (BER) programs and performed at Oak Ridge National Laboratory (ORNL) under US Department of Energy contract DE-AC05-00OR22725. CH was supported by the Centre for Ecology and Hydrology "Science Budget". EK was supported by the Global Environment Research Fund (S-10) of the Ministry of Environment of Japan. GrvdW was supported by the European Research Council. BDS was supported by the Swiss National Science Foundation. AA acknowledges the Mistra-SWECIA programme and the strategic research areas MERGE, BECC and LUCCI.

References

Ahlström, A., Miller, P. A., and Smith, B.: Too early to infer a global NPP decline since 2000, Geophys. Res. Lett., 39, L15403, doi:10.1029/2012GL052336, 2012.

Andres, R. J., Boden, T. A., Bréon, F.-M., Ciais, P., Davis, S., Erickson, D., Gregg, J. S., Jacobson, A., Marland, G., Miller, J., Oda, T., Olivier, J. G. J., Raupach, M. R., Rayner, P., and Treanton, K.: A synthesis of carbon dioxide emissions from fossil-fuel combustion, Biogeosciences, 9, 1845–1871, doi:10.5194/bg-9-1845-2012, 2012.

Archer, D., Eby, M., Brovkin, V., Ridgwell, A., Cao, L., Mikolajewicz, U., Caldeira, K. M., K., Munhoven, G., Montenegro, A., and Tokos, K.: Atmospheric Lifetime of Fossil Fuel Carbon Dioxide, Annu. Rev. Earth Pl. Sc., 37, 117–134, 2009.

Assmann, K. M., Bentsen, M., Segschneider, J., and Heinze, C.: An isopycnic ocean carbon cycle model, Geosci. Model Dev., 3, 143–167, doi:10.5194/gmd-3-143-2010, 2010.

Aufdenkampe, A. K., Mayorga, E., Raymond, P. A., Melack, J. M., Doney, S. C., Alin, S. R., Aalto, R. E., and Yoo, K.: Riverine coupling of biogeochemical cycles between land, oceans and atmosphere, Frontiers Ecology Environ., 9, 53–60, 2011.

Aumont, O. and Bopp, L.: Globalizing results from ocean in situ iron fertilization studies, Global Biogeochem. Cy., 20, GB2017, doi:10.1029/2005GB002591, 2006.
Baccini, A., Goetz, S. J., Walker, W. S., Laporte, N. T., Sun, M., Sulla-Menashe, D., Hackler, J., Beck, P. S. A., Dubayah, R., Friedl, M. A., Samanta, S., and Houghton, R. A.: Estimated carbon dioxide emissions from tropical deforestation improved by carbon-density maps, Nature Clim. Change, 2, 182–186, 2012.
Ballantyne, A. P., Alden, C. B., Miller, J. B., Tans, P. P., and White, J. W. C.: Increase in observed net carbon dioxide uptake by land and oceans during the last 50 years, Nature, 488, 70–72, 2012.
Ballhorn, U., Siegert, F., Mason, M., and Limin, S.: Derivation of burn scar depths and estimation of carbon emissions with LIDAR in Indonesian peatlands, P. Natl. Acad. Sci., 106, 21213–21218, doi:10.1073/pnas.0906457106, 2009.
Battin, T. J., Kaplan, L. A., Findlay, S., Hopkinson, C. S., Marti, E., Packman, A. I., Newbold, J. D., and Sabater, F.: Biophysical controls on organic carbon fluxes in fluvial networks, Nat. Geosci., 1, 95–100, 2008.
Statistical Review of World Energy 2012: http://www.bp.com/sectionbodycopy.do?categoryId=7500&contentId=7068481, last access: October 2012.
Buitenhuis, E. T., Rivkin, R. B., Sailley, S., and Le Quéré, C.: Biogeochemical fluxes through microzooplankton, Global Biogeochem. Cy., 24, Gb4015, doi:10.1029/2009gb003601, 2010.
Canadell, J. G., Le Quéré, C., Raupach, M. R., Field, C. B., Buitenhuis, E. T., Ciais, P., Conway, T. J., Gillett, N. P., Houghton, R. A., and Marland, G.: Contributions to accelerating atmospheric CO_2 growth from economic activity, carbon intensity, and efficiency of natural sinks, P. Natl. Acad. Sci. USA, 104, 18866–18870, doi:10.1073/pnas.0702737104, 2007.
Canadell, J. G., Ciais, P., Gurney, K., Le Quéré, C., Piao, S., Raupach, M. R., and Sabine, C. L.: An international effort to quantify regional carbon fluxes, EOS, 92, 81–82, 2011.
Clark, D. B., Mercado, L. M., Sitch, S., Jones, C. D., Gedney, N., Best, M. J., Pryor, M., Rooney, G. G., Essery, R. L. H., Blyth, E., Boucher, O., Harding, R. J., Huntingford, C., and Cox, P. M.: The Joint UK Land Environment Simulator (JULES), model description – Part 2: Carbon fluxes and vegetation dynamics, Geosci. Model Dev., 4, 701–722, doi:10.5194/gmd-4-701-2011, 2011.
Conway, T. J. and Tans, P. P.: Trends in atmospheric carbon dioxide: http://www.esrl.noaa.gov/gmd/ccgg/trends, last access: 16 November 2012.
Cox, P. M.: Description of the "TRIFFID" dynamic global vegetation model, Hadley Centre, Technical Note 24, 2001.

Davis, S. J., Peters, G. P., and Caldeira, K.: The supply chain of CO_2 emissions, P. Natl. Acad. Sci. USA, 108, 18554–18559, 2011.
Denman, K. L., Brasseur, G., Chidthaisong, A., Ciais, P., Cox, P. M., Dickinson, R. E., Hauglustaine, D., Heinze, C., Holland, E., Jacob, D., Lohmann, U., Ramachandran, S., Leite da Silva Dias, P., Wofsy, S. C., and Zhang, X.: Couplings Between Changes in the Climate System and Biogeochemistry, in: Climate Change 2007: The Physical Science Basis. Contribution of Working Group I to the Fourth Assessment Report of the Intergovernmental Panel on Climate Change, edited by: Solomon, S., Qin, D., Manning, M., Chen, Z., Marquis, M., Averyt, K. B., Tignor, M., and Miller, H. L., Cambridge University Press, Cambridge, United Kingdom and New York, NY, USA.
Doney, S. C., Lima, I., Feely, R. A., Glover, D. M., Lindsay, K., Mahowald, N., Moore, J. K., and Wanninkhof, R.: Mechanisms governing interannual variability in upper-ocean inorganic carbon system and air-sea CO_2 fluxes: Physical climate and atmospheric dust, Deep-Sea Res. Pt. II, 56, 640–655, 2009.
Earles, J. M., Yeh, S., and Skog, K. E.: Timing of carbon emissions from global forest clearance, Nature Climate Change, 2, 682–685, 2012.
Enting, I. G., Wigley, T. M. L., and Heimann, M.: Future emissions and concentrations of carbon dioxide: Key ocean/atmosphere/land analyses, Melbourne, 1994.
Falkowski, P., Scholes, R. J., Boyle, E., Canadell, J. G., Canfield, D., Elser, J., Gruber, N., Hibbard, K., Högberg, P., Linder, S., Mackenzie, F. T., Moore III, B., Pedersen, T., Rosenthal, Y., Seitzinger, S., Smetacek, V., and Steffen, W.: The Global Carbon Cycle: A Test of Our Knowledge of Earth as a System, Science, 290, 291–296, 2000.
FAO: Global Forest Resource Assessment 2010, 378 pp., 2010.
Food and Agriculture Organization Statistics Division: http://faostat.fao.org/, 2010.
Friedlingstein, P., Houghton, R. A., Marland, G., Hackler, J., Boden, T. A., Conway, T. J., Canadell, J. G., Raupach, M. R., Ciais, P., and Le Quéré, C.: Update on CO_2 emissions, Nat. Geosci., 3, 811–812, doi:10.1038/ngeo1022, 2010.
Giglio, L., Randerson, J. T., van der Werf, G. R., Kasibhatla, P. S., Collatz, G. J., Morton, D. C., and DeFries, R. S.: Assessing variability and long-term trends in burned area by merging multiple satellite fire products, Biogeosciences, 7, 1171–1186, doi:10.5194/bg-7-1171-2010, 2010.
Gitz, V. and Ciais, P.: Amplifying effects of land-use change on future atmospheric CO_2 levels, Global Biogeochem. Cy., 17, 1024, doi:10.1029/2002GB001963, 2003.

Goldewijk, K. K., Beusen, A., van Drecht, G., and de Vos, M.: The HYDE 3.1 spatially explicit database of human-induced global land-use change over the past 12,000 years, Global Ecol. Biogeogr., 20, 73–86, 2011.
Gregg, J. S., Andres, R. J., and Marland, G.: China: Emissions pattern of the world leader in CO_2 emissions from fossil fuel consumption and cement production, Geophys. Res. Lett., 35, L08806, doi:10.1029/2007gl032887, 2008.
Hooijer, A., Page, S., Canadell, J. G., Silvius, M., Kwadijk, J., Wösten, H., and Jauhiainen, J.: Current and future CO_2 emissions from drained peatlands in Southeast Asia, Biogeosciences, 7, 1505–1514, doi:10.5194/bg-7-1505-2010, 2010.
Houghton, R. A.: Revised estimates of the annual net flux of carbon to the atmosphere from changes in land use and land management 1850–2000, Tellus B, 55, 378–390, doi:10.1034/j.1600-0889.2003.01450.x, 2003.
Houghton, R. A., van der Werf, G. R., DeFries, R. S., Hansen, M. C., House, J. I., Le Quéré, C., Pongratz, J., and Ramankutty, N.: Chapter G2 Carbon emissions from land use and land-cover change, Biogeosciences Discuss., 9, 835–878, doi:10.5194/bgd-9-835-2012, 2012.
Hurtt, G. C., Chini, L. P., Frolking, S., Betts, R. A., Feddema, J., Fischer, G., Fisk, J. P., Hibbard, K., Houghton, R. A., Janetos, A., Jones, C. D., Kindermann, G., Kinoshita, T., Klein Goldewijk, K., Riahi, K., Shevliakova, E., Smith, S., Stehfest, E., Thomson, A., Thornton, P., van Vuuren, D. P., and Wang, Y. P.: Harmonization of land-use scenarios for the period 1500–2100: 600 years of global gridded annual land-use transitions, wood harvest, and resulting secondary lands, Climatic Change, 109, 117–161, 2011.
Jain, A. K., Meiyappan, P., Song, Y., and House, J. I.: Estimates of carbon emissions from historical land-use and land-cover change, Glob. Change Biol., revised, 2012.
Kato, E., Kinoshita, T., Ito, A., Kamamiya, M., and Yamagata, Y.: Evaluation of spatially explicit emission scenario of land-use change and biomass burning using a process-based biogeochemical model, Journal of Land Use Science, doi:10.1080/1747423X.2011.628705, in press, 2012.
Keeling, C. D., Bacastow, R. B., Bainbridge, A. E., Ekdhal, C. A., Guenther, P. R., and Waterman, L. S.: Atmospheric carbon dioxide variations at Mauna Loa Observatory, Hawaii, Tellus, 28, 538–551, 1976.
Keeling, R. F., Piper, S. C., and Heimann, M.: Global and hemispheric CO_2 sinks deduced from changes in atmospheric O_2 concentration, Nature, 381, 218–222, 1996.
Kirschke, S., Bousquet, P., Ciais, P., Saunois, M., Dlugokencky, E. J., Bergamaschi, P., Bergmann, D., Blake, D. R., Bruhwiler, L., Cameron-Smith, P., Canadell, J. G., Castaldi, S.,

Chevallier, F., Feng, L., Fraser, A., Fraser, P. J., Heimann, M., Hodson, E. L., Houweling, S., Josse, B., Krummel, P. B., Lamarque, J.-F., Le Quéré, C., Montzka, S. A., Naik, V., O'Doherty, S., Palmer, P. I., Pison, I., Plummer, D., Poulter, B., Prinn, R. G., Rigby, M., Ringeval, B., Santini, M., Schmidt, M., Shindell, D. T., Simpson, I. J., Spahni, R., Steele, L. P., Strode, S. A., Sudo, K., Szopa, S., van der Werf, G. R., Voulgarakis, A., van Weele, M., Weiss, R. F., Williams, J. E., and Zeng, G.: Three decades of methane sources and sinks: budgets and variations, Nat. Geosci., in review, 2012.
Krinner, G., Viovy, N., de Noblet-Ducoudre, N., Ogee, J., Polcher, J., Friedlingstein, P., Ciais, P., Sitch, S., and Prentice, I. C.: A dynamic global vegetation model for studies of the coupled atmosphere-biosphere system, Global Biogeochem. Cy., 19, Gb1015, doi:10.1029/2003gb002199, 2005.
Lawrence, D. M., Oleson, K. W., Flanner, M. G., Thornton, P. E., Swenson, S. C., Lawrence, P. J., Zeng, X., Yang, Z.-L., Levis, S., Sakaguchi, K., Bonan, G. B., and Slater, A. G.: Parameterization improvements and functional and structural advances in version 4 of the Community Land Model, Journal of Advances in Modeling Earth Systems, 3, M03001, doi:10.1029/2012MS000165, 2011.
Le Quéré, C.: Closing the global budget for CO_2, Glob. Change, 74, 28–31, 2009.
Le Quéré, C., Rödenbeck, C., Buitenhuis, E. T., Conway, T. J., Langenfelds, R., Gomez, A., Labuschagne, C., Ramonet, M., Nakazawa, T., Metzl, N., Gillett, N., and Heimann, M.: Saturation of the Southern Ocean CO_2 sink due to recent climate change, Science, 316, 1735–1738, doi:10.1126/science.1136188, 2007.
Le Quéré, C., Raupach, M. R., Canadell, J. G., Marland, G., Bopp, L., Ciais, P., Conway, T. J., Doney, S. C., Feely, R. A., Foster, P., Friedlingstein, P., Gurney, K., Houghton, R. A., House, J. I., Huntingford, C., Levy, P. E., Lomas, M. R., Majkut, J., Metzl, N., Ometto, J. P., Peters, G. P., Prentice, I. C., Randerson, J. T., Running, S. W., Sarmiento, J. L., Schuster, U., Sitch, S., Takahashi, T., Viovy, N., van der Werf, G. R., and Woodward, F. I.: Trends in the sources and sinks of carbon dioxide, Nat. Geosci., 2, 831–836, 2009.
Levy, P. E., Cannell, M. G. R., and Friend, A. D.: Modelling the impact of future changes in climate, CO_2 concentration and land use on natural ecosystems and the terrestrial carbon sink, Global Environ. Chang., 14, 21–30, doi:10.1016/j.gloenvcha.2003.10.005, 2004.
Marland, G.: Uncertainties in accounting for CO_2 from fossil fuels, J. Ind. Ecol., 12, 136–139, doi:10.1111/j.1530-9290.2008.00014.x, 2008.

Manning, A. C. and Keeling, R. F.: Global oceanic and land biotic carbon sinks from the Scripps atmospheric oxygen flask sampling network, Tellus B, 58, 95–116, doi:10.1111/j.1600-0889.2006.00175.x, 2006.
Marland, G., Andres, R. J., Blasing, T. J., Boden, T. A., Broniak, C. T., Gregg, J. S., Losey, L. M., and Treanton, K.: Energy, industry and waste management activities: An introduction to CO_2 emissions from fossil fuels, in: A report by the US Climate Change Science Program and the Subcommittee on Global Change Research, in The First State of the Carbon Cycle Report (SOCCR): The North American Carbon Budget and Implications for the Global Carbon Cycle, edited by: King, A. W., Dilling, L., Zimmerman, G. P., Fairman, D. M., Houghton, R. A., Marland, G., Rose, A. Z., and Wilbanks, T. J., Asheville, NC, 57–64, 2007.
Marland, G., Hamal, K., and Jonas, M.: How Uncertain Are Estimates of CO_2 Emissions?, J. Ind. Ecol., 13, 4–7, doi:10.1111/j.1530-9290.2009.00108.x, 2009.
Masarie, K. A. and Tans, P. P.: Extension and integratino of atmospheric carbon dioxide data into a globally consistent measurement record, J. Geophys. Res.-Atmos., 100, 11593–11610, doi:10.1029/95jd00859, 1995.
McNeil, B. I., Matear, R. J., Key, R. M., Bullister, J. L., and Sarmiento, J. L.: Anthropogenic CO_2 uptake by the ocean based on the global chlorofluorocarbon data set, Science, 299, 235–239, doi:10.1126/science.1077429, 2003.
Meiyappan, P. and Jain, A. K.: Three distinct global estimates of historical land-cover change and land-use conversions for over 200 years, Front. Earth Sci., 6, 122–139, 2012.
Mikaloff Fletcher, S. E., Gruber, N., Jacobson, A. R., Doney, S. C., Dutkiewicz, S., Gerber, M., Follows, M., Joos, F., Lindsay, K., Menemenlis, D., Mouchet, A., Müller, S. A., and Sarmiento, J. L.: Inverse estimates of anthropogenic CO_2 uptake, transport, and storage by the oceans, Global Biogeochem. Cy., 20, GB2002, doi:10.1029/2005GB002530, 2006.
National Accounts Main Aggregates Database: http://unstats.un.org/unsd/snaama/Introduction.asp, last access: November 2012.
NOAA/ESRL calculation of global means: http://www.esrl.noaa.gov/gmd/ccgg/about/global_means.html, last access: November 2012.
Peters, G. P., Andrew, R., and Lennos, J.: Constructing a multi-regional input-output table using the GTAP database, Economic Systems Research, 23, 131–152, 2011a.
Peters, G. P., Minx, J. C., Weber, C. L., and Edenhofer, O.: Growth in emission transfers via international trade from 1990 to 2008, P. Natl. Acad. Sci. USA, 108, 8903–8908, doi:10.1073/pnas.1006388108, 2011b.

Peters, G. P., Andrew, R. M., Boden, T., Canadell, J. G., Ciais, P., Le Quéré, C., Marland, G., Raupach, M. R., and Wilson, C.: The challenge to keep global warming below 2 °C, Nature Climate Change, doi:10.1038/nclimate1783, in press, 2012a.
Peters, G. P., Marland, G., Le Quéré, C., Boden, T. A., Canadell, J. G., and Raupach, M. R.: Correspondence: Rapid growth in CO_2 emissions after the 2008–2009 global financial crisis, Nature Climate Change, 2, 2–4, 2012b.
Peylin, P., Bousquet, P., Le Quéré, C., Sitch, S., Friedlingstein, P., McKinley, G., Gruber, N., Rayner, P., and Ciais, P.: Multiple constraints on regional CO_2 flux variations over land and oceans, Global Biogeochem. Cy., 19, GB1011, doi:10.1029/2003GB002214, 2005.
Poulter, B., AragÃo, L., Heyder, U., Gumpenberger, M., Heinke, J., Langerwisch, F., Rammig, A., Thonicke, K., and Cramer, W.: Net biome production of the Amazon Basin in the 21st century, Glob. Change Biol., 16, 2062–2075, 2010.
Prater, M. J., Holmes, C. D., and Hsu, J.: Reactive greenhouse gas scenarios: Systematic exploration of uncertainties and the role of atmospheric chemistry, Geophys. Res. Lett., 39, L09803, doi:10.1029/2012GL051440, 2012.
Prentice, I. C., Farquhar, G. D., Fasham, M. J. R., Goulden, M. L., Heimann, M., Jaramillo, V. J., Kheshgi, H. S., Le Quéré, C., Scholes, R. J., and Wallace, D. W. R.: The Carbon Cycle and Atmospheric Carbon Dioxide, in: Climate Change 2001: The Scientific Basis. Contribution of Working Group I to the Third Assessment Report of the Intergovernmental Panel on Climate Change, edited by: Houghton, J. T., Ding, Y., Griggs, D. J., Noguer, M., van der Linden, P. J., Dai, X., Maskell, K., and Johnson, C. A., Cambridge University Press, Cambridge, United Kingdom and New York, NY, USA, 183–237, 2001.
Quay, P. D., Tilbrook, B., and Wong, C. S.: Oceanic Uptake of Fossil Fuel CO_2: Carbon-13 Evidence, Science, 256, 74–79, 1992.
Raupach, M. R., Marland, G., Ciais, P., Le Quéré, C., Canadell, J. G., Klepper, G., and Field, C. B.: Global and regional drivers of accelerating CO_2 emissions, P. Natl. Acad. Sci. USA, 104, 10288–10293, doi:10.1073/pnas.0700609104, 2007.
Schimel, D., Alves, D., Enting, I., Heimann, M., Joos, F., Raynaud, D., Wigley, T., Prater, M., Derwent, R., Ehhalt, D., Fraser, P., Sanhueza, E., Zhou, X., Jonas, P., Charlson, R., Rodhe, H., Sadasivan, S., Shine, K. P., Fouquart, Y., Ramaswamy, V., Solomon, S., Srinivasan, J., Albritton, D., Derwent, R., Isaksen, I., Lal, M., and Wuebbles, D.: Radiative Forcing of Climate Change, in: Climate Change 1995: The Science of Climate Change. Contribution of Working Group I to the Second Assessment Report of the Intergovernmental Panel on Climate Change, edited by: Houghton, J. T., Meira Filho, L. G., Callander, B. A., Harris, N.,

Kattenberg, A., and Maskell, K., Cambridge University Press, Cambridge, United Kingdom and New York, NY, USA, 1995.
Sitch, S., Smith, B., Prentice, I. C., Arneth, A., Bondeau, A., Cramer, W., Kaplan, J. O., Levis, S., Lucht, W., Sykes, M. T., Thonicke, K., and Venevsky, S.: Evaluation of ecosystem dynamics, plant geography and terrestrial carbon cycling in the LPJ dynamic global vegetation model, Glob. Change Biol., 9, 161–185, doi:10.1046/j.1365-2486.2003.00569.x, 2003.
Sitch, S., Friedlingstein, P., Gruber, N., Jones, S., Murray-Tortarolo, G., Ahlström, A., Doney, S. C., Graven, H., Heinze, C., Huntingford, C., Levis, S., Levy, P. E., Lomas, M., Poulter, B., Viovy, N., Zaehle, S., Zeng, N., Arneth, A., Bonan, G., Bopp, L., Canadell, J. G., Chevallier, F., Ciais, P., Ellis, R., Gloor, M., Peylin, P., Piao, S., Le Quéré, C., Smith, B., Zhu, Z., and Myneni, R.: Trends and drivers of regional sources and sinks of carbon dioxide over the past two decades, Biogeosciences Discuss., in review, 2012.
Smith, B., Prentice, I. C., and Sykes, M. T.: Representation of vegetation dynamics in the modelling of terrestrial ecosystems: comparing two contrasting approaches within European climate space, Global Ecol. Biogeogr., 10, 621–637, doi:10.1046/j.1466-822X.2001.t01-1-00256.x, 2001.
Stocker, B. D., Strassmann, K., and Joos, F.: Sensitivity of Holocene atmospheric CO_2 and the modern carbon budget to early human land use: analyses with a process-based model, Biogeosciences, 8, 69–88, doi:10.5194/bg-8-69-2011, 2011a.
Stocker, B. D., Strassmann, K., and Joos, F.: Sensitivity of Holocene atmospheric CO_2 and the modern carbon budget to early human land use: analyses with a process-based model, Biogeosciences, 8, 69–88, doi:10.5194/bg-8-69-2011, 2011b.
Strassmann, K. M., Joos, F., and Fischer, G.: Simulating effects of land use changes on carbon fluxes: past contributions to atmospheric CO_2 increases and future commitments due to losses of terrestrial sink capacity, Tellus, 60B, 583–603, 2008.
Tans, P. P., Fung, I. Y., and Takahashi, T.: Observational contraints on the global atmospheric CO_2 budget, Science, 247, 1431–1439, 1990.
Thomas, H., Prowe, A. E. F., Lima, I. D., Doney, S. C., Wanninkhof, R., Greatbatch, R. J., Schuster, U., and Corbiere, A.: Changes in the North Atlantic Oscillation influence CO_2 uptake in the North Atlantic over the past 2 decades, Global Biogeochem. Cy., 22, Gb4027, doi:10.1029/2007gb003167, 2008.
Tian, H., Melillo, J. M., Kicklighter, D. W., McGuire, A. D., Helfrich, J. V. K., Moore III, B., and Vorosmarty, C. J.: Effect of interannual climate variability on carbon storage in Amazonian ecosystems, Nature, 396, 644–667, 1998.

Tjiputra, J. F., Roelandt, C., Bentsen, M., Lawrence, D. M., Lorentzen, T., Schwinger, J., Seland, Ø., and Heinze, C.: Evaluation of the carbon cycle components in the Norwegian Earth System Model (NorESM), Geosci. Model Dev. Discuss., 5, 3035–3087, doi:10.5194/gmdd-5-3035-2012, 2012.
Trends in atmospheric carbon dioxide: http://www.esrl.noaa.gov/gmd/ccgg/trends, last access: July 2012.
US Geological Survey: Minerals Commodities Summaries, in: US Geological Survey, 198 pp., 2012.
United Nations Statistics Division – Energy Statistics: http://unstats.un.org/unsd/energy/, last access: October 2012a.
United Nations Statistics Division – Industry Statistics: http://unstats.un.org/unsd/industry/default.asp, last access: October 2012b.
van der Werf, G. R., Dempewolf, J., Trigg, S. N., Randerson, J. T., Kasibhatla, P., Giglio, L., Murdiyarso, D., Peters, W., Morton, D. C., Collatz, G. J., Dolman, A. J., and DeFries, R. S.: Climate regulation of fire emissions and deforestation in equatorial Asia, P. Natl. Acad. Sci. USA, 15, 20350–20355, 2008.
van der Werf, G. R., Randerson, J. T., Giglio, L., Collatz, G. J., Mu, M., Kasibhatla, P. S., Morton, D. C., DeFries, R. S., Jin, Y., and van Leeuwen, T. T.: Global fire emissions and the contribution of deforestation, savanna, forest, agricultural, and peat fires (1997–2009), Atmos. Chem. Phys., 10, 11707–11735, doi:10.5194/acp-10-11707-2010, 2010.
Van Oss, H. G.: 2009 Minerals Yearbook, in: US Geological Survey, July 2011, 16.01–16.36, 2011.
Watson, R. T., Rodhe, H., Oeschger, H., and Siegenthaler, U.: Greenhouse Gases and Aerosols, in: Climate Change: The IPCC Scientific Assessment, Intergovernmental Panel on Climate Change (IPCC), edited by: Houghton, J. T., Jenkins, G. J., and Ephraums, J. J., Cambridge University Press, Cambridge, 1–40, 1990.
Woodward, F. I. and Lomas, M. R.: Vegetation dynamics – simulating responses to climatic change, Biological Rev., 79, 643–670, doi:10.1017/s1464793103006419, 2004.
Zaehle, S., Ciais, P., Friend, A. D., and Prieur, V.: Carbon benefits of anthropogenic reactive nitrogen offset by nitrous oxide emissions, Nat. Geosci., 4, 601–605, doi:10.1038/ngeo1207, 2011.
Zeng, N., Mariotti, A., and Wetzel, P.: Terrestrial mechanisms of interannual CO_2 variability, Global Biogeochem. Cy., 19, GB1016, doi:10.1029/2004gb002273, 2005.

Table 1. Data sources used to compute each component of the global CO_2 budget.

Component	Process	Data source	Data reference
E_{FF}	Fossil fuel combustion and gas flaring	UN Statistics Division to 2009 BP for 2010–2011	UN (2012a, b) BP (2012)
	Cement production	US Geological Survey	Van Oss (2011) US Geological Survey (2012)
	Consumption-based country emissions	Global Trade and Analysis Project (GTAP)	Narayanan et al. (2012)
E_{LUC}	Land cover change (deforestation, afforestation, and forest regrowth)	Forest Resource Assessment (FRA) of the Food and Agriculture Organisation (FAO)	FAO (2010)
	Wood harvest	FAO Statistics Division	FAOSTAT (2010)
	Shifting agriculture	FAO FRA and Statistics Division	FAOSTAT (2010) FAO (2010)
	Peat fires and interannual variability from climate-land management interactions	Global Fire Emissions Database (GFED3)	van der Werf et al. (2010)
G_{ATM}	Change in CO_2 concentration	1959–1980: CO_2 Program at Scripps Institution of Oceanography and other research groups. 1980–2011: US National Oceanic and Atmospheric Administration Earth System Research Laboratory	Keeling et al. (1976) Conway and Tans (2012) and Ballantyne et al. (2012)
S_{OCEAN}	Uptake of anthropogenic CO_2	1990–1999 average: indirect estimates based on CFCs, atmospheric O_2, and other tracer observations	Manning and Keeling (2006); McNeil et al. (2003); Mikaloff Fletcher et al. (2006) as assessed by the IPCC Denman et al. (2007)
	Impact of increasing atmospheric CO_2, and climate change and variability	Ocean models	Le Quéré et al. (2009) and Table 3
S_{LAND}	Response of land vegetation to: Increasing atmospheric CO_2 concentration Climate change and variability Other environmental changes	Budget residual	

Table 2. Comparison of the processes included in the E_{LUC} of the global carbon budget and the DGVMs. See Table 3 for model references.

	CO_2 budget	VISIT	ISAM-HYDE	LPJmL	LPJ-Bern
Deforestion, afforestation, forest regrowth after abandonment of agriculture	yes	yes	yes	yes	yes
Wood harvest and forest degradation	yes	no	yes	no	no
Shifting cultivation	yes	yes	yes	no	no
Cropland harvest	yes	no	no	no	yes
Peat fires	from 1998	no	no	no	no
Fire suppression	for US only	no	no	no	no
Management-Climate interactions	from 1998	no	no	no	no
Climate change and variability	no	climate change is present but decadal mean response is used for regrowing uptake	climate variability present but not corresponding to observed years	yes	yes
CO_2 fertilisation	no	yes	yes	yes	yes
Nitrogen dynamics	no	no	yes	no	no

Table 3. References for the process models included in Fig. 3.

Model name	Reference
Dynamic Global Vegetation Models providing E_{LUC}	
VISIT	Kato et al. (2012) Climate forcing is changed to use CRU TS3.10.01 up to the year 2009.
ISAM-HYDE	Jain et al. (2012)
LPJmL	Poulter et al. (2010)
LPJ-Bern	Stocker et al. (2011a); Strassmann et al. (2008)
Dynamic Global Vegetation Models providing S_{LAND}	
Community Land Model 4CN	Lawrence et al. (2011)
Hyland	Levy et al. (2004)
JULES	Clark et al. (2011); Cox (2001)
LPJ	Sitch et al. (2003)
LPJ-GUESS	Smith et al. (2001); Ahlström et al. (2012) and references therein.
O-CN	Zaehle et al. (2011)
Orchidee	Krinner et al. (2005)
Sheffield-DGVM	Woodward and Lomas (2004)
VEGAS	Zeng et al. (2005)
Ocean Biogeochemistry Models providing S_{OCEAN}	
NEMO-PlankTOM5	Buitenhuis et al. (2010) with no nutrient restoring below the mixed layer depth
LSCE	Aumont and Bopp (2006)
CCSM-BEC	Doney et al. (2009)
MICOM-HAMOCC	Assmann et al. (2010) with updates to the physical model as described in Tjiputra et al. (2012)

Table 4. Decadal mean in the five components of the anthropogenic CO_2 budget for the periods 1980–1989, 1990–1999, 2000–2009 and the last decade available. All values are in PgC yr^{-1}.

	mean (PgC yr^{-1})					
	1960–1969	1970–1989	1980–1989	1990–1999	2000–2009	2002–2011
Emissions						
Fossil fuel combustion and cement production (E_{FF})	3.1 ± 0.2	4.7 ± 0.2	5.5 ± 0.3	6.4 ± 0.3	7.8 ± 0.4	8.3 ± 0.4
Land-Use Change emissions (E_{LUC})	1.5 ± 0.5	1.3 ± 0.5	1.4 ± 0.5	1.6 ± 0.5	1.0 ± 0.5	1.0 ± 0.5
Partitioning						
Atmospheric growth rate (G_{ATM})	1.7 ± 0.1	2.8 ± 0.1	3.4 ± 0.1	3.1 ± 0.1	4.0 ± 0.1	4.3 ± 0.1
Ocean sink (S_{OCEAN})	1.5 ± 0.5	1.7 ± 0.5	2.0 ± 0.5	2.2 ± 0.4	2.3 ± 0.5	2.5 ± 0.5
Residual terrestrial sink (S_{LAND})	1.3 ± 0.7	1.5 ± 0.8	1.5 ± 0.8	2.6 ± 0.8	2.5 ± 0.8	2.6 ± 0.8

Table 5. Actual CO_2 emissions from fossil fuel combustion and cement production (E_{FF}) compared to projections made the previous year based on world GDP and the fossil fuel intensity of GDP (I_{FF}). The "Actual" values and the Projected value for 2012 refer to those presented in this paper.

Component	2009[a]		2010[b]		2011[c]		2012
	Projected	Actual	Projected	Actual	Projected	Actual	Projected
E_{FF}	–2.8 %	–0.3 %	> 3 %	5.1 %	3.1 ± 1.5 %	3.1 %	2.6 (1.9–3.5) %
GDP	–1.1 %	0.1 %	4.8 %	5.3 %	4.0 %	3.9 %	3.3 %
I_{FF}	–1.7 %	–0.4 %	> –1.7 %	+0.2 %	–0.9 ± 1.5 %	–0.8 %	–0.7 %

[a] Le Quéré et al. (2009); [b] Friedlingstein et al. (2010); [c] Peters et al. (2012b).

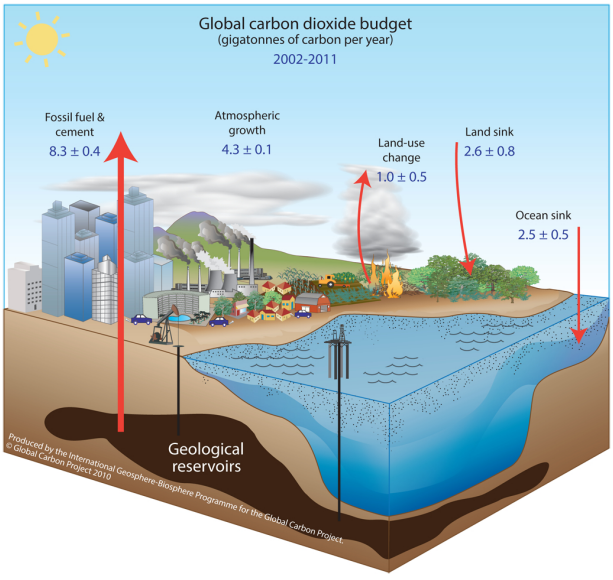

Fig. 1. Schematic representation of the overall perturbation of the global carbon cycle caused by anthropogenic activities, averaged globally for the decade 2002–2011. The arrows represent emission from fossil fuel burning and cement production; emissions from deforestation and other land-use change; and the carbon sinks from the atmosphere to the ocean and land reservoirs. The annual growth of carbon dioxide in the atmosphere is also shown. All fluxes are in units of PgC yr^{-1}, with uncertainties reported as ±1 sigma (68 % confidence that the real value lies within the given interval) as described in the text. This Figure is an update of one prepared by the International Geosphere Biosphere Programme for the GCP, first presented in Le Quéré (2009).

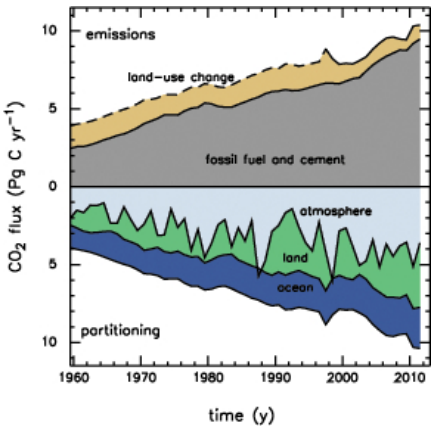

Fig. 2. Combined components of the global carbon budget illustrated in Fig. 1 as a function of time, for (top) emissions from fossil fuel combustion and cement production (E_{FF}; grey) and emissions from land-use change (E_{LUC}; brown), and (bottom) their partitioning among the atmosphere (G_{ATM}; light blue), land (S_{LAND}; green) and oceans (S_{OCEAN}; dark blue). All time-series are in PgC yr^{-1}. Land-use change emissions include management-climate interactions from year 1997 onwards, where the line changes from dashed to full.

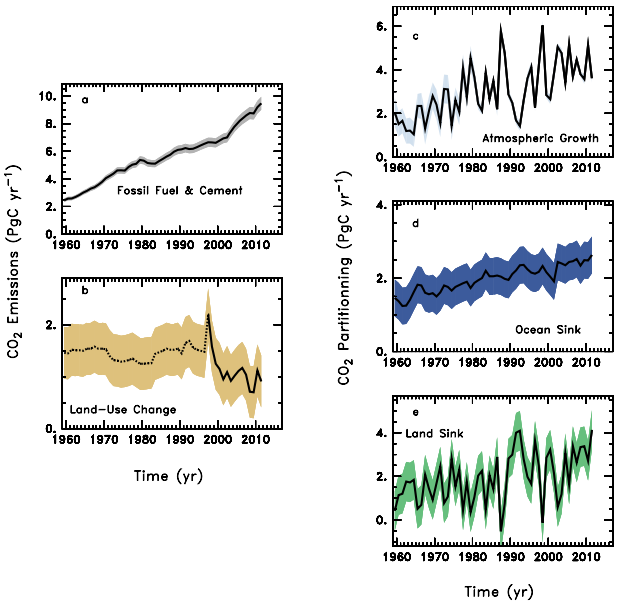

Fig. 3. Components of the global carbon budget and their uncertainties as a function of time, presented individually for **(a)** emissions from fossil fuel combustion and cement production (E_{FF}), **(b)** emissions from land-use change (E_{LUC}) with management-climate interactions based on fire activities in deforested areas (full line) or not (dashed line), **(c)** atmospheric CO_2 growth rate (G_{ATM}), **(d)** the ocean CO_2 sink (S_{OCEAN}, positive indicates a flux from the atmosphere to the ocean), and **(e)** the land CO_2 sink (S_{LAND}, positive indicates a flux from the atmosphere to the land). All time-series are in PgC yr^{-1} with the uncertainty bounds in shaded colour.

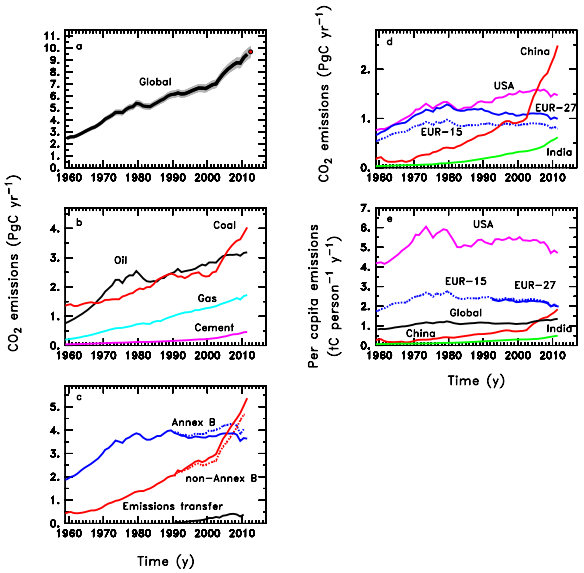

Fig. 4. CO_2 emissions from fossil fuel combustion and cement production for **(a)** the globe, including an uncertainty of ±5% (grey shading) and the emissions projection for year 2012 based on GDP projection (red dot), **(b)** global emissions by fuel type, including coal (red), oil (black), gas (light blue), and cement (purple), and excluding gas flaring which is small (0.7% in 2011), **(c)** territorial (full line) and consumption (dashed line) emissions for the countries listed in the Annex B of the Kyoto Protocol (blue lines; mostly advanced economies with emissions limitations) versus non-Annex B countries (red lines), also shown are the emissions transfer from non-Annex B to Annex B countries (black line) **(d)** territorial CO_2 emissions for the top three country emitters (USA – purple; China – red; India – green) and for the European Union (EU; full blue for the 27 states members of the EU in 2011; dash blue for the 15 states members of the EU in 1997 when the Kyoto Protocol was signed), and **(e)** per-capita emissions for the top three country emitters and the EU (all colours as in panel **d**). All time-series are in PgC yr^{-1} except the per-capita emissions (panel **e**), which are in tonnes of carbon per person per year.

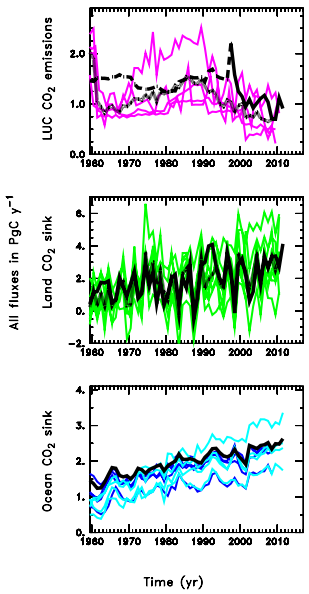

Fig. 5. Comparison of (top panel) CO_2 emissions from land-use change (LUC), (middle panel) land CO_2 sink (S_{LAND}), and (bottom panel) ocean CO_2 sink (S_{OCEAN}) between the CO_2 budget values estimated here (black line), and those estimated from process models (Table 3; coloured lines). The thin dotted black lines in the top and middle panels are the model averages. The LUC emissions from the CO_2 budget estimate is dashed before year 1997 to highlight the start of the satellite data from that year, as used to quantify the interannual variability from management-climate interactions based on fire activities in deforested areas. For the ocean CO_2 sink, the four models used in Le Quéré et al. (2009) are shown in dark blue, while the updated and models used to calculate interannual variability after 2008 are shown in pale blue.

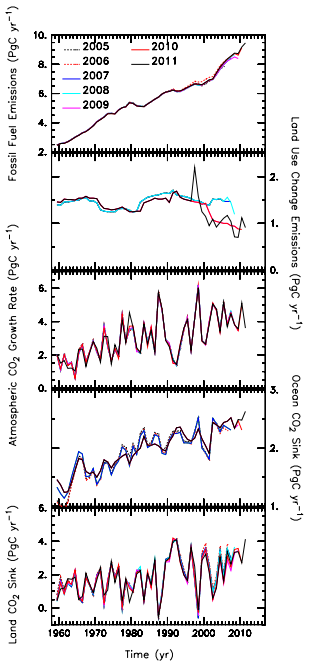

Fig. 6. Comparison of global carbon budget components released annually by GCP since 2005. CO_2 emissions from both **(a)** fossil fuel combustion and cement production, and **(b)** land-use change, and their partitioning among **(c)** the atmosphere, **(d)** the ocean, and **(e)** the land. The different curves were published in (dashed black) Raupach et al. (2007), (dashed red) Canadell et al. (2007), (dark blue) online only, (light blue) Le Quéré et al. (2009), (pink) Friedlingstein et al. (2010), (red) Peters et al. (2012b), and (black) this study. All values are in PgC yr^{-1}.

1157

Available online at www.sciencedirect.com
ScienceDirect
Current Opinion in Environmental Sustainability

Carbon–climate feedbacks: a review of model and observation based estimates

P Friedlingstein[1,2,3] and IC Prentice[2,4,5]

A growing number of studies investigated the feedback between the carbon cycle and the climate system. Modeling studies evolved from analysis based on simple land or ocean carbon cycle models to comprehensive Earth System Models accounting for state-of-the-art climate models coupled to land and ocean biogeochemical models. So far, there is a general agreement that climate change negatively affects the oceanic uptake of carbon. On land there was a similar agreement until recently where new studies showed that warming could reduce nitrogen limitation to growth, reducing the amplitude, or even changing the sign of, the land feedback. In parallel, alternative approaches used the observational record of atmospheric CO_2 and temperature, on time scales ranging from interannual to millennial, to estimate the climate–carbon cycle feedback. These studies confirmed that at the global scale, warming leads to a release of CO_2 from the land/ocean system to the atmosphere. Whether these observations can strongly constrain the magnitude of the feedback under future climate change is still under investigation.

Addresses
[1] IPSL/LSCE, CE-Saclay, Gif-sur-Yvette F-91191, France
[2] QUEST, University of Bristol, Bristol BS8 1RJ, UK
[3] University of Exeter, Exeter EX4 4QF, UK
[4] Department of Biological Sciences, Macquarie University, North Ryde, NSW 2109, Australia
[5] Grantham Institute of Climate Change, and Division of Biology, Department of Life, Sciences, Imperial College, Silwood Park, Ascot SL5 7BY, UK

Corresponding author: Friedlingstein, P (Pierre.Friedlingstein@bristol.ac.uk)

Current Opinion in Environmental Sustainability 2010, **2**:251–257

This review comes from a themed issue on Carbon and nitrogen cycles
Edited by Josep G Canadell

Received 1 February 2010; Accepted 1 June 2010
Available online 3rd July 2010

1877-3435/$ – see front matter
Crown Copyright © 2010 Published by Elsevier B.V. All rights reserved.

DOI 10.1016/j.cosust.2010.06.002

Introduction

The atmospheric content of long-lived greenhouse gases (GHG) represents the balance between anthropogenic emissions and natural sources and sinks. In the absence of anthropogenic emissions, sources and sinks are approximately balanced over multi-decadal time scales; atmospheric concentrations would therefore remain relatively constant over these time scales. But human-induced emissions of carbon dioxide (CO_2), methane (CH_4) and nitrous oxide (N_2O) have increased substantially, and at an accelerating rate, over the 2–3 centuries since the Industrial Revolution. The resulting increase in GHG concentrations has been the principal driver of the observed increase in global mean temperature especially since the 1970s, when the anthropogenic signal began to emerge from the 'noise' associated with natural variations in volcanic aerosol emissions and solar output, changes in anthropogenic aerosol emissions, and natural modes of variability in climate [1••].

For CO_2, it has long been recognized that the change in atmospheric concentration has induced a change in the natural sink strengths (e.g. [2–4]). On the decadal average, about 55% of anthropogenic CO_2 emissions are being absorbed by the land and ocean; only about 45% remains in the atmosphere [5••]. Note that there is a non-negligible (about 10%) uncertainty in these numbers as both emissions arising from fossil fuel burning and deforestation activities are associated with significant uncertainty (respectively about 6% and 46%). Increasing atmospheric CO_2 concentration sets up a concentration gradient across the air–sea interface that leads to a net uptake of CO_2 into the surface ocean, which progressively mixes to deeper layers. Land plant photosynthesis is stimulated by increasing atmospheric CO_2 [6], a fact that (combined with the 20–30 year residence time of land carbon pools) provides a plausible, quantitative explanation for the continuing net uptake of CO_2 into vegetation and soils. The stimulation of photosynthesis is increased in semi-arid regions because of an additional physiological effect by which increasing CO_2 tends to reduce stomatal conductance and thus lead to reduced water loss per unit leaf area [7]. The land and ocean together thus exert a major negative feedback on the carbon cycle. In the absence of such feedback, present day CO_2 concentration would already be around 500 ppm.

Climate–carbon cycle interaction

All of the above has been known for decades, and has served as the basis for calculations of historical and future concentrations of CO_2 to be used for climate projections (e.g. for the IPCC Second and Third Assessment Reports). CO_2 concentration was estimated from anthropogenic emissions and natural sinks that were assumed to be determined only by the time course of CO_2 emissions. However, at the time of the Third Assessment Report (TAR), there was already modeling evidence suggesting

Figure 1

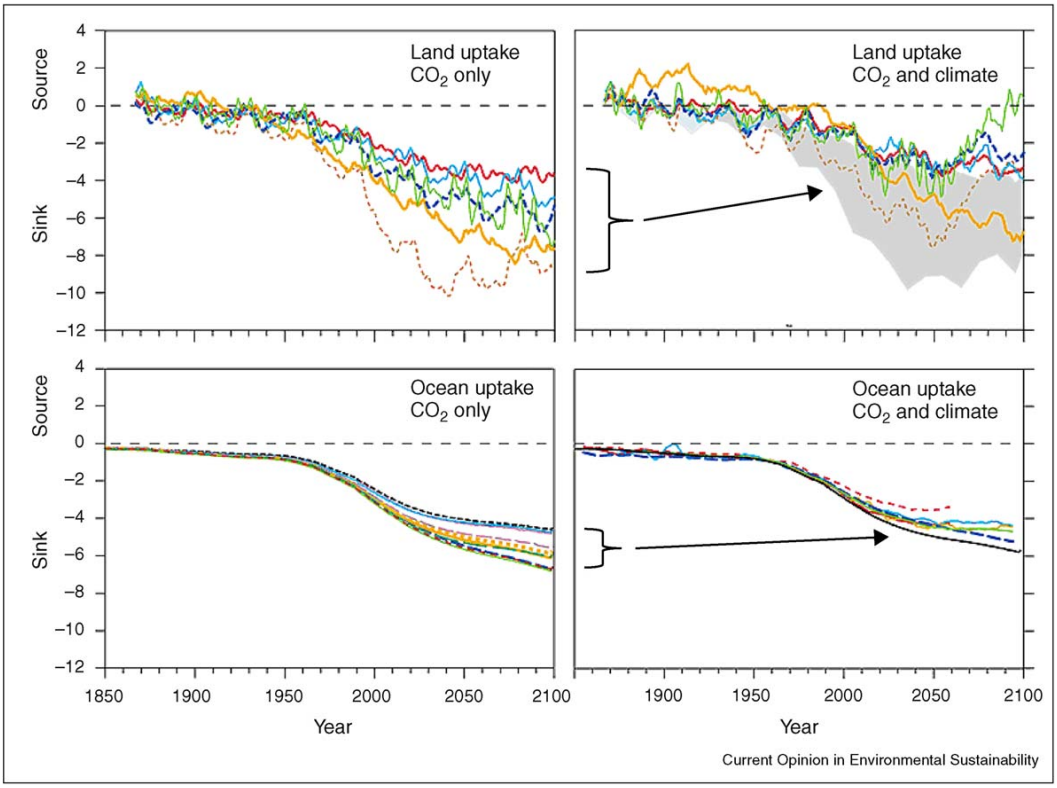

Land and ocean carbon sources/sinks as simulated by state-of-the-art models at the time of the IPCC Third Assessment Report. Panels **(a)** and **(b)** on the left side are respectively for land and ocean models driven by atmospheric CO_2 only, while panels **(c)** and **(d)** on the right side are for the same models but driven by atmospheric CO_2 and the associated climate change. Units are PgC/yr.

that this assumption was simplistic as it was missing a key player: the feedback of climate change on the land and ocean sinks. In the IPCC Third Assessment Report, [8••] assessed the existing knowledge of land and ocean carbon cycle responses to change in climate. In a landmark figure (Figure 3.10, reproduced here in Figure 1), it was shown that in state-of-the-art models of the time both land and ocean carbon uptake were reduced when the effect of climate change was accounted for. In other words, there was unequivocal model evidence for a positive climate–carbon cycle feedback: GHG-induced warming leading to reduced CO_2 uptake, which would then increase the rate of accumulation of CO_2 This chapter also calculated atmospheric concentration for several emission scenarios with reduced-form models (ISAM and Bern-CC) that accounted for climate–carbon cycle interactions in a way quantitatively consistent with state-of-the-art land and ocean carbon cycle models. For reasons of timing, the climate projections of the TAR did not use these simulated concentrations, but used previous estimates from simpler 'carbon cycle only' models.

Around the same time, two studies in which land and ocean carbon cycle modules were fully coupled into climate models had confirmed the indication of a positive climate–carbon cycle feedback [9•,10•]. The Hadley Centre study found a remarkable increase of 200 ppm in 2100 (i.e. an additional 200 ppm CO_2 remained in the atmosphere at 2100, compared to a simulation without climate–carbon cycle feedback) in a 'business as usual' emissions scenario. The IPSL study initially estimated the gain of the climate–carbon cycle feedback from off-line land and ocean carbon cycle calculations [11]. Although the two studies agreed upon the sign of the perturbation (a positive feedback), the climate–carbon cycle feedback gain in the IPSL study was only a third of that shown in the Hadley Centre study.

These new findings, and the large uncertainty they implied, stimulated a worldwide proliferation of coupled climate–carbon cycle model development. Five years on, 11 models could perform coupled climate–carbon cycle simulations analogous to those pioneered by the Hadley Centre and IPSL. The Coupled Climate–Carbon Cycle

Model Intercomparison Project (C^4MIP), engaging all 11 models, confirmed the original finding of a positive feedback, but did nothing to reduce the uncertainty in its magnitude [12••]. In these models both land and ocean showed a reduced uptake under a warming climate, both contributing to the positive feedback. The main processes leading to this reduced uptake are common to the models. Increased stratification of the surface ocean (due to warming at the sea surface) reduces the export of carbon from the surface to the deep ocean, and hence limits the air–sea exchange of CO_2. Declining productivity in tropical forests and a more general increase of the rate of soil carbon decomposition contribute to a partial offsetting of the CO_2 fertilization effect; however, responses of temperate ecosystems are highly variable among models.

The IPCC Fourth Assessment Report (AR4) included a chapter devoted to the coupling between changes in the climate system and biogeochemistry [13] and a section dealing with climate–carbon cycle feedbacks in climate projections [14]. The AR4 climate projection uncertainties for a given scenario (SRES) accounted for the climate–carbon cycle feedback. This is the main reason why the AR4 global warming estimates for 2100 exceed those of the TAR [1]. For the IPCC Fifth Assessment Report most climate modeling groups will use Earth System Models that at least account for climate–carbon cycle interactions. Using the new Representative Concentration Pathways (RCP), the models will estimate climate change and anthropogenic CO_2 emissions compatible with these scenarios [15].

Introducing carbon–nitrogen cycle coupling

A deficiency of the land and ocean carbon cycle models presented in the TAR, C^4MIP and AR4 is their lack of consideration of ways in which the global nitrogen cycle interacts with the carbon cycle and can thereby modify both CO_2 fertilization and climate–carbon cycle feedback. Nitrogen (in reactive forms such as ammonia, nitrogen oxides, NO_x, and nitrate) is the principal limiting nutrient in many land and ocean ecosystems [16] and strongly limits growth in high-latitude and temperate forests. Anthropogenic deposition of reactive N has relieved this limitation in the most populous and industrialized regions [17••]. Over the past couple of years, several modeling groups have improved the terrestrial components of Earth System models by including an explicit, prognostic nitrogen cycle [18–24]. From work in this area to date, accounting for nitrogen limitation on land appears to have two main implications for the global-scale analysis of feedbacks. First, in regions where N is limiting to plant growth, the CO_2 fertilization effect is restricted (compared to a reference case with no active nitrogen cycle), hence reducing the magnitude of the negative feedback due to CO_2 fertilization in the models. This effect is generic to all of these 'second generation' climate carbon/nitrogen cycle models [18–20,22,23]. Second, the effect of warming on soil organic matter decomposition has two aspects: soil carbon is released from soil more quickly as CO_2 (a positive feedback as before), but this process also accelerates soil nitrogen mineralization (the conversion of N from organic to inorganic forms in the soil solution) and hence the amount of nitrogen available for plant growth in N-limited ecosystems, thus imposing an additional negative feedback. Again, this effect is generic to all of the above-mentioned C–N models. These results are broadly consistent with the response observed in soil warming manipulative experiments [25].

The introduction of C–N interactions in coupled models has then a direct effect on the estimate of the climate–carbon cycle feedbacks. Interestingly, although it tends to reduce that feedback, it also tends to increase the growth rate of atmospheric CO_2 (as CO_2 fertilization is reduced). Indeed, all these new models agree that accounting for nitrogen does reduce the land response to CO_2 increase (reduction of the negative carbon–CO_2 feedback), leaving a larger fraction of the anthropogenic emissions in the atmosphere. However, for some [19,20] the climate induced release of nitrogen and its effect on productivity is so large that the overall sign of the climate–carbon cycle feedback is close to zero of even negative, that is, the growth enhancing effect of increased soil N mineralization outweighs both the effect of increased CO_2 loss from soil and the (rather small) effect of reduced carbon uptake in the oceans. Other models suggest little overall change in the land carbon sink because of compensation between a reduced response to CO_2 and an enhanced soil decomposition response to warming [22] or even a decrease in the land carbon sink, the simulated fertilization reduction being much larger than the N-induced growth enhancement [23].

In contrast to the C^4MIP models where most of the disagreement comes from the mid-latitudes, here the disagreement among models comes principally from the tropics. All these new models agree that the mid-latitudes will continue to be N-limited in the future and that warming will alleviate some of that limitation. For the tropics, two models show similar behavior [19,20] while two others [22,23] show little N limitation in the most productive tropical ecosystems. The two models simulating tropical N limitation argue that indeed productivity, while non-limited today, might be N or P limited in the future. We note that [20] does already simulate a strong GPP N-limitation by the end of the 20th century in contradiction with their hypothesis. [19] argues that for tropical lowland primary forest, phosphorous is the main limiting nutrient, but nitrogen is a useful proxy for phosphorous limitation (not represented in the model). As for the two models that do not simulate strong N limitation in the tropics, [22] only simulates the 20th

century. It is unclear how their model would behave in a warmer world. [23] argue that their findings are consistent with current observations but that does not necessarily imply that the future response is realistic. Clearly, more work to evaluate these models against available observations, including FACE CO_2 enriched and soil warming manipulative experiments that might help to infer the model response to future climate and atmospheric CO_2 conditions now seems to be an urgent priority. To our knowledge, so far only [26] performed such model evaluation with very encouraging results. Future modeling will also need to consider interactions of the carbon, nitrogen and phosphorus cycles, as this latter is the major limiting nutrient in many tropical and subtropical ecosystems.

None of the climate carbon or climate carbon–nitrogen models presented here have a realistic representation of land use and land cover changes (LULCC). LULCC was only treated as an external CO_2 emission source, as are fossil fuel emissions, affecting the climate system only via change in atmospheric CO_2 concentration. The real world is obviously more complex; with land cover changes having a direct impact on climate via biophysical effects. The sign and magnitude of this effect is regional, amplifying or reducing the LULCC impact on climate through atmospheric CO_2 [27]. Several land surface models are now accounting for human-driven land cover changes [27–29], which allow for quantification of the biophysical effect of LULCC in several climate models [30] and more recently in climate–carbon cycle models [31].

Constraints from observations

An alternative approach to assessing the realism of modeled climate–carbon cycle feedbacks involves the examination of independent global observations of CO_2 and climate. On several timescales, the CO_2 response to climate anomalies can provide constraints on the magnitude of the global carbon cycle sensitivity to climate (represented by γ in [12]). The year-to-year variation in atmospheric CO_2 growth rate is strongly correlated with climate variability. In particular, El Niño years are associated with higher than average CO_2 growth rates.

Figure 2

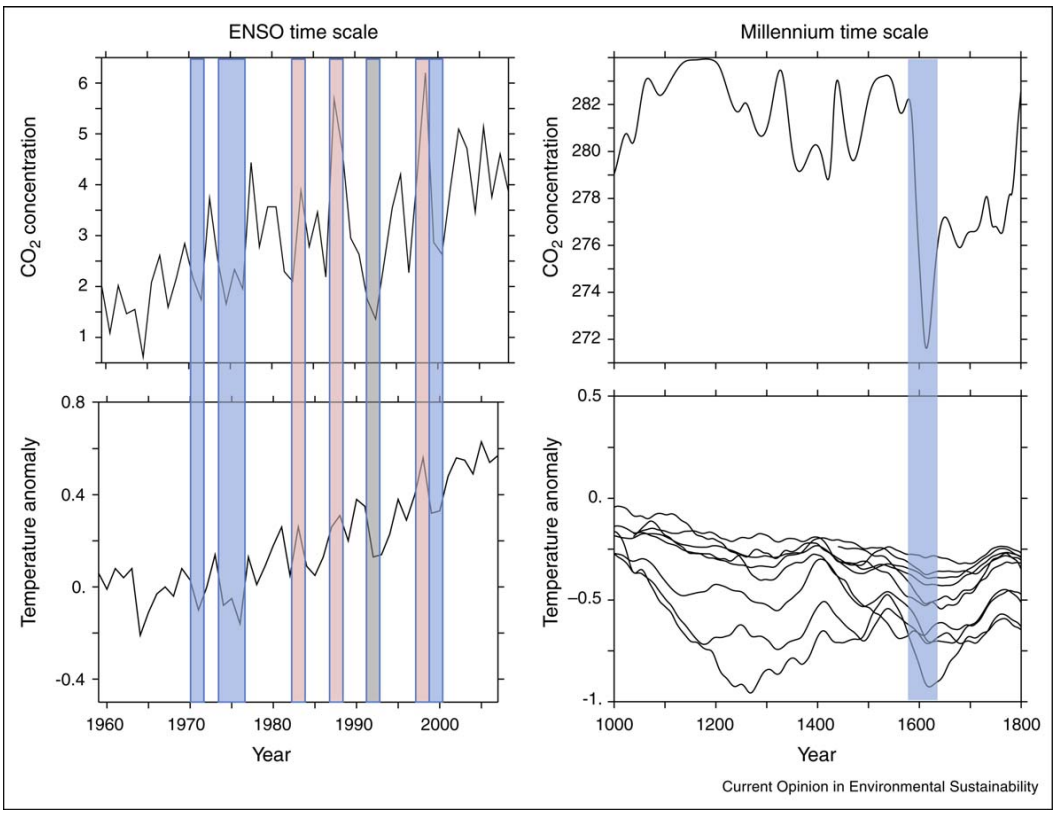

CO_2 and global temperature variability on interannual and millennium time scales. Panels **(a)** and **(b)** on the left side are respectively annual atmospheric CO_2 growth rate (ppm/yr) at Mauna Loa (Hawaii) and global temperature anomalies (°C). Blue and red stripes indicate El Nino and La Nina years respectively, while the grey stripe Panels **(c)** and **(d)** on the right side are respectively CO_2 concentrations from ice core (ppm) over the past millennium and several reconstruction of Northern Hemisphere temperature anomalies (°C) from different proxies. The blue stripe indicates the timing of the Little Ice Age.

[32•] first reported this, although he wrongly attributed the observed CO_2 growth rate anomalies to changes in the ocean carbon cycle. Many more recent studies have analyzed CO_2 variability on El Niño-Southern Oscillation (ENSO) time scales either using carbon cycle models or top-down methods such as deconvolution or inversion of atmospheric CO_2 and $^{13}CO_2$ data [33–36]. All evidence now points to a major terrestrial carbon source during El Niño events, with the global ocean showing a slightly enhanced sink.

Interannual variations in the CO_2 growth rate have been used to constrain global climate–carbon cycle models [37] and to estimate γ, the carbon cycle sensitivity to climate [38]. Tropical lands are anomalous sources of CO_2 during El Niño events, implying a positive γ at these time scales (Figure 2a and b). This observation provides a constraint on the tropical ecosystem response to climate anomalies. As the new carbon nitrogen models diverge in their tropical response to future warming, the ENSO sensitivity could be a discriminating test. So far, Zaehle is the only one of the new C–N land models who showed evidences that his model does perform well on ENSO timescale (see [26], Figure 4).

Short-lived climatic events such as the global cooling following the eruption of Mount Pinatubo are also associated with atmospheric CO_2 growth rate anomalies [34] (Figure 2a and b). Again, the observation indicates a positive γ, as the cold anomaly leads to an increased sink, generally attributed to the Northern Hemisphere ecosystems [39,40]. The degree to which these findings can inform analysis of future climate–carbon cycle feedback is unclear, however, as the processes in play might be different.

On centennial time scales, there are several potential approaches. The 20th century signal of CO_2 and climate is hard to use, as the CO_2 increase has been essentially driven by anthropogenic emissions and not by the response of the natural carbon cycle to climate change. Uncertainties in emissions (mainly not only those from land use, but also to some extent those from fossil fuel combustion), lack of full understanding of the mechanisms driving the land sinks, and natural decadal variability still make it challenging to isolate the climate impact on natural sinks (e.g. by examining the time course of the 'airborne fraction' of anthropogenic CO_2, which has remained stubbornly constant over decades). Remaining uncertainties still prevent unequivocal statistical detection of a trend in the efficiency of natural carbon sinks and attribution of such a trend to the climate change of the 20th century [5,41]. Nevertheless, within the data uncertainties, coupled climate–carbon and now nitrogen cycle models do generally produce a realistic magnitude of CO_2 uptake by the land and ocean. However, when compared to their carbon-only parent models, the carbon-nitrogen models generally simulate a reduced CO_2 fertilization driven sink. However, they also represent the additional land carbon sink driven by atmospheric nitrogen deposition, which does compensate for the reduced CO_2 fertilization. The historical observations of atmospheric CO_2 are incapable of disentangling these two effects. Also, it should be noted that none of these models properly account for ecosystem disturbances and land management (e.g. as in [29]).

The use of ice-core archives allows us to examine other periods further back in the past, albeit at the cost of reduced temporal resolution. CO_2 and climate variability over the past millennium are relatively well documented, in particular the low CO_2 and temperature excursion associated with the Little Ice Age (Figure 2c and d). The main problems with using the data are first the multiple sources (different proxies for temperature and different sets of ice-core measurements for atmospheric CO_2), and second the necessary choices made as to the treatment of the data (analysis period, smoothing, age calibration, consideration of time lags, and handling of uncertainties). Several studies have nevertheless used the past millennium record to derive γ [42,43]. The most comprehensive study to date is that of [44]. Combining all known sources of uncertainties, they estimated a median value of $\gamma = 7.7$ ppm/°C. They concluded that their estimate is twice as likely to fall in the lowermost than in the uppermost quartile of the γ values characteristic of the various C^{4}MIP models.

Glacial/interglacial changes in atmospheric CO_2 and the concurrent changes in global temperature have also been used to derive the climate–carbon cycle feedback [45]. This time scale is of little help for constraining climate–carbon cycle feedbacks during the next century as the glacial/interglacial CO_2 rise is thought to be dominated by (still largely unexplained) changes in the ocean carbon cycle that may not be relevant to the contemporary world. The glacial–interglacial shift does however provide a semi-quantitative constraint on the CO_2 fertilization effect. The difference between full-glacial (~200 ppm) and full interglacial (~280 ppm) CO_2 concentrations is large enough to have caused major changes in the global distribution of vegetation types through physiological effects (on the productivity of trees, and stomatal conductance) as well as an increase in terrestrial carbon storage broadly consistent with the CO_2 fertilization effect as represented in land carbon models [46–48].

Conclusions

Several independent lines of evidence point toward a positive climate–carbon cycle feedback. At multiple time scales relevant for the anthropogenic perturbation, a warmer world leads to higher CO_2 concentration in the atmosphere. This is true for singular climate events such as the Pinatubo perturbation, on the ENSO time scale,

possibly on multi-decadal time scales, and on centennial time scales over the past millennium. In addition, most models simulate a positive climate–carbon cycle feedback. The exceptions combine a negative land climate–carbon cycle feedback with a weak positive ocean feedback. The best way to reduce the large model uncertainty is to test how far the models can reproduce climate–carbon cycle variations on the time scales listed above, where robust observations can be used as a benchmark.

Acknowledgements

P. Friedlingstein was supported by CNRS while in sabbatical at University of Bristol within the NERC funded QUEST program. We wish to thank P. Cadule, P. Cox, J. Gregory, and S. Zaehle for useful discussions.

References and recommended reading

Papers of particular interest, published within the annual period of review, have been highlighted as:

- • of special interest
- •• of outstanding interest

1. •• IPCC: **Summary for policymakers**. In *Climate Change 2007: The Physical Science Basis. Contribution of Working Group I to the Fourth Assessment Report of the Intergovernmental Panel on Climate Change.* Edited by Solomon S, Qin D, Manning M, Chen Z, Marquis M, Averyt KB, Tignor M, Miller HL. Cambridge, United Kingdom and New York, NY, USA: Cambridge University Press; 2007.

The most comprehensive assessment on the science of climate change.

2. Bolin B, Eriksson E: **Changes in the carbon dioxide content in the atmosphere and sea due to fossil fuel combustion**. In *The Atmosphere and Sea in Motion.* Edited by Bolin B. New York: The Rockefeller Institute Press; 1959:130-142.

3. Siegenthaler U, Oeschger H: **Predicting future atmospheric carbon dioxide levels**. *Science* 1978, **199**:388-395.

4. Broecker WS, Takahashi T, Simpson HJ, Peng T-H: **Fate of fossil fuel carbon dioxide and the global carbon budget**. *Science* 1979, **206**:409-418.

5. •• Le Quéré C, Raupach MR, Canadell JG, Marland G, Bopp L, Ciais C, Conway TJ, Doney SC, Feely RA, Foster P *et al.*: **Trends in the sources and sinks of carbon dioxide**. *Nat Geosci* 2009, **2**:831-836 doi: 10.1038/ngeo689.

The most up to date estimate of the present-day global carbon budget.

6. Norby RJ, DeLucia EH, Gielen B, Calfapietra C, Giardina CP, King JS, Ledford J, McCarthy HR, Moore DJP, Ceulemans R *et al.*: **Forest response to elevated CO_2 is conserved across a broad range of productivity**. *Proc Natl Acad Sci USA* 2005, **102**:18052-18056.

7. Field CB: **Ecological scaling of carbon gain to stress and resource availability**. In *Response of Plants to Multiple Stresses.* Edited by Mooney HA, Winner WE, Pell EJ. San Diego, CA: Academic Press; 1991:35-65.

8. •• Prentice IC, Farquhar GD, Fasham MJR, Goulden ML, Heimann M, Jaramillo VJ, Kheshgi HS, Le Quéré C, Scholes RJ, Wallace DWR: **The carbon cycle and atmospheric carbon dioxide**. In *Climate Change 2001: The Scientific Basis. Contribution of Working Group I to the Third Assessment Report of the Intergovernmental Panel on Climate Change.* Edited by Houghton JT, Ding Y, Griggs DJ, Noguer M, van der Linden PJ, Dai X, Maskell K, Johnson CA. Cambridge, UK: Cambridge University Press; 2001:183-237.

Although it is not from the most recent IPCC assessment, it is still the most comprehensive 'textbook' on the global carbon cycle.

9. • Cox PM, Betts RA, Jones CD, Spall SA, Totterdell IJ: **Acceleration of global warming due to carbon-cycle feedbacks in a coupled climate model**. *Nature* 2000, **408**:184-187.

The first paper describing a climate–carbon cycle model simulation and revealing the positive feedback between climate change and terrestrial carbon.

10. • Dufresne J-L, Friedlingstein P, Berthelot M, Bopp L, Ciais P, Fairhead L, Le Treut H, Monfray P: **On the magnitude of positive feedback between future climate change and the carbon cycle**. *Geophys Res Lett* 2002, **29**: doi: 10.1029/2001GL013777.

As reference [9•], but with a different model, showing a much reduced feedback.

11. Friedlingstein P, Bopp L, Ciais P, Dufresne J-L, Fairhead L, LeTreut H, Monfray P, Orr J: **Positive feedback of the carbon cycle on future climate change**. *Geophys Res Lett* 2001, **28**:1543-1546.

12. •• Friedlingstein P, Cox P, Betts R, Bopp L, vonBloh W, Brovkin V, Cadule P, Doney S, Eby M, Fung I *et al.*: **Climate–carbon cycle feedback analysis, results from the C4MIP model intercomparison**. *J Clim* 2006, **19**:3337-3353.

The synthesis paper presenting the coupled climate–carbon cycle models intercomparison.

13. Denman KL, Brasseur G, Chidthaisong A, Ciais P, Cox PM, Dickinson RE, Hauglustaine D, Heinze C, Holland E, Jacob D *et al.*: **Couplings between changes in the climate system and biogeochemistry**. In *Climate Change 2007: The Physical Science Basis. Contribution of Working Group I to the Fourth Assessment Report of the Intergovernmental Panel on Climate Change.* Edited by Solomon S, Qin Q, Manning M, Chen Z, Marquis M, Averyt KB, Tignor M, Miller HL. Cambridge, United Kingdom and New York, NY, USA: Cambridge University Press; 2007.

14. Meehl GA, Stocker TF, Collins WD, Friedlingstein P, Gaye AT, Gregory JM, Kitoh A, Knutti R, Murphy JM, Noda A *et al.*: **Global climate projections**. In *Climate Change 2007: The Physical Science Basis. Contribution of Working Group I to the Fourth Assessment Report of the Intergovernmental Panel on Climate Change.* Edited by Solomon S, Qin D, Manning M, Chen Z, Marquis M, Averyt KB, Tignor M, Miller HL. Cambridge, United Kingdom and New York, NY, USA: Cambridge University Press; 2007.

15. Hibbard KA, Meehl GA, Cox PM, Friedlingstein P: **A strategy for climate change stabilization experiments**. *EOS* 2007, **88**:217-221.

16. Vitousek PM, Howarth RW: **Nitrogen limitation on land and in the sea: how can it occur?** *Biogeochemistry* 1991, **13**:87-115 doi: 10.1007/BF00002772.

17. •• Galloway JN, Dentener FJ, Capone DG, Boyer EW, Howarth RW, Seitzinger SP, Asner GP, Cleveland CC, Green PA, Holland EA *et al.*: **Nitrogen cycles: past, present and future**. *Biogeochemistry* 2004, **70**:153-226.

Extensive review on the global nitrogen cycle.

18. Thornton PE, Lamarque J-F, Rosenbloom NA, Mahowald NM: **Influence of carbon–nitrogen cycle coupling on land model response to CO_2 fertilization and climate variability**. *Global Biogeochem Cycles* 2007, **21**:GB4018 doi: 10.1029/2006GB002868.

19. Thornton PE, Doney SC, Lindsay K, Moore JK, Mahowald N, Randerson JT, Fung I, Lamarque J-F, Feddema JJ, Lee YL: **Carbon–nitrogen interactions regulate climate–carbon cycle feedbacks: results from an atmosphere-ocean general circulation model**. *Biogeosciences* 2009, **6**:2099-2120.

20. Sokolov AP, Kicklighter DW, Melillo JM, Felzer B, Schlosser CA, Cronin TW: **Consequences of considering carbon/nitrogen interactions on the feedbacks between climate and the terrestrial carbon cycle**. *J Clim* 2008, **21**:3776-3796 doi: 10.1175/2008JCLI2038.1.

21. Xu-Ri, Prentice IC: **Terrestrial nitrogen cycle simulation with a dynamic global vegetation model**. *Global Change Biol* 2008, **14(8)**:1745-1764 doi: 10.1111/j.1365-2486.2008.01625.x.

22. Jain A, Yang X, Kheshgi H, McGuire AD, Post W, Kicklighter D: **Nitrogen attenuation of terrestrial carbon cycle to global environmental factors**. *Global Biogeochem Cycles* 2009, **23**:GB4028 doi: 10.1029/2009GB003519.

23. Zaehle S, Friedlingstein P, Friend AD: **Terrestrial nitrogen feedbacks may accelerate future climate change**. *Geophys Res Lett* 2010, **37**:L01401 doi: 10.1029/2009GL041345.

24. Gerber SL, Hedin O, Oppenheimer M, Pacala SW, Shevliakova E: **Nitrogen cycling and feedbacks in a global dynamic land**

model. *Global Biogeochem Cycles* 2010, **24**:GB1001 doi: 10.1029/2008GB003336.

25. Melillo JM, Steudler PA, Aber JD, Newkirk K, Lux H, Bowles FP, Catricala C, Magill A, Ahrens T, Morrisseau S: **Soil warming and carbon-cycle feedbacks to the climate system**. *Science* 2002, **298**:2173-2176 doi: 10.1126/science.1074153.

26. Zaehle S, Friend AD, Dentener F, Friedlingstein P, Peylin P, Schulz M: **Carbon and nitrogen cycle dynamics in the O-CN land surface model: 2. The role of the nitrogen cycle in the historical terrestrial carbon balance**. *Global Biogeochem Cycles* 2010:GB1006 doi: 10.1029/2009GB003522.

27. Pongratz J, Reick CH, Raddatz T, Claussen M: **Effects of anthropogenic land cover change on the carbon cycle of the last millennium**. *Global Biogeochem Cycles* 2009, **23**:GB4001 doi: 10.1029/2009GB003488.

28. Piao SL, Friedlingstein P, Ciais P, Ducoudré N, Labat D, Zaehle S: **Climate and land use changes have a larger impact than rising CO_2 on global river runoff trends**. *Proc Natl Acad Sci USA* 2007, **104**:15242-15247.

29. Shevliakova E, Pacala SW, Malyshev S, Hurtt GC, Milly PCD, Caspersen JP, Sentman LT, Fisk JP, Wirth C, Crevoisier C: **Carbon cycling under 300 years of land use change: importance of the secondary vegetation sink**. *Global Biogeochem Cycles* 2009, **23**:GB2022 doi: 10.1029/2007GB003176.

30. Pitman AJ, deNoblet-Ducoudré N, Cruz FT, Davin EL, Bonan GB, Brovkin V, Claussen M, Delire C, Ganzeveld L, Gayler V *et al.*: **Uncertainties in climate responses to past land cover change: first results from the LUCID intercomparison study**. *Geophys Res Lett* 2009, **36**:L14814 doi: 10.1029/2009GL039076.

31. Pongratz J, Reick CH, Raddatz T, Claussen M: **Biogeophysical versus publications biogeochemical climate response to historical anthropogenic land cover change**. *Geophys Res Lett* 2010, **37**:L08702 doi: 10.1029/2010GL043010.

32. • Bacastow RB: **Modulation of atmospheric carbon cycle by the Southern Oscillation**. *Nature* 1976, **261**:116-118.
One of the very first paper on atmospheric CO_2 and ENSO variability.

33. Francey RJ, Tans PP, Allison CE, Entng IG, White JWC, Trolier M: **Change in terrestrial and oceanic uptake since 1982**. *Nature* 1995, **373**:326-330.

34. Keeling CD, Whorf T, Whalen M, der Plicht JV: **Interannual extremes in the rate of rise of atmospheric carbon dioxide since 1980**. *Nature* 1995, **375**:666-670.

35. Bousquet P, Peylin P, Ciais P, Le Quéré C, Friedlingstein P, Tans PP: **Regional changes in carbon dioxide fluxes of land and oceans since 1980**. *Science* 2000, **290**:1342-1346.

36. Jones CD, Collins M, Cox PM, Spall SA: **The carbon cycle response to ENSO: a coupled climate–carbon cycle model study**. *J Clim* 2001, **14**:4113-4129.

37. Cadule P, Friedlingstein P, Bopp L, Sitch S, Jones CD, Ciais P, Piao SL, Peylin P: **Benchmarking coupled climate–carbon models against long-term atmospheric CO_2 measurements**, *Global Biogeochem Cycles* 2010, doi:10.1029/2009GB003556, in press.

38. Cox P, Jones CD: **Illuminating the modern dance of climate and CO_2**. *Science* 2008, **321**:1642-1644.

39. Lucht W, Prentice IC, Myneni RB, Sitch S, Friedlingstein P, Cramer W, Bousquet P, Buermann W, Smith B: **Climatic control of the high-latitude vegetation greening trend and Pinatubo effect**. *Science* 2002, **296**:1687-1689.

40. Peylin P, Bousquet P, Le Quéré C, Sitch S, Friedlingstein P, McKinley G, Gruber N, Rayner P, Ciais P: **Multiple constraints on regional CO_2 flux variations over land and oceans**. *Global Biogeochem Cycles* 2005, **19**:GB1011 doi: 10.1029/2003GB002214.

41. Knorr W: **Is the airborne fraction of anthropogenic CO_2 emissions increasing?** *Geophys Res Lett* 2009, **36**:L21710 doi: 10.1029/2009GL040613.

42. Joos F, Prentice IC: **A paleo-perspective on changes in atmospheric CO_2 and climate**. In *The Global Carbon Cycle: Integrating Humans, Climate and the Natural World*. Edited by Field CB, Raupach MR. Washington, DC: Island Press; 2004:165-186.

43. Scheffer M, Brovkin V, Cox P: **Positive feedback between global warming and atmospheric CO_2 concentration inferred from past climate change**. *Geophys Res Lett* 2006, **33**:L10702 doi: 10.1029/2005GL025044.

44. Frank DC, Esper J, Raible CC, Buntgen U, Trouet V, Stocker B, Joos F: **Ensemble reconstruction constraints on the global carbon cycle sensitivity to climate**. *Nature* 2010, **463**:527-530.

45. Torn MS, Harte J: **Missing feedbacks, asymmetric uncertainties, and the underestimation of future warming**. *Geophys Res Lett* 2006, **33**:L10703 doi: 10.1029/2005GL025540.

46. Friedlingstein P, Prentice KC, Fung IY, John JG, Brasseur GP: **Climate–Vegetation–Carbon interactions in the LGM climate**. *J Geophys Res* 1995, **100**:7203-7221.

47. Harrison SP, Prentice IC: **Climate and CO_2 controls on global vegetation distribution at the last glacial maximum: analysis based on palaeovegetation data, biome modeling and palaeoclimate simulations**. *Global Change Biol* 2003, **9**:983-1004.

48. Prentice IC, Harrison SP: **Ecosystem effects of CO_2 concentration: evidence from past climates**. *Clim Past* 2009, **5**:297-307.

Hydrol. Earth Syst. Sci., 15, 967–981, 2011
www.hydrol-earth-syst-sci.net/15/967/2011/
doi:10.5194/hess-15-967-2011
© Author(s) 2011. CC Attribution 3.0 License.

Hydrology and Earth System Sciences

Magnitude and variability of land evaporation and its components at the global scale

D. G. Miralles[1], **R. A. M. De Jeu**[1], **J. H. Gash**[1], **T. R. H. Holmes**[1,2], **and A. J. Dolman**[1]

[1]Department of Hydrology, VU University, Amsterdam, The Netherlands
[2]Hydrology and Remote Sensing Lab, USDA-ARS, Beltsville, MD, USA

Received: 10 December 2010 – Published in Hydrol. Earth Syst. Sci. Discuss.: 3 January 2011
Revised: 11 March 2011 – Accepted: 14 March 2011 – Published: 17 March 2011

Abstract. A process-based methodology is applied to estimate land-surface evaporation from multi-satellite information. GLEAM (Global Land-surface Evaporation: the Amsterdam Methodology) combines a wide range of remotely-sensed observations to derive daily actual evaporation and its different components. Soil water stress conditions are defined from a root-zone profile of soil moisture and used to estimate transpiration based on a Priestley and Taylor equation. The methodology also derives evaporationfrom bare soil and snow sublimation. Tall vegetation rainfall interception is independently estimated by means of the Gash analytical model. Here, GLEAM is applied daily, at global scale and a quarter degree resolution. Triple collocation is used to calculate the error structure of the evaporation estimates and test the relative merits of two different precipitation inputs. The spatial distribution of evaporation – and its different components – is analysed to understand the relative importance of each component over different ecosystems. Annual land evaporation is estimated as 67.9×10^3 km^3, 80% corresponding to transpiration, 11% to interception loss, 7% to bare soil evaporation and 2% snow sublimation. Results show that rainfall interception plays an important role in the partition of precipitation into evaporation and water available for runoff at a continental scale. This study gives insights into the relative importance of precipitation and net radiation in driving evaporation, and how the seasonal influence of these controls varies over different regions. Precipitation is recognised as an important factor driving evaporation, not only in areas that have limited soil water availability, but also in areas of high rainfall interception and low available energy.

Correspondence to: D. G. Miralles
(diego.miralles@falw.vu.nl)

1 Introduction

Despite the importance of latent heat flux as the link between water, carbon and energy cycles, land-surface evaporation remains one of the most uncertain terms in the world's water balance (Dolman and de Jeu, 2010). Estimates of evaporation from land surface models and Global Circulation Models (GCMs) differ greatly both in their global numbers (see Dirmeyer et al., 2006; Lim and Roderick, 2009) and their spatial distribution (Jiménez et al., 2009). This creates the need for observation-based evaporation benchmark datasets to evaluate GCM performance (Blyth et al., 2009). Such datasets would help GCM developers to improve their evaporation schemes and consequently their model predictions of future climate.

Jung et al. (2009) presented an approach to upscale eddy-covariance measurements of latent heat flux and produce observation-based global fields of evaporation at monthly timescale. Complementary, satellite observations – able to measure the spatial and temporal variation in the main drivers of evaporation – also contribute a powerful alternative to fulfilling the need for accurate global estimates of evaporation. Such estimates have been derived from remote sensing information previously (Choudhury, 1998; Mu et al., 2007; Fisher et al., 2008; Zhang et al., 2010). These studies show that global methodologies require: (a) estimating evaporation at the appropriate temporal and spatial resolution, (b) specifically accounting for soil moisture and its coupling to plant transpiration, and (c) treating forest rainfall interception as an individual process (see Jiménez et al., 2011). Here we satisfy these requirements by using the approach described by Miralles et al. (2011) at a global scale. The methodology, named GLEAM (Global Land-surface Evaporation: the Amsterdam Methodology), is based on the Priestley and Taylor (PT) evaporation formula and the Gash analytical model

Published by Copernicus Publications on behalf of the European Geosciences Union.

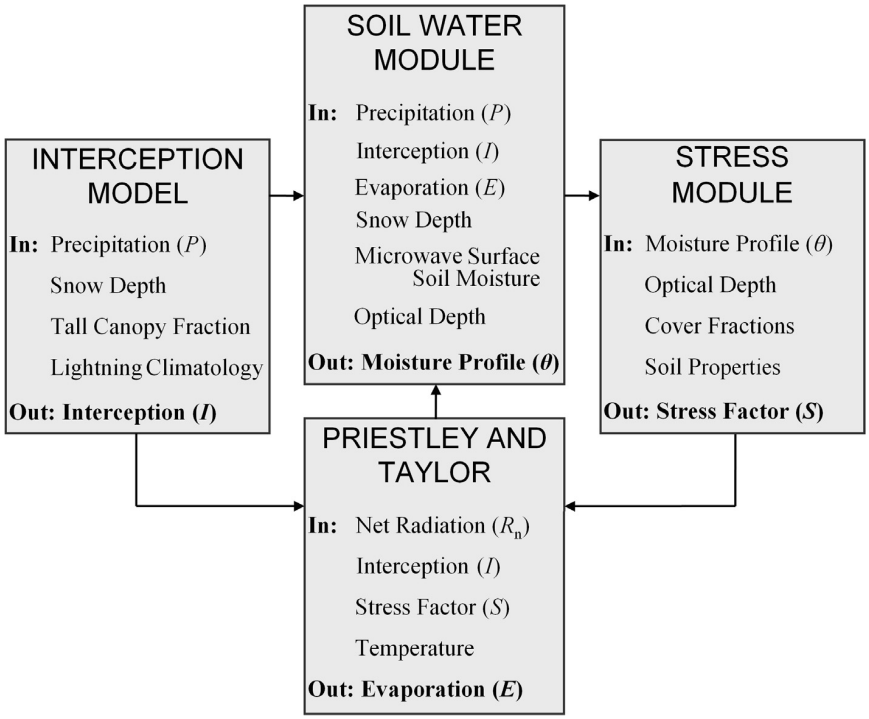

Fig. 1. Schematic overview of GLEAM (adapted from Miralles et al., 2011).

of forest rainfall interception (Gash, 1979; Valente et al., 1997).

GLEAM uses a broad range of independent remotely-sensed observations as a basis for estimating daily actual evaporation (and its different components) at a quarter-degree spatial resolution. The approach is based on the parameterization of physical processes and although it contains some empirical parameters these have been derived from the results of separate field studies. The evaporation product has been successfully validated at site level over different vegetation and climate conditions using in situ observations from 43 stations of the FLUXNET global network of micrometeorological flux measurements (see Miralles et al., 2011). The extensive use of observational data, the coupling between evaporation and soil moisture conditions and the separate estimation of rainfall interception allow application of the methodology in land-atmosphere feedback studies and tests of GCM performance.

Here, triple collocation (TC) is used to map the error of the evaporation estimates following the methodology in Miralles et al. (2010a). GLEAM is then applied at a watershed scale to validate the estimated long-term partitioning of incoming precipitation (P) into evaporation (E) and water available for runoff ($P-E$) using observations of river discharge from the Global Runoff Data Centre (GRDC). The methodology is finally applied at a global scale to study the global distribution of land evaporation and its different components. The role of rainfall interception and soil moisture on both the long-term partitioning of precipitation, and the seasonal distribution of the main drivers of evaporation (i.e. net radiation and precipitation), are analysed in detailed.

2 Methodology

2.1 GLEAM

The model is driven by a large set of remote sensing observations from different satellites (see Miralles et al., 2011, for a detailed description of the different input datasets and full details of the methodology). GLEAM produces daily estimates of land evaporation at a 0.25° spatial resolution. It is structured in four interconnected units (see Fig. 1): (a) the interception model, (b) the soil water module, (c) the stress module, and (d) the PT module. The scheme is independently formulated for three land surface types with specific physical characteristics: (a) land covered by tall canopies, (b) land covered by short vegetation, and (c) bare soil.

The interception model in GLEAM is based on the revised version of Gash's analytical model (Valente et al., 1997). It calculates daily fields of global tall canopy rainfall interception at 0.25° resolution (I) using remotely-sensed observations of precipitation (P) and forest cover. The interception

component of GLEAM is described in detail by Miralles et al. (2010b).

The soil water module consists of a multilayer bucket model driven by P and calculating soil moisture for different layers within the root-zone. Satellite-measured surface soil moisture is assimilated into the first layer of the profile by means of a Kalman filter. The Kalman filter is based on the uncertainty of soil moisture observations, which is calculated using satellite-derived vegetation optical depth (the higher the optical depth, the higher the uncertainty in surface soil moisture – see De Jeu et al., 2008). Optimised estimates of soil moisture (θ) are subsequently translated into estimates of evaporative stress represented by a factor (S), ranging from 0 (maximum stress) to 1 (no stress). PT estimates of potential evaporation are multiplied by S to estimate plant transpiration (in vegetated cover) and bare soil evaporation. The final estimate of actual evaporation for each pixel is the result of aggregating the fluxes from the three different land cover types (tall canopy interception loss, tall canopy transpiration, short vegetation transpiration, bare soil evaporation) weighted by the percentage of each cover type within the pixel. In pixels covered by ice and snow, E is independently calculated by adapting the PT equation to estimate sublimation as described by Murphy and Koop (2005).

2.2 Error analysis

A traditional way to estimate the uncertainty of model outputs is through error propagation studies. These studies account for the sensitivity of the output to uncertainties in the input data but do not give information on the quality of the model itself. Triple collocation (TC – Stoffelen, 1998; Scipal et al., 2008), however, allows the estimation of the entire error structure of the estimates of a model. This is done by simultaneously inter-comparing the product to two other datasets that observe the same physical phenomenon and present uncorrelated errors. Here, we are not only interested in the sensitivity of GLEAM estimates to errors in the set of inputs, but also in the uncertainties introduced by the parameterization of the physical processes within the methodology. Consequently, an error analyses based on TC has been undertaken to evaluate the evaporation product.

Requirements for the application of TC are: (a) the three datasets must refer to the same physical phenomenon, (b) the number of triplets has to be large (i.e. sufficient time steps in which the three datasets report an estimate), and (c) errors of the different datasets must be uncorrelated. If these three requisites are fulfilled the estimated errors of a single product are not sensitive to the choice of the two other datasets (see Dorigo et al., 2010).

In order to meet the requirement of uncorrelated errors the products need to be mutually independent. To perform the TC-based evaluation of GLEAM, two (a priori) independent global daily evaporation datasets were selected: (a) the Princeton University product (Sheffield et al., 2010), and (b) the Modern Era Retrospective-analysis for Research and Applications (MERRA) product. The Princeton University product is based on the application of a modified Penman-Monteith equation driven by a collection of satellite data. MERRA evaporation is a reanalysis product from NASA that uses the Goddard Earth Observing System Data Assimilation System (GEOS-5 DAS – Bosilovich, 2008).

The TC analysis presented here is limited to the spatial domain and the period (2003–2006) in which the three selected products overlap. Ideally, an infinite number of common observations is required in the application of TC to obtain unbiased results. However, statistical tests revealed that a minimum number of 100 triplets is sufficient to allow the application of the method (Scipal et al., 2008).

A disadvantage of TC is that it does not retrieve any information about biases. Consequently – and in order to ease the interpretation of the results – the analyses presented here are based on characterising the error of the anomalies of evaporation as calculated relative to a seasonally-varying climatology. Therefore the feature of GLEAM that is evaluated in this study is its skill in representing short-term changes in evaporation (e.g. after rainfall events), and how that skill changes from region to region. This error analysis follows closely the methodology presented in Miralles et al. (2010a) and Dorigo et al. (2010).

For each pixel, the three datasets are decomposed into climatology mean and anomaly components:

$$E_i = E_i' + \langle E \rangle_{D(i)}^{N}, \tag{1}$$

where $\langle E \rangle_{D(i)}^{N}$ is the climatological expectation for land-surface evaporation at the day-of-year (D) associated with time step i, and E_i' is the actual anomaly relative to this expectation. Values of $\langle E \rangle_{D(i)}^{N}$ are calculated using a moving window averaging of multi-year data with a window size of 31 days centered on D.

Subsequently, the time series of anomalies of the three products need to be scaled to the same dynamic range. This scaling is done by first selecting one of the datasets as the reference. Then the time series of the other two are normalised at every pixel to match the standard deviation of the time series of the reference one. To retrieve the errors within the dynamic range of GLEAM the dataset selected as reference must be GLEAM. Note that the choice of the reference dataset does not influence the relative magnitude of the errors of the three products at a given pixel.

TC assumes a linear relation between the three independent estimates of a physical variable and the hypothetical true value (Stoffelen, 1998). In our case the time series of anomalies of the three evaporation products (E_{G}' for GLEAM, E_{PU}' for the Princeton University product and E_{M}' for MERRA) can be expressed as a function of the hypothetical true evaporation anomalies (E_{TRUE}'):

$$E_{\mathrm{G}}' = E_{\mathrm{TRUE}}' + \epsilon_{\mathrm{G}}, \tag{2}$$

Table 1. GRDC stations used in the comparison of $P-E$ and observed annual river runoff (Q). Results correspond to the period 2003–2006.

River	Location of the station			Area (10^3 km^2)	Q (mm)	$P-E$ (mm)		E (mm)	
	Lat (deg)	Long (deg)	Country			CMORPH	GPCP	CMORPH	GPCP
Alabama	7.80	6.77	USA	55.6	581	661	654	884	892
Apalachicola	29.95	−85.02	USA	49.7	443	515	596	895	910
Arkansas	34.79	−92.36	USA	409.3	83	405	115	735	647
Columbia	46.18	−123.18	USA	665.4	284	104	209	467	463
Danube	45.22	28.72	Romania	807.0	296	286	455	438	457
Elbe	53.23	10.89	Germany	132.0	151	216	450	321	347
Fraser	49.38	−121.45	Canada	217.0	361	194	369	468	514
Glomma	59.61	11.12	Norway	40.5	501	646	646	296	295
Liard	61.75	−121.22	Canada	275.0	284	136	160	380	390
Mackenzie	67.46	−133.74	Canada	1660.0	177	83	97	329	344
Mississippi	37.22	−89.46	USA	1847.2	81	369	199	523	487
Missouri	38.71	−91.44	USA	1357.7	37	322	120	521	468
Nelson	56.40	−94.37	Canada	1060.0	105	136	156	386	414
Niger	7.80	6.77	Nigeria	1331.6	125	381	156	368	327
Ohio	38.28	−85.80	USA	236.1	570	486	622	634	649
Rhine	51.84	6.11	Netherlands	160.8	378	253	520	408	440
St. Lawrence	45.42	−73.62	Canada	959.1	265	212	478	492	546
Snake	46.10	−116.98	USA	240.8	107	90	70	454	377
Susquehanna	39.66	−76.18	USA	70.2	697	421	761	579	630
Tanana	64.57	−149.09	USA	66.3	346	251	251	314	314
Tennessee	35.23	−88.26	USA	85.8	822	820	670	793	791
Tombigbee	31.76	−88.13	USA	47.7	641	712	566	929	932
Wabash	38.40	−87.75	USA	74.2	424	628	691	555	559
Yukon	61.93	−162.88	USA	831.4	254	178	179	314	314

$$E'_{\mathrm{PU}} = E'_{\mathrm{TRUE}} + \epsilon_{\mathrm{PU}}, \quad (3)$$

$$E'_{\mathrm{M}} = E'_{\mathrm{TRUE}} + \epsilon_{\mathrm{M}}, \quad (4)$$

where ϵ_{G}, ϵ_{PU} and ϵ_{M} are the residual errors relative to E'_{TRUE}. Subtracting Eqs. (3) and (4) from Eq. (2) leads to

$$E'_{\mathrm{G}} - E'_{\mathrm{PU}} = \epsilon_{\mathrm{G}} - \epsilon_{\mathrm{PU}}, \quad (5)$$

$$E'_{\mathrm{G}} - E'_{\mathrm{M}} = \epsilon_{\mathrm{G}} - \epsilon_{\mathrm{M}}. \quad (6)$$

Multiplying Eqs. (5) and (6) and taking the average in time (indicated by "$\langle - \rangle$") leads to

$$\langle (E'_{\mathrm{G}} - E'_{\mathrm{PU}})\,(E'_{\mathrm{G}} - E'_{\mathrm{M}}) \rangle = \langle \epsilon_{\mathrm{G}}^2 \rangle - \langle \epsilon_{\mathrm{G}}\,\epsilon_{\mathrm{PU}} \rangle - \langle \epsilon_{\mathrm{G}}\,\epsilon_{\mathrm{M}} \rangle + \langle \epsilon_{\mathrm{PU}}\,\epsilon_{\mathrm{M}} \rangle. \quad (7)$$

If the errors of the three datasets are uncorrelated the residual covariances can be assumed to be zero. Therefore Eq. (7) can be expressed as

$$\langle (E'_{\mathrm{G}} - E'_{\mathrm{PU}})\,(E'_{\mathrm{G}} - E'_{\mathrm{M}}) \rangle = \langle \epsilon_{\mathrm{G}}^2 \rangle. \quad (8)$$

The root mean square error (RMSE) of the GLEAM-estimated evaporation anomalies will therefore be

$$\mathrm{RMSE}\,(E'_{\mathrm{G}},\, E'_{\mathrm{TRUE}}) = \sqrt{\langle (E'_{\mathrm{G}} - E'_{\mathrm{PU}})\,(E'_{\mathrm{G}} - E'_{\mathrm{M}}) \rangle}. \quad (9)$$

The results of this TC error analysis are presented in Sect. 4.1.

3 Validation using river discharge

This validation at basin-scale of GLEAM evaporation estimates uses river discharge measurements from the Global Runoff Data Centre (GRDC) in Koblenz, Germany. It is complementary to the validations of the independent modules described by Miralles et al. 2010b, 2011).

The study covers a period of 4 years (2003–2006). Cumulative GLEAM estimates of $P-E$ at 24 catchments are compared to observations of river runoff; the description of the river basins is presented in Table 1. Catchments were selected according to the availability of GRDC data during the complete study period and only rivers with an average annual discharge larger than 20 km^3 were considered for the study.

Estimates of P used in GLEAM (both in the interception model and the soil moisture module) are normally derived from the Climate Prediction Center morphing technique precipitation product (CMORPH – Joyce et al., 2004). This precipitation product is based only on satellite observations and has a high spatial resolution (0.07°). Previous studies have shown that CMORPH is in better agreement with in situ observations than the majority of existing precipitation products (e.g. Ebert et al., 2007). However CMORPH presents two practical disadvantages when applied in GLEAM: (a) its

spatial domain (60° N–60° S) does not cover the entire globe, and (b) precipitation is severely underestimated at higher latitudes during winter time (see Zeweldi and Gebremichael, 2009). Consequently, the 1° resolution Global Precipitation Climatology Project (GPCP-1DD) product (Huffman et al., 2001) is used in GLEAM outside the CMORPH domain and when the temperature drops below 0 °C.

Due to the obvious sensitivity of the $P-E$ estimates to uncertainties in P, this validation study is repeated using exclusively GPCP-1DD as P. Note that the choice of precipitation product implicitly affects the calculation of E in GLEAM. However, the sensitivity of $P-E$ estimates to P will be higher than the sensitivity of E estimates to P (this can also be noted in Table 1).

Figure 2 shows the results of the comparison between GLEAM catchment estimates of $P-E$ and river runoff measurements from the 24 rivers for the period 2003–2006. The figure shows the statistics of the correlation when the methodology is run with CMORPH ($R = 0.71$, bias = 20.4 mm yr^{-1}) and when it is run with GPCP-1DD ($R = 0.85$, bias = 46.5 mm yr^{-1}). The higher correlation coefficient found for the GPCP-based $P-E$ estimates can be explained by the high positive bias of the CMORPH-based $P-E$ estimates in the rivers of central United States (see Table 1). This is in agreement with the findings of Tian et al. (2007), who reported a clear overestimation of CMORPH rainfall during the warm season in this area. This hypothesis is further analysed in Sect. 4.1.

The correlation in Fig. 2 depends on the validity of three assumptions: (a) the entire volume of river water extracted for human use returns to the river, (b) the catchment is watertight, and (c) both the lag-time between a rainfall peak in the watershed and the discharge peak in the measuring station, and the long-term change in soil water storage, can be neglected by considering a relatively long (4 year) period. Moreover, as GLEAM is not a tuned or calibrated hydrological model, Fig. 2 should be interpreted with a consideration of the magnitude and different origins of the various uncertainties. Because river discharge estimates are usually derived from a stage-discharge rating curve, they include the errors in the measurements of river height and in the discharge data used to calibrate the rating curve, as well as the errors from the interpolation and extrapolation due to changes in river bed roughness, hysteresis effects, etc (see Di Baldassarre and Montanari, 2009). On top of those, the volumes of Q are also affected by the uncertainties in the estimation of the discharge-contributing area (given that the observations are presented in mm). On the vertical axes, the uncertainty in $P-E$ estimates will result from the uncertainty associated with the precipitation product and with GLEAM estimates of land evaporation. The later include the errors in the satellite data used to drive GLEAM (including therefore the uncertainties in P as well), the scaling of those to the desired 0.25° resolution, and the model structure itself (see Miralles et al., 2011).

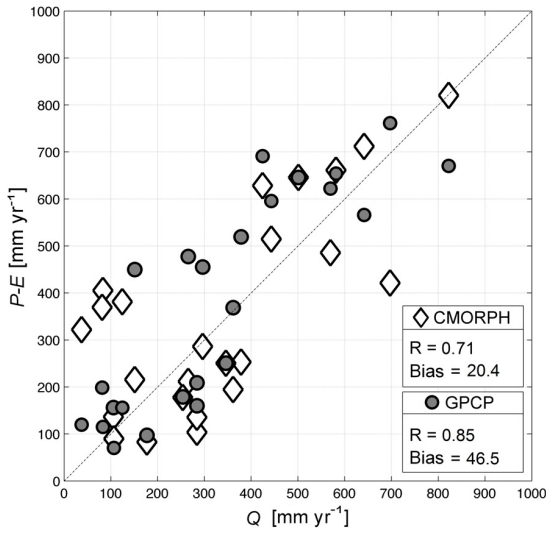

Fig. 2. GLEAM estimates of $P-E$ are compared to the runoff (Q) from 24 different catchments for the period 2003–2006. Correlation coefficients (R) and mean bias errors (bias) are listed for both the validation exercise using GPCP and the one using CMORPH (gap-filled with GPCP as explained in Sect. 3).

Despite all the possible sources of uncertainty a level of correlation remains as seen in Fig. 2. Furthermore, the $P-E$ estimates are of the right order of magnitude and overall lack a systematic bias relative to the one-to-one line. A global analysis of the spatial distribution of $P-E$ estimates is presented in Sect. 4.2; as in previous applications of GLEAM (i.e. Miralles et al., 2010b, 2011), the CMORPH-based P is chosen for the global run of the methodology. This choice is mainly justified by the better resolution of CMORPH compared to GPCP-1DD and the overall better performance of the methodology when CMORPH is applied as reported by the results of the error analyses in Sect. 4.1.

4 Results

4.1 Error analysis

Figure 3a presents the map of the absolute error of GLEAM evaporation anomalies as calculated through Eq. (9) – the RMSE is presented in units of mm day^{-1}. The Amazon delta presents the largest errors, probably because of the large volumes of open water and their negative effect on microwave observations. High absolute errors in the rest of Amazonia and south-eastern Asia partly respond to the larger variance of the anomalies in those regions.

The quality of the product seems to be generally higher in Europe than in North America. As mentioned in Sect. 3, the low performance of CMORPH over central United States has been reported in the past (see Tian et al., 2007). To test if

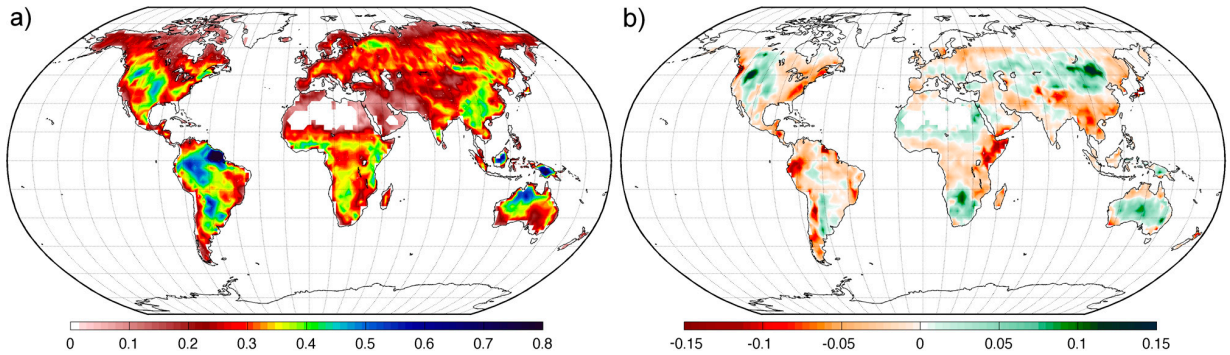

Fig. 3. Results of the triple collocation error analyses: **(a)** absolute error of the evaporation anomalies of GLEAM expressed as RMSE, **(b)** difference between the RMSE of the evaporation anomalies of GLEAM when it is run with CMORPH and when it is run with GPCP-1DD (red colour represents the areas where using CMORPH improves the evaporation product). Units are mm day^{-1}.

the high errors of GLEAM in the Great Plains respond to uncertainties in CMORPH, the analysis is repeated using only GPCP-1DD as input of the model. Figure 3b presents the difference between the absolute error of GLEAM E anomalies when the methodology is run with CMORPH and when it is run with GPCP-1DD only (in units of mm day^{-1}). It can be noted that applying GPCP-1DD improves the evaporation estimates not only over central North America but also around Mongolia, South Africa and the Australian desert. However, Fig. 3b also shows higher quality for the CMORPH-driven evaporation product in the majority (63%) of the domain common to both precipitation products (60° N–60° S). The improvement is significant over the east coast of North America, west coast of South America, Horn of Africa and China. Overall the application of CMORPH leads to better evaporation estimates in all the large regions with complex topography (except for the Rocky Mountains); this finding is in agreement with previous precipitation inter-product comparisons over complex terrains (e.g. Dinku et al., 2007; Hirpa et al., 2009). This type of information about the spatial distribution of GLEAM errors can be used to selectively pick the inputs that allow a better performance of the model over each region. Notice again that bias errors are not detected by a TC analyses.

The rationale of these three approaches is fundamentally different and the assumption of uncorrelated errors appears therefore justified. However, it may be argued that some degree of interdependence exists between the Princeton University product and GLEAM due to the relation between the inputs of net radiation in each of the two models. GLEAM uses the NASA/GEWEX Surface Radiation Budget (SRB) net radiation (Stackhouse et al., 2004); the Princeton University product is run with the International Satellite Cloud Climatology Project (ISCCP) net radiation (Zhang et al., 2004). Like ISCCP net radiation, SRB is also based on ISCCP cloud products. However, SRB net radiation uses different ancillary data sources and radiative transfer codes. Both datasets still present fundamental differences (Zhang et al., 2007; Lin et al., 2008). In addition, the level of agreement between the two is lower at daily timescales (see Troy and Wood, 2009); in this sense the extraction of the seasonally-varying climatology in this exercise will make their errors more uncorrelated. Moreover, if this source of dependency was large enough to preclude the TC application, areas in which evaporation estimates are highly dependent on net radiation (see Sect. 4.2.3 for the global distribution of those areas) would be likely to present lower values of TC-calculated RMSE; this pattern is not indicated by Fig. 3. Finally it is worth mentioning that this potential dependency would not affect the results presented in Fig. 3b.

4.2 Global application

The methodology has been applied globally for the period 2003–2007 using the satellite data products listed by Miralles et al. (2011) as driving data. Results are analysed in terms of the magnitude of evaporation and its separate components at a continental scale and the range of variation of the different fluxes over the Earth's ecosystems. Special emphasis is given to the role of interception loss in the long-term recycling of land precipitation and its repercussions on runoff generation. The daily time-resolution of the model allows a correspondingly high resolution analysis of the temporal correlations between evaporation and external factors limiting the flux; an analysis of the distribution and seasonality of these correlations is also presented. Results underline the importance of the accurate estimation of the flux of wet canopy evaporation and the coupling between soil moisture and transpiration if we are to understand the dynamics and trends of evaporation over the complete globe.

Table 2. Annual precipitation (P), evaporation (E) and water available for runoff ($P-E$) divided by continents for the period 2003–2007. The contribution of rainfall interception loss (I) to E is also presented.

Continent	P	E			$P-E$			I		
	mm	mm	10^3 km^3	$\%P$	mm	10^3 km^3	$\%P$	mm	10^3 km^3	$\%P$
Africa	930	545	16.2	59	385	11.4	41	38	1.1	4
Antarctica	199	21	0.3	11	177	2.5	89	0	0.0	0
Asia	648	388	16.8	60	260	11.3	40	38	1.7	6
Europe	638	369	3.5	58	269	2.6	42	54	0.5	9
N. America	665	413	9.5	62	252	5.8	38	42	1.0	6
Oceania	795	519	4.6	65	276	2.5	35	50	0.4	6
S. America	1712	967	17.0	56	745	13.1	44	144	2.5	8
Total	799	463	67.9	58	336	49.0	42	50	7.2	6

4.2.1 Overview of the global hydrological fluxes

For a certain region, and over a sufficiently long period to allow the net change of water storage in the soil to be neglected, the land-incoming precipitation is either recycled back into the atmosphere through evaporation, or it drains into the water bodies in the region. Figure 4 presents a graphic overview of the latitudinal partitioning of precipitation according to GLEAM. Average annual volumes of the different hydrological fluxes are illustrated for the period 2003–2007. All the fluxes are larger close to the Equator due to the higher average incoming radiation, temperature and specific humidity.

Table 2 shows the volumes of total precipitation (P), evaporation (E – which includes transpiration, soil evaporation, snow sublimation and interception loss) and water available for runoff ($P-E$) for each continent. The right-hand columns present the contribution of tall vegetation rainfall interception (I) to the long-term partitioning of P into E and $P-E$. The volume of annual global land-surface evaporation is estimated as 67.9×10^3 km^3. Tall vegetation interception amounts to 11% of the continental evaporation or 6% of the continental precipitation. Fluxes are larger in South America due to the faster dynamics of the hydrological cycle over Amazonia which results from the majority of South America's land mass being located within the ITCZ; this is more easily recognised when the fluxes are expressed per unit area.

To better understand the role of I in the partitioning of incoming precipitation over forested ecosystems, the land-use classification scheme of the International Geosphere-Biosphere Programme (IGBP) is used in Table 3 to present the same hydrological fluxes allocated to biome types. Given that I is calculated for the fraction of tall canopy within each pixel, it can still occur within pixels in which the dominant land use is not forest. Tropical forests contribute to 29% of the global land-surface evaporation and 57% of the global canopy interception loss. In these ecosystems, 20% of the evaporation corresponds to the flux of rainfall interception; this flux is equivalent to 22% of the water available for river discharge. At higher latitudes the relative contribution of interception loss to land-surface evaporation is also large. In temperate forests, the volume of I is on average 13% of the incoming precipitation (19% of evaporation).

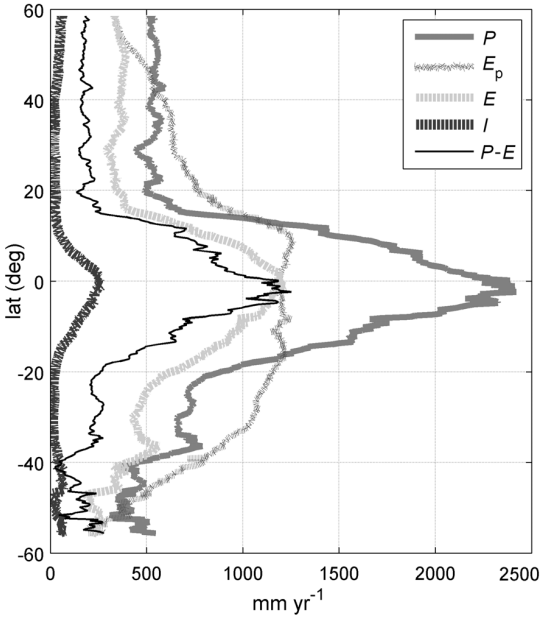

Fig. 4. Magnitude of the different hydrological fluxes as average along the latitudinal bands (modified from Fisher et al., 2008). The results correspond to the application of GLEAM for the period 2003–2007. E_p refers to potential evaporation.

4.2.2 Spatial distribution of evaporation and its different components

The ability of GLEAM to estimate the components of the evaporative flux in a separate manner is exploited to show the relative importance of each component over different

Table 3. Annual precipitation (P), evaporation (E), water available for runoff ($P-E$) and rainfall interception loss (I) per biome type for 2003–2007.

Biome	P	E			$P-E$			I		
	mm	mm	10^3 km^3	$\%P$	mm	10^3 km^3	$\%P$	mm	10^3 km^3	$\%P$
Tropical forest	2250	1182	19.6	53	1068	17.7	47	232	3.8	10
Temperate forest	718	512	4.7	71	207	1.9	29	95	0.9	13
Boreal forest	594	372	2.9	63	222	1.7	37	79	0.6	13
Shrubland	502	315	8.2	63	187	4.9	37	9	0.2	2
Savanna	1339	806	14.7	60	533	9.7	40	51	0.9	4
Grassland	689	462	4.2	67	227	2.1	33	15	0.1	2
Cropland	878	542	10.7	62	336	6.6	38	31	0.6	4
Permanent snow	225	27	0.4	12	198	3.3	88	0	0.0	0
Desert	167	112	2.6	67	54	1.2	33	0	0.0	0
TOTAL	799	463	67.9	58	336	49.0	42	50	7.2	6

ecosystems. The global distribution of the average annual evaporation during the period 2003–2007 is presented in Fig. 5. The spatial distribution and latitudinal profile for the different components of evaporation is also shown (both in mm yr^{-1} and in km^3 yr^{-1}). Transpiration contributes to the majority of global land evaporation. It is the largest in the humid tropics due to the sufficient availability of soil moisture during the entire year and the dependency of transpiration on the incoming radiation. Overall, the contribution of canopy interception to the global volume of evaporation is larger than the contribution from bare soil evaporation and snow sublimation. Evaporation from bare soil is important in desert regions even though it only happens during (and shortly after) the sporadic rainfall events. Peaks of snow sublimation occur in the Himalayas where annual net radiation is higher than in other permanent snow-covered areas due to its location closer to the Equator.

Figure 6 illustrates the contribution to global land-surface evaporation from: (a) each continent, and (b) each biome type. It also shows the relative magnitude of the four constituents of the evaporative flux. As seen in Tables 2 and 3, the continent evaporating the largest volume of water is South America (25%), followed by Asia (24.5%) and Africa (23.5%). 29% of world's evaporation occurs in tropical forests and 21% in savannas. The contribution from transpiration amounts to 80% of the total evaporative flux from land; 11% is interception loss, 7% bare soil evaporation and 2% to snow sublimation.

The seasonal distribution of the main inputs and outputs of the methodology is explored in Fig. 7. Global maps of R_n, P, E, I and $P-E$ for 2003–2007 are presented as an average for two different periods: the months of June, July and August (JJA), and December, January and February (DJF). The global distributions of both I and $P-E$ are dominated by the seasonal cycle of P. The observed patterns also indicate the lower importance of seasonal changes in E – compared to changes in P – in the availability of water for runoff at different times of the year. The seasonal distribution of E is mainly dominated by the cycle of R_n over most of the world (see also Sect. 4.2.2). The largest seasonal variations in E are found in subtropical areas with sufficient input of P during the summer period; in some of these regions the volume of E in summer-time becomes almost one order of magnitude larger than during winter-time (see for instance Northern Australia, Southern Africa or the east coast of United States). In desert regions where rainfall events rarely happen (like central Australia or the Arabian Peninsula) the volumes of evaporation remain low during the entire year and the seasonal distribution of E is independent of the cycle of R_n.

4.2.3 Drivers of evaporation

The main factors that limit land evaporation are the available energy and the volume of precipitation. The spatial and temporal distribution of these limiting factors, and the strength of the correlation of evaporation with one particular driver, can provide valuable information on the seasonal dynamics of evaporation in a particular area. Teuling et al. (2009) hypothesised that regional trends in land evaporation respond to trends in the limiting drivers. Only when we know to what extent a specific driver is controlling the evaporation process, known changes in that controlling factor may be translated into long-term changes in evaporation.

Here, the GLEAM-estimated relationship between land evaporation and its external drivers is analysed at a global scale. Figure 8 gives a global overview of such analysis for the period 2003–2007. This figure has been made using the technique by Teuling et al. (2010) for plots with bivariate colour maps. Figure 8a shows for JJA the global distribution of the correlation coefficient between daily time series of E and R_n and the correlation coefficient between E and θ (volumetric water content for the whole root-zone). Figure 8b shows the same inferences for the period DJF. Figure 8c,d

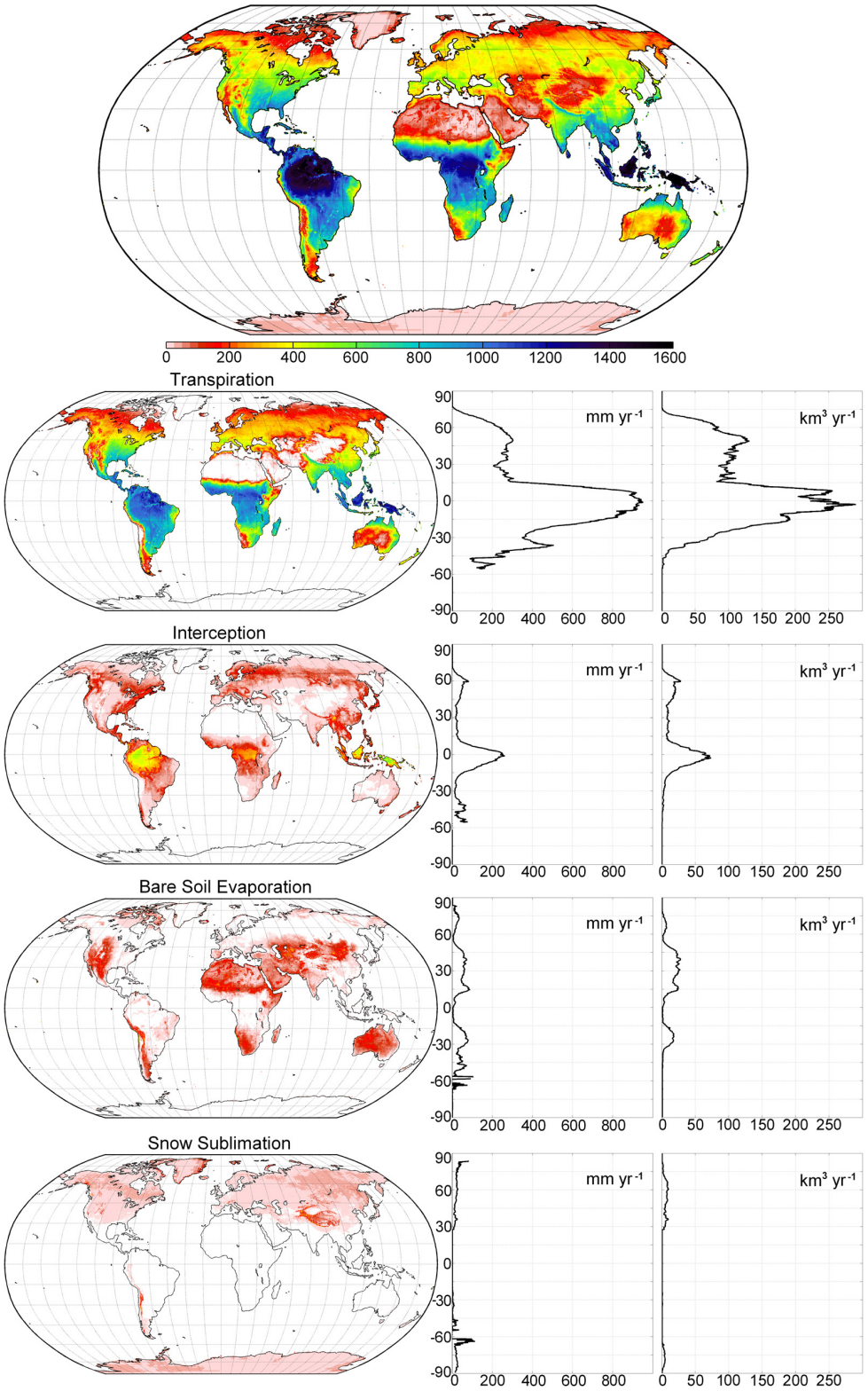

Fig. 5. Decomposition of 2003–2007 average annual evaporation (mm) into its contributing fluxes. The latitudinal profiles are shown in units of mm yr^{-1} and $km^3\,yr^{-1}$.

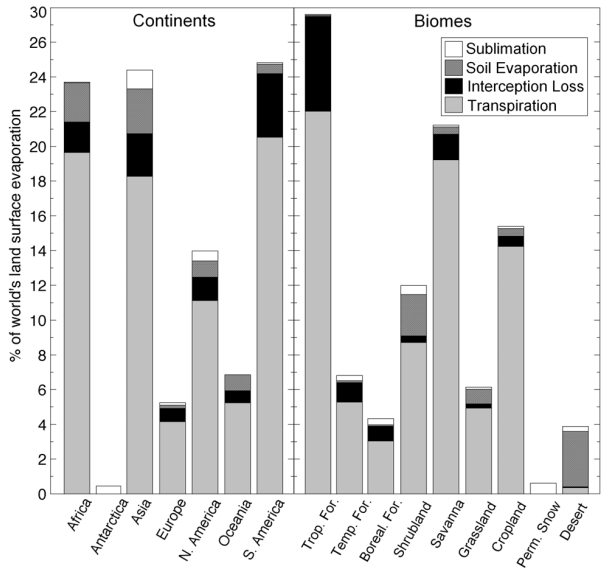

Fig. 6. Contribution to global land-surface evaporation (in %) for each: **(a)** continent, and **(b)** biome type. The relative contribution of the constituents of evaporation is presented separately.

present the global distribution of the correlation between E and R_n, and E and P for JJA and DJF, respectively.

The model predicts that most of the JJA daily variability of E over Central Europe and North America can be explained by the dynamics in R_n (see high correlation between E and R_n in Fig. 8a). In forested areas in boreal winter-time P becomes important (see Fig. 8d) and the relation with R_n is weaker. Despite the high correlation between E and P, E remains relatively uncorrelated with θ; this suggests that the soil remains under no stress for transpiration. The component of forest evaporation that is affected by P (and governing the dynamics of E) is therefore not the transpiration flux but the rainfall interception loss. For tropical rain forests, despite the fact that R_n remains in general the largest controlling factor, P is also identified as an important driver of evaporation in both seasons.

Areas presenting high correlations between E and θ correspond mainly to arid and semi-arid regions, and especially during summer-time (see Fig. 8a and b). In these regions the correlation of E with the time series of P is lower than the correlation between E and θ; this is because soil moisture is a more direct indicator of plant water stress. The areas where soil moisture is likely to limit the evaporative flux can also be seen in Fig. 9. This figure presents the global average (2003–2007) distribution of the estimates of daily stress factor, S – which equals $(E-I)/E_p$ (see Sect. 2.1). The left map represents the months of JJA; the right map shows DJF. GLEAM calculates S at daily time-step based on estimates of soil moisture and vegetation optical depth (see Miralles et al., 2011). Values of $S = 1$ correspond to areas where there is sufficient water to meet the atmospheric evaporative demand; values of $S = 1$ are present in areas where the shortage of water restricts the actual rate of evaporation under its potential value. It can be seen that over the majority of the world's land surface, land conditions regulate to certain extent the flux of evaporation. In high latitudes the availability of water is generally sufficient to meet the atmospheric demand. Arid and semi-arid regions, however, remain under evaporative stress during almost the entire year. The seasonal spatial patterns of S are strongly related to the seasonal distribution of P (Fig. 7c and d) and the distribution of the correlation between E and θ (Fig. 8a and b).

5 Discussion

The average annual land-surface evaporation estimated by GLEAM for the period 2003–2007 is 67.9×10^3 km^3. This number is comparable to other estimates of average annual land evaporation – e.g. the 71×10^3 km^3 found by Baumgartner and Reichel (1975) (see Dolman and Gash, 2010), the 65.5×10^3 km^3 found by Oki and Kanae (2006), the 65×10^3 km^3 reported by Jung et al. (2010) or the 65.8×10^3 km^3 by Schlosser and Gao (2010). Lim and Roderick (2009) analysed the global partitioning of precipitation over land making use of the GCMs from the Intergovernmental Panel on Climate Change (IPCC) Fourth Assessment Report (AR4). Despite referring to a different period than the one presented here (2003–2007 versus 1970–1999) the volume of incoming precipitation is similar in both studies. While the ensemble of GCMs estimated that 70% of the global land precipitation was evaporated and 30% was available for runoff ($P-E$), the global partitioning in GLEAM is somewhat different: 58% evaporation and 42% water available for runoff. Despite this difference the relative contribution from each continent to global E and global $P-E$ agrees well in both studies. One exception is South America in which the GCMs estimated 51% less $P-E$ than GLEAM. It is worth mentioning that this dissimilarity responds mainly to the different volumes of precipitation and not of evaporation.

Results shown in Table 2 are also in good agreement with the average volumes of P, E and $P-E$ reported for each continent by Sellers (1965) and Baumgartner and Reichel (1975) (see Peixoto and Oort, 1992). The GLEAM-estimated fraction of P that is evaporated over Africa (58%) is however much lower than the 76% and 84% reported by Sellers (1965) and by Baumgartner and Reichel (1975) respectively. These differences come again from discrepancies in the volume of precipitation (and not evaporation). The low density of the rainfall observational network in Africa makes traditional gauge-based estimates of precipitation for this continent – like the ones by Sellers (1965) and Baumgartner and Reichel (1975) – highly uncertain (see Love et al., 2004). The use of satellite information in CMORPH reduces

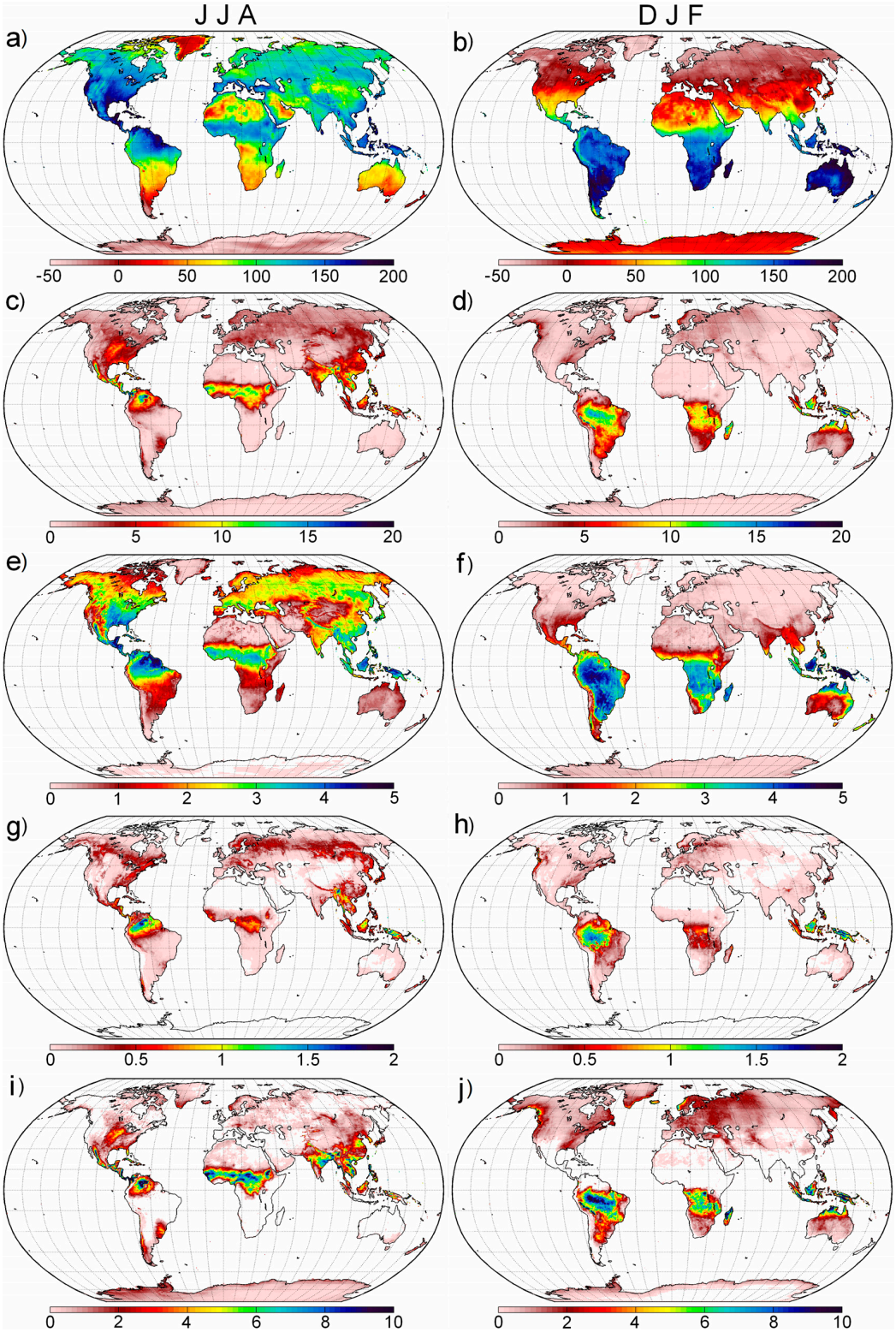

Fig. 7. Average fluxes for the period 2003–2007 separately presented for JJA (left panel) and DJF (right panel): **(a)** and **(b)** show the distribution of R_n, **(c)** and **(d)** represent P, **(e)** and **(f)** are E, **(g)** and **(h)** are I, and **(i)** and **(j)** present the estimated distribution of $P - E$. Units are mm day^{-1} except for R_n which is presented in W m^{-2}.

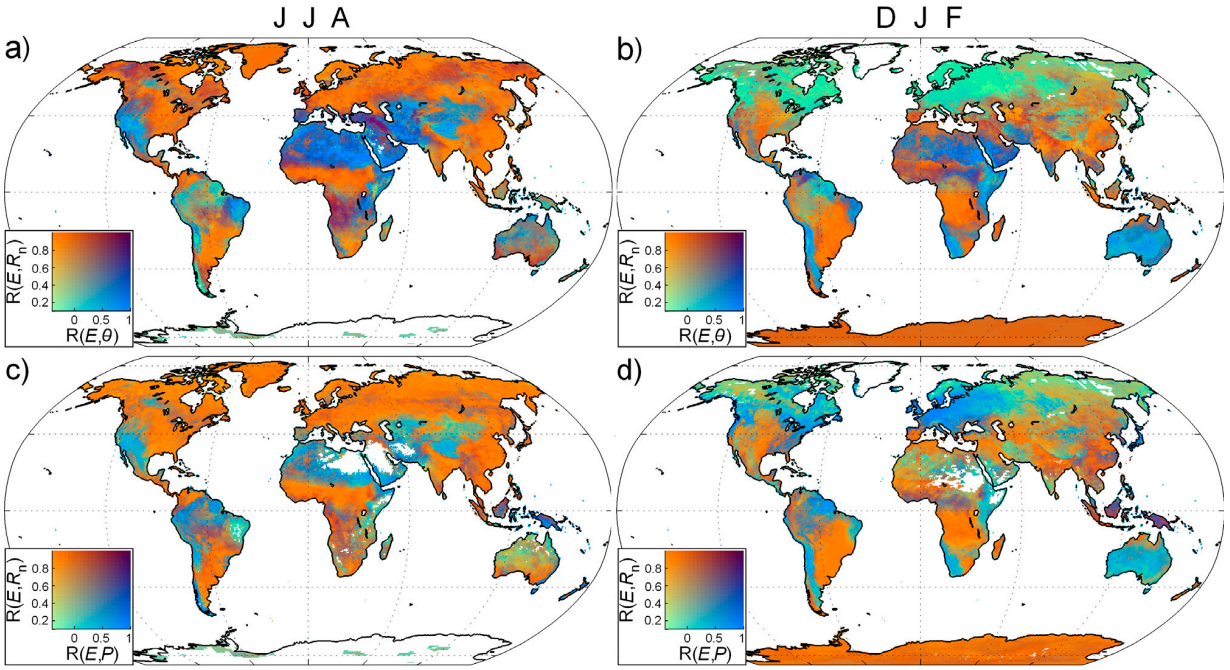

Fig. 8. The upper panel shows the estimated correlation (R) of daily time series of E with R_n and θ for **(a)** JJA and **(b)** DJF. The bottom figures show the correlation of daily E with R_n and P during **(c)** JJA and **(d)** DJF. All the results correspond to the period 2003–2007.

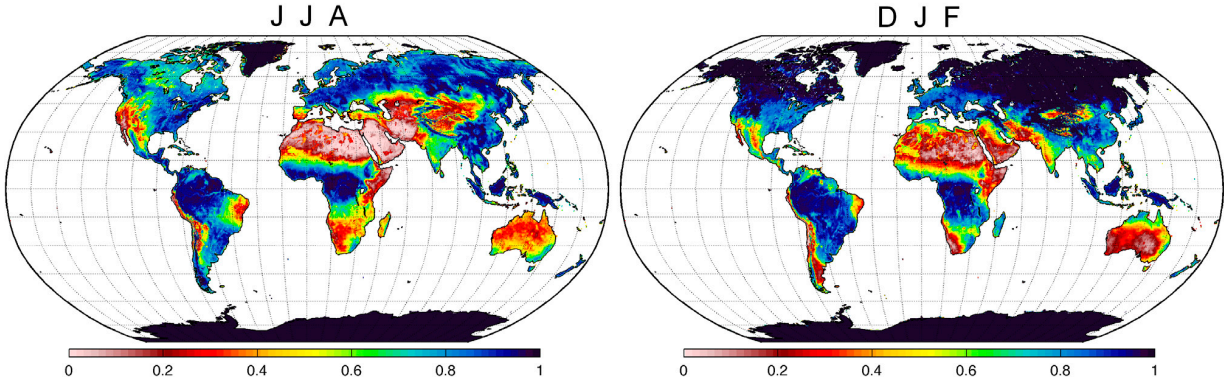

Fig. 9. Estimated stress factor (S) as averaged for the months of JJA and DJF

this uncertainty and enhances the reliability of GLEAM estimates of E and $P - E$ in areas of sparse observations like Africa.

Fisher et al. (2008) obtained similar results (both in absolute and in relative terms) to the ones presented in the latitudinal profile of annual fluxes shown in Fig. 4. Humid tropics show a value of land evaporation around 50% of the incoming precipitation, in accordance with the level of rainfall recycling in these areas reported by Salati and Vose (1984). This latitudinal profile is in agreement with the hypothesis that at high latitudes in winter-time, the flux of interception loss – dominated by the aerodynamic forces rather than by the available energy – can represent the main source of evaporation in forested regions. When considering interception loss, evaporation can reach and even exceed the available energy (Stewart, 1977) (see also the results in Fig. 7). The different bio-physical processes behind interception loss and transpiration make wet canopy evaporation more dependent on the volume and duration of rainfall and less on the net radiation (see Shuttleworth and Calder, 1979). Under low energy availability, rates of wet canopy evaporation can become several times higher than the rates of transpiration which would be occurring under dry conditions (see commentary by Gash and Shuttleworth, 2007). In the context of

the Penman-Monteith equation, the aerodynamic term (and not the energy one) is responsible for the major part of the flux. This is the main reason why interception loss requires a separate estimation, and why PT energy-based approaches are not suitable for its estimation.

Traditionally, studies on evaporation drivers have been focused on net radiation and soil moisture (considered only as the link between precipitation and evaporation). However, an important component of the evaporative flux from forests, canopy-intercepted rainfall, will not be directly affected by the soil moisture dynamics. Moreover, as stated above, the flux of evaporated water from wet canopies is relatively independent from the net radiation. Teuling et al. (2009) analysed in detail the drivers of the evaporative flux over Europe and North America focusing on net radiation and precipitation, but considering the latter only as a surrogate for soil moisture. Their results were extensively validated using FLUXNET data but rain-days were not included in this validation and therefore the role of interception could not be identified. The daily frequency and separate estimation of interception within GLEAM allows a detailed study of these interactions. However, while Teuling et al. (2009) compared independent estimates, in the study presented in Sect. 4.2.3 the estimates of E are dependent on the values of P, R_n and θ, and therefore the results rely on the sensitivity of GLEAM E to these variables. Consequently this study merely aims to understand how GLEAM reproduces interactions between land and atmosphere and how it estimates the relative importance of the evaporation drivers in different regions in the world.

Figure 8a and c shows how in summer-time and over Central Europe and North America, most of the variability of daily GLEAM estimates of E can be explained by the dynamics in R_n. This is in agreement with Fig. 7a,b,e,f that illustrate how in the majority of the world's land surface the seasonality of E follows closely the seasonality of the incoming solar energy. However, in forested regions and during winter-time the relationship is not obvious (see Fig. 8b). This low dependency between the time series of E and the time series of R_n is a response to the higher relative importance of I as a component of E. This happens because of the low volumes of transpiration in winter-time. As can be appreciated from Fig. 8d, in forested regions under conditions of low incoming radiation, the model identifies the availability of water on the canopy (dominated by the volume of P and its duration) as an important factor determining the dynamics of evaporation. The low correlations found with θ over the same areas, suggest that the correlation with P is not a response to conditions of soil water deficit.

Trends in soil moisture can be responsible for the long-term changes in land evaporation; this happens over regions where water availability is the main control on the evaporation (see Teuling et al., 2009). Jung et al. (2010) analysed the results of their FLUXNET data-based approach (Jung et al., 2009) to reveal a positive trend in global land-surface evaporation from 1982 to 1997; from 1998 this trend slowed down, attributed to the decrease in soil moisture over the Southern Hemisphere. Dark blue-coloured regions in Fig. 8a and b represent the areas where GLEAM identifies that a long-term decrease in soil moisture could potentially induce a negative trend in land evaporation. They are mainly arid and semi-arid regions, where the rate of actual evaporation rarely matches the potential rate (especially during summer-time) and it is the availability of water in the soil that will determine the volume of daily evaporation (see also Fig. 9). This dependency on the soil moisture underlines the importance of correctly parameterising the soil water content and the stress conditions for those areas.

6 Conclusions

Large differences in the estimates of land-surface evaporation from the currently existing methodologies (Jiménez et al., 2011; Müller et al., 2011) indicate that land evaporation remains one of the most uncertain terms in the global water cycle. GLEAM is a new alternative to estimate global evaporation and its different components by combining satellite-observable variables within a simple bio-physical approach. It aims to fill the gaps from previous satellite-based evaporation models acknowledging the importance of estimating interception loss through a widely-tested model (Gash's analytical model), and moderating PT estimates of latent heat flux by considering the soil water stress conditions over the entire root-zone. As with every model, GLEAM is a simplification of reality: results presented here are affected by the assumptions taken in the parameterisation of the bio-physical processes within the methodology. However, the constituent parts of GLEAM have been successfully validated by comparison with in situ data over different ecosystems and the error structure of the estimates has been analysed in detail; this sets the level of credibility of the results presented in this paper.

An average annual land evaporation of 67.9×10^3 km^3 is estimated for the period 2003–2007, which represents 58% of the incoming precipitation. South America, Asia and Africa are found to contribute together to 73% of the evaporative flux over land, while only 5% occurs in Europe. Half of the world's land evaporation is originated in tropical forests and savannas. Transpiration contributes to 80% of global land-surface evaporation. Canopy interception loss is estimated as 11% and plays a major role in the long-term partition of rainfall and the volume of runoff generated in forested ecosystems. Precipitation is identified as an important factor driving evaporation in forest regions due to the effect of evaporation of canopy-intercepted rainfall. Soil moisture limited regions where trends on land evaporation are likely respond to trends in soil available water are located by the methodology.

Ongoing activities include the application of GLEAM to develop a 24 year database (from 1984 to 2007), and an inter-product comparison with existing global fields of evaporation within the LandFlux-EVAL initiative of the GEWEX Radiation Panel (Jiménez et al., 2011; Müller et al., 2011). The applicability of triple collocation will be further explored using the longer record of evaporation; different sources of evaporation will be applied to test the sensitivity of the estimated errors to the potential dependency between GLEAM and Princeton University products. The dataset could additionally be used to investigate trends in land evaporation and their relation to ocean oscillations, the effects of land-use changes such as desertification or deforestation on the hydrological cycle, and the coupling between land and atmospheric processes.

All GLEAM products will become freely available through the web portal hosted at the VU University Amsterdam Geo-services website (http://geoservices.falw.vu.nl).

Acknowledgement. The work was undertaken as part of the European Union (FP6) funded Integrated Project called WATCH (Contract No. 036946). The data used in the validation of the $P-E$ estimates was provided by the Global Runoff Data Centre, 56068 Koblenz, Germany. We would like to thank A. J. Teuling for his feedback on the application of the technique explained in Teuling et al. (2010) and his valuable comments. We also thank C. Jiménez for his detailed review, and R. H. Reichle and J. Sheffield for providing the datasets used in the triple collocation study.

Edited by: B. van den Hurk

References

Baumgartner, A. and Reichel, E.: The World Water Balance: Mean Annual Global Continental and Maritime Precipitation, Evaporation and Runoff, Elsevier Scientific Publishing Company, Amsterdam, The Netherlands, Oxford, UK and New York, USA, 1975.

Blyth, E. M., Shuttleworth, W. J, and Harding, R. J.: Summary of the GEWEX International Symposium on Global Land-surface Evaporation and Climate, Hydrol. Process., 23, 3411–3412, 2009.

Bosilovich, M.: NASA's Modern Era Retrospective-analysis for Research and Applications: Integrating Earth Observations, Earth-Zine, E-Zine article, 2008.

Choudhury, B. J. and DiGirolamo, N. E.: A biophysical process-based estimate of global land surface evaporation using satellite and ancillary data; I. Model description and comparison with observations, J. Hydrol., 205, 164–185, 1998.

De Jeu, R. A. M., Wagner, W., Holmes, T. R. H., Dolman, A. J., van de Giesen, N. C., and Friesen, J.: Global soil moisture patterns observed by space borne microwave radiometers and scatterometers, Surv. Geophys., 29, 399–420, 2008.

Di Baldassarre, G. and Montanari, A.: Uncertainty in river discharge observations: a quantitative analysis, Hydrol. Earth Syst. Sci., 13, 913–921, doi:10.5194/hess-13-913-2009, 2009.

Dinku, T., Ceccato, P., Grover-Kopec, E., Lemma, M., Connor, S. J., and Ropelewski, C. F.: Validation of satellite rainfall products over East Africa's complex topography, Int. J. Remote Sens., 28, 1503–1526, doi:10.1080/01431160600954688, 2007.

Dirmeyer, P. A., Gao, X. A., Zhao, M., Guo, Z. C., Oki, T., and Hanasaki, N.: GSWP-2 Multimodel anlysis and implications for our perception of the land surface, B. Am. Meteorol. Soc., 87, 1381–1397, 2006.

Dolman, A. J. and De Jeu, R. A. M.: Evaporation in focus, Nat. Geosci., 3, 296, 2010.

Dolman, A. J. and Gash, J. H.: Evaporation in the global hydrological cycle, in: Treatise on Water Science, edited by: Wilderer, P., Treatise on Water Science, vol. 2, Academic Press, Oxford, 79-87, 2010.

Dorigo, W. A., Scipal, K., Parinussa, R. M., Liu, Y. Y., Wagner, W., de Jeu, R. A. M., and Naeimi, V.: Error characterisation of global active and passive microwave soil moisture datasets, Hydrol. Earth Syst. Sci., 14, 2605–2616, doi:10.5194/hess-14-2605-2010, 2010.

Ebert, E. E., Janowiak, J. E., and Kidd, C.: Comparison of near-real time precipitation estimates from satellite observations and numerical models, B. Am. Meteorol. Soc., 88, 47–64, 2007.

Fisher, J. B., Tu, K. P., and Baldocchi, D. D.: Global estimates of the land-atmosphere water flux based on monthly AVHRR and ISLSCP-II data, validated at 16 FLUXNET sites, Remote Sens. Environ., 112, 901–919, 2008.

Gash, J. H.: An analytical model of rainfall interception by forests, Q. J. Roy. Meteorol. Soc., 105, 43–55, 1979.

Gash, J. H. and Shuttleworth, W. J.: Vegetation controls on evaporation – commentary, in: Benchmark Papers in Hydrology: Evaporation, edited by: Gash, J. H. and Shuttleworth, W. J., IAHS Press, Wallingford, 233–239, 2007.

Hirpa, F. A., Gebremichael, M., and Hopson, T.: Evaluation of high resolution satellite precipitation products over very complex terrain in Ethiopia, J. Appl. Meteorol. Clim., 49, 1044-1051, doi:10.1175/2009JAMC2298.1, 2009.

Huffman, G. J., Adler, R. F., Morrissey, M. M., Bolvin, D. T., Curtis, S., Joyce, R., McGavock, B., and Susskind, J.: Global precipitation at one-degree daily resolution from multisatellite observations, J. Hydrometeorol., 2, 36–50, 2001.

Jiménez, C., Prigent, C., and Aires, F.: Toward an estimation of global land surface heat fluxes from multisatellite observations, J. Geophys. Res.-Atmos., 114, D06305, doi:10.1029/2008JD011392, 2009.

Jiménez, C., Prigent, C., Müller, B., Seneviratne, S. I., McCabe, M. F., Wood, E. F., Rossow, W. B., Balsamo, G., Betts, A. K., Dirmeyer, P. A., Fisher, J. B., Jung, M., Kanamitsu, M., Reichle, R. H., Reichstein, M., Rodell, M., Sheffield, J., Ku, T., and Wang, K.: Global inter-comparison of 12 land surface heat flux estimates, J. Geophys. Res.-Atmos., 116, D02102, doi:10.1029/2010JD014545, 2011.

Joyce, R. J., Janowiak, J. E., Arkin, P. A., and Xie, P.: CMORPH: A method that produces global precipitation estimates from passive microwave and infrared data at high spatial and temporal resolution, J. Hydrometeorol., 5, 487–503, 2004.

Jung, M., Reichstein, M., and Bondeau, A.: Towards global empirical upscaling of FLUXNET eddy covariance observations: validation of a model tree ensemble approach using a biosphere model, Biogeosciences, 6, 2001–2013, doi:10.5194/bg-6-2001-2009, 2009.

Jung, M., Reichstein, M., Ciais, P., Seneviratne, S., Sheffield, J., Goulden, M., Bonan, G., Cescatti, A., Chen, J., de Jeu, R., Dolman, A. J., Eugster, W., Gerten, D., Gianelle, D., Gobron, N., Heinke, J., Kimball, J., Law, B., Montagnani, L., Mu, Q., Mueller, B., Oleson, K., Papale, D., Richardson, A., Roupsard, O., Running, S., Tomelleri, E., Viovy, N., Weber, U., Williams, C., Wood, E., Zaehle, S., and Zhang, K.: Recent decline in the global land evapotranspiration trend due to limited moisture supply, Nature, 467, 951–954, doi:10.1038/nature09396, 2010.

Lim, W. H. and Roderick, M. L.: An Atlas of the Global Water Cycle: Based on the IPCC AR4 models, ANU E Press, Canberra, 2009.

Lin, B., Stackhouse Jr., P. W., Minnis, P., Wielicki, B. A., Hu, Y., Sun, W., Fan, T.-F., and Hinkelman, L. M.: Assessment of global annual atmospheric energy balance from satellite observations, J. Geophys. Res., 113, D16114, doi:10.1029/2008JD009869, 2008.

Love, T. B., Kumar, V., Xie, P. and Thiaw, W.: A 20-year daily Africa precipitation climatology using satellite and gauge data. In Proceedings of the 84th AMS Annual Meeting, P5.4. Conference on Applied Climatology, Seattle, WA, 2004.

Miralles, D. G., Crow, W. T., and Cosh, M. H.: Estimating spatial sampling errors in coarse-scale soil moisture estimates derived from point-scale observations, J. Hydrometeorol., 11, 1423–1429, doi:10.1175/2010JHM1285.1, 2010a.

Miralles, D. G., Gash, J. H., Holmes, T. R. H., De Jeu, R. A. M., and Dolman, A. J.: Global canopy interception from satellite observations, J. Geophys. Res.-Atmos., 115, D16122, doi:10.1029/2009JD013530, 2010b.

Miralles, D. G., Holmes, T. R. H., De Jeu, R. A. M., Gash, J. H., Meesters, A. G. C. A., and Dolman, A. J.: Global land-surface evaporation estimated from satellite-based observations, Hydrol. Earth Syst. Sci., 15, 453–469, doi:10.5194/hess-15-453-2011, 2011.

Mu, Q., Heinsch, F. A., Zhao, M., and Running, S. W.: Development of a global evapotranspiration algorithm based on MODIS and global meteorology data, Remote Sens. Environ., 111, 519–536, 2007.

Müller, B., Seneviratne, S. I., Jiménez, C., Corti, T., Hirschi, M., Balsamo, G., Ciais, P., Dirmeyer, P., Fisher, J. B., Guo, Z., Jung, M., Maignan, F., McCabe, M. F., Reichle, R., Reichstein, M., Rodell, M., Sheffield, J., Teuling, A. J., Wang, K., Wood, E. F., and Zhang, Y.: Evaluation of global observations-based evapotranspiration datasets and IPCC AR4 simulations, Geophys. Res. Lett., doi:10.1029/2010GL046230, in press, 2011.

Murphy, D. M. and Koop, T.: Review of the vapour pressures of ice and supercooled water for atmospheric applications, Q. J. Roy. Meteorol. Soc., 131, 1539–1565, 2005.

Oki, T. and Kanae, S: Global hydrological cycles and world water resources, Science, 313, 1068-1072, 2006.

Peixoto, J. P. and Oort, A. H.: Physics of Climate, American Institute of Physics, New York, USA, 172 pp., 1992.

Salati, E. and Vose, P. B.: Amazon Basin: a system in equilibrium, Science, 225, 129–138, 1984.

Schlosser, C. A. and Gao, X.: Assessing evapotranspiration estimates from the second Global Soil Wetness Project (GSWP-2) simulations, J. Hydrometeor, 11, 880-897, doi:10.1175/2010JHM1203.1, 2010.

Scipal, K., Holmes, T., de Jeu, R., Naeimi, V., and Wagner, W.: A possible solution for the problem of estimating the error structure of global soil moisture data sets, Geophys. Res. Lett., 35, L24403, doi:10.1029/2008gl035599, 2008.

Sellers W. D.: Physical Climatology, University of Chicago Press, Chicago, IL, USA, 1965.

Sheffield, J., Wood, E. F., and Munoz-Arriola, F.: Long-term regional estimates of evapotranspiration for Mexico based on downscaled ISCCP data, J. Hydrometeorol., 11, 253–275, 2010.

Shuttleworth, W. J. and Calder, I. R.: Has the Priestley-Taylor equation any relevance to forest evaporation?, J. Appl. Meteorol., 18, 639–646, 1979.

Stackhouse, P. W., Gupta, S. K., Cox, S. J., Mikovitz, J. C., Zhang, T., and Chiacchio ,M.: 12 year surface radiation budget data set GEWEX News, 14, 2004.

Stewart, J. B: Evaporation from the wet canopy of a pine forest, Water Resour. Res., 13, 915–921, 1977.

Stoffelen, A.: Toward the true near-surface wind speed: Error modeling and calibration using triple collocation, J. Geophys. Res., 103, 7755-7766, doi:10.1029/97jc03180, 1998.

Teuling, A. J., Hirschi, M., Ohmura, A., Wild, M., Reichstein, M., Ciais, P., Buchmann, N., Ammann, C., Montagnani, L., Richardson, A. D., Wohlfahrt, G., and Seneviratne, S. I.: A regional perspective on trends in continental evaporation, Geophys. Res. Lett., 36, L02404, doi:10.1029/2008GL036584, 2009.

Teuling, A. J., Stöckli, R., and Seneviratne, S. I.: Bivariate colour maps for visualizing climate data (short communication), Int. J. Climatol., doi:10.1002/joc.2153, in press, 2010.

Tian, Y., Peters-Lidard, C. D., Chaudhury, B. J., and Garcia, M.: Multitemporal analysis of TRMM-based satellite precipitation products for land data assimilation applications, J. Hydrometeorol., 8, 1165–1183, 2007.

Troy, T. J. and Wood, E. F.: Comparison and evaluation of gridded radiation products across northern Eurasia, Environ. Res. Lett., 4, 045008, doi:10.1088/1748-9326/4/4/045008, 2009.

Valente, F., David, J. S., and Gash, J. H.: Modelling interception loss for two sparse eucalypt and pine forests in Central Portugal using reformulated Rutter and Gash analytical models, J. Hydrol., 190, 141–162, 1997.

Zeweldi, D. A. and Gebremichael, M.: Evaluation of CMORPH precipitation products at fine space-time scales, J. Hydrometeorol., 10, 300–308, 2009.

Zhang, K., Kimball, J. S., Nemani, R. R., and Running, S. W.: A continuous satellite-derived global record of land surface evapotranspiration from 1983 to 2006, Water Resour. Res., 46, W09522, doi:10.1029/2009WR008800, 2010.

Zhang, Y., Rossow, W. B., Lacis, A. A., Oinas, V. and Mishchenko, M. I.: Calculation of radiative fluxes from the surface to top of atmosphere based on ISCCP and other global data sets: Refinements of the radiative transfer model and the input data, J. Geophys. Res., 109, D19105, doi:10.1029/2003JD004457, 2004.

Zhang, Y., Rossow, W. B., and Stackhouse Jr., P. W.: Comparison of different global information sources used in surface radiative flux calculation: Radiative properties of the surface, J. Geophys. Res., 112, D01102, doi:10.1029/2005JD007008, 2007.

Hydrol. Earth Syst. Sci. Discuss., 10, 769–805, 2013
www.hydrol-earth-syst-sci-discuss.net/10/769/2013/
doi:10.5194/hessd-10-769-2013
© Author(s) 2013. CC Attribution 3.0 License.

Hydrology and Earth System Sciences Discussions

This discussion paper is/has been under review for the journal Hydrology and Earth System Sciences (HESS). Please refer to the corresponding final paper in HESS if available.

Benchmark products for land evapotranspiration: LandFlux-EVAL multi-dataset synthesis

B. Mueller[1], M. Hirschi[1], C. Jimenez[2], P. Ciais[3], P. A. Dirmeyer[4], A. J. Dolman[5], J. B. Fisher[6], M. Jung[7], F. Ludwig[8], F. Maignan[3], D. Miralles[9], M. F. McCabe[10], M. Reichstein[7], J. Sheffield[11], K. C. Wang[12], E. F. Wood[11], Y. Zhang[13], and S. I. Seneviratne[1]

[1]Institute for Atmospheric and Climate Science, ETH Zurich, Zurich, Switzerland
[2]LERMA, Observatoire de Paris, Paris, France
[3]LSCE, UMR CEA-CNRS, Gif-sur-Yvette, France
[4]George Mason University, Fairfax, Virginia, USA
[5]VU University Amsterdam, The Netherlands
[6]Jet Propulsion Laboratory, California Institute of Technology, Pasadena, USA
[7]Max Planck Institute for Biogeochemistry, Jena, Germany
[8]Wageningen University, Wageningen, The Netherlands
[9]School of Geographical Sciences, University of Bristol, UK
[10]Water Desalination and Reuse Center, King Abdullah University of Science and Technology, Saudi Arabia

[11]Department of Civil and Environmental Engineering, Princeton University, Princeton, USA
[12]College of Global Change and Earth System Science, Beijing Normal University, Beijing, China
[13]CSIRO Land and Water, Canberra, Australia

Received: 19 December 2012 – Accepted: 6 January 2013 – Published: 17 January 2013

Correspondence to: B. Mueller (brigitte.mueller@env.ethz.ch),
S. I. Seneviratne (sonia.seneviratne@env.ethz.ch)

Published by Copernicus Publications on behalf of the European Geosciences Union.

Abstract

Land evapotranspiration (ET) estimates are available from several global datasets. Here, monthly global land ET synthesis products, merged from these individual datasets over the time periods 1989–1995 (7 yr) and 1989–2005 (17 yr), are presented. The merged synthesis products over the shorter period are based on a total of 40 distinct datasets while those over the longer period are based on a total of 14 datasets. In the individual datasets, ET is derived from satellite and/or in-situ observations (diagnostic datasets) or calculated via land-surface models (LSMs) driven with observations-based forcing and atmospheric reanalyses. Statistics for four merged synthesis products are provided, one including all datasets and three including only datasets from one category each (diagnostic, LSMs, and reanalyses). The multi-annual variations of ET in the merged synthesis products display realistic responses. They are also consistent with previous findings of a global increase in ET between 1989 and 1997 (1.15 mm yr^{-2} in our merged product) followed by a decrease in this trend (−1.40 mm yr^{-2}), although these trends are relatively small compared to the uncertainty of absolute ET values. The global mean ET from the merged synthesis products (based on all datasets) is 1.35 mm per day for both the 1989–1995 and 1989–2005 products, which is relatively low compared to previously published estimates. We estimate global runoff (precipitation minus ET) to 34 406 km^3 per year for a total land area of 130 922 km^2. Precipitation, being an important driving factor and input to most simulated ET datasets, presents uncertainties between single datasets as large as those in the ET estimates. In order to reduce uncertainties in current ET products, improving the accuracy of the input variables, especially precipitation, as well as the parameterizations of ET are crucial.

1 Introduction

In recent years, several global multi-year evapotranspiration datasets based on in-situ observations or satellite retrievals of different indirect variables have been derived. In

Mueller et al. (2011b), an evaluation of their performance within the LandFlux-EVAL (see www.iac.ethz.ch/url/LandFlux-EVAL) initiative over the time period 1989–1995 was presented, while the study of Jimenez et al. (2011) assessed a subset of these datasets over a shorter period but also assessing the radiative and sensible fluxes. These studies considered dedicated datasets that derive ET from combinations of observations or observations-based estimates together with targeted algorithms (referred to as *diagnostic datasets*), ET from land surface model *(LSM) simulations driven with observations-based forcing* as well as ET from atmospheric *reanalyses* (i.e. computed with LSMs within a global model assimilating mostly atmospheric observations). The general main geographical structures related to the principal climatic regimes are present in all products, but relatively large differences in the absolute values among some of the products were observed (Mueller et al., 2011b; Jimenez et al., 2011).

Even though a large number of ET datasets is currently available and has been analyzed in these studies, a global benchmark for ET is missing. Such a benchmark dataset would be useful for several purposes. Land-surface modellers and hydrologists often use ET to validate their model output, because it is one of the main components in the land water and energy budgets as well as a key driver for droughts (e.g. Sheffield et al., 2012; Seneviratne, 2012). Furthermore, agricultural and water-management communities estimate the water needed for irrigation with information on ET. Apart from mean ET values, corresponding uncertainty estimates are necessary for all kinds of applications. For these reasons, benchmark synthesis products of ET derived from existing datasets have been developed in the present study with the provision of different estimates of uncertainty.

The previous studies by Mueller et al. (2011b) and Jimenez et al. (2011) focused on spatial patterns of multi-year means and seasonal variations, respectively. However, the behavior of the LandFlux-EVAL datasets with respect to ET trends or multi-annual variations has not yet been investigated. Knowledge of the temporal changes of ET is important since it is a major component of the global water cycle. Within a changing climate, changes in the hydrological cycle are also expected, but very difficult

to determine. Observations indicate that precipitation over land increased by about 2.4 mm per decade from 1900 to 1988 (Dai et al., 1997, excluding North Africa in their analysis). Extending the analysis to the entire 20th century indicates a similar large trend (reduced by about 25 %, New et al., 2001). While some publications relate this behavior to a possible *intensification* of the hydrological cycle, this term is not well defined. Indeed, while evaporation from ocean surfaces is expected to increase with increasing temperature (as warmer air can hold more water vapour), it is unclear whether ET from land surfaces could similarly increase due to possible limitations imposed by soil moisture content and vegetation physiology. Due to a lack of relevant observations, respective trends of land ET could not be assessed until recently. The studies by Wang et al. (2010b) and Jung et al. (2010) are the first to investigate this issue over a relatively short time span from 1982 to 2002 and 1982 to 2008, respectively. Wang et al. (2010b) found an increase in global land ET of 15 mm per year, using 1120 globally distributed stations (Wang et al., 2010a). Jung et al. (2010) performed a trend analysis based on a global dataset empirically derived from in-situ measurements of ET from the FLUXNET project and satellite remote sensing and surface meteorological data (Jung et al., 2009, hereafter referred to as *MPIBGC* dataset), but also including eight other datasets. A tendency of increasing ET was found for the years 1982 to 1997, which indicates a possible intensification of the hydrological cycle. However, this trend was found to vanish after 1998. The decline in global land ET trend after 1998 was attributed to a decrease in moisture availability in Southern Hemisphere supply- (i. e. water-) limited evaporative regimes, which might indicate that a limit to the temperature-driven acceleration of the hydrological cycle was reached during the 1998–2008 time period. Nonetheless, the article also mentioned that whether this tendency was related to a long-term trend or only decadal variability could not be assessed given the short time period considered (see also Douville et al., 2013). Another study based on satellite retrievals also found that the increasing trend in global land ET disappeared after 2000 (Yao et al., 2012). However, it is important to note that uncertainties in forcing datasets used to derive such ET trends are large and may entail spurious features

linked to the use of reanalyses products assimilating non-homogeneous satellite products or variations in the density of stations considered in gridded precipitation products (e.g. Bengtsson et al., 2004; Seneviratne et al., 2004; Lorenz and Kunstmann, 2012; Sheffield et al., 2012).

Decreasing ET in soil moisture-limited regions would lead to a further increase in air temperature, since more available energy would be partitioned into sensible heat. Thus, understanding changes in the hydrological cycle is not only important to reduce the uncertainty in climate change projections, but also to assess the impacts of these changes on water availability, as well as for the occurrence of droughts, floods and hot extremes (see, e.g. Sheffield et al., 2012; Mueller and Seneviratne, 2012; IPCC, 2011; Seneviratne et al., 2010).

The benchmark synthesis products presented in this study are used to assess the inter-annual variations of ET on the global scale and encompasses the largest number of ET products to date. Besides the evaluation of temporal variability of the benchmark products and the single datasets contributing to them, the present study also compares these to precipitation, which is one of the most important drivers of ET, especially in soil moisture-limited regions (see, e.g. Teuling et al., 2009; Seneviratne et al., 2010).

2 Datasets and method

2.1 Merged benchmark synthesis products of evapotranspiration

We present here new multi-year merged synthesis products based on the analyses of existing land ET datasets. A first product spans the time period 1989–1995 and includes 40 products, while the second is available for the longer time period 1989–2005 and includes 14 products. Consistent with a previous analysis (Mueller et al., 2011b), the type of datasets included can be classified as diagnostic datasets, LSMs and reanalyses (see Sect. 1). Besides the two merged synthesis products based on all types of datasets, merged synthesis products from each of the individual dataset

types are also produced (see Table 1). The output statistics for each of the merged synthesis products are: Mean, median, 25th-percentile, 75th-percentile, interquartile range, standard deviation and minimum and maximum values of the ensemble of underlying datasets. All products are available in monthly and yearly temporal resolution, and as multi-year statistics. All merged synthesis products are made available through the internet (www.iac.ethz.ch/url/LandFlux-EVAL).

2.2 Overview of included datasets

An overview of the diagnostic datasets, LSMs and reanalyses considered for the preparation of the merged synthesis products is provided in Table 2. The subset of datasets available over the period 1989–2005 (cross in 5th column in Table 2) forms the basis of the merged synthesis products over this longer time period (see also Sect. 2.1). The table also lists information on the single datasets, such as the ET schemes, the number of soil layers used in the case of LSMs, the precipitation forcing datasets and other forcing variables used for the derivation of the respective datasets or, in the case of reanalyses, the land-surface schemes.

We considered here several additional datasets compared to the earlier analysis of Mueller et al. (2011b). These additional datasets are the diagnostic dataset GLEAM (Global Land-surface Evaporation: The Amsterdam Methodology, Miralles et al., 2011a), as well as LSM estimates from the Water Model Intercomparison Project WaterMIP (Haddeland et al., 2011). Simulations from the Global Land Data Assimilation System I (GLDAS-I, Rodell et al., 2004) were included in Mueller et al. (2011b) but excluded in the present study because of spurious trends (see Fig. A1 and Rui, 2011), which arised because the source of forcing data changed several times over the GLDAS-I time period (Matt Rodell, personal communication, 2012). However, we included GLDAS-II simulations (see Rui, 2011) from one of these models (NOAH version 3.3) which has been produced recently with a consistent forcing dataset (Princeton forcing, see Sheffield et al., 2006).

In GLEAM, the calculation of ET is based on the Priestley-Taylor equation and the Gash analytical model of forest rainfall interception (Miralles et al., 2011b). The model discriminates the different evapotranspiration components, i. e. interception, bare soil evaporation, transpiration and sublimation, and ET is coupled to soil moisture (Miralles et al., 2011a). Note that not all diagnostic estimates separately calculate these components or account for all of them, which leads to large differences especially in the Amazon region. The forcing data for GLEAM were all obtained from remote sensing products and synthesis of rain gauges (CPC, see Appendix A).

All WaterMIP simulations are driven with the same forcing dataset (WATCH forcing, see Weedon et al., 2011), but the employed forcing variables and time steps differ. For a list of these variables as well as references for each model, see Haddeland et al. (2011). The differences between the WaterMIP models are large. Some models, for example, solve both the water and the energy balances at the land surface and are classified as (classical) *LSMs*, while others solve the water balance only and are classified as *global hydrological models, GHMs* (following the classification proposed by Haddeland et al., 2011, note that for simplicity, we refer to both as LSMs in most of the present article). Further, the WaterMIP models vary substantially in their complexity in the representation of ET (e.g. including or excluding interception and transpiration), runoff, groundwater, snow or frozen soil (for more details, see Haddeland et al., 2011). For more information on all other datasets, the reader is referred to Mueller et al. (2011b) and Jimenez et al. (2011).

2.3 Processing of ET datasets and merged synthesis products

In order to prepare the merged synthesis products, we first interpolated all datasets on a common global grid of 1 degree longitude and latitude and aggregated daily values to monthly values where necessary. A spatial matching of the datasets was done, and if one gridpoint was covered by less than 70 % of the datasets, it was excluded from the final synthesis product (for the number of datasets originally available, see Fig. A2). Some of the datasets exhibit unrealistically large values (especially in the northern

latitudes due to the viewing angle of satellites). For the merged synthesis products, we applied a physical constraint to exclude such values. An upper limit to the latent heat flux is given by the energy balance, i. e. ET should not exceed net surface radiation at a scale as large as our grid cells. For each gridpoint of the merged synthesis products, we calculated a seasonal cycle of net radiation (from the Surface Radiation Budget (SRB) version 3) based on the monthly maxima of all available years (1984–2007). Monthly ET values exceeding the seasonal maxima cycle's net radiation of that month by more than 25 % were excluded, unless ET was smaller than 0.3 mm day^{-1}, since for such small values, ground heat flux cannot be neglected. Note, however, that if interception plays an important role, such as during winter time, ET can be larger than radiation. A further possible constraint might be applied from the assumption that ET should not exceed precipitation over a longer time period. However, we did not apply such a constraint because soil moisture depletion might play a role in some regions, and based on a small scale analysis (such as single pixels), atmospheric water fluxes or runon could provide additional water input for ET. In order to exclude single dataset values that were very different from those of the other datasets, we performed a statistical outlier detection after the application of the physical constraint, similar to that described in Weedon (2011), but applied on monthly values. A movie in the Supplement shows the number of datasets at each gridpoint and time step after all these steps. Finally, the mean, median, 25th-percentile, 75th-percentile, interquartile range, standard deviation and minimum and maximum statistics of the ensemble of underlying datasets are derived and provided as monthly, yearly and multi-year statistics.

3 Results

3.1 Merged synthesis products

The different merged synthesis products created from single categories only (*diagnostic datasets*, *LSMs* and *reanalyses*) and from all categories (see Table 1) coincide to

a large extent in their global land mean ET (Fig. 1), with highest values in the merged product based on reanalyses only (563 mm per year) and lowest in that based on LSMs only (423 mm per year). The interquartile ranges (IQRs, 75th-percentile minus 25th-percentile) are largest in the merged products based on diagnostic datasets and reanalyses. The variation of global mean ET for the 1989–2005 (*long*) as well as for the 1989–1995 (*short*) merged product created from all dataset categories (median) is shown in Fig. 2. The long merged product shows slightly higher values. The largest difference in the list of datasets in the short and long merged synthesis products is the inclusion of 28 LSMs (*short*) versus only 5 LSMs (*long*). WaterMIP and GSWP simulations are not available for the *long* version, and are therefore, due to their consistently low ET values (see Mueller et al., 2011b), the main reason for lower ET in the *short* product. The small difference in the temporal variations between the *short* and the *long* merged synthesis products is a strong indication that including a large number of dependent datasets (i.e. model simulations driven with the same forcing data, such as GSWP and WaterMIP runs) does not have a strong influence.

Global mean ET shows a slight increase between 1989 and 1997 followed by a decrease until 2005 (Fig. 2). The merged synthesis product (long) shows a nearly identical inter-annual variation as that found in the MPIBGC dataset in Jung et al. (2010). However, if we consider this variation in relation to the IQRs or the standard deviations, both shown in Fig. 2, the absolute ET trend change is very small and the interannual variations nearly vanish.

The reason for the large IQRs and standard deviations are the large differences in the absolute ET values of the single datasets. The IQRs and standard deviations based on the yearly anomalies of the underlying datasets (i. e. setting the mean of all datasets to zero before calculating the statistics), which is the quantity shown in Jung et al. (2010), are much smaller (can partly be seen also in Fig. 3). Note also that we consider more estimates than in the previous analyses from Jung et al. (2010).

The ET anomalies from all long merged synthesis products are shown in Fig. 3 (top left). The comparison reveals a very similar temporal evolution of ET in all four merged

synthesis products. Therefore, in the remainder of this study, only the merged products based on all dataset categories (long and short) will be analysed.

3.2 Single datasets

The temporal variations of the 14 single datasets contributing to the long merged synthesis products are shown in Fig. 3. In these analyses of single datasets, we excluded unrealistically high ET values, setting a threshold of 12.5 mm day^{-1}. The LSMs (bottom left) and reanalyses (bottom right) are more consistent amongst one another in their yearly variations than the diagnostic datasets (top right). The ET timeseries of all LSMs and reanalyses peak between 1997 and 1999. Some of the diagnostic datasets peak in other years, such as 2001 in the case of PRUNI and 2000 in GLEAM and AWB. The trends for the two time periods 1989–1997 and 1998–2005 are listed in Table 3. The merged product as well as 5 single datasets display a significant negative trend (italic font) for 1998–2005, indicating a decrease in global ET during that period. The positive trend found in Jung et al. (2010) for the previous period is only significantly positive in GLEAM. The reason for this could be that we calculate the trends over a shorter time period compared to Jung et al. (2010), who calculated them over 1982–1997 and 1998–2008.

3.3 Analyses of climate regions

We analyze here the two merged products (i.e. short and long, based on all dataset categories) as well as precipitation data (average of CRU, GPCC, GPCP and CPC, for references and information on these datasets, see Appendix A and Biemans et al., 2009) in climate regions using the classification of Koeppen-Geiger (data available from http://koeppen-geiger.vu-wien.ac.at). In order to facilitate the interpretation of the results, subregions have been merged to larger regions. The regions considered are displayed in Fig. 4.

Mean ET and precipitation are listed for the various climate regions in Table 4. Also included are the ET and precipitation trends (Theil-Sen estimator) from 1998–2005, i. e. for the period for which a decline in ET trend was found in Jung et al. (2010, see also previous section). The sum of the areas of all climate regions (third column) represents over 90 % of the global land area.

The global mean ET from the merged synthesis amounts to 1.35 mm day^{-1} for both the 1989–2005 and 1989–1995 products. This value is well within the range, and sometimes at the lower boundary, of other studies. For example Trenberth et al. (2009) reported a range of 1.38 to 1.82 mm day^{-1}, Haddeland et al. (2011) 1.14 to 1.61, Wang and Dickinson (2012) 1.2 to 1.5 and Dirmeyer et al. (2006) a mean of 1.36 mm day^{-1} for different time periods. The larger values from Trenberth et al. (2009) can be explained by their reliance on reanalysis products, which were found here to display a tendency for high ET values. The mean value of precipitation (average of CRU, GPCC, GPCP and CPC) amounts to 2.07 mm day^{-1}. The difference between global precipitation and land ET corresponds to the water that leaves the continents as runoff and amounts to 34 406 km^3 per year. This value is in good agreement with values from other studies summarized in Syed et al. (2009).

The largest contribution to the global ET trend over 1998–2005, which amounts to 18.9 km^3 yr^{-2}, stems from the equatorial winter dry (Aw), arid desert (BW) and arid steppe (BS) climate regions, even though the latter two are characterized by very low per area values of ET. The study of Jung et al. (2010) showed that the decline in trend change is mainly due to Southern Hemisphere dry regions. We therefore treated the northern and Southern Hemisphere of these regions (BW and BS) separately. Indeed, we find that even though they belong to the same climate regions, the Southern Hemisphere parts of the arid steppe (BS) and arid desert (BW) regions exhibit a large negative trend, while the Northern Hemisphere parts show very small (and positive) trends.

The signs of the trends in precipitation agree with the signs of the ET trends, except for the polar climate region (E). The opposite trends in the northern and southern

hemispere parts of the BS and BW regions can also be found in the precipitation datasets. Furthermore, the table shows that global ET has decreased much stronger than global precipitation over the period 1998–2005.

3.4 Precipitation forcing

The 1989–1995 global mean land ET of each dataset contributing to the synthesis product (short) is plotted against precipitation in Fig. 5. The precipitation value was taken from the forcing data of the respective ET dataset as listed in Table 2. If precipitation was not available (for some diagnostic datasets), the average of four currently available observational datasets (CRU, GPCP, GPCC and CPC) was taken. Global mean values of these four precipitation datasets range from 2 to 2.2 mm day^{-1}. The dataset-median of the merged synthesis ET product is indicated with a solid line, and the IQRs with dash-dotted lines. The single datasets are indicated with different symbols (groups) and colors (ET schemes).

We first compare simulations from the GSWP and the WaterMIP projects, which are each based on common forcing datasets (filled circles and stars/rhombi, respectively). The spread within the GSWP and WaterMIP simulations is similar, both globally and in most climate regions (see Fig. A3). However, the spread in the WaterMIP ensemble is smaller in some dry regions (Cs, Dw and Df), and larger in wetter regions (all equatorial regions). Looking at the WaterMIP *GHMs* and *LSMs* separately, we find that the *GHMs* (stars) are not separated from the *LSMs* (rhombi), which supports the findings from Haddeland et al. (2011), that this classification does not fully account for differences among the WaterMIP models.

In order to compare the influence of uncertainties in precipitation forcing to model structure, sensitivity simulations using the same model (here, the COLA model) and different precipitation forcing have been performed in the framework of GSWP (Schlosser and Gao, 2010) and are included in the Fig. A3. Evapotranspiration from simulations with differing precipitation (GSWP sens, noted with empty circles) shows a smaller range than from GSWP simulations from different models using the same forcing (filled

circles), which has also been shown in Schlosser and Gao (2010). However, note that global mean ET from these sensitivity simulations is relatively low, indicating dry conditions in the COLA model, even if a forcing with high precipitation was employed. This possibly points to a dry bias of the model independently of the applied precipitation forcing, which could be the reason for the separation of this GSWP model in the cluster analyses reported in Mueller et al. (2011b).

The merged synthesis product based on all datasets exhibits a value of 1.5 mm day^{-1}. Note that the global mean values in the analyses for Fig. 5 are higher than the ones given in Table 4. The reason is that for the analyses of single datasets, we only included those pixels of the merged product that were also available in all other datasets. Table 4, on the other hand, includes all land pixels.

The largest exceedance of precipitation over ET, on average, is found in the wettest climate regimes (Af, Am, Aw, Cw, Cf and Df), as expected. In several dry regions, especially the arid desert (BW) and arid steppe (BS) regions, some datasets reveal an ET exceedance over precipitation (see bisecting line through origin in Fig. A3). The reasons could be (1) ET is too high, (2) precipitation is too low, (3) both ET and precipitation are correct, but the net depletion of soil water storage is larger than the volume of runoff generated over the period 1989–1995.

A comparison of the range between the lowest and highest values in precipitation and ET shows that the uncertainties in precipitation are larger than those of the ET datasets. This is not only the case for the global mean values, but also for single climate regions (Fig. A3). Large uncertainties in precipitation datasets have also recently been highlighted in Lorenz and Kunstmann (2012). The reason for smaller uncertainties in ET than in precipitation could be that ET estimates are constrained not only by the water, but also by the energy balance. This indicates that the uncertainty range in ET estimates will be difficult to reduce as long as the uncertainties in precipitation and radiation are not reduced. Jimenez et al. (2011), e.g. showed that the spread in net radiation datasets is nearly as large as the one in ET.

4 Conclusions

The intensity of the hydrological cycle determines the water availability and influences the climate system in various ways. Despite the important impacts of the hydrological cycle and one of its key variable, ET, a global benchmark ET dataset has long been missing. In the framework of the LandFlux-EVAL initiative (www.iac.ethz.ch/url/LandFlux-EVAL), several ET datasets based on observations (diagnostic datasets, LSMs and reanalyses) have been evaluated in previous studies (Mueller et al., 2011b; Jimenez et al., 2011), focusing on multi-annual means and seasonal cycles. The present study further investigates ET datasets. Global merged benchmarking ET products are derived and trends are analyzed in single LandFlux-EVAL datasets as well as the merged ET products.

The benchmark synthesis products provide monthly estimates for the time periods 1989–1995 (*short*) and 1989–2005 (*long*), respectively. For the creation of the *short* benchmark products, 7 diagnostic datasets, 29 LSMs and 4 reanalyses are considered, for the *long* products 5 diagnostic, 5 LSMs and 4 reanalyses. In order to address several demands on benchmark datasets, we created *short* and *long* merged synthesis products based on all datasets as well as based on each category. Monthly radiation is used as a physical constraint on maximum ET, and a statistical outlier detection is applied on the monthly ET estimates.

Evapotranspiration from the merged synthesis benchmark products shows realistic interannual variations that correspond to those found in a previous study based on a smaller number of ET datasets (Jung et al., 2010). The negative trend in *global land ET*[1] between 1998–2005 amounts to 18.9 $km^3 yr^{-2}$. Most of this trend is attributed to the equatorial winter dry, arid desert and arid steppe regions. The latter two regions are determined by low per area ET and precipitation, but cover very large areas of the northern and Southern Hemisphere. Dividing these arid desert and steppe regions into

[1] After a space and time matching of all datasets, data coverage of roughly 90 % of the land surface was attained.

northern and Southern Hemisphere fractions, we find that the negative trend change arises from the southern part only, which is consistent with the results of Jung et al. (2010). However it is important to note that the signal is very small compared to the overall global land ET as well as compared to the uncertainty of absolute ET values (interquartile range or standard deviations of the merged synthesis products). In addition, it is still unclear whether this signal corresponds to a long-term trend or decadal variability. Finally, because of the reliance of all ET datasets on atmospheric input datasets, the influence of spurious trends in these datasets cannot be excluded.

Large uncertainties in absolute values of ET are found, which can partly be related to uncertainties in precipitation. Precipitation is both one of the main drivers for ET in water-limited evaporation regimes and overall in forests where interception can be large. As a consequence, it belongs to one of the main forcing variables for ET used in most diagnostic datasets and LSMs. Indeed, the spread in ET datasets is smaller than the spread in the corresponding precipitation datasets in our global analyses as well as in most climatic regions, which indicates that ET is not only constrained by precipitation, but also by other variables such as radiation. In general, the absolute values of precipitation are higher than ET, as expected, globally and in wet climate regions. Global mean ET in the merged synthesis product amounts to 1.35 mm per day, while precipitation to 2.07 mm per day (average of four observations-based datasets). The difference of 34 406 $km^3 yr^{-1}$ (runoff) is in agreement with previous studies (an overview can be found in Syed et al., 2009). In dry regions, ET exceeds precipitation in several datasets. The merged synthesis product's (median) ET is always lower than average precipitation.

In summary, we have presented here the first benchmark synthesis products for monthly, global land ET estimates. A reproduction of a negative trend in global ET during 1998–2005 with these benchmark synthesis products supports previous findings of a declining global ET trend over that period. However, caution is necessary when analyzing trends, because the considered time period is very short for trend analyses, the analyzed ET datasets are not totally independent from each other (e.g. same forcing

data, similar methodologies), and agreement between them is not necessarily an indicator of their validity. Furthermore, spurious trends can be introduced through changes in the observing systems for the forcing variables (e.g. precipitation, radiation) of ET. In order to gain more confidence in ET estimates, not only are improvements in model parameterizations necessary, but so is a reduction of uncertainties in precipitation and radiation data in order to better constrain ET.

Appendix A

Precipitation datasets

A The observation-based precipitation datasets are from the Climate Research Unit (CRU) at the University of East Anglia, the Global Precipitation Climatology Centre (GPCC), the Global Precipitation Climatology Project (GPCP) and the unified gauge-based analysis of global daily preciptation from the climate prediction center (CPC) from the National Oceanic and Atmospheric Administration (NOAA Chen et al., 2008). These datasets are chosen for this investigation because (a) they are mainly based on observations, (b) they cover the period 1989–2005, and (c) they are forcing datasets employed for the diagnostic ET datasets used in this study.

The CRU precipitation data are based on rain gauge data, whose number varies over time between around 5000 and nearly 15 000 stations. The CRU TS3.1 dataset covers the period 1901–2009. It has not been corrected for gauge biases, which vary with gauge type and can result in inhomogeneities in the records (New et al., 2000).

The NOAA CPC unified precipitation dataset is created from quality-controlled daily precipitation gauge data, taking advantage of the optimal interpolation objective analysis technique (Chen et al., 2008). The retrospective version, covering 1979 to 2005, includes more than 30 000 gauge station data.

The GPCC monitoring product for the period 1986 to present is based on quality-controlled data from 7000 stations, which are interpolated into monthly area averages.

This product delivers the in-situ component for the satellite (microwave and infrared)-gauge combination GPCP (Huffman et al., 1995; Adler et al., 2003). The GPCP product includes gauge-bias corrections, but due to the limited length of satellite records, inhomogeneities arise (Adler et al., 2003).

Supplementary material related to this article is available online at: http://www.hydrol-earth-syst-sci-discuss.net/10/769/2013/hessd-10-769-2013-supplement.zip.

Acknowledgements. The LandFlux-EVAL project was coordinated under the Global Energy and Water Exchanges (GEWEX) LandFlux initiative. We also acknowledge the support of the Integrated Land Ecosystem-Atmosphere Processes Study, iLEAPS, in the development of the synthesis products. CRU data were obtained from the University of East Anglia Climate Research Unit (CRU), British Atmospheric Data Centre, 2008, available from http://badc.nerc.ac.uk/data/cru. The GPCP combined precipitation data were developed and computed by the NASA/Goddard Space Flight Center's Laboratory for Atmospheres as a contribution to the GEWEX Global Precipitation Climatology Project. GPCC precipitation data are available from the GPCC Homepage: http://gpcc.dwd.de. CPC merged analysis of precipitation data were provided by the NOAA/OAR/ESRL PSD, Boulder, Colorado, USA, from their Web site at http://www.esrl.noaa.gov/psd/. We acknowledge the Global Modeling and Assimilation Office and the GES DISC for the dissemination of MERRA and MERRA-LAND, and the ECMWF for the dissemination of ERA-Interim data. The CFSR data are from the Research Data Archive which is maintained by the Computational and Information Systems Laboratory at the National Center for Atmospheric Research (NCAR). NCAR is sponsored by the National Science Foundation. The original data are available from the RDA (http://dss.ucar.edu) in dataset number ds093.0. We would further like to acknowledge the Japanese 25-yr ReAnalysis and JMA Climate Data Assimilation System (JCDAS) for the dissemination of JRA-25 data. JBF contributed to this work at the Jet Propulsion Laboratory, California Institute of Technology, under a contract with the National Aeronautics and Space Administration. In addition, several authors were partially funded by EU-PF7 projects. We would like to thank Zhichang Guo from COLA for providing the GSWP sensitivity simulations.

References

Adler, R. F., Huffman, G. J., Chang, A., Ferraro, R., Xie, P. P., Janowiak, J., Rudolf, B., Schneider, U., Curtis, S., Bolvin, D., Gruber, A., Susskind, J., Arkin, P., and Nelkin, E.: The version-2 global precipitation climatology project (GPCP) monthly precipitation analysis (1979-present), J. Hydrometeorol., 4, 1147–1167, 2003. 786

Bengtsson, L., Hagemann, S., and Hodges, K. I.: Can climate trends be calculated from reanalysis data?, J. Geophys. Res.-Atmos., 109, D11111, doi:10.1029/2004JD004536, 2004. 774

Biemans, H., Hutjes, R. W. A., Kabat, P., Strengers, B. J., Gerten, D., and Rost, S.: Effects of precipitation uncertainty on discharge calculations for main river basins, J. Hydrometeorol., 10, 1011–1025, doi:10.1175/2008JHM1067.1, 2009. 779

Bosilovich, M. G.: NASA's modern era retrospective-analysis for research and applications: Integrating Earth observations, available at: www.earthzine.org/2008/09/26/nasas-modern-era-retrospective-analysis (last access: 20 December 2012), 26 September 2008. 795

Chen, M. Y., Shi, W., Xie, P. P., Silva, V. B. S., Kousky, V. E., Higgins, R. W., and Janowiak, J. E.: Assessing objective techniques for gauge-based analyses of global daily precipitation, J. Geophys. Res.-Atmos., 113, D04 110. doi:10.1029/2007JD009132, 2008. 785

Dai, A., Fung, I. Y., and DelGenio, A. D.: Surface observed global land precipitation variations during 1900–88, J. Climate, 10, 2943–2962, doi:10.1175/1520-0442(1997)010<2943:SOGLPV>2.0.CO;2, 1997. 773

Dee, D. P., Uppala, S. M., Simmons, A. J., Berrisford, P., Poli, P., Kobayashi, S., Andrae, U., Balmaseda, M. A., Balsamo, G., Bauer, P., Bechtold, P., Beljaars, A. C. M., van de Berg, L., Bidlot, J., Bormann, N., Delsol, C., Dragani, R., Fuentes, M., Geer, A. J., Haimberger, L., Healy, S. B., Hersbach, H., Hólm, E. V., Isaksen, L., Kållberg, P., Köhler, M., Matricardi, M., McNally, A. P., Monge-Sanz, B. M., Morcrette, J.-J., Park, B.-K., Peubey, C., de Rosnay, P., Tavolato, C., Thépaut, J.-N., and Vitart, F.: The ERA-Interim reanalysis: configuration and performance of the data assimilation system, Q. J. Roy. Meteorol. Soc., 137, 553–597, 2011. 795

Dirmeyer, P. A., Gao, X. A., Zhao, M., Guo, Z. C., Oki, T. K., and Hanasaki, N.: GSWP-2 – multimodel anlysis and implications for our perception of the land surface, B. Am. Meteorol. Soc., 87, 1381–1397, 2006. 780, 794

Douville, H., Ribes, A., Decharme, B., Alkama, R., and Sheffield, J.: Anthropogenic influence on multidecadal changes in reconstructed global evapotranspiration, Nature Climate Change, 3, 59–62, doi:10.1038/nclimate1632, 2013. 773

Fisher, J. B., Tu, K. P., and Baldocchi, D. D.: Global estimates of the land-atmosphere water flux based on monthly AVHRR and ISLSCP-II data, validated at 16 FLUXNET sites, Remote Sens. Environ., 112, 901–919, doi:10.1016/j.rse.2007.06.025, 2008. 794

Haddeland, I., Clark, D. B., Franssen, W., Ludwig, F., Voss, F., Arnell, N. W., Bertrand, N., Best, M., Folwell, S., Gerten, D., Gomes, S., Gosling, S. N., Hagemann, S., Hanasaki, N., Harding, R., Heinke, J., Kabat, P., Koirala, S., Oki, T., Polcher, J., Stacke, T., Viterbo, P., Weedon, G. P., and Yeh, P.: Multimodel Estimate of the global terrestrial water balance: setup and first results, J. Hydrometeorol., 12, 869–884, doi:10.1175/2011JHM1324.1, 2011. 775, 776, 780, 781, 794

Huffman, G. J., Adler, R. F., Rudolf, B., Schneider, U., and Keehn, P. R.: Global precipitation estimates based on a technique for combining satellite-based estimates, rain-gauge analysis, and NWP model precipitation information, J. Climate, 8, 1284–1295, doi:10.1175/1520-0442(1995)008<1284:GPEBOA>2.0.CO;2, 1995. 786

IPCC: Summary for policymakers, in: Intergovernmental Panel on Climate Change Special Report on Managing the Risks of Extreme Events and Disasters to Advance Climate Change Adaptation, Cambridge University Press, edited by: Field, C. B., Barros, V., Stocker, T. F., Qin, D., Dokken, D. J., Ebi, K. L., Mastrandrea, M. D., Mach, K. J., Plattner, G.-K., Allen, S. K., Tignor, M., and Midgley, P. M., Cambridge, UK and New York, NY, USA, 2011. 774

Jimenez, C., Prigent, C., Mueller, B., Seneviratne, S. I., McCabe, M. F., Wood, E. F., Rossow, W. B., Balsamo, G., Betts, A. K., Dirmeyer, P. A., Fisher, J. B., Jung, M., Kanamitsu, M., Reichle, R. H., Reichstein, M., Rodell, M., Sheffield, J., Tu, K., and Wang, K.: Global intercomparison of 12 land surface heat flux estimates, J. Geophys. Res.-Atmos., 116, D02102, doi:10.1029/2010JD014545, 2011. 772, 776, 782, 783

Jung, M., Reichstein, M., and Bondeau, A.: Towards global empirical upscaling of FLUXNET eddy covariance observations: validation of a model tree ensemble approach using a biosphere model, Biogeosciences, 6, 2001–2013, doi:10.5194/bg-6-2001-2009, 2009. 773, 794

Jung, M., Reichstein, M., Ciais, P., Seneviratne, S. I., Sheffield, J., Goulden, M. L., Bonan, G., Cescatti, A., Chen, J. Q., de Jeu, R., Dolman, A. J., Eugster, W., Gerten, D., Gianelle, D., Gobron, N., Heinke, J., Kimball, J., Law, B. E., Montagnani, L., Mu, Q. Z., Mueller, B., Oleson, K., Papale, D., Richardson, A. D., Roupsard, O., Running, S., Tomelleri, E., Viovy, N.,

Weber, U., Williams, C., Wood, E., Zaehle, S., and Zhang, K.: Recent decline in the global land evapotranspiration trend due to limited moisture supply, Nature, 467, 951–954, doi:10.1038/nature09396, 2010. 773, 778, 779, 780, 783, 784

Krinner, G., Viovy, N., de Noblet-Ducoudre, N., Ogee, J., Polcher, J., Friedlingstein, P., Ciais, P., Sitch, S., and Prentice, I. C.: A dynamic global vegetation model for studies of the coupled atmosphere-biosphere system, Global Biogeochem. Cy., 19, GB1015, doi:10.1029/2003GB002199, 2005. 795

Lorenz, C. and Kunstmann, H.: The hydrological cycle in three state-of-the-art reanalyses: intercomparison and performance analysis, J. Hydrometeor, 13, 1397–1420, doi:10.1175/JHM-D-11-088.1, 2012. 774, 782

Miralles, D. G., De Jeu, R. A. M., Gash, J. H., Holmes, T. R. H., and Dolman, A. J.: Magnitude and variability of land evaporation and its components at the global scale, Hydrol. Earth Syst. Sci., 15, 967–981, doi:10.5194/hess-15-967-2011, 2011a. 775, 776, 794

Miralles, D. G., Holmes, T. R. H., De Jeu, R. A. M., Gash, J. H., Meesters, A. G. C. A., and Dolman, A. J.: Global land-surface evaporation estimated from satellite-based observations, Hydrol. Earth Syst. Sci., 15, 453–469, doi:10.5194/hess-15-453-2011, 2011b. 776, 794

Mueller, B. and Seneviratne, S. I.: Hot days induced by precipitation deficits at the global scale, P. Natl. Acad. Sci. USA, 109, 12398–12403, doi:10.1073/pnas.1204330109, 2012. 774

Mueller, B., Hirschi, M., and Seneviratne, S. I.: New diagnostic estimates of variations in terrestrial water storage based on ERA-Interim data, Hydrol. Process., 25, 996–1008, doi:10.1002/hyp.7652, 2011a. 794

Mueller, B., Seneviratne, S. I., Jimenez, C., Corti, T., Hirschi, M., Balsamo, G., Ciais, P., Dirmeyer, P., Fisher, J. B., Guo, Z., Jung, M., Maignan, F., McCabe, M. F., Reichle, R., Reichstein, M., Rodell, M., Sheffield, J., Teuling, A. J., Wang, K., Wood, E. F., and Zhang, Y.: Evaluation of global observations-based evapotranspiration datasets and IPCC AR4 simulations, Geophys. Res. Lett., 38, L06402, doi:10.1029/2010GL046230, 2011b. 772, 774, 775, 776, 778, 782, 783

New, M., Hulme, M., and Jones, P.: Representing twentieth-century space-time climate variability. Part II: Development of 1901–96 monthly grids of terrestrial surface climate, J. Climate, 13, 2217–2238, 2000. 785

New, M., Todd, M., Hulme, M., and Jones, P.: Precipitation measurements and trends in the twentieth century, Int. J. Climatol., 21, 1899–1922, 2001. 773

Onogi, K., Tslttsui, J., Koide, H., Sakamoto, M., Kobayashi, S., Hatsushika, H., Matsumoto, T., Yamazaki, N., Kaalhori, H., Takahashi, K., Kadokura, S., Wada, K., Kato, K., Oyama, R., Ose, T., Mannoji, N., and Taira, R.: The JRA-25 reanalysis, J. Meteorol. Soc. Jpn., 85, 369–432, 2007. 795

Reichle, R., Koster, R., De Lannoy, G., Forman, B., Liu, Q., Mahanama, S., and Toure, A.: Assessment and enhancement of MERRA land surface hydrology estimates, J. Climate, 24, 6322–6338, doi:10.1175/JCLI-D-10-05033.1, 2011. 795

Rodell, M., Famiglietti, J. S., Chen, J., Seneviratne, S. I., Viterbo, P., Holl, S., and Wilson, C. R.: Basin scale estimates of evapotranspiration using GRACE and other observations, Geophys. Res. Lett., 31, L20504, doi:10.1029/2004GL020873, 2004. 775

Rui, H.: README Document for Global Land Data Assimilation System Version 2 (GLDAS-2) Products, GES DISC, 2011. 775

Saha, S., Moorthi, S., Pan, H. L., Wu, X. R., Wang, J. D., Nadiga, S., Tripp, P., Kistler, R., Woollen, J., Behringer, D., Liu, H. X., Stokes, D., Grumbine, R., Gayno, G., Wang, J., Hou, Y. T., Chuang, H. Y., Juang, H. M. H., Sela, J., Iredell, M., Treadon, R., Kleist, D., Van Delst, P., Keyser, D., Derber, J., Ek, M., Meng, J., Wei, H. L., Yang, R. Q., Lord, S., Van den Dool, H., Kumar, A., Wang, W. Q., Long, C., Chelliah, M., Xue, Y., Huang, B. Y., Schemm, J. K., Ebisuzaki, W., Lin, R., Xie, P. P., Chen, M. Y., Zhou, S. T., Higgins, W., Zou, C. Z., Liu, Q. H., Chen, Y., Han, Y., Cucurull, L., Reynolds, R. W., Rutledge, G., and Goldberg, M.: The NCEP climate forecast system reanalysis, B. Am. Meteorol. Soc., 91, 1015–1057, doi:10.1175/2010BAMS3001.1, 2010. 795

Schlosser, C. A. and Gao, X. A.: Assessing Evapotranspiration Estimates from the Second Global Soil Wetness Project (GSWP-2) Simulations, J. Hydrometeorol., 11, 880–897, doi:10.1175/2010JHM1203.1, 2010. 781, 782

Seneviratne, S. I.: Climate science: historical drought trends revisited, Nature, 491, 338–339, doi:10.1038/491338a, 2012. 772

Seneviratne, S. I., Viterbo, P., Lüthi, D., and Schär, C.: Inferring changes in terrestrial water storage using ERA-40 reanalysis data: the Mississippi River basin, J. Climate, 17, 2039–2057, 2004. 774

Seneviratne, S. I., Corti, T., Davin, E. L., Hirschi, M., Jaeger, E. B., Lehner, I., Orlowsky, B., and Teuling, A. J.: Investigating soil moisture-climate interactions in a changing climate: a review, Earth-Sci. Rev., 99, 125–161, doi:10.1016/j.earscirev.2010.02.004, 2010. 774

Sheffield, J. and Wood, E. F.: Characteristics of global and regional drought, 1950–2000: analysis of soil moisture data from off-line simulation of the terrestrial hydrologic cycle, J. Geophys. Res.-Atmos., 112, D17115-1-21, doi:10.1029/2006JD008288, 2007. 795

Sheffield, J., Goteti, G., and Wood, E. F.: Development of a 50-year high-resolution global dataset of meteorological forcings for land surface modeling, J. Climate, 19, 3088–3111, doi:10.1175/JCLI3790.1, 2006. 775, 794, 795

Sheffield, J., Wood, E. F., and Munoz-Arriola, F.: Long-term regional estimates of evapotranspiration for Mexico based on downscaled ISCCP data, J. Hydrometeorol., 11, 253–275, doi:10.1175/2009JHM1176.1, 2010. 794

Sheffield, J., Wood, E. F., and Roderick, M. L.: Little change in global drought over the past 60 years, Nature, 491, 435–438, doi:10.1038/nature11575, 2012. 772, 774

Syed, T. H., Famiglietti, J. S., and Chambers, D. P.: GRACE-based estimates of terrestrial freshwater discharge from basin to continental scales, J. Hydrometeorol., 10, 22–40, doi:10.1175/2008JHM993.1, 2009. 780, 784

Teuling, A. J., Hirschi, M., Ohmura, A., Wild, M., Reichstein, M., Ciais, P., Buchmann, N., Ammann, C., Montagnani, L., Richardson, A. D., Wohlfahrt, G., and Seneviratne, S. I.: A regional perspective on trends in continental evaporation, Geophys. Res. Lett., 36, L02404, doi:10.1029/2008GL036584, 2009. 774

Trenberth, K. E., Fasullo, J. T., and Kiehl, J.: Earth's global energy budget, B. Am. Meteorol. Soc., 90, 311–323, 2009. 780

Wang, K. C. and Dickinson, R. E.: A review of global terrestrial evapotranspiration: observation, modeling, climatology, and climatic variability, Rev. Geophys., 50, RG2005, doi:10.1029/2011RG000373, 2012. 780

Wang, K. C. and Liang, S. L.: An improved method for estimating global evapotranspiration based on satellite determination of surface net radiation, vegetation index, temperature, and soil moisture, J. Hydrometeorol., 9, 712–727, doi:10.1175/2007JHM911.1, 2008. 794

Wang, K. C., Dickinson, R. E., Wild, M., and Liang, S. L.: Evidence for decadal variation in global terrestrial evapotranspiration between 1982 and 2002: 1. Model development, J. Geophys. Res.-Atmos., 115, D20112, doi:10.1029/2009JD013671, 2010a. 773

Wang, K. C., Dickinson, R. E., Wild, M., and Liang, S. L.: Evidence for decadal variation in global terrestrial evapotranspiration between 1982 and 2002: 2. Results, J. Geophys. Res.-Atmos., 115, D20113, doi:10.1029/2010JD013847, 2010b. 773

Weedon, G. P.: WATCH Technical Report Number 37, Creation of the WATCH 20th Century Ensemble Product, Tech. rep., UK Met Office, Exeter, UK, 2011. 777

Weedon, G. P., Gomes, S., Viterbo, P., Shuttleworth, W. J., Blyth, E., Osterle, H., Adam, J. C., Bellouin, N., Boucher, O., and Best, M.: Creation of the WATCH forcing data and its use to assess global and regional reference crop evaporation over land during the twentieth century, J. Hydrometeorol., 12, 823–848, doi:10.1175/2011JHM1369.1, 2011. 776, 794

Yao, Y. J., Liang, S. L., Qin, Q. M., Wang, K. C., Liu, S. M., and Zhao, S. H.: Satellite detection of increases in global land surface evapotranspiration during 1984–2007, International Journal of Digital Earth, 5, 299–318, doi:10.1080/17538947.2011.598953, 2012. 773

Zhang, Y. Q., Leuning, R., Hutley, L. B., Beringer, J., McHugh, I., and Walker, J. P.: Using long-term water balances to parameterize surface conductances and calculate evaporation at 0.05 degrees spatial resolution, Water Resour. Res., 46, W05512, doi:10.1029/2009WR008716, 2010. 794

Table 1. Number and type of datasets included in the 8 different merged synthesis products.

Merged synthesis products based on	Number of datasets 1989–1995 (denoted *short*)	Number of datasets 1989–2005 (denoted *long*)
All dataset categories	40	14
Diagnostic	7	5
LSMs	29	5
Reanalyses	4	4

Table 2. Overview of ET datasets, including their ET scheme or land-surface schemes (LSS), along with the number of soil layers, precipitation forcing dataset and atmospheric forcing variables. Model names with a star are classified as global hydrological models (GHMs, see text). Forcing variables are P: precipitation; T: air temperature; W: wind speed; Q: specific humidity; R: radiation; SP: surface pressure. "na" denotes either not applicable or information currently not available. Note that GS-VISA and GS-CLMTOP cannot strictly be classified as aerodynamic approaches, since they include a carbon cycle and photosynthetic control on transpiration. Models with an x are included in the 1989–2005 merged synthesis product.

	Group	Name	ET scheme/ LSS for reanalyses	89-05	No. soil layers	Precipitation forcing datasets	Atmosph. forcing variables	Reference
Diagnostic		PT-JPL*	Priestley-Taylor		0	Not required	T,Q,R,red/NIR reflectances	Fisher et al. (2008)
		MAUNI	Empirical		na	Not required	na	Wang and Liang (2008)
		PRUNI	Penman-Monteith	x	na	Sheffield et al. (2006)	na	Sheffield et al. (2010)
		MPIBGC	Empirical	×	na	GPCC	na	Jung et al. (2009)
		CSIRO	Penman-Monteith	×	na	GPCC	na	Zhang et al. (2010)
		GLEAM v1A	Priestley-Taylor	×	3	CPC unified precip	na	Miralles et al. (2011b,a)
		AWB	None	×	na	GPCP	na	Mueller et al. (2011a)
LSMs and GHMs	GSWP	GS-COLA	Aerodynamic		6	NCEP, GPCC, GPCP (CRU for spin-up)	P,T,W,Q,R, SP	Dirmeyer et al. (2006)
		GS-NOAH	Penman-Monteith		4		P,T,W,Q,R, SP	
		GS-NSIPP	Aerodynamic		3		P,T,W,Q,R, SP	
		GS-VISA	Aerodynamic		10		P,T,W,Q,R, SP	
		GS-ISBA	Aerodynamic		3		P,T,W,Q,R, SP	
		GS-BUCKET	Aerodynamic		1		P,T,W,Q,R, SP	
		GS-CLMTOP	Aerodynamic		10		P,T,W,Q,R, SP	
		GS-HY-SSIB	Aerodynamic		3		P,T,W,Q,R, SP	
		GS-LAD	Aerodynamic		1		P,T,W,Q,R, SP	
		GS-MOSAIC	Penman-Monteith		3		P,T,W,Q,R, SP	
		GS-MOSES2	Penman-Monteith		4		P,T,W,Q,R, SP	
		GS-SIBUC	Aerodynamic		3		P,T,W,Q,R, SP	
		GS-SWAP	Penman-Monteith		2		P,T,W,Q,R, SP	
	WaterMIP	WM-GWAVA*	Penman-Monteith		multi	WATCH (Weedon et al., 2011)	P,T,W,Q,R, SP	Haddeland et al. (2011)
		WM-H08	Aerodynamic		1		P,T,W,Q,R, SP	
		WM-HTESSEL	Penman-Monteith		4		P,T,W,Q,R, SP	
		WM-JULES	Penman-Monteith		4		P,T,W,Q,R, SP	
		WM-LPJmL*	Priestley-Taylor		2		P,T,R	
		WM-MacPDM*	Penman-Monteith		multi		P,T,W,Q,R	
		WM-MATSIRO	Aerodynamic		5		P,T,W,Q,R, SP	
		WM-MPI*	Thornthwaite		1		P,T	
		WM-Orchidee	Aerodynamic		11		P,T,W,Q,R, SP	
		WM-VIC	Penman-Monteith		2		P,T,W,Q,R, SP	
		WM-WaterGAP*	Priestley-Taylor		multi		P,T,R	

* Referred to as UCB in Mueller et al. (2011a).

Table 2. Continued.

	Group	Name	ET scheme/ LSS for reanalyses	89-05	No. soil layers	Precipitation forcing datasets	Atmosph. forcing variables	Reference
	ORCH	EI-ORCH	Aerodynamic	×	2	ERA-Interim	P,T,W,Q,R, SP	Krinner et al. (2005)
		CRU-ORCH	Aerodynamic	×	11	CRU, NCEP	P,T,W,Q,R, SP	
	VIC	VIC	Penman-Monteith	×	2	obs. and NCEP	P,T,W,Q,R, SP	Sheffield and Wood (2007)
	NOAH-PF	GL-NOAHPF	Penman-Monteith	×	4	Sheffield et al. (2006)	P,T,W,Q,R, SP	
	MERRA-LAND	M-LAND	Penman-Monteith	×	na	Replay of MERRA-reanalysis	P,T,W,Q,R, SP	Reichle et al. (2011)
Reanalyses		ERAINT (ERA-Interim)	TESSEL	×	na			Dee et al. (2011)
		CFSR (CFSR-NCEP)	NOAH	×	na			Saha et al. (2010)
		JRA (JRA-25)	SiB	×	na			Onogi et al. (2007)
		MERRA	GEOS-5 Catchment LSM	×	na			Bosilovich (2008)

Table 3. Slope of trends for the two time periods 1989–1997 and 1998–2005 of the merged (all) product and the single datasets. The slopes are estimated with the Theil-Sen estimator, which is robust against outliers. Significant values (non parametric Mann-Kendal two-sided test at 90 %-level) are printed in italic font.

Dataset	Trend 1989–1997 mm yr^{-2}	Trend 1998–2005 mm yr^{-2}
Merged (all)	1.15	*−1.40*
AWB	−2.12	0.95
PRUNI	0.76	4.37
MPIBGC	0.39	0.06
CSIRO	1.78	−1.41
GLEAM	*1.69*	−2.96
VIC	−0.10	−0.26
EI-ORCH	0.82	*−1.28*
CRU-ORCH	−0.19	−1.27
GL-NOAHPF	0.75	*−1.30*
M-LAND	−0.18	*−2.33*
ERAINT	1.75	*−2.98*
MERRA	3.41	−0.45
JRA	−0.11	*−4.07*
CFSR	2.40	−0.78

Table 4. Mean ET of merged synthesis products 1989–2005 (*long*), 1989–1995 (*short*), mean precipitation 1989–2005 (average of CRU, GPCC, GPCP and CPC) and ET and precipitation trends 1998–2005 in climate regions. Slope of trends (Theil-Sen) and significance (italic font, Mann-Kendal) estimated as for Table 3.

Climate region	Abbreviation	Area [10^3 km^2]	Mean ET synthesis long [mm d^{-1}]	Mean ET synthesis short [mm d^{-1}]	Mean precip CRU,GPCC, GPCP,CPC [mm d^{-1}]	ET trend 1998–2005 [km^3 yr^{-2}]	Mean precipitation trend 1998–2005 [km^3 yr^{-2}]
Equatorial fully humid	Af	5914	3.34	3.23	6.78	*−2.6*	−0.1
Equatorial monsoonal	Am	4822	3.16	3.02	5.55	*−1.6*	−2.4
Equatorial winter dry	Aw	16 687	2.52	2.49	3.47	*−9.0*	−4.6
Equatorial summer dry	As	745	2.05	2.09	2.77	0.0	1.0
Arid desert	BW north	19 247	0.27	0.27	0.29	1.9	5.9
Arid desert	BW south	4766	0.60	0.61	0.69	−4.1	−5.8
Arid steppe	BS north	9993	0.91	0.99	1.03	3.4	2.2
Arid steppe	BS south	6455	1.24	1.25	1.44	−6.5	−6.9
Warm temp. summer dry	Cs	3901	1.22	1.24	1.62	0.4	1.3
Warm temp. winter dry	Cw	5802	2.03	1.97	2.95	−0.7	−2.8
Warm temp. fully humid	Cf	11 533	1.87	2.03	3.11	−0.8	−8.0
Snow summer dry	Ds	1060	0.87	0.84	1.15	0.2	0.7
Snow winter dry	Dw	4777	1.05	1.08	1.33	0.5	3.7
Snow fully humid	Df	26 207	0.97	0.95	1.49	0.3	3.7
Polar	E	9012	0.46	0.42	1.05	−0.4	*4.9*
Global land		130 922	1.35	1.35	2.07	−18.9	−7.2

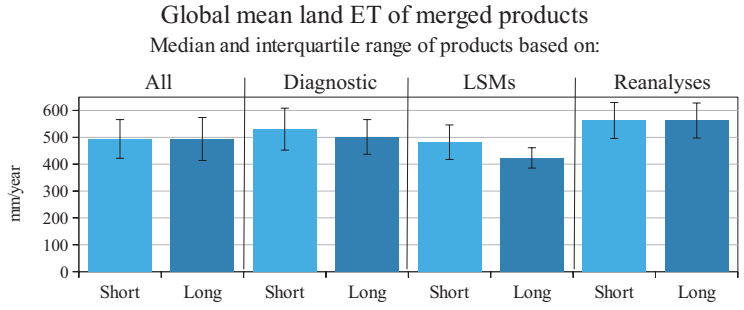

Fig. 1. Global mean ET of merged synthesis products based on all datasets, only the diagnostic, only LSMs and only reanalyses. The medians and interquartile ranges for the short (1989–1995) and long (1989–2005) merged products are shown.

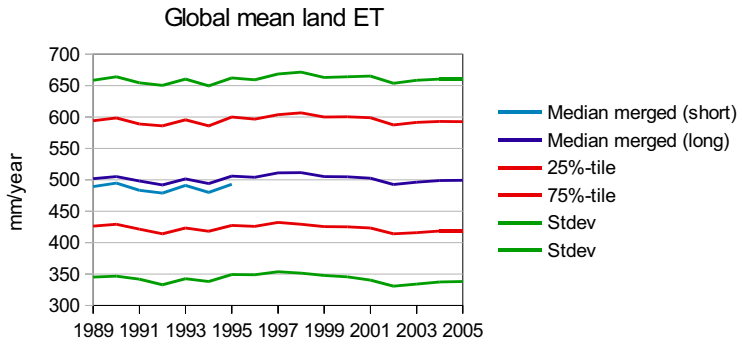

Fig. 2. Variation of global mean ET of merged synthesis products (based on all datasets). The median for both short (1989–1995) and long (1989–2005) products as well as the interquartile range and the standard deviation (median ±1 standard deviation) of the long product are shown.

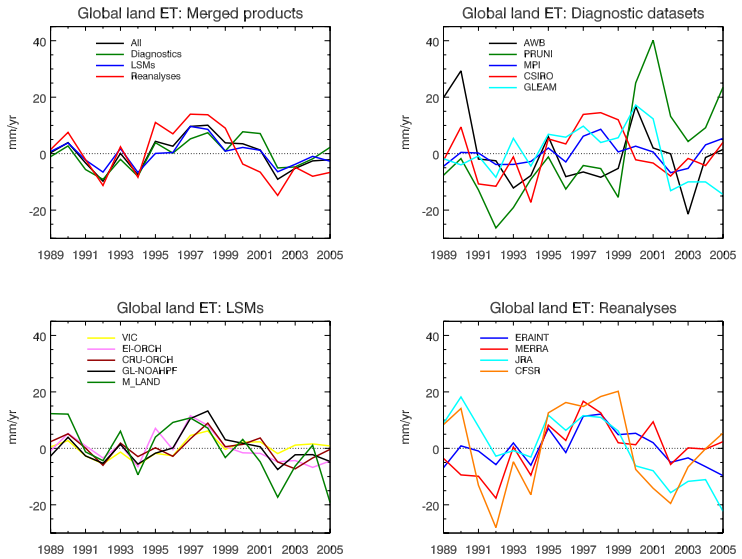

Fig. 3. Anomaly timeseries (1989–2005) of the four merged synthesis benchmark products (top left) and the individual diagnostic datasets (top right), LSMs (bottom left) and reanalyses (bottom right) that contribute to the long merged synthesis product.

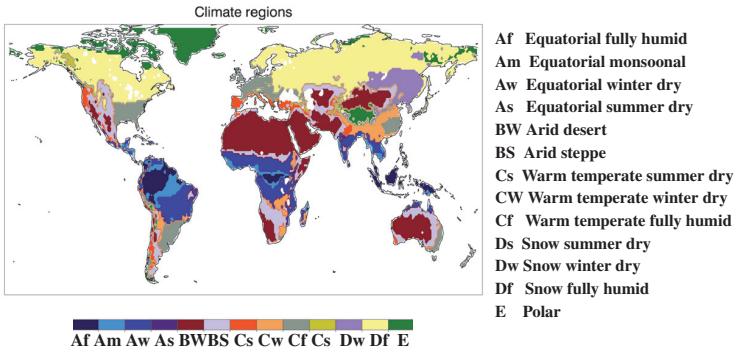

Fig. 4. Climate regions (Koeppen–Geiger classification).

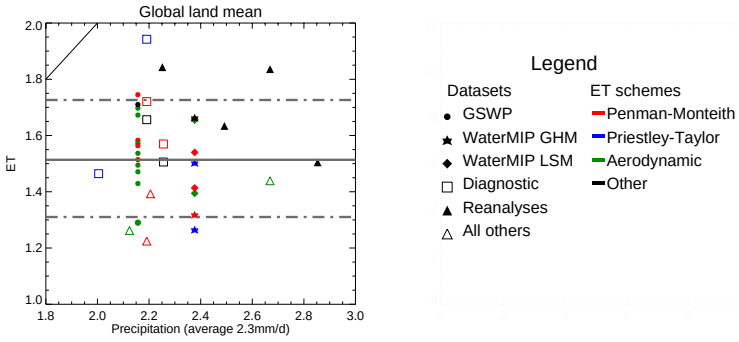

Fig. 5. Scatter plot of ET (in mm day^{-1}) from each dataset that is included in the short merged product (1989–1995) versus precipitation from the corresponding forcing dataset. If no precipitation data is used for the derivation of ET, the average of CRU, GPCP, CPC and GPCC has been used instead (see Table 2). The merged synthesis product's median is indicated with a full line, the IQR with dash-dotted lines. The precipitation value indicated is the average of all datasets.

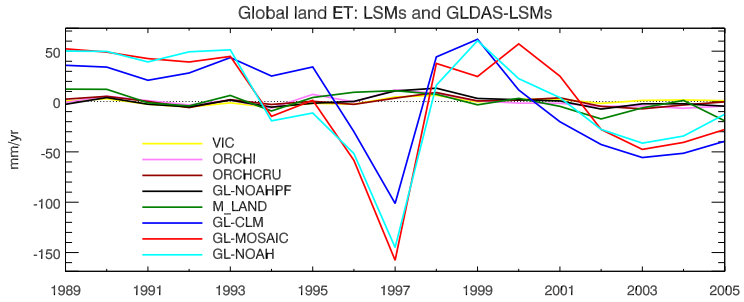

Fig. A1. Timeseries 1989–2005 of LSMs. In addition to the LSMs that contribute to the long merged synthesis product, GLDAS-I simulations from the models CLM, MOSAIC and NOAH are shown.

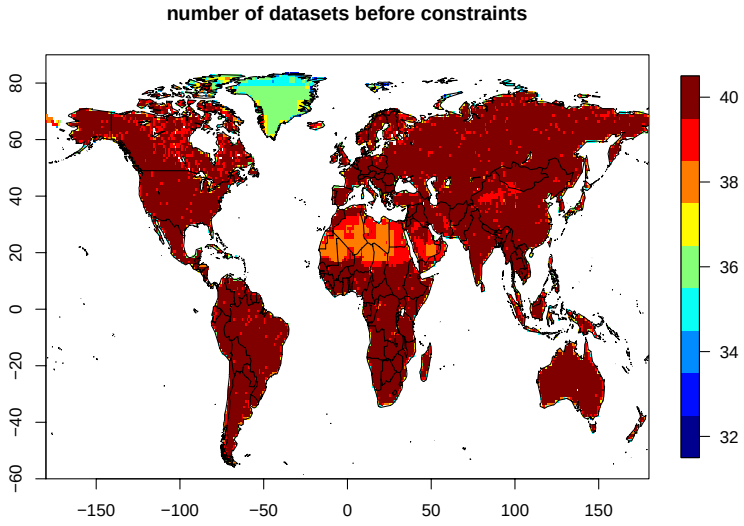

Fig. A2. Number of datasets available before applying the constraints at each pixel. For the number of datasets included in the final merged synthesis product (after constraints) at each month, see movie in Supplement online information.

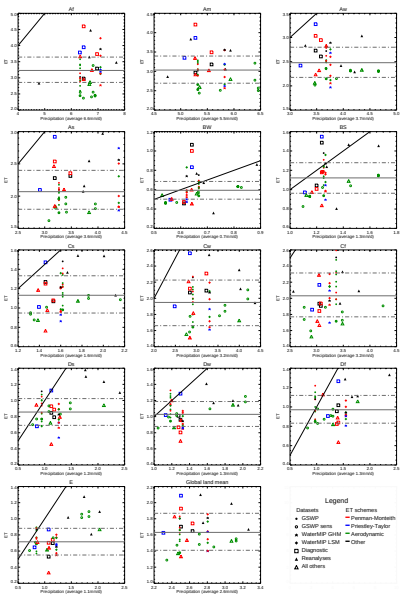

Fig. A3. Scatter plot for all different climate regions of ET (in mm day^{-1}) from each dataset that is included in the short merged products (1989–1995) as well as the GSWP sensitivity runs versus precipitation from the corresponding forcing dataset. If no precipitation data is used for the derivation of ET, the average of CRU, GPCP, CPC and GPCC has been used instead (see Table 2). The merged synthesis product's median is indicated with a full line, the IQR with dash-dotted lines. For abbreviations of climate regions, see Table 4.

Professor. Martin Todd
Department of Geography, University of Sussex, UK

CURRENT APPOINTMENT

2009-present. Professor of Climate Change, Department of Geography, University of Sussex
2009-present. Visiting Professor, Department of Geography, UCL, UK
Webpage: http://www.sussex.ac.uk/geography/profile249692.html

PREVIOUS EMPLOYMENT, RESEARCH POSITIONS AND EDUCATION

2006-2009: Reader in Climate Science, Department of Geography, UCL
2000-2006: Lecturer, Department of Geography, UCL
1996-2000: Lecturer, School of Geography, University of Oxford
1996-2000: Lecturer in Physical Geography, St. John's College, Oxford
1993-1996: Post-Doctoral Research Associate, University of Bristol
1992: PhD: University of Bristol, *'Estimating rainfall from satellite'*
1988-1989: Research Assistant, University of Stirling
1988: BSc Environmental Science (First Class Honours), University of Stirling

RESEARCH ACTIVITIES

- An internationally renowned climate scientist with over 20 years research experience
- 80 peer-reviewed publications
- H-Index of 29
- PI/Co-I on numerous international research projects
- Major research themes: climate change impacts; the water cycle; atmospheric aerosols.
- Research aims: To improve climate information and services for adaptation planning
- Strong multi-disciplinary emphasis
- Regional specialisation in African climate

SELECTED RECENT GRANTS

Total grant income exceeds £6 million. Recent examples:

- The Saharan Climate system ('Fennec'), NERC Consortium, 2010-2014, Co-I (£3.5M)
- 'Enhancing water for food: poverty reduction through improved management of ecosystem services for sustainable food production in sub-Saharan Africa' NERC/DFID/ESRC ESPA [£48k]**, Co-I**
- Global-scale impacts of climate change: an integrated multi-sectoral assessment (QUEST-GSI), NERC QUEST Theme III, 2007-9, Co-I (£1.75M)
- Simulating potential future threats to biodiversity of the Okavango Delta, Botswana (ACCORD), Defra Darwin Initiative, 2005-9, PI (£190K)
- The Bodélé Dust Experiment (BoDEx 2005), RGS, NERC, 2004-5, PI (£20K)
- Assessing regional climate signals from $\delta^{18}O$ diatom records in annually laminated lake sediments, NERC small grant, 2003-6, Co-I (£35K)
- Water and Ecosystem Resources in Regional Development (WERRD), EU FP5 INCO-DEV, 2002-5 (£1.9M)

KNOWLEDGE EXCHANGE ACTIVITIES AND RESEARCH IMPACT

Media activities: Research cited frequently in the popular media. Numerous papers featured in journal highlights. Advisor to BBC on popular science documentary series.

Stakeholder engagement and training activities: HFP Pilot Humanitarian agencies -Science Exchange Programme, 2009-present; Organiser: Training programme in 'Climate Information for Adaptation': GTZ, June 2010; Organiser: Training programme in 'Climate change', University of Botswana, 2009; Co-organizer: NERC QUEST GSI workshop 'Quantifying uncertainty in the impacts of climate change and development on freshwater availability', UCL, 2009; Workshop: The role of hydrological models in Stakeholder dialogues. Johannesburg, 2004

Policy influence: Research has directly informed water management policy notably at the international and national level for the Okavango River basin.

PUBLICATIONS

In press

1. McQuaid and co-authors Overview and Insights gained by Airborne Observations over the Sahara during Fennec 2011 and 2012. Journal of Geophysical Research
2. Todd, M.C. and co-authors. Meteorological and dust aerosol conditions over the Western Saharan region observed at Fennec supersite-2 during the Intensive Observation Period in June 2011. Journal of Geophysical Research

2013

3. Ambrosino, C, Chandler, R.E. and Todd, M.C., Rainfall-derived growing season characteristics for agricultural impact assessments in South Africa. *Theor Appl Climatol. DOI 10.1007/s00704-013-0896-y*
4. Hobby, M. et al. The Fennec Automatic Weather Station (AWS) Network: monitoring the Saharan Climate System. *J. Atmos. Oceanic Tech.. 3*0, 709–724.doi: http://dx.doi.org/10.1175/JTECH-D-12-00037.1
5. Marsham, J.M., and co-authors. Meteorology and dust over the central Sahara. Observations from Fennec supersite-1 during the June 2011 intensive observation period., J. Geophys. Res. Atmos., 2013, doi: 10.1002/jgrd.5021

2012

6. Bouet and co-authors, 2012: Sensitivity of desert dust emissions modeling to horizontal resolution: a case study during the Bodélé Dust Experiment 2005. Atmospheric Environment, 50, 377-380
7. Davidson, T et al., Seasonal and spatial hydrological variability drives aquatic biodiversity in a flood-pulsed, sub-tropical wetland, Freshwater Biology, 57, 1253-1265
8. Cavazos-Guerra, C and Todd, M.C., 2012. Model Simulations of Complex Dust Emissions over the Sahara during the West African Monsoon Onset, Advances in Meteorology, 2012, Article ID 351731, doi:10.1155/2012/351731.
9. Haustein, K., C. Pérez, J. M. Baldasano, O. Jorba, S. Basart, R. L. Miller, Z. Janjic, T. Black, S. Nickovic, M. C. Todd, and R.Washington., 2012.Atmospheric dust modeling from meso to global scales with the online NMMB/BSC-Dust model: 2. Regional experiments in North Africa. Atmospheric Chemistry and Physics
10. Hobby, M. et al. The Fennec Automatic Weather Station (AWS) Network: monitoring the Saharan Climate System. Journal of Atmospheric and Oceanic Technology, doi: 10.1175/JTECH-D-12-00037.1
11. Taylor, R.G Todd, M.C., Kongola, L., Maurice, L., Nahozya, E., Sanga, H., and MacDonald, A., 2012: Evidence of the dependence of groundwater resources on extreme rainfall in East Africa. Nature Climate Change. doi:10.1038/nclimate1731
12. Wolski, P., Todd, M.C, Murray-Hudson, M., Tadross, M., 2012. Multidecadal variability in hydro-climate of Okavango river system, southwest Africa, in the past and under future climate. Journal of Hydrology, 475, 294–305

2011

13. Ambrosino, C., Chandler, R.E. and Todd, M.C., Southern African Monthly Rainfall variability: an analysis based on generalised linear models. Journal of Climate doi: 10.1175/2010JCLI3924.1
14. Gosling, S.N., Taylor, R.G., Arnell, N.W. and Todd, M.C., 2011: A comparative analysis of projected impacts of climate change on river runoff from global and catchment-scale hydrological models, Hydrol. Earth Syst. Sci., 15, 279–294, 201
15. Hughes D.A., Kingston D.G, and Todd M.C., Uncertainty in water resources availability in the O,kavango River basin as a result of climate change. Hydrol. Earth Syst. Sci. 15, 931-941, 2011
16. Knippertz, P and Todd, M.C., Mineral dust aerosols over the Sahara: Processes of emission and transport, and implications for modelling. Reviews of Geophysics, doi:10.1029/2011RG000362
17. Mackay, A., Davidson, T., Wolski, P., Woodward, S., Mazabedi, R., Masamba, W.R.L., and Todd, M.C, 2011: Diatom sensitivity to hydrological and nutrient variability in a subtropical flood-pulse wetland, Ecohydrology, 5, 491-502, : 10.1002/eco.24
18. Mackay, A., Davidson, T., Wolski, P., Mazabedi, R., Masamba, W.R.L., huntsman-Mapila, P., and Todd, M.C, 2011: Spatial and Seasonal Variability in Surface Water Chemistry in the Okavango Delta, Botswana: A Multivariate Approach , Wetlands, 31, 815-829, DOI: 10.1007/s13157-011-0196-1

19. Okin, G and co-authors, 2011: Dust: small-scale processes with global consequences, EOS, 92, 241-2
20. Todd M.C. and co-authors, Uncertainty in climate change impacts on basin-scale freshwater resources – preface to the special issue: the QUEST-GSI methodology and synthesis of results, Hydrol. Earth Syst. Sci., 15, 1035-1046, 2011
21. Todd, M.C. and co-authors., 2011, Climate change impacts on hydrology in Africa: Case studies of river basin water resources. In Williams, C. and Kniveton, D., (Eds.) African Climate and Climate Change: Physical, Social and Political Perspectives, Springer.

2010

22. Xu, H.M., Taylor, R.G., Kingston, D.G., Jiang, T., Thompson, J.R. and Todd, M.C., 2011L Hydrological modeling of River Xiangxi using SWAT2005: A comparison of model parameterizations using station and gridded meteorological observations, Quaternary International, 226, 1-2, 54-59
23. Knippertz, P and Todd, M.C., The central west Saharan dust hot spot and its relation to African easterly waves and extratropical disturbances . Journal of Geophysical Research, doi:10.1029/2009JD012819 (in press)
24. Taylor, R, Longuevergne, L, Harding, R, Todd, M, Hewitson, B, Lall, U, Hiscock, K, Treidel, H, Dev Sharma, K, Kukuric, N, Stuckmeier, W and Shamsudduha, M (2010) . Groundwater and global hydrological change: Current challenges and new insight. IAHS-AISH Publication, 338. pp. 51-61.

2009

25. Bou Karam, D., C. Flamant, P. Tulet, J. Chaboureau, A. Dabas, and M. C. Todd, 2009, Estimate of Sahelian dust emissions in the intertropical discontinuity region of the West African Monsoon, J. Geophys. Res., 114, D13106, doi:10.1029/2008JD011444.
26. Bou Karam, D., Flamant, C., Tulet, P., Todd, M.C., Pelon, J., and Williams, E., 2009. Dry cyclogenesis and dust mobilization in the Inter Tropical Discontinuity of the West African Monsoon: a case study. Journal of Geophysical Research, 114, D05115, doi:10.1029/2008JD010952.
27. Cavazos, C., M. C. Todd, and K. Schepanski (2009), Numerical model simulation of the Saharan dust event of 6–11 March 2006 using the Regional Climate Model version 3 (RegCM3), J. Geophys. Res., 114, D12109, doi:10.1029/2008JD011078
28. Flamant, C., Lavaysse, C., Todd, M.C., Cahaboureau, J-P, and Pelon, J., 2009. Multi-platform observations of a representative springtime case of Bodélé and Sudan dust emission, transport and scavenging over West Africa. Quarterly Journal of the Royal Meteorological Society, DOI: 10.1002/qj.376
29. Kingston, D., Todd, M.C., Taylor, R. and Thompson, R.T., 2009. Uncertainty in future freshwater availability associated with the estimation of potential evapotranspiration. Geophysical Research Letters, VOL. 36, L20403, doi:10.1029/2009GL040267, 2009
30. Mileham, L., Taylor, R.T., Todd M.C., Tindimugaya, C. The Impact of Climate Change on Groundwater Recharge and Runoff in a Humid, Equatorial catchment, Uganda. Hydrological Sciences Journa, 54, 727-738
31. Schepanski, K., I. Tegen, M. C. Todd, B. Heinold, G. Boenisch, B. Laurent, and A. Macke (2009), Meteorological processes forcing Saharan dust emission inferred from MSG-SEVIRI observations of subdaily dust source activation and numerical models, J. Geophys. Res., 114, D10201, doi:10.1029/2008JD010325.
32. Todd, M.C. and co-authors., 2008 Simulating climate impacts on water resources: Experience from the Okavango River, southern Africa. In Sorooshian, S.; Hsu, K.-l.; Coppola, E.; Tomassetti, B.; Verdecchia, M.; Visconti, G. (Eds.) Hydrological modelling and water cycle. Coupling of the atmospheric and hydrological model, Springer, 291pp ISBN: 978-3-540-77842-4

2008

33. Mileham L., Taylor R.T., Thompson., J., Todd M.C, and Tindimugaya, C., 2008. Impact of rainfall distribution on the parameterisation of a soil-moisture balance model of groundwater recharge in equatorial Africa. Journal of Hydrology, 359 , 46-58
34. Todd, M.C., Washington, R., Lizcano, G., Ragvahan, S and Knippertz, P., 2008. Regional model simulations of the Bodélé low-level jet of Northern Chad during BoDEx 2005. Journal of Climate, 21, 995-1012
35. Todd, M.C. and co-authors, 2008. Quantifying uncertainty in estimates of mineral dust flux: an inter-comparison of model performance over the Bodélé Depression, Northern Chad, Journal of Geophysical Research 113, D24107, doi:10.1029/2008JD010476

2007

36. Bouet, C., Cautenet, G., Washington, R, Todd., M.C., Laurent, B., Marticorena, B, and Bergametti, G., 2007. Mesoscale modeling of aeolian dust emission during the BoDEx 2005 experiment. Geophysical Research Letters, 34, 34, L07812, doi:10.1029/2006GL029184.2007

37. Rose, N, Benedictow, A., Metcalfe, S., Todd M.C., Nicholson, J, And Tarrason, L., 2007. National, International and Global Sources of Contamination at Lochnagar, in Rose, N (ed.) Lochnagar: The Natural history of a mountain lake, Springer. Dordrecht. c. 505pp.
38. Warren, A., Todd, M.C., Bristow, C., Chappell, A., Engelstaedter, S., M'Bainayell, S, Martins, V. and Washington, R., 2007. The Bodele depression, Chad: Observations form the dustiest place on earth. Geomorphology, doi:10.1016/j.geomorph.2007.02.007
39. Todd, M.C., Martins, V., Washington, R., Lizcano, G, Dubovik, O., M'Bainayel, S., and Engelstaedter, S., 2007. Mineral dust emission from the Bodele Depression, Chad during BoDEx. 2005. Journal of Geophysical Research 112, D06207, doi:10.1029/2006JD007170

2006

40. Andersson, L., Wilk, J., Todd, M.C., Hughes, D., Kniveton, D., Layberry, R., and Savenije, H.H.G., 2006. Scenarios of the impact of changes of climate and water use on water flow in the Okavango River. Journal of Hydrology, 331, 43-57
41. Kniveton, D.R. and Todd, M.C., 2006: Water Resources in Regional Development: The Okavango River, Journal of Hydrology, 331, 1-2
42. Koren, I., Kaufman, Y.J., Washington, R., Todd, M.C., Rudich, Y., Martins, V. J. and Rosenfeld, D., 2006. The Bodélé depression—a single spot in the Sahara that provides most of the mineral dust to the Amazon forest. Env. Res. Lett., 1, 1-5
43. Layberry, R, Kniveton, D., Todd, M.C., Bellerby, T.J. and Kidd, C., 2006. Daily precipitation over southern Africa: a new resource for climate studies. Journal of Hydrometeorology, 7, 149-159
44. Tegen, I., Heinold, B., Todd, M.C., Helmert, J., Washington, R. and Dubovik, O., 2006. Modelling soil dust aerosol in the Bodélé depression during the BoDEx campaign. Atmospheric Chemistry and Physics, 6, 4345-4359
45. Washington, R., Harrison, M., Conway, D., Black, E., Challinor, A., Grimes, D., Jones, R., Morse, A., Kay, G., and Todd, M.C., 2006. African climate change: taking the shorter route. Bulletin of the American Meteorological Society, 87, 1355-1366
46. Washington, R., Todd, M.C., Engelstaedter, S., Mbainayel, S., and Mitchell, F., 2006. Dust and the low-level circulation over the Bodele Depression, Chad: Observations from BoDEx 2005, Journal of Geophysical Research, 111, D03201, doi:10.1029/2005JD006502.
47. Washington, R., Todd, M.C., Lizcano, G., Tegen, I., Flamant, C., Koren, I., Ginoux, P., Engelstaedter, S., Bristow, C., Zender, C.S., Goudie, A., Warren A., and Prospero, J.M., 2006. Links between topography, wind, deflation, lakes and dust: The case of the Bodele depression, Chad. Geophysical Research Letters, 33, L09401, doi 10/1029 2006GL025827
48. Wilk, J., Kniveton, D., Andersson, L., Ringrose, S., Layberry, R., and Todd, M.C., 2006. Rainfall and water balance of the Okavango basin. Journal of Hydrology, 331, 18-29

2005

49. Kniveton, D.R., Todd M.C., Sciare, J. and Mihalopoulos, N., 2005, The net effect of ultraviolet radiation on Variability of atmospheric dimethylsulphide over the Southern Indian Ocean, Philosophical Transactions of the Royal Society, 363, 187-189
50. Lizcano, G. and Todd, M.C., 2005. Non-ENSO control on Southern Africa precipitation variability, Philosophical Transactions of the Royal Society, 363, 61-62
51. Washington, R. and Todd, M.C., 2005. Atmospheric controls on mineral dust emission from the Bodele depression, Chad: The role of the low level jet. Geophysical Research Letters 32, (17), L17701 10.1029/2005GL023597.

2004

52. Todd, M.C. and Kniveton, D.R, 2004. Short term variability in satellite-derived cloud cover and galactic cosmic rays: An update. Journal of Atmospheric and Solar-Terrestrial Physics, 66, 1205-1211
53. Todd, M.C. and Washington, R., 2004. Climate variability in Central Equatorial Africa: Influence from the Atlantic sector. Geophysical Research Letters 10.1029/2004GL020975
54. Todd, M.C., Palmer, P. and Washington, R. 2004. Water vapour sources associated with major rainfall events over Southern Africa. International Journal of Climatology, 24, 555-568

2003

55. Andersson, L., Gumbricht, T., Hughes, D., Kniveton, D., Savinije, H., Todd M.C., Wilk, J., Wolski, P., 2003. Water flow dynamics in the Okavango River and delta: A pre-requisite for the ecosystems of the delta. Physics and Chemistry of the Earth, 28, 1165-1178
56. Goudie, A., Washington, R., Todd, M and Swann, M., 2003. North African dust production: Source areas and variability. CLIVAR Exchanges, 27
57. Kidd, C.K., Kniveton, D.R, Todd, M.C and Bellerby, T.J., 2003. Satellite rainfall estimation using a combined passive microwave and infrared algorithm. Journal of Hydrometeorology, 4, 1088-1104

58. Kniveton, D.R., Todd M.C., Sciare, J. and Mihalopoulos, N., 2003. Variability of atmospheric dimethylsulphide over the Southern Indian Ocean due to changes in ultraviolet radiation. Global Biogeochemical Cycles 17 (4)
59. Todd, M.C and Mackay, A.W., 2003. Large scale climatic controls on Lake Baikal ice cover. Journal of Climate, 16, 3186-3199.
60. Todd, M.C and Washington, R., 2003. Climate variability in central equatorial Africa: Evidence of extra-tropical influence. CLIVAR Exchanges, 27
61. Todd, M.C., Washington, R., and James, T, 2003. Characteristics of summertime daily rainfall variability over South America and the South Atlantic Convergence Zone. Meteorology and Atmospheric Physics, 83, 1-2, 89-109
62. Washington, R., Todd, M.C., Goudie, A.S and Middleton, N, 2003. Global dust storm source areas determined by the total ozone monitoring spectrometer and ground observations. Annals of the Association of American Geographers, 93, 297-313
63. Washington, R, Preston, A, and Todd M.C, 2003. Sea surface temperature influences on African rainfall variability. Bulletin of the American Meteorological Society, 84, 899-901

2002

64. Todd, M.C., Washington, R., Cheke, R.A., and Kniveton D.R., 2002. Brown locust outbreaks and climate variability in southern Africa, Journal of Applied Ecology, 39, 31-42

2001

65. Kniveton, D.R. and Todd, M.C., 2001. On the relationship of cosmic ray flux and precipitation. Geophysical Research Letters, 28, 1527-1530
66. Murphy, S., Washington, R., Downing, T., Martin, R., Ziervogel, G., Preston, A., Todd, M.C., Butterfield, R., Briden, J., 2001. Seasonal forecasting for climate hazards: Prospects and responses. Natural Hazards, 23, 171-196
67. New, M., Todd, M.C., Hulme, M. Jones, P., 2001. Precipitation measurements and trends in the twentieth Century. International Journal of Climatology, 21, 1889-1922
68. Todd, M.C. and Kniveton, D.R., 2001. Changes in cloud cover associated with Forbush decreases in galactic cosmic rays. Journal of Geophysical Research-Atmospheres, 106 (D23), 32031-32042
69. Todd, M.C., Kidd, C.K., Kniveton, D.R. and Bellerby, T.J., 2001. A combined satellite infrared and passive microwave technique for estimation of small scale rainfall over the global tropics and subtropics. Journal of Atmospheric and Oceanic technology, 18, 742-755

2000

70. Bellerby, T.J., Todd, M.C., Kniveton, D.R. and Kidd, C.K., 2000. Rainfall estimation from a combination of TRMM precipitation radar and GOES multi-spectral satellite imagery through the use of an artificial neural network. Journal of Applied Meteorology 39, 12, 2115-2128

1999

71. Tait, A., Barrett, E.C., Beaumont, M.J and Todd, M.C., 1999. Interpretation of an atlas of passive microwave-derived rainfall over the Eastern North Atlantic Ocean and North Sea. International Journal of Climatology, 19, 231-252
72. Todd, M.C. and Washington, R., 1999. A method to retrieve 3-hourly estimates of global tropical and subtropical precipitation from International Satellite Cloud Climatology Program (ISCCP) D1 data. Journal of Atmospheric and Oceanic Technology, 16, 146-155.
73. Todd, M.C. and Washington, R., 1999. Circulation anomalies associated with tropical-temperate troughs over Southern Africa and the South West Indian Ocean. Climate Dynamics, 15, 937-951
74. Todd, M.C., Barrett, E.C., Beaumont, M.J. and Bellerby, T.J., 1999. Estimation of daily rainfall over the upper Nile river basin using a continuously calibrated satellite infrared technique. Meteorological Applications, 6, 201-210
75. Washington, R. and Todd, M.C., 1999. Tropical temperate links in Southern African and Southwest Indian Ocean daily rainfall, International Journal of Climatology, 19, 1601-1616.

1998

76. Todd, M.C. and Washington, R., 1998. Extreme daily rainfall in Southern African and Southwest Indian Ocean tropical-temperate links. South African Journal of Science, 94, 64-70

1996

77. Dewhurst, N., Barrett, E., Beaumont, M.J. and Todd, M.C., 1996: Satellite monitoring of rainfall and surface water balances: In search of the optimum rain/no-rain boundary. In Parlow, E. (Ed.), Progress in Environmental Remote Sensing Research and Applications, Balkema, Rotterdam, p393-398
78. Todd, M.C. and Barrett, E.C. 1996: Rainfall and drought over the Mediterranean Sea and neighbouring countries: Preparation of a satellite passive microwave climatology from 1978-1995. In Spiteri, A. (Ed.) Remote Sensing 96:

Integrated Applications for Risk Assessment and Disaster Prevention for the Mediterranean. Balkema, Rotterdam p87-95.

1995

79. Todd, M.C. and Bailey, J., 1995. Estimation of rainfall over the UK and surrounding seas from the SSM/I, using the Polarisation Corrected Temperature Algorithm. Journal of Applied Meteorology, 34, 1254-1265.
80. Todd, M.C., Barrett, E.C., Beaumont, M.J. and Green, J., 1995. Satellite identification of rain days over the upper Nile river basin using an optimum infrared rain/no rain threshold temperature model. Journal of Applied Meteorology, 34, 2600-2611.

nature climate change

LETTERS

PUBLISHED ONLINE: 11 NOVEMBER 2012 | DOI: 10.1038/NCLIMATE1731

Evidence of the dependence of groundwater resources on extreme rainfall in East Africa

Richard G. Taylor[1]*, Martin C. Todd[2], Lister Kongola[3], Louise Maurice[4], Emmanuel Nahozya[3], Hosea Sanga[3] and Alan M. MacDonald[4]

Groundwater recharge sustains the groundwater resources on which there is global dependence for drinking water and irrigated agriculture[1]. For many communities, groundwater is the only perennial source of water. Here, we present a newly compiled 55-year record of groundwater-level observations in an aquifer of central Tanzania that reveals the highly episodic occurrence of recharge resulting from anomalously intense seasonal rainfall. Episodic recharge interrupts multiannual recessions in groundwater levels, maintaining the water security of the groundwater-dependent communities in this region. This long-term record of groundwater storage changes in the semi-arid tropics demonstrates a nonlinear relationship between rainfall and recharge wherein intense seasonal rainfall associated with the El Niño Southern Oscillation and the Indian Ocean Dipole mode of climate variability[2,3] contributes disproportionately to recharge. Analysis of the Intergovernmental Panel on Climate Change AR4 and AR5 multi-model ensembles for the twenty-first century indicates that projected increases in extreme monthly rainfall, responsible for observed recharge, are of much greater magnitude than changes to mean rainfall. Increased use of groundwater may therefore prove a potentially viable adaptation to enhanced variability in surface-water resources and soil moisture resulting from climate change[4–7]. Uncertainty in the projected behaviour of the El Niño Southern Oscillation and associated teleconnections remains, however, high[8].

Groundwater is the world's largest accessible store of fresh water and supplies 36% of the world's drinking water and ~42% of the water used for irrigation[1]. Groundwater is the only reliable source of fresh water in many semi-arid and arid regions where surface waters are seasonally or perennially absent[9]. The long-term viability of groundwater resources as well as the ecosystems and livelihoods that they sustain, depends on replenishment of groundwater by recharge. Over the past 50 years, groundwater depletion has been estimated and observed in several aquifers throughout the tropics and sub-tropics[10–13]. Such depletion not only threatens ecosystem function and the livelihoods of groundwater-dependent communities in some of the world's poorest regions but is also estimated to contribute to sea-level rise[12,13]. A conceptual understanding of the relationship between rainfall and recharge is fundamental to the development of robust estimates and projections of not only groundwater recharge and depletion but of all components of the terrestrial water balance under changing climates and increasing freshwater demand.

Recharge results from effective precipitation (that is, precipitation minus losses from evapotranspiration) infiltrating the subsurface where hydraulic gradients are downward. Diffuse groundwater recharge occurs directly through the soil matrix in saturated soils and through soil macropores and fractures that bypass the soil matrix. Focused groundwater recharge takes place indirectly by way of leakage from runoff and surface-water sources including ephemeral streams and is often a critical source of recharge in semi-arid environments[14–16]. The magnitude of effective precipitation is highly sensitive to changes in precipitation and evapotranspiration, particularly in semi-arid environments where differences between these fluxes are small[16,17]. Soil-moisture balance modelling studies in the tropics[18–20] suggest a nonlinear relationship between rainfall and recharge in which recharge is biased to heavy rainfall events ($>10\,\mathrm{mm\,d^{-1}}$) that temporarily exceed high rates of prevailing evapotranspiration. A key uncertainty is whether soil infiltration capacities are able to transmit, in practice, modelled increases in recharge generated by heavy rainfall. Indeed, the relationship between precipitation and groundwater recharge remains poorly resolved in many regions owing to a lack of long-term observational data.

Here we present empirical evidence of the relationship between rainfall and groundwater recharge in semi-arid tropical East Africa from a recently compiled near-continuous, 55-year (1955–2010) record of coincidental, *in situ* groundwater-level observations (variable time step with gaps) and monthly rainfall (Fig. 1a,b). Observations derive from the Makutapora Wellfield (35° 45′ E, 5° 55′ S) in central Tanzania where groundwater is abstracted from an aquifer comprising deeply weathered granite overlain by alluvium. This unique time series, the longest observed record yet published for any location in the tropics, reveals the highly episodic nature of recharge events indicated by positive deflections in groundwater levels that result from anomalously intense rainfall during the austral summer monsoon (November–April). These recharge events interrupt multiannual recessions in groundwater levels. Rates of groundwater-level decline have increased substantially from $\sim 0.5\,\mathrm{m\,yr^{-1}}$ (1955–1979) to $\sim 1.7\,\mathrm{m\,yr^{-1}}$ since 1990. This change is a response to pronounced increases in monthly groundwater abstraction from 0.1 to 0.9 million $\mathrm{m^3}$ to supply potable water to the national capital, Dodoma (Fig. 1c). Intensive groundwater abstraction is sustained by natural, inter-annual groundwater storage that is replenished on a decadal timescale by episodic recharge.

The observed relationship between seasonal rainfall and groundwater recharge is nonlinear (Fig. 2a) as recharge is largely restricted to anomalously intense seasonal rainfall. The cumulative recharge distribution (Fig. 2b) shows that the top 7 (11) seasons of rainfall account for 60% (75%) of the total recharge observed over 55 years from 1955 to 2010; remaining recharge is confined to seasons that

[1]Department of Geography, University College London, Gower Street, London WC1E 6BT, UK, [2]Department of Geography, University of Sussex, Brighton BN1 9QS, UK, [3]Ministry of Water and Irrigation, PO Box 9153, Dar es Salaam, Tanzania, [4]British Geological Survey, West Mains Road, Edinburgh EH9 3LA, UK. *e-mail: richard.taylor@ucl.ac.uk.

© 2012 Macmillan Publishers Limited. All rights reserved.

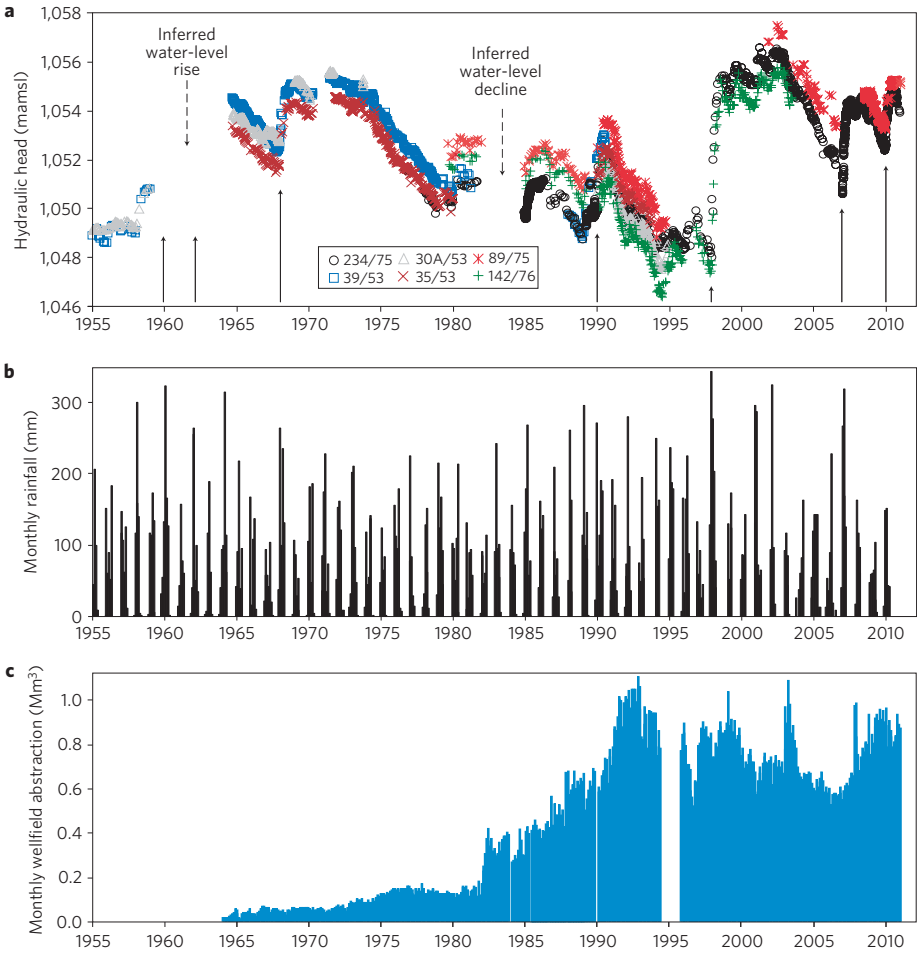

Figure 1 | 55-year observational record of groundwater levels, rainfall and groundwater abstraction from central Tanzania. a–c, Time series of groundwater-level observations from 6 monitoring wells (**a**), monthly rainfall (**b**) and monthly groundwater abstraction (**c**) at the Makutapora Wellfield from 1955 to 2010. The vertical solid arrows in **a** denote the seven greatest recharge events considered in the composite analyses. Monthly rainfall data for 2010 are missing in **b**. Records of monthly abstraction in **c** are unavailable for September 1993 and from May 1994 to September 1995 mamsl, metres above mean sea level.

feature individual months of statistically extreme (>95th percentile) rainfall (Fig. 2a). For nearly two-thirds of the 55-year record, no recharge is observed. Indeed, the Makutapora record suggests that unless monthly rainfall exceeds 200 mm (>95th percentile) or seasonal rainfall is greater than 670 mm (third quartile), little or no recharge occurs. These observed thresholds reflect the requirement of intense rainfall to overcome the high rates of potential evapotranspiration that prevail in the tropics, estimated locally to be 160 mm month^{-1} during the monsoon season, to generate recharge. Recharge pathways to the Makutapora Wellfield are both diffuse, through surficial sediments within the wellfield depression, and focused by way of ephemeral streams flowing over the coarse-grained soils within alluvial fans at the margins of the depression[21] (see Supplementary Information).

We examine anomalously intense seasonal rainfall that generates recharge in central Tanzania in terms of the wider regional and global climate system. Composite analysis of regional-scale rainfall anomalies associated with the seven largest episodic groundwater recharge events indicates a marked north–south dipole pattern of precipitation over tropical southeast Africa (Fig. 3a) with opposing positive (negative) precipitation anomalies north (south) of ~10° S. This dipole pattern is congruent with the most important structure of rainfall variability across southeast Africa as defined by the leading empirical orthogonal function (EOF) of monsoon season rainfall[2] (see Supplementary Information). The leading EOF is itself strongly correlated with tropical sea-surface temperature anomalies (SSTAs) indicative of both the Indian Ocean Dipole (IOD) and the El Niño Southern Oscillation (ENSO), the dominant modes of coupled ocean–atmosphere interaction in the tropical global and Indian oceans, respectively[2]. Figure 3b clearly shows the close association among the time series of the leading EOF, ENSO and groundwater recharge events. Of the seven largest recharge events, all but one are in the top eight events of the EOF time series and five coincide with El Niño events. The other groundwater recharge event (1959–1960) is associated with locally high rainfall (Fig. 1b) that does not have a strong regional expression.

The complex interaction of ENSO teleconnections and IOD variability is known to be the key driver of climate variability over southeast Africa[2,3]. Major ENSO warm (El Niño) events and the positive phase of the IOD lead to wet extremes in the East African sector and our study region. The most striking example is that the greatest recharge event (521 mm) observed in the Makutapora record (Fig. 1a) resulted from the heaviest season of monsoonal rainfall (1997–1998) recorded. This event is associated not only with the strongest ENSO warm event of the past century but also a positive IOD event[22]. From the above analysis, we conclude

© 2012 Macmillan Publishers Limited. All rights reserved.

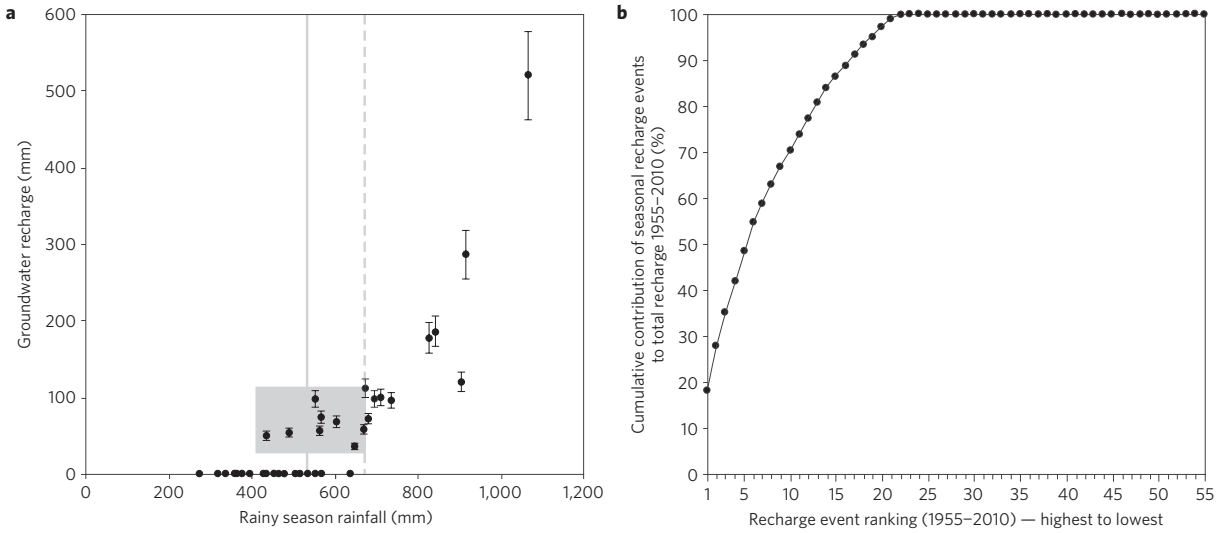

Figure 2 | Analysis of the relationship between groundwater recharge and rainfall. a, Cross plot of observed recharge from groundwater-level fluctuations versus rainy season (November to April) rainfall. **b**, Cumulative contribution of annual recharge to the total recharge received at the Makutapora Wellfield from 1955 to 2010. The shaded region in **a** indicates seasons featuring a month of statistically extreme (>95th percentile) rainfall, the solid vertical line in **a** indicates the median (50th percentile), and the dashed line indicates the third quartile (75th percentile) rainy season rainfall.

that the infrequent and episodic groundwater recharge events at Makutapora are primarily driven by regional-scale extreme precipitation anomalies associated with major events of the dominant modes of tropical climate variability in the region. Some of the more minor recharge events are associated with more localized rainfall anomalies (see Supplementary Information). It is unclear at present whether climate change will strengthen or weaken the influence of ENSO on East African rainfall[8]. An increase in the probability of positive IOD modes associated with heavy monsoonal rainfall in East Africa has recently been suggested as a response to anthropogenic warming from a review of AR4 models[23]. At present, the complex interactions of ENSO and IOD and their teleconnections preclude, however, firm conclusions on the impact of global warming on ENSO and IOD modes of variability and their influence on heavy rainfall in central Tanzania. This uncertainty represents a key question to be investigated using new output from AR5 models.

A robust signal of projected global warming is an increase in the intensity of heavy rainfall events. This intensification is expected to be especially pronounced in tropical wet seasons as a result of the $\sim$6.5% K^{-1} increase in atmospheric humidity defined by the Clausius–Clapeyron relation and the sensitivity of tropical convective rainfall to total moisture content[4,5,23], verified by observational studies[6]. Analysis of general circulation model (GCM) projections for the twenty-first century over the region surrounding the study site (Fig. 4) suggests an increase in mean precipitation over the study region, associated with projected increases over equatorial East Africa more widely (see Supplementary Information). This result is similar in the analysis of GCMs contributing to the Intergovernmental Panel on Climate Change AR4 and forthcoming AR5 (+9.7 and +5.2 mm d^{-1} by the end of the twenty-first century, respectively), although the uncertainty is higher in the latter case, reflecting some important regional differences (see Supplementary Information). At the broader scale, this is part of a wider quasi-global rich-get-richer pattern in which regions of moisture convergence (divergence) are expected to experience increased (decreased) precipitation[6], consistent between the AR4 and AR5 models. However, of particular importance to this study is that projected changes to extreme monthly rainfall driving groundwater recharge observed in the Makutapora record are of much greater magnitude (+22.5 and +25.4 mm $month^{-1}$ for AR4 and AR5 GCMs, respectively) than changes projected for mean monthly rainfall. These changes in the higher moments of the rainfall distribution are an important dimension to non-stationarity in future climate and, as shown here, have important implications for groundwater processes.

Anomalously intense seasonal and monthly rainfall has been associated with negative socio-economic consequences[3] that include the loss of crops and livestock, and the destruction of homes, yet the Makutapora record shows that these episodic events sustain groundwater resources on which there is often complete dependence for freshwater in tropical semi-arid environments. The observed dependence of episodic groundwater recharge on intense rainfall is consistent with evidence from semi-arid areas of Australia[24], southwestern USA[14] and West Africa[15]. The projected shift towards more intensive monthly rainfall favouring groundwater recharge suggests that greater use of groundwater may form a viable adaptation to increased variability in surface-water resources and soil moisture resulting from climate change. In light of the observed dependence of groundwater recharge on ENSO and IOD, the limited ability of GCMs to represent these modes of climate variability and their teleconnections remains a key impediment to understanding climate-change impacts on freshwater supplies in East Africa and regional climate change scenarios more widely.

Methods

The near-continuous time series of groundwater-level measurements drawn from 6 monitoring wells over a variable time step (daily to monthly) and monthly pumping volumes from the Makutapora Wellfield was constructed from observations collected by the Ministry of Water and Irrigation (Tanzania) and the Dodoma Urban Water Supply and Sanitation Authority. Data were assembled from computer files, hardcopy plots and notebooks stored in Wamaruvu Basin Office. Monthly rainfall at the Makutapora Wellfield (35° 45′ E, 5° 55′ S) was monitored by the Tanzanian Meteorological Agency; daily records are unavailable. Groundwater recharge (q) was estimated from changes in groundwater levels (∂h) through time (∂t) assuming that changes in groundwater storage are controlled by the balance of recharge and net groundwater drainage (D) from a monitoring well where the specific yield (S_y) is the storage coefficient through the equation[25]: $q = S_y(\partial h/\partial t) + D$. The Makutapora Wellfield resides within a large, local depression wherein recharge occurs both directly, through the direct infiltration of rainfall, and indirectly, through ephemeral streams (see Supplementary Information). D occurs both as a result of intensive groundwater abstraction for the city of Dodoma (Fig. 1c) and natural discharges. D was estimated from recessionary trends in groundwater levels during extended periods of absent recharge ($q = 0$). S_y was estimated from the statistically significant ($r^2 = 0.94$, $p = 0.001$) correlation

© 2012 Macmillan Publishers Limited. All rights reserved.

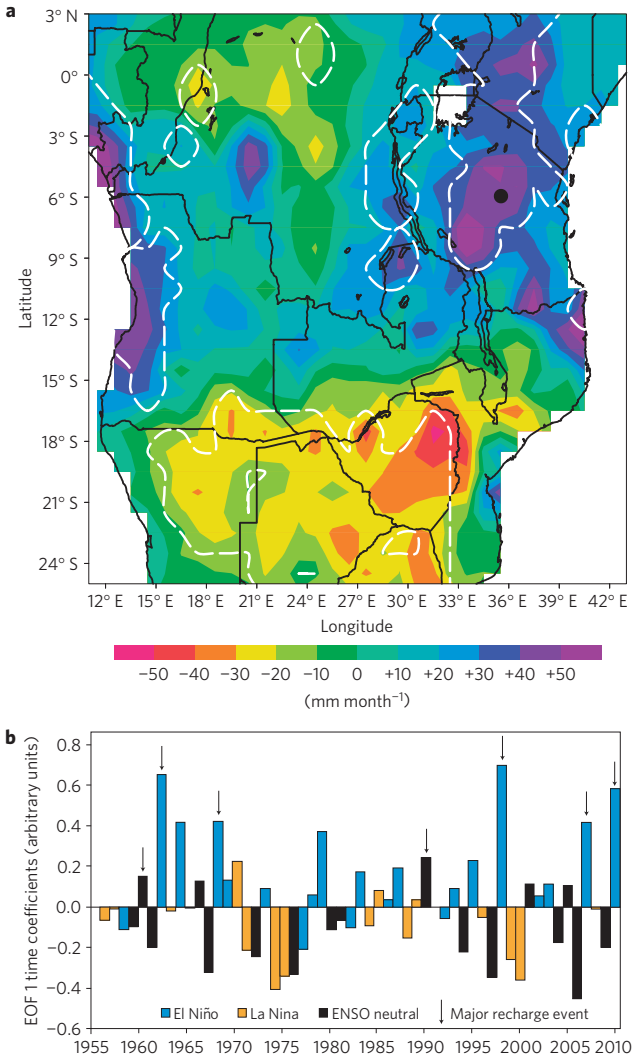

Figure 3 | Analysis of climate variability associated with major groundwater recharge events. a, Composite precipitation anomalies (colour scale) of the peak monsoon season (December–February) for the sample years coincident with the seven largest recharge events. Grid cells where composite mean anomalies are significant at the 0.05 level are indicated by the white dashed contour. The location of the Makutapora study site is indicated by the black dot. **b**, Time series of the leading EOF of regional monsoon season precipitation (November–March, Global Precipitation Climatology Centre (GPCC) data) over the domain 25° S–5° N, 10°–45° E. Note, the EOF aggregates over calendar years (for example 1997–1998 El Niño is plotted as 1998); and the value for 2010 is based on projection of the EOF onto data from the GPCC monitoring product. The seven largest groundwater recharge events are indicated with arrows.

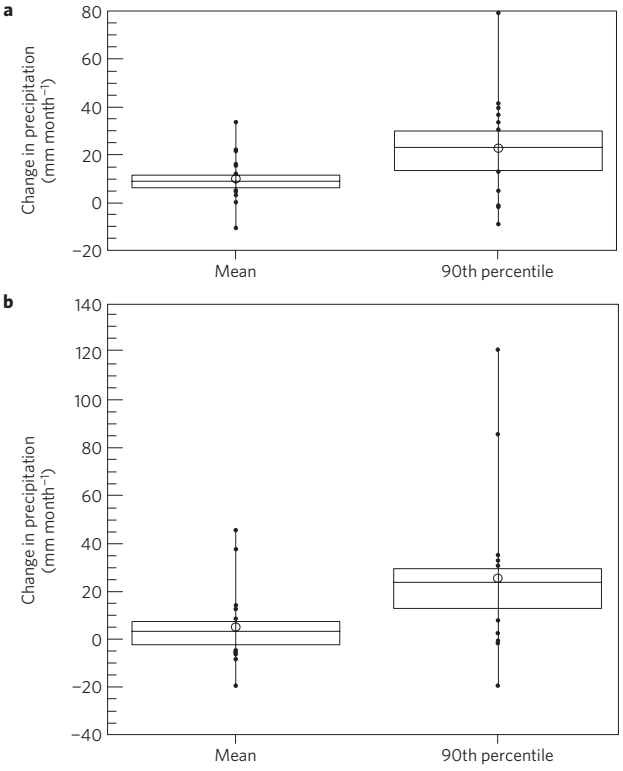

Figure 4 | Projected changes in mean and extreme monthly rainfall in central Tanzania. a,**b**, Projected changes in precipitation over the period 2070–2099 relative to 1961–1990 for a 10° box centred on the Makutapora Wellfield in central, semi-arid Tanzania from multi-model ensembles of CMIP3 (AR4) under the A1B emissions scenario (23 GCMs) (**a**) and CMIP5 (AR5) under the RCP8.5 scenario (21 GCMs) (**b**). Box plots are of changes in monthly precipitation for each model in the MME. Dots indicate individual models within the MME sample, boxes show the inter-quartile range and median and circles show the mean of the MME sample.

that was observed (see Supplementary Information) between cumulative wellfield abstraction ($-Q$) and groundwater-level recession ($-\delta h/\delta t$) within the wellfield ($A = 59\,\mathrm{km}^2$) wherein $S_y = (\partial t/-\partial h)(-Q/A)$. This relationship assumes that groundwater is drawn from pore storage evenly from multiple boreholes over the wellfield area. The derived value of S_y (0.064 ± 0.004) applies to groundwater-level fluctuations over a depth interval (1,046–1,058 m above mean sea level) comprising *in situ* weathered granite[26] and is consistent with that recently estimated from tracing experiments in weathered crystalline rock in Uganda[27]. Estimates of recharge during two gaps in the Makutapora record (1960–1965, 1980–1984) were imputed empirically from the statistically significant ($R^2 = 0.82$, $p < 10^{-4}$) relationship between heavy (>580 mm) seasonal rainfall and observed recharge; aggregate values imputed for each period were validated against the observed gap in the record ($\partial h/\partial t$) and estimated D (see Supplementary Information).

Analysis of historical climate over the wider region employed: gridded monthly precipitation at 0.5° resolution from the GPCC product version 5 from 1955 to 2009 (ref. 28); and gridded global SSTAs on a 1.0° global grid from the Hadley Centre Sea Ice and Sea Surface Temperature data set[29]. In both cases our results are insensitive to the choice of other available observed gridded data products (see Supplementary Information). We apply the following statistical analyses: composite analysis of gridded rainfall (Fig. 3a) and SSTA fields (see Supplementary Information) based on sample years of major groundwater recharge events; and EOF analysis of monthly rainfall over the region to determine objectively the spacetime structures of rainfall variability (see Supplementary Information). Climate-change projections were obtained from the multi-model ensemble (MME) compiled under the third (CMIP3) and fifth (CMIP5) Coupled Model Intercomparison Projects contributing to the Intergovernmental Panel on Climate Change fourth and (forthcoming) fifth Assessment Reports, AR4 and AR5, respectively. In total, the MME contained data from 23 GCMs for the CMIP3 data and 21 GCMs for the so far incomplete CMIP5 archive, of which 8 are Earth System Models (see Supplementary Information). We use data from a single greenhouse-gas emission scenario (Special Report on Emissions Scenario A1B) from the CMIP3 collection, and two emission Representative Concentration Pathway scenarios from the CMIP5 collection (RCP4.5 and RCP8.5). Changes in climate were calculated over a 10° box centred on the study site for three future epochs representing the early (2021–2050), mid (2035–2065) and late (2070–2099) twenty-first century. Here, we present only results from analysis of the RCP8.5 scenario, as this is the trajectory closest to recent greenhouse-gas emissions, and for the late twenty-first century alone (Fig. 4). The basic structure, if not the magnitude, of the projected changes to the mean and the 90th percentiles of monthly rainfall is essentially insensitive to both the epoch and the choice of RCP (see Supplementary Information).

© 2012 Macmillan Publishers Limited. All rights reserved.

Received 6 June 2012; accepted 2 October 2012; published online 11 November 2012

References

1. Döll, P. *et al.* Impact of water withdrawals from groundwater and surface water on continental water storage variations. *J. Geodyn.* **59–60,** 143–156 (2012).
2. Goddard, L. & Graham, N. E. The importance of the Indian Ocean for simulating precipitation anomalies over eastern and southern Africa. *J. Geophys. Res.* **104,** 19099–19116 (1999).
3. Conway, D. in *The East African Great Lakes: Limnology, Palaeolimnology and Biodiversity* (eds Odada, E. O. & Olago, D. O.) 62–92 (Kluwer, 2002).
4. Allen, M. R. & Ingram, W. J. Constraints on future changes in climate and the hydrologic cycle. *Nature* **419,** 224–232 (2002).
5. Trenberth, K. *et al.* The changing character of precipitation. *Bull. Am. Meteorol. Soc.* **84,** 1205–17 (2003).
6. Allan, R. P. & Soden, B. J. Atmospheric warming and the amplification of precipitation extremes. *Science* **321,** 1481–1484 (2008).
7. IPCC *Managing the Risks of Extreme Events and Disasters to Advance Climate Change Adaptation* (eds Field, C. B. *et al.*) (Cambridge Univ. Press, 2012); available at http://ipcc-wg2.gov/SREX/.
8. Latif, M. & Keenlyside, N. S. El Niño/Southern Oscillation response to global warming. *Proc. Natl Acad. Sci. USA* **106,** 20578–20583 (2009).
9. MacDonald, A. *et al.* Quantitative maps of groundwater resources in Africa. *Environ. Res. Lett.* **7,** 024009 (2012).
10. Rodell, M. *et al.* Satellite-based estimates of groundwater depletion in India. *Nature* **460,** 999–1002 (2009).
11. Shamsudduha, M., Taylor, R. G. & Longuevergne, L. Monitoring groundwater storage changes in the Bengal Basin: Validation of GRACE measurements. *Wat. Resour. Res.* **48,** W02508 (2012).
12. Konikow, L. Contribution of global groundwater depletion since 1900 to sea-level rise. *Geophys. Res. Lett.* **38,** L17401 (2011).
13. Wada, Y. *et al.* Past and future contribution of global groundwater depletion to sea-level rise. *Geophys. Res. Lett.* **39,** L09402 (2012).
14. Pool, D. R. Variations in climate and ephemeral channel recharge in southeastern Arizona, United States. *Wat. Resour. Res.* **41,** W11403 (2005).
15. Favreau, G. *et al.* Land clearing, climate variability, and water resources increase in semiarid southwest Niger: A review. *Wat. Resour. Res.* **45,** W00A16 (2009).
16. Scanlon, B. R. *et al.* Global synthesis of groundwater recharge in semiarid and arid regions. *Hydrol. Proc.* **20,** 3335–3370 (2006).
17. deWit, M. & Stankiewicz, J. Changes in surface water supply across Africa with predicted climate change. *Science* **311,** 1917–1921 (2006).
18. Taylor, R. G. & Howard, K. W. F. Groundwater recharge in the Victoria Nile basin of East Africa: Support for the soil-moisture balance method using stable isotope and flow modelling studies. *J. Hydrol.* **180,** 31–53 (1996).
19. Eilers, V. H., Carter, R. C. & Rushton, K. R. A single layer soil water balance model for estimating deep drainage (potential recharge): An application to cropped land in semi-arid North-east Nigeria. *Geoderma* **140,** 119–131 (2007).
20. Mileham, L. *et al.* Climate change impacts on the terrestrial hydrology of a humid, equatorial catchment: Sensitivity of projections to rainfall intensity. *Hydrol. Sci. J.* **54,** 727–738 (2009).
21. Onodera, S., Kitaoka, K. & Shindo, S. in *Models for Assessing and Monitoring Groundwater* (eds Wagner, B. J., Illangasekare, T. H. & Jensen, K. H.) 75–83 (IAHS Publ., 1995).
22. Latif, M., Dommenget, D., Dima, M. & Grötzner, A. The role of Indian Ocean sea surface temperature in forcing East African rainfall anomalies during December–January 1997/98. *J. Clim.* **12,** 3497–3504 (1999).
23. Shongwe, M. W. *et al.* Projected changes in mean and extreme precipitation in Africa under global warming. Part II: East Africa. *J. Clim.* **24,** 3718–3733 (2009).
24. Crosbie, R., McCallum, J., Walker, G. & Chiew, F. Episodic recharge and climate change in the Murray–Darling basin, Australia. *Hydrogeol. J.* **20,** 245–261 (2012).
25. Cuthbert, M. An improved time series approach for estimating groundwater recharge from groundwater level fluctuations. *Wat. Resour. Res.* **46,** W09515 (2010).
26. Nkotagu, H. Application of environmental isotopes to groundwater recharge studies in a semi-arid fractured crystalline basement area of Dodoma, Tanzania. *J. Afr. Earth Sci.* **22,** 443–457 (1996).
27. Taylor, R.G. *et al.* Convergent radial tracing of viral and solute transport in gneiss saprolite. *Ground Water* **48,** 284–294 (2010).
28. Rudolf, B. *et al.* in *Global Precipitations and Climate Change* (eds Desbois, M. & Desalmond, F.) 173–186 (NATO ASI Series I, Vol . 26, Springer, 1994).
29. Rayner, N. A. *et al.* Global analyses of sea surface temperature, sea ice, and night marine air temperature since the late nineteenth century. *J. Geophys. Res.* **108,** 4407 (2003).

Acknowledgements

The study was supported by a grant (Ref. GA/09F/094) from the UK Department for International Development (DFID), Groundwater resilience to climate change in Africa. The authors are grateful to the climate modelling groups and the CMIP projects for making model data available and to the Dodoma Urban Water Supply and Sewerage Authority for access to water supply records. The views expressed in this paper are those of the authors alone.

Author contributions

The Makutapora record was compiled by L.K., E.N., R.G.T., L.M. and H.S. Recharge analyses were conducted by R.G.T., M.C.T., A.M.M. and L.M. M.C.T. performed the analysis of climate data and model projections. R.G.T., M.C.T. and L.M. conceived the paper and R.G.T. and M.C.T. wrote the paper with feedback from all other authors.

Additional information

Supplementary information is available in the online version of the paper. Reprints and permissions information is available online at www.nature.com/reprints. Correspondence and requests for materials should be addressed to R.G.T.

Competing financial interests

The authors declare no competing financial interests.

© 2012 Macmillan Publishers Limited. All rights reserved.

INSTITUTE OF PHYSICS PUBLISHING ENVIRONMENTAL RESEARCH LETTERS
Environ. Res. Lett. **1** (2006) 014005 (5pp) doi:10.1088/1748-9326/1/1/014005

The Bodélé depression: a single spot in the Sahara that provides most of the mineral dust to the Amazon forest

Ilan Koren[1], Yoram J Kaufman[2], Richard Washington[3], Martin C Todd[4], Yinon Rudich[1], J Vanderlei Martins[2,5,6] and Daniel Rosenfeld[7]

[1] Department of Environmental Sciences, Weizmann Institute, Israel
[2] NASA Goddard Space Flight Center, Greenbelt, MD 20771, USA
[3] Climate Research Lab, Oxford University Centre for the Environment, UK
[4] Department of Geography, University College London, UK
[5] Joint Center for Earth Systems Technology, University of Maryland, Baltimore County, USA
[6] Institute of Physics, University of Sao Paulo, Brazil
[7] Institute of Earth Sciences, The Hebrew University, Jerusalem 91904, Israel

Received 27 July 2006
Accepted for publication 4 October 2006
Published 30 October 2006
Online at stacks.iop.org/ERL/1/014005

Abstract
About 40 million tons of dust are transported annually from the Sahara to the Amazon basin. Saharan dust has been proposed to be the main mineral source that fertilizes the Amazon basin, generating a dependence of the health and productivity of the rain forest on dust supply from the Sahara. Here we show that about half of the annual dust supply to the Amazon basin is emitted from a single source: the Bodélé depression located northeast of Lake Chad, approximately 0.5% of the size of the Amazon or 0.2% of the Sahara. Placed in a narrow path between two mountain chains that direct and accelerate the surface winds over the depression, the Bodélé emits dust on 40% of the winter days, averaging more than 0.7 million tons of dust per day.

Keywords: Sahara, Amazon, dust, aerosols, rainforest, fertilization

M This article features online multimedia enhancements

1. Introduction

Satellite observations show continuous dust transport across 5000 km from the Saharan sources to the Caribbean Sea and North America in the Northern summer and to the Amazon basin during the Northern winter [1, 2]. Due to the annual cycle in winds over the Sahara, the winter Saharan dust sources are different from the summer sources [3]. In the summer, dust fluxes reaching the Tropical Atlantic shore originate mainly from the northwest and central-west parts of the Sahara. During winter, strong surface winds (the Harmattan winds) occur along the southern border of the Sahara, activating sources on the border of the Sahel, notably the Bodélé depression in Northern Chad.

Analysis of satellite data [4] shows that out of the 240 ± 80 Tg (1 Tg = 10^{12} g = one million tons) of dust transported annually from Africa to the Atlantic ocean, 140 Tg are transported in the summer and 100 Tg in the winter. A total of 140 ± 40 Tg is deposited in the Atlantic ocean and 50 ± 15 Tg reach and fertilize the Amazon basin. This is four times an older estimate, explaining a paradox regarding the source of nutrients to the Amazon forest. Swap *et al* suggested [5] that while the source for minerals and nutrients in the Amazon is the dust from Africa, it was estimated that only 13 Tg of dust per year actually arrive in the Amazon. However, they pointed out that 50 Tg are needed to balance the Amazon nutrient budget.

Here we show a remarkable arrangement in nature in which the mineral dust arriving at the Amazon [6, 7] basin from the Sahara actually originates from a single source of only ∼0.5% of the size of the Amazon or ∼0.2% of the Sahara: the Bodélé depression. Located northeast of Lake

 © 2006 IOP Publishing Ltd Printed in the UK

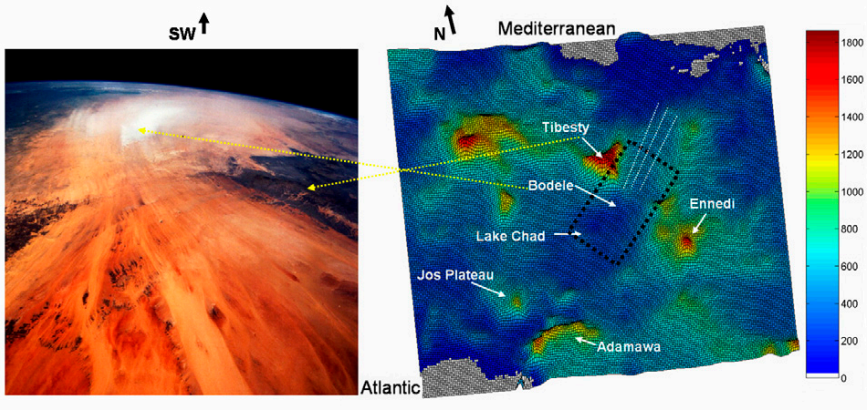

Figure 1. The surface wind focusing toward the Bodélé. Right: 3D topography of the Sahara; left: a rare shuttle image of emission from the Bodélé between the Tibesti and the Ennedi mountains (the projection of the shuttle image is marked in black on the map and the viewing direction is towards the southwest). The most significant pass between the northeast of the Sahara and the southwest is the one between the Tibesti and the Ennedi mountains. The structure of the mountains creates a caldera shape that guides and accelerates the surface winds from the northeast through the narrow pass located at the southwest. The Bodélé is located downwind directly after the pass. Several wind tunnels can be seen on the shuttle image starting as far north as 1000 km from the pass and focusing towards it, activating the Bodélé downwind from the passage (marked as white lines in the topographic map). A heavy dust storm leaving the Bodélé towards the Sahel is can be seen in the distance. The white dust emitted from the Bodélé is shown in the middle of the narrow path between the Tibesti (the black mountains on the right) and the Ennedi (left) approaching Lake Chad (see on the right near the horizon). The focusing effect can be seen as the distance between the wind tunnels become smaller near the Tibesti–Ennedi narrow path.

Chad (17°N, 18°E) near the northern border of the Sahel, it is known to be the most vigorous source for dust over the entire globe [3, 8]. Unlike most of the large sources in the Sahara that emit mainly during the summer months, the Bodélé depression emission pattern reaches its peak during the winter months. This depression is a unique dust source due to its location at a bottle neck of two large magmatic formations that serves as a 'wind lens', guiding and focusing the surface winds to the Bodélé.

The Tibesti mountains to the north and the Ennedi mountains southeast of the Bodélé form a large (more than 44 300 km^2) caldera-like valley [9]. Downwind, on the southwest corner, the caldera forms a cone with a narrow pass that accelerates the surface winds towards the Bodélé, which is located in a depression along the pass (see figure 1 right). A unique low level wind jet (LLJ) forms over the Bodélé [10, 11], and the maximum dust production occurs in the winter when the LLJ is strongest.

During the winter, the near surface winds are consistently northeasterly, making the Tibesti–Ennedi structure very efficient in focusing and guiding the winds over the Bodélé with an average of more than two days per week of winds stronger than 12 m s^{-1} [9, 11]. The surface winds over the Bodélé have a pronounced diurnal pattern, reaching the critical velocity for dust emission in the early morning and weakening toward the evening [12]. Therefore a clear 'dust parcel' forms, travelling away from the Bodélé, shown as an area covered by heavy dust with clear borders. This parcel can be detected by satellites on the day following the emission (figure 3: see the parcel in the right satellite image) and sometimes can be followed up to 3–4 days downwind, southwestward towards the Atlantic. In the same season, the Sahel biomass burning reaches its peak [13]. Therefore, the dust from the Bodélé may mix with the smoke, making retrievals of the dust properties over the Sahel much more difficult. Actual transport of a dust parcel from the Bodélé to the Atlantic ocean can be seen on an ozone monitoring instrument (OMI) [14] movie (available at stacks.iop.org/ERL/1/014005).

The rate of emission from the Bodélé depression has not been measured yet from space or otherwise, due to its remote, isolated location and difficulties in analysis of traditional satellite data of dust over the bright desert. Here we take advantage of recent advancement in satellite instrumentation to produce the first quantitative estimate of the amount of dust emitted from the Bodélé and transported across the Atlantic ocean to the Amazon. The analysis of emission combines data from two satellite instruments: MODIS (moderate-resolution imaging spectroradiometer), which provides daily observations of dust emitting days and dust parcel area but no quantitative estimates of dust concentration over the bright desert; and MISR (multi-angle imaging spectroradiometer), which provides estimates of the average dust optical depth of the parcel that in turn is used to derive the dust column mass but has only a nine-day revisit frequency.

2. Methods and results

The analysis over land is aimed at estimating the contribution of the Bodélé to the total dust flux reaching the African coast, followed by detailed analysis of dust fluxes reaching the Amazon coast, over the Atlantic ocean. Data from the MODIS blue channel (0.47 μm), with 1 km resolution, are used for detecting the area of the dust parcel emitted from the Bodélé. By using information from two satellites carrying the instrument, observing the same spot on ground 3 h apart (Terra $\sim$ 10:30 AM, Aqua 1:30 PM), we observed the patterns

of the dust activity. The dust (wind) speed and direction are calculated from the difference in the location of the dust front in the two satellites [9]. Then the emission starting time is estimated from the wind speed, the location of the source and the location of the dust front, and the duration of the emission is extracted from the wind velocity and the length of the dust parcel along the wind direction. Similarly, these properties can be calculated when using the location of the dust parcel from satellite images of the day after the emission. The optical parameters of the dust plume are derived from MISR data [15]. Each MISR pixel is measured from nine different angles, enabling the use of the directional variability of the dust in order to retrieve optical parameters over bright surfaces. The dust flux was calculated by converting the MISR optical thickness into dust mass [4] and integrating it over the entire parcel.

Dust emission starts with saltation and blasting of the surface crust by larger particles that release and lift the finer dust particles [16]. The large particles sink relatively quickly and are not transported to large distances from the source. The aerosol optical depth near the Bodélé may contain a contribution from the large particles. Therefore, to estimate the amount of fine dust that can be transported over large distances we focus on the day following the emission, where the average dust parcel is more than 1200 km away from the source.

The mass column concentration for Saharan dust M is estimated from the dust optical depth τ_d using the following ratio:

$$\frac{M}{\tau_d} = 2.7 \text{ g m}^{-2}, \quad (1)$$

as estimated in several field experiments combined with Aeronet measurements and models [17–21]. The mass flux of a particular event over land is the product of the average mass column concentration (calculated from the average dust optical thickness) and the parcel area.

The analysis of the MODIS and MISR satellite data over the desert was complemented with calculations of the dust flux over the Atlantic ocean. To do so, we separated the satellite measurements of aerosol optical depth into dust, marine aerosol and smoke. The amount of marine aerosol is estimated using the NCEP surface winds [22]. Dust and smoke are separated by estimating the contribution of the fine particles to the optical depth derived from MODIS. The flux of dust transported from Africa to Brazil is then calculated by applying the westward NCEP winds to the dust concentration, and the longitudinal length between 20°S and 10°N of the segment through which the flux is being computed near the African and the Brazilian coasts (*the method and results are described in detail in* [4]).

All dust outbreaks over the Saharan Atlantic zone from October 2003 to October 2004 were analysed in this study. Figure 2 (blue line) shows the accumulated distribution of days that the Bodélé emitted dust form October 2003 to October 2004 defined from MODIS data. Dust emission was highest during the winter time and occurred on 50% of the days during late winter and spring (February–April). The average duration of each event is about four days. The emission decreased sharply in May–June and occurred on less than 20% of the days during July–September.

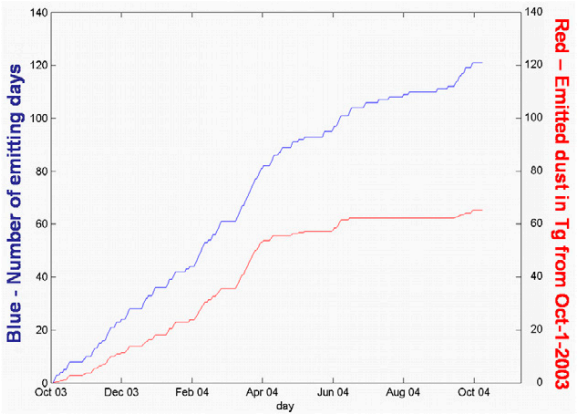

Figure 2. Dust emission from the Bodélé. The blue line shows a cumulative histogram of the Bodélé emission days between October 2003 to October 2004 and the red line is the corresponding cumulative histogram of the estimated dust mass emitted from the Bodélé. This analysis indicates that more than 60 Tg of dust were emitted during this year.

The average measured wind near the source derived from the Aqua–Terra difference for 40 cases is 13.2 ± 1 m s^{-1} with azimuth direction of $250° \pm 6°$, in line with previous measurements [7]. Moreover, during the winter–spring period the wind of the one-day-old dust parcel has a similar average wind speed of 13.0 ± 1.5 m s^{-1} and direction of $247° \pm 9°$. The average daily duration of emission is 8 ± 2 h, starting at 5 am $\pm$ 2 h. The average length of the dust package is $L = 370 \pm 100$ km, and the average width is $W = 700 \pm 300$ km.

Based on 21 cases of MISR analysis, the one-day-old dust parcel has an average optical depth of 1.1 ± 0.4 (with standard error of 0.1), and neutral spectral reflection of sunlight (Angstrom exponent of 0.2), indicating that the aerosol is pure dust [23]. The error estimate includes the error due to averaging for the entire parcel and the error of the dust retrieval [24]. The total mass of dust emitted from the Bodélé and observed by MODIS on the next day parcel is calculated as the product of the average MISR aerosol optical depth and the average parcel area covered by the dust, yielding $M_{tot} = 2.7\ \tau_{du} A$, where A is the averaged parcel area, $M_{tot} = 0.77 \pm 0.1$ Tg/day. The accumulation of emitted dust mass from October 2003 to October 2004 is plotted in red in figure 2.

The analysis of the satellite data shows that during the winter–spring time of 2003–2004 more than 58 ± 8 Tg of dust were emitted from the Bodélé, as measured 1300 km downwind from the source. At this distance the dust parcel is mostly free of the large particles that were removed earlier by gravitational settling. The estimates of dust flux emitted from the Bodélé depression are compared here to the dust fluxes across the Atlantic ocean to the Amazon [4]. In figure 3, we show the results of calculation for average of two years (2003–2004) of emissions and two cross section of the Atlantic ocean, one next to the African coast (brown frame) and one next to the South American coast (yellow frame). Out of 80 ± 8 Tg of dust transported to the ocean from Africa (between 20°S and 10°N), 40 ± 13 Tg arrive at South America. If we assume that the

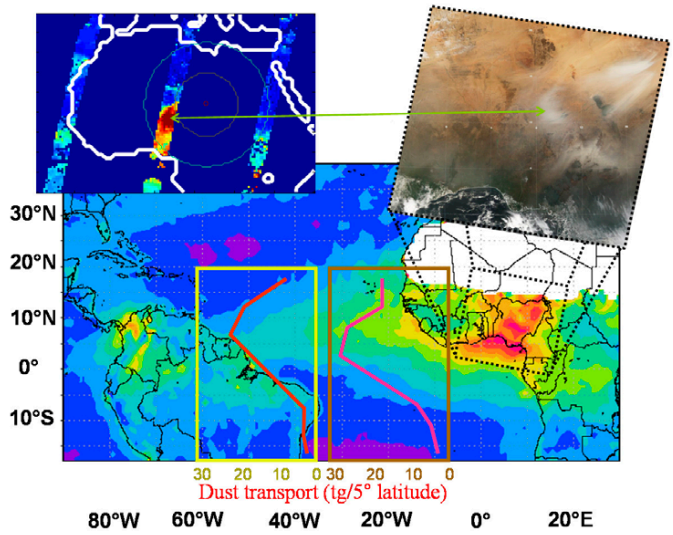

Figure 3. Dust production and transport across the Atlantic ocean from the Bodélé depression northeast of Lake Chad (17°N, 18°E) to the Amazon basin. Main image: distribution of the average aerosol optical depth as a measure for the column aerosol concentration derived from MODIS data for January 2003–March 2003 (http://g0dup05u.ecs.nasa.gov/OPS/Giovanni/). The upper right MODIS true colour image shows a huge dust plume leaving the Bodélé depression in the top right corner. The dust parcel emitted on the previous day, 1300 km downwind from the Bodélé, is shown closer to the ocean. The parcel is marked with an arrow connecting to the parcels optical depth measured by the MISR instrument (upper left). High dust concentrations follow all the way to the Amazon, with cross section profiles of dust western transport flux shown as a function of latitude (averaged for 5° of latitude and longitude) centred at 17°W and 37°W.

deposition rates over West Africa are similar to those over the Atlantic ocean we find that out of the 58 ± 8 Tg of dust emitted from the Bodélé depression, about 45 ± 6 Tg are loaded on the westward trade winds to be transported across the ocean. This amounts to 56% of the total annual burden, all coming from a single source.

3. Discussion

Using satellite data and reanalysis wind fields we have identified a remarkable connection between the Amazon forest and a single dust source in the Sahara: the Bodélé depression and its wind regime. A unique combination of global wind pattern and topography forms a vigorous dust source that emits an average of more than 0.7 Tg of dust per emission day and is active mostly during the winter–spring, which is different from most other Saharan dust sources. We estimate that between November and March, the Bodélé depression sends more than half of the dust that is deposited annually in the Amazon forest. Our direct measurements are consistent with a recent modelling study showing that the Bodélé is responsible for $>40\%$ of dust optical depth over the Amazon in the winter season [25].

The soil of the Amazon tropical rainforest is shallow, poor in nutrients and almost without soluble minerals. Heavy rains have washed away the nutrients in the soil obtained from weathered rocks. The rainforest has a short nutrient cycle, and due to the heavy washout, a stable supply of minerals is required to keep the delicate nutrient balance [26]. Kimmins [27] showed that any change in the nutrient supply will convert tropical forests to 'wet deserts'.

Despite the insight we gained into the role of the Bodélé in fertilization of the Amazon forest, some key questions remain open. What is the relationship of the mineralogical content of the dust to the local surface mineralogy? What is the size of the reservoir of mineral dust there? And since when has the Bodélé emitted such a huge amount of dust, and for how long will it continue to do so?

Such questions, among others, were the motivation for the BoDEx Field Experiment [28]. An expedition to the Bodélé during the spring of 2005 aimed at collecting *in situ* measurements of the emitted dust, and characterizing the local meteorology and the surface properties [29]. Answers to these questions are needed to understand the nature of the emissions in the past, and the future capability of the Bodélé to fertilize the Amazon.

Acknowledgments

We thank Gala Wind for the help with the MISR analysis. This work was supported by NASA. IK is incumbent of the Benjamin H Swig and Jack D Weiler career development chair. This research was partly funded by the Weizmann–Argentina Cooperation program.

References

[1] Prospero J M and Carlson T N 1972 Vertical and areal distribution of Saharan dust over the western equatorial North Atlantic ocean *J. Geophys. Res.* **77** 5255–65

[2] Carlson T N 1979 Atmospheric turbidity in Saharan dust outbreaks as determined by analysis of satellite brightness data *Mon. Weather Rev.* **107** 322–35

[3] Prospero J M, Ginoux P, Torres O, Nicholson S E and Gill T E 2002 Environmental characterization of global sources of atmospheric soil dust identified with the NIMBUS 7 total ozone mapping spectrometer (TOMS) absorbing aerosol product *Rev. Geophys.* **40** 1002
[4] Kaufman Y J, Koren I, Remer L A, Tanré D, Ginoux P and Fan S 2005 Dust transport and deposition observed from the Terra-MODIS space observations *J. Geophys. Res.* **110** D10S12
[5] Swap R *et al* 1992 Saharan dust in the Amazon basin *Tellus* B **44** 133–49
[6] Talbot R W *et al* 1990 Aerosol chemistry during the wet season in Central Amazonia: the influence of long-range transport *J. Geophys. Res.* **95** (D10) 16955–9
[7] Artaxo P *et al* 1990 Aerosol characteristics and sources for the Amazon Basin during the wet season *J. Geophys. Res.* **95** 16971–86
[8] Washington R, Todd M, Middleton N J and Goudie A S 2003 Dust-storm source areas determined by the total ozone monitoring spectrometer and surface observations *Ann. Assoc. Am. Geogr.* **93** 297–313
[9] Koren I and Kaufman Y J 2004 Direct wind measurements of Saharan dust events from Terra and Aqua satellites *Geophys. Res. Lett.* **31** (6)
[10] Washington R, Todd M C, Engelstaedter S, Mbainayel S and Mitchell F 2006 Dust and the low-level circulation over the Bodélé depression, Chad: observations from BoDEx 2005 *J. Geophys. Res.* **111** D03201
[11] Washington R and Todd M C 2005 Atmospheric controls on mineral dust emission from the Bodélé depression, Chad: the role of the low level jet *Geophys. Res. Lett.* **32** L17701
[12] Ginoux P and Torres O 2003 Empirical TOMS index for dust aerosol: applications to model validation and source characterization *J. Geophys. Res.* **108** 4534
[13] Herman J R *et al* 1997 Global distribution of UV-absorbing aerosols from Nimbus 7/TOMS data *J. Geophys. Res.* **102** 16911–22
[14] Torres O, Decae R, Veefkind P and de Leeuw G 2002 OMI aerosol retrieval algorithm *Algorithm Theoretical Baseline Document: Clouds, Aerosols, and Surface UV Irradiance* vol III, ed P Stammes *ATBD-OMI-03* version 2.0
[15] Kahn R, Gaitley B, Martonchik J, Diner D, Crean K and Holben B 2005 Multiangle imaging spectroradiometer (MISR) global aerosol optical depth validation based on two years of coincident AERONET observations *J. Geophys. Res.—Atmos.* **110** D10S04
[16] Shao Y and Raupach M 1993 Effect of saltation bombardment by wind *J. Geophys. Res.* **98** 12719–26
[17] Haywood J, Francis P, Osborne S, Glew M, Loeb N, Highwood E, Tanré D, Myhre G, Formenti P and Hirst E 2003 Radiative properties and direct radiative effect of Saharan dust measured by the C-130 aircraft during SHADE: 1. Solar spectrum *J. Geophys. Res.* **108** 8577
[18] Tanré D *et al* 2001 Climatology of dust aerosol size distribution and optical properties derived from remotely sensed data in the solar spectrum *J. Geophys. Res.* **106** 18205–17
[19] Maring H, Savoie D L, Izaguirre M A, Custals L and Reid J S 2003 Mineral dust aerosol size distribution change during atmospheric transport *J. Geophys. Res.* **108** 8592
[20] Ginoux P *et al* 2001 Sources and distributions of dust aerosols simulated with the GOCART model *J. Geophys. Res.* **106** 20255–74
[21] Fan S, Horowitz L W, Levy H II and Moxim W J 2004 Impact of air pollution on wet deposition of mineral dust aerosols *Geophys. Res. Lett.* **31** L02104
[22] Kalnay E *et al* 1996 The NCEP/NCAR 40-year reanalysis project *Bull. Am. Meteorol. Soc.* **77** 437–71
[23] Tanré D, Kaufman Y J, Holben B N, Chatenet B, Karnieli A, Lavenu F, Blarel L, Dubovik O, Remer L A and Smirnov A 2001 Climatology of dust aerosol size distribution and optical properties derived from remotely sensed data in the solar spectrum *J. Geophys. Res.* **106** 18205–18
[24] Martonchik J V, Diner D J, Kahn R and Gaitley B 2004 Comparison of MISR and AERONET aerosol optical depths over desert sites *Geophys. Res. Lett.* **31** L16102
[25] Tegen I *et al* 2006 Modeling soil dust aerosol in the Bodélé depression during the BoDEx campaign *Atmos. Chem. Phys.* **6** 4345–59
[26] Vitousek P M and Stanford R L Jr 1986 Nutrient cycling in moist tropical forest *Annu. Rev. Ecol. Syst.* **17** 137–67
[27] Kimmins J P 1997 *Forest Ecology: a Foundation for Sustainable Management* 2nd edn (Upper Saddle River, NJ: Prentice-Hall) p 596
[28] BoDEx Field Experiment—Chad 2005 http://www.geog.ox.ac.uk/research/projects/bodex/index.html
[29] Giles J 2005 Climate science: the dustiest place on earth *Nature* **434** 816–9

MINERAL DUST AEROSOLS OVER THE SAHARA: METEOROLOGICAL CONTROLS ON EMISSION AND TRANSPORT AND IMPLICATIONS FOR MODELING

Peter Knippertz[1] and Martin C. Todd[2]

Received 29 April 2011; revised 31 October 2011; accepted 6 December 2011; published 14 February 2012.

[1] Atmospheric mineral dust has recently become an important research field in Earth system science because of its impacts on radiation, clouds, atmospheric dynamics and chemistry, air quality, and biogeochemical cycles. Studying and modeling dust emission and transport over the world's largest source region, the Sahara, is particularly challenging because of the complex meteorology and a very sparse observational network. Recent advances in satellite retrievals together with ground- and aircraft-based field campaigns have fostered our understanding of the spatiotemporal variability of the dust aerosol and its atmospheric drivers. We now have a more complete picture of the key processes in the atmosphere associated with dust emission. These cover a range of scales from (1) synoptic scale cyclones in the northern sector of the Sahara, harmattan surges and African easterly waves, through (2) low-level jets and cold pools of mesoscale convective systems (particularly over the Sahel), to (3) microscale dust devils and dusty plumes, each with its own pronounced diurnal and seasonal characteristics. This paper summarizes recent progress on monitoring and analyzing the dust distribution over the Sahara and discusses implications for numerical modeling. Among the key challenges for the future are a better quantification of the relative importance of single processes and a more realistic representation of the effects of the smaller-scale meteorological features in dust models. In particular, moist convection has been recognized as a major limitation to our understanding because of the inability of satellites to observe dust under clouds and the difficulties of numerical models to capture convective organization.

Citation: Knippertz, P., and M. C. Todd (2012), Mineral dust aerosols over the Sahara: Meteorological controls on emission and transport and implications for modeling, *Rev. Geophys.*, *50*, RG1007, doi:10.1029/2011RG000362.

1. INTRODUCTION

[2] Atmospheric aerosols are an important component of the climate system by virtue of their direct radiative impacts, indirect effect on cloud properties, the semidirect effect of these on atmospheric dynamics [*Forster et al.*, 2007], and finally their role in global terrestrial and oceanic biogeochemical cycles [e.g., *Jickells et al.*, 2005; *Mahowald et al.*, 2010]. Of the aerosol species, mineral dust is the dominant type by mass [*Textor et al.*, 2006], yet many processes associated with atmospheric dust and the associated climate impacts are poorly understood. Uncertainty in the magnitude of radiative forcing from dust aerosols remains high, especially at the regional scale [*Uno et al.*, 2006; *Todd et al.*, 2008a]. Efforts to quantify these processes and their representation in models are at the cutting edge of climate science and represent one of the major challenges for Earth system modeling. In addition, dust affects living conditions for humans through affecting air quality, aviation and road safety, and human health by fostering respiratory diseases and meningitis epidemics [*Molesworth et al.*, 2002]. As a result, there is increasing demand for dust storm forecasts.

[3] The Sahara Desert is by far the most important dust source globally [*Prospero et al.*, 2002; *Washington et al.*, 2003], as such there is a critical need to understand aerosol processes in this region. The Saharan atmosphere is particularly interesting as it is characterized by extreme features, notably (1) record high temperatures and the deepest planetary boundary layer (PBL) on Earth reaching up to 5–6 km above ground [*Gamo*, 1996]; (2) very high aerosol optical thickness (AOT) during most of the year (Figure 1); and (3) the summertime Saharan heat low (SHL), which colocates with aerosol maxima and is pivotal for the West

[1]School of Earth and Environment, University of Leeds, Leeds, UK.
[2]Department of Geography, University of Sussex, Brighton, UK.

Copyright 2012 by the American Geophysical Union.

8755-1209/12/2011RG000362
Paper number 2011RG000362

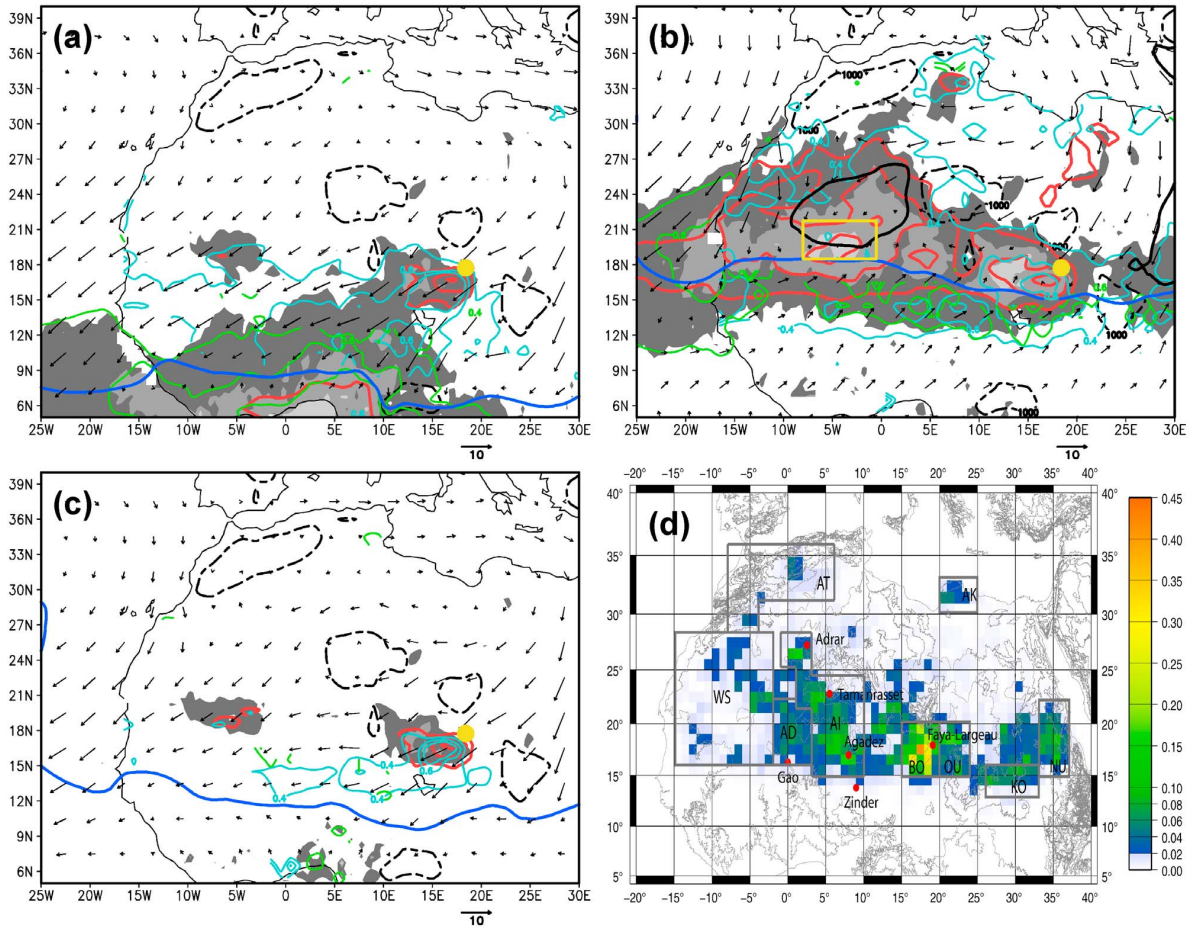

Figure 1. Aerosols over the Sahara as estimated by satellite. (a–c) Average seasonal AOT from MISR (gray shaded), MODIS Deep Blue (cyan contour), MODIS collection 5 (green contour, over ocean and dark land surfaces south of ~15°N only), and the absorbing *AI* from TOMS (red contours). Seasons shown are the January–March (Figure 1a) and June–September dust seasons (Figure 1b) and the October–November dust-minimum season (Figure 1c). AOT shading and contour intervals are 0.4, 0.6, and 0.8; *AI* contours are 1.5, 2.0, and 2.5. To illustrate structural controls on dust distribution, the plots also show the mean 925 hPa winds (arrows), the mean position of the intertropical discontinuity (solid blue line, as defined by the 10 g kg^{-1} contour of 925 hPa specific humidity from ECMWF Re-Analysis (ERA)-Interim data), and the 1000 m surface elevation contour (dashed black contour). In Figure 1b, the mean position of the Saharan heat low core is indicated by the 1008 hPa contour of mean sea level pressure (thick black solid line). The Bodélé Depression (yellow dot) and the West African summertime dust hot spot (yellow box) are marked. Note that particularly during winter months, the AOT estimates south of ~13°N include contributions from both dust and biomass burning aerosols. (d) Mean annual dust source activation frequency as estimated from the SEVIRI dust product [*Schepanski et al.*, 2009, Figure 1].

African monsoon system [*Peyrillé et al.*, 2007; *Biasutti et al.*, 2009]. The Sahara is also a key location for tropical-extratropical interactions [*Knippertz*, 2007].

[4] Until recently, the climate of the region remained relatively poorly understood, in part because of a lack of observations. However, there have been a number of important recent developments, which have combined to advance our understanding of the emission and transport of Saharan dust. Several field studies have provided invaluable observational data, which illuminate our understanding of dust processes. These include the Bodélé Dust Experiment (BoDEx) in 2005 [*Washington et al.*, 2006; *Todd et al.*, 2007], the African Monsoon Multidisciplinary Analysis (AMMA) in 2006 [*Redelsperger et al.*, 2006], the Dust and Biomass Experiment (DABEX) in 2006 [*Haywood et al.*, 2008], Dust Outflow and Deposition to the Ocean (DODO) in 2006 [*McConnell et al.*, 2008], the Geostationary Earth Radiation Budget Intercomparison of Longwave and Shortwave Radiation (GERBILS) in 2007 [*Haywood et al.*, 2011a], the Saharan Mineral Dust Experiment (SAMUM) in 2006 and 2008 [*Heintzenberg*, 2009; *Ansmann et al.*, 2011], and Fennec in 2011. Figure 2 gives an overview of the study

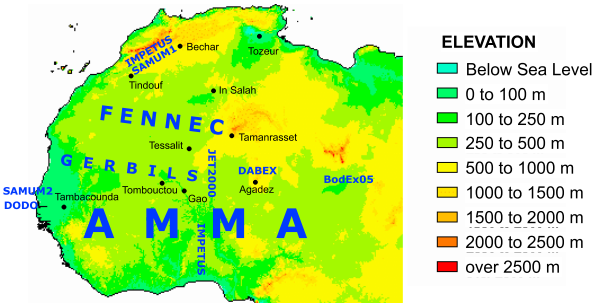

Figure 2. Study areas of recent dust field campaigns (in blue, see text for more details). The map also shows surface topography (shaded) and the locations of currently or formerly active radiosonde stations of interest for Saharan dust emission (in black). Map developed by U.S. Geological Survey EROS Data Center.

areas of these campaigns showing a bias toward the desert margins that are logistically more accessible. Only Fennec took measurements in the central Sahara, a region more than half the size of Europe. Eastern parts have received even less attention, so that the Sahara as a whole still remains a vastly undersampled region.

[5] The advent of new satellite sensors with improved observing capabilities for dust (notably the Meteosat Second Generation (MSG) Spinning Enhanced Visible and Infrared Imager (SEVIRI) [*Brindley and Ignatov*, 2006; *Thomas et al.*, 2007], Multiangle Imaging Spectroradiometer (MISR) [*Kalashnikova and Kahn*, 2008; *Kahn et al.*, 2009], and Cloud-Aerosol Lidar with Orthogonal Polarization (CALIOP) [*Winker et al.*, 2009]) as well as new algorithms for other satellite data (e.g., Moderate Resolution Imaging Spectroradiometer (MODIS) Deep Blue [*Hsu et al.*, 2004]) have combined to radically improve our ability to monitor and understand aerosol processes. At the same time, there has been a rapid development of off-line and coupled dust aerosol–atmosphere models for operational weather, air quality, and dust hazard forecasting and for Earth system research purposes.

[6] Aided by these developments there has been a substantive advance in our understanding of dust aerosols from the Sahara. This review will provide a synthesis of these developments and provide a comprehensive account of the state-of-the-art knowledge of the meteorological processes by which Saharan mineral dust aerosol is generated, distributed, and transported over the region as well as implications for representation of these in models and for weather forecast and climate prediction. This paper focuses on the most fundamental stages of the dust "cycle": the lifting of dust aerosol and the subsequent vertical and horizontal mixing and advection. It is these processes that determine the fine detail of the 3-D structure of the large-scale dust plumes over the region. This in turn strongly influences the nature of the direct, indirect, and semidirect effects on climate. Specifically, this paper considers recent advances in understanding the various multiscale meteorological phenomena that generate dust plumes, from microscale dry convective vortices; through mesoscale circulation features including low-level jets (LLJ) and those associated with moist convection; to synoptic scale weather systems in the tropical, subtropical, and midlatitude atmosphere. These processes characteristically have a strong relationship with diurnal and seasonal cycles. The recent advances listed above are such that we now have a more complete picture of dust generation processes, although many details and their relative importance are still unclear.

[7] This paper is organized as follows: Section 2 provides the relevant background information that motivates our interest in this topic, including an overview of the role of mineral dust in the Earth system and the state of the art in monitoring and modeling the global dust budget. More detailed discussions of these aspects can be found in recent review articles by *Maher et al.* [2010] and *Shao et al.* [2011]. Section 3 then provides detail on the spatiotemporal structure of the dust plume and its meteorological drivers as well as implications for modeling. We conclude with a reflection on the state of the art and perspective on priorities for the future in Section 4.

2. THE CONTEXT

2.1. Dust in the Earth System

[8] The direct and indirect effects of aerosols constitute the largest uncertainties in our knowledge of the radiative forcing of the climate system [*Forster et al.*, 2007]. Mineral dust released from natural soils through wind erosion is estimated to contribute at least 80% to the total dust budget [*Forster et al.*, 2007] and more than half to the total global aerosol burden [*Textor et al.*, 2006]. Once airborne, dust can be mixed to great heights and can be transported over long distances. Dust in the atmosphere affects both climate and weather through the following processes:

[9] 1. Dust aerosols have a direct effect on the shortwave and longwave radiative flux through scattering and absorption. The global net top-of-the-atmosphere direct radiative forcing is on the order of -0.3 W m^{-2} with a range of -0.56 to $+0.1$ on the basis of model studies [*Forster et al.*, 2007]. There are large regional variations depending on the characteristics of the underlying surface [*Haywood et al.*, 2001, 2011b].

[10] 2. Dust aerosols have an indirect effect on the radiation budget through affecting cloud microphysical processes. Dust particles that have undergone chemical or physical processing in the atmosphere, for example, through coating with sulphates, can act as cloud condensation nuclei, affecting radiation indirectly through factors such as cloud albedo, precipitation efficiency, cloud lifetime, and cloud height [e.g., *Rosenfeld et al.*, 2001; *Kaufman et al.*, 2005; *Min et al.*, 2009; *Klüser and Holzer-Popp*, 2010]. In addition, mineral dust particles are the dominant natural ice-nucleating aerosol, leading to a faster glaciation of convective clouds [*Richardson et al.*, 2007].

[11] 3. A semidirect effect of dust is generated by absorptional heating within dust layers, which changes relative humidity and vertical stability with potential effects on

clouds, precipitation [*Solmon et al.*, 2008; *Klüser and Holzer-Popp*, 2010], and even tropical cyclone development [*Dunion and Velden*, 2004].

[12] 4. Dust provides a surface for atmospheric chemistry and can thereby mediate chemical cycles of, e.g., sulphates [*Desboeufs and Cautenet*, 2005; *Kandler et al.*, 2007] and ozone [*de Reus et al.*, 2000; *Michel et al.*, 2003].

[13] It has been shown that including effects of airborne dust into numerical models has a positive impact on weather and climate simulations [*Tompkins et al.*, 2005; *Pérez et al.*, 2006; *Chaboureau et al.*, 2007; *Rodwell and Jung*, 2008].

[14] Dust is removed from the atmosphere through gravitational sedimentation and turbulence (dry deposition) and through scavenging in precipitating clouds (wet deposition). Deposition affects climate by changing the albedo of snow and ice surfaces [*Warren and Wiscombe*, 1980; *Painter et al.*, 2007] and through biogeochemical processes in the ocean (phytoplankton) [*Erickson et al.*, 2003; *Fasham*, 2003; *Jickells et al.*, 2005] and on land [*Swap et al.*, 1992; *Okin et al.*, 2004] with important ramifications on the carbon cycle (see *Shao et al.* [2011] for a review on this topic). *Swap et al.* [1992] were the first to suggest that Saharan dust contributes to the nutrient budget of the Amazon ecosystems, which has been quantified in more recent studies [*Koren et al.*, 2006; *Ansmann et al.*, 2009a; *Ben-Ami et al.*, 2010; *Bristow et al.*, 2010]. The amount and characteristics of dust deposited in soils, glaciers, and sediments are used as indicators of climate and environmental changes on long timescales [*Lambert et al.*, 2008; *Sima et al.*, 2009; *Stuut et al.*, 2009; *Maher et al.*, 2010, and references therein; *Mulitza et al.*, 2010]. Dust has been discussed as a potential climate feedback in glacial-interglacial cycles [*Krinner et al.*, 2006; *Winckler et al.*, 2008] and for the modern climate because of interactions between dust, precipitation, and the land surface [*Rosenfeld et al.*, 2001; *Yoshioka et al.*, 2007; *Hui et al.*, 2008]. Given the complex role of dust aerosols in the Earth system, reliable quantitative estimates of the three main processes of the global dust budget, emission, transport, and deposition, are necessary for a full understanding of its role in the Earth system.

2.2. Monitoring the Dust Distribution

[15] Scientists utilize ground-based, airborne, and satellite instruments to measure various aspects of atmospheric dust including AOT, size distribution, mass concentration, vertical distribution, shape, and optical properties. Particularly because emission and deposition are rarely measured in situ and difficult to estimate from space, the current network does not provide enough observational constraints for a complete quantification of the dust budget [*Tegen and Schepanski*, 2009]. Nevertheless, advances in satellite sensors in recent years have illuminated our understanding considerably. A summary of existing satellite records of relevance with their relative strengths and weaknesses is provided in Table 1. For a more detailed review of recent developments, see *Mishchenko et al.* [2007] and *Tanré* [2010]. By their nature, satellite instruments provide indirect observations of radiances, from which parameters such as amount, size, shape, optical properties, and elevation must be inferred. The most important products of the now extensive satellite record are (1) a near-global, long-term record of aerosol indices and AOT available from early satellite sensors such as Total Ozone Mapping Spectrometer (TOMS); (2) the ability to distinguish aerosol types in transport plumes on the basis of physical properties; and (3) more spatially and temporally resolved properties of atmospheric aerosols from the more recent sensors, including estimates directly over the Sahara desert, most notably from MODIS Deep Blue, MISR, Ozone Monitoring Instrument (OMI), CALIOP, ICESat, and SEVIRI (see Table 1 for more details). Recent developments of particular relevance to understanding Saharan dust processes are (1) the ability to retrieve quantitative AOT estimates over bright desert surfaces at high spatial resolution from nadir-viewing MODIS data (the "Deep Blue" algorithm of *Hsu et al.* [2004]) and from multiangle visible data from MISR [*Diner et al.*, 2005]; (2) estimates of AOT at 15 min temporal resolution from SEVIRI visible and infrared channels [*Brindley and Ignatov*, 2006; *Thomas et al.*, 2007; *Carboni et al.*, 2007], in addition to the qualitative SEVIRI dust product (see "Best practices for RGB compositing of multi-spectral imagery," European Organisation for the Exploitation of Meteorological Satellites guide, available at http://oiswww.eumetsat.org/SDDI/html/doc/best_practices.pdf; an example is shown in Figure 3a); (3) estimates of aerosol properties from Polarization and Anisotropy of Reflectances for Atmospheric Sciences coupled with Observations from a Lidar (PARASOL); and (4) remarkably detailed vertical profiles of aerosol backscatter from the CALIOP (and to a lesser extent ICESat) spaceborne lidar, albeit with a limited temporal sampling. The example given in Figure 3b demonstrates clear evidence of a widespread deep dust layer over the Sahara. The remainder of the paper will further illustrate how these new data sources have enabled notable advances in our understanding of aerosol emission and transport processes as well as our ability to validate model performance and highlight model limitations.

[16] It should be pointed out, however, that no single satellite instrument or retrieval is without limitations. Uncertainties have manifold causes including cloud contamination and assumptions on optical properties and perhaps most importantly by variability in surface albedo and emissivity over land. No current sensor can detect aerosols beneath thick cloud layers and thick dust is difficult to distinguish from cirrus clouds at visible wavelengths [*Roskovensky and Liou*, 2005]. All AOT products are originally designed to sample all aerosol types together and only a few studies have attempted to filter out a dust signal by making certain assumptions about optical properties [*Evan et al.*, 2006; *Ginoux et al.*, 2010; *Klüser et al.*, 2011]. The desert dust retrieval intercomparison (initial results of *Carboni et al.* [2009]) compared a sample of 15 satellite algorithms over the Sahara for a limited period during March 2006. Results show that although most algorithms correlate well with Aerosol Robotic Network (AERONET) AOT, the standard error in mean monthly AOT between the methods varied between ~0.5 and 1.0, broadly proportional to mean AOT,

TABLE 1. Summary of Satellite Sensors for Aerosol Retrievals[a]

Instrument	Spectral Characteristics	Record Length	Space/Time Resolution	AOT	Retrieval Coverage					Other Strengths/Limitations and Key References
					Desert	Other Land	Sea	Day	Night	
OMI[b]	UV channels (312–380 nm)	2004 to present	13 × 24 km; daily	Yes	Yes	Yes	Yes	Yes	No	AOT, single scattering albedo, and absorbing aerosol index; longest near continuous record (with OMI). Subpixel cloud contamination, sensitivity to aerosol layer height [*Torres et al.*, 1998].
TOMS[b]	UV channels (312–380 nm)	1979–1993; 1996–2005	50 km; daily	Yes	Yes	Yes	Yes	Yes	No	AOT, single scattering albedo, and absorbing aerosol index; longest near continuous record (with OMI). Subpixel cloud contamination, sensitivity to aerosol layer height [*Torres et al.*, 1998].
MODIS 5.1 standard algorithm	Visible channels (412–670 nm)	2000 to present	10 km; twice daily (daytime)	Yes	No	Yes	Yes	Yes	No	AOT and Ångström coefficient; fine mode fraction, effective radius (ocean only); asymmetry factor (ocean only); and high spatial resolution with extensive time coverage. Cloud free only [*Remer et al.*, 2005].
MODIS Deep Blue[b]	Visible channels plus UV blue (412–670 nm)	2002 to present	10 km; twice daily	Yes	Yes	Yes	Yes	Yes	No	AOT over oceans and land and near global spatial extent at high spatial resolution and with extensive time coverage. Cloud free only [*Hsu et al.*, 2004].
MISR[b]	Visible and near infrared channels with multiple viewing angles	2000 to present	17.6 km; 9 day global repeat cycle	Yes	Yes	Yes	Yes	Yes	No	AOT; Ångström exponent; small, medium, and large fractions; nonspherical fraction; and single scattering albedo over land and ocean with high accuracy. Cloud free only [*Diner et al.*, 2005].
SEVIRI[b]	Visible, near, mid-, and thermal infrared channels	2002 to present	3 km nadir; 15 min	Yes	Yes	Yes	Yes	Yes	Yes (false color only)	AOT and dust false color product; high space-time resolution. Day and night for qualitative products. Cloud free only [*Brindley and Ignatov*, 2006; *Thomas et al.*, 2007].
Advanced very high resolution radiometer (AVHRR)	Visible and near infrared channels	1981 to present	4 km; daily	Yes	No	No	Yes	Yes	No	AOT and Ångström coefficient; long continuous record. Cloud free only [*Husar et al.*, 1997; *Evan et al.*, 2006].
Advanced Along Track Scanning Radiometer (AATSR)	Visible and near infrared channels	1995 to present	3 × 4 km; 3 day repeat cycle	Yes	No	Yes	Yes	Yes	No	AOT and Ångström coefficient. High spatial resolution. Cloud free only [*Thomas et al.*, 2009].
Medium-Resolution Imaging Spectrometer (MERIS)	Visible channels	1995 to present	~1 km; 3 day repeat cycle	Yes	No	Yes	Yes	Yes	No	AOT and Ångström coefficient. High spatial resolution. Cloud free only [*Ramon and Santer*, 2001].

TABLE 1. (continued)

Instrument	Spectral Characteristics	Record Length	Space/Time Resolution	AOT	Retrieval Coverage					Other Strengths/Limitations and Key References
					Desert	Other Land	Sea	Day	Night	
POLDER	Spectral, directional, and polarized visible radiances	1997 to present	20 km; daily	Yes	No[c]	No[c]	Yes	Yes	No	AOT, Ångström coefficient, fine mode, and nonspherical fractions over ocean (operational) and land (under development). Cloud free only [*Herman et al.*, 2005; *Dubovik et al.*, 2011].
Atmospheric Infrared Sounder (AIRS)	Infrared hyperspectral sounding channels	2003 to present	1°; twice daily (day and night)	Yes	No[c]	No[c]	Yes	Yes	Yes	AOT at 10 μm, aerosol effective radius, and mean aerosol layer height. Day and night retrievals.
Infrared Atmospheric Sounding Interferometer (IASI)	Infrared hyperspectral sounding channels	2007 to present	1°; twice daily (day and night)	Yes	No	No	Yes	Yes	Yes	AOT at 10 μm, aerosol effective radius, mean aerosol layer height. Day and night retrievals. Cloud free only.
CALIOP[b]	Polarization lidar (532 and 1064 nm)	2006 to present	30 m vertical, 300 m horizontal; 16 day repeat cycle	Yes	Yes	Yes	Yes	Yes	Yes	Vertical profile of aerosol backscatter and aerosol mask over land and ocean; cloud contamination; poor temporal sampling [*Winker et al.*, 2009].
ICESat[b]	Laser altimeter and green channel	2003–2010 (3 months per year)	91 day repeat cycle	No	Yes	Yes	Yes	Yes	Yes	Vertical profile of aerosol over land and ocean. Cloud contamination; very low temporal sampling [*Schutz et al.*, 2005; *Spinhirne et al.*, 2005].

[a]All sensors provide near global coverage except SEVIRI which has a geostationary satellite view centered on 0°N, 0°E.
[b]These rows highlight those instruments which currently provide estimates directly over desert surfaces.
[c]Land retrievals under development [*DeSouza-Machado et al.*, 2006; *Pierangelo et al.*, 2004; *Peyridieu et al.*, 2010].

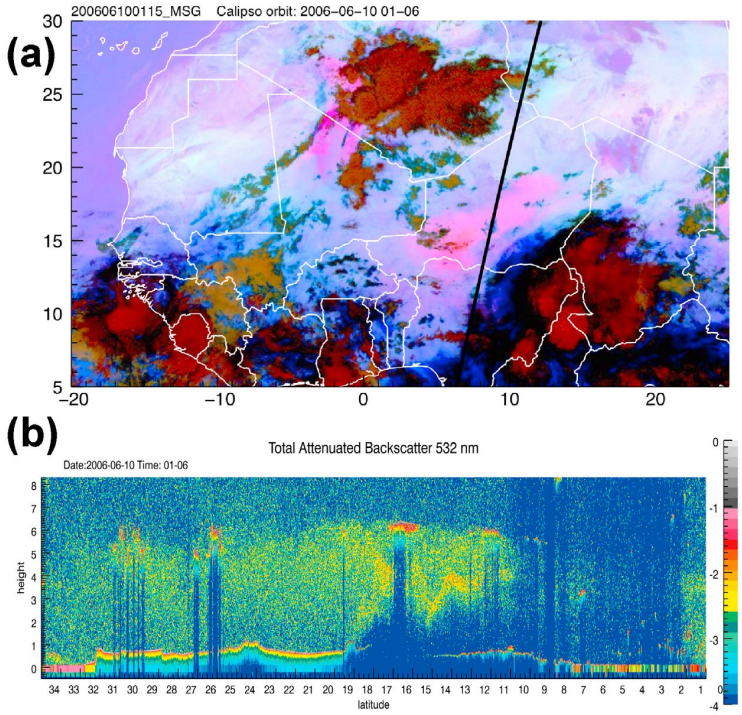

Figure 3. Example of a recent advance in Earth observation of dust aerosols. (a) MSG SEVIRI IR dust product for 0115 UTC 10 June 2006. Dust appears pink in these images and clouds appear red (deep, high), black (shallow, high), orange (midlevel), and green/blue (low). (b) The 532 nm total attenuated backscatter (km^{-1} sr^{-1}) from CALIOP with latitude marked on the *x* axis (horizontal track shown in black in Figure 3a, only section between Nigeria and the Libyan coast shown) around the same time. The deep dust layer over the Sahara between 20°N and 25°N and Saharan dust overriding the shallow monsoon layer over southern West Africa south of ~19°N stand out in Figure 3b.

such that absolute uncertainties remain relatively high. Global scale intercomparisons indicate far greater agreement between aerosol algorithms over ocean than land [*Poulsen et al.*, 2009; *Mishchenko et al.*, 2010; *Kittaka et al.*, 2011]. There is a clear need for more extensive, quantitative intercomparison and understanding of the sources of uncertainty, especially over deserts. We can anticipate that further advances in Earth observation of aerosols will emerge from new algorithm development and integration of multiple sensors [e.g., *Christopher et al.*, 2011].

[17] While satellites provide unparalleled spatial and temporal coverage, surface-based sensors play an important role too (not least as validation for satellite products). The global AERONET network of almost 500 surface-based Sun photometers [*Holben et al.*, 1998] provides high-quality retrievals of AOT and of aerosol optical and physical properties. However, coverage in the Sahara is particularly sparse. The recent field campaigns over North Africa listed in section 1 (see Figure 2) have involved the deployment of sophisticated surface-based instrumentation to directly measure aerosol and related meteorological properties with high precision. These include standard meteorological instruments, aerosol lidar, optical particle counters, and various dust samplers to measure emission and deposition as well as detailed optical and physical properties of aerosols (see Figures 5a and 14b for examples). In many cases (AMMA, DABEX, SAMUM, and Fennec), these surface observations are complemented with similar measurements from airborne instruments on research aircraft, providing very detailed information on processes in horizontal and vertical directions. All, however, are limited by relatively short observation periods over limited domains.

2.3. Issues in Modeling Dust Processes

[18] Recent years have seen a veritable boom in the development and implementation of dust modules in weather and climate models for a large range of applications reaching from modeling systems for regional or global air quality and dust forecasting (e.g., Global and Regional Earth-System Monitoring Using Satellite and In Situ Data (GEMS) [*Hollingsworth et al.*, 2008], Monitoring Atmospheric Composition and Climate (MACC) [*Morcrette et al.*, 2008], Dust Regional Atmospheric Model (DREAM) [*Nickovic et al.*, 2001], and Integrated Community Limited Area Modeling System (ICLAMS) [*Solomos et al.*, 2011]), through global off-line aerosol-chemistry transport models used for process

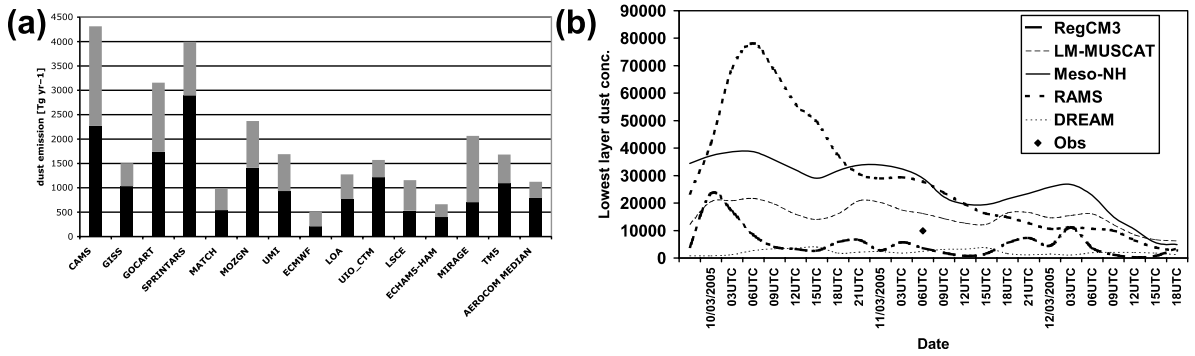

Figure 4. Uncertainty in model estimates of dust emission at the global and local scales. (a) AeroCom model intercomparison of annual global (gray bars) and North African (black bars) dust emission based on data from *Huneeus et al.* [2011]. (b) Time series of model simulated dust concentration in lowest layer (μg m^{-3}) at the location of Chicha, Chad, during the BoDEx field campaign in March 2005 showing marked model disagreement and temporal trends [*Todd et al.*, 2008a, Figure 8]. Only one observation is available for this period (marked as a black diamond).

studies (e.g., Global Model of Aerosol Processes (GLOMAP) [*Spracklen et al.*, 2005] and CHIMERE-DUST [*Menut et al.*, 2009]), to fully coupled Earth system models employed for climate projections (e.g., Quantifying and Understanding the Earth System (QUEST) Earth System Model (QESM; http://www.quest-esm.ac.uk/) and Community Climate System Model (CCSM) [*Mahowald et al.*, 2011]). It is notable that the World Meteorological Organization (WMO) recently

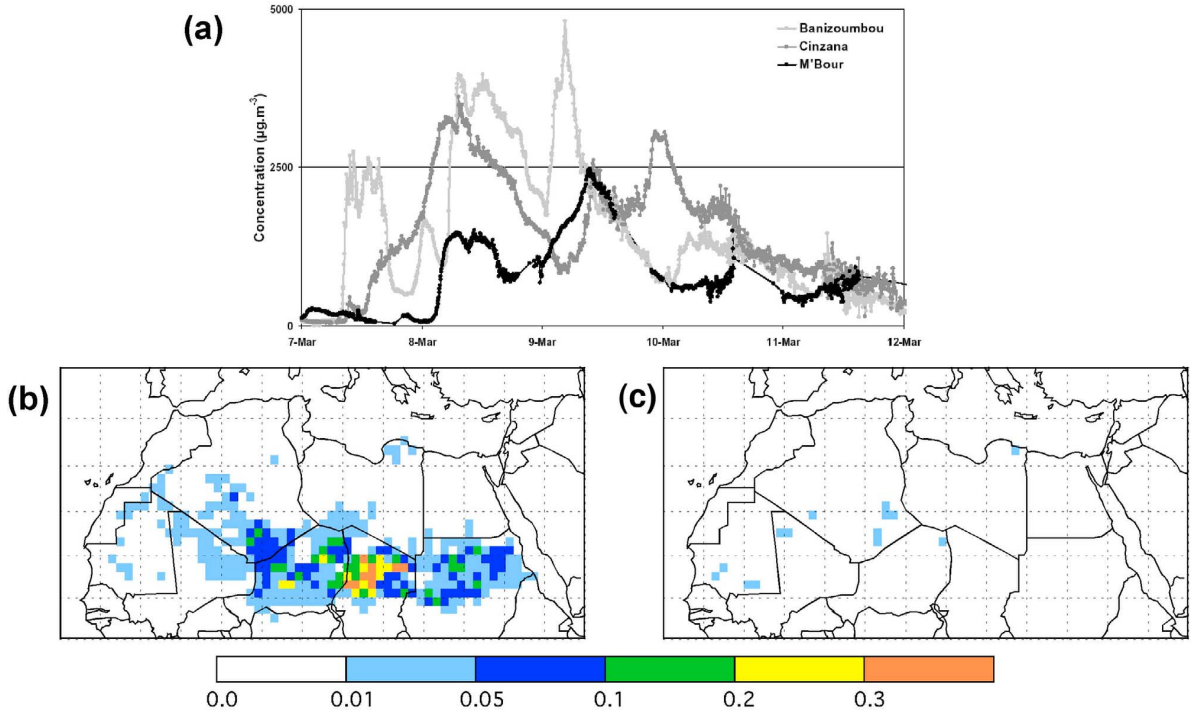

Figure 5. Diurnal cycle of dust emission. (a) The 5 min mean PM_{10} concentrations measured along the AMMA Sahelian dust transect at Banizoumbou (Niger), Cinzana (Mali), and M'Bour (Senegal) from 7 to 12 March 2006 [*Marticorena et al.*, 2010, Figure 10]. The time evolution shows rapid changes in surface concentrations due to changes in local wind speed and advection from sources upstream. Frequencies of dust source activation as identified from the infrared channels of SEVIRI during boreal winter (December–February) for (b) 0300–0900 and (c) 1200–0000 UTC [from *Schepanski et al.*, 2009, Figure 2]. The shorter morning period shows substantially more emission events across large parts of the southern Sahara.

established the Sand and Dust Storm Warning Advisory and Assessment System (SDS-WAS; http://www.wmo.int/pages/prog/arep/wwrp/new/Sand_and_Dust_Storm.html) to enhance the ability of countries to deliver timely and quality sand and dust storm forecasts, observations, information, and knowledge to users. Within this program, the Northern Africa-Middle East-Europe Regional Center aims to lead the development and implementation of a system for dust observation and forecast and currently distributes forecasts over North Africa from eight modeling centers.

[19] In the framework of the Global Aerosol Model Intercomparison (AeroCom) initiative [*Schulz et al.*, 2009], the dust budget in 15 global models driven by prescribed or nudged analyzed meteorological fields were compared [*Textor et al.*, 2006; *Huneeus et al.*, 2011]. All diagnostic parameters characterizing the dust budget show a large spread with estimates for both global and North African dust emissions differing by a factor of about 5 (Figure 4a). These uncertainties are attributed to differences in (1) dust emission parameterization [*Zender et al.*, 2004]; (2) soil properties, including soil moisture; and (3) representation of peak winds. Because of the high sensitivity of dust flux to the high tail of the wind speed distribution, the usage of different meteorological "driver" fields (e.g., European Centre for Medium-Range Weather Forecasts (ECMWF) versus National Centers for Environmental Prediction reanalysis) alone can produce larger differences than different dust emission schemes [*Luo et al.*, 2003; *Menut*, 2008]. Using wind fields generated by free running regional or global models, as necessary for air quality forecasts or climate projections, further enhances the wind-related uncertainties [*Timmreck and Schulz*, 2004]. A regional dust model intercomparison for the Bodélé Depression during BoDEx by *Todd et al.* [2008a] shows differences in emission and loading of around 1 order of magnitude (Figure 4b). Major obstacles to reducing these uncertainties are the lack of available dust emission measurements to validate emission parameterizations near source areas (see section 2.2 for more details).

[20] Uncertainties in emissions have impacts on the entire dust budget. Because of a stronger observational constraint on dust burden through satellite AOT retrievals, models are often "tuned" with respect to this parameter (see section 2.3.1 for more details), resulting in a diversity among the AeroCom models of 40%, which is smaller than that for emission and deposition [*Textor et al.*, 2006]. Prescribing emissions has a surprisingly small effect on dust burden [*Textor et al.*, 2007, Table 2], suggesting that tuning creates compensational effects between emission and deposition. It is, therefore, believed that source strength is one of the major limiting factors in simulating aerosol fields [*Textor et al.*, 2006]. Any improvement in the representation of dust emission in models will therefore improve estimates of both dust loading and deposition, calling for a better understanding of the involved mechanisms at the process level [*Textor et al.*, 2007]. This in turn is crucial for radiative forcing and cloud effects (loading) and biogeochemical and surface albedo effects (deposition).

2.3.1. Dust Emission Parameterization

[21] Dust emission involves complex, nonlinear processes governed by meteorology and the state and properties of land surfaces. Direct in situ field measurement typically observe emission over a few tens of square meters at most [e.g., *Houser and Nickling*, 2001], so that measurement at the scale of most atmospheric models are rather difficult. The currently ongoing project DO4 Models: Dust Observation (http://www.geog.ox.ac.uk/research/climate/projects/do4models.html) aims to observe emission at a coarse, model-relevant scale at a field site in Botswana. To date, much of what is known about these processes has been obtained from microscale (local) experiments in the field and wind tunnels and theoretical studies [e.g., *Marticorena and Bergametti*, 1995; *Alfaro et al.*, 1998; *Shao and Mikami*, 2005; *Ishizuka et al.*, 2008; *Okin*, 2008; *Li et al.*, 2010; *Kok*, 2011]. The early work of *Bagnold* [1935, 1937] suggested that dust particles are released to the atmosphere through three mechanisms: (1) the direct aerodynamic entrainment or suspension of particles, (2) saltation bombardment, and (3) aggregate disintegration. Emission schemes parameterize some or all of these processes and are classified as more or less physically based, depending on the number of processes explicitly represented. Dust emission models are too numerous to describe here individually, but, in general, global models tend to incorporate simple schemes and regional models utilize more physically based schemes (see short summary in chapter 6.1 of *Shao et al.* [2011]).

[22] Simple schemes parameterize the vertical flux of emitted mineral aerosols into the atmosphere as a function of the third (or fourth) power of the difference between the surface wind speed u and a fixed threshold u_t for $u > u_t$. Other schemes use the friction velocity, u_*, instead. Here u_* is the square root of the kinematic stress at the surface and is usually calculated from wind at 10 m and surface roughness. In contrast, more physically based schemes [*Marticorena and Bergametti*, 1995; *Shao et al.*, 1996] explicitly calculate (1) the size-resolved horizontal flux (saltation) as a function of friction velocity above the threshold, which depends on the surface characteristics of soil grain size distribution, crusting, moisture content, snow, and vegetation cover and then (2) the resulting vertical dust fluxes from soil aggregate bombardment and disintegration, either as a function of particle kinetic energy [*Shao et al.*, 1996; *Alfaro and Gomes*, 2001] or through a volume removal relationship [*Lu and Shao*, 1999; *Shao*, 2004]. Many schemes include a scaling parameter to represent source "intensity" to tune emissions. For example, preferential sources have been identified by colocation of peak TOMS aerosol index (*AI*) and topographic lows [*Ginoux et al.*, 2001; *Prospero et al.*, 2002]. Others use more physical parameters such as the grid cell erodible fraction, i.e., the part of the surface which is not protected from wind erosion by roughness elements [e.g., *Laurent et al.*, 2006]. Generally speaking there is a substantial disagreement between different methods to identify sources [see *Formenti et al.*, 2011, Figure 1].

[23] Dust emission schemes require both meteorological and land surface characteristics at the temporal and spatial scales pertinent to dust emission processes such as high-resolution surface stresses, particle size distribution, binding energies, etc. Such information is hardly ever available, even for the highest-resolution regional models (a few kilometers grid spacing). As a result, because of remaining large uncertainties associated with representing the very heterogeneous soil and land surface physical characteristics and wind regimes, many modelers have introduced explicit or implicit tuning parameters into the schemes, which enables emission to be calibrated such that the resulting dust burden in the atmosphere is consistent with measured AOTs from surface or satellite [*Cakmur et al.*, 2006]. Even in applying the most physically based schemes many parameters, especially soil characteristics, are not sufficiently well constrained, so empirically derived constants are commonly used in process equations. Examples include the constants in the soil moisture correction and in the derivation of vertical dust flux from horizontal saltation flux (the "sandblasting efficiency") [*Marticorena and Bergametti*, 1995; *Alfaro and Gomes*, 2001; *Shao*, 2004]. It is highly likely that these constants are in effect scale and location dependent and that varying these could be used to tune emission.

[24] Not surprisingly, model intercomparison projects typically indicate high uncertainty in dust emission estimates [e.g., *Textor et al.*, 2006; *Todd et al.*, 2008a; *Huneeus et al.*, 2011], but identifying and ranking the specific sources of model error is difficult. To address this, a number of recent studies have sought to systematically quantify the uncertainty associated with each stage in various physically based dust schemes. *Darmenova et al.* [2009] noted from the sensitivity experiments of the *Marticorena and Bergametti* [1995] and *Shao et al.* [1996] schemes that horizontal dust flux is most sensitive to friction velocity, with land surface parameters important only for lower wind speed events, highlighting the priority need to reduce uncertainty in meteorological fields. Nevertheless, sensitivity experiments using identical meteorology show that differences in monthly emission over the main Asian dust source regions can greatly exceed a factor of 2 as a result of the combined differences between two schemes. *Kang et al.* [2011] explicitly analyzed the sensitivity to three different vertical flux parameterizations for a 5 day Asian dust event. Total emission estimates vary by more than a factor of 6. Note that differences in scale and location between these two studies make direct quantitative comparison difficult. It is clear, however, that uncertainty associated with parameterization of the dust emission processes remains very high, resulting from incomplete physics coupled with a lack of critical land surface information.

[25] Whatever dust scheme is used, a key requirement is an accurate representation of the high tail of the u_* distribution. Despite the high sensitivity of emissions to near-surface peak winds [*Uno et al.*, 2006] and the comparatively large amount of available measurements of this parameter in source regions, surprisingly few studies have addressed the problem of improving the representation of u_*, which is often simply considered as an external driving parameter. Atmospheric models used for dust simulations are mostly based on numerical weather prediction or climate models, which have not been optimized for the complex and highly energetic desert PBL. It has been suggested that coarse-resolution models cannot sufficiently represent many meteorological processes crucial for peak wind generation and that a parameterization of subgrid wind variance is desirable [e.g., *Cakmur et al.*, 2004]. First attempts to tackle this problem in a physical way by computing probability density functions for wind speed using turbulent kinetic energy (TKE) estimates from the model's PBL scheme report significant improvements [*Cakmur et al.*, 2004; *Grini et al.*, 2005], consistent with higher correlations of dust loadings with gustiness than with mean wind [*Engelstaedter and Washington*, 2007].

2.3.2. Deposition

[26] Dust deposition occurs through both dry deposition and wet deposition associated with cloud and precipitation processes. As such, deposition involves a complex set of physical processes for which understanding requires detailed knowledge of dust size distribution, density, particle shape, hygroscopicity, and cloud and precipitation microphysics. As it is not a focus of this review, only a very short summary is given here for completeness. Overall, the uncertainty in deposition processes and rates are at least as great as those for emission processes but have received far less attention in the literature, and there has been limited systematic evaluation in dust models [*Huneeus et al.*, 2011]. Estimates of total deposition based on global aerosol models range from about 700 to over 4000 Tg yr^{-1}, with wet deposition contributing from over 60% to well under 20% [*Huneeus et al.*, 2011, Table 3]. Measurements of dust deposition are conducted with traps over land and ocean but are generally few and incomplete, particularly for dry deposition. *McTainsh* [1999], for example, measured deposition rates of about 200 g m^{-2} yr^{-1} in Niger. Observations established during AMMA [*Rajot et al.*, 2008] and the International Global Atmospheric Chemistry - Deposition of Biogeochemically Important Trace Species Africa (IDAF) network (http://idaf.sedoo.fr/spip.php?rubrique3) have improved our knowledge over Sahelian and tropical West Africa. There is a large interest in the magnitude of dust input into the world's oceans because of biogeochemical implications, but current estimates disagree by a considerable amount [see *Shao et al.*, 2011, Table 2]. Because of the great source strength of the Sahara and predominant easterly flow at low levels, the North Atlantic is one of the regions with the largest dust input (on the order of 180–260 Tg yr^{-1}).

3. METEOROLOGICAL CONTROLS ON DUST DISTRIBUTION

[27] In this section, we summarize the key characteristics of the dust distribution over the Sahara (section 3.1) and review the recent research, which has sought to provide a physical explanation of these structures (section 3.2).

3.1. Spatiotemporal Structure of Saharan Dust

[28] Despite the growth of integrated surface-based observational networks such as AERONET, there remains precious few direct in situ observation of the dust budget from the Sahara. However, advances in satellite systems (see section 2.2) have facilitated new insights into the characteristic patterns of Saharan dust emission and transport and the associated effects on climate. Here we describe some of the key features of the mean horizontal and vertical dust distributions as well as their seasonal and diurnal cycles.

3.1.1. Mean Dust Distribution and Associated Seasonal Cycle

[29] Annual mean dust burden derived from all the long-term satellite data sets currently available (TOMS, OMI, MISR, and MODIS Deep Blue; see Table 1 and section 2.2 for details) show similar spatial patterns with peaks ("hot spots") immediately downwind of the Bodélé Depression in Chad and a larger area over the western Sahara (WS) with a large downwind transport plume extending from the continent over the subtropical east Atlantic (Figure 1). *Ben-Ami et al.* [2011] have recently described the mean seasonal pattern of emission and transport over the subtropical North Atlantic as an annual "triplet" of two strong dust seasons and one season with low dust loadings. The first dust season extending from November to March (Figure 1a) involves episodic dust emission events, notably from the Bodélé Depression, and dust transport within a more southern latitude and over West Africa and the Atlantic at ~5°N, where the dust often mixes with biomass burning aerosol [e.g., *Knippertz et al.*, 2011]. The second dust season during May–September (Figure 1b) has more uniform emission frequency with strong contributions from the Bodélé Depression and WS. At this time of year, the broad WS dust hot spot is colocated with the SHL (Figure 1b). Smaller areas of high dust loadings are located along the southern foothills of the Atlas Mountains and in Libya and Egypt. The westward dust transport plume advances northward to reach about 20°N. The third season of October–December experiences low dust loadings (Figure 1c). Differences in the satellite products shown in Figure 1 are nicely illustrated by the different size of the Bodélé Plume during this season, illustrating the uncertainties discussed in section 2.2.

[30] Regarding the location of continental dust sources, work in the last decade sought to interpret the patterns of dust burden in terms of local source regions [*Prospero et al.*, 2002; *Washington et al.*, 2003; *Engelstaedter and Washington*, 2007]. This is relatively unproblematic in the case of the Bodélé Depression, where the extraordinary frequency of emission during winter from localized lacustrine deposits combined with a dominant southwestward transport ensures that the hot spot in satellite fields directly represents the activity of this singular source. Recent work on the Bodélé Depression has provided a comprehensive climatological and geomorphological explanation for its dominance as a dust source [*Washington et al.*, 2006; *Koren et al.*, 2006; *Todd et al.*, 2007]. Of course, other sources are active in winter too (notably those in the great event of March 2006 [*Slingo et al.*, 2006; *Cavazos et al.*, 2009]), but their frequency of emission is so much lower than that of the Bodélé Depression that their emission does not emerge strongly in mean aerosol burden fields (Figure 1a).

[31] Explaining the existence of the WS hot spot is more difficult and has been a source of lively debate in the literature for a number of reasons: (1) the high dust burden is dispersed over a wider area (Figure 1b), (2) there is no single major source region with a well-understood geomorphological history [*Prospero et al.*, 2002; *Washington et al.*, 2003], (3) the few available surface station observations are not fully consistent with the strong increase in summer that some satellite products show [*Klose et al.*, 2010], and (4) the dust "season" occurs during the West African summer monsoon when the atmospheric circulation in the region leads to multiple meteorological emission mechanisms and trajectories of dispersion [*Knippertz and Todd*, 2010] (see also section 3.2). High-temporal-resolution imagery from the MSG SEVIRI has enabled more precise identification of sources through a qualitative backtracking of specific dust plumes to their sources of origin [*Schepanski et al.*, 2007]. The resulting maps of dust source activation frequency (DSAF; irrespective of magnitude, Figures 1d, 5b, and 5c) confirm the importance of the Bodélé Depression and broadly the WS but illustrate the importance of the margins of topographic features, notably the Hoggar and Aïr Mountains for the latter region. The disparity over WS between DSAF and the satellite-derived mean aerosol burden is consistent with the explanation of *Knippertz and Todd* [2010], which suggests that multiple, multiscale emission mechanisms associated with the climatological distribution of synoptic and mesoscale processes activate the various dust sources identified in the DSAF and drive the subsequent vertical and horizontal transport processes over the WS and West African sector, with the resulting distribution exhibited in Figure 1b. In the following, we will examine the meteorological processes of emission and transport that in effect drive this complex seasonal pattern in more detail.

3.1.2. Diurnal Cycle

[32] Early studies on the diurnal cycle of dustiness used synoptic station observations of horizontal visibility as an indicator and found an increase during the daytime hours with some variations between the Sahel and Sahara [*N'Tchayi Mbourou et al.*, 1997]. High-resolution surface concentrations from the AMMA Sahelian dust transect show remarkably complex diurnal changes with abrupt increases but generally confirm the daytime maximum (Figure 5a). Until recently, satellite aerosol products were limited to a fixed daily observation time by either characteristics of the satellite platform (polar-orbiting satellites in the case or TOMS, OMI, MISR, and MODIS) or the algorithm (the Infrared Difference Dust Index) [*Legrand et al.*, 1994]. As such our perspective on dust was strongly biased toward the near-noon time period. Analysis of the twice daily time series of MODIS data revealed a strong diurnal pulsing of emission from the Bodélé Depression during winter, indicating discrete "packets" of emission during daytime hours [*Koren and Kaufman*, 2004]. Subsequent analysis of the

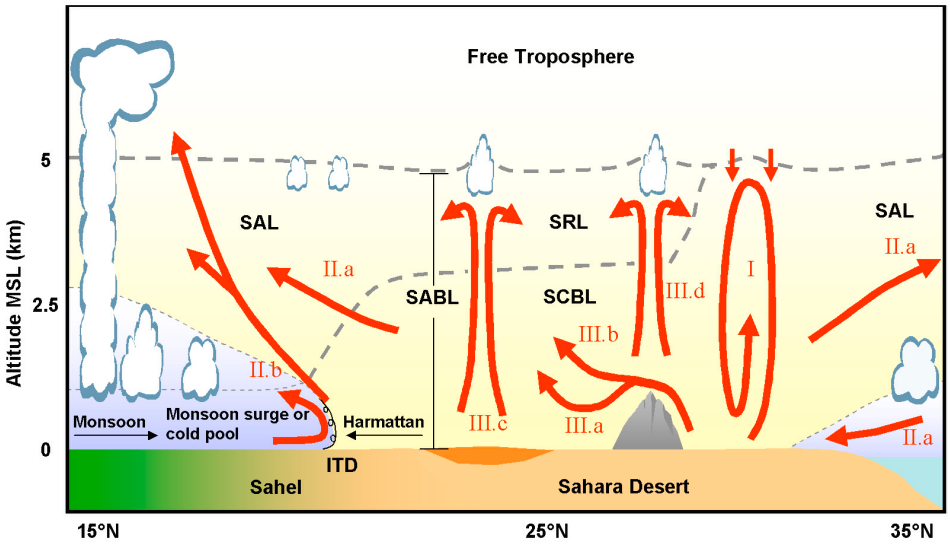

Figure 6. Schematic of the mechanisms which control the structure of the Saharan PBL and dust vertical redistribution [*Cuesta et al.*, 2009, Figure 1]. Shading (yellow or light blue) indicates air mass origin and temperature. Abbreviations stand for intertropical discontinuity (ITD), Saharan air layer (SAL), Saharan atmospheric boundary layer (SABL), Saharan convective boundary layer (SCBL), and Saharan residual layer (SRL). The numerical labels in the figure refer to sections of *Cuesta et al.* [2009]; the associated processes are described here in section 3.2.4.

number of plume trajectories across the entire Sahara from the novel 15 min SEVIRI imagery [*Schepanski et al.*, 2007, 2009] revealed the dominance of the midmorning period for dust plume initiation in all source regions in all seasons (Figures 5b and 5c show boreal winter as an example).

3.1.3. Vertical Distribution

[33] Most passive satellite and ground-based instruments can only provide column-integrated information on dust loading such as AOT (see section 2.2). Most of our knowledge on the vertical structure of dust plumes results from aircraft, surface-based, and satellite-borne aerosol lidars. While the former two are usually restricted to field campaigns or locations relatively far away from Saharan dust sources, spaceborne CALIOP now provides north-south cross sections through Saharan dust plumes in cloud-free regions (e.g., Figure 3b). Although the temporal resolution of CALIOP is poor, the widespread distribution and relatively slow dust transport allows a robust picture to emerge. These measurements have added substantial detail to our knowledge of the characteristic vertical patterns in the dust distribution, first investigated through aircraft measurements in the 1970s, particular over the continent. During winter, dust plumes remain close to the surface during transport from sources across the Sahara [*Chiapello et al.*, 1995; *Johnson et al.*, 2008; *Peyridieu et al.*, 2010; *Knippertz et al.*, 2011], with high concentrations at stations in the Sahel [*Klose et al.*, 2010; *Marticorena et al.*, 2010]. South of 10°N there is evidence of dust aerosol (often mixed with biomass burning aerosol) above 1.5 km, probably associated with vertical transport around cumulus congestus cloud systems over southern West Africa [*Knippertz et al.*, 2011].

[34] During the boreal summer, the PBL and therefore the dust layer over the Sahara and the adjacent Atlantic Ocean is substantially deeper and frequently reaches altitudes of up to 6 km above sea level [*Gamo*, 1996; *Léon et al.*, 2009; *Tesche et al.*, 2009; *Cavalieri et al.*, 2010; *Peyridieu et al.*, 2010]. This deep, hot, and dusty air mass has been termed the Saharan air layer (SAL) by *Carlson and Prospero* [1972]. Toward the fringes of the Sahara the SAL usually glides up onto the cooler low-level air masses of the southwesterly monsoon flow to the south and the maritime air of the subtropical Atlantic and Mediterranean Sea to the west and north, leading to an elevated dust layer [*Prospero and Carlson*, 1972; *Karyampudi and Carlson*, 1988]. For the continent, this behavior is nicely summarized in a schematic by *Cuesta et al.* [2009], reproduced as Figure 6 here. The example aerosol profile from CALIOP shown in Figure 3b clearly shows (1) dusty air that appears well mixed throughout the PBL ("SCBL" in Figure 6) over the Sahara, thereby extending from the distinct "cap" at about 6 km height all the way to the ground and (2) how this dust air layer overrides the low-level monsoonal southwesterlies to the south of about 18°N. Observations of surface concentrations in the Sahel show relatively low values in summer [e.g., *Marticorena et al.*, 2010, Figure 4] despite considerable AOTs, confirming the upgliding of dusty air over the monsoon layer.

3.2. Meteorological Conditions for Dust Emission and Vertical Mixing

[35] Analysis of dust and driving meteorological fields from a combination of observations from satellite and field campaigns with model simulations has advanced our

understanding of the role of the multiscale meteorological processes involved in dust emission and transport. This new knowledge provides at least qualitative explanations for the observed spatiotemporal characteristics of the Saharan dust distribution described in section 3.1. To summarize these findings, we will structure this section according to the scale of the meteorological processes from synoptic (section 3.2.2), through mesoscale (section 3.2.3), to microscale aspects (section 3.2.4). In addition, section 3.2.1 will discuss the diurnal cycle of the PBL over the Sahara and how it influences wind speed near the surface, focusing on the role of LLJs. Section 3.2.5 will conclude with some remarks on vertical and horizontal transports. Each of these sections will also discuss implications for modeling the respective process.

3.2.1. Low-Level Jets

[36] Recent studies have indicated that LLJs play a key role in Saharan dust emission and transport. The peak morning emission from the single greatest dust source of the Bodélé Depression [*Washington et al.*, 2006] and more widely across the Sahara [*Schepanski et al.*, 2009] (Figures 5b and 5c) is now known to be phase locked to the LLJ diurnal cycle. The mechanism of LLJ formation, which is found in all subtropical desert regions and which governs the (out of phase) diurnal cycles of LLJ and surface winds (and hence dust emission), is described as follows. In the free troposphere, wind speed and direction for a given location is mainly controlled by the ambient pressure gradient, leading to flow close to geostrophic balance away from the equator. Closer to the surface, turbulence and frictional effects create substantial deviations from geostrophy depending on factors such as surface roughness, wind shear, and vertical stability. Particularly, the last factor can create substantial systematic differences between day and night within the PBL and surface layer. Cloud-free and dry conditions in desert regions cause most of the high insolation during the day to be converted into sensible heating at the surface, leading to a hot, often rather deep, dry convective PBL.

[37] During the night, strong radiative cooling stabilizes the very lowest layers and effectively decouples most of the air that used to be within the PBL during the day from surface friction [*Todd et al.*, 2008b]. In areas of sufficient background pressure gradient, this decoupling leads to an inertial oscillation around the equilibrium wind (usually well approximated by the geostrophic wind) [*Blackadar*, 1957; *Van de Wiel et al.*, 2010] as schematically depicted in Figure 7a. The amplitude of the oscillation depends on the magnitude of the ageostrophic component at the time of decoupling (*D* in Figure 7a) and therefore on the background pressure gradient, latitude, and roughness of the underlying surface. Rough surfaces exert a strong frictional force and therefore a high-amplitude inertial oscillation. The oscillation period is given by 2π divided by the Coriolis parameter, *f*. For 23°N, a typical latitude in the Sahara, the oscillation period is 30.7 h. Assuming a decoupled period of 10–12 h, only about 1/3 of the oscillation can be completed, leading to highly supergeostrophic LLJ peaking before sunrise (as shown from model experiments over the Bodélé Depression in Figure 7b).

[38] The importance of the LLJ to dust results from its relationship with surface winds. After sunrise, surface heating causes the PBL to grow in depth and mixes momentum from the jet level down to the surface. This creates the distinctive diurnal cycle with peak surface winds and dust emissions from morning to midday (Figures 5a, 7c, and 8) and the resulting erosion of the LLJ above and hence the out of phase diurnal cycle of LLJ and surface winds (Figure 7c) [*Knippertz*, 2008*; Todd et al.*, 2008b]. There are very few radiosonde observations of LLJs in the Sahara (Figure 2), but analysis data suggest a frequent occurrence throughout the year (Figure 7d shows January as an example). It should be noted here that the degree of decoupling critically depends on factors suppressing turbulence near the surface during the night. On one hand, clouds or high-column water vapor weaken the radiative cooling and therefore keep stability relatively low, leading to generally less decoupling in summer. This can lead to one or several breakdowns of the jet during the night, when the vertical shear underneath the jet core has reached a critical level, creating so-called intermittent mixing events [*Banta et al.*, 2003]. On the other hand, in situations of very strong background pressure gradients, stability might never become high enough to suppress the mechanically induced turbulence near the surface and therefore impedes a complete decoupling (see, for example, Figure 8a showing surface winds during the main dust storm days during BoDEx and Figure 5a showing a dust emission case over the Sahel).

[39] The close spatial similarity in the frequency of LLJs (Figure 7d) and dust source activation (Figures 5b and 5c) provides compelling evidence of the often dominant role of LLJs in emission, most notable in winter. Accurate model representation of the LLJ processes is therefore crucial. While state-of-the-art numerical models usually reproduce the large-scale pressure gradients that drive LLJs satisfactorily, they often struggle to reproduce the distinct diurnal cycle in near-surface winds (Figure 8a). Several studies have shown problems with temperature inversions over arid areas being too weak, leading to an underestimation of stability in the lowest layers, too little decoupling, and therefore too much vertical dispersion during the night resulting in large wind forecast errors and even phase errors [*Hanna and Yang*, 2001; *Zhong and Fast*, 2003]. These results are sensitive to vertical resolution, PBL scheme, and roughness length [*Zhang and Zheng*, 2004; *Todd et al.*, 2008b] (Figure 8b), suggesting that there is an opportunity to optimize forecast models for the Saharan sector. The work of *Todd et al.* [2008b] notwithstanding, a systematic investigation of the representation of LLJs in dust models and potential implications for emission and transport strength and diurnal cycle remains lacking.

3.2.2. Synoptic Scale

[40] It has long been known that the episodic nature of large dust events is primarily controlled by synoptic scale meteorological features [e.g., *Dubief*, 1979; *Washington and Todd*, 2005; *Schepanski and Knippertz*, 2011], but more

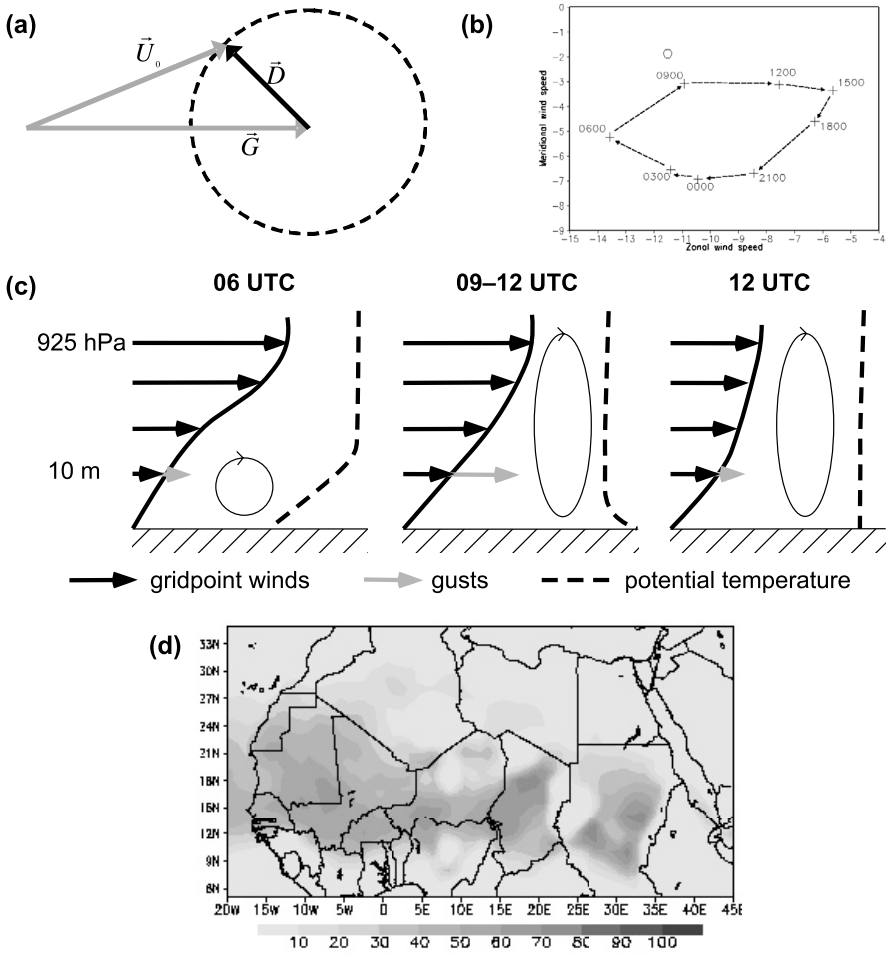

Figure 7. The LLJ and its role for dust emission. (a) Schematic showing a low-level wind vector in the evening (U_0) together with the geostrophic (G) and ageostrophic (D) wind components [*Van de Wiel et al.*, 2010, Figure 1]. The decoupling from surface friction during the night causes a clockwise (in the Northern Hemisphere) inertial oscillation of the wind vector following the dashed circle with a period of $2\pi/f$. (b) Mean diurnal cycle of winds at 940 hPa from numerical simulations over the Bodélé Depression during BoDEx in February and March 2005 providing clear evidence of an inertial oscillation [*Todd et al.*, 2008b, Figure 9a]. (c) Schematic depiction of typical changes in the vertical profile of low-level wind, gusts, potential temperature, and turbulence over the Sahara during morning hours [*Knippertz*, 2008, Figure 1] (http://www.schweizerbart.de/). The key for dust emission is the downward mixing of momentum from the nocturnal LLJ during the morning buildup of the PBL. (d) Frequency of LLJ events during January for ERA-Interim reanalysis data showing widespread occurrence through large parts of the Sahara [*Schepanski et al.*, 2009, Figure 4]. Note similarity of LLJ frequency and dust storm activation frequency in Figure 5. Figures 7a and 7b are © American Meteorological Society. Reprinted with permission.

recent analysis of the space-time distribution of dust AOT has added considerable detail to our understanding. The most important prerequisite for dust storms on this scale is the establishment of a sufficiently large surface pressure gradient to drive strong winds capable of dust emission and long-range transport. From many analyses of case study events and statistical analysis of long-term records, we now have more evidence to identify the dominant synoptic types by season.

[41] During the cool season from November to April, two patterns appear especially important. First, upper level troughs over northern Africa can trigger intense Saharan cyclones along the northern margin of the Sahara [*Alpert and Ziv*, 1989; *Bou Karam et al.*, 2010]. These systems are often related to lee cyclogenesis to the south of the Atlas Mountains and then track eastward along the Mediterranean coast (Figure 9a). They are often referred to as Khamsin cyclones in Libya and Egypt and Sharav cyclones in the Middle East. Many tracks turn northward into Turkey, but some systems continue moving eastward. Incorporating moisture from the Mediterranean Sea can lead to a rapid intensification of the system and cause significant rainfall.

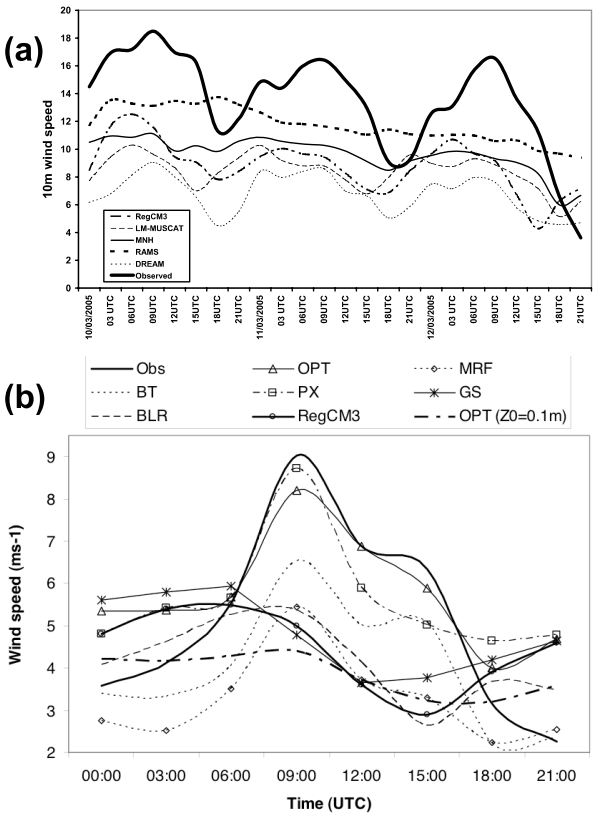

Figure 8. Modeling low-level jets and associated surface winds over the Bodélé Depression. (a) Comparison between observations (solid line) and simulations with five different regional models (horizontal resolutions between 7 and 26 km [*Todd et al.*, 2008a, Figure 4]). Most models tend to underestimate the diurnal cycle and the absolute magnitude of the winds. (b) Mean diurnal cycle in observations (solid) and simulations with the same model in different PBL configurations [*Todd et al.*, 2008b Figure 7a]. Different PBL representations can lead to large differences in wind magnitude and diurnal cycle. Figure 8b is © American Meteorological Society. Reprinted with permission.

This type of event is most frequent during spring, when the baroclinicity along the Mediterranean coast is maximized and supports cyclone intensification [*Alpert and Ziv*, 1989]. Figure 9b shows an example of a Khamsin cyclone with its core over Turkey, which caused widespread dust emission over Libya and Egypt. The dust emitted by Khamsin cyclones often gets carried over the Mediterranean Sea and sometimes even into Europe with the southerly winds ahead of the system.

[42] Second, ridging of the subtropical high increases the south-north pressure gradient over the Sahara and leads to a surge in the northeasterly harmattan or Etesian winds with strong effects on the central and southern Sahara and the Sahel [*Washington and Todd*, 2005; *Knippertz and Fink*, 2006; *Knippertz et al.*, 2011]. Examples for this type of situation include an intensified Libyan high associated with dust outbreaks from the Bodélé Depression [*Washington and Todd*, 2005; *Washington et al.*, 2006] (Figure 10) as well as an intensified and southeastward extended Azores high activating dust sources in Mauritania, Mali, and Algeria [*Knippertz et al.*, 2011]. In both cases, dust emission and surface winds show a clear diurnal cycle affected by the formation of LLJs (see section 3.2.1). Long-lasting, extensive events with high dust amounts are often associated with explosive anticyclogenesis behind a surface cold front penetrating into the northern Sahara. Prominent examples of this type, which generated considerable research interest, occurred during 2–7 March 2004 [*Knippertz and Fink*, 2006; *Min et al.*, 2009; *Mangold et al.*, 2011; *Shao et al.*, 2010] and 7–13 March 2006 [*Slingo et al.*, 2006; *Tulet et al.*, 2008; *Cavazos et al.*, 2009; *Mallet et al.*, 2009; *Stanelle et al.*, 2010]. The evaporating precipitation along the cold front can play an important role in the early stages of these events [*Knippertz and Fink*, 2006]. Generally, numerical models satisfactorily reproduce such large-scale dust outbreaks [*Cavazos et al.*, 2009; *Shao et al.*, 2010] (Figure 11) in that the meteorological drivers of emission and transport provide accurate depiction of timing/transport of dust and AOT with respect to satellite observations. Indeed, in the study of *Cavazos et al.* [2009], model dust estimate errors are dominated by poor representation of specific local sources as a result of inadequate soil information.

[43] In summer, there is a large background pressure gradient into the SHL (Figure 1b), which frequently generates high surface winds, often associated with LLJ formation. This is particularly true for the dry northerly, westerly, and easterly inflow [*Knippertz*, 2008; *Grams et al.*, 2010]. On the moist side of the "intertropical discontinuity" (ITD), which separates Saharan and tropical air masses over Africa, surface inversions are weaker, leading to less decoupling and LLJ formation (see section 3.2.1). Nevertheless, the often large monsoon pressure gradient allows a substantial acceleration of the near-surface wind in stable conditions during the night [*Parker et al.*, 2005], which can lead to dust emissions near the leading edge of the monsoon flow [*Flamant et al.*, 2007; *Bou Karam et al.*, 2008], possibly associated with intermittent LLJ mixing events. The example north-south lidar transect across southern West Africa shown in Figure 12 indicates two regions of dust uplift within the northward progressing monsoon flow. One is the actual leading edge of the monsoonal air; the southern one has been speculated to be the remnants of a convective cold pool (see section 3.2.2) [see also *Marsham et al.*, 2008a]. Rather little is known about the vertical wind structure of these events. The representation of this feature in numerical models has not been systematically investigated but will be closely linked to the representation of the monsoon circulation, which is a large challenge for many coarse-resolution models [*Cook and Vizy*, 2006; *Marsham et al.*, 2011].

[44] The dominant synoptic scale weather systems over summertime West Africa are African easterly waves (AEWs). It has long been known that AEWs modify dust transport over the tropical Atlantic [*Karyampudi and Carlson*, 1988; *Westphal et al.*, 1988], but their role for the dust distribution over the continent is less clear. Recently,

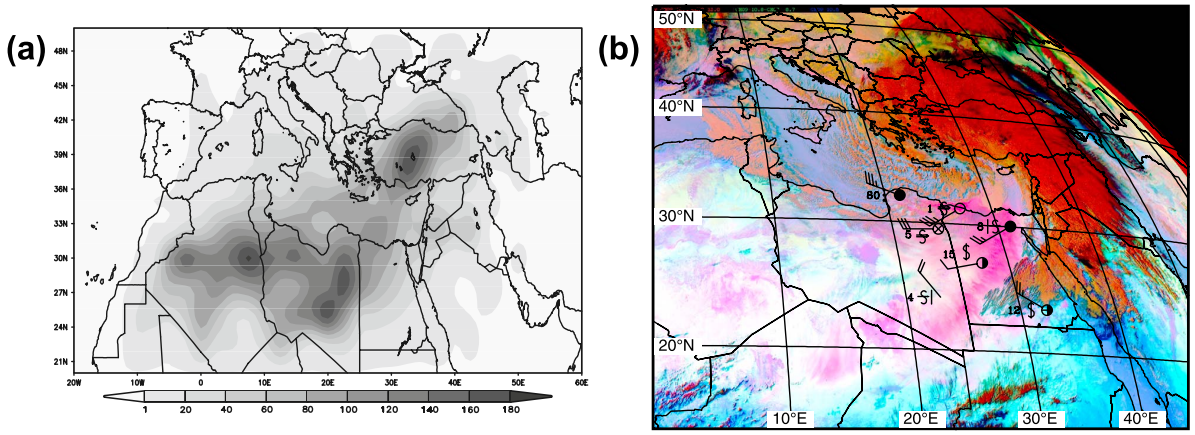

Figure 9. Characteristic synoptic scale weather system associated with dust emission: the Saharan cyclone. (a) Climatology of Saharan cyclone counts in 2.5° × 2.5° grid boxes for March–May 1958–2006 showing maximum activity across the Algerian and Libyan Sahara [*Hannachi et al.*, 2010, Figure 6]. With kind permission from Springer Science + Business Media. (b) Example of a Saharan cyclone on 22 January 2004 in the SEVIRI dust product overlaid with synoptic station reports from Libya and Egypt. The dark red colors show the main cloud mass of the cyclone and cold front, while pink colors indicate dust emission behind the front (also see the Figure 3 caption).

Knippertz and Todd [2010] suggested that AEWs contribute to the synoptic scale variability of the WS hot spot through (1) the organization of dust transport, (2) dust emission around the AEW surface vortex if it is strong enough, and (3) dust emission in connection with convective cold pools (see section 3.2.2) forming in the moist southerlies to the east of the AEW trough upstream of the WS (Figure 13). The same authors provide evidence that interactions between AEWs and subtropical upper level troughs play a role in creating extended areas of southerly moisture advection into the Sahara and northerly dust advection into the WS. Such interactions have been proposed to create dust-generating, traveling surface disturbances called Soudano-Saharan Depressions, but this concept has recently been questioned

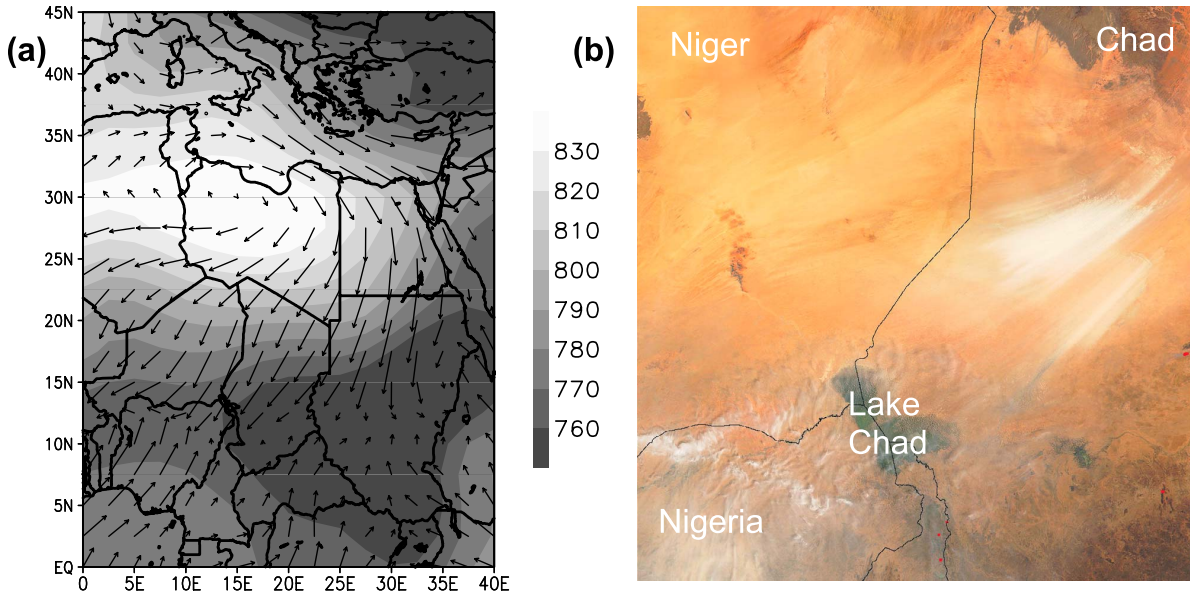

Figure 10. Characteristic synoptic scale weather system associated with dust emission: ridging of subtropical high. (a) Composite mean geopotential height at 925 hPa (geopotential meters, shading) and wind vectors (m s^{-1}) for 10–12 March 2005 associated with dust outbreaks from the Bodélé Depression in Chad. The strong anticyclone over Libya increases the north-south pressure gradient and causes a surge in the northeasterly harmattan flow [*Todd et al.*, 2008a, Figure 2b]. (b) Visible satellite image of a Bodélé Depression dust outbreak [*Washington and Todd*, 2005, Figure 1].

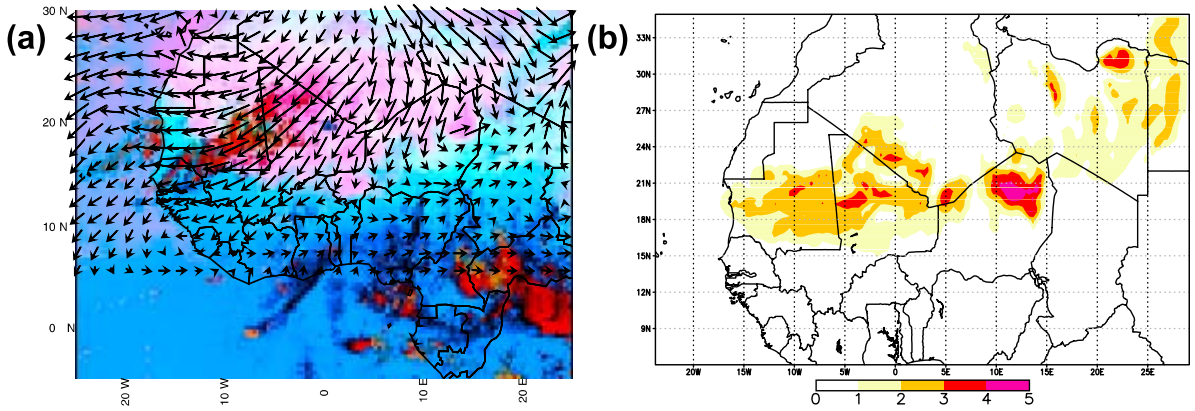

Figure 11. Characteristic synoptic scale weather system associated with dust emission: explosive anticyclogenesis. (a) SEVIRI false color dust composite at 1200 UTC 7 March 2006 (see the Figure 3 caption for explanation) overlain with 925 hPa winds from a regional climate model version 3 (RegCM3) simulation. (b) Corresponding AOT from the same model simulation showing good qualitative agreement with the observations. Figures 11a and 11b are from *Cavazos et al.* [2009, Figure 3].

on the basis of modern reanalysis and satellite data [*Schepanski and Knippertz*, 2011]. AEWs are reasonably well represented in state-of-the-art weather prediction models, although interactions with moist convection and the land surface can lead to errors in both strength and propagation [*Sander and Jones*, 2008; *Shen et al.*, 2010]. Systematic evaluation of model representation of tropical-temperate interactions over the Sahara in relations to these specific synoptic scale features has yet to be conducted.

3.2.3. Mesoscale

[45] A prominent dust storm type on scales of several hundred kilometers is the so-called "haboob," which is caused by evaporationally driven, cold near-surface outflow from organized moist convection. In particular, the squall lines of the Sahel have long been connected to this kind of dust storm [*Sutton*, 1925; *Farquharson*, 1937; *Freeman*, 1952]. The strong gust winds at the leading edge of the cold pool can lead to dramatic moving "walls of dust" (Figure 14a) and very sharp increases in wind speed and particle concentrations (Figure 14b). Haboobs have been documented for the northern [*Knippertz et al.*, 2007; *Emmel et al.*, 2010] and southern margins of the Sahara [*Lawson*, 1971; *Marsham et al.*, 2008a; *Williams et al.*, 2008; *Knippertz and Todd*, 2010] and other deserts worldwide [*Idso et al.*, 1972; *Membery*, 1985; *Chen and Fryrear*, 2002; *Takemi*, 2005; *Miller et al.*, 2008]. Because of the diurnal cycle of deep moist convection haboobs tend to cluster in the late afternoon until early morning [*Emmel et al.*, 2010]. There is an ongoing debate in the scientific community on how much haboobs contribute to total dust emission, partly caused by the difficulties of satellites to detect dust underneath convective cloud shields and problems in distinguishing and tracking specific events [*Engelstaedter and Washington*, 2008; *Williams*, 2008]. Another aspect of debate is subsequent wet deposition of dust particles by convective rains, but SEVIRI dust imagery has recently revealed that at least the northern parts of many large dusty cold pools can move sufficiently far away from the precipitation area (see *Knippertz and Todd* [2010] for examples). Figure 14d shows a CALIOP lidar cross section through the cold pool of an extended haboob penetrating from Niger into southern Algeria (Figure 14c). The sharp, inclined leading edge is clearly visible in the lidar profile connecting with an elevated dust layer from the previous day further south. Their enormous spatial scale and vigor make haboobs one of the most spectacular features in dust research.

[46] Modeling haboobs is a great challenge closely tied to a realistic representation of organized moist convection with a clear dependence on horizontal resolution and convection parameterization [*Knippertz et al.*, 2009a; *Reinfried et al.*, 2009; C. Cavazos and M. C. Todd, Model simulations of a complex dust event over the Sahara during the West African monsoon onset, submitted to *Advances in Meteorology*, 2011] (Figures 14e and 14f). Recent results by *Marsham et al.* [2011] have shown that the contribution from

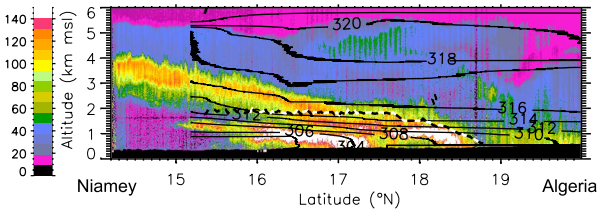

Figure 12. Characteristic summertime dust emission process: the monsoon nocturnal surge. Airborne lidar-derived atmospheric reflectivity at 732 nm along a vertical cross section between Niamey (Niger) and southern Algeria observed during the AMMA special observation period 2 peak monsoon (0602–0658 UTC 7 July 2006) [*Bou Karam et al.*, 2008, Figure 7]. The high reflectivity between 18°N and 19°N marks the leading edge of the southwesterly monsoon flow that accelerates in the course of the night. The black lines are lines of constant potential temperature indicating the stable stratification in the early morning hours.

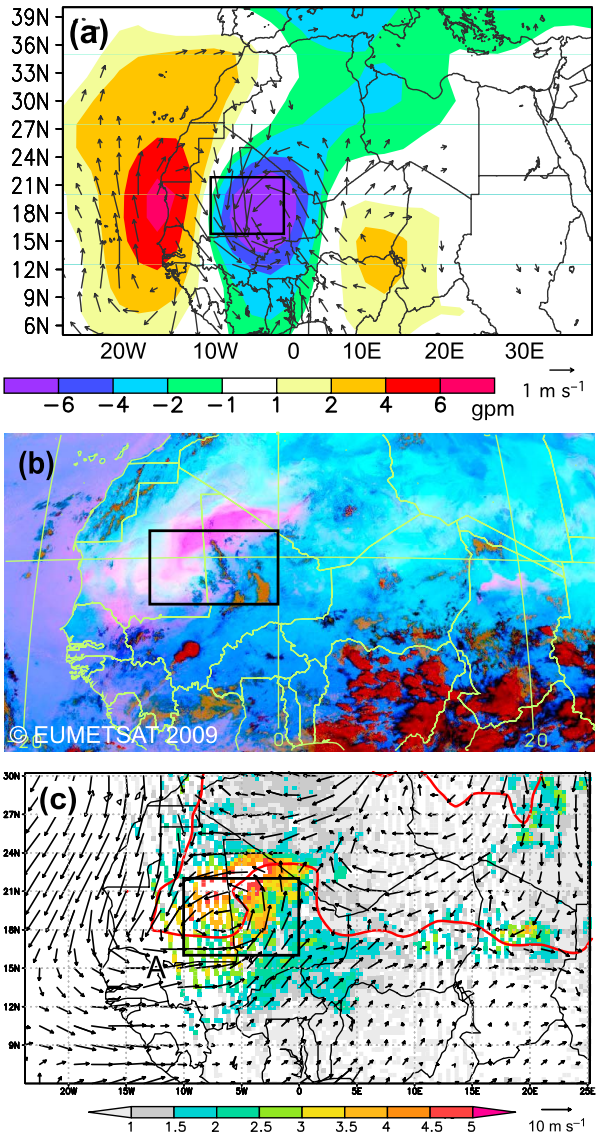

Figure 13. Characteristic summertime dust emission processes: the synoptic scale surface trough. (a) Mean sea level pressure and 925 hPa wind anomalies associated with large positive perturbations in TOMS *AI* over the western Sahara (black box in all figures) during June–September 1979–1993. The patterns indicate enhanced cyclonic winds in the area of the surface trough of an African easterly wave during dust events. (b) SEVIRI dust product (see the Figure 3 caption for explanation) for an example case on 18 July 2006 showing a marked dust plume over the western Sahara. (c) OMI *AI* (shading), 925h Pa winds (vectors), and the intertropical discontinuity (red line) for the same time. Strongest dust signals occur in the northeasterly flow around the cyclonic center and are associated with convection and haboob dust events in the southerly flow [*Knippertz and Todd*, 2010, Figures 4g, 5c, and 5d].

haboob dust emission changes dramatically between simulations using the same model with and without convective parameterization. There are examples of large haboobs over the Sahara, which are not even represented in analysis data because of a lack of observations and difficulties with getting the model to generate the parent convection [*Knippertz et al.*, 2009b]. The key problem is that convective parameterizations are designed to release convective instability within a model grid box and therefore do not allow for the spatial separation of the up- and downdrafts that are crucial to the mesoscale organization and the formation of cold pools, which in reality can easily reach dimensions of many grid boxes of a typical regional model as shown by Figures 14c–14f. Another issue is the correct initiation of convection in the model, which is sensitive to surface topography and soil moisture heterogeneity [*Taylor et al.*, 2011]. Moist convection can also be associated with very small-scale and short-lived intense wind events, sometimes referred to as "dry microbursts" [*Wakimoto*, 2001]. These can be expected to cause dust emission too, but there is very limited research on this topic so far. These results, in particular, those of *Marsham et al.* [2011], suggest that an important dust emission mechanism is not satisfactory represented in the majority of dust models, which has important ramifications on the diurnal cycle and the activation of source regions in the Sahel, where haboobs are most common. There is a need to better quantify the contribution of haboobs to dust emission, transport, and deposition and to explore cost-effective ways to better represent their impacts in models.

3.2.4. Microscale

[47] On scales of a few to several hundred meters, turbulent circulations in the dry convective daytime PBL over deserts can cause considerable emission over bare dry lands on days with high insolation and weak background winds [*Sinclair*, 1969; *Ansmann et al.*, 2009b]. These can take the form of more compact rotating dust devils and larger, longer-lived nonrotating dusty plumes [e.g., *Koch and Renno*, 2005]. There are relatively few high-quality observations of these features over the Sahara. Satellite data is clearly too coarse to monitor microscale systems and in situ measurements are challenging because of logistics. Figure 15a shows lidar measurements from summertime southern Morocco, which give a good indication of the frequency and depths of dusty plumes that stand out as areas of high depolarization (red colors). Clearly identifiable plumes occur on timescales of 10–30 min. Maximum depth increases in the course of the morning reaching values of up to 2 km above the ground (3 km above sea level) around midday.

[48] The contribution of dust devils and dusty plumes to the global dust emission is unknown, but extrapolations of limited observations in North America suggest values of up to 35% [*Koch and Renno*, 2005]. The applicability of these measurements to the Sahara, however, is not clear because of differences in land surface and PBL characteristics and most evidence from satellite data and field campaigns suggests that synoptic and mesoscale processes dominate. The increase in computer capacities in recent years has made it

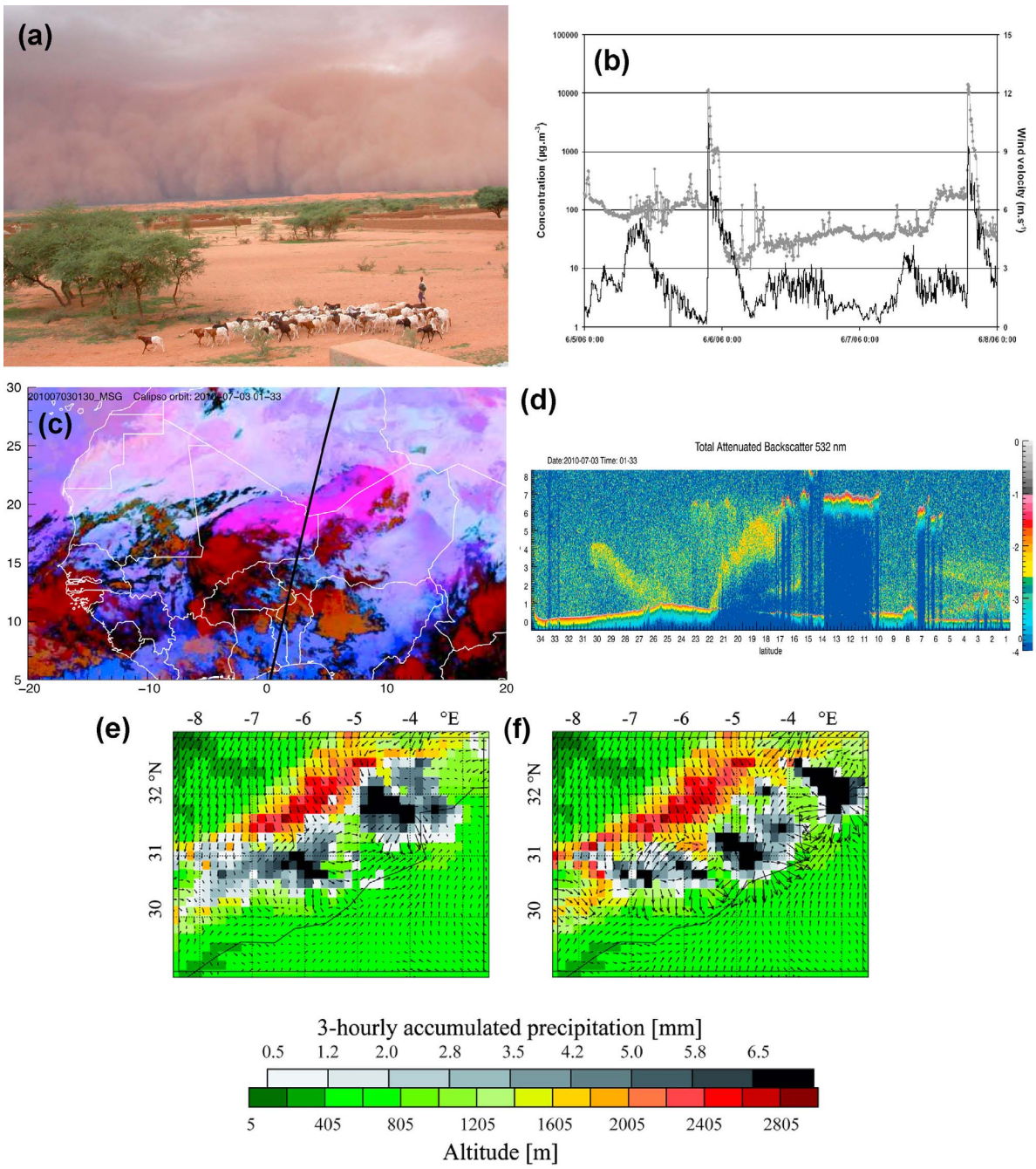

Figure 14. Characteristic summertime dust emission process: haboobs. (a) Photograph of the leading edge of a haboob in Hombori, Mali (photo courtesy of Françoise Guichard, CNRS Photothèque). (b) Surface measurements of PM_{10} concentrations and wind speed at Cinzana (Mali) showing the passage of two haboobs during 5–7 June 2006 [*Marticorena et al.*, 2010, Figure 15]. View from space of a haboob around 0130 UTC 3 July 2010 showing (c) MSG SEVIRI and (d) CALIOP data as in Figure 3. Going south to north the CALIOP section shows altocumulus clouds over southern West Africa, elevated dust from the previous day around 17°N, the sharp inclined leading edge of the haboob, and possibly dust gliding onto cooler Mediterranean air in the north. (e and f) Simulations of a haboob near the High Atlas in Morocco on 3 June 2006. Shown are model topography, 10 m winds, and precipitation. While the simulation using 7 km grid spacing and the Kain-Fritsch convection scheme (Figure 14e) struggles to reproduce the event, a 2.8 km simulation with explicit deep convection (Figure 14f) performs much better [*Reinfried et al.*, 2009, Figure 8].

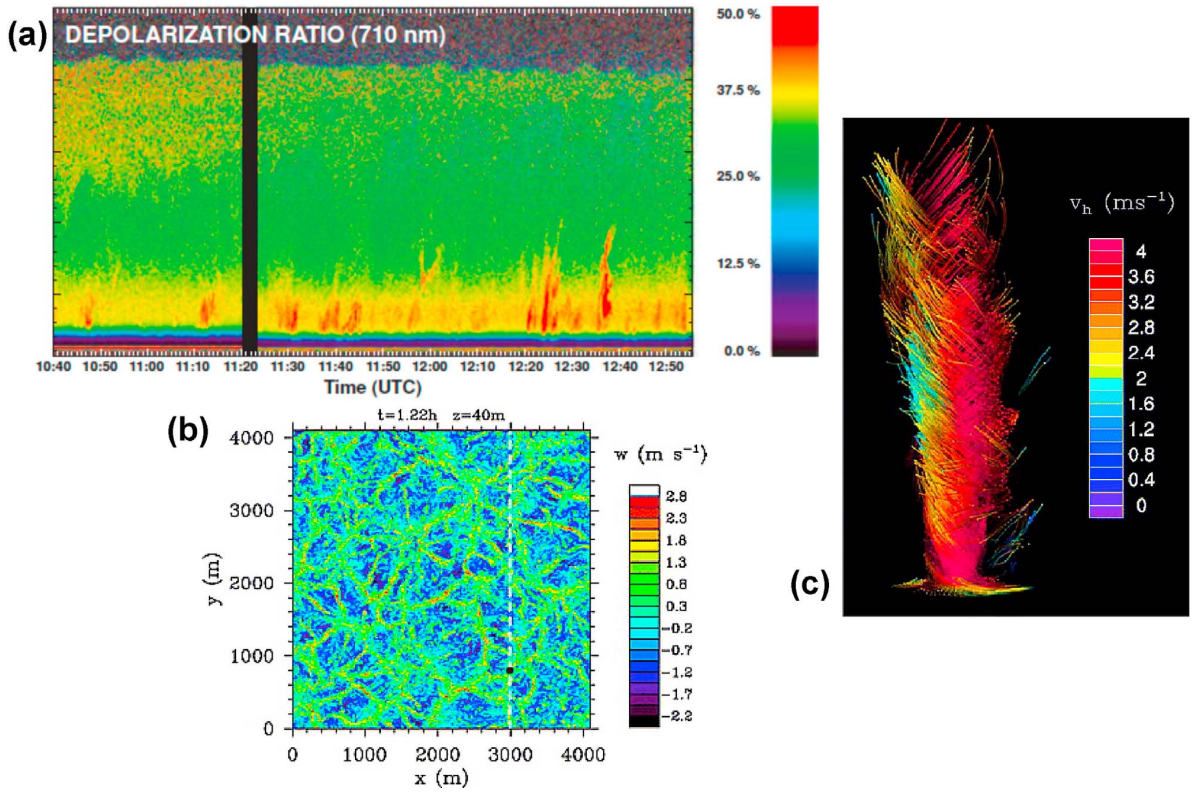

Figure 15. Microscale emission processes. (a) Observations of dusty plumes by lidar taken on 16 May 2006 between 1040 and 1258 UTC in Ouarzazate, southern Morocco, during SAMUM-1. The dust plumes stand out as regions of high depolarization reaching up to 2 km above ground level [*Ansmann et al.*, 2009b, Figure 2]. (b) High-resolution large eddy simulations of dry convection in an active daytime desert boundary layer with a forming dust devil marked by a black dot. Shown is vertical motion at 40 m above ground. (c) Flow visualization using trajectories with colors showing horizontal wind speed [from *Raasch and Franke*, 2011, Figures 2 and 11].

possible to generate idealized large eddy simulations of dust devils with resolutions down to a few meters for research purposes [*Kanak*, 2005; *Ohno and Takemi*, 2010; *Raasch and Franke*, 2011; *Sullivan and Patton*, 2011]. An example from such a conceptual simulation is shown in Figure 15b. The structure of vertical motions at 40 m above ground indicates PBL eddies bounded by areas of strong uplift. The associated horizontal convergence at the surface is most likely associated with dusty plumes in the more intense regions. In addition, the model shows the formation of a rotating dust devil at the intersection of several uplift branches (marked by a black dot). Theoretical, observational, and modeling studies show that dust devils are sensitive to sensible heat flux, background wind, and PBL depth [*Rennó et al.*, 1998]. The effects of dust devils are not considered in dust models so far and are unlikely to be reflected in TKE approaches as the one by *Cakmur et al.* [2004] (see end of section 2.3.1), as these assume isotropic eddies in the PBL.

3.2.5. Vertical Dust Transport

[49] As described in section 3.1.3, the summertime vertical structure of the dust distribution is complex. Recent measurements have revealed a variety of dynamical control mechanisms for mixing and transport. These are summarized by *Cuesta et al.* [2009] and schematically depicted in Figure 6. Dust emitted over the Sahara (most often in the hours after sunrise, see section 3.1.2) will be mixed vertically through the Saharan convective boundary layer (SCBL). This occurs most strongly during the hot summer season when observations reveal that the SCBL extends up to ~5–6 km across a vast extent of the central Sahara north of the ITD (Feature I in Figure 6). Dust is typically well mixed throughout this layer within a day or two of emission as exemplified in Figure 3.

[50] Dynamical lifting occurs when cooler air intrudes into the Sahara most commonly along the ITD where the monsoon flow undercuts the SAL or when midlatitude weather systems advect cooler air from the Atlantic sector (Features II.b and II.a, respectively, in Figure 6). The resulting slanting isentropes cause an upgliding of the dusty SAL over the monsoon or midlatitude air. The elevated SAL is clearly visible as a ubiquitous feature in CALIOP lidar profiles south of the ITD (Figure 3). Further, more detailed features in the vertical structure of the SCBL are associated with the

effects of topography and surface albedo patterns. Horizontal flow over and around major topographic barriers (e.g., the Hoggar and Tibesti Mountains) can induce variations in wind speed and in the depth of the SCBL (a hydraulic "jump") downwind of mountains [e.g., *Drobinski et al.*, 2005] (Features II.a and II.b in Figure 6). Localized heating over regions of low albedo associated with particular geological features and mountains can result in hot spots driving deeper convection during daytime (Features III.c and III.d, respectively, in Figure 6). This has implication for vertical mixing in those areas and for the compensating circulation and vertical structure of the SCBL in the surrounding areas [*Marsham et al.*, 2008b].

[51] Fine detail on the vertical structure of dust was provided by lidar observations during SAMUM-1 in southern Morocco, providing the first surface lidar observations of the full diurnal cycle of dust transport and mixing. These observations have shown that during stable nighttime conditions differential advection can lead to complicated layering in the lowest ~5 km of the atmosphere, which are then mixed vertically in the course of the following day [*Knippertz et al.*, 2009b]. The different layers can be separated by weak lids, which are often poorly resolved in numerical models because of insufficient vertical resolution. This can cause a too early mixing of air from difference layers. Similarly, simulations of summertime dust events with the Weather Research and Forecasting (WRF) regional model reveal that too weak inversions at the SCBL top allow dust to be mixed to excessive heights (Cavazos and Todd, submitted manuscript, 2011).

4. CONCLUSIONS AND FUTURE DIRECTIONS

[52] Mineral dust aerosol is an important component of the Earth system and efforts to incorporate the effects of dust in weather and climate models is at the cutting edge of the discipline. The Sahara desert is by far the world's dominant dust source with implications for the local, regional, and global climate. This paper summarizes the advances made in recent years in our understanding of mineral dust processes over the Sahara, emerging primarily from analysis of (1) new satellite observations, (2) intensive field and airborne observational campaigns, and (3) high-resolution regional model simulations. The emphasis here is specifically on the meteorological processes of dust emission and transport. What has emerged from this research is (1) a greatly improved quantitative representation of the 4-D structure of Saharan dust plumes, (2) a more complete list of the multiscale meteorological processes responsible, and (3) a deeper understanding of the utility and key limitations of models in representing these processes.

[53] There are fundamental differences between the winter and summer conditions. The former is characterized more by synoptic scale processes and often dry dynamics leading to episodic strong dust events affecting mostly the lowest 1.5 km of the atmosphere. Cyclonic storms in the northern Sahara and surges in the harmattan or Etesian winds farther south associated with a pulsing of subtropical high-pressure systems are dominating. The summertime is more complex involving a wider range of sources and mechanisms, leading to a much deeper dust layer that frequently gets elevated when advected over cooler air surrounding the Sahara. Important meteorological features include AEWs and interactions with midlatitude troughs, the SHL, the monsoon circulation, haboobs, and dust devils and dusty plumes in the dry convective PBL. Nocturnal LLJs are common during both winter and summer and are an important control on diurnal variations in dust distribution.

[54] We can identify a number of critical challenges that should be addressed in future research substantially associated with the representation of peak winds.

[55] 1. The role of moist convective processes and cloud/precipitation systems is clearly central to dust emission, transport, and deposition in the Sahara and the Sahel during summer, most vividly expressed through the dramatic haboob dust events. However, even regional models running at grid spacings as low at 10 km do not adequately represent these processes, neither in climatological terms nor for weather forecasting. Addressing this is especially problematic as it requires improvements both in models and in detailed observations of aerosols under cloud systems, which is not currently possible from any of the satellite or ground-based observational systems. Representing moist convective processes has long been recognized as a challenge to models and was part of the rationale for the AMMA and other campaigns. However, the overwhelming emphasis in previous research has understandably been on representing precipitation processes and there is a clear need for a focused effort to observe and simulate the extreme wind events associated with moist convective processes.

[56] 2. The role of dry convective processes in the PBL on dust emission and mixing. There are two components to this. First, the contribution of dry convective eddies (dust devils) to dust emission remains essentially unknown. During summer, in particular, the deep SAL has a high background aerosol load. It is not clear to what extent this is the result of mixing and transport of dust from episodic synoptic and mesoscale events or from microscale dust devil–like processes. The latter are not at all well observed from satellite and existing surface observations over the Sahara are not adequate to resolve them. The "Fennec" project, combining detailed surface observations and high-resolution, eddy-resolving modeling, should provide valuable insights in this regard. Second, while the LLJ features have been highlighted as central to dust emission and transport, there remain substantial uncertainties in model representation of LLJs through inadequate handling of the fine detail of the nocturnal stable PBL as well as the downward mixing of LLJ momentum during the buildup of the PBL in the morning. The timing and height of vertical mixing of dust during the day is controlled by often subtle layering in the atmosphere, which models struggle to resolve. In addition, there remains the problem of a lack of detailed information on land surface characteristics (soil texture, moisture, roughness, and land cover characteristics) and its temporal variations, required by physically based emission schemes.

[57] Addressing these challenges requires a combination of (1) more extensive, fine-grained observational programs, such as the recent Fennec field campaign; (2) further advances in satellite retrievals with high-resolution modeling; (3) more thorough testing, evaluation, and sensitivity studies of model parameterization of meteorological processes (e.g., PBL, convection, and microphysics schemes) and dust processes (emission and deposition); and (4) a concerted effort to develop model parameterizations specifically tested for the unique conditions of the Sahara desert. The last is the goal of the recently started "Desert Storms" project at the University of Leeds (http://www.see.leeds.ac.uk/research/icas/working-groups/knippertz/projects/desert-storms/). Representing subgrid-scale wind variability through probability density functions on the basis of measures of turbulence [*Cakmur et al.*, 2004] is a promising general concept that will be followed in this project. This approach, however, is of limited advantage if the process generating the turbulence (the LLJ or its breakdown, the haboobs, the dust devil, etc.) is not satisfactorily represented in the model in the first place, calling for further parameterization efforts on the level of single meteorological processes involved in peak wind generation. We expect that for the time being, dust modeling will have to rely on some degree of tuning to account for the lack of high-resolution soil information, but that the new insights gained in recent years will lead the way to a more physical representation of smaller-scale meteorological processes that will ultimately improve geographical variations, vertical structure, seasonality, and the diurnal cycle of the dust distribution in models as well as short-term forecasts of dust hazards and air quality.

[58] **ACKNOWLEDGMENTS.** P.K. acknowledges funding from ERC grant 257543 Desert Storms. The authors would like to thank three anonymous reviewers and the editor Greg Okin for their thoughtful and constructive comments that helped to improve an earlier version of this paper.

[59] The Editor responsible for this paper was Greg Okin. He thanks Beatrice Marticorena and two anonymous reviewers.

REFERENCES

Alfaro, S. C., and L. Gomes (2001), Modeling mineral aerosol production by wind erosion: Emission intensities and aerosol size distributions in source areas, *J. Geophys. Res.*, *106*(D16), 18,075–18,084, doi:10.1029/2000JD900339.

Alfaro, S., A. Gaudichet, L. Gomes, and M. Maillé (1998), Mineral aerosol production by wind erosion: Aerosol particle sizes and binding energies, *Geophys. Res. Lett.*, *25*, 991–994, doi:10.1029/98GL00502.

Alpert, P., and B. Ziv (1989), The Sharav cyclone: Observations and some theoretical considerations, *J. Geophys. Res.*, *94*(D15), 18,495–18,514, doi:10.1029/JD094iD15p18495.

Ansmann, A., H. Baars, M. Tesche, D. Muller, D. Althausen, R. Engelmann, T. Pauliquevis, and P. Artaxo (2009a), Dust and smoke transport from Africa to South America: Lidar profiling over Cape Verde and the Amazon rainforest, *Geophys. Res. Lett.*, *36*, L11802, doi:10.1029/2009GL037923.

Ansmann, A., M. Tesche, P. Knippertz, E. Bierwirth, D. Althausen, D. Müller, and O. Schulz (2009b), Vertical profiling of convective dust plumes in southern Morocco during SAMUM, *Tellus B*, *61*, 340–353, doi:10.1111/j.1600-0889.2008.00384.x.

Ansmann, A., A. Petzold, K. Kandler, I. Tegen, M. Wendisch, D. Müller, B. Weinzierl, T. Müller, and J. Heintzenberg (2011), Saharan Mineral Dust Experiments SAMUM-1 and SAMUM-2: What have we learned?, *Tellus B*, *63*, 403–429, doi:10.1111/j.1600-0889.2011.00555.x.

Bagnold, R. A. (1935), The movement of desert sand, *Geogr. J.*, *85*(4), 342–365, doi:10.2307/1785593.

Bagnold, R. A. (1937), The transport of sand by wind, *Geogr. J.*, *89*(5), 409–438, doi:10.2307/1786411.

Banta, R. M., Y. L. Pichugina, and R. K. Newsom (2003), Relationship between low-level jet properties and turbulence kinetic energy in the nocturnal stable boundary layer, *J. Atmos. Sci.*, *60*, 2549–2555, doi:10.1175/1520-0469(2003)060<2549:RBLJPA>2.0.CO;2.

Ben-Ami, Y., I. Koren, Y. Rudic, P. Artaxo, S. T. Martin, and M. O. Andreae (2010), Transport of North African dust from the Bodélé Depression to the Amazon Basin: A case study, *Atmos. Chem. Phys.*, *10*, 7533–7544, doi:10.5194/acp-10-7533-2010.

Ben-Ami, Y., I. Koren, O. Altaratz, A. B. Kostinski, and Y. Lehahn (2011), Discernible rhythm in the spatio/temporal distributions of transatlantic dust, *Atmos. Chem. Phys. Discuss.*, *11*, 23,513–23,539, doi:10.5194/acpd-11-23513-2011.

Biasutti, M., A. H. Sobel, and S. J. Camargo (2009), The role of the Sahara Low in Sahel rainfall variability and change in the CMIP3 models, *J. Clim.*, *22*, 5755–5771, doi:10.1175/2009JCLI2969.1.

Blackadar, A. K. (1957), Boundary layer wind maxima and their significance for the growth of nocturnal inversions, *Bull. Am. Meteorol. Soc.*, *38*, 282–290.

Bou Karam, D., C. Flamant, P. Knippertz, O. Reitebuch, J. Pelon, M. Chong, and A. Dabas (2008), Dust emissions over the Sahel associated with the West African monsoon intertropical discontinuity region: A representative case study, *Q. J. R. Meteorol. Soc.*, *134*, 621–634, doi:10.1002/qj.244.

Bou Karam, D., C. Flamant, J. Cuesta, J. Pelon, and E. Williams (2010), Dust emission and transport associated with a Saharan depression: The February 2007 case, *J. Geophys. Res.*, *115*, D00H27, doi:10.1029/2009JD012390.

Brindley, H., and A. Ignatov (2006), Retrieval of mineral aerosol optical depth and size information from Meteosat Second Generation solar reflectance bands, *Remote Sens. Environ.*, *102*, 344–363, doi:10.1016/j.rse.2006.02.024.

Bristow, C. S., K. A. Hudson-Edwards, and A. Chappell (2010), Fertilizing the Amazon and equatorial Atlantic with West African dust, *Geophys. Res. Lett.*, *37*, L14807, doi:10.1029/2010GL043486.

Cakmur, R. V., R. L. Miller, and O. Torres (2004), Incorporating the effect of small-scale circulations upon dust emission in an atmospheric general circulation model, *J. Geophys. Res.*, *109*, D07201, doi:10.1029/2003JD004067.

Cakmur, R. V., R. L. Miller, J. Perlwitz, I. V. Geogdzhayev, P. Ginoux, D. Koch, K. E. Kohfeld, I. Tegen, and C. S. Zender (2006), Constraining the magnitude of the global dust cycle by minimizing the difference between a model and observations, *J. Geophys. Res.*, *111*, D06207, doi:10.1029/2005JD005791.

Carboni, E., G. Thomas, R. Grainger, C. Poulsen, R. Siddans, D. Peters, E. Campmany, A. Sayer, and H. Brindley (2007), Retrieval of aerosol properties from SEVIRI using visible and infrared channels, paper presented at Joint 2007 EUMETSAT/AMS Conference, Amsterdam, 24–28 Sep.

Carboni, E., et al. (2009), Desert-dust satellite retrieval intercomparison, *Geophys. Res. Abs.*, *11*, Abstract EGU2009-0.

Carlson, T. N., and J. M. Prospero (1972), The large-scale movement of Saharan air outbreaks over the northern equatorial Atlantic, *J. Appl. Meteorol.*, *11*, 283–297, doi:10.1175/1520-0450(1972)011<0283:TLSMOS>2.0.CO;2.

Cavalieri, O., et al. (2010), Variability of aerosol vertical distribution in the Sahel, *Atmos. Chem. Phys.*, *10*, 12,005–12,023, doi:10.5194/acp-10-12005-2010.

Cavazos, C., M. C. Todd, and K. Schepanski (2009), Numerical model simulation of the Saharan dust event of 6–11 March 2006 using the regional climate model version 3(RegCM3), *J. Geophys. Res.*, *114*, D12109, doi:10.1029/2008JD011078.

Chaboureau, J.-P., P. Tulet, and C. Mari (2007), Diurnal cycle of dust and cirrus over West Africa as seen from Meteosat Second Generation satellite and a regional forecast model, *Geophys. Res. Lett.*, *34*, L02822, doi:10.1029/2006GL027771.

Chen, W., and D. Fryrear (2002), Sedimentary characteristics of a haboob dust storm, *Atmos. Res.*, *61*, 75–85, doi:10.1016/S0169-8095(01)00092-8.

Chiapello, I., G. Bergametti, L. Gomes, B. Chatenet, F. Dulac, J. Pimenta, and E. S. Suares (1995), An additional low layer transport of Sahelian and Saharan dust over the northeastern tropical Atlantic, *Geophys. Res. Lett.*, *22*, 3191–3194, doi:10.1029/95GL03313.

Christopher, S. A., P. Gupta, B. Johnson, C. Ansell, H. Brindley, and J. Hawood (2011), Multi-sensor satellite remote sensing of dust aerosols over North Africa during GERBILS, *Q. J. R. Meteorol. Soc.*, *137*, 1168–1178, doi:10.1002/qj.863.

Cook, K. H., and E. K. Vizy (2006), Coupled model simulations of the West African monsoon system: Twentieth- and twenty-first-century simulations, *J. Clim.*, *19*, 3681–3703, doi:10.1175/JCLI3814.1.

Cuesta, J., J. H. Marsham, D. J. Parker, and C. Flamant (2009), Dynamical mechanisms controlling the vertical redistribution of dust and the thermodynamic structure of the west Saharan atmospheric boundary layer during summer, *Atmos. Sci. Lett.*, *10*, 34–42, doi:10.1002/asl.207.

Darmenova, K., I. N. Sokolik, Y. Shao, B. Marticorena, and G. Bergametti (2009), Development of a physically based dust emission module within the Weather Research and Forecasting (WRF) model: Assessment of dust emission parameterizations and input parameters for source regions in central and East Asia, *J. Geophys. Res.*, *114*, D14201, doi:10.1029/2008JD011236.

de Reus, M., F. Dentener, A. Thomas, S. Borrmann, J. Ström, and J. Lelieveld (2000), Airborne observations of dust aerosol over the North Atlantic Ocean during ACE 2: Indications for heterogeneous ozone destruction, *J. Geophys. Res.*, *105*(D12), 15,263–15,275, doi:10.1029/2000JD900164.

Desboeufs, K. V., and G. Cautenet (2005), Transport and mixing zone of desert dust and sulphate over tropical Africa and the Atlantic Ocean region, *Atmos. Chem. Phys. Discuss.*, *5*, 5615–5644, doi:10.5194/acpd-5-5615-2005.

DeSouza-Machado, S. G., L. L. Strow, S. E. Hannon, and H. E. Motteler (2006), Infrared dust spectral signatures from AIRS, *Geophys. Res. Lett.*, *33*, L03801, doi:10.1029/2005GL024364.

Diner, D. J., J. V. Martonchik, R. A. Kahn, B. Pinty, N. Gobron, D. L. Nelson, and B. N. Holben (2005), Using angular and spectral shape similarity constraints to improve MISR aerosol and surface retrievals over land, *Remote Sens. Environ.*, *94*, 155–171, doi:10.1016/j.rse.2004.09.009.

Drobinski, P., B. Sultan, and S. Janicot (2005), Role of the Hoggar massif on the West African monsoon onset, *Geophys. Res. Lett.*, *32*, L01705, doi:10.1029/2004GL020710.

Dubief, J. (1979), Review of the North African climate with particular emphasis on the production of Eolian dust in the Sahel zone and in the Sahara, in *Saharan Dust*, edited by C. Morales, pp. 27–48, John Wiley, Chichester, U. K.

Dubovik, O., M. Herman, A. Holdak, T. Lapyonok, D. Tanré, J. L. Deuzé, F. Ducos, A. Sinyuk, and A. Lopatin (2011), Statistically optimized inversion algorithm for enhanced retrieval of aerosol properties from spectral multi-angle polarimetric satellite observations, *Atmos. Meas. Tech.*, *4*, 975–1018, doi:10.5194/amt-4-975-2011.

Dunion, J., and C. Velden (2004), The impact of the Saharan air layer on Atlantic tropical cyclone activity, *Bull. Am. Meteorol. Soc.*, *85*, 353–365, doi:10.1175/BAMS-85-3-353.

Emmel, C., P. Knippertz, and O. Schulz (2010), Climatology of convective density currents in the southern foothills of the Atlas Mountains, *J. Geophys. Res.*, *115*, D11115, doi:10.1029/2009JD012863.

Engelstaedter, S., and R. Washington (2007), Atmospheric controls on the annual cycle of North African dust, *J. Geophys. Res.*, *112*, D03103, doi:10.1029/2006JD007195.

Engelstaedter, S., and R. Washington (2008), Reply to comment by E. Williams on "Atmospheric controls on the annual cycle of North African dust," *J. Geophys. Res.*, *113*, D23110, doi:10.1029/2008JD010275.

Erickson, D. J., III, J. L. Hernandez, P. Ginoux, W. W. Gregg, C. McClain, and J. Christian (2003), Atmospheric iron delivery and surface ocean biological activity in the Southern Ocean and Patagonian region, *Geophys. Res. Lett.*, *30*(12), 1609, doi:10.1029/2003GL017241.

Evan, A. T., A. K. Heidinger, and M. J. Pavolonis (2006), Development of a new over-water advanced very high resolution radiometer dust detection algorithm, *Int. J. Remote Sens.*, *27*, 3903–3924, doi:10.1080/01431160600646359.

Farquharson, M. (1937), Haboobs and instability in the Sudan, *Q. J. R. Meteorol. Soc.*, *63*, 393–414, doi:10.1002/qj.49706327111.

Fasham, M. J. R. (2003), *Ocean Biogeochemistry*, Springer, Heidelberg, Germany.

Flamant, C., J.-P. Chaboureau, D. J. Parker, C. M. Taylor, J.-P. Cammas, O. Bock, F. Timouk, and J. Pelon (2007), Airborne observations of the impact of a convective system on the planetary boundary layer thermodynamics and aerosol distribution in the inter-tropical discontinuity region of the West African monsoon, *Q. J. R. Meteorol. Soc.*, *133*, 1175–1189, doi:10.1002/qj.97.

Formenti, P., L. Schütz, Y. Balkanski, K. Desboeufs, M. Ebert, K. Kandler, A. Petzold, D. Scheuvens, S. Weinbruch, and D. Zhang (2011), Recent progress in understanding physical and chemical properties of African and Asian mineral dust, *Atmos. Chem. Phys.*, *11*, 8231–8256, doi:10.5194/acp-11-8231-2011.

Forster, P., et al. (2007), Changes in atmospheric constituents and in radiative forcing, in *Climate Change 2007: The Physical Science Basis: Working Group I Contribution to the Fourth Assessment Report of the Intergovernmental Panel on Climate Change*, edited by S. Solomon et al., pp. 129–234, Cambridge Univ. Press, New York.

Freeman, M. (1952), *Duststorms of the Anglo-Egyptian Sudan*, *Meteorol. Rep. Ser.*, vol. 11, 22 pp., Her Majesty's Stn. Off., London.

Gamo, M. (1996), Thickness of the dry convection and large-scale subsidence above deserts, *Boundary Layer Meteorol.*, *79*(3), 265–278, doi:10.1007/BF00119441.

Ginoux, P., et al. (2001), Sources and distributions of dust aerosols simulated with the GOCART model, *J. Geophys. Res.*, *106*(D17), 20,255–20,273, doi:10.1029/2000JD000053.

Ginoux, P., D. Garbuzov, and N. C. Hsu (2010), Identification of anthropogenic and natural dust sources using Moderate Resolution Imaging Spectroradiometer (MODIS) Deep Blue level 2 data, *J. Geophys. Res.*, *115*, D05204, doi:10.1029/2009JD012398.

Grams, C. M., S. C. Jones, J. M. Marsham, D. J. Parker, J. M. Haywood, and V. Heuveline (2010), The Atlantic inflow to the Saharan heat low: Observations and modelling, *Q. J. R. Meteorol. Soc.*, *136*, 125–140, doi:10.1002/qj.429.

Grini, A., G. Myhre, C. S. Zender, and I. S. A. Isaksen (2005), Model simulations of dust sources and transport in the global atmosphere: Effects of soil erodibility and wind speed variability, *J. Geophys. Res.*, *110*, D02205, doi:10.1029/2004JD005037.

Hanna, S., and R. Yang (2001), Evaluations of mesoscale model's simulations of near-surface winds, temperature gradients, and mixing depths, *J. Appl. Meteorol.*, *40*, 1095–1104, doi:10.1175/1520-0450(2001)040<1095:EOMMSO>2.0.CO;2.

Hannachi, A., A. Awad, and K. Ammar (2010), Climatology and classification of spring Saharan cyclone tracks, *Clim. Dyn.*, *37*, 473–491, doi:10.1007/s00382-010-0941-9.

Haywood, J. M., P. N. Francis, M. D. Glew, and J. P. Taylor (2001), The optical properties and direct radiative effect of Saharan Dust: A case study of two Saharan dust outbreaks using aircraft data, *J. Geophys. Res.*, *106*(D16), 18,417–18,430, doi:10.1029/2000JD900319.

Haywood, J. M., et al. (2008), Overview of the Dust and Biomass-burning Experiment and African Monsoon Multidisciplinary Analysis Special Observing Period-0, *J. Geophys. Res.*, *113*, D00C17, doi:10.1029/2008JD010077.

Haywood, J. M., et al. (2011a), Motivation, rationale and key results from the GERBILS Saharan dust measurement campaign, *Q. J. R. Meteorol. Soc.*, *137*, 1106–1116, doi:10.1002/qj.797.

Haywood, J. M., B. T. Johnson, S. R. Osborne, J. Mulcahy, M. E. Brooks, M. Harrison, S. F. Milton, and H. Brindley (2011b), Observations and modelling of the solar and terrestrial radiative effects of Saharan dust: A radiative closure case-study over oceans during the GERBILS campaign, *Q. J. R. Meteorol. Soc.*, *137*, 1211–1226, doi:10.1002/qj.770.

Heintzenberg, J. (2009), The SAMUM-1 experiment over southern Morocco: Overview and introduction, *Tellus B*, *61*, 2–11, doi:10.1111/j.1600-0889.2008.00403.x.

Herman, M., J. L. Deuzé, A. Marchand, B. Roger, and P. Lallart (2005), Aerosol remote sensing from POLDER/ADEOS over the ocean: Improved retrieval using a nonspherical particle model, *J. Geophys. Res.*, *110*, D10S02, doi:10.1029/2004JD004798.

Holben, B. N., et al. (1998), AERONET—A federated instrument network and data archive for aerosol characterization, *Remote Sens. Environ.*, *66*, 1–16, doi:10.1016/S0034-4257(98)00031-5.

Hollingsworth, A., et al. (2008), Toward a monitoring and forecasting system for atmospheric composition: The GEMS project, *Bull. Am. Meteorol. Soc.*, *89*, 1147–1164, doi:10.1175/2008BAMS2355.1.

Houser, C. A., and W. G. Nickling (2001), The emission and vertical flux of particulate matter <10 μm from a disturbed clay-crusted surface, *Sedimentology*, *48*, 255–267, doi:10.1046/j.1365-3091.2001.00359.x.

Hsu, N. C., S. C. Tsay, M. D. King, and J. R. Herman (2004), Aerosol properties over bright-reflecting source regions, *IEEE Trans. Geosci. Remote Sens.*, *42*, 557–569, doi:10.1109/TGRS.2004.824067.

Hui, W. J., B. I. Cook, S. Ravi, J. D. Fuentes, and P. D'Odorico (2008), Dust-rainfall feedbacks in the West African Sahel, *Water Resour. Res.*, *44*, W05202, doi:10.1029/2008WR006885.

Huneeus, N., et al. (2011), Global dust model intercomparison in AeroCom phase I, *Atmos. Chem. Phys.*, *11*, 7781–7816, doi:10.5194/acp-11-7781-2011.

Husar, R. B., J. M. Prospero, and L. L. Stowe (1997), Characterization of tropospheric aerosols over the oceans with the NOAA advanced very high resolution radiometer optical thickness operational product, *J. Geophys. Res.*, *102*, 16,889–16,909, doi:10.1029/96JD04009.

Idso, S., R. S. Ingram, and J. M. Pritchard (1972), An American haboob, *Bull. Am. Meteorol. Soc.*, *53*, 930–935, doi:10.1175/1520-0477(1972)053<0930:AAH>2.0.CO;2.

Ishizuka, M., M. Mikami, J. F. Leys, Y. Yamada, S. Heidenreich, Y. Shao, and G. H. McTainsh (2008), Effects of soil moisture and dried raindroplet crust on saltation and dust emission, *J. Geophys. Res.*, *113*, D24212, doi:10.1029/2008JD009955.

Jickells, T., et al. (2005), Global iron connections between desert dust, ocean biogeochemistry, and climate, *Science*, *308*, 67–71, doi:10.1126/science.1105959.

Johnson, B. T., B. Heese, S. A. McFarlane, P. Chazette, A. Jones, and N. Bellouin (2008), Vertical distribution and radiative effects of mineral dust and biomass burning aerosol over West Africa during DABEX, *J. Geophys. Res.*, *113*, D00C12, doi:10.1029/2008JD009848.

Kahn, R., et al. (2009), Desert dust aerosol air mass mapping in the western Sahara, using particle properties derived from space-based multi-angle imaging, *Tellus B*, *61*, 239–251, doi:10.1111/j.1600-0889.2008.00398.x.

Kalashnikova, O. V., and R. A. Kahn (2008), Mineral dust plume evolution over the Atlantic from MISR and MODIS aerosol retrievals, *J. Geophys. Res.*, *113*, D24204, doi:10.1029/2008JD010083.

Kanak, K. (2005), Numerical simulation of dust devil-scale vortices, *Q. J. R. Meteorol. Soc.*, *131*, 1271–1292, doi:10.1256/qj.03.172.

Kandler, K., N. Benker, U. Bundke, E. Cuevas, M. Eberta, P. Knippertz, S. Rodríguez, L. Schütz, and S. Weinbruch (2007), Chemical composition and complex refractive index of Saharan mineral dust at Izaña, Tenerife (Spain) derived by electron microscopy, *Atmos. Environ.*, *41*, 8058–8074, doi:10.1016/j.atmosenv.2007.06.047.

Kang, J.-Y., S.-C. Yoon, Y. Shao, and S.-W. Kim (2011), Comparison of vertical dust flux by implementing three dust emission schemes in WRF/Chem, *J. Geophys. Res.*, *116*, D09202, doi:10.1029/2010JD014649.

Karyampudi, V. M., and T. N. Carlson (1988), Analysis and numerical simulations of the Saharan air layer and its effect on easterly wave disturbances, *J. Atmos. Sci.*, *45*, 3102–3136, doi:10.1175/1520-0469(1988)045<3102:AANSOT>2.0.CO;2.

Kaufman, Y. J., I. Koren, and L. A. Remer (2005), The effect of smoke, dust, and pollution aerosol on shallow cloud development over the Atlantic Ocean, *Proc. Natl. Acad. Sci. U. S. A.*, *102*, 11,207–11,212, doi:10.1073/pnas.0505191102.

Kittaka, C., D. M. Winker, M. A. Vaughan, A. Omar, and L. A. Remer (2011), Intercomparison of column aerosol optical depths from CALIPSO and MODIS-Aqua, *Atmos. Meas. Tech.*, *4*, 131–141, doi:10.5194/amt-4-131-2011.

Klose, M., Y. Shao, M. K. Karremann, and A. H. Fink (2010), Sahel dust zone and synoptic background, *Geophys. Res. Lett.*, *37*, L09802, doi:10.1029/2010GL042816.

Klüser, L., and T. Holzer-Popp (2010), Relationships between mineral dust and cloud properties in the West African Sahel, *Atmos. Chem. Phys.*, *10*, 6901–6915, doi:10.5194/acp-10-6901-2010.

Klüser, L., D. Martynenko, and T. Holzer-Popp (2011), Thermal infrared remote sensing of mineral dust over land and ocean: A spectral SVD based retrieval approach for IASI, *Atmos. Meas. Tech.*, *4*, 757–773, doi:10.5194/amt-4-757-2011.

Knippertz, P. (2007), Tropical-extratropical interactions related to upper-level troughs at low latitudes, *Dyn. Atmos. Oceans*, *43*, 36–62, doi:10.1016/j.dynatmoce.2006.06.003.

Knippertz, P. (2008), Dust mobilization in the West African heat trough—The role of the diurnal cycle and of extratropical synoptic disturbances, *Meteorol. Z.*, *17*, 553–563, doi:10.1127/0941-2948/2008/0315.

Knippertz, P., and A. H. Fink (2006), Synoptic and dynamic aspects of an extreme springtime Saharan dust outbreak, *Q. J. R. Meteorol. Soc.*, *132*, 1153–1177, doi:10.1256/qj.05.109.

Knippertz, P., and M. C. Todd (2010), The central west Saharan dust hot spot and its relation to African easterly waves and extratropical disturbances, *J. Geophys. Res.*, *115*, D12117, doi:10.1029/2009JD012819.

Knippertz, P., C. Deutscher, K. Kandler, T. Müller, O. Schulz, and L. Schütz (2007), Dust mobilization due to density currents in the Atlas region: Observations from the SAMUM 2006 field campaign, *J. Geophys. Res.*, *112*, D21109, doi:10.1029/2007JD008774.

Knippertz, P., J. Trentmann, and A. Seifert (2009a), High-resolution simulations of convective cold pools over the

northwestern Sahara, *J. Geophys. Res.*, *114*, D08110, doi:10.1029/2008JD011271.

Knippertz, P., et al. (2009b), Dust mobilization and transport in the northern Sahara during SAMUM 2006—A meteorological overview, *Tellus B*, *61*, 12–31, doi:10.1111/j.1600-0889.2008.00380.x.

Knippertz, P., M. Tesche, B. Heinold, K. Kandler, C. Toledano, and M. Esselborn (2011), Dust mobilization and aerosol transport from West Africa to Cape Verde–A meteorological overview of SAMUM-2, *Tellus B*, *63*, 430–447, doi:10.1111/j.1600-0889.2011.00544.x.

Koch, J., and N. O. Renno (2005), The role of convective plumes and vortices on the global aerosol budget, *Geophys. Res. Lett.*, *32*, L18806, doi:10.1029/2005GL023420.

Kok, J. F. (2011), A scaling theory for the size distribution of emitted dust aerosols suggests climate models underestimate the size of the global dust cycle, *Proc. Natl. Acad. Sci. U. S. A.*, *108*, 1016–1021, doi:10.1073/pnas.1014798108.

Koren, I., and Y. J. Kaufman (2004), Direct wind measurements of Saharan dust events from Terra and Aqua satellites, *Geophys. Res. Lett.*, *31*, L06122, doi:10.1029/2003GL019338.

Koren, I., Y. J. Kaufman, R. Washington, M. C. Todd, Y. Rudich, V. J. Martins, and D. Rosenfeld (2006), The Bodélé depression—A single spot in the Sahara that provides most of the mineral dust to the Amazon forest, *Environ. Res. Lett.*, *1*, 014005, doi:10.1088/1748-9326/1/1/014005.

Krinner, G., O. Boucher, and Y. Balkanski (2006), Ice-free glacial northern Asia due to dust deposition on snow, *Clim. Dyn.*, *27*(6), 613–625, doi:10.1007/s00382-006-0159-z.

Lambert, F., B. Delmonte, J. R. Petit, M. Bigler, P. Kaufmann, M. Hutterli, T. F. Stocker, U. Ruth, J. P. Steffensen, and V. Maggi (2008), New constraints on the dust-climate couplings from the 800,000-year EPICA Dome C ice core, *Nature*, *452*, 616–619, doi:10.1038/nature06763.

Laurent, B., B. Marticorena, G. Bergametti, and F. Mei (2006), Modeling mineral dust emissions from Chinese and Mongolian deserts, *Global Planet. Change*, *52*, 121–141, doi:10.1016/j.gloplacha.2006.02.012.

Lawson, T. J. (1971), Haboob structure at Khartoum, *Weather*, *26*, 105–112.

Legrand, M., C. N'Doume, and I. Jankowiak (1994), Satellite-derived climatology of the Saharan aerosol, in *Passive Infrared Remote Sensing of Clouds and the Atmosphere II*, edited by D. K. Lynch, pp. 127–135, Soc. of Photo-Opt. Instrum. Eng., Bellingham, Wash.

Léon, J.-F., Y. Derimian, I. Chiapello, D. Tanré, T. Podvin, B. Chatenet, A. Diallo, and C. Deroo (2009), Aerosol vertical distribution and optical properties over M'Bour (16.96°W; 14.39°N), Senegal from 2006 to 2008, *Atmos. Chem. Phys.*, *9*, 9249–9261, doi:10.5194/acp-9-9249-2009.

Li, J., G. S. Okin, J. E. Herrick, J. Belnap, S. M. Munson, and M. E. Miller (2010), A simple method to estimate threshold friction velocity of wind erosion in the field, *Geophys. Res. Lett.*, *37*, L10402, doi:10.1029/2010GL043245.

Lu, H., and Y. Shao (1999), A new model for dust emission by saltation bombardment, *J. Geophys. Res.*, *104*, 16,827–16,842, doi:10.1029/1999JD900169.

Luo, C., N. M. Mahowald, and J. del Corral (2003), Sensitivity study of meteorological parameters on mineral aerosol mobilization, transport, and distribution, *J. Geophys. Res.*, *108*(D15), 4447, doi:10.1029/2003JD003483.

Maher, B. A., J. M. Prospero, D. Mackie, D. Gaiero, P. P. Hesse, and Y. Balkanski (2010), Global connections between aeolian dust, climate and ocean biogeochemistry at the present day and at the last glacial maximum, *Earth Sci. Rev.*, *99*, 61–97, doi:10.1016/j.earscirev.2009.12.001.

Mahowald, N. M., et al. (2010), Observed 20th century desert dust variability: Impact on climate and biogeochemistry, *Atmos. Chem. Phys.*, *10*, 10,875–10,893, doi:10.5194/acp-10-10875-2010.

Mahowald, N., K. Lindsay, D. Rothenberg, S. C. Doney, J. K. Moore, P. Thornton, J. T. Randerson, and C. D. Jones (2011), Desert dust and anthropogenic aerosol interactions in the Community Climate System Model coupled-carbon-climate model, *Biogeosciences*, *8*, 387–414, doi:10.5194/bg-8-387-2011.

Mallet, M., P. Tulet, D. Serça, F. Solmon, O. Dubovik, J. Pelon, V. Pont, and O. Thouron (2009), Impact of dust aerosols on the radiative budget, surface heat fluxes, heating rate profiles and convective activity over West Africa during March 2006, *Atmos. Chem. Phys.*, *9*, 7143–7160, doi:10.5194/acp-9-7143-2009.

Mangold, A., et al. (2011), Aerosol analysis and forecast in the European Centre for Medium-Range Weather Forecasts Integrated Forecast System: 3. Evaluation by means of case studies, *J. Geophys. Res.*, *116*, D03302, doi:10.1029/2010JD014864.

Marsham, J. H., D. J. Parker, C. M. Grams, C. M. Taylor, and J. M. Haywood (2008a), Uplift of Saharan dust south of the intertropical discontinuity, *J. Geophys. Res.*, *113*, D21102, doi:10.1029/2008JD009844.

Marsham, J. H., D. J. Parker, C. M. Grams, B. T. Johnson, W. M. F. Grey, and A. N. Ross (2008b), Observations of mesoscale and boundary-layer scale circulations affecting dust transport and uplift over the Sahara, *Atmos. Chem. Phys.*, *8*, 6979–6993, doi:10.5194/acp-8-6979-2008b.

Marsham, J. H., P. Knippertz, N. S. Dixon, D. J. Parker, and G. M. S. Lister (2011), The importance of the representation of deep convection for modeled dust-generating winds over West Africa during summer, *Geophys. Res. Lett.*, *38*, L16803, doi:10.1029/2011GL048368.

Marticorena, B., and G. Bergametti (1995), Modeling the atmospheric dust cycle: 1. Design of a soil-derived dust emission scheme, *J. Geophys. Res.*, *100*(D8), 16,415–16,430, doi:10.1029/95JD00690.

Marticorena, B., B. Chatenet, J. L. Rajot, S. Traoré, M. Coulibaly, A. Diallo, I. Koné, A. Maman, T. N. Diaye, and A. Zakou (2010), Temporal variability of mineral dust concentrations over West Africa: Analyses of a pluriannual monitoring from the AMMA Sahelian Dust Transect, *Atmos. Chem. Phys.*, *10*, 8899–8915, doi:10.5194/acp-10-8899-2010.

McConnell, C. L., E. J. Highwood, H. Coe, P. Formenti, B. Anderson, S. Osborne, S. Nava, K. Desboeufs, G. Chen, and M. A. J. Harrison (2008), Seasonal variations of the physical and optical characteristics of Saharan dust: Results from the Dust Outflow and Deposition to the Ocean (DODO) experiment, *J. Geophys. Res.*, *113*, D14S05, doi:10.1029/2007JD009606.

McTainsh, G. H. (1999), Dust transport and deposition, in *Aeolian Environments, Sediments and Landforms*, edited by A. S. Goudie, I. Livingstone, and S. Stokes, chap. 9, pp. 181–211, John Wiley, Chichester, U. K.

Membery, D. (1985), A gravity-wave haboob?, *Weather*, *40*, 214–221.

Menut, L. (2008), Sensitivity of hourly Saharan dust emissions to NCEP and ECMWF modeled wind speed, *J. Geophys. Res.*, *113*, D16201, doi:10.1029/2007JD009522.

Menut, L., I. Chiapello, and C. Moulin (2009), Predictability of mineral dust concentrations: The African Monsoon Multidisciplinary Analysis first short observation period forecasted with CHIMERE-DUST, *J. Geophys. Res.*, *114*, D07202, doi:10.1029/2008JD010523.

Michel, A. E., C. R. Usher, and V. H. Grassian (2003), Reactive uptake of ozone on mineral oxides and mineral dusts, *Atmos. Environ.*, *37*, 3201–3211, doi:10.1016/S1352-2310(03)00319-4.

Miller, S. S. D., A. P. Kuciauskas, M. Liu, Q. Ji, J. S. Reid, D. W. Breed, A. L. Walker, and A. A. Mandoos (2008), Haboob dust storms of the southern Arabian Peninsula, *J. Geophys. Res.*, *113*, D01202, doi:10.1029/2007JD008550.

Min, Q.-L., R. Li, B. Lin, E. Joseph, S. Wang, Y. Hu, V. Morris, and F. Chang (2009), Evidence of mineral dust altering

cloud microphysics and precipitation, *Atmos. Chem. Phys.*, *9*, 3223–3231, doi:10.5194/acp-9-3223-2009.

Mishchenko, M. I., I. V. Geogdzhayev, B. Cairns, B. E. Carlson, J. Chowdhary, A. A. Lacis, L. Liu, W. B. Rossow, and L. D. Travis (2007), Past, present, and future of global aerosol climatologies derived from satellite observations: A perspective, *J. Quant. Spectrosc. Radiat. Transfer*, *106*, 325–347, doi:10.1016/j.jqsrt.2007.01.007.

Mishchenko, M. I., L. Liu, L. D. Travis, B. Cairns, and A. A. Lacis (2010), Toward unified satellite climatology of aerosol properties: Part 3. MODIS versus MISR versus AERONET, *J. Quant. Spectrosc. Radiat. Transfer*, *111*, 540–552, doi:10.1016/j.jqsrt.2009.11.003.

Molesworth, A. M., L. E. Cuevas, A. P. Morse, J. R. Herman, and M. C. Thomson (2002), Correspondence: Dust clouds and spread of infection, *Lancet*, *359*, 81–82, doi:10.1016/S0140-6736(02)07304-X.

Morcrette, J.-J., A. Beljaars, A. Benedetti, L. Jones, and O. Boucher (2008), Sea-salt and dust aerosols in the ECMWF IFS model, *Geophys. Res. Lett.*, *35*, L24813, doi:10.1029/2008GL036041.

Mulitza, S., et al. (2010), Increase in African dust flux at the onset of commercial agriculture in the Sahel region, *Nature*, *466*, 226–228, doi:10.1038/nature09213.

Nickovic, S., A. Papadopoulos, O. Kakaliagou, and G. Kallos (2001), Model for prediciton of desert dust cycle in the atmosphere, *J. Geophys. Res.*, *106*, 18,113–18,129, doi:10.1029/2000JD900794.

N'Tchayi Mbourou, G., J. J. Bertrand, and S. E. Nicholson (1997), The diurnal and seasonal cycles of wind-borne dust over Africa north of the equator, *J. Appl. Meteorol.*, *36*, 868–882, doi:10.1175/1520-0450(1997)036<0868:TDASCO>2.0.CO;2.

Ohno, H., and T. Takemi (2010), Mechanisms for intensification and maintenance of numerically simulated dust devils, *Atmos. Sci. Lett.*, *11*, 27–32.

Okin, G. S. (2008), A new model of wind erosion in the presence of vegetation, *J. Geophys. Res.*, *113*, F02S10, doi:10.1029/2007JF000758.

Okin, G. S., N. Mahowald, O. A. Chadwick, and P. Artaxo (2004), Impact of desert dust on the biogeochemistry of phosphorus in terrestrial ecosystems, *Global Biogeochem. Cycles*, *18*, GB2005, doi:10.1029/2003GB002145.

Painter, T. H., A. P. Barrett, C. C. Landry, J. C. Neff, M. P. Cassidy, C. R. Lawrence, K. E. McBride, and G. L. Farmer (2007), Impact of disturbed desert soils on duration of mountain snow cover, *Geophys. Res. Lett.*, *34*, L12502, doi:10.1029/2007GL030284.

Parker, D. J., R. R. Burton, A. Diongue-Niang, R. J. Ellis, M. Felton, C. M. Taylor, C. D. Thorncroft, P. Bessemoulin, and A. M. Tompkins (2005), The diurnal cycle of the West African monsoon circulation, *Q. J. R. Meteorol. Soc.*, *131*, 2839–2860, doi:10.1256/qj.04.52.

Pérez, C., S. Nickovic, G. Pejanovic, J. M. Baldasano, and E. Özsoy (2006), Interactive dust-radiation modeling: A step to improve weather forecasts, *J. Geophys. Res.*, *111*, D16206, doi:10.1029/2005JD006717.

Peyridieu, S., A. Chédin, D. Tanré, V. Capelle, C. Pierangelo, N. Lamquin, and R. Armante (2010), Saharan dust infrared optical depth and altitude retrieved from AIRS: A focus over North Atlantic—Comparison to MODIS and CALIPSO, *Atmos. Chem. Phys.*, *10*, 1953–1967, doi:10.5194/acp-10-1953-2010.

Peyrillé, P., J.-P. Lafore, and J.-L. Redelsperger (2007), An idealized two-dimensional framework to study the West African monsoon. Part I: Validation and key controlling factors, *J. Atmos. Sci.*, *64*, 2765–2782, doi:10.1175/JAS3919.1.

Pierangelo, C., A. Chédin, S. Heilliette, N. Jacquinet-Husson, and R. Armante (2004), Dust altitude and infrared optical depth from AIRS, *Atmos. Chem. Phys.*, *4*, 1813–1822, doi:10.5194/acp-4-1813-2004.

Poulsen, C. A., R. Siddans, G. E. Thomas, A. Sayer, R. G. Grainger, O. Perez-Navarro, O. Portela-Arjona, and P.-Y. Deschamps (2009), ESA GlobAerosol: Final validation and intercomparison report, version 3.2, report, Eur. Space Agency, Paris. [Available at http://www.globaerosol.info/docs/globaer_fvir_v3p2.pdf.]

Prospero, J. M., and T. N. Carlson (1972), Vertical and areal distributions of Saharan dust over the western equatorial North Atlantic Ocean, *J. Geophys. Res.*, *77*, 5255–5265, doi:10.1029/JC077i027p05255.

Prospero, J. M., P. Ginoux, O. Torres, S. Nicholson, and T. Gill (2002), Environmental characterization of global sources of atmospheric soil dust identified with the NIMBUS7 Total Ozone Mapping Spectrometer (TOMS) absorbing aerosol product, *Rev. Geophys.*, *40*(1), 1002, doi:10.1029/2000RG000095.

Raasch, S., and T. Franke (2011), Structure and formation of dust devil-like vortices in the atmospheric boundary layer: A high-resolution numerical study, *J. Geophys. Res.*, *116*, D16120, doi:10.1029/2011JD016010.

Rajot, J. L., et al. (2008), AMMA dust experiment: An overview of measurements during the dry season special observation period (SOP0) at the Banizoumbou (Niger) supersite, *J. Geophys. Res.*, *113*, D00C14, doi:10.1029/2008JD009906.

Ramon, D., and R. Santer (2001), Operational remote sensing of aerosols over land to account for directional effects, *Appl. Opt.*, *40*, 3060–3075, doi:10.1364/AO.40.003060.

Redelsperger, J. L., C. D. Thorncroft, A. Diedhiou, T. Lebel, D. J. Parker, and J. Polcher (2006), African monsoon multidisciplinary analysis—An international research project and field campaign, *Bull. Am. Meteorol. Soc.*, *87*, 1739–1746, doi:10.1175/BAMS-87-12-1739.

Reinfried, F., I. Tegen, B. Heinold, O. Hellmuth, K. Schepanski, U. Cubasch, H. Hübener, and P. Knippertz (2009), Density currents in the Atlas Region leading to dust mobilization: A model sensitivity study, *J. Geophys. Res.*, *114*, D08127, doi:10.1029/2008JD010844.

Remer, L. A., et al. (2005), The MODIS aerosol algorithm, products and validation, *J. Atmos. Sci.*, *62*, 947–973, doi:10.1175/JAS3385.1.

Rennó, N. O., M. L. Burkett, and M. P. Larkin (1998), A simple thermodynamical theory for dust devils, *J. Atmos. Sci.*, *55*, 3244–3252, doi:10.1175/1520-0469(1998)055<3244:ASTTFD>2.0.CO;2.

Richardson, M., et al. (2007), Measurements of heterogeneous ice nuclei in the western United States in springtime and their relation to aerosol characteristics, *J. Geophys. Res.*, *112*, D02209, doi:10.1029/2006JD007500.

Rodwell, M. J., and T. Jung (2008), Understanding the local and global impacts of model physics changes: An aerosol example, *Q. J. R. Meteorol. Soc.*, *134*, 1479–1497, doi:10.1002/qj.298.

Rosenfeld, D., Y. Rudich, and R. Lahav (2001), Desert dust suppressing precipitation: A possible desertification feedback loop, *Proc. Natl. Acad. Sci. U. S. A.*, *98*, 5975–5980, doi:10.1073/pnas.101122798.

Roskovensky, J. K., and K. N. Liou (2005), Differentiating airborne dust from cirrus clouds using MODIS data, *Geophys. Res. Lett.*, *32*, L12809, doi:10.1029/2005GL022798.

Sander, N., and S. C. Jones (2008), Diagnostic measures for assessing numerical forecasts of African easterly waves, *Meteorol. Z.*, *17*, 209–220, doi:10.1127/0941-2948/2008/0269.

Schepanski, K., and P. Knippertz (2011), Soudano-Saharan depressions and their importance for precipitation and dust: A new perspective on a classical synoptic concept, *Q. J. R. Meteorol. Soc.*, *137*, 1431–1445, doi:10.1002/qj.850.

Schepanski, K., I. Tegen, B. Laurent, B. Heinold, and A. Macke (2007), A new Saharan dust source activation frequency map derived from MSG-SEVIRI IR-channels, *Geophys. Res. Lett.*, *34*, L18803, doi:10.1029/2007GL030168.

Schepanski, K., I. Tegen, M. C. Todd, B. Heinold, G. Bönisch, B. Laurent, and A. Macke (2009), Meteorological processes forcing Saharan dust emission inferred from MSG-SEVIRI observations of subdaily dust source activation and numerical

models, *J. Geophys. Res.*, *114*, D10201, doi:10.1029/2008JD010325.

Schulz, M., M. Chin, and S. Kinne (2009), The Aerosol Model Comparison Project, AeroCom, Phase II: Clearing up diversity, *IGAC Newsl.*, *41*, 2–11.

Schutz, B. E., H. J. Zwally, C. A. Shuman, D. Hancock, and J. P. DiMarzio (2005), Overview of the ICESat Mission, *Geophys. Res. Lett.*, *32*, L21S01, doi:10.1029/2005GL024009.

Shao, Y. (2004), Simplification of a dust emission scheme and comparison with data, *J. Geophys. Res.*, *109*, D10202, doi:10.1029/2003JD004372.

Shao, Y., and M. Mikami (2005), Heterogeneous saltation: Theory, observation and comparison, *Boundary Layer Meteorol.*, *115*, 359–379, doi:10.1007/s10546-004-7089-2.

Shao, Y., M. R. Raupach, and J. F. Leys (1996), A model for predicting aeolian sand drift and dust entrainment on scales from paddock to region, *Aust. J. Soil Res.*, *34*, 309–342, doi:10.1071/SR9960309.

Shao, Y., A. H. Fink, and M. Klose (2010), Numerical simulation of a continental-scale Saharan dust event, *J. Geophys. Res.*, *115*, D13205, doi:10.1029/2009JD012678.

Shao, Y., K.-H. Wyrwoll, A. Chappell, J. Huang, Z. Lin, G. H. McTainsh, M. Mikami, T. Y. Tanaka, X. Wang, and S. Yoon (2011), Dust cycle: An emerging core theme in Earth system science, *Aeolian Res.*, *2*(4), 181–204, doi:10.1016/j.aeolia.2011.02.001.

Shen, B.-W., W.-K. Tao, and M.-L. C. Wu (2010), African easterly waves in 30-day high-resolution global simulations: A case study during the 2006 NAMMA period, *Geophys. Res. Lett.*, *37*, L18803, doi:10.1029/2010GL044355.

Sima, A., D. D. Rousseau, M. Kageyama, G. Ramstein, M. Schulz, Y. Balkanski, A. Antoine, F. Dulac, and C. Hatte (2009), Imprint of North-Atlantic millennial-timescale variability on western European loess deposits as viewed in a dust emission model, *Quat. Sci. Rev.*, *28*, 2851–2866, doi:10.1016/j.quascirev.2009.07.016.

Sinclair, P. (1969), General characteristics of dust devils, *J. Appl. Meteorol.*, *8*, 32–45, doi:10.1175/1520-0450(1969)008<0032:GCODD>2.0.CO;2.

Slingo, A., et al. (2006), Observations of the impact of a major Saharan dust storm on the atmospheric radiation balance, *Geophys. Res. Lett.*, *33*, L24817, doi:10.1029/2006GL027869.

Solmon, F., M. Mallet, N. Elguindi, F. Giorgi, A. Zakey, and A. Konaré (2008), Dust aerosol impact on regional precipitation over western Africa, mechanisms and sensitivity to absorption properties, *Geophys. Res. Lett.*, *35*, L24705, doi:10.1029/2008GL035900.

Solomos, S., G. Kallos, J. Kushta, M. Astitha, C. Tremback, A. Nenes, and Z. Levin (2011), An integrated modeling study on the effects of mineral dust and sea salt particles on clouds and precipitation, *Atmos. Chem. Phys.*, *11*, 873–892, doi:10.5194/acp-11-873-2011.

Spinhirne, J. D., S. P. Palm, W. D. Hart, D. L. Hlavka, and E. J. Welton (2005), Cloud and aerosol measurements from GLAS: Overview and initial results, *Geophys. Res. Lett.*, *32*, L22S03, doi:10.1029/2005GL023507.

Spracklen, D. V., K. J. Pringle, K. S. Carslaw, M. P. Chipperfield, and G. W. Mann (2005), A global off-line model of size-resolved aerosol microphysics: Part I. Model development and prediction of aerosol properties, *Atmos. Chem. Phys.*, *5*, 2227–2252, doi:10.5194/acp-5-2227-2005.

Stanelle, T., B. Vogel, H. Vogel, D. Bäumer, and C. Kottmeier (2010), Feedback between dust particles and atmospheric processes over West Africa during dust episodes in March 2006 and June 2007, *Atmos. Chem. Phys.*, *10*, 10,771–10,788, doi:10.5194/acp-10-10771-2010.

Stuut, J.-B., I. Smalley, and K. O'Hara Dhandt (2009), Aeolian dust in Europe: African sources and European deposits, *Quat. Int.*, *198*, 234–245, doi:10.1016/j.quaint.2008.10.007.

Sullivan, P. P., and E. G. Patton (2011), The effect of mesh resolution on convective boundary layer statistics and structures generated by large-eddy simulation, *J. Atmos. Sci.*, *68*, 2395–2415, doi:10.1175/JAS-D-10-05010.1.

Sutton, L. J. (1925), Haboobs, *Q. J. R. Meteorol. Soc.*, *51*, 25–30, doi:10.1002/qj.49705121305.

Swap, R., M. Garstang, S. Greco, R. Talbot, and P. Kållberg (1992), Saharan dust in the Amazon basin, *Tellus B*, *44*, 133–149, doi:10.1034/j.1600-0889.1992.t01-1-00005.x.

Takemi, T. (2005), Explicit simulations of convective-scale transport of mineral dust in severe convective weather, *J. Meteorol. Soc. Jpn.*, *83A*, 187–203, doi:10.2151/jmsj.83A.187.

Tanré, D. (2010), Derivation of tropospheric aerosol properties from satellite observations, *C. R. Geosci.*, *342*, 403–411, doi:10.1016/j.crte.2010.02.003.

Taylor, C. M., A. Gounou, F. Guichard, P. H. Harris, R. J. Ellis, F. Couvreux, and M. DeKauwe (2011), Frequency of Sahelian storm initiation enhanced over mesoscale soil-moisture patterns, *Nat. Geosci.*, *4*, 430–433, doi:10.1038/ngeo1173.

Tegen, I., and K. Schepanski (2009), The global distribution of dust, *IOP Conf. Ser. Earth Env. Sci.*, *7*, 012001, doi:10.1088/1755-1307/7/1/012001.

Tesche, M., et al. (2009), Vertical profiling of Saharan dust with Raman lidars and airborne HSRL during SAMUM, *Tellus B*, *61*, 144–164, doi:10.1111/j.1600-0889.2008.00390.x.

Textor, C., et al. (2006), Analysis and quantification of the diversities of aerosol life cycles within AeroCom, *Atmos. Chem. Phys.*, *6*, 1777–1813, doi:10.5194/acp-6-1777-2006.

Textor, C., et al. (2007), The effect of harmonized emissions on aerosol properties in global models—An AeroCom experiment, *Atmos. Chem. Phys.*, *7*, 4489–4501, doi:10.5194/acp-7-4489-2007.

Thomas, G. E., C. A. Poulsen, R. L. Curier, G. De Lewuw, S. H. Marsh, E. Carboni, R. G. Grainger, and R. Siddans (2007), Comparison of AATSR and SEVIRI aerosol retrievals over the Northern Adriatic, *Q. J. R. Meteorol. Soc.*, *133*, 85–95, doi:10.1002/qj.126.

Thomas, G. E., C. A. Poulsen, A. M. Sayer, S. H. Marsh, S. M. Dean, E. Carboni, R. Siddans, R. G. Grainger, and B. N. Lawrence (2009), The GRAPE aerosol retrieval algorithm, *Atmos. Meas. Tech.*, *2*, 679–701, doi:10.5194/amt-2-679-2009.

Timmreck, C., and M. Schulz (2004), Significant dust simulation differences in nudged and climatological operation mode of the AGCM ECHAM, *J. Geophys. Res.*, *109*, D13202, doi:10.1029/2003JD004381.

Todd, M. C., V. Martins, R. Washington, G. Lizcano, O. Dubovik, S. M'Bainayel, and S. Engelstaedter (2007), Mineral dust emission from the Bodélé Depression, Chad during BoDEx 2005, *J. Geophys. Res.*, *112*, D06207, doi:10.1029/2006JD007170.

Todd, M. C., et al. (2008a), Quantifying uncertainty in estimates of mineral dust flux: An intercomparison of model performance over the Bodélé Depression, northern Chad, *J. Geophys. Res.*, *113*, D24107, doi:10.1029/2008JD010476.

Todd, M. C., R. Washington, S. Raghavan, G. Lizcano, and P. Knippertz (2008b), Regional model simulations of the Bodélé low-level jet of northern Chad during the Bodélé Dust Experiment (BoDEx 2005), *J. Clim.*, *21*, 995–1012, doi:10.1175/2007JCLI1766.1.

Tompkins, A. M., C. Cardinali, J.-J. Morcrette, and M. Rodwell (2005), Influence of aerosol climatology on forecasts of the African Easterly Jet, *Geophys. Res. Lett.*, *32*, L10801, doi:10.1029/2004GL022189.

Torres, O., P. K. Bhartia, J. R. Herman, Z. Ahmad, and J. Gleason (1998), Derivation of aerosol properties from satellite measurements of backscattered ultraviolet radiation: Theoretical basis, *J. Geophys. Res.*, *103*(D14), 17,099–17,110, doi:10.1029/98JD00900.

Tulet, P., M. Mallet, V. Pont, J. Pelon, and A. Boone (2008), The 7–13 March 2006 dust storm over West Africa: Generation,

transport, and vertical stratification, *J. Geophys. Res.*, *113*, D00C08, doi:10.1029/2008JD009871.

Uno, I., et al. (2006), Dust model intercomparison (DMIP) study over Asia: Overview, *J. Geophys. Res.*, *111*, D12213, doi:10.1029/2005JD006575.

Van de Wiel, B. J. H., A. F. Moene, G. J. Steeneveld, P. Baas, F. C. Bosveld, and A. A. M. Holtslag (2010), A conceptual view on inertial oscillations and nocturnal low-level jets, *J. Atmos. Sci.*, *67*, 2679–2689, doi:10.1175/2010JAS3289.1.

Wakimoto, R. M. (2001), Convectively driven high wind events, in *Severe Convective Storms*, *Meteorol. Monogr. Ser.*, vol. 28, edited by C. A. Doswell III, pp. 255–298, Am. Meteorol. Soc., Boston.

Warren, S., and W. Wiscombe (1980), A model for the spectral albedo of snow. Part II: Snow containing atmospheric aerosols, *J. Atmos. Sci.*, *37*, 2734–2745, doi:10.1175/1520-0469(1980)037<2734:AMFTSA>2.0.CO;2.

Washington, R., and M. C. Todd (2005), Atmospheric controls on mineral dust emission from the Bodélé Depression, Chad: The role of the low level jet, *Geophys. Res. Lett.*, *32*, L17701, doi:10.1029/2005GL023597.

Washington, R., M. C. Todd, A. S. Goudie, and N. Middleton (2003), Global dust storm source areas determined by the total ozone monitoring spectrometer and ground observations, *Ann. Assoc. Am. Geogr.*, *93*, 297–313, doi:10.1111/1467-8306.9302003.

Washington, R., M. C. Todd, S. Engelstaedter, S. Mbainayel, and F. Mitchell (2006), Dust and the low-level circulation over the Bodélé Depression, Chad: Observations from BoDEx 2005, *J. Geophys. Res.*, *111*, D03201, doi:10.1029/2005JD006502.

Westphal, D., O. Toon, and T. Carlson (1988), A case study of mobilization and transport of Saharan dust, *J. Atmos. Sci.*, *45*, 2145–2175, doi:10.1175/1520-0469(1988)045<2145:ACSOMA>2.0.CO;2.

Williams, E. (2008), Comment on "Atmospheric controls on the annual cycle of North African dust" by S. Engelstaedter and R. Washington, *J. Geophys. Res.*, *113*, D23109, doi:10.1029/2008JD009930.

Williams, E., N. Nathou, E. Hicks, C. Pontikis, B. Russell, M. Miller, and M. Bartholomew (2008), The electrification of dust-lofting gust fronts ('haboobs') in the Sahel, *Atmos. Res.*, *91*, 292–298, doi:10.1016/j.atmosres.2008.05.017.

Winckler, G., R. F. Anderson, M. Q. Fleisher, D. McGee, and N. Mahowald (2008), Covariant glacial-interglacial dust fluxes in the equatorial Pacific and Antarctica, *Science*, *320*, 93–96, doi:10.1126/science.1150595.

Winker, D. M., M. A. Vaughan, A. Omar, Y. Hu, K. A. Powell, Z. Liu, W. H. Hunt, and S. A. Young (2009), Overview of the CALIPSO Mission and CALIOP data processing algorithms, *J. Atmos. Oceanic Technol.*, *26*, 2310–2323, doi:10.1175/2009JTECHA1281.1.

Yoshioka, M., N. M. Mahowald, A. J. Conley, W. D. Collins, D. W. Fillmore, C. S. Zender, and D. B. Coleman (2007), Impact of desert dust radiative forcing on Sahel precipitation: Relative importance of dust compared to sea surface temperature variations, vegetation changes, and greenhouse gas warming, *J. Clim.*, *20*, 1445–1467, doi:10.1175/JCLI4056.1.

Zender, C. S., R. L. Miller, and I. Tegen (2004), Quantifying mineral dust mass budgets: Terminology, constraints, and current estimates, *Eos Trans. AGU*, *85*(48), 509,512, doi:10.1029/2004EO480002.

Zhang, D.-L., and W.-Z. Zheng (2004), Diurnal cycles of surface winds and temperatures as simulated by five boundary layer parameterizations, *J. Appl. Meteorol.*, *43*, 157–169, doi:10.1175/1520-0450(2004)043<0157:DCOSWA>2.0.CO;2.

Zhong, S., and J. D. Fast (2003), An evaluation of MM5, RAMS, and Meso Eta at sub-kilometer resolution using the VTMX field campaign data in the Salt Lake Valley, *Mon. Weather Rev.*, *131*, 1301–1322, doi:10.1175/1520-0493(2003)131<1301:AEOTMR>2.0.CO;2.

P. Knippertz, School of Earth and Environment, University of Leeds, Leeds LS2 9JT, UK. (p.knippertz@leeds.ac.uk)

M. C. Todd, Department of Geography, University of Sussex, Brighton BN1 9RH, UK.

JOURNAL OF GEOPHYSICAL RESEARCH, VOL. 115, D12117, doi:10.1029/2009JD012819, 2010

Click Here for Full Article

The central west Saharan dust hot spot and its relation to African easterly waves and extratropical disturbances

Peter Knippertz[1] and Martin C. Todd[2,3]

Received 13 July 2009; revised 16 February 2010; accepted 23 February 2010; published 23 June 2010.

[1] A vast, arid, and virtually uninhabited region covering eastern Mauritania and northern Mali appears in satellite estimates of dust loading as the global maximum during boreal summer. Here the complex meteorological conditions that create this central western Sahara (CWS) dust hot spot are investigated on the basis of regression analyses and case study examples using a wide range of satellite analysis products. The results confirm the importance of African easterly waves (AEWs), previously hypothesized on the basis of case studies. The main ingredients to create this connection are as follows. (1) Strengthened southerlies to the east of an AEW trough advect moist air into the southern Sahara. Daytime heating and orography trigger moist convection in this air mass. Strong evaporation in dry midlevel air generates extended cold pools and haboob dust storms. (2) Vertical mixing brings dust into the upper parts of the deep Saharan boundary layer, from where it can be advected back into the CWS region with the northerlies ahead of the next AEW trough. (3) If the associated surface vortex is strong enough, more dust emission occurs within or just upstream of the CWS. (4) High-amplitude waves in the subtropics enhance the meridional flow associated with the AEW. Although there is a considerable case-to-case variability, it can be concluded that AEWs in concert with extratropical disturbances substantially contribute to the hot spot creation both through emission and the organization of transport. Disagreement between different satellite products and the presence of clouds complicate the analysis and underline the necessity for new observations.

Citation: Knippertz, P., and M. C. Todd (2010), The central west Saharan dust hot spot and its relation to African easterly waves and extratropical disturbances, *J. Geophys. Res.*, *115*, D12117, doi:10.1029/2009JD012819.

1. Introduction

[2] It is now widely recognized that mineral dust aerosols are an important part of the climate system [*Forster et al.*, 2007]. This is by virtue of the direct effect on the radiation budget [e.g., *Haywood et al.*, 2001], the indirect effect on cloud properties [e.g., *Richardson et al.*, 2007], and the semidirect effect of this on the atmospheric circulation. Dust deposits also influence terrestrial and oceanic ecosystems and therefore the global carbon cycle [e.g., *Jickells et al.*, 2005].

[3] Climatological analyses of atmospheric mineral dust loadings based upon different satellite estimates consistently point to a vast, arid, and virtually uninhabited region in eastern Mauritania and northern Mali as one of the most active hot spots worldwide, particularly during the months of June to September [*Brooks and Legrand*, 2000; *Prospero et al.*, 2002; *Washington et al.*, 2003; *Engelstaedter et al.*, 2006]. For the lack of a better terminology the authors will refer to this region as the central western Sahara (CWS) for the rest of this paper. Due to its remote location and hostile climate, the CWS region has only been analyzed on the basis of satellite observations and model experiments. The CWS hot spot is evident in independent satellite products including Aerosol Optical Thickness (AOT) estimates from Multiangle Imaging SpectroRadiometer (MISR) visible data and the Aerosol Indices (AIs) from the Total Ozone Mapping Spectrometer (TOMS) and the Ozone Monitoring Instrument (OMI), which both observe at UV wavelengths (Figure 1; see section 2.1 for more information on the data). It is often assumed that high dust loadings imply collocated strong surface sources. This assumption is probably not justified for most synoptic-scale single emission events, when the strong winds that mobilize the dust also transport it away rather quickly, and might not even be true in a climatological sense for regions with a clear prevalence of wind direction. A possible indication of this problem is the shift in activity maxima over West Africa between some of the long-term satellite aerosol products (compare Figure 3 of *Engelstaedter et al.* [2006] with Figure 2 of *Brooks and Legrand* [2000]). In fact, a recent 2 year source activation

[1]Institute for Climate and Atmospheric Science, School of Earth and Environment, University of Leeds, Leeds, UK.
[2]Department of Geography, University College London, London, UK.
[3]Now at Department of Geography, University of Sussex, Brighton, UK.

Copyright 2010 by the American Geophysical Union.
0148-0227/10/2009JD012819

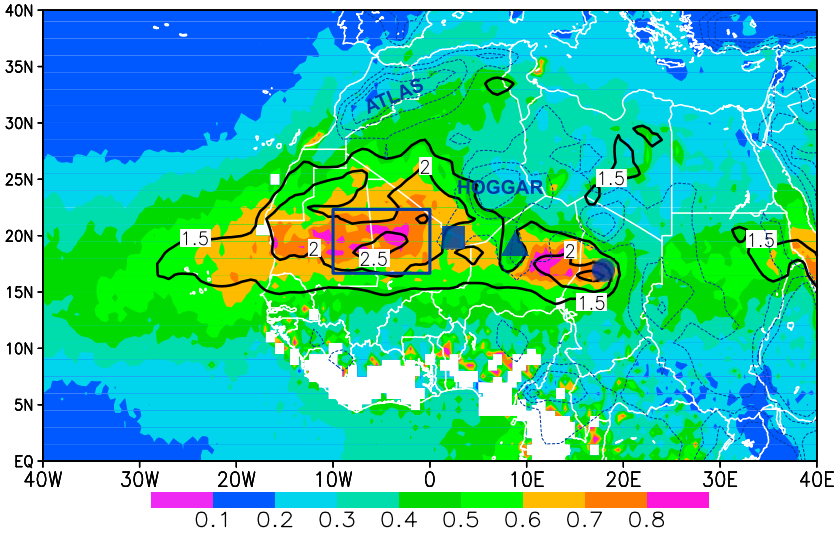

Figure 1. Climatological mean aerosol loading over North Africa during June–September. Mean MISR AOT at 558 nm wavelength 2000–2006 (shading) and mean TOMS AI 1979–1992 (solid contours). Also shown are 500, 750, and 1000 m surface elevation (blue dashed contours) and relevant geographical features (blue box marks central western Sahara region, circle marks Bodélé Depression, triangle marks Aïr Mountains, and square marks Adrar des Iforas Uplands).

climatology based upon data in 15 min temporal resolution from the Spinning Enhanced Visible and Infrared Imager (SEVIRI) flying on the geostationary Meteosat Second Generation satellites points to regions to the east and north of the CWS as more important dust sources [see *Schepanski et al.*, 2009, Figure 1]. Another issue in this context is the near-noontime sampling of some satellites leading to a misrepresentation of sources activated by afternoon convective activity [*Schepanski et al.*, 2007].

[4] While the meteorological mechanisms controlling dust emissions from prominent local sources such as the Bodélé Depression in northern Chad are now much better understood [*Washington and Todd*, 2005; *Washington et al.*, 2006; *Todd et al.*, 2008], the geological, geomorphological, and meteorological reasons that make the vast CWS region such a prominent hot spot are still unclear. *Prospero et al.* [2002] and *Washington et al.* [2003] describe the region as a complex low-relief terrain with few distinctive features, which may have received alluvial deposits from the Niger river and from wadis draining the Hoggar and Adrar des Iforas uplands to the north and east in the past, as indicated by several ancient lake beds. The source activation frequency map of *Schepanski et al.* [2009] does in fact indicate localized sources, associated substantially with surface drainage features, rather than the broad area of high aerosol loadings from the AI and MISR AOT products (Figure 1).

[5] Meteorological processes of potential importance to dust emission in the Sahara range from microscale to continental scale and can be grouped into four different mechanisms: mechanism A, dry boundary layer convection such as dust devils and dust plumes [*Koch and Renno*, 2005; *Ansmann et al.*, 2009]; mechanism B, mesoscale "haboob" dust storms related to the gust fronts of organized convective systems, mostly originating from the Sahel [*Sutton*, 1925; *Lawson*, 1971; *Williams et al.*, 2008]; mechanism C, synoptic-scale emissions related to a downward mixing of momentum from nocturnal low-level jets (LLJs) in the northeasterly harmattan flow [*Knippertz*, 2008]; and mechanism D, strong winds and high turbulence at the leading edge of the southerly monsoon flow (called the Intertropical Discontinuity (ITD))[*Flamant et al.*, 2007; *Bou Karam et al.*, 2008].

[6] *Engelstaedter and Washington* [2007] investigated the mean annual cycle of dust loading over the CWS region as estimated from the TOMS AI and found a better correlation of dustiness with 10 m wind convergence and gustiness than with mean wind speed. They concluded that this points to a prevalence of small-scale processes (mechanism A). *Marsham et al.* [2008] on the other hand showed a relation between dustiness and downdraft convective potential energy and interpreted this to underline the importance of haboobs (mechanism B). *Knippertz* [2008] argued that the strong diurnal cycle involved in mechanism C can create a close relationship between gustiness and dust on the mesoscale and synoptic scale in agreement with the analysis of the diurnal cycle of dust plume emissions by *Schepanski et al.* [2009]. There is a clear need to better understand these individual processes and their relative importance, not least to evaluate the fidelity of the aerosol components of climate models.

[7] Synoptic-scale variability over West Africa during summer is dominated by African Easterly Waves (AEWs) [*Burpee*, 1974; *Kiladis et al.*, 2006, and references therein]. Previous work based upon case studies [*Karyampudi and Carlson*, 1988; *Westphal et al.*, 1988; *Karyampudi et al.*, 1999] and dust model simulations driven by analyzed wind fields [*Jones et al.*, 2003] has shown that AEWs modify dustiness over the downstream eastern Atlantic. For the dust generation in the CWS region itself, *Knippertz*

[2008] discusses impacts of occasional shifts of the position of the heat trough over West Africa related to extratropical disturbances. The precise role of AEWs in this process remains to be determined. Possible mechanisms relating AEWs and dust emission are variations in the near-surface pressure that lead to stronger nighttime accelerations toward the pressure trough (mechanisms C and D) or by favoring the occurrence of haboob dust storms at the southern margin of the Sahara through the northward advection of moisture (mechanism B) [*Fink and Reiner*, 2003].

[8] The aim of this paper is to provide the most comprehensive analysis of the association of AEWs and extratropical disturbances with dust generation over the CWS region conducted to date. Unlike previous studies, this will be achieved by statistical analysis of long-term satellite aerosol and meteorological products (section 3) and through detailed analysis of representative case study events (section 4). The main objective is to assess the relative importance of mechanisms B–D as explained above and to better understand their relation to AEWs. A meaningful assessment of mechanism A is difficult to make from the available data. In addition, section 2 contains a description of the employed data and methods, and section 5 provides a discussion of the results and the main conclusions.

2. Data and Methods

[9] Understanding the association of AEWs with dust generation and transport is strongly aided by observational data with extensive space/time coverage. The only such source of information on aerosols over the CWS is satellite data. In this study we utilize a number of independent, long-term satellite aerosol products to ensure robust results from statistical analysis. To provide insights into atmospheric controls on dust mechanisms the day-to-day variability in the aerosol loading over the CWS in conjunction with information on the state of the atmosphere is examined. Our approach here is to undertake a self-consistent analysis of both (1) the generalized statistical association of CWS dust variability and the large-scale circulation from long-term data (section 3) and (2) detailed analysis of case studies objectively selected from these same aerosol data (section 4).

2.1. Observational Data

[10] Three different types of satellite data are used in this study. The AI from TOMS and OMI is derived from the spectral contrast of measurements in two UV channels (340 nm and 380 nm) providing a dimensionless index, which has been shown to have an approximately linear relationship to the column AOT for smoke and dust aerosols [*Herman et al.*, 1997; *Hsu et al.*, 1999; *Torres et al.*, 2007; *Christopher et al.*, 2008]. Over summertime West Africa the AI predominantly reflects dust, but smaller contributions from other aerosols cannot be excluded. Both OMI and TOMS AI are sensitive to the vertical distribution of the aerosol. There is an ongoing debate about how well the AI is able to capture dust below about 1.5 km [*Herman and Celarier*, 1997; *Torres et al.*, 2002]. The potential height bias would underestimate atmospheric dust content in regions with low-level dust transport or a shallow boundary layer [*Mahowald and Dufresne*, 2004]. The TOMS AI covers the period 1979–1992 at 1.25° longitude by 1° latitude resolution, whilst the OMI AI product covers the period 2005–2007 with a resolution of 0.25°. The higher resolution of OMI substantially reduces, but certainly does not eliminate, the likelihood of subpixel cloud contamination [*Ahn et al.*, 2008].

[11] The second data set used is retrievals of AOT at 558 nm wavelength from MISR onboard the National Aeronautic and Space Administration (NASA) Terra spacecraft with a local equatorial crossing time of 1030 h. MISR observes the Earth using nine cameras distributed at different angles in four wavelengths, allowing quantification of tropospheric aerosols [*Bothwell et al.*, 2002]. The spatial resolution is about 20 km but the narrow swath limits the temporal resolution to around one week, impeding a robust statistical analysis of the relationship with the large-scale atmospheric circulation on a daily basis. Here the 0.5° daily gridded product for 2000–2007 is used.

[12] For the case studies in section 4 we employ a fairly new (available since 2004) product based on brightness temperatures (BTs) from three SEVIRI infrared (IR) channels. These images are composited using BT differences 10.8 μm minus 12.0 μm for red, 10.8 μm minus 8.7 μm for green, and BTs at 10.8 μm for blue (for more details see http://oiswww.eumetsat.org/WEBOPS/msg_interpretation/atmospheric_constituents.php). Although this product only provides a qualitative estimate of dust loading, the high temporal resolution of 15 min allows a detailed analysis of dust emission and transport [*Schepanski et al.*, 2007]. It is particularly suited to detect freshly emitted dust due to the sensitivity of IR channels to the existence of a coarse mode [*Sokolik et al.*, 1998]. The red color in these images is closely related to dust particle size, while the blue color is more sensitive to dust optical depth [*Li et al.*, 2007]. A decrease in IR signals relative to products based on shorter wavelengths (such as OMI) with transport distance has been observed [*Pierangelo et al.*, 2004]. In contrast to OMI, most IR techniques including the SEVIRI dust product are not very sensitive to dust layer height [*Wald et al.*, 1998]. There is, however, a sensitivity of the employed IR channels to water vapor, which leads to problems with detecting dust over the moist southern parts of West Africa in summer [*Chaboureau et al.*, 2007; *Flamant et al.*, 2007].

[13] Information on the state of the atmosphere was obtained from two independent reanalysis products, the National Center for Environmental Prediction (NCEP) reanalysis (daily means, 2.5° grid, 1979–2007 [*Kalnay et al.*, 1996]) and the European Centre for Medium-Range Weather Forecasts (ECMWF) ERA-Interim reanalysis (1200 UTC fields, 1° grid, 1989–2007 [*Uppala et al.*, 2008]). Atmospheric fields of geopotential height and winds at 1000 hPa and 700 hPa, and specific humidity at 1000 hPa were chosen to enable diagnosis of AEW activity and controls on dust emission and convection. In addition, satellite outgoing longwave radiation (OLR) observations from the National Oceanic and Atmospheric Administration (NOAA; 2.5° daily mean [*Liebmann and Smith*, 1996]) were employed as a proxy for deep convection over the region. For the case studies in section 4 operational ECMWF analyses of 1200 UTC mean sea-level pressure (MSLP) and its anomalies with respect to long-term monthly means were used.

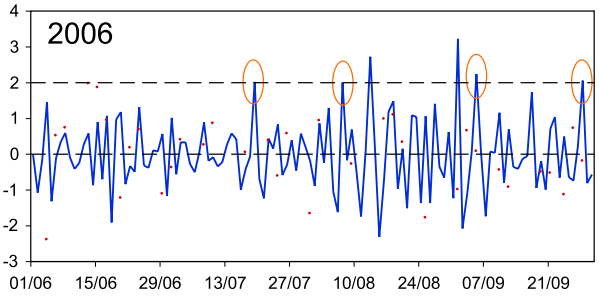

Figure 2. Time series of $AI(OMI)_{CWS}$ (blue line) and AOT_{CWS} (red dots) for boreal summer 2006 (dates given as dd/mm). The 2 standard deviation line and the four events studied in section 4 are marked. For more details on how the indices are computed, see section 2.

2.2. Time Series Generation

[14] Daily time series of AI from TOMS and OMI, and MISR AOT for the CWS region were created by averaging the gridded satellite products over the region 16°N–22°N, 0°–10°W, broadly encompassing the zone of mean maximum aerosol loading during June–September in both the AI and MISR AOT products (blue box in Figure 1). The narrow swath of MISR precludes full coverage of this region during one overpass and therefore only those satellite passes with more than 25% coverage were included in creating the daily area average to ensure representative sampling. For each time series daily anomalies were calculated with respect to the 30 day running mean of the daily climatology (i.e., the mean of each day averaged over the period of the particular data record). These daily anomalies were then standardized separately for each data type (TOMS, OMI and MISR) by dividing by the standard deviation of daily anomalies for that particular data set. This way the resulting time series are comparable between the different sensors. In the case of TOMS and OMI AIs, high-pass filtering was applied to retain variance at time scales less than 10 days associated with synoptic-scale disturbances (irregular temporal sampling from MISR precludes time filtering). Data for the months June–September were then extracted for statistical analysis. These time series, hereafter referred to as $AI(TOMS)_{CWS}$, $AI(OMI)_{CWS}$, and AOT_{CWS}, represent the standardized variability in dust over the CWS over extended periods. The time series for boreal summer 2006 is shown in Figure 2, and forms the basis of the selection of case study events in section 4. Note that the poor temporal and spatial sampling of MISR together with the time filtering applied to the OMI data make a comparison between the two time series difficult.

2.3. Method

[15] The association of AEWs and CWS dust is determined by projecting the atmospheric fields onto the dust time series by linear regression. This method has been successfully applied to dynamical structures in the tropical atmosphere including AEWs in many previous studies [*Kiladis and Wheeler*, 1995; *Kiladis et al.*, 2006]. The time series of the dynamical field (technically the predictand, e.g., NCEP 1000 hpa geopotential height) at each grid cell within a wider North African/European domain is first converted to daily anomalies with respect to the 30 day running mean of the climatological value (1961–1990) and then filtered to retain high-frequency variance at time scales less than 10 days. These gridded anomaly time series are then regressed against the CWS dust time series (technically the predictor, e.g., $AI(OMI)_{CWS}$). The resulting regression coefficients at each grid cell represent the linear dependence of the predictand at that location on variability in the aerosol loading over the CWS region. Using regressions, in which the predictand leads or lags the predictor by −5 to +5 days, the time evolution of the anomalies can be inferred. In the following text our notation is such that LAG-3 refers to the regression where the atmospheric field lead the aerosol time series by 3 days. The results can then be presented as maps of the anomalies in the large-scale dynamical field associated with a particular perturbation in aerosol over CWS, in this case +2 standard deviations. We will refer to these as "representative perturbations" for the rest of the paper. This term is chosen to indicate that the shown circulation anomalies are not associated with specific real events but represent conditions associated with "typical" major dust outbreaks (see Figure 2). Statistical significance (at the 0.05 level) at each grid cell is determined from the correlation coefficient of the two time series.

[16] The real cases studied in section 4 complement this analysis. Specific examples of major CWS dust events are identified from the time series of $AI(OMI)_{CWS}$, specifically those events greater in magnitude than +2 standard deviations. These are then analyzed independently to reveal the involved specific circulation structures. Unlike the bulk statistical analysis described above the case study analysis is able to utilize high-resolution (but qualitative) information on dust emission from the SEVIRI instrument, to reveal the role of mesoscale circulation features and their relationship to the broader structures of AEWs.

3. Statistical Relationship of Dust and Atmospheric Circulation

[17] The bulk statistical relationships between CWS aerosol load and the large-scale circulation are quite insensitive to the choice of reanalysis data and aerosol product. We therefore present only results for the combination of data with the greatest temporal coverage, namely the TOMS AI and NCEP reanalyses during 1979–1992. Conditions where other data give substantially different results are highlighted. Figure 3 shows a time-longitude plot of geopotential height anomalies at 1000 and 700 hPa along 15°–20°N associated with a representative perturbation in $AI(TOMS)_{CWS}$. The former level was chosen for its importance for dust mobilization, while 700 hPa reflects both AEW activity and upper-level disturbances from the extratropics. The time dimension here is derived from the lag/lead regression of the aerosol time series and atmospheric data. The results clearly indicate a westward propagation of alternating positive and negative geopotential anomalies over the West African domain (10°E–20°W) during the period leading and following the aerosol anomaly over the CWS with a propagation speed of approximately 800 km d^{-1} (around 9 m s^{-1}) and a wavelength of around 3500 km. The 700 hPa trough is displaced eastward (i.e., upstream) relative to 1000 hPa, indicative of low-level baroclinicity. Such a structure is characteristic of AEW

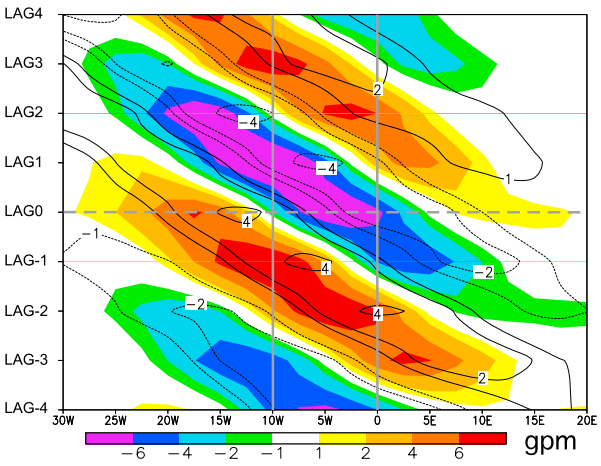

Figure 3. Time-longitude plot of perturbation in geopotential height (15°N–20°N) associated with a +2 standard deviation in high-pass filtered TOMS AI averaged over the CWS region (marked with grey lines). Shading is 1000 hPa, while contours show 700 hPa. All analysis is based on daily data during June–September for 1979–1992.

activity centered on 15°N in the study of *Kiladis et al.* [2006]. With zero lag in the regression analysis, the CWS region lies within or just to the west of the AEW low-level trough and in the northerly sector at 700 hPa. This basic structure is essentially the same for analysis of all the other aerosol data used (OMI AI and MISR AOT, not shown) and can therefore be considered a robust result. Regressions of $AI(TOMS)_{CWS}$ ($AI(OMI)_{CWS}$) against TOMS (OMI) AI anomalies averaged over 15°N–20°N give evidence of a dust signal propagating across the CWS from about 5°E (not shown). This suggests a contribution from dust emission from sources to the east of the CWS associated with the propagating AEW. This issue is considered in more detail below. The poor temporal sampling of MISR precludes a usefully regression of AOT_{CWS} against gridded AOT.

[18] Figure 4 shows the equivalent results as latitude-longitude maps for LAG-3 to LAG0, presenting geopotential height and wind at 1000 and 700 hPa with the former overlaid by specific humidity anomalies and the latter by satellite OLR anomalies. For LAG-3, a clear and statistically significant signal in 1000 hPa geopotential height is found (Figure 4a). The anomalies over West Africa show the typical structure of an AEW with a negative anomaly of about 7 gpm centered near 16°N, 12.5°W and a positive anomaly of similar shape and magnitude about 16° farther east. The corresponding low-latitude anomalies at 700 hPa are shifted eastward by several degrees longitude, reflecting the low-level baroclinic structure of the waves (Figure 4b). Particularly at this higher level the AEW trough is connected with a pronounced extratropical negative geopotential height anomaly with a center over the Canary Islands. LAG-4 maps indicate an origin of this anomaly over the Iberian Peninsula (not shown). Together the two disturbances create an extended region of strong southerly flow that stretches from the Gulf of Guinea to the southern side of the Atlas Mountains. This flow significantly enhances the moisture content over western Niger and northern Mali (red line in Figure 4a), mainly to the east of the study region (marked with a box in Figure 4). A conspicuous negative OLR anomaly over the western part of the moist anomaly indicates enhanced convective activity (red line in Figure 4b). Anomaly wind vectors at 1000 hPa indicate a highly ageostrophic and divergent flow out of this region toward the northwest indicative of convective downdrafts (Figure 4a). Anomalous wind speeds are higher than in other parts of the AEW structure and point to some potential for dust emission. These results are consistent with an enhanced haboob activity in the moist southerly sector of the wave (mechanism B from section 1), which is strengthened through the interaction with the extratropical disturbance. The affected regions have been identified to be preferred dust sources due to fluvial deposits on the western and southern slopes of the Aïr, Hoggar and Adrar des Iforas massifs [*Schepanski et al.*, 2009]. Certainly, details cannot be expected to be well resolved in the coarse-resolution data used here, but the net effects in a statistical sense are likely reflected in both wind analyses and OLR measurements. Presumably most dust detection methods from satellites will have problems to identify the associated emissions due to cloud contamination (see the discussion on this subject by *Williams* [2008]).

[19] The same images for LAG-2 show the westward propagation of the wave structure, a weakening of the negative anomalies over the west coast of West Africa, and the emergence of an upstream AEW trough over southern Chad (Figures 4c and 4d). The AEW ridge at 700 hPa, which has now entered the study region from the east, shows a strong connection to a high geopotential region over the Iberian Peninsula and the adjacent western Mediterranean Sea, again leading to extended regions of meridional flow anomalies. The area of negative OLR anomalies, positive specific humidity anomalies, and strong southerly wind anomalies at 1000 hPa has moved into the study region (Figures 4c and 4d), but haboob-related dust emissions, if they occur, are again most likely undetectable from satellites due to cloud cover. OMI data indicate more dust emissions within the northerly 1000 hPa wind anomaly over Niger and Chad (not shown). The analysis for LAG-1 (Figures 4e and 4f) is almost a mirror image of LAG-3. The AEW surface ridge is now located over southern Mali and connected with a high geopotential anomaly over northwestern Africa, while the upstream trough lies over Niger. In between there is a region with strong northerly 1000 hPa wind anomalies from southern Algeria to northern Togo, which is probably associated with dust emission in its northern parts. There are still indications for potential haboob activity just to the west of the study region. The easterly anomalies over northern Niger at both levels are likely to help transporting dust, which has been emitted farther east on the previous day, toward the CWS.

[20] Finally for LAG0, the AEW ridge has propagated to the Mauritanian Atlantic coast, while the upstream trough reaches Mali (Figures 4g and 4h). Both show connections to subtropical features of equal sign, particularly at 700 hPa, creating extended areas of anomalous meridional flow. Low-level wind anomalies peak in the northerlies around the intensified AEW vortex, i.e., right over the study region and to the south of it. The vectors are clearly less ageostrophic than for LAG-1, LAG-2 and LAG-3, but are of a comparable magnitude so that additional dust emission can

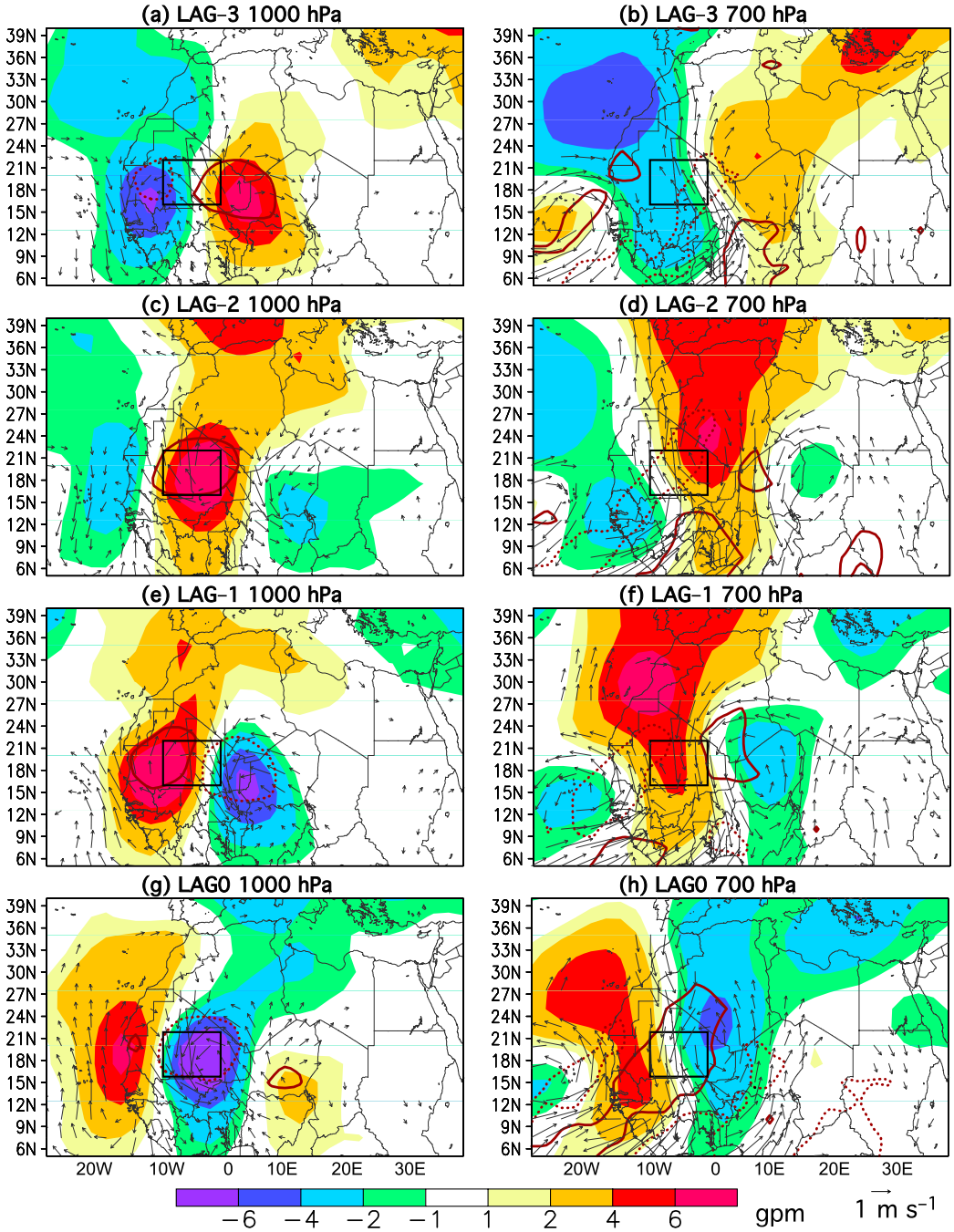

Figure 4. Perturbation in dynamical fields associated with a +2 standard deviation in high-pass filtered TOMS AI averaged over the CWS region (black boxes). (a, c, e, and g) The 1000 hPa geopotential height anomalies with wind perturbations and specific humidity (-0.4 g kg^{-1} (dotted contour) and $+0.4$ g kg^{-1} (solid contour)). (b, d, f, and h) Same as Figures 4a, 4c, 4e, and 4g but for 700 hPa and contours showing OLR perturbations (-4 W m^{-2} (dotted contour) and $+4$ W m^{-2} (solid contour)). For winds, humidity, and OLR, only statistically significant perturbations are shown. Each row corresponds to a different lag relative to the AI(TOMS)$_{CWS}$. All analysis is based on daily data during June–September for 1979–1992.

be expected. This pattern is consistent with mechanism C from section 1. The strong northerlies at 700 hPa from the Atlas Mountains toward the Guinea Coast (Figure 4h) might advect some of the dust, which has been mobilized in the AEW southerly sector and then mixed to higher levels, back into the study region, where it contributes to the high $AI(TOMS)_{CWS}$ values. This process would be particularly effective, if a detection of dust below 1.5 km is problematic as has been suggested [*Herman and Celarier*, 1997; *Mahowald and Dufresne*, 2004]. As an interesting side remark it is noted that the positive geopotential anomaly in the subtropics moves faster westward than the low-latitude AEW disturbances (Figures 4b, 4d, 4f, and 4h). LAG0 is also characterized by negative specific humidity and very strong positive OLR anomalies over the study region that suggest cloud-free conditions (red lines in Figures 4g and 4h). Given that TOMS has a rather large view of sensor (50 by 50 km at nadir), resulting in a high likelihood of subpixel cloud contamination, highest AI values are presumably biased toward cloud-free conditions and therefore toward the northerly sectors of AEWs.

[21] The picture that emerges from these results suggests a clear association of dustiness over the CWS region and AEWs. The connection involves dust emission from multiple sources over the CWS and upstream resulting from different mesoscale to synoptic-scale processes. AEWs act to both initiate dust emission and to organize subsequent transport into the CWS region. We hypothesize that this occurs as follows.

[22] 1. Haboobs in the southerly sector of an AEW mobilize dust within and to the east of the CWS region in the period up to 3 days prior to the CWS dust peak. This dust is transported northward by the haboob outflow embedded in the large-scale southerlies associated with the AEW and subsequently is mixed into the upper parts of the Saharan boundary layer.

[23] 2. In the following northerly sector, dust is readvected westward and southward into the CWS and more emission takes place in the CWS region itself and upstream in connection with the AEW cyclonic surface vortex, most likely involving the LLJ mechanism.

[24] 3. The meridional extent of the southerly and northerly sectors are increased by interactions with extratropical disturbances.

[25] 4. Enhanced cloudiness associated with item 1 potentially creates a bias in the satellite estimates of dust toward item 2.

4. Case Study Examples

[26] To further illustrate the statistical results discussed in section 3, detailed case studies of four marked dust events over the CWS region will be presented that exemplify typical synoptic situations. The cases are all taken from the period of June–September 2006, for which both OMI AI and SEVIRI dust data are available. The four cases have the third to sixth largest daily OMI anomalies over the CWS for this period and therefore constitute significant events (Figure 2). The two top events (12 and 31 August 2006) are not shown because of widespread cloud cover over the Sahara prior to the peak in OMI AI. Both cases, however, do share many common features with the four cases presented here.

[27] For a discussion of the relation to the larger-scale circulation, 1000 hPa wind fields for 1200 UTC on the days under study are shown. The 8 g kg^{-1} specific humidity contour at 1000 hPa is used to delineate the northern edge of the moist monsoonal air. This value is closely related to a 2 m dew point of 11°C and therefore slightly drier than standard ITD definitions that use the 14°C or 15°C contour [e.g., *Bou Karam et al.* 2008].

4.1. A Strong AEW Cyclonic Vortex

[28] From 17 to 18 July 2006 the $AI(OMI)_{CWS}$ increased from −0.07 to 2.02 units, the fifth highest value of the period June–September 2006 (Figure 2). Around midday on 17 July 2006, low-level winds show a distinct cyclonic vortex centered over eastern Mali (Figure 5b). This feature causes northerly flow over large parts of the CWS region. Despite the missing anticyclonic circulation over the coast, the situation has some resemblance to the structures identified in the statistical analysis (Figure 4g) and can therefore serve as an illustration of a typical case.

[29] Animations of SEVIRI images (see auxiliary material Animation S1) show the emergence of major dust plumes from the paleolake deposits of Taoudenni in northern Mali (23°N, 4°W) around 1000 UTC on 17 July.[1] These plumes intensify and spread southwestward in the course of the day (see feature A in Figure 5a for the situation at 1330 UTC). This evolution is consistent with ECMWF analyses, which show an increase in both mean wind and gustiness near the surface from morning to midday (not shown), suggesting a relation to the LLJ mechanism [see *Schepanski et al.*, 2009]. The OMI signal (Figure 5b) also highlights feature A, but additionally indicates widespread dustiness over large parts of Mauritania (feature B). Considering the OMI height bias and the larger sensitivity to smaller particles (see section 2.1), this suggests that this dust was emitted over the previous days and has been mixed to the top of the Saharan boundary layer. The higher moisture contents closer to the coast (red line in Figure 5b) might also contribute to a weaker SEVIRI signal.

[30] To the east of the vortex center southwesterlies reach across eastern Mali to the Algerian border leading to a bulge in the 8 g kg^{-1} specific humidity contour (Figure 5b; see also the corresponding divide between brighter and darker colors in Figure 5a). Farther south, there is strong convective activity in the southerlies (feature C in Figure 5a), which might have supported the northward push of the ITD through the emergence of convective cold pools [*Flamant et al.*, 2009]. A similar, yet weaker pattern is found over eastern Nigeria and eastern Niger (feature D in Figure 5a).

[31] In the course of the afternoon and evening of 17 July, deep convection forms along the southwestern border of Algeria and moves into northern Mali in the course of the night (see auxiliary material Animation S1). This convection generates westward propagating cold pools, which activate dust over the CWS. In the morning of 18 July, further emission from the Taoudenni deposits occur, creating a region of large signals for dust in both SEVIRI and OMI by midday (feature E in Figures 5c and 5d; note the slight downstream shift in the OMI data, which might be related to

[1] Auxiliary materials are available in the HTML. doi:10.1029/2009JD012819.

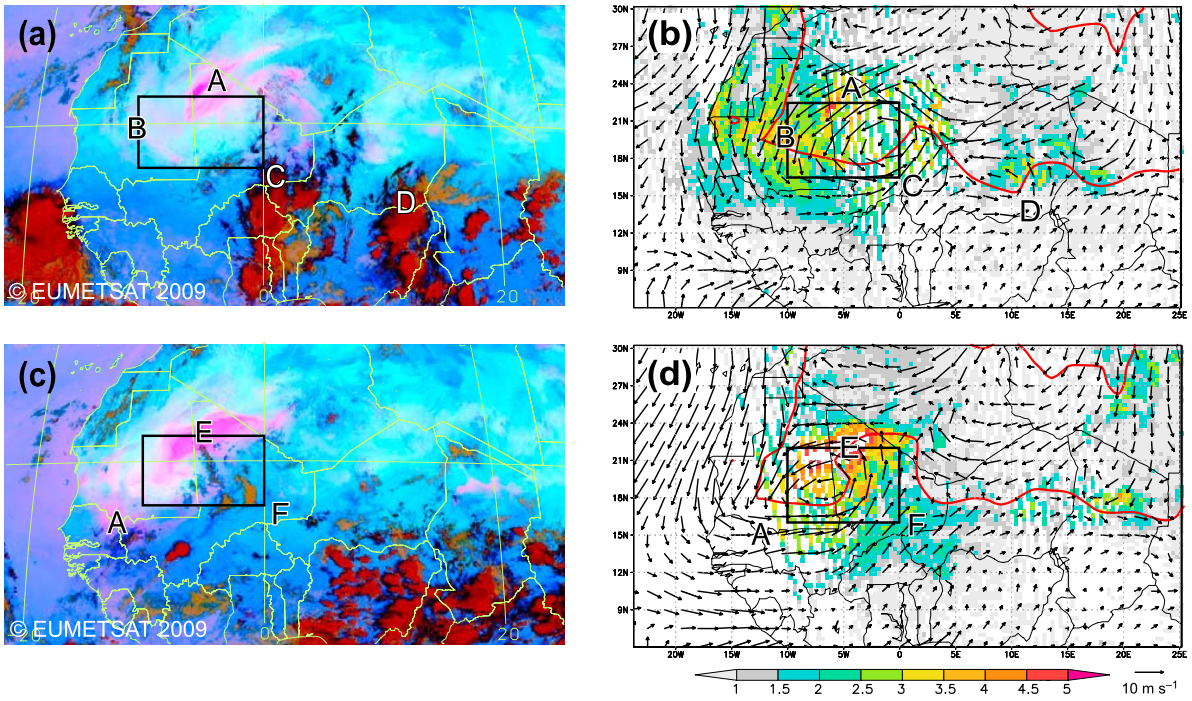

Figure 5. Dustiness and low-level circulation during 17–18 July 2006. (a) SEVIRI dust product and (b) OMI AI at 1330 UTC 17 July 2006. Dust appears in pink and high clouds in red colors. In Figure 5b, vectors are 1000 hPa winds and the thick red line is the 8 g kg^{-1} specific humidity contour at 1000 hPa used to delineate the northern edge of the moist monsoonal air. Both are taken from ECMWF operational analyses at 1200 UTC. (c and d) Same as Figures 5a and 5b but for 18 July 2006. Black boxes mark the study region, and letters label cloud or dust features referred to in the text. Note the difference in map projection between SEVIRI and OMI images.

the height bias). Dust feature A has already reached the eastern border of Senegal by this time. The 1000 hPa winds at 1200 UTC 18 July indicate that the vortex has propagated westward to the border of Mali with Mauritania without a significant change to the wind pattern (Figure 5d). The northward extension of moist monsoonal air is much larger now and covers most of northern Mali. The SEVIRI product clearly struggles to highlight dust in this region (compare feature F in Figures 5c and 5d).

[32] One day later, the 1000 hPa vortex center lies over western Mauritania (not shown) indicating a propagation of about 6–7° longitude per day. This suggests that the cyclonic circulation is the surface reflection of the northern vortex of an AEW, which typically has propagation velocities of this order [*Burpee*, 1974]. More evidence that AEW activity is present during this period is the fairly large-scale organization of convection seen in Figure 5a. The exact dynamical reasons why the surface vortex is so strong in this case (MSLP anomalies reach 3 and 4 hPa on 17 and 18 July compared to 1.1 hPa for a composite by *Burpee* [1974]) is beyond the scope of the present paper, but will be subject of future work.

[33] This case illustrates how an AEW trough passing through the CWS can generate dust in both the strong northeasterly winds to the northwest of the cyclonic center and through convective cold pools in the moist southerly flow to the east. This dust is subsequently transported over the CWS in northeasterly flow. These conditions are broadly consistent with the bulk statistical analysis discussed in section 3.

4.2. A Subtropical Wave

[34] The example of 26–27 September 2006 is characterized by an increase in AI(OMI)$_{CWS}$ from 0.22 to 2.05 units, the latter being the fourth highest value during the entire summer. On both days dust emission takes place in the strong northeasterly flow across the study region, to the north of the ITD (see Figure 6 and auxiliary material Animation S2). Strongest activity from morning to midday points to an importance of the LLJ mechanism as in the previous case. The plumes appear to emerge from localized sources in the extreme south of Algeria on 26 September and from northern Mali on the next day (feature A in Figures 6a and 6b). Again there is a downstream shift between the SEVIRI and OMI signals. MISR AOT (not shown) confirms much of the AI structure underlying the qualitative nature of the SEVIRI product, which also does not indicate the strong increase from 26 to 27 September evident from OMI AI. It is not clear to what extent these discrepancies reflect OMI vertical bias and/or SEVIRI sensitivity to particle size and moisture. The comparably cloud-free conditions in the northerlies agree with the statistical results in section 3 (see positive OLR anomaly in Figure 4g) and make cloud contamination an unlikely reason for the large differences to the SEVIRI product.

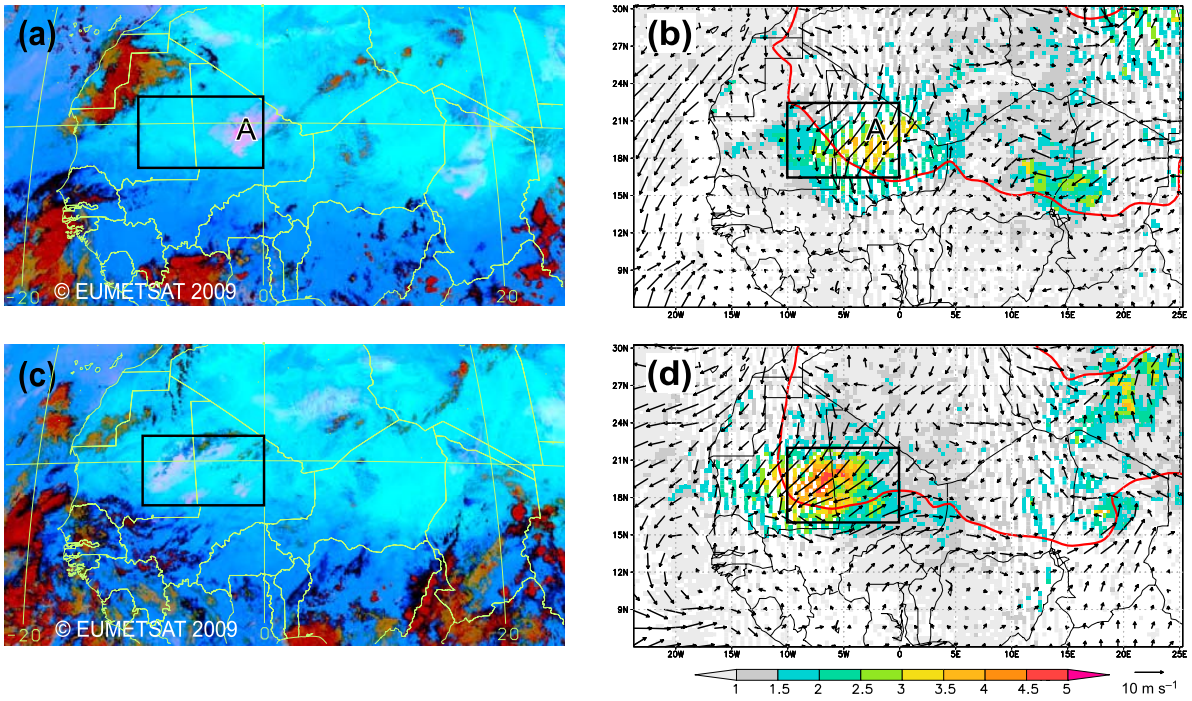

Figure 6. Same as Figure 5 but for 26–27 September 2006.

[35] The northeasterly flow across the CWS in Figures 6b and 6d is in good agreement with the statistical results for LAG0 (see section 3). However, in contrast to these results and to the example discussed in section 4.1, there is little indication of a cyclonic vortex and the 8 g kg^{-1} specific humidity contour is only slightly deformed, suggesting weak AEW activity during this period. Instead, the strong northerlies across Algeria and Mali, which cause most of the dust emission, are related to a wave in the subtropics. It is associated with a strengthening and southeastward excursion of the subtropical high into West Africa, and with the development of a surface depression over the Central Mediterranean, which extends a low-pressure zone across Libya well into the tropics (Figure 7). MSLP anomalies associated with this pattern reach +4 hPa over Mauritania and −8 hPa over the Libyan coast. The unusually high amplitude of this wave appears to be related to the presence of ex-hurricane Helene (45°N, 23°W [see, e.g., *Davis et al.*, 2008]), which was already weakening on 26 September, but had a core pressure of 968 hPa on the previous day (not shown). This case illustrates how synoptic-scale pressure fluctuations in the subtropics can cause dustiness in the CWS region.

4.3. A Hybrid Case

[36] Another significant dust event with an increase in AI $(OMI)_{CWS}$ from 0.07 to 2.24 units (third highest value of June–September 2006) occurred during 3–4 September 2006. The evolution is in some sense a hybrid of the cases discussed in sections 4.1 and 4.2 and also shows good agreement with the bulk regression results in section 3. Wind vectors at 1000 hPa indicate a cyclonic vortex, whose center propagates westward from eastern Mali/western Niger to central Mali by 4 September (Figures 8b and 8d). This feature is associated with MSLP anomalies of −4 and −2 hPa (not shown). Particularly on 4 September, there are strong winds all around the vortex, but again dust emission is most intense in the easterlies to the north of the center from sources in southern Algeria (feature A in Figures 8c and 8d).

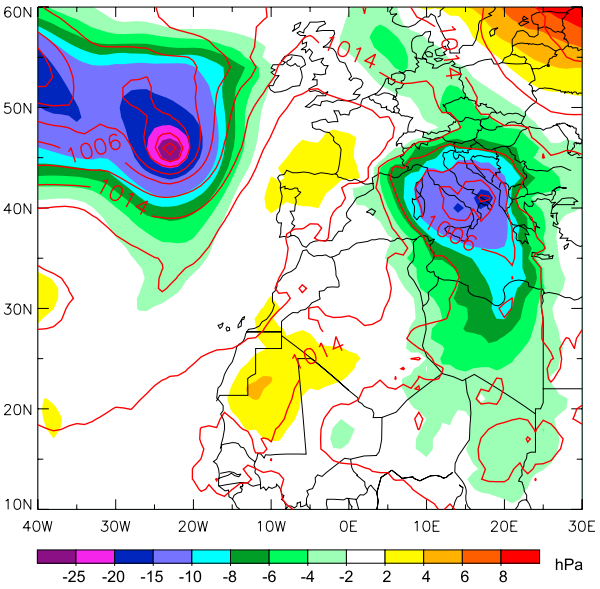

Figure 7. MSLP (red contours every 4 hPa) and the pertinent anomalies with respect to long-term monthly means (shading) for 1200 UTC 26 September 2006.

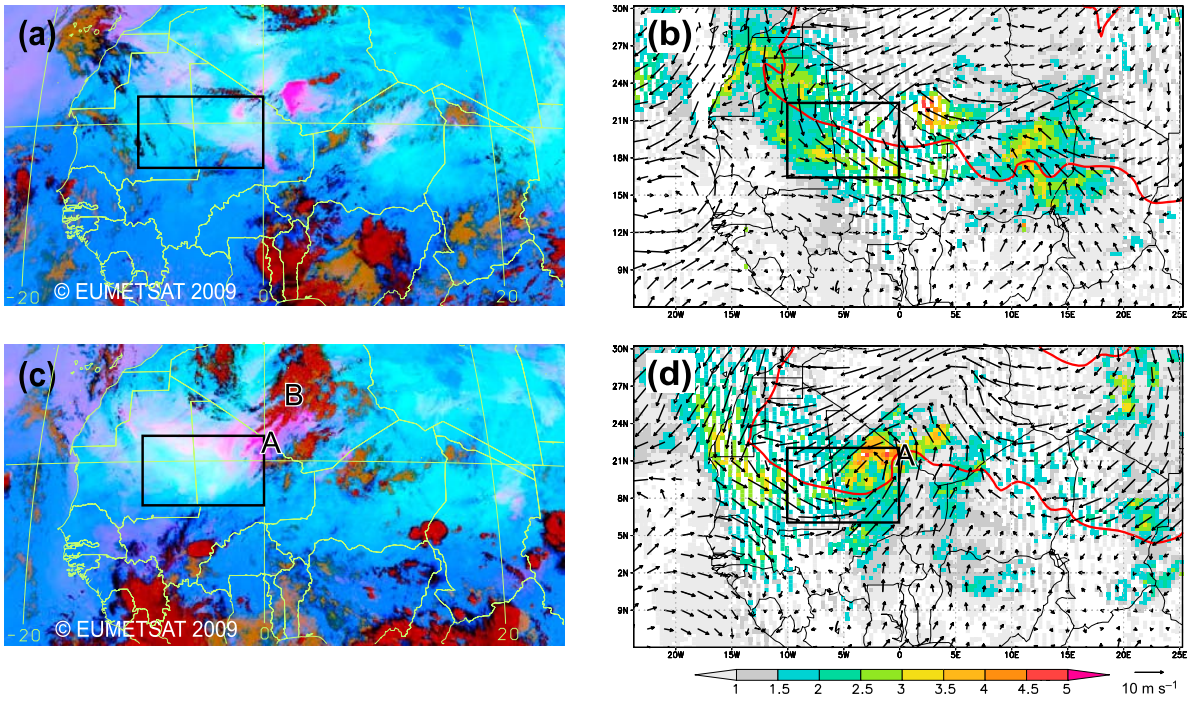

Figure 8. Same as Figure 5 but for 3–4 September 2006.

The accelerated flow over the Sahara is related to anomalously high MSLP over the Mediterranean region (not shown), which enhances the south-north pressure gradient. An increase in dust activity in the morning hours evident from the SEVIRI data points to an importance of LLJs (see auxiliary material Animation S3). In addition, moist air is advected northward to the east of the AEW vortex with southerlies reaching far into southern Algeria. The SEVIRI images show deep convection there (feature B in Figure 8c), but do not reveal to what extent the dust mobilization is due to the strong background flow or through cold pools. Again the SEVIRI signal is shifted upstream with respect to OMI AI and does not show the strong increase on day 2 of the dust event. This case illustrates how tropical and extratropical disturbances can act in concert to enhance dustiness in the CWS region.

4.4. A Monsoon Surge

[37] The last example is a significant dust event that deviates somewhat from the picture evolving from the statistical analysis in section 3. Between 5 and 6 August 2006 the $AI(OMI)_{CWS}$ jumped from −1.62 to 2.00 units, the sixth highest value of the period June–September 2006 (Figure 2). An animation of SEVIRI images show that the dust outbreak begins in connection with the gust fronts of two massive convective systems that form over eastern Mali and western Niger in the early afternoon of 3 August, and then rapidly intensify and merge until midnight (see auxiliary material Animation S4). There is some agreement between this real case and the representative perturbation used in the statistical analysis in section 3, as LAG-3 equally shows indications for convection in this area (Figure 4b).

[38] By midday on 4 August (should be compared to LAG-2) the remnants of the western convective system have reached western Mali (feature A in Figure 9a), while the SEVIRI dust signal shows a very pronounced convex maximum stretching from northern Mali across southern Algeria into northern Niger (feature B), similar to a case investigated by *Westphal et al.* [1988]. There is a substantial northward excursion of moist air and strong southwesterly flow to the east of a cyclonic circulation center over Mauritania (Figure 9b), whose size, strength, and propagation over the previous days suggest the surface signature of an AEW trough. This northward surge of the monsoon is supported by a high-amplitude wave in the extratropics. The MSLP chart for 4 August shows a low-pressure system over the Atlantic, a strongly deformed subtropical high stretching toward the British Isles, and low pressure over the Mediterranean Sea and adjacent Africa (Figure 10). The juxtaposition of the AEW trough (MSLP anomaly of −7 hPa) with an extratropical low over Tunisia (anomaly of −9 hPa) creates the pressure gradients necessary for the meridionally extended region of southerly flow that advects moisture and dust into Algeria.

[39] In the afternoon of 4 August several smaller convective cells form within this air mass (see auxiliary material Animation S4), the remnants of which are still evident in the satellite image at 1330 UTC on 5 August (Figure 9c). These systems generate their own rather small and short-lived cold pools and thereby contribute more dust to the widespread maximum covering large parts of the central Sahara on 5 August (feature C in Figures 9c and 9d). The cyclonic center is still located over Mauritania, slightly farther west than on the previous day, and the northward extension of the moist southwesterly flow is now even more pronounced (Figure 9d).

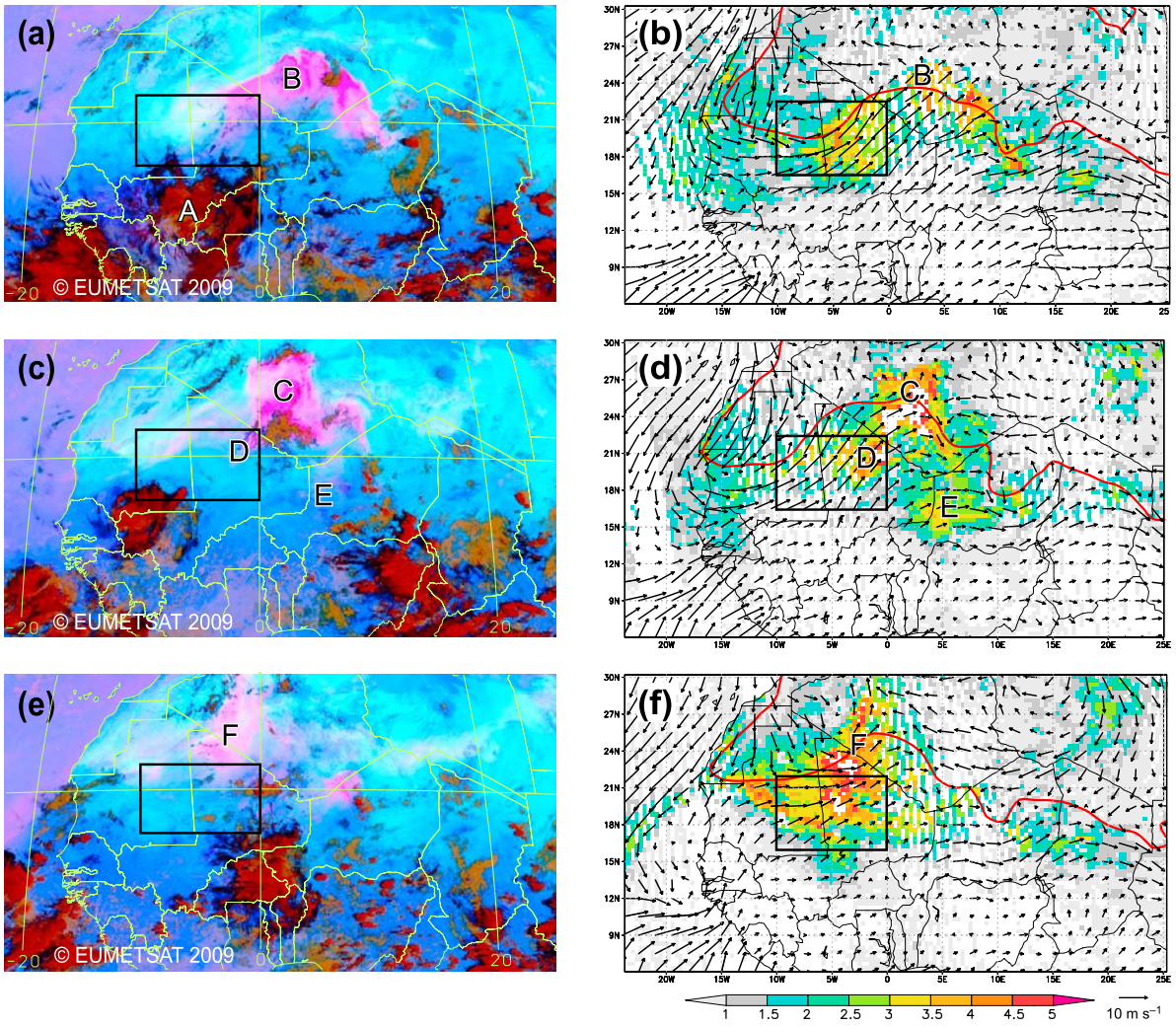

Figure 9. (a–d) Same as Figure 5 but for 4–5 August 2006. (e and f) Corresponding images for 6 August 2006.

Although the SEVIRI images for 4 and 5 August suggest comparable dustiness, the corresponding OMI AI distributions indicates a marked increase as in previous cases. The OMI AI signals over northern Mali and western Niger (features D and E in Figure 9) are not matched by SEVIRI, possibly indicating the presence of aged dust in these regions or SEVIRI bias in moist air. Unfortunately there are no MISR data in this region to confirm the OMI signal.

[40] By midday of 6 August the cyclonic center has moved from Mauritania to western Algeria, still associated with southwesterly or southerly flow over large parts of the western Sahara and a northward shifted moist zone (Figure 9f). This is clearly not in agreement with the regression results for LAG0 in Figure 4g. The unusual track and slow propagation of the cyclonic center together with the very extended southerly sector is not compatible with the typical evolution of an AEW and is presumably closely related to the disturbance by the extratropical circulation. The dust signal weakens in the SEVIRI product on 6 August and slowly drifts westward into northern Mali and western Algeria (feature F in Figure 9e), while the OMI AI reaches extremely high values farther downstream over the almost cloud-free study region (Figure 9f). This discrepancy is similar to that observed the previous day. Notably, on 6 August the MISR AOT data confirm the high OMI AI south within the moist zone, suggesting that SEVIRI is underrepresenting dust in these conditions.

[41] This case demonstrates how the complex interaction of convective, AEW, and synoptic activity in the subtropics can act together to generate a strong dust event over the CWS involving several mechanisms discussed in this paper, most notably haboob events upstream of the CWS.

5. Summary and Conclusions

[42] The broad central west Saharan (CWS) region centered around 19°N, 5°W appears in most satellite products to have the highest dust loadings anywhere in the world during

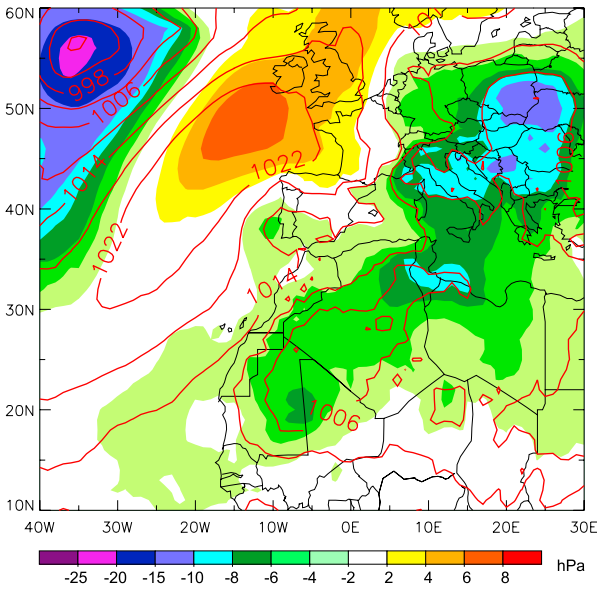

Figure 10. Same as Figure 7 but for 4 August 2006.

the boreal summer. In this paper, the complex physical mechanisms of dust emission and transport that create this dust hot spot have been investigated on the basis of a regression analysis relating daily time series of area-averaged satellite dust products to the analyzed atmospheric circulation and moist convective activity. This bulk statistical analysis is complemented with detailed examinations of carefully selected case study examples.

[43] The results show a clear relation between dustiness over the CWS on one hand and tropical AEW disturbances and synoptic activity in the subtropics on the other hand. The results confirm some of the key features of the idealized view of the great Saharan dust plumes proposed by *Karyampudi and Carlson* [1988] and *Karyampudi et al.* [1999] based on a more restricted analysis of case study events. Most notably, they suggest that dust generation occurs over the Sahara in the northeasterlies around the Saharan heat low when surface pressure gradients are enhanced by the passage of an AEW surface trough. This dust is then mixed throughout the Saharan Air Layer and transported out over the Atlantic in the easterly midtropospheric flow. Here we confirm the importance of the northeasterlies around the near-surface trough over the CWS but provide important additional detail, which illustrates the complexity of processes resulting in the CWS dust hot spot. The two important mechanisms that have not been documented previously are as follows.

[44] 1. During the 2–3 days before the peak in dustiness over the CWS region, a high-amplitude extratropical wave over northern Africa interacts with an AEW, leading to an extended region of low-level southerly flow upstream of and over the CWS, which in some cases mobilizes dust at the leading edge of the monsoon flow (mechanism D in section 1), but more importantly brings moisture into the southern Sahara. Moist convection that develops in this air mass is subject to considerable evaporation of hydrometeors in the usually extremely dry midlevel air over the desert. This causes haboob dust storms as far north as the central Sahara (mechanism B). Over the following days this dust mixes through the deep Saharan boundary layer and eventually gets transported over the CWS region with the northerlies between the ridge and trough of the following AEW disturbance.

[45] 2. More dust emission can occur over the CWS itself in the associated northeasterly flow at the surface, in particular during the morning hours when momentum from nocturnal LLJs is mixed downward (mechanism C). Again, variations in the pressure distribution in the subtropics can enhance or even dominate this process as discussed by *Knippertz* [2008]. As such, the summertime CWS dust hot spot results from emissions from local sources and advection of dust generated to the east and north from a combination of large-scale and mesoscale processes involving a complex interplay between the tropical and the extratropical circulations. The fact that AEWs are often better organized and more strongly involved in the organization of moist convection to the west of the Greenwich Meridian [*Fink and Reiner*, 2003] supports the prominence of the CWS region.

[46] Our work presents the most comprehensive analysis of dust variability over the CWS region conducted to date. We utilize independent long-term satellite data sets from the TOMS/OMI and the MISR sensors. The results are to some degree sensitive to the employed data. The TOMS/OMI AI has a bias toward aerosols at higher elevation such that it is best in detecting dust loadings in the upper parts of the deep Saharan boundary layer, whilst MISR suffers from poor temporal sampling. Neither data set resolves dust loadings under cloud. The temporal resolution of the SEVIRI dust product facilitates much more detailed identification of dust sources [*Schepanski et al.*, 2009] but the qualitative information is not suitable for statistical analysis. There are at times large discrepancies between the SEVIRI dust product and the OMI AI that are probably related to problems of the former in detecting dust in humid air to the south of the ITD and to a sensitivity to particle size. Separating the limitations in these data is problematic and requires further work in the future, which should include the quantitative Moderate Resolution Imaging Spectroradiometer (MODIS) deep blue AOT estimates and lidar observations from CALIPSO. Generally the discrepancies between the different satellite products limit our ability to resolve the processes involved in more detail. This highlights the need for in situ observations of meteorological and aerosol processes in the CWS region. Previous field campaigns in the Sahara, including SHADE, AMMA, SAMUM, and GERBILS have been focussed on the periphery of the CWS. There is a clear need to fill this gap in our observational record.

[47] **Acknowledgments.** Part of this work was made possible through funding to the first author within the Emmy Noether program of the German Science Foundation DFG (grant KN 581/2–3). The authors are grateful to the ESSC at the University of Reading for access to SEVIRI dust product data through the Radagast project Web page. We would like to thank the three anonymous reviewers, whose thoughtful and constructive comments helped to improve an earlier version of the paper.

References

Ahn, C., O. Torres, and P. Bhartia (2008), Comparison of Ozone Monitoring Instrument UV aerosol products with Aqua/Moderate Resolution Imaging Spectroradiometer and Multiangle Imaging Spectroradiometer

observations in 2006, *J. Geophys. Res.*, *113*, D16S27, doi:10.1029/2007JD008832.
Ansmann, A., M. Tesche, P. Knippertz, E. Bierwirth, D. Althausen, D. Müller, and O. Schulz (2009), Vertical profiling of convective dust plumes in southern Morocco during SAMUM, *Tellus, Ser. B*, *61*, 340–353.
Bothwell, G., E. Hansen, R. Vargo, and K. Miller (2002), The Multi-angle Imaging SpectroRadiometer science data system, its products, tools, and performance, *IEEE Trans. Geosci. Remote Sens.*, *40*(7), 1467–1476.
Bou Karam, D., C. Flamant, P. Knippertz, O. Reitebuch, J. Pelon, M. Chong, and A. Dabas (2008), Dust emissions over the Sahel associated with the West African monsoon intertropical discontinuity region: A representative case-study, *Q. J. R. Meteorol. Soc.*, *134*, 621–634.
Brooks, N., and M. Legrand (2000), Dust variability over northern Africa and rainfall in the Sahel, in *Linking Land Surface Change to Climate Change*, edited by D. McLarena and S. Kniverton, pp. 1–25, Kluwer Acad., Dordrecht, Netherlands.
Burpee, R. (1974), Characteristics of North African easterly waves during the summers of 1968 and 1969, *J. Atmos. Sci.*, *31*, 1556–1570.
Chaboureau, J.-P., P. Tulet, and C. Mari (2007), Diurnal cycle of dust and cirrus over West Africa as seen from Meteosat Second Generation satellite and a regional forecast model, *Geophys. Res. Lett.*, *34*, L02822, doi:10.1029/2006GL027771.
Christopher, S., J. Haywood, and G. Greed (2008), Aerosol optical thicknesses over North Africa: 1. Development of a product for model validation using Ozone Monitoring Instrument, Multiangle Imaging Spectroradiometer, and Aerosol Robotic Network, *J. Geophys. Res.*, *113*, D00C04, doi:10.1029/2007JD009446.
Davis, C., S. Jones, and M. Riemer (2008), Hurricane vortex dynamics during Atlantic extratropical transition, *J. Atmos. Sci.*, *65*, 714–736.
Engelstaedter, S., and R. Washington (2007), Atmospheric controls on the annual cycle of North African dust, *J. Geophys. Res.*, *112*, D03103, doi:10.1029/2006JD007195.
Engelstaedter, S., I. Tegen, and R. Washington (2006), North African dust emissions and transport, *Earth Sci. Rev.*, *79*, 73–100.
Fink, A., and A. Reiner (2003), Spatio-temporal variability of the relation between African easterly waves and West African squall lines in 1998 and 1999, *J. Geophys. Res.*, *108*(D11), 4332, doi:10.1029/2002JD002816.
Flamant, C., J.-P. Chaboureau, D. Parker, C. Taylor, J.-P. Cammas, O. Bock, F. Timouk, and J. Pelon (2007), Airborne observations of the impact of a convective system on the planetary boundary layer thermodynamics and aerosol distribution in the inter-tropical discontinuity region of the West African Monsoon, *Q. J. R. Meteorol. Soc.*, *133*, 1175–1189.
Flamant, C., P. Knippertz, D. Parker, J.-P. Chaboureau, C. Lavaysse, A. Augusti-Panareda, and L. Kergoat (2009), The impact of a mesoscale convective system cold pool on the northward propagation of the intertropical discontinuity over West Africa, *Q. J. R. Meteorol. Soc.*, *135*, 139–159.
Forster, P., et al. (2007), Changes in atmospheric constituents and in radiative forcing, in *Climate Change 2007: The Physical Science Basis. Contribution of Working Group I to the Fourth Assessment Report of the Intergovernmental Panel on Climate Change*, edited by S. Solomon et al., chap. 2, pp. 129–234, Cambridge Univ. Press, Cambridge, U. K.
Haywood, J., P. Francis, M. Glew, and J. Taylor (2001), Optical properties and direct radiative effect of Saharan dust: A case study of two Saharan dust outbreaks using aircraft data, *J. Geophys. Res.*, *106*(D16), 18,417–18,430.
Herman, J., and E. Celarier (1997), Earth surface reflectivity climatology at 340–380 nm from TOMS data, *J. Geophys. Res.*, *102*(D23), 28,003–28,011.
Herman, J. R., P. Bhartia, O. Torres, C. Hsu, C. Seftor, and E. Celarier (1997), Global distribution of UV-absorbing aerosols from Nimbus 7/TOMS data, *J. Geophys. Res.*, *102*(D14), 16,911–16,922.
Hsu, N., J. Herman, O. Torres, D. T. B. Holben, T. Eck, A. Smirnov, B. Chatenet, and F. Lavenu (1999), Comparisons of the TOMS aerosol index with Sun-photometer aerosol optical thickness: Results and applications, *J. Geophys. Res.*, *104*(D6), 6269–6279.
Jickells, T., et al. (2005), Global iron connections between desert dust, ocean biogeochemistry, and climate, *Science*, *308*(5718), 67–71.
Jones, C., N. Mahowald, and C. Luo (2003), The role of easterly waves on African desert dust transport, *J. Clim.*, *16*, 3617–3628.
Kalnay, E., et al. (1996), The NCEP/NCAR 40-year reanalysis project, *Bull. Am. Meteorol. Soc.*, *77*, 437–471.
Karyampudi, V., and T. Carlson (1988), Analysis and numerical simulations of the Saharan air layer and its effect on easterly wave disturbances, *J. Atmos. Sci.*, *45*, 3102–3136.
Karyampudi, V., et al. (1999), Validation of the Saharan dust plume conceptual model using lidar, Meteosat, and ECMWF data, *Bull. Am. Meteorol. Soc.*, *80*, 1045–1075.
Kiladis, G., and M. Wheeler (1995), Horizontal and vertical structure of observed tropospheric equatorial Rossby waves, *J. Geophys. Res.*, *100*(D11), 22,981–22,997.
Kiladis, G., C. Thorncroft, and N. Hall (2006), Three-dimensional structure and dynamics of African Easterly Waves. Part I: Observations, *J. Atmos. Sci.*, *63*, 2212–2230.
Knippertz, P. (2008), Dust emissions in the West African heat trough—The role of the diurnal cycle and of extratropical disturbances, *Meteorol. Z.*, *17*(5), 553–563.
Koch, J., and N. O. Renno (2005), The role of convective plumes and vortices on the global aerosol budget, *Geophys. Res. Lett.*, *32*, L18806, doi:10.1029/2005GL023420.
Lawson, T. (1971), Haboob structure at Khartoum, *Weather*, *26*, 105–112.
Li, J., P. Zhang, T. Schmit, J. Schmetz, and W. Menzel (2007), Technical note: Quantitative monitoring of a Saharan dust event with SEVIRI on Meteosat-8, *Int. J. Remote Sens.*, *28*, 2181–2186.
Liebmann, B., and C. Smith (1996), Description of a complete (interpolated) outgoing longwave radiation dataset, *Bull. Am. Meteorol. Soc.*, *77*, 1275–1277.
Mahowald, N., and J. Dufresne (2004), Sensitivity of TOMS aerosol index to boundary layer height: Implications for detection of mineral aerosol sources, *Geophys. Res. Lett.*, *31*, L03103, doi:10.1029/2003GL018865.
Marsham, J., D. Parker, C. Grams, C. Taylor, and J. Haywood (2008), Uplift of Saharan dust south of the intertropical discontinuity, *J. Geophys. Res.*, *113*, D21102, doi:10.1029/2008JD009844.
Pierangelo, C., A. Chédin, S. Heilliette, N. Jacquinet-Husson, and R. Armante (2004), Dust altitude and infrared optical depth from AIRS, *Atmos. Chem. Phys.*, *4*, 1813–1822.
Prospero, J., P. Ginoux, O. Torres, S. Nicholson, and T. Gill (2002), Environmental characterization of global sources of atmospheric soil dust identified with the NIMBUS 7 Total Ozone Mapping Spectrometer (TOMS) absorbing aerosol product, *Rev. Geophys.*, *40*(1), 1002, doi:10.1029/2000RG000095.
Richardson, M., et al. (2007), Measurements of heterogeneous ice nuclei in the western United States in springtime and their relation to aerosol characteristics, *J. Geophys. Res.*, *112*, D02209, doi:10.1029/2006JD007500.
Schepanski, K., I. Tegen, B. Laurent, B. Heinold, and A. Macke (2007), A new Saharan dust source activation frequency map derived from MSG-SEVIRI IR-channels, *Geophys. Res. Lett.*, *34*, L18803, doi:10.1029/2007GL030168.
Schepanski, K., I. Tegen, M. Todd, B. Heinold, G. Bönisch, B. Laurent, and A. Macke (2009), Meteorological processes forcing Saharan dust emission inferred from MSG-SEVIRI observations of subdaily dust source activation and numerical models, *J. Geophys. Res.*, *114*, D10201, doi:10.1029/2008JD010325.
Sokolik, I., O. Toon, and R. Bergstrom (1998), Modeling the radiative characteristics of airborne mineral aerosols at infrared wavelengths, *J. Geophys. Res.*, *103*(D8), 8813–8826.
Sutton, L. (1925), Haboobs, *Q. J. R. Meteorol. Soc.*, *51*, 25–30.
Todd, M., R. Washington, G. Lizcano, S. Ragvahan, and P. Knippertz (2008), Regional model simulations of the Bodélé low-level jet of northern Chad during BoDEx 2005, *J. Clim.*, *21*, 995–1012.
Torres, O., P. Bhartia, J. Herman, A. Sinyuk, P. Ginoux, and B. Holben (2002), A long term record of aerosol optical depth from TOMS observations and comparison to AERONET measurements, *J. Atmos. Sci.*, *59*, 398–413.
Torres, O., A. Tanskanen, B. Veihelmann, C. Ahn, R. Braak, P. K. Bhartia, P. Veefkind, and P. Levelt (2007), Aerosols and surface UV products from Ozone Monitoring Instrument observations: An overview, *J. Geophys. Res.*, *112*, D24S47, doi:10.1029/2007JD008809.
Uppala, S., D. Dee, S. Kobayashi, P. Berrisford, and A. Simmons (2008), Towards a climate data assimilation system: Status update of ERA-interim, *ECMWF Newsl.*, *115*, 12–18.
Wald, A., Y. Kaufman, D. Tanré, and B.-C. Gao (1998), Daytime and nighttime detection of mineral dust over desert using infrared spectral contrast, *J. Geophys. Res.*, *103*(D24), 32,307–32,313.
Washington, R., and M. Todd (2005), Atmospheric controls on mineral dust emission from the Bodélé depression, Chad: The role of the low level jet, *Geophys. Res. Lett.*, *32*, L17701, doi:10.1029/2005GL023597.
Washington, R., M. Todd, N. Middleton, and A. Goudie (2003), Dust-storm source areas determined by the Total Ozone Monitoring Spectrometer and surface observations, *Ann. Assoc. Am. Geogr.*, *93*(2), 297–313.
Washington, R., M. Todd, S. Engelstaedter, S. Mbainayel, and F. Mitchell (2006), Dust and the low-level circulation over the Bodélé depression, Chad: Observations from BoDEx 2005, *J. Geophys. Res.*, *111*, D03201, doi:10.1029/2005JD006502.
Westphal, D., O. Toon, and T. Carlson (1988), A case study of mobilization and transport of Saharan dust, *J. Atmos. Sci.*, *45*, 2145–2175.

Williams, E. (2008), Comment on "Atmospheric controls on the annual cycle of North African dust" by S. Engelstaedter and R. Washington, *J. Geophys. Res.*, *113*, D23109, doi:10.1029/2008JD009930.

Williams, E., N. Nathou, E. Hicks, C. Pontikis, B. Russell, M. Miller, and M. Bartholomew (2008), The electrification of dust-lofting gust fronts ("haboobs") in the Sahel, *Atmos. Res.*, *91*, 292–298, doi:10.1016/j.atmosres.2008.05.017.

P. Knippertz, Institute for Climate and Atmospheric Science, School of Earth and Environment, University of Leeds, Leeds LS2 9JT, UK. (p.knippertz@leeds.ac.uk)

M. C. Todd, Department of Geography, University of Sussex, Chichester I Bldg., Rm. 301, Falmer, Brighton BN1 9QJ, UK. (m.todd@sussex.ac.uk)

CURRICULUM VITAE

Name:	Ms CHEE, Yoke Ling
Date of Birth:	14 May, 1959
Nationality:	Malaysian
Address:	131 Macalister Road 10400 Penang Malaysia
Email:	yokeling@twnetwork.org

Academic Qualifications:	LLB (First Class Honours), University of Malaya, Malaysia (1982) LLM (Honours), University of Cambridge, UK (1984)
Work Experience:	Director of Programmes, Third World Network (2009 -) Environmental Programme Coordinator, Third World Network (2004-2009) Legal Advisor, Third World Network (1993-2004) Executive Secretary, Friends of the Earth Malaysia (1989-1993) Legal Consultant, Meena Thayalan & Partners (1989-1993) Law lecturer, University of Malaya (1984-1989)
Affiliations:	Lead Author, Working Group III on Mitigation, Intergovernmental Panel on Climate Change, Chapter IV on Sustainable Development and Equity (2010 -) Member of the Civil Society Reflection Group on Global Development Perspectives (2011 -) Board Member, Dag Hammarskjöld Foundation (2011 -) Co-editor of the bi-monthly Mandarin Chinese language Bulletin on Biodiversity and Traditional Knowledge (2006 -) Member of the Genetic Resources Policy Committee of the Consultative Group on International Agricultural Research (CGIAR) (2007- 2010) Member of the FAO Panel of Eminent Experts on Ethics in Food and Agriculture (2004 - 2007) Board of Governors, International Development Research Center (IDRC), Canada (2003 - 2006)

Policy research and participation in international fora:

1. **United Nations Conference on Environment and Development (UNCED)** Participated in three preparatory negotiation sessions and the Summit Conference (1990-1992), initially as an NGO observer and then as a technical adviser on the Malaysian delegation.

2. **UN Commission on Sustainable Development**
   Participation at the annual meetings of the Commission in New York to implement Agenda 21 of UNCED) (1993-2002; 2010-2011) as part of TWN technical team working with key G77 delegations.

3. **World Summit on Sustainable Development (2002)**
   a) Member of the Malaysian National preparatory Committee for WSSD
   b) Co-facilitating point for NGO inputs into the multi-stakeholder dialogues and events, nominated by the WSSD Secretariat
   c) Coordinator of Third World Network's WSSD activities and part of the TWN technical team working with the Malaysian and other key delegations of the G77)
   d) Participation in the Asia-Pacific regional consultation in Phnom Penh (November 2001), three preparatory meetings (2001-2002) and the WSSD in Johannesburg (August-September 2002)
   e) Research and publication of a report on International Environmental Governance at the request of the Chair of G77 for the WSSD negotiations and related UNEP GMEF negotiations (2001-2002)

3. **UN Conference on Sustainable Development (June 2012)**

   a) Preparatory meetings (UN headquarters, New York, 2010-2011)
   b) High Level Symposium on UNCSD (Beijing, September 2011)
   c) UN Conference on Sustainable Development (Rio de Janeiro, June, 2012)

4. **Convention on Biological Diversity**
   a) Preparatory meetings of the Inter-Governmental Committee on the Convention on Biological Diversity (1993-4)
   b) Meetings of the Conference of the Parties (1994, 1995, 1996, 1998, 1999, 2004, 2008)
   c) Negotiations on a legally binding international Biosafety Protocol (1996-2000)
   d) Member of the International Steering Committee of, and participant at, the Norway/UN Conference on Technology Transfer and Capacity Building (June 2003) in preparation for COP 7
   e) 9th Meeting of the Subsidiary Body on Science, Technical and Technological Advice (2003)
   f) Member of the Technical Committee for CBD COP7, Malaysian Ministry of Science, Technology and Environment that will host COP 7 in February 2004
   g) CBD COP acting as the First Meeting of the Parties to the Cartagena Protocol on Biosafety (2004)
   h) Technical adviser to the Malaysian delegation to the Experts' Meeting of the Like-Minded Group of Megadiverse Countries (July 2003); prepared the Draft Action Plan for the Group's discussion and adoption
   i) Third Meeting of the CBD Ad Hoc Open-ended Working Group on Access and Benefit Sharing (February 2005)
   j) Fourth Meeting of the CBD Ad Hoc Open-ended Working Group on Access and Benefit Sharing (February 2006)
   k) Fifth Meeting of the CBD Ad Hoc Open-ended Working Group on Access and Benefit Sharing (October 2007)
   l) Sixth to Ninth Meetings of the CBD Ad Hoc Open-ended Working Group on Access and Benefit Sharing (2008 to 2010)

m) 9th Meeting of the CBD COP (November 2008)
n) 10th Meeting of the CBD COP (November 2010)
o) First and Second meetings of the Intergovernmental Committee on the Nagoya Protocol on Access and benefit Sharing (6-10 June 2011; 2-6 July 2012)
p) Quito Seminar Dialogue on Scaling-up Biodiversity Financing (6-9 March 2012)
q) 11th Meeting of the CBD COP (October 2012)

5. Biotechnology and Biosafety (as paper presenter, discussant or participant)

a) Biotechnology/biosafety meetings with NGOs, agriculture/environment officials, and media to prepare for the 2nd meeting of the Conference of the Parties to the Convention on Biological Diversity (Indonesia, August, 1995)
b) Conference on Sustainable Use of Biotechnology, organised by the Norwegian Government (Oslo, September 1995)
c) Negotiations on the Cartagena Protocol on Biosafety (1996-2000): 6 meetings of the Working Group on Biosafety, an experts' meeting, 2 meetings of the Extraordinary Session of the Conference of the Parties to the Convention on Biological Diversity and one informal consultation of the negotiators
d) First meeting of the Intergovernmental Committee on the Cartagena Protocol on Biosafety (Montpellier, 2001)
e) Sustainable Agriculture in the New Millennium: The impact of biotechnology on developing countries (Brussels, May 2000)
f) OECD Consultation on Biotechnology, Agriculture and Food Security (Bangkok, 2001)
g) UNEP-GEF Biosafety Capacity Project: Asia Pacific regional workshop on Risk Assessment and Public Participation to implement the Cartagena Protocol (Kuala Lumpur, 2002)
h) First Meeting of the Parties to the Cartagena Protocol on Biosafety (Kuala Lumpur, 2004)

Also co-organiser of the following

i) International Workshop on Biosafety: Environmental Impacts and Safety Regulation of Genetically Modified Organisms (Nanjing, 2005)
j) Second International Workshop on Biosafety (Beijing, 2007)
k) Third International Workshop on Biosafety (Beijing, 2009)
l) Fourth International Workshop on Biosafety (Beijing, 2011)

6. Climate Change

a) Meetings of the Ad Hoc Working Group on Long Term Cooperative Action under the UN Framework Convention on Climate Change (UNFCCC) and the Ad Hoc Working Group on Further Commitments of Annex I Parties under the Kyoto Protocol (2008 to 2012)
b) Annual Meetings of the Conference of Parties to the UNFCCC and Kyoto Protocol (2008 to 2012)
c) Symposia and Conferences on climate change (Beijing, 2009, 2010, 2011, 2012)

Policy research and participation in national fora:

1. Project coordinator/lead researcher: Regulation of Medical Devices in ASEAN, Ministry of Health (Malaysia) (2005-2007)

2. Alternative Member of the Genetic Modification Advisory Committee, Ministry of Natural Resources and Environment (2003-2006)

3. Member of the Ministry of Natural Resources and Environment Task Force on the Biosafety Bill (2005)

4. Committee Member of the Malaysian Environmental NGOs coalition (2005-2006)

5. Member of TWN consultancy team on Globalisation for the National Economic Action Council, Prime Minister's Department focusing on global negotiations and national implementation of the CBD and Cartagena Protocol; WTO-TRIPS in relation to access to medicines and the TRIPS and CBD relationship (2001 - 2004)

6. Member of the Malaysian National Committee for CBD COP7 (2003-2004)

7. Consultant to the Ministry of Science, Technology and Environment for a DANIDA-supported project on Compliance and Opportunity Analysis relating to the CBD, Cartagena Protocol on Biosafety, Ramsar Convention and CITES (2002)

8. Member of the National WSSD Preparatory Committee chaired by the Economic Planning Unit, Prime Minister's Department (2002)

9. Consultant to the Task Force set up by the National Biodiversity Committee to draft 3 national laws (1999-2000):

   a) National Biosafety Act
   b) Access to Biological Resources Act
   c) National Biodiversity Council Act.

10. Member of the National Organising Committee for the Global Knowledge Conference II chaired by the Chief Secretary of the Government (1999-2000)

11. Consultation on the Draft Plant Varieties Protection Act (April, 1999)

12. Member of the Independent Review Panel of Environmental Impact Assessments for the following projects:
    a) Penang Hills development (1991)
    b) Sungei Buloh Forest Reserve development (1992)

13. Annual NGO consultations of the Ministry of Environment, Science and Technology (1990-1993)

14. Review of the Environmental Quality Act 1974 (NGO member of the review panel set up by the Ministry of Environment, Science and Technology, 1991-1992)

Book chapters, research papers and conference papers (selected):

1. Environmental Law in Malaysia: Socio-legal Perspectives (1982)
2. Legal Education and Social Change in South-east Asia (editor) (1987) and author of chapter on "A Move towards Public Interest Law Education in Malaysia"
3. Humanity Must Protect Nature (1988) (booklet)
4. Third World Domination: The Use and Abuse of International Law (1988) (booklet)
5. Land Tenure and Use in Malaysia: Law and Practice (1988)
6. Malaysian Forests: A Call for Sustainable Management (1990)
7. The Forest Crisis: Will UNCED be able to resolve it? (1991)
8. The Global Environment Facility: A Model for Post-UNCED Financial Mechanisms? (1992)
9. Current and Future Environmental Issues: Policy, law and Practice in Malaysia (1992)
10. Current Developments in International Environmental Law (1992)
11. Integrating Economics and Environment in Development Planning (1993)
12. A Southern Perspective on Sustainable Consumption (1994)
13. Global Environmental Issues and the Role of NGOs: Meeting the Challenges of Sustainable Development (1994)
14. The Future of Environmental and Developmental Funding (1994)
15. Linkages between the Convention on Biological Diversity and Agenda 21 (1994)
16. IPRs and Biodiversity: A Southern Perspective (1995)
17. Biosafety: Scientific Findings and Elements of a Protocol (1996) – co-author as member of the Independent Group of Scientific and Legal Experts on Biosafety
18. The Asian Financial Crisis and its Social Effects (1999)
19. Biosafety Protocol in danger of being pre-empted by the WTO (1999)
20. The "Cartagena/Vienna setting": towards more transparent and democratic global negotiations – case study of the Biosafety Protocol negotiations (2000)
21. Choices in agricultural production techniques, consumption patterns and safety regulations: Potentials and threats to sustainable agriculture (2000)
22. Sustainable Agriculture in the New Millennium: Biotechnology for the Third World? (2000)
23. Polluter nations torpedo UN climate change treaty (2001)
24. Climate change talks almost hijacked (2001)
25. South-south cooperation in science and technology: implementing equitable access and benefit sharing, and biosafety (2002) – paper prepared at the request of the G77 Secretariat for a G77 Science and Technology meeting
26. International regime to promote and safeguard the fair and equitable sharing of benefits arising out of the utilisation of biological resources (2003)
27. Technology transfer and cooperation, and capacity building under the CBD: Enabling environments (2003)
28. The challenges of the WTO on the biotechnology industry in Malaysia (2003)
29. "Biotechnological inventions": Social, ethical, economic and scientific concerns (2003) – co-author
30. The economics of biotechnology: implications for developing countries (2003) – co-author
31. "Promoting and facilitating informed public participation in the implementation of the Biosafety Protocol at the national and international levels" – co-author in a CBD Secretariat/UNEP publication on Cartagena Protocol: From Negotiation to Implementation (2003)
32. Sustainable development and the WTO (2003) (co-author)
33. The US-Singapore FTA: Preliminary comments, focusing on Chapter 16 on IPRs (2003)
34. Malaysia's commitments under the WTO and other multilateral/regional agreements on IPRs: scenarios, implications and recommended stand (2003)

35. Intellectual Property Rights: Issues and Challenges (2003)
36. Quest for Fair and Equitable Exchange and Benefit Sharing of Genetic Resources (2004)
37. Some Key Issues for CBD COP7 (2004)
38. Intellectual property, genetic resources and traditional knowledge: the state of current international negotiations and implications for development (2005)
39. Overview of Genetic Engineering (2005)
40. Malaysia's Experience in Increasing Access to Antiretroviral Drugs: Exercising the "Government Use" option (2006) (booklet)
41. New type of strategic partnership for China-Africa (2006)
42. Patents and medicines: Enforce the right to public health (2006)
43. Thailand uses compulsory licence for cheaper AIDS drug (2006)
44. Africans propose draft CBD access and benefit-sharing protocol (2006)
45. Access and Benefit Sharing from a Southern Perspective (2007)
46. Biopiracy meeting ends with no progress (2007) (co-author)
47. Reforming the WHO avian flu virus sharing system to ensure fair and equitable benefit sharing for developing countries (2007)
48. Intellectual property rights and access to affordable medicines: Some Asian Experiences (2008) – co-author (published in Mandarin Chinese by the China State Intellectual Property Office)
49. CBD meeting dominated by talks on access and benefit-sharing regime (2008)
50. Negotiations finally begin on access and benefit-sharing (2009)
51. International negotiations to prevent biopiracy resume (2010)
52. Progress in shaping protocol on access and benefit-sharing (2010)
53. Optimism for a new treaty to combat biopiracy (2010)
54. Access and benefit-sharing protocol gaining shape (2010)
55. Rocky road still ahead for ABS protocol (2010)
56. Benefit-sharing protocol text negotiations finally start (2010)
57. Access and benefit-sharing protocol negotiations resume in September (2010)
58. Biodiversity treaty adopts landmark decisions (2010)
59. Mixed reactions on new access and benefit sharing treaty (2010)
60. Developing countries propose TRIPS amendment to fight biopiracy (2011)
61. "REDD-plus" decision further shapes actions on forests (2011)
62. Kyoto Protocol "second commitment period" remains uncertain (2011)
63. BASIC ministers on Durban expectation, caution against unilateralism (2011)
64. Nagoya Protocol on Access and Benefit Sharing inches on (2012)
65. Nagoya Protocol: Some progress, but divergence remains in implementation preparations (2012)
66. Nagoya Protocol: Differences over compliance system (2012)
67. Targets for new and additional biodiversity finance a must, say developing countries (2012)
68. North-South divide on resource mobilization for biodiversity (2012)
69. Doubled biodiversity funding by 2015 amidst doubts by developed countries (2012)
70. From Fragmentation to Integration: Environment and Sustainable Development Challenges in Malaysia (2013) (book chapter co-author)
71. Nagoya Protocol on Access and Benefit Sharing: Background and Analysis (2013) (book co-author and editor)